frontiers | Research Topics

Methods and applications in invertebrate physiology

Edited by
Tetsuya Tanaka, Natraj Krishnan, Graziano Fiorito, Fernando Ariel Genta and Pamela Imperadore

Published in
Frontiers in Physiology

ISSN 1664-8714
ISBN 978-2-83251-789-5
DOI 10.3389/978-2-83251-789-5

About Frontiers

Frontiers is more than just an open access publisher of scholarly articles: it is a pioneering approach to the world of academia, radically improving the way scholarly research is managed. The grand vision of Frontiers is a world where all people have an equal opportunity to seek, share and generate knowledge. Frontiers provides immediate and permanent online open access to all its publications, but this alone is not enough to realize our grand goals.

Frontiers journal series

The Frontiers journal series is a multi-tier and interdisciplinary set of open-access, online journals, promising a paradigm shift from the current review, selection and dissemination processes in academic publishing. All Frontiers journals are driven by researchers for researchers; therefore, they constitute a service to the scholarly community. At the same time, the *Frontiers journal series* operates on a revolutionary invention, the tiered publishing system, initially addressing specific communities of scholars, and gradually climbing up to broader public understanding, thus serving the interests of the lay society, too.

Dedication to quality

Each Frontiers article is a landmark of the highest quality, thanks to genuinely collaborative interactions between authors and review editors, who include some of the world's best academicians. Research must be certified by peers before entering a stream of knowledge that may eventually reach the public - and shape society; therefore, Frontiers only applies the most rigorous and unbiased reviews. Frontiers revolutionizes research publishing by freely delivering the most outstanding research, evaluated with no bias from both the academic and social point of view. By applying the most advanced information technologies, Frontiers is catapulting scholarly publishing into a new generation.

What are Frontiers Research Topics?

Frontiers Research Topics are very popular trademarks of the *Frontiers journals series*: they are collections of at least ten articles, all centered on a particular subject. With their unique mix of varied contributions from Original Research to Review Articles, Frontiers Research Topics unify the most influential researchers, the latest key findings and historical advances in a hot research area.

Find out more on how to host your own Frontiers Research Topic or contribute to one as an author by contacting the Frontiers editorial office: frontiersin.org/about/contact

Methods and applications in invertebrate physiology

Topic editors

Tetsuya Tanaka — Kagoshima University, Japan
Natraj Krishnan — Mississippi State University, United States
Graziano Fiorito — Department of Biology and Evolution of Marine Organisms, Stazione Zoologica Anton Dohrn, Italy
Fernando Ariel Genta — Oswaldo Cruz Foundation (Fiocruz), Brazil
Pamela Imperadore — Department of Biology and Evolution of Marine Organisms, Zoological Station Anton Dohrn, Italy

Citation

Tanaka, T., Krishnan, N., Fiorito, G., Genta, F. A., Imperadore, P., eds. (2023). *Methods and applications in invertebrate physiology*. Lausanne: Frontiers Media SA.
doi: 10.3389/978-2-83251-789-5

Table of contents

frontiers | Frontiers in Physiology

TYPE Editorial
PUBLISHED 17 February 2023
DOI 10.3389/fphys.2023.1158972

OPEN ACCESS

EDITED AND REVIEWED BY
Sylvia Anton,
Institut National de recherche pour l'agriculture, l'alimentation et l'environnement (INRAE), France

*CORRESPONDENCE
Natraj Krishnan,
nk260@msstate.edu

SPECIALTY SECTION
This article was submitted to Invertebrate Physiology, a section of the journal Frontiers in Physiology

RECEIVED 04 February 2023
ACCEPTED 10 February 2023
PUBLISHED 17 February 2023

CITATION
Krishnan N, Tanaka T, Fiorito G, Genta FA and Imperadore P (2023), Editorial: Methods and applications in invertebrate physiology.
Front. Physiol. 14:1158972.
doi: 10.3389/fphys.2023.1158972

Editorial: Methods and applications in invertebrate physiology

Natraj Krishnan[1]*, Tetsuya Tanaka[2], Graziano Fiorito[3], Fernando Ariel Genta[4] and Pamela Imperadore[5]

[1]Department of Biochemistry, Molecular Biology, Entomology and Plant Pathology, Mississippi State University, Starkville, MS, United States, [2]Laboratory of Infectious Diseases, Joint Faculty of Veterinary Medicine, Kagoshima University, Korimoto, Kagoshima, Japan, [3]Department of Biology and Evolution of Marine Organisms, Stazione Zoologica Anton Dohrn, Naples, Italy, [4]Laboratório de Bioquímica e Fisiologia de Insetos, Instituto Oswaldo Cruz, Fundação Oswaldo Cruz (IOC/FIOCRUZ), Rio de Janeiro, RJ, Brazil, [5]Department of Biology and Evolution of Marine Organisms, Stazione Zoologica Anton Dohrn, Napoli, Italy

KEYWORDS

invertebrate animal models, invertebrate physiology, *Drosophila melanogaster*, RNAi—RNA interference, cephalopod, gene expression, fluorescent *in situ* hybridization (FISH), *Bombyx mori*

Editorial on the Research Topic
Methods and applications in invertebrate physiology

Interest and research on invertebrate animal models has increased over the past decades and new methods and applications are being developed leading to fundamental physiological discoveries with applications ranging from biology to medicine. Invertebrate study systems thus have become cornerstones of biological and biomedical research, providing key insights into fields from genetics to behavioral ecology. Species being investigated and used as models range from terrestrial invertebrates such as insects and nematodes to freshwater and marine life including crustaceans, molluscs and many others. While the use of *Drosophila* for genetic studies was established in the early 20th century, it has since been used for many other applications including developmental biology, stem cell biology, endocrine function and metabolism, innate immunity, neurobiology, toxicology, etc. (Beckingham et al., 2005; Gilbert, 2008). Similarly, the nematode *Caenorhabditis elegans* has been utilized as a model system to investigate biological and physiological processes common to all animals (Strange, 2007). In recent years, there has been an increased use of other invertebrates to both understand the evolution of these organisms but also to throw light on developmental processes in higher animals (Holland and Gibson-Brown, 2003; Bicker, 2005; Darling et al., 2005; Swalla, 2006; Bicker, 2007; Arendt et al., 2008; Wessel et al., 2010; Wilson-Sanders, 2011; Castillo and de la Guardia, 2017).

This Research Topic focuses on some of the recent advances in Methods and Applications in Invertebrate Physiology and is a compilation of ten original research articles dealing with methods (six) or research (four) and one review article (a total of eleven articles) dealing with invertebrate physiology.

Sellamuthu et al., describe a method for selecting reference genes for normalizing gene expression results for different experimental conditions for an important wood-boring destructive coleopteran beetle *Ips sexdentatus*. Currently practiced management strategies have proven inadequate to stem the outbreak of bark beetle populations, which necessitates

investigations into novel mitigation strategies using state-of-the-art molecular methods. In this context, gene expression and functional genomics studies are crucial to generate alternative strategies. This work represents the first reference gene validation study in *I. sexdentatus*, an ecologically important wood-boring beetle which provides valuable information on reference genes for future molecular studies on host-beetle interactions and functional genomic studies on this bark beetle or other Ips beetles (Coleoptera: Curculionidae: Scolytinae).

In another study on identification and validation of reference genes for beetles of the genus *Monochamus* that serve as vector for the pine wood nematode (PWN) *Bursaphelenchus xylophilus*, Li et al., evaluate the stability of fourteen candidate reference genes in *Montipora saltuarius*. This was conducted at different developmental stages associated with infection of PWN or PWN treatment conditions and was evaluated using delta Ct, geNorm, NormFinder, BestKeeper and RefFinder algorithms. Based on this study, *RPL7* and *RPS5* were considered the most stable reference genes in the pupae treated with PWN. *RPS5* and *SNX6* could be used as reference genes in the adults treated with PWN. *RPL7*, *EF1-γ*, and *RPS5* could be used as stable reference genes in all the samples. This study lays the groundwork for understanding the phoretic relationship between *M. saltuarius* and *B. xylophilus*.

Restoration of reef building corals are crucial for a healthy marine ecosystem. Guo et al., provide a possible solution for the decline in reef building corals due to climate change, ocean acidification and also by invasive species. They report on the sequencing of the transcriptome of the fibroblast growth factor (FGF) and its receptor (FGFR) involved in coral budding morphogenesis of four common and dominant reef building corals *Pocillopora damicornis*, *Montipora capricornis*, *Acropora muricata*, and *Pocillopora verrucosa*. Phylogenetic analysis revealed that FGF8 and FGFR3 are widely distributed in hydrozoan animals. Employing three dimensional models of FGF8 and FGFR3 as well as reconstruction of binding models, they found that FGFR3 is a tyrosine kinase receptor and the ligand is FGF8 in *A. muricata*, *P. damicornis*, and *Montipora capricomis*, but not in *P. verrucosa*. In *P. verrucosa* FGF8 is not the ligand for FGFR3 but its receptor needs activation by other TK-ligands. Given this understanding of the morphogenesis signaling mechanism, they postulate the possibility of using biological agents that could activate morphogenesis as a restorative measure for reef building corals.

Zabelina et al., provide a method that determines the exact timing of microinjection of silkworm *Bombyx mori* L embryos to generate successful pathenogenetic clonal lines. This technique addresses a critical hurdle in utilizing parthenogenetic strains of silkworms in transgenesis and increases efficiency of transgene injection and survival. The authors determine 18 h after egg activation as the optimal time for transgene microinjection and also provide a detailed troubleshooting guide to help other researchers improve the survival rate of injected embryos.

RNA interference (RNAi) strategy is a strategy that is being widely used by researchers to knock-down specific genes to interrogate their function in life science research as well as has potential to be used in pest management strategies. A major obstacle to this technique is the generation of large quantities of double stranded RNA (dsRNA) in an economic and cost effective manner. Verdonckt and Vanden Broeck compare and report on methods for large-scale production of high-quality dsRNA from the *E. coli* HT115 bacterial system. They also determine the efficiency of the dsRNAs thus produced at inducing knockdowns in a lepidopteran cell line. It is expected that these results will provide researchers with an efficient and cost effective method to generate dsRNA for their knock-down studies.

The major component of insect cuticle is the polysaccharide chitin. To understand cuticle metabolism and biology, it is important to study chitin structure in chitin deficient phenotypes of insects. Current methods rely on expensive and labor intensive electron microscopy studies. To circumvent this, Flaven-Pouchon and Moussian describe a fluorescent-microscopy based technique that leverages utilizing the common polysaccharide marker Fluorescent brightener 28 (FB28) in whole-mount *Drosophila melanogaster*. To ensure effective penetration, they recommend performing the staining at 65°C. This technique will have applicability to a large variety of insects.

In situ hybridization enables the detection and precise localization of a specific nucleic acid sequence within an individual cell. *In situ* hybridization (ISH) combines three main advantages: great sensitivity, precise anatomical localization, and the possibility of quantification. It is extensively used in evolutionary and developmental biology. Paganos et al., describe a rapid, reliable and accurate fluorescent *in situ* hybridization (FISH) protocol that can be utilized for a variety of marine species—five species of echinoderms, species representatives of the mollusks, tunicates and cephalochordates. This protocol is expected to be of great utility to the Evo-Devo community with the possibility of being extended to other non-marine species.

Elagoz et al., provide an optimized protocol for visualizing and imaging Octopus embryo neurogenesis. A major challenge to visualizing and investigating organ functioning is the ability to effectively detect gene expression patterns in whole organ or embryo. Here, the authors describe a whole mount multiplexed RNA *in situ* hybridization chain reaction version 3.0 (HCR v3.0) in combination with immunohistochemistry (IHC), followed by fructose-glycerol clearing and light sheet fluorescence microscopy (LSFM) imaging on *Octopus vulgaris* embryos. The authors hypothesize that the developed experimental pipeline can be adapted to other model and non-model organisms.

The Cephalopod digestive tract physiology has been the Research Topic of several studies particularly because of its importance from the standpoint of contributing to comparative and evolutionary studies. In their comprehensive review on the physiology of the digestive system of *O. vulgaris*, Andrews et al., describe a variety of techniques, gaps that exist in knowledge and future research areas in this aspect.

With the inclusion of cephalopods in the legislation related to ethical use of animals for experimental purposes, handling cephalopod mollusks in research is challenging and sedation and/or anesthesia is necessary whenever more invasive procedures are required. Sprecher et al., test the physiological effects of ethanol and magnesium chloride as anesthetics in the squid *Loligo vulgaris* embryos. The authors conclude that ethanol had a faster onset of

action and faster recovery than magnesium chloride, being potentially more adequate as an anesthetic for shorter procedures. Also, the authors suggest that the late developmental stages of *L. vulgaris* embryos could represent a good model to evaluate anesthetics for cephalopods.

The neural control of coordinated limb movements have long been a Research Topic of investigations in invertebrates as well as vertebrates. Insects have served as preeminent models in such studies. Hammel et al., investigated the mechanisms underlying curve walking in the stick insect *Carausius morosus* during optomotor-induced turning. This study presents evidence that the motor output to the three main leg joints of the meso- and the metathoracic legs of the stick insect, during turning is not only joint-specific, but also differs depending on the thoracic segment. Also, changes in the activity during turning are most likely mediated by influences on local central pattern generating network (CPG) activities, and the respective influences on segmental CPGs weaken caudally towards the metathorax. The authors conclude that the turning-related motor output strongly depends on local or inter-leg sensory feedback.

In conclusion, the articles in this Research Topic e-collection is a compilation of contributions of different experts in the field of invertebrate physiology and their applications, in a wide variety of invertebrate species. These articles address specific methods as well as extend our knowledge while providing new insights and perspectives in the field of invertebrate physiology.

Author contributions

All authors listed have made a substantial, direct, and intellectual contribution to the work and approved it for publication.

Acknowledgments

The authors are thankful to the contributors to this Research Topic as well as the Editorial support of the Journal.

Conflict of interest

The authors declare that the research was conducted in the absence of any commercial or financial relationships that could be construed as a potential conflict of interest.

Publisher's note

References

Arendt, D., Denes, A. S., Jekely, G., and Tessmar-Raible, K. (2008). The evolution of nervous system centralization. *Philos.Trans. R. Soc. Lond. B. Biol. Sci.* 363 (1496), 1523–1528. doi:10.1098/rstb.2007.2242

Beckingham, K. M., Armstrong, J. D., Texada, M. J., Munjaal, R., and Baker, D. A. (2005). *Drosophila melanogaster*: The model organism of choice for complex biology of multi-cellular organisms. *Gravit. Space Biol. Bull.* 18 (2), 17–29.

Bicker, G. (2007). Pharmacological approaches to nitric oxide signalling during neural development of locusts and other model insects. *Arch. Insect Biochem. Physiol.* 64 (1), 43–58. doi:10.1002/arch.20161

Bicker, G. (2005). STOP and GO with NO: Nitric oxide as a regulator of cell motility in simple brains. *Bioessays* 27 (5), 495–505. doi:10.1002/bies.20221

Castillo, A., and de la Guardia, Y. (2017). Spineless solutions: The potential of invertebrate animal models for advancing science in the developing world. *EMBO Rep.* 18, 1885–1888. doi:10.15252/embr.201744113

Darling, J. A., Reitzel, A. R., Burton, P. M., Mazza, M. E., Ryan, J. F., Sullivan, J. C., et al. (2005). Rising starlet: The starlet sea anemone, *Nematostella vectensis*. *Bioessays* 27 (2), 211–221. doi:10.1002/bies.20181

Gilbert, L. I. (2008). *Drosophila* is an inclusive model for human diseases, growth and development. *Mol. Cell Endocrinol.* 293 (1-2), 25–31. doi:10.1016/j.mce.2008.02.009

Holland, L. Z., and Gibson-Brown, J. J. (2003). The *Ciona intestinalis* genome: When the constraints are off. *Bioessays* 25 (6), 529–532. doi:10.1002/bies.10302

Strange, K. (2007). Revisiting the krogh principle in the post-genomic era: *Caenorhabditis elegans* as a model system for integrative physiology research. *J. Exp. Biol.* 210 (9), 1622–1631. doi:10.1242/jeb.000125

Swalla, B. J. (2006). Building divergent body plans with similar genetic pathways. *Heredity* 97 (3), 235–243. doi:10.1038/sj.hdy.6800872

Wessel, G. M., Reich, A. M., and Klatsky, P. C. (2010). Use of sea stars to study basic reproductive processes. *Syst. Biol. Reprod. Med.* 56 (3), 236–245. doi:10.3109/19396361003674879

Wilson-Sanders, S. E. (2011). Invertebrate models for biomedical research, testing, and education. *ILAR J.* 52 (2), 126–152. doi:10.1093/ilar.52.2.126

frontiers in Physiology

ORIGINAL RESEARCH
published: 27 October 2021
doi: 10.3389/fphys.2021.752768

Reference Gene Selection for Normalizing Gene Expression in *Ips Sexdentatus* (Coleoptera: Curculionidae: Scolytinae) Under Different Experimental Conditions

*Gothandapani Sellamuthu[1], Shan Amin[1,2], Jan Bílý[1], Jirí Synek[1], Roman Modlinger[1], Madhab Kumar Sen[3], Amrita Chakraborty[4] and Amit Roy[1,4]**

[1] Excellent Team for Mitigation (ETM), Faculty of Forestry and Wood Sciences, Czech University of Life Sciences Prague, Prague, Czechia, [2] Department of Biology, Lund University, Lund, Sweden, [3] Department of Agroecology and Crop Production, Faculty of Agrobiology, Food and Natural Resources, Czech University of Life Sciences Prague, Prague, Czechia, [4] EVA 4.0 Unit, Faculty of Forestry and Wood Sciences, Czech University of Life Sciences Prague, Prague, Czechia

OPEN ACCESS

Edited by:
Fernando Ariel Genta, Oswaldo Cruz Foundation (FIOCRUZ), Brazil

Reviewed by:
Xue-Qing Yang, Shenyang Agricultural University, China
Jia Fan, Institute of Plant Protection (CAAS), China

***Correspondence:**
Amit Roy
roy@fld.czu.cz

Specialty section:
This article was submitted to Invertebrate Physiology, a section of the journal Frontiers in Physiology

Received: *03 August 2021*
Accepted: *24 September 2021*
Published: *27 October 2021*

Citation:
Sellamuthu G, Amin S, Bílý J, Synek J, Modlinger R, Sen MK, Chakraborty A and Roy A (2021) Reference Gene Selection for Normalizing Gene Expression in Ips Sexdentatus (Coleoptera: Curculionidae: Scolytinae) Under Different Experimental Conditions. Front. Physiol. 12:752768. doi: 10.3389/fphys.2021.752768

Ips sexdentatus (Coleoptera: Curculionidae: Scolytinae) is one of the most destructive and economically important forest pests. A better understanding of molecular mechanisms underlying its adaptation to toxic host compounds may unleash the potential for future management of this pest. Gene expression studies could be considered as one of the key experimental approaches for such purposes. A suitable reference gene selection is fundamental for quantitative gene expression analysis and functional genomics studies in *I. sexdentatus*. Twelve commonly used reference genes in Coleopterans were screened under different experimental conditions to obtain accurate and reliable normalization of gene expression data. The majority of the 12 reference genes showed a relatively stable expression pattern among developmental stages, tissue-specific, and sex-specific stages; however, some variabilities were observed during varied temperature incubation. Under developmental conditions, the *Tubulin beta-1 chain* (*β-Tubulin*) was the most stable reference gene, followed by *translation elongation factor* (*eEF2*) and *ribosomal protein S3* (*RPS3*). In sex-specific conditions, *RPS3, β-Tubulin*, and *eEF2* were the most stable reference genes. In contrast, different sets of genes were shown higher stability in terms of expression under tissue-specific conditions, i.e., *RPS3* and *eEF2* in head tissue, *V-ATPase-A* and *eEF2* in the fat body, *V-ATPase-A* and *eEF2* in the gut. Under varied temperatures, *β-Tubulin* and *V-ATPase-A* were most stable, whereas *ubiquitin (UbiQ)* and *V-ATPase-A* displayed the highest expression stability after Juvenile Hormone III treatment. The findings were validated further using real-time quantitative reverse transcription PCR (RT-qPCR)-based target gene expression analysis. Nevertheless, the present study delivers a catalog of reference genes under varied experimental conditions for the coleopteran forest pest *I. sexdentatus* and paves the way for future gene expression and functional genomic studies on this species.

Keywords: *Ips sexdentatus*, reference gene, RT-qPCR, differential gene expression, housekeeping genes, bark beetles, Scolytinae

INTRODUCTION

Differential gene expression (DGE) studies are fundamental to evaluate the effects of physiological responses on biological variation in insect populations at the molecular level. Real-time quantitative reverse transcription PCR (RT-qPCR) is a reliable technique and is widely used to analyze the expression of target genes due to its high sensitivity, accuracy, specificity, reproducibility, and speed (Heid et al., 1996; Bustin et al., 2005; VanGuilder et al., 2008; Wang et al., 2020). In addition, RT-qPCR allows simultaneous measurement of gene expression in many different samples for a limited number of target genes and is particularly suitable when only a limited number of samples are available (Higuchi et al., 1993; Vandesompele et al., 2002). Nevertheless, expression results vary due to initial sample size, RNA integrity (quantity and quality), reverse transcription, messenger RNA (mRNA) recovery, PCR efficiency, and primer design (Gao et al., 2020). Therefore, internal control genes (alternatively called reference genes) are commonly used to normalize mRNA levels for more accurate gene expression quantification as their expression should not vary under different biological or experimental conditions (Nicot et al., 2005; Lu et al., 2018). Furthermore, it is strongly recommended to use multiple reference genes for target gene expression normalization for more authenticity (García-Reina et al., 2018; Shakeel et al., 2018; Wang et al., 2020). There are several studies on gene function analysis in insects using reference genes such as β-actin (*Actin*), glyceraldehyde-3-phosphate dehydrogenase (*GAPDH*), elongation factor 1α (*EF1A*), β-Tubulin (*β-Tubulin*), ribosomal proteins (*RPs*), ubiquitin (*UbiQ*), superoxide dismutase (*SOD*), heat shock protein 90 (*HSP90*), and vacuolar-type H+-ATPase subunit B (*V-ATPase-B*) for gene expression normalization (Lu et al., 2018; Qu et al., 2018; Gao et al., 2020; Wang et al., 2020). This suggests that reference genes can be differentially expressed in insects under varied experimental conditions. Alternatively, no universal reference gene is available, which is stably expressed under different experimental conditions (Lu et al., 2018). Therefore, identification and validation of reference genes under different experimental conditions, life stages, and tissue-specific stages are essential on a case-by-case basis for accurate quantification of gene expression in any insects, including *I. sexdentatus* (Pfaffl et al., 2004; Rodrigues et al., 2014; Qu et al., 2018; Basu et al., 2019; Gao et al., 2020; Gurusamy et al., 2021; Xie et al., 2021).

The wood-boring insect *I. sexdentatus* (Coleoptera: Curculionidae: Scolytinae; hereby referred to as ISx), also known as the six-toothed bark beetle, is one of the most destructive and economically important insects, causing severe damage to coniferous species throughout Europe and Asia (Etxebeste and Pajares, 2011; Seidl et al., 2017; Douglas et al., 2019). ISx is an opportunistically aggressive species of bark beetles (Wermelinger et al., 2008; Chakraborty et al., 2020a). It usually attacks old scots pine trees and can occupy young trees up to a diameter of 10 cm in dbh (diameter at breast height). It was primarily a sparse specimen (Pfeffer, 1955; Postner, 1974) in the past, but now ISx is considered a significant pest in some European countries (Gregoire and Evans, 2004). Several drought periods during the last decade highly favored its current upliftment on the pest status, and we are registering higher population densities of ISx in most of the Czech forests. At least from 2018, the south Moravian forests suffered from the severe outbreak of this species. The volume of the harvested pine due to bark beetles in the most affected region was 12 times higher than in the previous years (Lubojacký and Knížek, 2020).

Bark beetles preferentially colonize weakened, wilted, or recently dead trees. However, favorable conditions such as drought can lead to an outbreak (epidemic phase). Beetles start attacking the healthy standing trees due to weakened defenses caused by warmer temperatures (Bouhot et al., 1988; Marini et al., 2017; Pettit et al., 2020) and larger windthrows (Kausrud et al., 2012; Biedermann et al., 2019; Sommerfeld et al., 2020). Furthermore, conifers have self-defense mechanisms to ward off bark beetle infestations with secondary metabolites such as terpenes (Ferrenberg et al., 2014; Denham et al., 2019). These defense mechanisms can also be overcome during mass insect attacks by detoxifying plant-derived secondary metabolites with the help of symbiotic microbes (Chakraborty et al., 2020b; Huang et al., 2020). To elucidate molecular underpinnings shaping environment-conifer-bark beetle (i.e., *I. sexdentatus*) interactions, gene expression studies need to be conducted in the future. Such studies advocate the requirements for stable reference genes under different experimental conditions.

Hence, we extensively evaluated 12 commonly known reference genes in Colepterans and other insects (**Supplementary Figure 1** and **Supplementary Table 1**) for the expression stability in ISx under varied experimental conditions in the present study. Using available in-house transcriptome data of ISx, we have obtained gene sequences of *β-actin* (*Actin*), *translation EF 2* (*eEF2*), *Tubulin beta-1 chain* (*β-Tubulin*), *myosin regulatory light chain 2* (*Myosin L*), *V-type proton ATPase catalytic subunit A* (*V-ATPase-A*), *NADH dehydrogenase subunit 1* (*NADH*), *ubiquitin C variant* (UbiQ), *glyceraldehyde-3-phosphate dehydrogenase* (*GAPDH*), *arginine kinase isoform X1*(*ArgK*), *RPS3*, *RPL17*, and *HSP83* for expression stability evaluation. The candidate reference genes were screened using different parameters, such as developmental stages (i.e., larvae, pupae, and adult stages), tissue- and sex-specific [head, gut, fat body, and whole body (WB) except the head, gut, fat body], and different treatments [such as temperature; Juvenile hormone III (JHIII); wild-collected vs. long-term laboratory-reared; and different host feeding] to obtain accurate reference genes for future genomic and functional studies. Our study delivers a catalog of genes that should be used for DGE studies on ISx under varied experimental conditions and commences the possibility for aggressive management of bark beetles using molecular approaches such as RNA interference (RNAi) (Joga et al., 2021).

MATERIALS AND METHODS

Bark Beetles

Ips sexdentatus (ISx)-infested *Pinus sylvestris* were collected from Kostelec nad Cernými lesy (50°00'07.2"N 14°50'56.3"E, under School Forest Enterprise) maintained insect rearing chambers

at Faculty of Forestry and Wood Sciences, Czech University of Life Sciences, Prague. Beetles were maintained with fresh pine logs at 27 ± 1°C under 70 ± 5% humidity and a 16:8-h light/dark (L:D) photoperiod. ISx is the largest beetle of the genus *Ips*, at 6-8 mm in length. The life stages include three larval stages, pupae, callow (just emerged), and fed adult stage (flying for new host colonization). Both sexes have six spines at each side of the elytral declivity. The fourth spine is the largest and is capitate. The wild population was supplied with fresh pine logs for the next generation and maintained for 40–45 days for one life cycle. Similarly, the wild population was continuously maintained for three generations to study the difference between wild and lab-reared beetle conditions.

Sample Preparation

Development Stages and Different Tissue Types

Samples were collected from different life stages of ISx: three larval stages (L1, L2, and L3), pupae, (P), callow (newly emerged) male (CM) and female (CF), and fed adult (mature adults move toward trunks of pines to lay eggs for next-generation) male (AMF) and female (AFF). For sufficient nucleic acid extraction for downstream processing, each biological replicate was prepared using pooled individuals from various developmental stages, such as five first instar larvae (L1)/replicate, three second and third instar larvae (L2 and L3)/ replicate, three pupae/ replicate, and two adults/replicate. Four biological replicates were used in all experiments.

Tissues such as head, fat body, gut, and WB minus head, fat body, and gut (hereby referred to as WB) were dissected from the callow and fed adult stage of both male and female ISx producing experimental samples, such as CMH, callow male beetle head; CMFB, callow male beetle fat body; CMMG, callow male beetle midgut; CMWB, callow male beetle WB; CFH, callow female beetle head; CFFB, callow female beetle fat body; CFMG, callow female beetle midgut; CFWB, callow female beetle WB; and AMFH, fed adult male head; AMFFB, fed adult male fat body; AMFMG, fed adult male midgut; AMFWB, fed adult male WB; AFFH, fed adult female head; AFFFB, fed adult female fat body; AFFMG, fed adult female midgut; and AFFWB, fed adult female WB. Four independent biological replicates were collected and stored at −80°C. Each replicate was derived by pooling tissues from 10 individual beetles.

Temperature and JHIII Treatment

For the temperature treatment, the freshly emerged adults were placed in small glass tubes and exposed to a range of temperatures (4, 27, and 37°C) for 72 h in a temperature-controlled chamber. After exposure, survivors were frozen in liquid nitrogen and stored at −80°C. Adults maintained at 27°C were used as control. At least four beetles were randomly collected per replication, and four independent biological replications were used from each temperature treatment.

For JHIII treatment, emerged beetles were sorted based on gender and kept at 4°C on moist paper towels. Beetles were treated topically on the ventral surface of the abdomen with 10 μg JHIII (dissolved in acetone) (Sigma-Aldrich, St. Louis, MO, USA) and only acetone as control (Aw et al., 2010; Sun et al., 2021). The beetles were incubated at 27 ± 1°C under 70 ± 5% humidity and a 16:8-h light/dark (L:D) photoperiod in groups of 20 in 60 ml plastic containers for 72 h. After incubation, beetles were immediately shock frozen in liquid nitrogen and stored at −80°C for downstream processing. Four biological replicates were used for JHIII treatment and control.

Different Host Feeding

Under different host feeding treatments, ISx was placed into the phloem tissue of freshly cut lodgepole pine and spruce. Beetles were placed under the bark in randomly chosen male-female pairs and maintained under standard rearing conditions. ISx was allowed to feed under the bark for one generation (40–45 days). We removed ISx adults from galleries showing the excavation of frass (an indication of feeding). The beetles were collected and immersed in insect ringer solution; the gut tissues were excised. Gut tissues were gently purged of their contents (i.e., malpighian tubules, fat body) and then frozen in liquid nitrogen and stored at −80°C.

Total RNA Extraction and Complementary DNA Synthesis

Total RNA from bark beetle tissue samples was extracted using TRIzol® (Invitrogen, Carlsbad, CA) following the protocol of the manufacturer. Isolated RNA was further treated with DNases using a TURBO DNAase Kit (Ambion, USA) to remove any DNA contamination. RNA quantity and quality were evaluated using 1.5% agarose gel and quantified by NanoDrop 2000/2000c from Thermo Fisher Scientific® (Waltham, MA, USA) and stored at −80°C. Complementary DNA (cDNA) (first-strand) was synthesized from 1 μg of total RNA in triplicate using the high-capacity cDNA reverse transcription kits (Applied Biosystems-Life Technologies) following the recommendations of the manufacturer and stored at −20°C.

Selection of Candidate Reference Genes for Evaluation

This study selected 12 potential reference genes (**Supplementary Table 2**) that function as reference genes in other Coleoptera species (**Supplementary Figure 1** and **Supplementary Table 1**). These genes were obtained from our functionally annotated in-house transcriptome of ISx (manuscript in preparation). The primers for those selected genes were designed *via* Integrated DNA Technologies, Inc. (IDT) (**Table 1**).

Quantitative RT-qPCR Analysis

cDNA samples were diluted 1:20 before being used in RT-qPCR. Four independent biological replicates from each treatment, developmental stage, and tissue-type were included in each RT-qPCR run. RT-qPCR run was performed using the Applied Biosystems™ StepOne™ Real-Time PCR System (Applied Biosystems) with a reaction mix containing 5.0 μL of SYBR® Green PCR Master Mix (Applied Biosystems), 1.0 μL of cDNA, 1.0 μL optimized concentrations of primers (**Table 1**), and RNase-free water (Invitrogen) to a total volume of 10.0 μL. Amplification conditions were as follows: initial denaturation at

TABLE 1 | Details of primer sequence, amplicon length, and RT-qPCR analysis of candidate reference genes and target genes.

Gene symbol	Gene name	Primer sequences (5′-3′)	Amplicon length (bp)	PCR efficiency %	Regression coefficient
Actin	β-actin	**FP**: GCATACGGTCAGCAATACC	118	101.14	0.988
		RP: CACGAAACCGTCTACAACTC			
eEF2	Translation elongation factor	**FP**: CGATGGCCTCAACGTAAC	142	101.30	0.981
		RP: CGTGTGTTCTCCGGTAAAG			
β-Tubulin	Tubulin beta-1 chain	**FP**: CATCTCGTCCATACCCTCT	126	105.85	0.987
		RP: GCCACCTTCATCGGTAAC			
Myosin L	Myosin regulatory light chain 2	**FP**: GACCCAACAACTGGGTAAG	140	98.69	0.990
		RP: CCACGACAAAGACGGTATC			
V-ATPase-A	V-type proton ATPase catalytic subunit A	**FP**: CGTTTGGCCTCCTTCTAC	125	110.71	0.9999
		RP: GTGACAGGATCGGAGAAATC			
NADH	NADH dehydrogenase subunit 1	**FP**: GTGTGAGTGCAGACCAAC	148	108.07	0.9941
		RP: GAACGAGAGCCGAAGAAAC			
UbiQ	Ubiquitin C variant	**FP**: TGAGGCTAAGAGGAGGAATG	120	98.17	0.989
		RP: CGTCCTTGTCCTGGATCT			
GAPDH	Glyceraldehyde-3-phosphate dehydrogenase	**FP**: CACCCAGAAGACTGTTGAC	129	107.06	0.977
		RP: CCGTTCAGGGAAGGAATAAC			
ArgK	Arginine kinase isoform X1	**FP**: CCGTCTTCTCTGACTTGTTC	144	106.49	0.9802
		RP: GGGTGGACACAACGTATTC			
RPS3	Ribosomal protein S3	**FP**: GAACGGACCGTGTTCTTG	128	98.32	0.973
		RP: CAGACCTCTGTTGACTACCT			
RPL17	60S ribosomal protein L17	**FP**: ACGTGCACTTCACACTTC	102	106.54	0.9895
		RP: TCCTCACCTCTCACCTAAAG			
HSP83	Heat shock protein 83	**FP**: GCTTTCTGGCGTAGGTTT	138	110.00	0.974
		RP: CGGATGGACTGCCAATATG			
Target gene					
Kr-h1	Kruppel homolog 1	**FP:** GCTGTTCTCAATTCTCCATGC	168	113.9	0.833
		RP: ACGGTGTAAGGCATCAGAATG			
Hsp70	Heat shock protein 70	**FP:** GACTATGGGTATTGAGACTGTG	140	104.9	0.961
		RP: CACCTTCGTACACCTGAATAG			

95°C for 10 min, followed by 40 cycles of 95°C for 15 s, and 60°C for 1 min. In order to confirm the primer specificity, we performed melt curve analysis using default parameters by a steady increase in temperature from 60 to 95°C. All RT-qPCR assays were carried out in four biological replicates, including two or three technical replicates.

Data Analyses

The raw cycle threshold (Ct) values were obtained with 7500 software v2.0.5 (Applied Biosystems®). Gene expression and stability were analyzed using four different commonly used tools and algorithms such as geNorm (Vandesompele et al., 2002), BestKeeper (Pfaffl et al., 2004), NormFinder (Andersen et al., 2004), and ΔCt method (Silver et al., 2006).

Precisely, geNorm assesses the expression stability value (M) as the average pairwise variation of one of the genes against all control genes present in the experiment. The program estimates the mean pairwise variation between genes across all samples, and the gene with the lowest M value is considered most stable (Vandesompele et al., 2002). NormFinder calculates the SD for each target gene and juxtaposes it with other gene expressions. The gene displaying the lowest variation between intra- and inter-group comparisons is considered most stable (Andersen et al., 2004). On the contrary, BestKeeper is a data processing method based on crossing points that compares all genes across all samples and provides a stability index for each reference gene (Pfaffl et al., 2004). The comparative delta-Ct method juxtaposes Ct values and the relative expression of "gene pairs" within each sample (Silver et al., 2006). The sample-specific mean Ct values of each reference gene from each experiment are given as input data and subsequently processed using the web-based tool RefFinder (https://www.heartcure.com.au/reffinder/).

Furthermore, pairwise variation (V), estimated by geNorm, was used to decide the optimal number of reference genes for accurate RT-qPCR normalization. The Vn/Vn+1 value reflected the pairwise variation between two sequential normalization factors. A cutoff threshold, i.e., Vn/Vn+1 = 0.15, was set for a valid normalization (Vandesompele et al., 2002).

Validation of Selected Reference Genes

We analyzed the relative expression levels of *Kr-h1* and *Hsp70* genes after JHIII treatment and different temperature exposure to evaluate the selected reference genes. To compare the impact of different normalization strategies, the expression of target genes was normalized using both selected reference genes individually and in combinations using the $2^{-\Delta\Delta Ct}$ method (Livak and

Schmittgen, 2001). Target genes expression were analyzed using one-way ANOVA using GraphPad Prism software. *P*-value < 0.05 was considered to identify significant differences between samples.

RESULTS

Primer Specificity and PCR Efficiency

In the current study, 12 genes, namely *Actin*, *eEF2*, *β-Tubulin*, *Myosin L*, *V-ATPase-A*, *NADH*, *UbiQ*, *GAPDH*, *ArgK*, *RPS3*, *RPL17*, and *HSP83,* were screened for identifying suitable reference gene or gene combination from ISx. RT-qPCR products generated with each primer set (forward+ reverse) against target genes were evaluated by the occurrence of a single peak in melting curve analyses (**Supplementary Figure 2**) and specific bands of the expected size in agarose gel electrophoresis (**Supplementary Figure 3**). The amplification efficiency for each primer pair ranged from 98.17 to 107.06%, and the correlation coefficients (R^2) were greater than 0.98 (**Table 1**). The Ct values of the 12 candidate reference genes ranged from 19.87 to 34.78 and covered all experimental conditions (**Figure 1A**). While most Ct values ranged from 19 to 27, *Actin, eEF2, β-Tubulin*, and *RPS3* were the most abundant transcripts under almost all experimental conditions. The least frequently expressed reference genes were *NADH, RPL17*, and *HSP83*. The five remaining reference genes were expressed at moderate levels.

Expression Stability of Putative Reference Genes Under Biotic Conditions

For identifying stable reference genes, four different algorithms (geNorm, NormFinder, BestKeeper, and delta-Ct) were deployed to evaluate the stability of candidate reference genes under different experimental conditions [(i.e., developmental stages, tissue-specific, sex-specific) and different treatments (JHIII; wild-collected vs. long-term laboratory-reared; and different host feeding)] by using the RefFinder web-based tool that ranks reference genes.

Reference Gene for Developmental Stages

For the developmental stages, the order of stability of the first four most stable genes, namely *β-Tubulin, eEF2, RPS3*, and *GADPH*, identified by four programs, was inconsistent (**Table 2**). The least stable genes nominated by four programs were *Actin, RPL17*, and *HSP83*. The most stable genes were *β-Tubulin*, *eEF2,* and *RPS3* determined based on Normfnder rankings of 0.343, 0.347, and 0.379, respectively (**Table 2**). As per RefFinder, the stability ranking of the reference genes from most stable to least stable across different developmental stages were as follows: *eEF2, β-Tubulin, Actin, UbiQ, GAPDH, V-ATPase-A, RPS3, Myosin L, HSP83, RPL17, ArgK,* and *NADH* (**Figure 1B**). RefFinder identified the top three candidates, *eEF2, β-Tubulin*, and *Actin*, across developmental stages by integrating the results from all four programs.

Reference Gene for Tissue Stages

Target Gene Expression in Male and Female Tissues

Sex-specific reference gene expressions were calculated separately for male (callow and fed adult) and female (callow and fed adult) insect tissues (i.e., head, fat body, gut, WB except for the head, fat body, and gut collected from male and female, or in short, abdomen). In male tissues, the order of stability of the first four most stable genes (*RPS3, GAPDH, eEF2*, and *β-Tubulin*) determined by four programs was inconsistent (**Table 3**). The least stable genes recommended by four programs were *Actin, RPL17,* and *Myosin L*. The stability ranking of the reference genes of the most stable and the top three candidates, *β-Tubulin, GAPDH,* and *RPS3*, was constant according to RefFinder (**Figure 2A**). In contrast, the female genes *eEF2, RPS3, β-Tubulin*, and *UbiQ* were the most stable genes (**Table 3**). The least stable gene was *ArgK*. The top three most stable reference genes, namely *eEF2, β-Tubulin*, and *RPS3,* were constant for females in the RefFinder analysis (**Figure 2B**).

Target Gene Expression in Various Tissues

Tissue sections were obtained to evaluate the stability of candidate reference genes among different tissue (i.e., head, fat body, gut, and WB). In head tissues, the order of stability of the first four most stable genes (i.e., *RPS3, eEF2, ArgK*, and *V-ATPase-A*) recognized by four programs was inconsistent (**Table 4**). The least stable genes determined by four programs were *GAPDH, RPL17*, and *HSP83*. According to RefFinder, the stability ranking of reference genes from the most stable and the top three candidates were *eEF2, NADH*, and *RPS3* within head tissues (**Figure 2C**). Whereas among fat body tissues, *V-ATPase-A, eEF2, NADH,* and *β-Tubulin* genes were the most consistently expressed (**Table 4**). The least stable genes were *RPL17, Myosin L*, and *Actin*. The stability ranking (top three) of the reference genes was *eEF2, β-Tubulin*, and *V-ATPase-A* (**Figure 2D**) in the RefFinder analysis for the fat body. However, *V-ATPase-A, eEF2, RPL17*, and *NADH* were the most stable genes in the gut tissue (**Table 4**). The least stable genes in the gut were *HSP83, Myosin L*, and *Actin*. The final top three stable reference genes after RefFinder analysis were *eEF2, V-ATPase-A,* and *GAPDH* in gut tissues (**Figure 2E**). Similarly, WB tissue showed that *RPS3, β-Tubulin, HSP83,* and *eEF2* genes were highly expressed and the most stable genes within these tissues (**Table 4**), while *RPL17, UbiQ,* and *ArgK* genes were found to be least stably expressed (**Figure 2F**). The best reference gene combination and stability ranking for WB tissues were *GAPDH, RPS3,* and *Myosin L*. The most stable reference gene among all four tissue stages was *eEF2* after assessing all expression results. The optimal reference genes for all tissue stages combined (head, fat body, gut, and WB) conditions were *β-Tubulin, eEF2,* and *RPS3* based on all algorithms (**Supplementary Table 3**).

Identification of Candidate Reference Genes Under Abiotic Conditions

The same four algorithms were used to identify the most appropriate reference genes under four different abiotic conditions such as temperature, JHIII treatment, laboratory-reared vs. wild beetles, and pine-fed vs. spruce-fed beetles. For

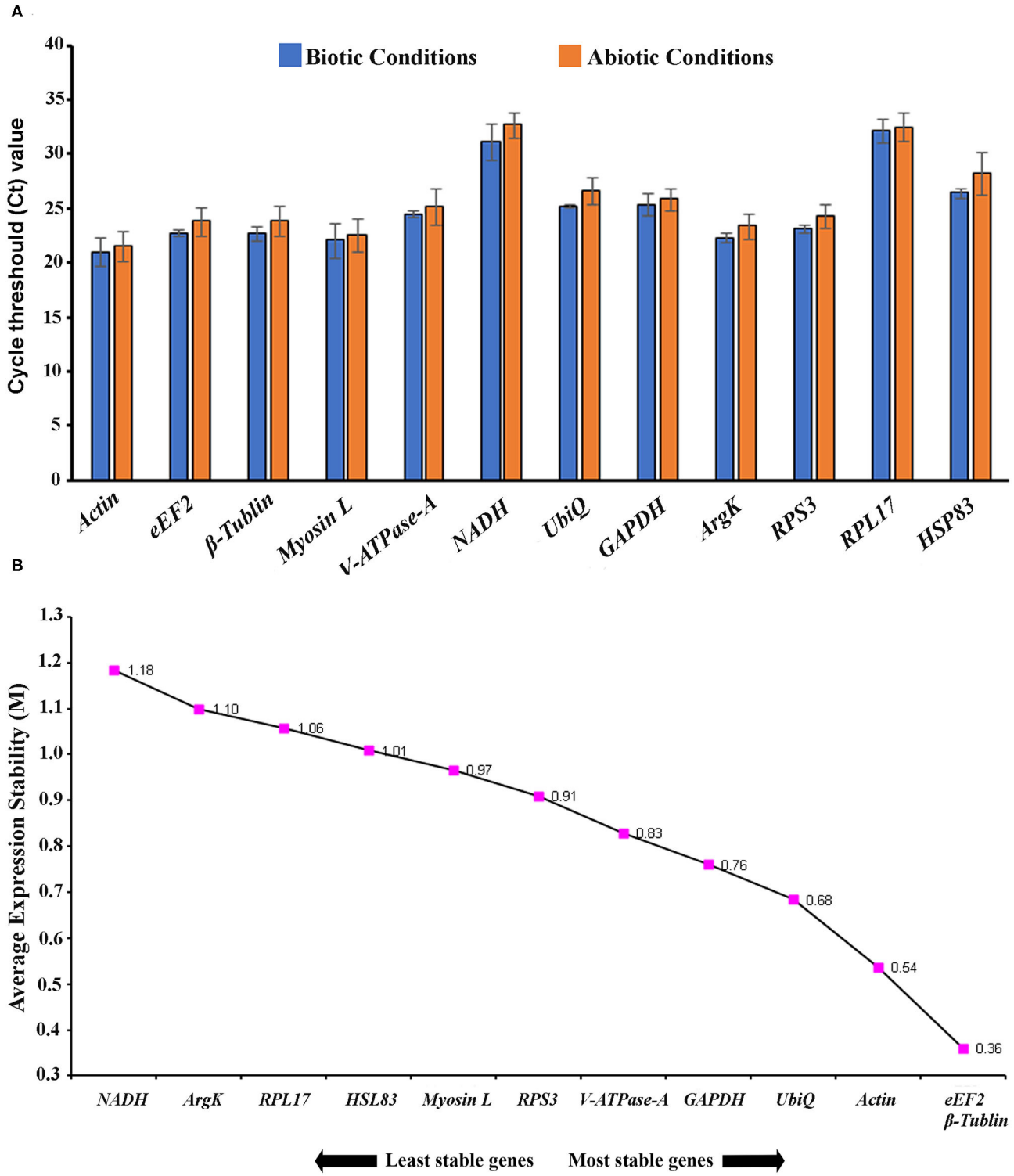

FIGURE 1 | (A) Expression range of cycle threshold (Ct) values of candidate reference genes under different experimental conditions in *I. sexdentatus* (ISx). The different conditions included in biotic conditions: developmental stages (i.e., larvae, pupae, and adult stages), sex-specific (male and female), tissue types [head, midgut, fat body, and whole body (WB) except head, gut, fat body (Abdomen)] and abiotic conditions: different treatments (such as temperature; Juvenile hormone III; wild-collected vs. long-term laboratory-reared; and different host feeding). **(B)** The average expression stability values (M) of 12 reference genes in different developmental stages (larvae, pupae, and adult stages) were plotted from the least stable (left) to the most stable (right).

TABLE 2 | Ranking of the candidate reference genes based on stability values performed by Delta Ct, BestKeeper, RefFinder, and NormFinder, in different developmental stages [i.e., larval stages (L1, L2, and L3), pupae (P), callow (newly emerged) male (CM), and female (CF)] and fed adult (mature adults move toward trunks of pines to lay eggs for next-generation) male (AMF) and female (AFF).

Genes	ΔCt method		Best keeper		RefFinder		NormFinder		Recommended genes
	Stability	Rank	Stability	Rank	Stability	Rank	Stability	Rank	
β-Tubulin	3.1	1	1.79	4	1.86	1	0.343	1	*β-Tubulin*,
GAPDH	3.19	2	1.89	6	3.94	5	0.388	5	*eEF2*
eEF2	3.24	3	1.85	5	3.08	3	0.374	2	and *RPS3*
RPS3	3.26	4	1.6	3	2.63	2	0.379	3	
Myosin-L	3.35	5	1.58	2	3.66	4	0.420	9	
V-ATPase-A	3.37	6	2.18	7	4.92	7	0.380	4	
ArgK	3.54	7	1.43	1	3.96	6	0.429	10	
UbiQ	4.15	8	2.5	8	8.24	8	0.389	6	
NADH	4.21	9	4.11	10	9.21	9	0.639	12	
HSP83	4.53	10	3.08	9	9.72	10	0.405	7	
RPL17	4.98	11	4.94	11	10.74	11	0.523	11	
Actin	8.45	12	7.62	12	12	12	0.415	8	

TABLE 3 | Ranking of the candidate reference genes based on stability values performed by Delta Ct, BestKeeper, RefFinder, and NormFinder, in sex-specific conditions (male and female).

Conditions	Genes	ΔCt method		Best keeper		RefFinder		NormFinder		Recommended genes
		Stability	Rank	Stability	Rank	Stability	Rank	Stability	Rank	
Male	*eEF2*	1.44	1	1.68	7	2.43	1	0.210	5	*RPS3*, *GAPDH*
	β-Tubulin	1.6	2	1.95	8	4	5	0.145	2	and *eEF2*
	NADH	1.63	3	1.34	5	3.41	4	0.274	9	
	GAPDH	1.63	4	2.15	10	6.16	7	0.145	1	
	UbiQ	1.66	5	1.12	3	4.16	6	0.210	6	
	RPS3	1.71	6	0.71	1	2.45	2	0.151	3	
	ArgK	1.79	7	0.79	2	3.15	3	0.234	8	
	V-ATPase-A	1.86	8	1.48	6	7.14	8	0.227	7	
	HSP83	1.89	9	2.08	9	8.97	10	0.294	10	
	RPL17	2.04	10	1.31	4	7.27	9	0.351	12	
	Myosin L	2.32	11	2.71	11	11	11	0.159	4	
	Actin	2.42	12	2.9	12	12	12	0.343	11	
Female	*eEF2*	1.31	1	1.5	4	1.41	1	0.255	1	*eEF2*, *RPS3* and
	RPS3	1.44	2	1.17	2	1.86	2	0.266	3	*β-Tubulin*
	β-Tubulin	1.51	3	1.48	3	4.05	4	0.274	6	
	NADH	1.63	4	1.63	8	5.26	6	0.373	4	
	UbiQ	1.64	5	1.09	1	2.94	3	0.350	10	
	GAPDH	1.67	6	2.08	10	7.33	8	0.273	5	
	HSP83	1.71	7	1.59	7	7	7	0.326	9	
	RPL17	1.78	8	1.17	2	4.76	5	0.402	11	
	Myosin L	1.91	9	2.48	12	9.93	10	0.265	2	
	V-ATPase-A	1.95	10	1.52	5	8.19	9	0.274	7	
	Actin	1.98	11	1.94	9	10.46	11	0.470	12	
	ArgK	2.02	12	2.17	11	11.74	12	0.325	8	

the temperature treatment, *β-Tubulin, V-ATPase-A, ArgK,* and *GAPDH* genes were shown to have the most stable expression using the four algorithms (**Table 5**). RefFinder confirmed that the three most stable gene expressions were *V-ATPase-A, ArgK,* and *β-Tubulin* (**Figure 3A**). After JHIII treatment, the stability of the first four most stable genes, such as *UbiQ, V-ATPase-A, RPS3,* and *Myosin L* determined by four programs was inconsistent (**Table 5**). The least stable genes were found to be

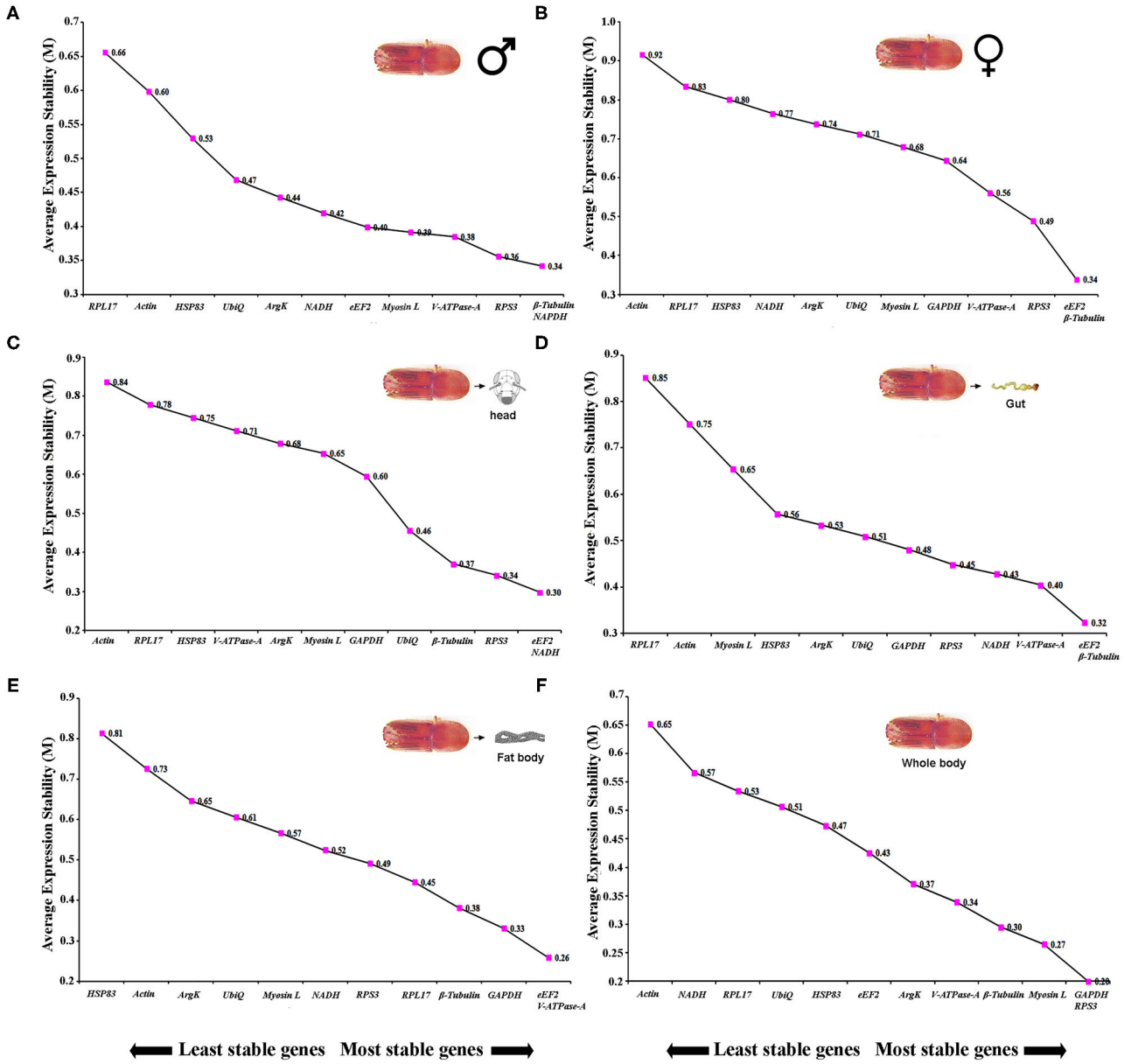

FIGURE 2 | The average expression stability values (M) of 12 reference genes under different conditions (sex-specific and tissue types) were calculated by geNorm from the least stable (left) to the most stable (right). **(A)** male, **(B)** female, **(C)** head, **(D)** gut, **(E)** fat body, and **(F)** whole body (WB).

Actin, RPL17, and *NADH*. According to RefFinder, the stability ranking of the reference genes of the most stable and the top three candidates were *RPS3, HSP83,* and *UbiQ* (**Figure 3B**). However, in beetles from wild and laboratory rearing conditions, most stable expressions were observed for *Actin, ArgK, Myosin L,* and *GAPDH via* ΔCt method (**Table 5**). The top three most stable reference genes *via* RefFinder were *Actin, β-Tubulin,* and *V-ATPase-A* (**Figure 3C**). Similarly, pine- and spruce-fed beetle gut showed stable expression for *V-ATPase-A, UbiQ, ArgK,* and *β-Tubulin* in RefFinder (**Table 5** and **Figure 3D**). The overall stability ranking and combination of reference genes among various tested abiotic conditions were *UbiQ, GAPDH,* and *β-Tubulin*.

Determination of the Minimum Number of Reference Genes for Normalization

To generate more accurate and reliable gene expression results, often more than one reference gene is recommended. According to Vandesompele et al. (2002), a Vn/Vn+1 value under 0.15 means adding the n+1 reference gene is unnecessary. Alternatively, the first reference gene is sufficient to normalize the target gene expression in those cases. We also

TABLE 4 | Ranking of the candidate reference genes based on stability values performed by Delta Ct, BestKeeper, RefFinder, and NormFinder in various tissue types [head, midgut, fat body, and whole body (WB) except head, gut, and fat body (Abdomen)].

Conditions	Genes	ΔCt method		Best keeper		RefFinder		NormFinder		Recommended genes
		Stability	Rank	Stability	Rank	Stability	Rank	Stability	Rank	
Head	*eEF2*	1.21	1	0.6	4	2	1	0.302	7	*RPS3*, *ArgK* and *eEF2*
	ArgK	1.33	2	0.72	6	2.91	3	0.266	4	
	V-ATPase-A	1.39	3	0.55	3	3.41	5	0.314	9	
	RPS3	1.41	4	0.3	1	2.11	2	0.191	1	
	β-Tubulin	1.49	5	1.52	8	5.79	6	0.314	10	
	UbiQ	1.5	6	0.92	7	6.24	7	0.266	5	
	NADH	1.54	7	0.52	2	3.15	4	0.306	8	
	Myosin L	1.63	8	1.71	10	8.46	8	0.257	3	
	Actin	1.7	9	1.71	11	9.72	11	0.371	12	
	HSP83	1.71	10	1.71	9	9.72	10	0.283	6	
	GAPDH	1.71	11	1.81	12	10.98	12	0.232	2	
	RPL17	1.74	12	0.68	5	9.64	9	0.335	11	
Fat body	*NADH*	0.97	1	1.18	6	2.21	1	0.363	9	*V-ATPase-A*, *eEF2* and *NADH*
	eEF2	1	2	1.3	7	2.55	3	0.245	4	
	V-ATPase-A	1	3	0.73	2	2.45	2	0.250	5	
	β-Tubulin	1.07	4	1.13	5	2.99	4	0.332	8	
	GAPDH	1.09	5	1.54	10	6.22	7	0.181	1	
	RPS3	1.11	6	0.99	4	5.63	6	0.294	6	
	UbiQ	1.13	7	0.72	1	3.96	5	0.230	3	
	HSP83	1.16	8	1.47	9	8.24	9	0.227	2	
	ArgK	1.3	9	0.98	3	7.56	8	0.315	7	
	Actin	1.31	10	1.71	11	9.97	10	0.606	11	
	Myosin L	1.32	11	1.95	12	10.44	11	0.435	10	
	RPL17	1.39	12	1.39	8	10.84	12	0.660	12	
Gut	*eEF2*	1.18	1	1.54	8	3.13	3	0.117	1	*V-ATPase-A*, *eEF2* and *RPL17*
	V-ATPase-A	1.18	2	1.15	7	1.93	1	0.130	2	
	NADH	1.24	3	1.09	6	3.57	4	0.270	7	
	RPL17	1.26	4	1.05	5	2.99	2	0.262	6	
	β-Tubulin	1.48	5	2.21	9	6.51	8	0.215	3	
	ArgK	1.54	6	0.7	1	3.81	5	0.396	10	
	RPS3	1.54	7	0.81	2	4.6	6	0.283	9	
	GAPDH	1.56	8	2.32	10	8.11	9	0.234	4	
	UbiQ	1.7	9	0.93	3	6.42	7	0.339	5	
	Myosin L	1.93	10	2.84	11	10.49	11	0.279	8	
	Actin	1.97	11	2.92	12	11.49	12	0.459	12	
	HSP83	1.99	12	0.95	4	8.71	10	0.440	11	
WB	*RPS3*	1.14	1	2.06	6	2.34	2	0.192	3	*RPS3*, *β-Tubulin* and *HSP83*
	Actin	1.18	2	2.16	7	2.3	1	0.375	12	
	eEF2	1.19	3	2.27	8	2.91	3	0.247	8	
	GAPDH	1.21	4	2.63	9	4.9	5	0.167	2	
	HSP83	1.23	5	2.04	5	4.4	4	0.201	4	
	β-Tubulin	1.24	6	2	3	5.05	6	0.079	1	
	V-ATPase-A	1.57	7	3.04	11	8.1	10	0.273	10	
	NADH	1.59	8	1.72	2	5.63	7	0.325	11	
	Myosin L	1.62	9	3.08	12	9.39	11	0.233	7	
	RPL17	1.75	10	2.01	4	7.95	9	0.215	6	
	UbiQ	1.81	11	1.36	1	6.04	8	0.259	9	
	ArgK	1.93	12	2.95	10	11.47	12	0.206	5	

TABLE 5 | Ranking of the candidate reference genes based on stability values performed by Delta Ct, BestKeeper, RefFinder, and NormFinder under the influence of various abiotic factors such as temperature (Temp), Juvenile hormone III (JHIII), laboratory-reared vs. wild beetles, and pine-fed vs. spruce-fed beetles.

Conditions	Genes	ΔCt method		Best keeper		RefFinder		NormFinder		Recommended genes
		Stability	Rank	Stability	Rank	Stability	Rank	Stability	Rank	
Temp	*β-Tubulin*	0.98	1	1.09	5	1.5	1	0.322	4	*β-Tubulin*, *V-ATPase-A* and *ArgK*
	V-ATPase-A	1.02	2	0.99	4	2	2	0.315	3	
	ArgK	1.06	3	1.37	7	3.98	4	0.252	2	
	GAPDH	1.07	4	0.93	3	3.66	3	0.356	5	
	Myosin L	1.08	5	1.61	9	5.73	6	0.251	1	
	Actin	1.13	6	1.29	6	5.73	5	0.519	7	
	eEF2	1.17	7	1.5	8	7.24	9	2.051	12	
	UbiQ	1.19	8	1.69	10	8.46	10	0.441	6	
	RPS3	1.43	9	0.88	2	6.18	8	0.614	8	
	NADH	1.59	10	1.79	11	10.24	11	0.668	10	
	RPL17	1.94	11	0.86	1	6.04	7	0.630	9	
	HSP83	2.6	12	2.73	12	12	12	1.446	11	
JHIII	*V-ATPase-A*	0.85	1	0.54	3	2.34	2	0.225	2	*UbiQ*, *V-ATPase-A* and *RPS3*
	UbiQ	0.87	2	0.45	2	1.86	1	0.208	1	
	Myosin L	0.9	3	0.58	4	2.45	3	0.432	10	
	ArgK	0.92	4	0.65	5	3.16	5	0.428	9	
	β-Tubulin	0.93	5	0.75	8	6.16	6	0.294	3	
	RPS3	0.93	6	0.37	1	3.13	4	0.297	4	
	eEF2	0.97	7	0.69	7	7.24	7	0.376	8	
	GAPDH	1.03	8	0.87	10	8.18	8	0.350	7	
	HSP83	1.06	9	0.89	11	9.72	10	0.314	5	
	Actin	1.08	10	0.69	6	8.78	9	0.510	12	
	RPL17	1.11	11	0.84	9	10.22	11	0.336	6	
	NADH	2.55	12	1.78	12	12	12	0.436	11	
Lab vs. Wild	*Actin*	0.9	1	1.68	9	3	2	0.068	2	*Actin*, *Myosin L* and *ArgK*
	Myosin L	0.9	2	1.26	5	2.66	1	0.088	6	
	ArgK	0.95	3	1.09	4	3.46	4	0.086	4	
	GAPDH	0.95	4	1.65	8	3.36	3	0.103	7	
	UbiQ	1.03	5	1.64	7	3.64	5	0.182	9	
	β-Tubulin	1.05	6	2.03	10	6.4	6	0.042	1	
	RPS3	1.06	7	1.44	6	6.48	8	0.221	10	
	V-ATPase-A	1.18	8	0.71	3	6.62	9	0.085	5	
	HSP83	1.23	9	2.28	11	9.19	11	0.072	3	
	eEF2	1.49	10	2.45	12	10.44	12	0.219	11	
	RPL17	1.49	11	0.48	2	7.01	10	0.124	8	
	NADH	1.98	12	0.47	1	6.45	7	0.282	12	
Pine vs. Spruce	*UbiQ*	0.65	1	0.52	4	2	2	0.102	2	*V-ATPase-A*, *UbiQ* and *ArgK*
	V-ATPase-A	0.71	2	0.29	1	1.86	1	0.155	4	
	GAPDH	0.73	3	0.61	8	4.68	5	0.072	1	
	ArgK	0.75	4	0.31	2	2.21	3	0.193	7	
	β-Tubulin	0.75	5	0.5	3	2.94	4	0.157	5	
	Myosin L	0.79	6	0.59	6	6	6	0.179	6	
	RPS3	0.82	7	0.52	5	6.85	7	0.202	8	
	eEF2	0.82	8	0.6	7	7.74	8	0.220	10	
	NADH	0.86	9	0.8	11	8.89	9	0.149	3	
	Actin	1.05	10	0.77	10	10	10	0.212	9	
	RPL17	1.3	11	0.74	9	10.46	11	0.393	12	
	HSP83	1.36	12	0.8	12	12	12	0.327	11	

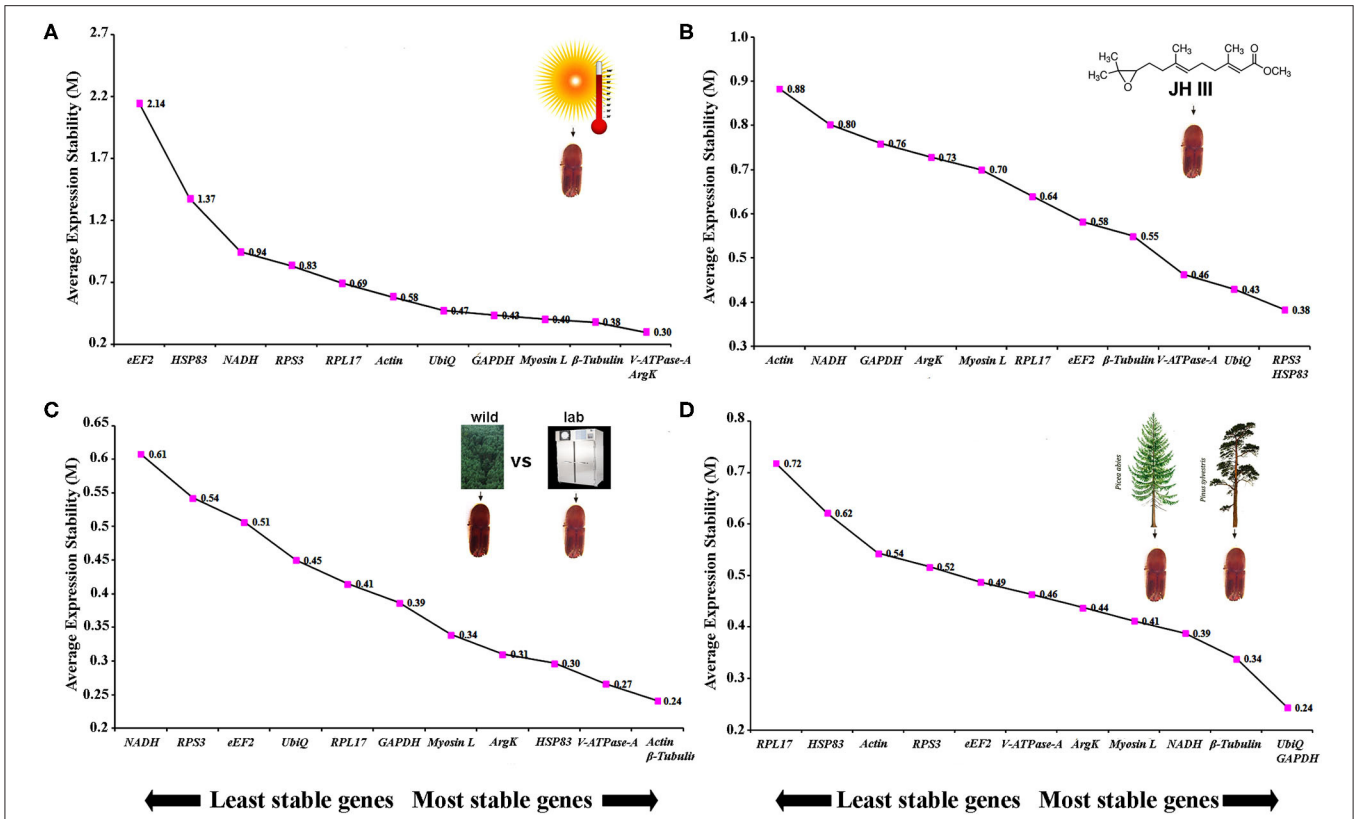

FIGURE 3 | The average expression stability values (M) of 12 reference genes under diverse conditions were calculated by geNorm from the least stable (left) to the most stable (right). **(A)** Temperature, **(B)** juvenile hormone III, **(C)** laboratory-reared vs. wild beetles, and **(D)** pine-fed vs. spruce-fed beetles.

calculated the optimal reference gene number based on geNorm algorithm analysis for each condition. We found that at least two reference genes were required for the head, female tissues, and temperature conditions based on the pairwise values (**Figures 4A,B**).

Validation of Reference Gene Selection

Krüppel-homolog 1 (*Kr-h1*) encodes a key transcription factor and plays a critical role in regulating insect metamorphosis within the juvenile hormone signaling pathway (Li et al., 2018a; Roy and Palli, 2018). The relative expression of *Kr-h1* in response to the JHIII treatment was normalized with single reference genes or gene combinations recommended by geNorm (**Figures 4A,B**). The two most stable reference genes, individually and in combination, and the least stable gene were used in this experiment. The results showed that the *Kr-h1* gene was expressed in male and female beetles (**Figure 5A**). The expression levels of *Kr-h1* normalized with *NADH* (least stable) in males reduced from 2.1 to 0.6 fold, and females were increased from 1.8 to 3.8 fold higher than those of *Kr-h1* normalized with stable reference gene or gene combinations, respectively. Similarly, *HSP70* is a key protein closely related to the molecular mechanism underlying insect resistance to the environment (Štětina et al., 2015). The relative expression of *Hsp70* showed a stable expression difference after normalizing with the single and most stable reference gene combination during temperature exposure. On the contrary, the *Hsp70* gene expression level after normalizing with the least stable reference gene showed higher variation after different temperature incubation (**Figure 5B**). Henceforth, the most stable genes used for normalization, either individually or in combination, resulted in more consistent and trustworthy target gene expression patterns.

In addition, *Kr-h1* gene expression was evaluated for the various developmental stages to validate the reference gene findings taking the most and least stable gene for expression normalization. Results showed that the expression level of *Kr-h1* in the second instar larvae was almost 4-fold higher than the first instar larvae when normalization was performed based on the most stable reference gene (β-*Tubulin*) (**Figure 5C**). In contrast, when the least stable reference gene (*RPL17*) was used for normalization, the *Kr-h1* expression was considerably low. Furthermore, normalization with β-*Tubulin* resulted in lower expression in all stages except second instar larvae signifying the importance of having optimal reference genes for expression normalization.

DISCUSSIONS

The wood-boring coleopteran pest, ISx, is one of the most destructive forest pests, causing severe damage to coniferous

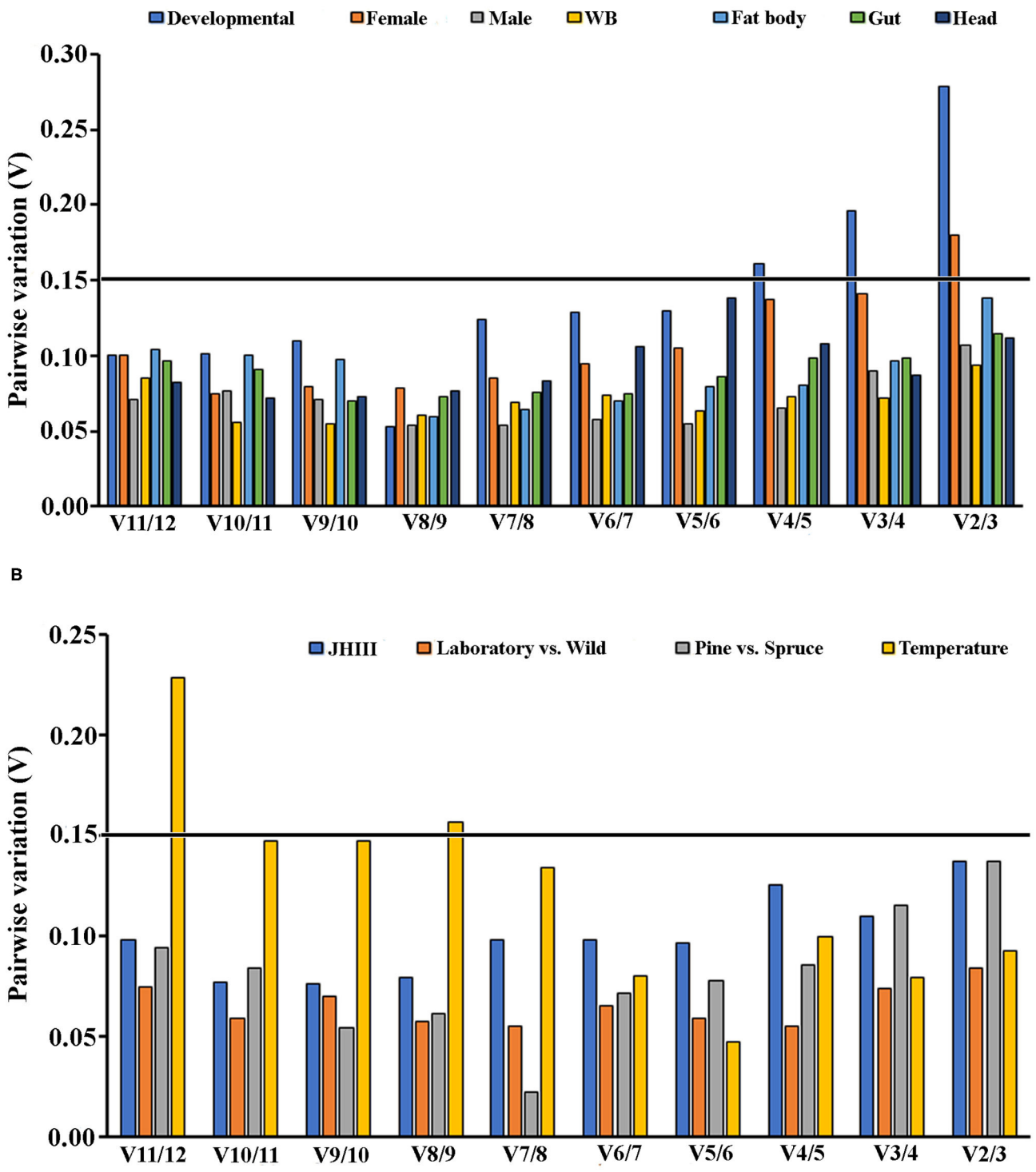

FIGURE 4 | An optimal number of reference genes for the normalization of ISx under selected extrinsic experimental conditions. Based on geNorm analysis, average pairwise variations were calculated between the normalization factors NFn and NFn + 1. Values <0.15 indicate that n + 1 genes were not required for the normalization of gene expression. **(A)** Biotic conditions: developmental stages (i.e., larvae, pupae, and adult stages), tissue types [head, midgut, fat body, and whole body (WB) except head, gut, fat body] and **(B)** Abiotic conditions: different treatments (temperature; Juvenile hormone III; wild-collected vs. long-term laboratory-reared; and different host feeding). Values <0.15 indicate that additional genes are not necessary for normalization.

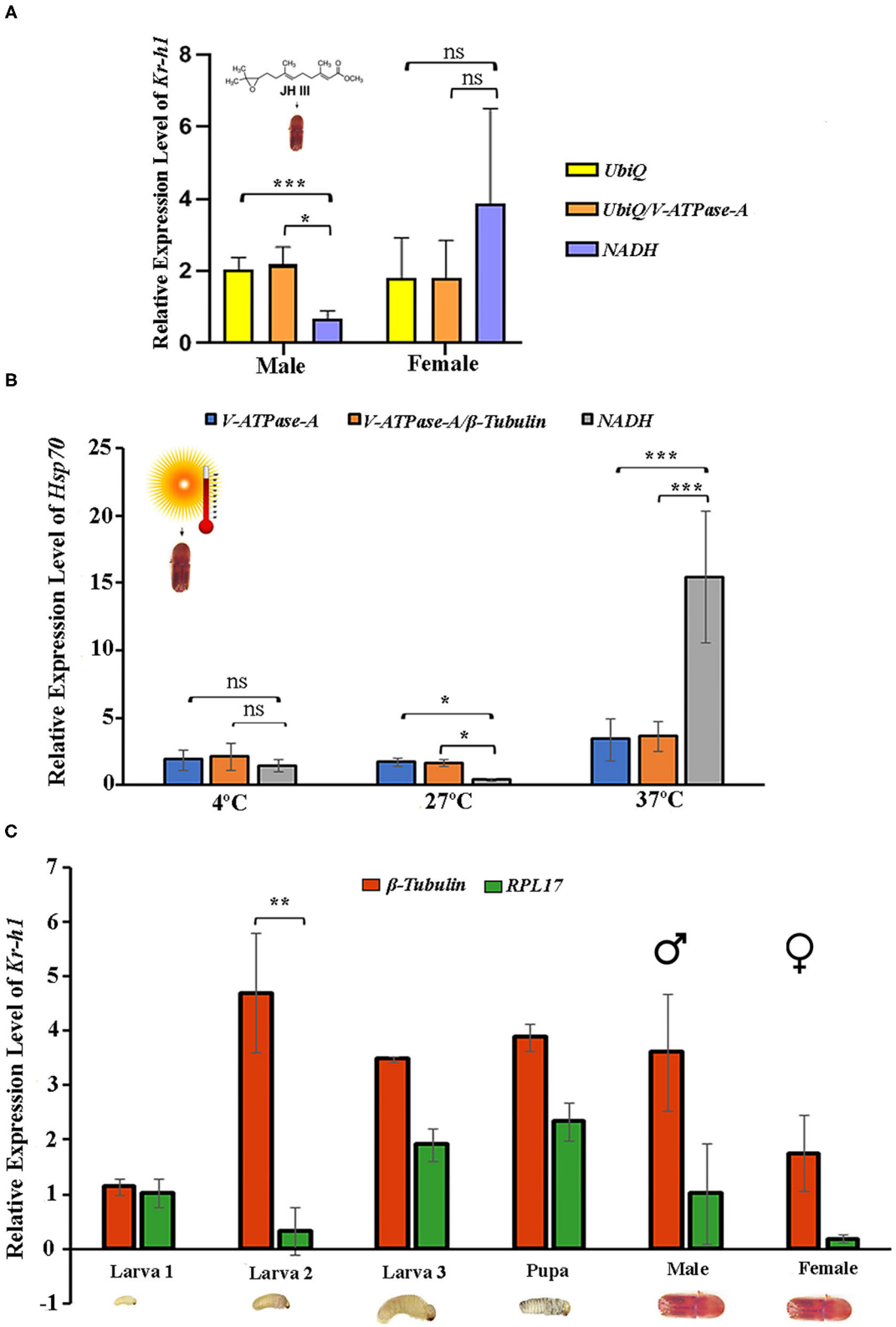

FIGURE 5 | Validation of the recommended reference genes. The relative expression levels of the target genes *Kr-h1* and *Hsp70* were studied under Juvenile hormone III treatment and temperature treatment by normalizing the selected reference gene. The most stable reference gene is *UbiQ* and V-*ATPase-A* for juvenile

(Continued)

FIGURE 5 | hormone III; *V-ATPase-A* and *β-Tubulin* for temperature, the least stable reference gene for both treatments *NADH*. The respective combination of stable reference genes UbiQ+V-*ATPase-A* and *V-ATPase-A*+*β-Tubulin*. **(A)** Juvenile hormone III and **(B)** Temperature. **(C)** The relative expression levels of the target gene *Kr-h1* were calculated under developmental stages (larvae, pupae, and adult stages), normalized with the most stable reference gene *β-Tubulin* and the least stable reference gene *RPL17*. Data represent mean values ± SD of four biological replicates. Asterisks indicate significant differences in the expression of the target gene normalized separately by different reference genes (***$P < 0.001$, **$P < 0.01$, *$P < 0.05$, ns indicate no significant difference).

species throughout Europe and Asia (Jeger et al., 2017). Environmental stress significantly affects host colonization and can provoke transitions from endemic to epidemic bark beetle development (Kausrud et al., 2012). However, to understand the molecular mechanisms of beetle-host interactions, the advent of high-throughput sequencing technologies must advance to increase genetic information. Reference genes with high expression stability under different environmental conditions will be needed to study further a particular gene expression (Fu and Meyer-Rochow, 2021). However, there is no universal reference gene for all samples and tissue types with diverse conditions to date. Therefore, evaluating the stable reference gene under various treatments is essential before aiming DGE study (Lu et al., 2018). The present study examined 12 reference genes commonly applied to Coleoptera using four algorithms (geNorm, NormFinder, BestKeeper, and the ΔCt method) under various biotic and abiotic conditions. There are copious studies regarding the validation of reference genes in other insects (Lu et al., 2018), but no information has previously been reported in any *Ips* species. Hence, this is the first report for suitable reference genes in any *Ips* bark beetles.

Accurate normalization using a stable reference gene is necessary to conduct gene expression studies under specific experimental conditions and to avoid erroneous differences in target gene expression (Andersen et al., 2004; Bustin et al., 2005; Ferguson et al., 2010; Cheng et al., 2013; García-Reina et al., 2018; Xie et al., 2021). The results obtained in this study indicate that the stability of reference genes in ISx can differ under various experimental conditions, including developmental stage, sex, and tissue-specific conditions, and exposure to abiotic conditions (**Tables 2**–**5** and **Figures 1B**–**4**) as observed in other reference gene finding studies in insects (Lu et al., 2018). Among the 12 reference genes studied in this study, we found that *β-Tubulin, eEF2, RPS3*, and *V-ATPase-A* were the most stable in the developmental stage, sex-specific, and tissue-specific conditions from all four algorithms (**Tables 2**–**4**); and geNorm (**Figures 1B**, **2A–F**). In addition, both *β-Tubulin* and *eEF2* were more stable than *V-ATPase-A* and *RPS3* at various developmental stages. Teng et al. (2012) reported EF (*eEF2*) as the most stably expressed gene in different developmental stages of *Plutella xylostella*. The higher stability of *β-Tubulin* and *eEF2* in two biotic factors (developmental stages and tissues) was also documented in reference gene analyses for *Agrilus planipennis* (Rajarapu et al., 2012); *Sogatella furcifera* (An et al., 2016); *Mythimna separata* (Li et al., 2018b); *Chilo partellus* (Adeyinka et al., 2019); and *Hippodamia variegate* (Xie et al., 2021). Alternatively, many studies have reported these genes as unsuitable for normalization because of expression variability in different experimental conditions (developmental stages, tissue stages) as in *Drosophila melanogaster* (Ponton et al., 2011). However, our results confirmed that tissue-specific expression of reference gene *eEF2* was highly stable. It was consistently the top-ranking gene for the developmental, head, fat body, and gut except for WB tissue in ISx.

Similarly, RPs have been evaluated and showed highly stable expression in different insects (Lu et al., 2018). Earlier research findings documented that RP-encoding genes are among the most stably expressed reference genes and have been widely used to normalize gene expression levels in insect molecular investigations during the past 10 years (Lu et al., 2018). For instance, *RPS13* and *RPS7* exhibited the most stable expression under larval-crowding conditions in *Mythimna separata* (Li et al., 2018b). *RPS3* also exhibited high stability under larval tissues in *Lucilia sericata* (Baumann et al., 2015). Similarly, *RPL9* and *RPL10* genes showed higher expression stability in different developmental stages and tissues of *Sogatella furcifera* (An et al., 2016), whereas *RPS26* and *RPL32* genes showed the same in *Thermobia domestica* (Bai et al., 2021). Furthermore, *RPS18* and *RPL13* genes showed the highest expression stability in *Rhopalosiphum padi* tissues (Li et al., 2021). Wang et al. (2014) reported *RPL22e* as the most stable reference gene comparing male and female *Mylabris cichorii*. Similarly, our results suggested that the RP, *RPS3,* was the most stable gene among the 12 candidates in sex-specific and tissue-specific (except fat body and gut) conditions tested in ISx (**Tables 3**, **4** and **Figure 2**).

Vacuolar-type ATPase (*V-ATPase-A*) is a proton translocating pump responsible for ATP hydrolysis, one of the most highly conserved eukaryotic proteins. The *V-ATPase-A* gene had been commonly used as a reference gene in *Amrasca biguttula* for experiments involving starvation stress and different life stages (Singh et al., 2018); for sex-specific experiments in *Cicindela campestris* (García-Reina et al., 2018). On the contrary, *V-ATPase-A* gene expression was highly unstable in the developmental and tissue stages of *Mythimna separata* (Li et al., 2018c). Nevertheless, our results demonstrated stable expression of *V-ATPase-A* in the fat body and gut tissues of ISx (**Table 4** and **Figures 2D,E**).

Experiments on ISx involving alteration of abiotic conditions revealed a varied set of genes as references, such as *V-ATPase-A*, *ArgK*, and *β-Tubulin* for temperature incubation; *UbiQ, V-ATPase-A,* and *RPS3* for JHIII treatment; *Actin, Myosin L,* and *β-Tubulin* in between laboratory vs. wild beetles, and *V-ATPase-A, UbiQ,* and *ArgK* among pine vs. spruce-fed beetle gut tissues (**Table 5** and **Figure 3**). The reference gene *V-ATPase-A* was used previously for normalization of *Mythimna separata* gene expression after temperature treatment (Li et al., 2018c), whereas *β-Tubulin* was applied for a similar purpose for *Bemisia tabaci* (Dai et al., 2017); *Phenacoccus solenopsis* (Arya et al., 2017);

Amphitetranychus viennensis (Yang et al., 2019); and *Hippodamia variegate* (Xie et al., 2021).

In the present study, host plants among all treatments caused the highest expression variations of the reference genes. In the dataset of gut samples collected from the adults fed on different plants (i.e., pine and spruce), the stability ranking of tested reference genes was different according to five algorithms. The most stable reference gene was *UbiQ* and *GAPDH* according to the geNorm algorithm (**Figure 3D**). However, *V-ATPase-A, UbiQ,* and *ArgK* were the most stable reference genes evaluated by the other four algorithms (delta Ct, BestKeeper, RefFinder, and Normfinder, respectively) (**Table 5**). Interestingly, similar studies in other arthropods have not found such dramatic variations so far (Arya et al., 2017). Furthermore, in laboratory-reared and wild-collected beetle gut tissues, *Actin, Myosin L*, and *ArgK* were the most stable reference genes after delta Ct, BestKeeper, RefFinder, and Normfinder analysis (**Table 5**), which differed from the geNorm algorithm analysis (**Figure 3C**). In our opinion, plant diet causes drastic changes at the gene expression level in ISx, hence higher variation in the reference gene expression.

Further, the expression of *Kr-h1* and *Hsp70* was evaluated in various developmental stages and respective treatments (JHIII and temperature) to corroborate the suitability of the identified reference genes. Although, the results demonstrated that the expression trends in different conditions were accordant using various reference gene or gene combinations. The *Kr-h1* gene expression was induced by JHIII, as expected from similar treatments on other beetles (Roy et al., 2017; Roy and Palli, 2018; Xu et al., 2018). However, our results displayed that using less stable reference genes may generate erroneous interpretation, whereas stable reference gene combinations can reduce bias during normalization (**Figure 5A**). Alternatively, there was no significant expression difference of *Hsp70* at 4°C temperature, but considerable expression differences were observed after 27 and 37°C incubation using the most stable reference gene (*β-Tubulin*) separately and together (*β-Tubulin/ V-ATPase-A*), and least reference gene (*NADH*) as normalizer. It is worth mentioning that the expression change was more extensive at 37°C for *Hsp70* when normalized with *NADH*, the least stable gene. Recently, elimination of such erroneous findings was achieved by normalization of gene expression with combinations of stable reference genes in different experimental conditions in *Helicoverpa armigera* (Zhang et al., 2015), *Aphis gossypii* (Ma et al., 2016), and *Cydia pomonella* (Wei et al., 2020). Additionally, with the selected single reference genes, such as *β-Tubulin* (most stable) and *RPL17* (least stable), we performed RT-qPCR to study *Kr-h1* expression patterns in several developmental stages of ISx (**Figure 5C**). More convincing results were obtained when two genes were used for expression normalization (**Figures 5A,B**). Our results corroborate the current notion of using two or three genes for target gene expression normalization to enhance accuracy (Arya et al., 2017; Li et al., 2018c; Wei et al., 2020; Bai et al., 2021; Fu and Meyer-Rochow, 2021).

Similar to other published studies in the field, our analyses also documented different results under diverse experimental conditions for all five algorithms; however, the results were comparable among some treatments. Interestingly, the most conclusive observation from the current assessments showed that *β-Tubulin* and *eEF2* were the most stable reference genes across all developmental stages, sex, and tissue-specific conditions investigated under the present study (**Tables 2–4** and **Figures 1A**, **2**). Our findings suggested that the recommended number of reference genes should be two for many comparisons in the study, based on the pairwise values (>0.15) obtained with geNorm (**Figures 4A,B**). Furthermore, these results imply that a single reference gene is not optimal to normalize the target gene expression in different experimental conditions. Hence, we endorsed optimal reference genes for the specific experimental conditions in ISx (**Table 6**).

In conclusion, temperate and boreal forests have recently undergone unprecedented pressure from bark beetle outbreaks, reducing forest biodiversity and their role in global carbon sequestration. It also affects their economic value and endangered wildlife habitat. Current management approaches are proven progressively deficient against outbreaking bark beetle populations, urging investigations into novel mitigation strategies using state-of-the-art molecular methodologies. Future gene expression and functional genomics studies are crucial to alleviate the ongoing bark beetle-mediated forest depletion. Hence, dedicated reference gene selection studies are of utmost importance on economically important bark beetles. The present work represents the first reference gene validation study in *I. sexdentatus*, an ecologically important wood-boring beetle. It provides valuable information on reference genes (**Table 6**) for future molecular studies (i.e., DGE studies) on host-beetle interactions and functional genomic studies (i.e., RNAi) on this bark beetle and similar *Ips* beetles (Coleoptera: Curculionidae: Scolytinae).

TABLE 6 | Summary of the recommended reference genes under different experimental conditions.

Conditions	Recommendation
Biotic conditions	
Developmental stage	*β-Tubulin, eEF2*, and *RPS3*
Sex-specific tissues	
Male	*RPS3, GAPDH*, and *eEF2*
Female	*eEF2, RPS3*, and *β-Tubulin*
Tissue	
Head	*RPS3*, *ArgK*, and *eEF2*
Fat body	*V-ATPase-A, eEF2*, and *NADH*
Gut	*V-ATPase-A, eEF2*, and *RPL17*
Abdomen (WB)	*RPS3*, *β-Tubulin*, and *HSP83*
Between tissues	*β-Tubulin, RPS3*, *and eEF2*
Abiotic conditions	
Temperature	*β-Tubulin*, *V-ATPase-A*, and *ArgK*
Juvenile hormone III	*UbiQ*, *V-ATPase-A*, and *RPS3*
Laboratory-reared vs. wild beetles	*Actin*, *Myosin L*, and *ArgK*
Pine-fed vs. spruce-fed	*V-ATPase-A*, *UbiQ*, and *ArgK*

DATA AVAILABILITY STATEMENT

The original contributions presented in the study are included in the article/**Supplementary Material**, further inquiries can be directed to the corresponding author/s. The reference gene sequences used in the study were submitted under the NCBI accession numbers from OK143445 to OK143455.

AUTHOR CONTRIBUTIONS

GS, AC, and AR conceived and designed the research and prepared the final manuscript. SA, RM, and JS collected, sorted, and dissected beetles. JB and SA prepared samples for in-house transcriptome. GS conducted real-time experiments and wrote the first draft. GS and MKS analyzed the data. All authors have read and approved the final manuscript.

FUNDING

The project was funded by the Internal Grant Agency (IGA) from the Faculty of Forestry and Wood Sciences, Czech University of Life sciences. Infrastructural support and salary for GS, JB, and AR are obtained from grant EXTEMIT-K, No. CZ.02.1.01/0.0/0.0/15_003/0000433 financed by OP RDE. The financial support for AC was provided by grant EVA 4.0, No. CZ.02.1.01/0.0 /0.0/16_019 /0000803 financed by OP RDE.

SUPPLEMENTARY MATERIAL

The Supplementary Material for this article can be found online at: https://www.frontiersin.org/articles/10.3389/fphys.2021.752768/full#supplementary-material

REFERENCES

Adeyinka, O. S., Tabassum, B., Nasir, I. A., Yousaf, I., and Husnain, T. (2019). Identification and validation of potential reference gene for effective dsRNA knockdown analysis in *Chilo partellus*. *Sci. Rep.* 9:13629. doi: 10.1038/s41598-019-49810-w

An, X. K., Hou, M. L., and Liu, Y. D. (2016). Reference gene selection and evaluation for gene expression studies using qRT-PCR in the white-backed Planthopper, *Sogatella furcifera* (Hemiptera: Delphacidae). *J. Econ. Entomol.* 109:879. doi: 10.1093/jee/tov333

Andersen, C. L., Jensen, J. L., and Orntoft, T. F. (2004). Normalization of real-time quantitative reverse transcription-PCR data: a model-based variance estimation approach to identify genes suited for normalization, applied to bladder and colon cancer data sets. *Cancer Res.* 64, 5245–5250. doi: 10.1158/0008-5472.CAN-04-0496

Arya, S. K., Jain, G., Upadhyay, S. K., Sarita, S. H., Dixit, S., and Verma, P. C. (2017). Reference genes validation in *Phenacoccus solenopsis* under various biotic and abiotic stress conditions. *Sci. Rep*. 7:13520. doi: 10.1038/s41598-017-13925-9

Aw, T., Schlauch, K., Keeling, C. I., Young, S., Bearfield, J. C., Blomquist, G. J., et al. (2010). Functional genomics of mountain pine beetle (*Dendroctonus ponderosae*) midguts and fat bodies. *BMC Genom*. 11:215. doi: 10.1186/1471-2164-11-215

Bai, Y., Lv, Y. N., Zeng, M., Jia, P. Y., Lu, H. N., Zhu, Y. B., et al. (2021). Selection of reference genes for normalization of gene expression in *Thermobia domestica* (Insecta: Zygentoma: Lepismatidae). *Genes* 12:21. doi: 10.3390/genes12010021

Basu, S., Pereira, A. E., Pinheiro, D. H., Wang, H., Valencia-Jiménez, A., Siegfried, B. D., et al. (2019). Evaluation of reference genes for real-time quantitative PCR analysis in southern corn rootworm, *Diabrotica undecimpunctata howardi* (Barber). *Sci. Rep.* 9:10703. doi: 10.1038/s41598-019-47020-y

Baumann, A., Lehmann, R., Beckert, A., Vilcinskas, A., and Franta, Z. (2015). Selection and evaluation of tissue specific reference genes in *Lucilia sericata* during an immune challenge. *PLoS ONE.* 10:e0135093. doi: 10.1371/journal.pone.0135093

Biedermann, P. H. W., Muller, J., Gregoire, J. C., Gruppe, A., Hagge, J., Hammerbacher, A., et al. (2019). Bark beetle population dynamics in the anthropocene: challenges and solutions. *Trends Ecol. Evol.* 34, 914–924. doi: 10.1016/j.tree.2019.06.002

Bouhot, L., Lieutier, F., and Debouzie, D. (1988). Spatial and temporal distribution of attacks by *Tomicus piniperda* L. and *Ips sexdentatus* Boern. (Col., Scolytidae) on *Pinus sylvestris*. *J. Appl. Entomol.* 106, 356–371. doi: 10.1111/j.1439-0418.1988.tb00604.x

Bustin, S. A., Benes, V., Nolan, T., and Pfaffl, M. W. (2005). Quantitative real-time RT-PCR–a perspective. *J. Mol. Endocrinol*. 34, 597–601. doi: 10.1677/jme.1.01755

Chakraborty, A., Ashraf, M. Z., Modlinger, R., Synek, J., Schlyter, F., and Roy, A. (2020b). Unravelling the gut bacteriome of Ips (Coleoptera: Curculionidae: Scolytinae): identifying core bacterial assemblage and their ecological relevance. *Sci. Rep*. 10:18572. doi: 10.1038/s41598-020-75203-5

Chakraborty, A., Modlinger, R., Ashraf, M. Z., Synek, J., Schlyter, F., and Roy, A. (2020a). Core mycobiome and their ecological relevance in the gut of five Ips bark beetles (Coleoptera: Curculionidae: Scolytinae). *Front. Microbiol.* 11:568853. doi: 10.3389/fmicb.2020.568853

Cheng, D., Zhang, Z., He, X., and Liang, G. (2013). Validation of reference genes in *Solenopsis invicta* in different developmental stages, castes and tissues. *PLoS ONE* 8:e57718. doi: 10.1371/journal.pone.0057718

Dai, T. M., Lü, Z. C., Liu, W. X., and Wan, F. H. (2017). Selection and validation of reference genes for qRT-PCR analysis during biological invasions: the thermal adaptability of *Bemisia tabaci* MED. *PLoS ONE* 12:e0173821. doi: 10.1371/journal.pone.0173821

Denham, S. O., Coyle, D. R., Oishi, A. C., Bullock, B. P., Heliövaara, H., and Novick, K. A. (2019). Tree resin flow dynamics during an experimentally induced attack by *Ips avulsus, I. calligraphus*, and *I. Grandicollis. Can. J. For. Res.* 49:1. doi: 10.1139/cjfr-2018-0024

Douglas, H. B., Cognato, A. I., Grebennikov, V., and Savard, K. (2019). Dichotomous and matrix-based keys to the *Ips* bark beetles of the World (Coleoptera: Curculionidae: Scolytinae). *Can. J. Arthropod. Identifi*. 38:234. doi: 10.3752/cjai.2019.38

Etxebeste, I., and Pajares, J. A. (2011). Verbenone protects pine trees from colonization by the six-toothed pine bark beetle, *Ips f sexdentatus* Boern. (Col.: Scolytinae). *J. Appl. Entomol.* 135, 258–268. doi: 10.1111/j.1439-0418.2010.01531.x

Ferguson, B. S., Nam, H., Hopkins, R. G., and Morrison, R. F. (2010). Impact of reference gene selection for target gene normalization on experimental outcome using real-time qRT-PCR in adipocytes. *PLoS ONE* 5:e15208. doi: 10.1371/journal.pone.0015208

Ferrenberg, S., Kane, J. M., and Mitton, J. B. (2014). Resin duct characteristics associated with tree resistance to bark beetles across lodgepole and limber pines. *Oecologia* 174, 1283–1292. doi: 10.1007/s00442-013-2841-2

Fu, X., and Meyer-Rochow, V. B. (2021). Selection and validation of suitable reference genes for RT-qPCR analysis in the rare aquatic firefly *Aquatica leii* (Coleoptera: Lampyridae). *Insects* 12:359. doi: 10.3390/insects12040359

Gao, P., Wang, J., and Wen, J. (2020). Selection of reference genes for tissue/organ samples of adults of *Eucryptorrhynchus scrobiculatus*. *PLoS ONE* 15:e0228308. doi: 10.1371/journal.pone.0228308

García-Reina, A., Rodríguez-García, M. J., and Galián, J. (2018). Validation of reference genes for quantitative real-time PCR in tiger beetles across sexes, body parts, sexual maturity and immune challenge. *Sci. Rep*. 8:10743. doi: 10.1038/s41598-018-28978-7

Gregoire, J. C., and Evans, H. F. (2004). "Damage and control of BAWBILT organisms an overview," in *Bark And Wood Boring Insects in Living Trees in Europe, A Synthesis*, eds F. Lieutier, K. R. Day, A. Battisti, J.-C. Grégoire, H. F. Evans (Dordrecht: Springer), 19–37. doi: 10.1007/978-1-4020-2241-8_4

Gurusamy, D., Howell, J. L., Chereddy, S. C. R. R., Mogilicherla, K., and Palli, S. R. (2021). Improving RNA interference in the southern green stink bug, *Nezara viridula*. *J. Pest Sci.* 4, 1461–1472. doi: 10.1007/s10340-021-01358-3

Heid, C. A., Stevens, J., Livak, K. J., and Williams, P. M. (1996). Real time quantitative PCR. *Genome Res.* 6, 986–994. doi: 10.1101/gr.6.10.986

Higuchi, R., Fockler, C., Dollinger, G., and Watson, R. (1993). Kinetic PCR analysis: real-time monitoring of DNA amplification reactions. *Biotechnology*. 11, 1026–1030. doi: 10.1038/nbt0993-1026

Huang, J., Kautz, M., Trowbridge, A. M., Hammerbacher, A., Raffa, K. F., Adams, H. D., et al. (2020). Tree defence and bark beetles in a drying world: carbon partitioning, functioning and modelling. *New Phytol.* 225, 26–36. doi: 10.1111/nph.16173

Jeger, M., Bragard, C., Caffier, D., Candresse, T., Chatzivassiliou, E., Dehnen-Schmutz, K., et al. (2017). Scientific Opinion on the pest categorisation of *Ips sexdentatus*. *EFSA J.* 15:4999. doi: 10.2903/j.efsa.2017.4999

Joga, M. R., Mogilicherla, K., Smagghe, G., and Roy, A. (2021). RNA interference-based forest protection products (FPPs) against wood-boring coleopterans: hope or hype? *Front. Plant Sci.* 12:733608. doi: 10.3389/fpls.2021.733608

Kausrud, K., Økland, B., Skarpaas, O., Grégoire, J. C., Erbilgin, N., and Stenseth, N. C. (2012). Population dynamics in changing environments: the case of an eruptive forest pest species. *Biol. Rev.* 87, 34–51. doi: 10.1111/j.1469-185X.2011.00183.x

Li, H. B., Dai, C. G., Zhang, C. R., He, Y. F., Ran, H. Y., and Chen, S. H. (2018b). Screening potential reference genes for quantitative real-time PCR analysis in the oriental armyworm, *Mythimna separata*. *PLoS ONE* 13:e0195096. doi: 10.1371/journal.pone.0195096

Li, K., Xu, N., Yang, Y. J., Zhang, J. H., and Yin, H. (2018c). Identification and validation of reference genes for RT-qPCR normalization in *Mythimna separata* (Lepidoptera: Noctuidae). *Biomed. Res. Int.* 14:1828253. doi: 10.1155/2018/1828253

Li, K. L., Yuan, S. Y., Nanda, S., Wang, W. X., Lai, F. X., Fu, Q., et al. (2018a). The roles of E93 and Kr-h1 in metamorphosis of *Nilaparvata lugens*. *Front. Physiol.* 9:1677. doi: 10.3389/fphys.2018.01677

Li, M., Li, X., Wang, C., Li, Q., Zhu, S., Zhang, Y., et al. (2021). Selection and validation of reference genes for qRT-PCR analysis of *Rhopalosiphum padi* (Hemiptera: Aphididae). *Front. Physiol.* 12:663338. doi: 10.3389/fphys.2021.663338

Livak, K. J., and Schmittgen, T. D. (2001). Analysis of relative gene expression data using real-time quantitative PCR and the 2[-Delta C(T)] method. *Methods* 25, 402–408. doi: 10.1006/meth.2001.1262

Lu, J., Yang, C., Zhang, Y., and Pan, H. (2018). Selection of reference genes for the normalization of RT-qPCR data in gene expression studies in insects: a systematic review. *Front. Physiol.* 9:1560. doi: 10.3389/fphys.2018.01560

Lubojacký, J., and Knížek, M. (2020). "Podkorní Hmyz," in Výskyt lesních škodlivých činitelu v roce 2019 a jejich očekávaný stav v roce 2020. Strnady, eds M. Knížek and J. Liška (VULHM), 22–35.

Ma, K. S., Li, F., Liang, P. Z., Chen, X. W., Liu, Y., and Gao, X. W. (2016). Identification and validation of reference genes for the normalization of gene expression data in qRT-PCR analysis in *Aphis gossypii* (Hemiptera: Aphididae). *J. Insect Sci.* 16:17. doi: 10.1093/jisesa/iew003

Marini, L., Okland, B., Jonsson, A. M., Bentz, B., Carroll, A., Forster, B., et al. (2017). Climate drivers of bark beetle outbreak dynamics in Norway spruce forests. *Ecography* 40, 1426–1435. doi: 10.1111/ecog.02769

Nicot, N., Hausman, J. F., Hoffmann, L., and Evers, D. (2005). Housekeeping gene selection for real-time RT-PCR normalization in potato during biotic and abiotic stress. *J. Exp. Bot.* 56, 2907–2914. doi: 10.1093/jxb/eri285

Pettit, J., Voelker, S., DeRose, R. J., and Burton, J. (2020). Spruce beetle outbreak was not driven by drought stress: evidence from a tree-ring iso-demographic approach indicate temperatures were more important. *Glob. Chang. Biol.* 2020, 1–15. doi: 10.1111/gcb.15274

Pfaffl, M. W., Tichopad, A., Prgomet, C., and Neuvians, T. P. (2004). Determination of stable housekeeping genes, differentially regulated target genes and sample integrity: BestKeeper - Excel-based tool using pairwise correlations. *Biotechnol. Lett.* 26, 509–515. doi: 10.1023/B:BILE.0000019559.84305.47

Pfeffer, A. (1955). *Fauna of Czechoslovakia: Bark beetles – Scolytoidea, Fauna CSR., svazek 6. Kurovci–Scolytoidea. 1. vyd*. Praha: Czechoslovak Academy of Sciences-Czechoslovak Academy of Sciences, 324.

Ponton, F., Chapuis, M. P., Pernice, M., Sword, G. A., and Simpson, S. J. (2011). Evaluation of potential reference genes for reverse transcription-qPCR studies of physiological responses in *Drosophila melanogaster*. *J. Insect Physiol.* 57, 840–850. doi: 10.1016/j.jinsphys.2011.03.014

Postner, M. (1974). "Scolytidae (=ipidae), borkenkaäfer," in *Die forstschaädlinge Europas, II Käfer, vol 2*, ed W. Schwenke (Hamburg: Verlag Paul Parey), 334–482.

Qu, C., Wang, R., Che, W., Zhu, X., Li, F., and Luo, C. (2018). Selection and evaluation of reference genes for expression analysis using quantitative real-time PCR in the Asian Ladybird *Harmonia axyridis* (Coleoptera: Coccinellidae). *PLoS ONE* 13:e0192521. doi: 10.1371/journal.pone.0192521

Rajarapu, S. P., Mamidala, P., and Mittapalli, O. (2012). Validation of reference genes for gene expression studies in the emerald ash borer (*Agrilus planipennis*). *Insect Sci.* 19, 41–46. doi: 10.1111/j.1744-7917.2011.01447.x

Rodrigues, T. B., Khajuria, C., Wang, H., Matz, N., Cunha, C. D., Valicente, F. H., et al. (2014). Validation of reference housekeeping genes for gene expression studies in western corn rootworm (*Diabrotica virgifera virgifera*). *PLoS ONE* 9:e109825. doi: 10.1371/journal.pone.0109825

Roy, A., George, S., and Palli, S. R. (2017). Multiple functions of CREB-binding protein during postembryonic development: identification of target genes. *BMC Genom.* 18:996. doi: 10.1186/s12864-017-4373-3

Roy, A., and Palli, S. R. (2018). Epigenetic modifications acetylation and deacetylation play important roles in juvenile hormone action. *BMC Genom.* 19:934. doi: 10.1186/s12864-018-5323-4

Seidl, R., Thom, D., Kautz, M., Martin-Benito, D., Peltoniemi, M., Vacchiano, G., et al. (2017). Forest disturbances under climate change. *Nat. Clim. Change.* 7, 395–402. doi: 10.1038/nclimate3303

Shakeel, M., Rodriguez, A., Tahir, U. B., and Jin, F. (2018). Gene expression studies of reference genes for quantitative real-time PCR: an overview in insects. *Biotechnol. Lett.* 40, 227–236. doi: 10.1007/s10529-017-2465-4

Silver, N., Best, S., Jiang, J., and Thein, S. L. (2006). Selection of housekeeping genes for gene expression studies in human reticulocytes using real-time PCR. *BMC Mol. Biol.* 7:33. doi: 10.1186/1471-2199-7-33

Singh, S., Gupta, M., Pandher, S., Kaur, G., Rathore, P., and Palli, S. R. (2018). Selection of housekeeping genes and demonstration of RNAi in cotton leafhopper, *Amrasca biguttula biguttula* (Ishida). *PLoS ONE* 13:e0191116. doi: 10.1371/journal.pone.0191116

Sommerfeld, A., Rammer, W., Heurich, M., Hilmers, T., Müller, J., and Seidl, R. (2020). Do bark beetle outbreaks amplify or dampen future bark beetle disturbances in Central Europe? *J. Ecol.* 2020, 1–13. doi: 10.1111/1365-2745.13502

Štětina, T., Koštál, V., and Korbelová, J. (2015). The role of inducible Hsp70, and other heat shock proteins, in adaptive complex of cold tolerance of the fruit fly (*Drosophila melanogaster*). *PLoS ONE* 10:e0128976. doi: 10.1371/journal.pone.0128976

Sun, Y., Fu, F., Kang, X., Liu, B., Ning, H., and Chen, H. (2021). Function of mevalonate pathway genes in the synthesis of frontalin in Chinese white pine beetle, *Dendroctonus armandi* (curculionidae: Scolytinae). *Arch. Insect Biochem. Physiol.* 107, 1–13. doi: 10.1002/arch.21828

Teng, X., Zhang, Z., He, G., Yang, L., and Li, F. (2012). Validation of reference genes for quantitative expression analysis by real-time RT-PCR in Four Lepidopteran insects. *J. Insect Sci.* 12, 1–17. doi: 10.1673/031.012.6001

Vandesompele, J., De Preter, K., Pattyn, F., Poppe, B., Roy, N. V., De Paepe, A., et al. (2002). Accurate normalization of real-time quantitative RT-PCR data by geometric averaging of multiple internal control genes. *Genome Biol.* 3, 1–11. doi: 10.1186/gb-2002-3-7-research0034

VanGuilder, H. D., Vrana, K. E., and Freeman, W. M. (2008). Twenty-five years of quantitative PCR for gene expression analysis. *Biotechniques* 44, 619–626. doi: 10.2144/000112776

Wang, Y., Wang, Z. K., Huang, Y., Liao, Y. F., and Yin, Y. P. (2014). Identification of suitable reference genes for gene expression studies by qRT-PCR in the blister beetle *Mylabris cichorii*. *J. Insect Sci.* 14:94. doi: 10.1673/031.014.94

Wang, Z., Meng, Q., Zhu, X., Sun, S., Liu, A., Gao, S., et al. (2020). Identification and evaluation of reference genes for normalization of gene expression in developmental stages, sexes, and tissues of *Diaphania caesalis* (Lepidoptera, Pyralidae). *J. Insect Sci.* 20:1. doi: 10.1093/jisesa/iez130

Wei, Z., Liu, M., Hu, C., and Yang, X. (2020). Overexpression of glutathione S-transferase genes in field λ-cyhalothrin-resistant population of *Cydia pomonella*: reference gene selection and expression analysis. *J. Agr. Food Chem.* 68, 5825–5834. 10.1021/acs.jafc.0c01367 doi: 10.1021/acs.jafc.0c01367

Wermelinger, B., Rigling, D., Schneider, M. D., and Dobbertin, M. (2008). Assessing the role of bark- and wood-boring insects in the decline of Scots pine (*Pinus sylvestris*) in the Swiss Rhone valley. *Ecol. Entomol.* 33, 239–249. doi: 10.1111/j.1365-2311.2007.00960.x

Xie, J., Liu, T., Khashaveh, A., Yi, C., Liu, X., and Zhang, Y. (2021). Identification and evaluation of suitable reference genes for RT-qPCR analysis in *Hippodamia variegata* (Coleoptera: Coccinellidae) under different biotic and abiotic conditions. *Front. Physiol.* 12:669510. doi: 10.3389/fphys.2021.669510

Xu, J., Roy, A., and Palli, S. R. (2018). CREB-binding protein plays key roles in juvenile hormone action in the red flour beetle, *Tribolium Castaneum*. *Sci. Rep*. 8:1426. doi: 10.1038/s41598-018-30083-8

Yang, J., Gao, Y., Liu, Z., Lu, J., Zhang, Y., Zhang, P., et al. (2019). Selection of reference genes for RT-qPCR analysis under intrinsic conditions in the hawthorn spider mite, *Amphitetranychus viennensis* (Acarina: Tetranychidae). *Front. Physiol.* 10:1427. doi: 10.3389/fphys.2019.01427

Zhang, S., An, S., Li, Z., Wu, F., Yang, Q., Liu, Y., et al. (2015). Identification and validation of reference genes for normalization of gene expression analysis using qRT-PCR in Helicoverpa armigera (Lepidoptera: Noctuidae). *Gene* 555, 393–402. doi: 10.1016/j.gene.2014.11.038

Conflict of Interest: The authors declare that the research was conducted in the absence of any commercial or financial relationships that could be construed as a potential conflict of interest.

Publisher's Note: All claims expressed in this article are solely those of the authors and do not necessarily represent those of their affiliated organizations, or those of the publisher, the editors and the reviewers. Any product that may be evaluated in this article, or claim that may be made by its manufacturer, is not guaranteed or endorsed by the publisher.

frontiers in Physiology

ORIGINAL RESEARCH
published: 04 January 2022
doi: 10.3389/fphys.2021.759370

Binding Pattern Reconstructions of FGF-FGFR Budding-Inducing Signaling in Reef-Building Corals

Zhuojun Guo[1], Xin Liao[2], J.-Y. Chen[3], Chunpeng He[1] and Zuhong Lu[1]**

[1] State Key Laboratory of Bioelectronics, School of Biological Science and Medical Engineering, Southeast University, Nanjing, China, [2] Guangxi Key Lab of Mangrove Conservation and Utilization, Guangxi Mangrove Research Center, Beihai, China, [3] Nanjing Institute of Geology and Paleontology, Nanjing, China

Reef-building corals play an important role in marine ecosystems. However, owing to climate change, ocean acidification, and predation by invasive crown-of-thorns starfish, these corals are declining. As marine animals comprise polyps, reproduction by asexual budding is pivotal in scleractinian coral growth. The fibroblast growth factor (FGF) signaling pathway is essential in coral budding morphogenesis. Here, we sequenced the full-length transcriptomes of four common and frequently dominant reef-building corals and screened out the budding-related FGF and FGFR genes. Thereafter, three-dimensional (3D) models of FGF and FGFR proteins as well as FGF-FGFR binding models were reconstructed. Based on our findings, the FGF8-FGFR3 binding models in *Pocillopora damicornis*, *Montipora capricornis*, and *Acropora muricata* are typical receptor tyrosine kinase-signaling pathways that are similar to the Kringelchen (FGFR) in hydra. However, in *P. verrucosa*, FGF8 is not the FGFR3 ligand, which is found in other hydrozoan animals, and its FGFR3 must be activated by other tyrosine kinase-type ligands. Overall, this study provides background on the potentially budding propagation signaling pathway activated by the applications of biological agents in reef-building coral culture that could aid in the future restoration of coral reefs.

Keywords: reef-building coral, budding reproduction, receptor tyrosine kinase, full-length transcriptome, FGF-FGFR binding models

OPEN ACCESS

Edited by:
Pamela Imperadore, Zoological Station Anton Dohrn, Italy

Reviewed by:
Bharat Bhusan Patnaik, Fakir Mohan University, India
Rossella Annunziata, Zoological Station Anton Dohrn, Italy

****Correspondence:***
Chunpeng He
cphe@seu.edu.cn
Zuhong Lu
zhlu@seu.edu.cn

Specialty section:
This article was submitted to Invertebrate Physiology, a section of the journal Frontiers in Physiology

Received: *16 August 2021*
Accepted: *30 November 2021*
Published: *04 January 2022*

Citation:
Guo Z, Liao X, Chen J.-Y, He C and Lu Z (2022) Binding Pattern Reconstructions of FGF-FGFR Budding-Inducing Signaling in Reef-Building Corals. Front. Physiol. 12:759370. doi: 10.3389/fphys.2021.759370

INTRODUCTION

Coral reefs mainly comprise large numbers of calcium carbonate skeletons produced by scleractinian corals. Coral reefs also serve as a living environment for more than 30% of marine animals and plants (Odum and Odum, 1955; Yu, 2012). Owing to biodiversity and efficient nutrient recycling, coral reefs can affect the physical and ecological conditions of surrounding ocean areas (Connell, 1978). Recently, due to global warming, changes in the physicochemical environment of the ocean, and massive encroachment of the predatory crown-of-thorns starfish (COTS), coral reefs are sharply declining (Moberg and Folke, 1999; Wilson et al., 2006; Nakamura et al., 2014; Reimer et al., 2019; Magel et al., 2020). Currently, scleractinian coral populations are beginning to display features similar to those exhibited during the last mass extinction, such as population shrinkage, the transplanting of colonies to the aphotic zone, and zygote dormancy (Dishon et al., 2020). Thus, determining how to promote the growth activity of reef-building corals is key to coral reef ecological restoration.

The hydra body plan is one of the two basic body plan types in the cnidaria. Anthozoa, including all neontological reef-building corals, have this body type (Kraus et al., 2015;

D'Ambra and Lauritano, 2020). Asexual reproduction by budding is a distinctive feature of hydrozoan animals, and is particularly important in maintaining the general skeletal growth of reef-building corals (Otto and Campbell, 1977). Reproduction by budding produces "clones" without going through the embryogenesis stage, and its morphogenesis is controlled by a cascade-inducing signaling pathway (Odum and Odum, 1955). Among these inducing signals, fibroblast growth factors (FGFs) play an important role in budding morphogenesis. The fibroblast growth factor receptor (FGFR) is a typically classic transmembrane dimer receptor activated by FGFs, insulin growth factors (IGFs), and insulin, etc., and belongs to the large class of receptor tyrosine kinases. Tyrosine kinases are enzymes that can transfer a phosphate group from ATP to the tyrosine residues of specific proteins to turn many cellular functions on or off, such as cell proliferation (Weiner and Zagzag, 2000; Lemmon and Schlessinger, 2010; Cadena and Gill, 2015; Ornitz and Itoh, 2015). During bud detachment, FGFR (Kringelchen) is the earliest gene demarcating the parent-bud boundary at the birth site of a new bud (Sudhop et al., 2004; Böttger and Hassel, 2012; Holz et al., 2017; Suryawanshi et al., 2020). FGF signaling molecules are also essential for bud growth as they contribute to tissue development (Lange et al., 2014; Chuang and Mitarai, 2020), including forming the endothelial system, patterning the oral-aboral axis, building the nervous system, etc., (Sudhop et al., 2004; Böttger and Hassel, 2012; Turwankar and Ghaskadbi, 2019). The FGF pathway is conserved at both the amino acid and structural levels. Further, all members of this family share a conserved core region/FGF domain that shows 30–60% sequence similarity (Krishnapati and Ghaskadbi, 2013; Ornitz and Itoh, 2015). Mapping the cell movements and changes in shape during the sprouting process has revealed that FGF and FGFR are used repeatedly to control branch budding and outgrowth (Savage et al., 1993; Tanaka and Gann, 1995; Böttger and Hassel, 2012; Krishnapati and Ghaskadbi, 2013; Tee et al., 2013; Ghaskadbi, 2020). Such findings indicate that from early metazoans to higher vertebrates, FGFs and FGFRs in the budding process are conserved in signaling pathway and functions. Reef-building corals show significant activation of the FGF signaling pathways during induction of polyp bail-out (Wecker et al., 2018; Chuang and Mitarai, 2020). These potential biological functions reveal that budding-inducing signals are crucial to the maintenance of the growth activity of hydrozoan animals. Currently, within the context of population decline of reef-building corals, offering external assistance to budding *via* budding-inducing proteins, such as FGFs, is a potential method for sustaining those populations.

Although reef-building coral transcriptomes have been sequenced by the Illumina platform, issues with short and error splicing triggered by Illumina sequencing can occur, as well as issues caused by individual amplification of target genes, which occurred during the early days of polymerase chain reactions and Sanger sequencing (Rhoads and Au, 2015; Lu et al., 2016; van Dijk et al., 2018). PacBio Sequel II sequencing technology can overcome the limitations of Illumina sequencing technology. To precisely identify the FGF-FGFR binding model in reef-building corals, we sequenced the full-length transcriptomes of four common and frequently dominant reef-building corals, including *Pocillopora damicornis*, *P. verrucosa*, *Montipora capricomis*, and *Acropora muricata*, using the PacBio Sequel II platform, screening out related FGFs and FGFRs genes by Nr, Nt, Pfam, KOG, Swiss-Prot, GO, and KEGG annotations, coding sequence predictions, and phylogenetic tree analyses. FGF and FGFR tertiary structures were reconstructed using the trRosetta algorithm and MOE software (Chemical Computing Group Inc., Montreal, Quebec, Canada). FGF-FGFR binding models were reconstructed with the ClusPro v2.0 software package. Illustrating the FGF-FGFR binding models in this manner can guide the generation of biological agents that are used to activate this signaling pathway and promote the budding of reef building corals, ultimately aiding in the recovery of marine ecosystems.

MATERIALS AND METHODS

Ethics

All coral samples were collected and processed in accordance with local laws for invertebrate protection.

Specimen Collection

The species in our study were collected from the Xisha Islands in the South China Sea (latitude 15°40′–17°10′ north, longitude 111°–113° east). All samples collected in this study were retrieved from the newly budded branches.

Coral Culture System

We used three sample replicates from the same newly budded branch for library construction and sequencing. The coral samples were cultured in our laboratory coral tank with conditions conforming to the environment of their habitat. All species were raised in a RedSea® tank (redsea575, Red Sea Aquatics Ltd.) at 26C and 1.025 salinity (Red Sea Aquatics Ltd.). The physical conditions of the coral culture system are as follows: three coral lamps (AI®, Red Sea Aquatics Ltd.), a protein skimmer (regal250s, Reef Octopus), a water chiller (tk1000, TECO Ltd.), two wave devices (VorTechTM MP40, EcoTech Marine Ltd.), and a calcium reactor (Calreact 200, Reef Octopus).

RNA Extraction

All RNA extraction procedures were carried out according to the manufacturer's instructions. Total RNA was isolated with TRIzol LS Reagent (Thermo Fisher Scientific, 10296028) and treated with DNase I (Thermo Fisher Scientific, 18068015). High-quality mRNA was isolated with a FastTrack MAG Maxi mRNA Isolation Kit (Thermo Fisher Scientific, K1580-02). Samples were separated from healthy *P. damicornis*, *P. verrucosa*, *M. capricomis*, and *A. muricata* to ensure that enough high-quality RNA (>10 μg) could be obtained for a full-length cDNA transcriptome library.

Library Construction

Before establishing the library, the quality of the total RNA was determined. Agarose gel electrophoresis was used to analyze

the degree of degradation of RNA and possible contamination. A Nanodrop nucleic acid quantifier was used to detect the purity of RNA (OD260/280 ratio), a Qubit RNA assay was used to accurately quantify the RNA concentration, and an Agilent 2200 TapeStation was used to accurately detect the integrity of the RNA. The Clontech SMARTer® PCR cDNA Synthesis Kit (Clontech Laboratories, 634926) and the BluePippin Size Selection System protocol, as described by Pacific Biosciences (PN 100-092-800-03), were used to prepare the Iso-Seq library according to the Isoform Sequencing protocol (Iso-Seq).

Sequencing and Data Processing

We used the PacBio Sequel II platform with single molecular real time (SMRT) sequencing technology and SMRTlink v7.0 software (minLength 50; maxLength 15,000; minPasses 1) to process sequencing samples. After polymer read bases were performed (Chin et al., 2016), the subreads.bam files were obtained by removing the joint and the original offline data, where the length was less than 50 bp. The circular consensus sequences (CCSs) were obtained using the subreads.bam file through the CCS algorithm, which is self-correcting for single molecule multiple sequencing. Consequently, the full-length-non-chimera (FLNC) and non-full-length (nFL; non-chimera) sequences were identified by determining whether CCSs contained 5′-primer, 3′-primer, and poly-A. FLNC sequences of the same transcript were clustered by a hierarchical n * log (n) algorithm to obtain consensus sequences. The corrected consensus reads were polished from consensus sequences (Arrow polishing) using LoRDEC v0.7 software and the RNA-seq data sequenced by the Illumina HiSeq X Ten platform (Salmela and Rivals, 2014). Using CD-HIT software (-c 0.95 -T 6 -G 0 -aL 0.00 -aS 0.99), all redundancies were removed in corrected consensus reads to acquire final full-length transcripts and unigenes for subsequent bioinformatics analysis (Fu et al., 2012).

Gene Functional Annotation

Gene function was annotated using the following databases: Nr (NCBI non-redundant protein sequences) (Li et al., 2002), Nt (NCBI non-redundant nucleotide sequences), Pfam (Protein family), KOG (Clusters of Orthologous Groups of proteins) (Tatusov et al., 2003), Swiss-Prot (a manually annotated and reviewed protein sequence database) (Bairoch and Apweiler, 2000), GO (Gene Ontology) (Ashburner et al., 2000), and KEGG (Kyoto Encyclopedia of Genes and Genomes) (Kanehisa et al., 2004). We use BLAST 2.7.1+ (Altschul et al., 1990) in NCBI to set the *e*-value "1e−5" for Nt database analysis; Diamond v0.8.36 BLASTX software to set the *e*-value to "1e−5" for Nr, KOG, Swiss-Prot, and KEGG database analyses; and the HMMER 3.1 package for Pfam database analysis.

Coding Sequence Analysis

Coding sequences were predicted by ANGEL v2.4 software in fault-tolerant mode, which maximizes the limited information from the input sequence to predict the coding sequence (Shimizu et al., 2006).

Phylogenetic Analysis

The amino acid sequences were constructed into phylogenetic trees using MEGA X software by the neighbor-joining (NJ) method (Saitou and Nei, 1987; Kumar et al., 2018). The evolutionary history of the analyzed taxa is represented by the bootstrap consensus tree drawn from 1,000 replicates (Felsenstein, 1985). The percentage of replicate trees next to the branches in which the associated taxa are together is presented. The Poisson correction method was used to compute the evolutionary distances in units of the number of amino acid substitutions per site (Zuckerkandl and Pauling, 1965). A matrix of pairwise distances was estimated by using the JTT model and then selecting the topology with the highest log likelihood value.

Homological Gene Selection

To precisely construct the phylogenetic trees, the FGF8 protein sequences of *P. damicornis* (Pd_FGF8), *P. verrucosa* (Pv_FGF8), *M. capricomis* (Mc_FGF8), *A. muricata* (Am_FGF8), *Hydra vulgaris* (XP_012554564.1), *Orbicella faveolata* (XP_020606946.1), *A. millepora* (XP_029189212.1), *A. digitifera* (XP_015756877.1), *Nematostella vectensis* (XP_032240538.1), *Actinia tenebrosa* (XP_031555139.1), *Stylophora pistillata* (XP_022781642.1), *Exaiptasia diaphana* (XP_020913607.1), *Denticeps clupeoides* (XP_028829118.1), *Trematomus bernacchii* (XP_033987865.1), *Kryptolebias marmoratus* (XP_017277162.1), *Astatotilapia calliptera* (XP_026046852.1), *Toxotes jaculatrix* (XP_040905908.1), *Melanotaenia boesemani* (XP_041865608.1), *Perca flavescens* (XP_028459575.1), *Etheostoma cragini* (XP_034754871.1), *E. spectabile* (XP_032367422.1), *Perca fluviatilis* (XP_039639039.1), *Cynoglossus semilaevis* (XP_016892646.1), *Sander lucioperca* (XP_016892646.1), *Maylandia zebra* (XP_004573854.1), *Cottoperca gobio* (XP_029305840.1), *Carcharodon carcharias* (XP_041065901.1), *Scyliorhinus canicular* (XP_038678019.1) and *Rhincodon typus* (XP_020371706.1) were selected and the FGFR protein sequences of *P. damicornis* (Pd_FGFR3), *P. verrucosa* (Pv_FGFR3), *M. capricomis* (Mc_FGFR3) *A. muricata* (Am_FGFR3), *H. vulgaris* (NP_001296694.1), *S. pistillata* (XP_022781630.1), *A. millepora* (XP_029189174.1), *A. digitifera* (XP_015756845.1), *N. vectensis* (XP_032231385.1), *E. diaphana* (KXJ23083.1), and *O. faveolata* (XP_020606906.1) were selected by setting the *e*-value threshold in BLAST to 1e−10 and then selecting FGFR sequences of which the species are Cnidarians and FGF sequences where species present an *e*-value lower than 1e−10.

Prediction of the Protein Tertiary Structure

The FGF8 tertiary structures were predicted using the trRosetta algorithm (Yang et al., 2020). trRosetta is an algorithm for fast and accurate *de novo* protein structure prediction that builds the protein structure based on direct energy minimization with a

restrained Rosetta. The restraints include inter-residue distance and orientation distributions, predicted by a deep residual neural network.

The template crystal FGFR3 structures were identified through BLAST (Camacho et al., 2009) and downloaded from the RCSB Protein Data Bank (PDB ID: 6PNX for Pd_FGFR3, Mc_FGFR3 and Am_FGFR3, 4ZSA for Pv_FGFR3). Homology modeling was conducted in MOE (Maier and Labute, 2014; Kandathil et al., 2019; Molecular Operating Environment [Moe], 2019). The protonation state of the protein and the orientation of the hydrogens were optimized by LigX at a pH of 7.0 and temperature of 26.85C. First, the target sequence was aligned to the template sequence, and ten independent intermediate models were built. These different homology models were the result of the permutational selection of different loop candidates and side chain rotamers. Thereafter, the intermediate model that scored the best, according to the GB/VI scoring function, was selected as the final model, and subjected to further energy minimization using the AMBER12/EHT force field.

Molecular Docking

Protein-protein docking with the ClusPro server (Kozakov et al., 2017) was used for molecular docking simulations of four complexes: Pd_FGFR3 with Pd_FGF8, Pv_FGFR3 with Pv_FGF8, Mc_FGFR3 with Mc_FGF8, and Am_FGFR3 with Am_FGF8. For protein docking, the smaller protein (a smaller number of residues) is often set as the ligand and the larger protein is often set as the receptor. The ligand was rotated 70,000 times. For each rotation, the ligand was translated in the x, y, and z axes relative to the receptor on a grid. One translation with the best score was selected from each rotation. Of the 70,000 rotations, 1,000 rotation/translation combinations that had the lowest scores were selected. Thereafter, a greedy clustering of these 1,000 ligand positions with a 9 Å C-alpha root mean squared deviation (RMSD) radius was performed to identify the ligand positions with the most "neighbors" within 9 Å (i.e., cluster centers). The top ten cluster centers with the most cluster members were then retrieved and individually inspected visually. The intermolecular contacts from the most probable position were further evaluated.

RESULTS

Full-Length Transcriptome Sequencing and Data Processing of Four Species of Coral

The SMRT-sequencing was performed with the PacBio Sequel II platform to acquire offline polymer read bases of full-length transcriptomes using SMRTlink v7.0 software (Methods). The offline polymer read bases of *P. damicornis*, *P. verrucosa*, *M. capricomis*, and *A. muricata* samples were 44.33G, 42.67G, 41.63G, and 27.8G, respectively. The polymer read bases, subreads, CCSs, FLNCs, consensus sequences, corrected consensus reads, and unigenes are shown in **Table 1**, which also contains the information revealed in subsequent analyses.

The full-length transcriptomes were annotated with Nr, Nt, Pfam, KOG, Swiss-Prot, GO, and KEGG databases, and the related unigene statistics are shown in **Table 2**. In protein-related databases, approximately 90% of the unigenes of investigated corals are annotated in Nr, which is the basic protein primary sequence database. Over 60% of the unigenes are annotated in Pfam, a conserved domain database. Over 70% of the unigenes are annotated in Swiss-Prot, a manually screened protein sequence database. As shown in **Supplementary Figures 1–4**, the Nr unigene annotations revealed that the genes of the four investigated corals are closest to the cnidarians *A. digitifera*, *Exaiptasia pallida*, and *N. vectensis*, with over 80% unigene overlap. Such findings indicate the accuracy and credibility of the annotation results. The coding sequences (CDS) were analyzed with ANGEL v2.4 software, and the ANGEL.pep files of the protein profiles were subsequently obtained (**Supplementary Material 2**) (Methods). Based on the Nr results and ANGEL.pep files, the FGF-FGFR budding inducing signals were identified in the four corals studied (Methods).

Phylogenetic Analysis of FGF-FGFR Budding Inducing Signals

In hydrozoan animals previously studied, the receptor tyrosine kinase related to the induction of polyp budding morphogenesis is FGFR3 (Kringelchen), and its general ligand is FGF8/17/18. To explore the evolutionarily homologous protein sequences

TABLE 1 | Sequencing data statistics of four full-length coral transcriptomes.

Sample name	*P. damicornis*	*P. verrucosa*	*M. capricomis*	*A. muricata*
Polymerase read base (G)	44.33	27.8	41.63	42.67
Subread base (G)	42.84	26.52	40.29	41.56
Subread (number)	19,729,634	16,171,363	17,878,457	14,983,676
Average subread length (Nt)	2,172	1,641	2,254	2,774
CCS (number)	602,185	292,565	634,369	646,298
FLNC (number)	463,766	249,577	452,189	496,518
Consensus read (number)	38,663	24,860	35,293	41,489
Corrected consensus (number)	38,663	24,860	35,293	41,489
Unigene (number)	22,408	13,173	20,263	23,499

TABLE 2 | Annotation result statistics of four full-length coral transcriptomes.

Sample name	*P. damicornis*	*P. verrucosa*	*M. capricomis*	*A. muricata*
NR (number)	20,749	11,787	19,149	22,668
NT (number)	6,052	3,299	13,562	22,826
KOG (number)	13,861	7,749	12,832	15,138
Swiss-Prot (number)	16,759	9,360	15,492	18,466
GO (number)	15,456	8,380	14,033	16,546
Pfam (number)	15,456	8,380	14,033	16,546
KEGG (number)	19,721	11,069	18,191	21,515

of FGF and FGFR in four corals, phylogenetic trees were constructed using MEGA X based on multiple sequence alignments, according to the FGF8 and FGFR3 protein sequence results of four corals in the ANGEL.pep files and NCBI database (**Figures 1**, **2**). Based on the phylogenetic trees, both FGF8 and FGFR3 are widely distributed in hydrozoan animals, and had evolved from the last common ancestor with the primary hydra body plan. After phylogenetic analysis, the FGF8 and FGFR3 protein sequences of the four corals were precisely determined, namely: Pd_FGF8, Pv_FGF8, Mc_FGF8, Am_FGF8, Pd_FGFR3, Pv_FGFR3, Mc_FGFR3, and Am_FGFR3 (**Supplementary Data**). Based on these definitive protein primary sequences, 3D modeling reconstructions were performed.

3D Modeling Reconstructions of FGF8 and FGFR3

The modeling results of Pd_FGF8, Pv_FGF8, Mc_FGF8, and Am_ FGF8 are depicted in **Figure 3** and **Supplementary Figure 5**. Protein structures revealed standard FGF features (**Figure 3**) while Ramachandran plots demonstrated

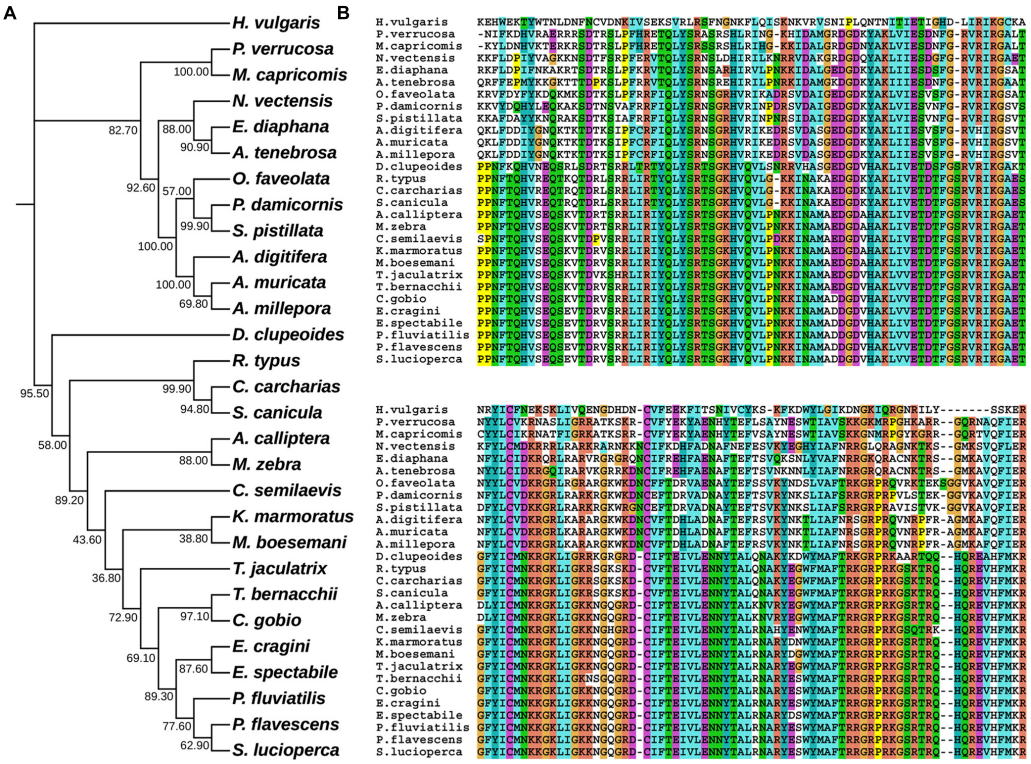

FIGURE 1 | Evolutionary phylogenetic tree of FGF8s. **(A)** Bootstrap consensus tree reconstructed with MEGA X using neighbor-joining with default settings. The values beside the branches represent the percentage of time that a node was supported over 1,000 bootstrap replications. **(B)** Partially conserved domains of FGF genes.

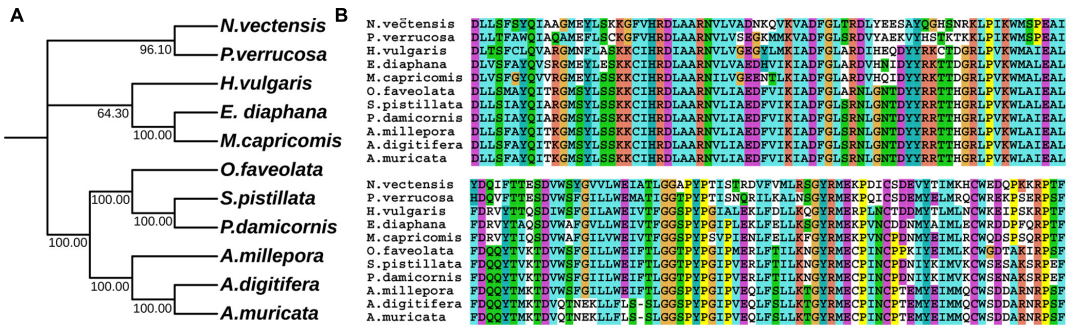

FIGURE 2 | Evolutionary phylogenetic tree of FGFR3s. **(A)** Bootstrap consensus tree reconstructed with MEGAX using neighbor-joining with default settings. The values beside the branches represent the percentage of time that a node was supported over 1,000 bootstrap replications. **(B)** Partially conserved domains of FGFR3 genes.

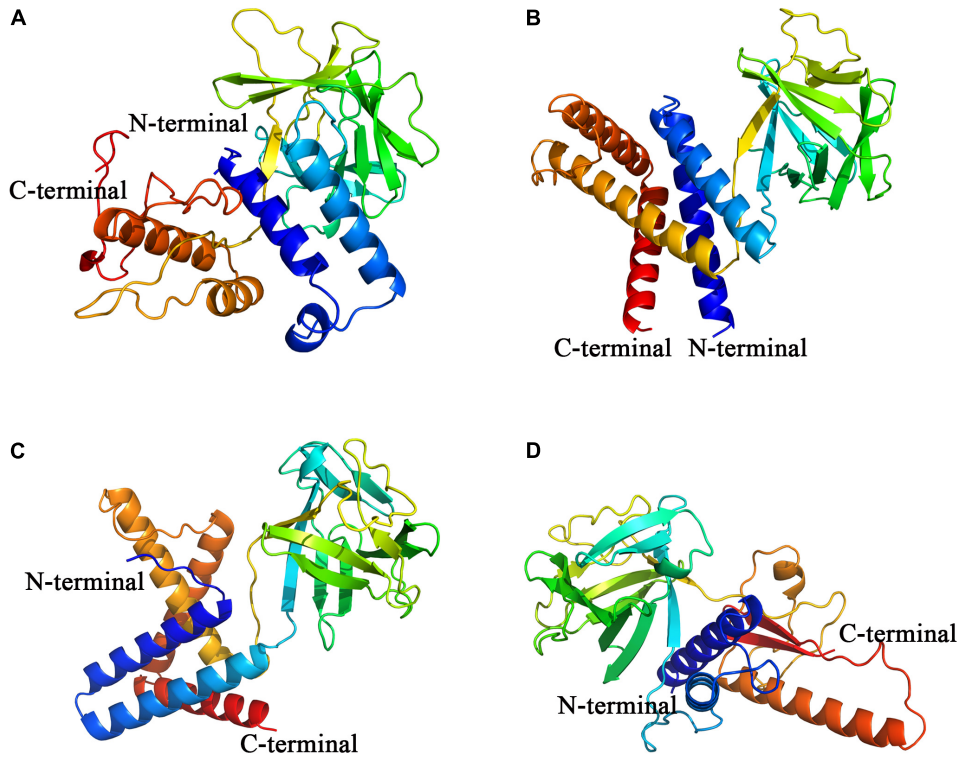

FIGURE 3 | Constructed *de novo* models of coral FGF8 proteins. **(A–D)** Are *de novo* FGF8 models of *P. damicornis*, *P. verrucosa*, *M. capricomis* and *A. muricata*, respectively. C-terminals are marked in red and N-terminals are marked in blue.

that 99% of the residues exist in allowed regions, indicating that the 3D structures of the FGF8 model are reasonable (**Supplementary Figure 5**). Pd_FGF8 has one main beta strand region and four alpha helix regions (**Figure 3A**), while Pv_FGF8 has one main beta strand region and five alpha helix regions (**Figure 3B**). Further, the structure of Mc_FGF8 has one main beta strand region and five alpha helix regions (**Figure 3C**), while Am_ FGF8 has two main beta strand regions and two alpha helix regions (**Figure 3D**).

Fibroblast growth factor receptors, including FGFR3, exist as a type of cellular transmembrane dimer. Dimer modeling results for Pd_FGFR3, Pv_FGFR3, Mc_FGFR3, and Am_FGFR3 are depicted in **Figure 4** and **Supplementary Figure 6**. **Figure 4** illustrates that the FGFRs of the four investigated reef-building corals are a type of classic receptor tyrosine kinase. Further, Ramachandran plots for FGFR3s revealed that 99% of the residues exist in allowed regions (**Supplementary Figure 6**). Structural analyses of the FGFR3 dimer modeling results are shown in **Figures 5, 6** and **Supplementary Figures 7–9**. The average RMSD values of the 3D structures overlapping with template structures for Pd_FGFR3, Pv_FGFR3, Mc_FGFR3, and Am_FGFR3 are 0.323Å, 0.214Å, 0.116Å, and 0.260Å. Both constructed dimer models and their template structures were found to have the same alpha helix and beta strand regions (**Figure 5**). The overall identities of the amino acid sequences for Pd_FGFR3, Pv_FGFR3, Mc_FGFR3, and Am_FGFR3 are 59.08, 36.57, 61.94, and 54.13% by BLAST, respectively (**Figure 6** and **Supplementary Figures 7–9**).

Binding Modes of Coral FGF8 and FGFR3

To investigate the binding mode of FGF8s and FGFR3s, docking simulation studies were carried out. The interaction between Pd_FGFR3 and Pd_FGF8 is shown in **Figures 7A,B**. The contact list between Pd_FGFR3 and Pd_FGF8 is shown in **Figure 7C** and **Supplementary Table 1**. Docking simulation studies indicate that amino acid residues of D310, F312, E313, D317, E318, K319, E321, Q348, T352, D369, E380, E384, and Q401 in chain A, and E335, K364, E365, and E371 in chain B bind with R67, R71, D87, R163, R168, R186, K201, E206, K224, R227, R231, S262, R264, S267, and R277 in Pd_FGF8 through salt bridges and hydrogen bond interactions (**Figure 7C**). A total of 279 residues were found in Pd_FGF8, of which fifteen interact with the Pd_FGFR3 dimer. Of these fifteen residues, Arg163, Arg168, Arg231, Arg67, and Lys224 interact with Glu318, Glu321, Thr352, Gln348, Phe312, Glu313, Gln401, Glu321, Glu380, and Glu384 in Pd_FGFR3 chain A by one binding to two models. Arg186, Arg227, Arg277, and Ser262 interact with Glu318, Asp317, Asp310, and Asp369 in Pd_FGFR3 chain A by one binding to one model. Arg71 and Asp87 simultaneously interact with Lys319 in Pd_FGFR3 chain A. Arg264, Glu206, Lys201, and Ser267 interact with Glu335, Glu365, Lys364, and Glu371 in Pd_FGFR3 chain B by one binding to one model (**Supplementary Table 1**).

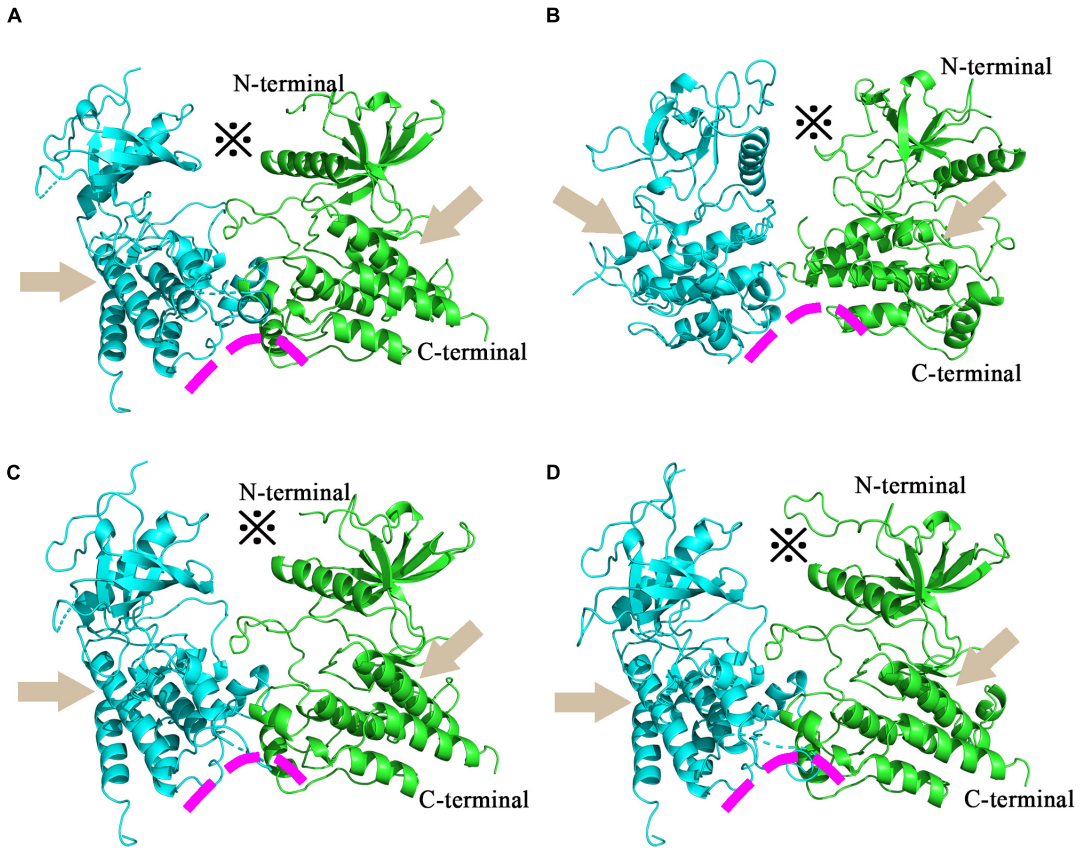

FIGURE 4 | Homology models of coral FGFR3 dimers. Homology models of *P. damicorni*, *P. verrucosa*, *M. capricomis* and *A. muricata* FGFR3 dimers are shown in panels **(A–D)**. These reconstructions illustrate that the FGFR3s of the four corals are all classic receptor tyrosine kinases with standard molecular architectural features, including extracellular ligand-binding domains (※), transmembrane helixes (arrows), and juxta-membrane regulatory regions (arcs).

The interaction between Pv_FGFR3 and Pv_FGF8 is shown in **Figures 8A,B**. The contact list between Pv_FGFR3 and Pv_FGF8 is shown in **Supplementary Table 2**. Docking simulation studies indicate that the amino acid residues of Q259, D262, P263, E299, E331, E332, E335, E336, E339, K342, R485, S508, D510, Y512, D537, and Q538 in chain A bind with R28, R62, R65, D81, Y139, K156, K157, K165, R167, R168, R171, K238, R242, and R249 in Pv_FGF8 through salt bridges and hydrogen bond interactions (**Figure 8C**). FGF8 only connects to residues in FGFR chain A and has no chemical connection to chain B.

The interaction between Mc_FGFR3 and Mc_FGF8 is shown in **Supplementary Figures 10A,B**. The contact list between Mc_FGFR3 and Mc_FGF8 is shown in **Supplementary Table 3**. Docking simulation studies indicate that the amino acid residues of E487, E489, D545, and R669 in chain A, and E487, R500, R516, L539, H546, D550, Y668, K670, and R675 in chain B bind with M1, Y12, Q24, Q29, R44, A211, K212, E214, D215, K218, D219, Y230, K231, R234, Q235, and R242 in Mc_FGF8 through salt bridges and hydrogen bond interactions (**Supplementary Figure 10C**). FGF8 is linked to FGFR chain A by eight residues, one of which is linked to two residues of FGFR chain A on position 234 of the residue (Arg234) and FGFR chain B by eleven residues. The 24th residue (Gln24) in FGF is linked to the 31st residue and the 54th residue of FGFR chain B. FGFR is also connected with two or more residues in FGF through three residues in chain A and three residues in chain B to further strengthen the structural stability of the receptor ligand.

The interaction between Am_FGFR3 and Am_FGF8 is depicted in **Supplementary Figures 11A,B**. The contact list between Am_FGFR3 and Am_FGF8 is shown in **Supplementary Table 4**. The docking simulation studies indicate that the amino acid residues of Y301, D303, and D307 in chain A, and T300, D303, D304, E360, S363, D364, and E366 in chain B bind with R162, R185, Y192, K193, R195, R196, K198, R212, R213, K214, T216, Y217, and L274 in Am_FGF8 through salt bridges and hydrogen bond interactions (**Supplementary Figure 11C**). The extracellular ligand-binding domains in Am_FGFR3 interact with Am_FGF8 through three residues in chain A and eight residues in chain B.

In summary, our research suggests that the FGF8-FGFR3 binding patterns in *A. muricata*, *P. damicornis*, and *M. capricomis* are typical of a receptor tyrosine kinase signaling pathway, with one FGF binding to an FGFR dimer in the active-binding region of extracellular ligand-binding domains. However, in *P. verrucosa*, the reconstruction result revealed that Pv_FGF8 only interacts with Pv_FGFR3 chain A, which is found in the middle of

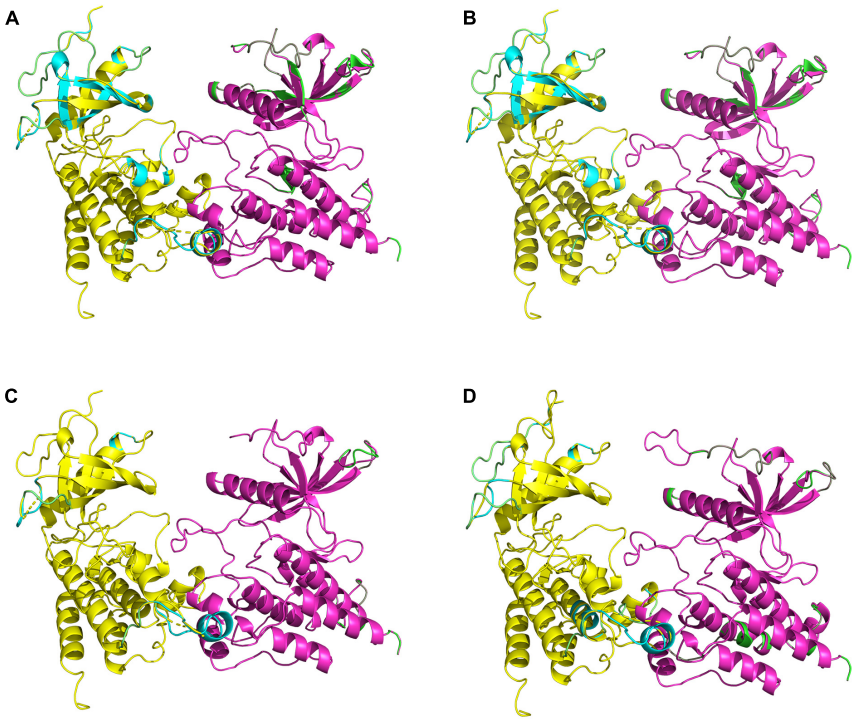

FIGURE 5 | Comparisons of homology-constructed coral FGFR3 dimers with receptor tyrosine kinase templates from the RCSB Protein Data Bank. Superposition results of FGFR3 dimer model structures and related template structures in *P. damicorni*, *P. verrucosa*, *M. capricomis*, and *A. muricata* are shown in panels **(A–D)**. The FGFR3 dimer structure is shown in yellow and purple, and the template structure is shown in green and cyan. The high degree of overlap indicates that coral FGFR3 dimers and receptor tyrosine kinase templates are highly coincident, confirming that the four coral FGFR3s are all tyrosine kinase receptors.

the lipid bilayer of the cell membrane, which is inexplicable based on real cellular processes. Such finding indicates that Pv_FGF8 is not the ligand of Pv_FGFR3; thus, it must be activated by other ligands.

DISCUSSION

Currently, the full-length transcriptome of marine organisms acquired by PacBio Sequel II sequencing technology enables researchers to directly obtain *de novo* completed unigene profile, including intact 5′UTR and 3′UTR in a more high-efficiency manner (Cheng et al., 2019). The provided data allow in-depth biological research. Further, bioinformatics researchers can also directly extract interesting gene data for phylogenetic studies. With these tools, researchers can accurately and more efficiently analyze all gene expression profile information, such as gene expression, variable splicing, gene fusion, expression regulation, CDS, and protein structure, overcoming the limitations and problems of next-generation sequencing technology (Rhoads and Au, 2015; Lu et al., 2016; van Dijk et al., 2018).

This study revealed the full-length transcriptomes and protein CDS profiles of four dominant reef-building corals. The goal of this computational study was to reconstruct the binding conformations and interactions between FGFs and FGFRs, and determine key FGF-FGFR binding patterns of reef-building corals. Based on full-length protein sequences, the results of multiple sequence alignment show that FGF and FGFR proteins in hydrozoan animals share sequence segments and features. Ramachandran plots of FGFR3s show that 99% of the residues exist in allowed regions and the RMSD values of FGFR3s are fairly low, indicating that all 3D model structures are reasonable (**Figure 6** and **Supplementary Figures 5–9**). 3D reconstructions of the FGFR dimers revealed the entire N-terminal amino acid residues exposed in the extracellular region, which was sufficient for calculating binding sites with ligands (Tavormina et al., 1995; Gupte et al., 2011). The N-terminal domain of receptor tyrosine kinase is composed of stranded β-sheets and α-helixes, and the C-terminal domain is a large cytoplasmic domain with α-helixes (Mohammadi et al., 1996; Linger et al., 2008; Trenker and Jura, 2020). As a typical receptor tyrosine kinase, the FGFR dimer has alpha-helical transmembrane domains and juxta-membrane regulatory regions found at sites where dimer structures are connected (Iwamoto et al., 2005). In our study, all reconstructed 3D FGFR3 dimers from four reef-building corals had molecular architecture features typical of tyrosine kinase receptors, including an extracellular ligand-binding domain, transmembrane helixes, and juxta-membrane regulatory regions (**Figures 4**, **5**).

Receptor tyrosine kinases become activated through autophosphorylation, which is thought to be induced through the mechanism of ligand-mediated receptor oligomerization (Ullrich and Schlessinger, 1990). Receptor activation results in a signal transduction cascade that leads to gene activation

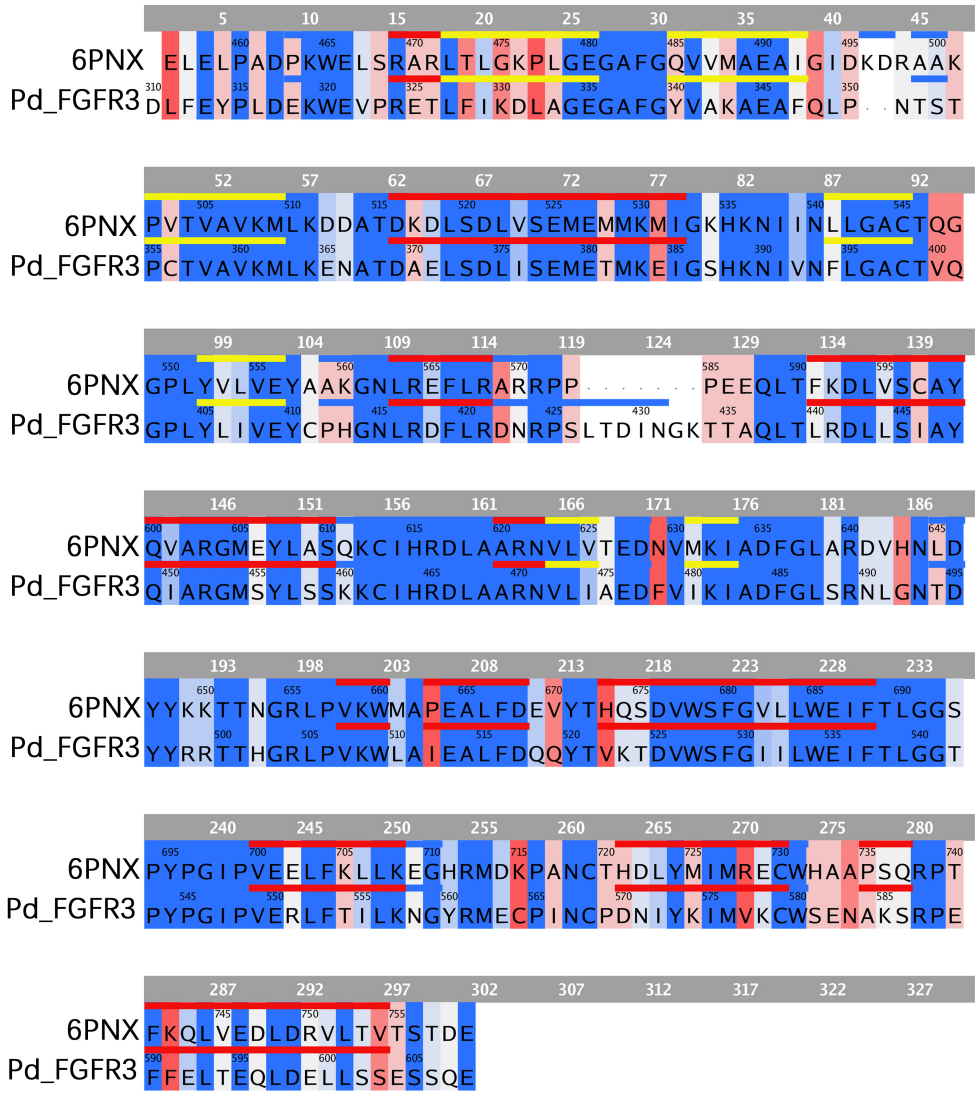

FIGURE 6 | Sequence comparison between FGFR3 in *P. damicornis* and its template. The same or similar residues are highlighted in blue and dissimilar ones are highlighted in red, with darker blue indicating more similar residues and darker red indicating more dissimilar residues. The sequences corresponding to alpha helixes and beta strands are marked with red and yellow lines, respectively. The FGFR3 dimer structure is basically consistent with the template structure.

and diverse biological responses (Johnson and Williams, 1993; Naski and Ornitz, 1998). Because the FGF8-FGFR3 binding pattern in *A. muricata*, *P. damicornis*, and *M. capricomis* belong to the pattern of a dimeric assemblage of one ligand and one receptor dimer, this type of binding pattern might be an evolutionary ancestral feature of reef-building corals inherited by most species (**Figures 7, 8** and **Supplementary Figures 10, 11**; Johnson and Williams, 1993; Stauber et al., 2000).

In this study, we sequenced and annotated the full-length transcriptomes of four common and frequently dominant reef-building corals, reconstructed their FGFR3 receptor tyrosine kinases, and found that FGF8 is the ligand of FGFR3 in *A. muricata*, *P. damicornis*, and *M. capricomis*, but not in *P. verrucosa*. These full-length transcriptomes could be exploited by other researchers to carry out phylogenetic studies as well as functional analyses. Applying controlled release of FGF8 produced on an industrial scale in the marine environment is a potential method to induce polyp survival, coral recovery, and growth, and should thus be further investigated.

Owing to this study, more knowledge regarding the FGF-FGFR binding patterns and mechanisms in reef-building corals has been gained. However, several questions remain unanswered. Although FGFs and FGFRs, which are potential budding reproduction proteins, have been identified in the four studied species, the specific mechanisms of the FGF signaling pathway in actual coral growth are still unclear. Further experiments on FGFR expression in the budding site are required to fully understand these mechanisms to enable its application to coral reef conservation and protection.

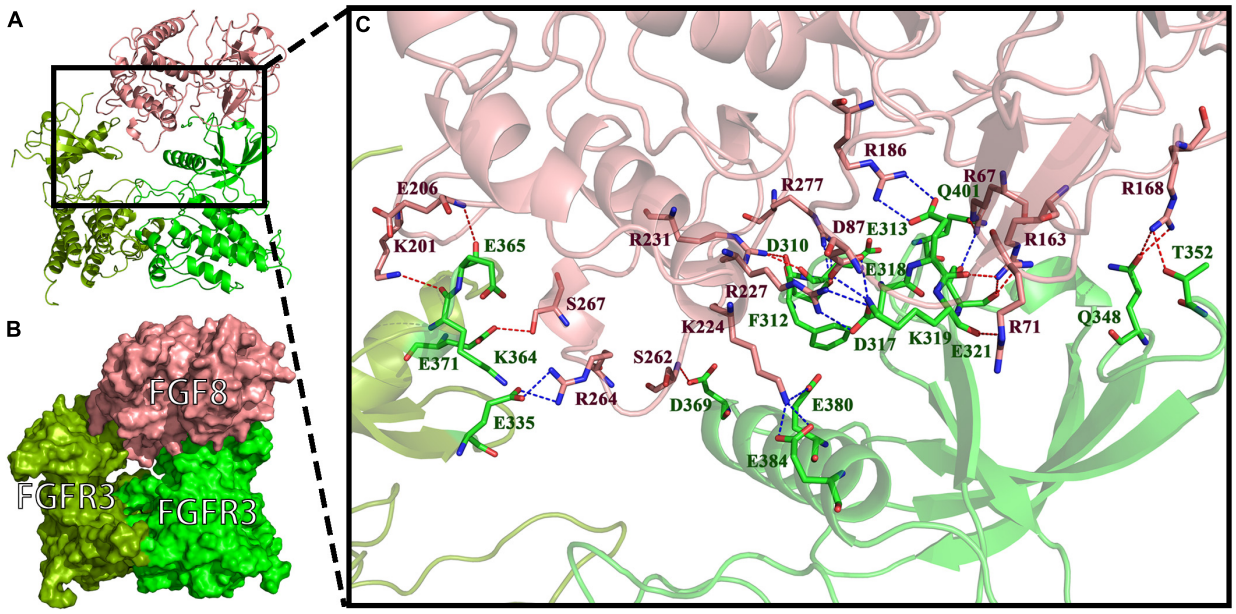

FIGURE 7 | FGF8-FGFR3 binding pattern docked by ClusPro in *P. damicornis*. **(A)** The interaction between Pd_FGF8 and Pd_FGFR3. **(B)** The surface binding model of Pd_FGF8 and Pd_FGFR3. Pd_FGFR3 chain A is bright green, Pd_FGFR3 chain B is colored pea green and Pd_FGF8 is colored pink. **(C)** Details of the interaction between Pd_FGF8 and Pd_FGFR3. The residues in Pd_FGFR3 are green, and in Pd_FGF8 are pink. The red dashes represent hydrogen bond interactions and the blue dashes represent salt bridges.

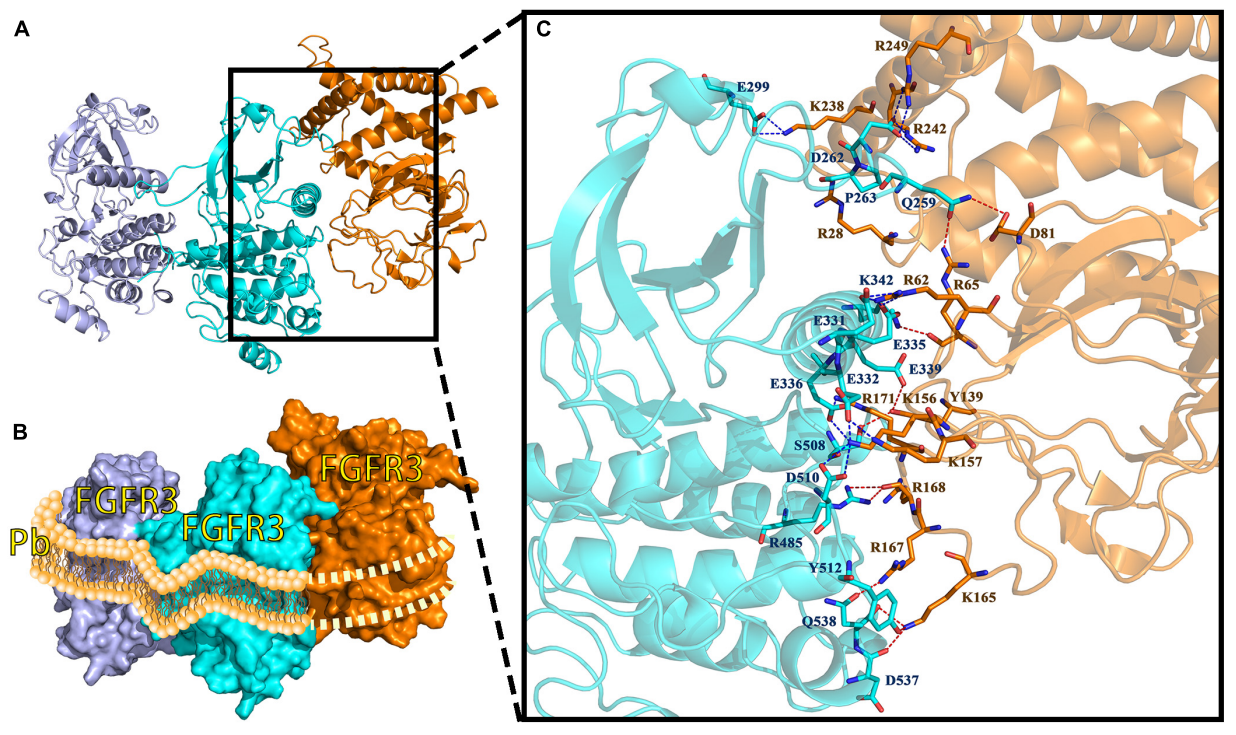

FIGURE 8 | FGF8-FGFR3 binding pattern docked by ClusPro in *P. verrucosa*. **(A)** The interaction between Pv_FGF8 and Pv_FGFR3. **(B)** Surface binding model of Pv_FGF8 and Pv_FGFR3. Pd_FGFR3 chain A is colored lightpurple, Pd-FGFR3 chain B is colored aquamarine, and Pd_FGF8 is orange. **(C)** Details of the interaction between Pv_FGF8 and Pv_FGFR3. The residues in Pv_FGFR3 are cyan, and in Pv_FGF8 they are orange. The red dashes represent hydrogen bond interactions and the blue dashes represent salt bridges. Interaction sites between FGFR3 and FGF8 occur only in FGFR3 chain A, which simultaneously falls into the lipid bilayer of the cell membrane, a situation that does not make sense. Pb, phospholipid bilayer of cell membrane.

DATA AVAILABILITY STATEMENT

The datasets presented in this study can be found in online repositories. The names of the repository/repositories and accession number(s) can be found in the article/ **Supplementary Material**.

AUTHOR CONTRIBUTIONS

ZG: experiment, writing and editing. ZL: reviewing. CH: supervision. XL: project approval. All authors contributed to the article and approved the submitted version.

FUNDING

This work was supported by the open research fund of State Key Laboratory of Bioelectronics, Southeast University (Sklb2021-k02), and open research fund program of Guangxi Key Lab of Mangrove Conservation and Utilization (Grant No. GKLMC-202002).

ACKNOWLEDGMENTS

We thank M. Zhu from the Nanjing Institute of Geology and Paleontology, CAS for scientific guidance, M. Zhu, J. Lu, and Z. Gai from the Institute of Vertebrate Paleontology and Paleoanthropology, CAS for technical and scientific guidance, Y. Loya from the Israel Academy of Sciences for scientific guidance.

SUPPLEMENTARY MATERIAL

The Supplementary Material for this article can be found online at: https://www.frontiersin.org/articles/10.3389/fphys.2021.759370/full#supplementary-material

REFERENCES

Altschul, S. F., Gish, W., Miller, W., Myers, E. W., and Lipman, D. J. (1990). Basic local alignment search tool. *J. Mol. Biol.* 215, 403–410. doi: 10.1016/S0022-2836(05)80360-2

Ashburner, M., Ball, C. A., Blake, J. A., Botstein, D., and Cherry, J. M. (2000). Gene ontology: tool for the unification of biology. the gene ontology consortium. *Nat. Genet.* 25, 25–29. doi: 10.1038/75556

Bairoch, A., and Apweiler, R. (2000). The SWISS-PROT protein sequence database and its supplement TrEMBL in 2000. *Nucleic Acids Res.* 28, 45–48. doi: 10.1093/nar/21.13.3093

Böttger, A., and Hassel, M. (2012). Hydra, a model system to trace the emergence of boundaries in developing eumetazoans. *Int. J. Dev. Biol.* 56, 583–591. doi: 10.1387/ijdb.113454ab

Cadena, D. L., and Gill, G. N. (2015). Receptor tyrosine kinases. *FASEB J.* 6, 2332–2337. doi: 10.1096/fasebj.6.6.1312047

Camacho, C., Coulouris, G., Avagyan, V., Ma, N., Papadopoulos, J., Bealer, K., et al. (2009). BLAST+: architecture and applications. *BMC Bioinformatics* 10:421. doi: 10.1186/1471-2105-10-421

Cheng, Y. W., Chen, Y. M., Zhao, Q. Q., Zhao, X., Wu, Y. R., Chen, D. Z., et al. (2019). Long read single-molecule real-time sequencing elucidates transcriptome-wide heterogeneity and complexity in esophageal squamous cells. *Front. Genet.* 10:915. doi: 10.3389/fgene.2019.00915

Chin, C. S., Peluso, P., Sedlazeck, F. J., Nattestad, M., Concepcion, G. T., Clum, A., et al. (2016). Phased diploid genome assembly with single-molecule real-time sequencing. *Nat. Methods* 13, 1050–1054. doi: 10.1038/nmeth.4035

Chuang, P. S., and Mitarai, S. (2020). Signaling pathways in the coral polyp bail-out response. *Coral Reefs* 39, 1535–1548. doi: 10.1007/s00338-020-01983-x

Connell, J. H. (1978). Diversity in tropical rain forests and coral reefs. *Science* 199, 1302–1310. doi: 10.1126/science.199.4335.1302

D'Ambra, I., and Lauritano, C. (2020). A review of toxins from Cnidaria. *Mar. Drugs* 18:507. doi: 10.3390/md18100507

Dishon, G., Grossowicz, M., Krom, M., Guy, G., Gruber, D. F., and Tchernov, D. (2020). Evolutionary traits that enable Scleractinian corals to survive mass extinction events. *Sci. Rep.* 10, 3903–3903. doi: 10.1038/s41598-020-60605-2

Felsenstein, J. (1985). Confidence limits on phylogenies: an approach using the bootstrap. *Evolution* 39, 783–791. doi: 10.1111/j.1558-5646

Fu, L., Niu, B., Zhu, Z., Wu, S., and Li, W. (2012). CD-HIT: accelerated for clustering the next-generation sequencing data. *Bioinformatics* 28, 3150–3152. doi: 10.1093/bioinformatics/bts565

Ghaskadbi, S. (2020). Cell signaling molecules in hydra: insights into evolutionarily ancient functions of signaling pathways. *Int. J. Dev. Biol.* 64, 141–149. doi: 10.1387/ijdb.190243sg

Gupte, J., Li, Y., Wu, X., Weiszmann, J., Hecht, R., Lemon, B., et al. (2011). The FGFR D3 domain determines receptor selectivity for fibroblast growth factor 21. *J. Mol. Biol.* 408, 491–502. doi: 10.1016/j.jmb.2011.03.003

Holz, O., Apel, D., Steinmetz, P., Lange, E., Hopfenmüller, S., Ohler, K., et al. (2017). Bud detachment in hydra requires activation of fibroblast growth factor receptor and a Rho-ROCK-myosin II signaling pathway to ensure formation of a basal constriction. *Dev. Dyn.* 246, 502–516. doi: 10.1002/dvdy.24508

Iwamoto, T., You, M., Li, E., Spangler, J., Tomich, J. M., and Hristova, K. (2005). Synthesis and initial characterization of FGFR3 transmembrane domain: consequences of sequence modifications. *Biochim. Biophys. Acta* 1668, 240–247. doi: 10.1016/j.bbamem.2004.12.012

Johnson, D. E., and Williams, L. T. (1993). Structural and functional diversity in the FGF receptor multigene family. *Adv. Cancer. Res.* 60, 1–41. doi: 10.1016/s0065-230x(08)60821-0

Kandathil, S. M., Greener, J. G., and Jones, D. T. (2019). Prediction of interresidue contacts with DeepMetaPSICOV in CASP13. *Proteins* 87, 1092–1099. doi: 10.1101/586800

Kanehisa, M., Goto, S., Kawashima, S., Okuno, Y., and Hattori, M. (2004). The KEGG resource for deciphering the genome. *Nucleic Acids Res.* 32, 277–280. doi: 10.1093/nar/gkh063

Kozakov, D., Hall, D. R., Xia, B., Porter, K. A., Padhorny, D., Yueh, C., et al. (2017). The ClusPro web server for protein-protein docking. *Nat. Protoc.* 12, 255–278. doi: 10.1038/nprot.2016.169

Kraus, J. E. M., Fredman, D., Wang, W., Khalturin, K., and Technau, U. (2015). Adoption of conserved developmental genes in development and origin of the medusa body plan. *EvoDevo* 6:23. doi: 10.1186/s13227-015-0017-3

Krishnapati, L. S., and Ghaskadbi, S. (2013). Identification and characterization of VEGF and FGF from Hydra. *Int. J. Dev. Biol.* 57, 897–906. doi: 10.1387/ijdb.130077sg

Kumar, S., Stecher, G., Li, M., Knyaz, C., and Tamura, K. (2018). MEGA X: molecular evolutionary genetics analysis across computing platforms. *Mol. Biol. Evol.* 35, 1547–1549. doi: 10.1093/molbev/msy096

Lange, E., Bertrand, S., Holz, O., Rebscher, N., and Hassel, M. (2014). Dynamic expression of a Hydra FGF at boundaries and termini. *Dev. Genes Evol.* 224, 235–244. doi: 10.1007/s00427-014-0480-1

Lemmon, M. A., and Schlessinger, J. (2010). Cell signaling by receptor tyrosine kinases. *Cell* 141, 1117–1134. doi: 10.1016/j.cell.2010.06.011

Li, W., Jaroszewski, L., and Godzik, A. (2002). Tolerating some redundancy significantly speeds up clustering of large protein databases. *Bioinformatics* 18, 77–82. doi: 10.1093/bioinformatics/18.1.77

Linger, R. M., Keating, A. K., Earp, H. S., and Graham, D. K. (2008). TAM receptor tyrosine kinases: biologic functions, signaling, and potential therapeutic

targeting in human cancer. *Adv. Cancer Res.* 100, 35–83. doi: 10.1016/S0065-230X(08)00002-X

Lu, H., Giordano, F., and Ning, Z. (2016). Oxford Nanopore MinION sequencing and genome assembly. *Genomics Proteomics Bioinformatics* 14, 265–279. doi: 10.1016/j.gpb.2016.05.004

Magel, J., Dimoff, S. A., and Baum, J. K. (2020). Direct and indirect effects of climate change-amplified pulse heat stress events on coral reef fish communities. *Bull. Ecol. Soc. Am.* 101:e01706. doi: 10.1002/bes2.1706

Maier, J. K., and Labute, P. (2014). Assessment of fully automated antibody homology modeling protocols in molecular operating environment. *Proteins* 82, 1599–1610. doi: 10.1002/prot.24576

Moberg, F., and Folke, C. (1999). Ecological goods and services of coral reef ecosystems. *Ecol. Econ.* 29, 215–233. doi: 10.1016/S0921-8009(99)00009-9

Mohammadi, M., Schlessinger, J., and Hubbard, S. R. (1996). Structure of the FGF receptor tyrosine kinase domain reveals a novel autoinhibitory mechanism. *Cell* 86, 577–587. doi: 10.1016/s0092-8674(00)80131-2

Molecular Operating Environment [Moe] (2019). *Chemical Computing Group ULC, 1010 Sherbooke St. West, Suite #910*. Montreal, QC: MOE.

Nakamura, M., Okaji, K., Higa, Y., Yamakawa, E., and Mitarai, S. (2014). Spatial and temporal population dynamics of the crown-of-thorns starfish, *Acanthaster planci*, over a 24-year period along the central west coast of Okinawa Island, Japan. *Mar. Biol.* 161, 2521–2530. doi: 10.1007/s00227-014-2524-5

Naski, M. C., and Ornitz, D. M. (1998). FGF signaling in skeletal development. *Front. Biosci.* 3:d781–d794. doi: 10.2741/a321

Odum, H. T., and Odum, E. P. (1955). Trophic structure and productivity of a windward coral reef community on Eniwetok atoll. *Ecol. Monogr.* 25, 291–320. doi: 10.2307/1943285

Ornitz, D. M., and Itoh, N. (2015). The fibroblast growth factor signaling pathway. *Wiley Interdiscip. Rev. Dev. Biol.* 4, 215–266. doi: 10.1002/wdev.176

Otto, J. J., and Campbell, R. D. (1977). Budding in *Hydra attenuata*: bud stages and fate map. *J. Exp. Zool.* 200, 417–428. doi: 10.1002/jez

Reimer, J. D., Kise, H., Wee, H. B., Lee, C. L., and Soong, K. (2019). Crown-of-thorns starfish outbreak at oceanic Dongsha Atoll in the northern South China Sea. *Mar. Biodivers.* 49, 2495–2497. doi: 10.1007/s12526-019-01021-2

Rhoads, A., and Au, K. F. (2015). PacBio sequencing and its applications. *Genomics Proteomics Bioinformatics* 13, 278–289. doi: 10.1016/j.gpb.2015.08.002

Saitou, N., and Nei, M. (1987). The neighbor-joining method: a new method for reconstructing phylogenetic trees. *Mol. Bio. Evol.* 4, 406–425. doi: 10.1093/oxfordjournals.molbev.a040454

Salmela, L., and Rivals, E. (2014). LoRDEC: accurate and efficient long read error correction. *Bioinformatics* 30, 3506–3514. doi: 10.1093/bioinformatics/btu538

Savage, M. P., Hart, C. E., Riley, B. B., Sasse, J., Olwin, B. B., and Fallon, J. F. (1993). Distribution of FGF-2 suggests it has a role in chick limb bud growth. *Dev. Dyn.* 198, 159–170. doi: 10.1002/aja.1001980302

Shimizu, K., Adachi, J., and Muraoka, Y. (2006). ANGLE: a sequencing errors resistant program for predicting protein coding regions in unfinished cDNA. *J. Bioinform. Comput. Biol.* 4, 649–664. doi: 10.1142/s0219720006002260

Stauber, D. J., Digabriele, D., and Hendrickson, W. A. (2000). Structural interactions of fibroblast growth factor receptor with its ligands. *Proc. Natl. Acad. Sci. U.S.A.* 97, 49–54. doi: 10.1073/pnas.97.1.49

Sudhop, S., Coulier, F., Bieller, A., Vogt, A., Hotz, T., and Hassel, M. (2004). Signalling by the FGFR-like tyrosine kinase, Kringelchen, is essential for bud detachment in *Hydra vulgaris*. *Development* 131, 4001–4011. doi: 10.1242/dev.01267

Suryawanshi, A., Schaefer, K., Holz, O., Apel, D., Lange, E., Hayward, D. C., et al. (2020). What lies beneath: *Hydra* provides cnidarian perspectives into the evolution of FGFR docking proteins. *Dev. Genes. Evol.* 230, 227–238. doi: 10.1007/s00427-020-00659-4

Tanaka, E. M., and Gann, A. F. (1995). Limb development. The budding role of FGF. *Curr. Biol.* 5, 594–597. doi: 10.1016/s0960-9822(95)00118-7

Tatusov, R. L., Fedorova, N. D., Jackson, J. D., Jacobs, A. R., Kiryutin, B., Koonin, E. V., et al. (2003). The COG database: an updated version includes eukaryotes. *BMC Bioinformatics* 4:41. doi: 10.1186/1471-2105-4-41

Tavormina, P. L., Rimoin, D. L., Cohn, D. H., Zhu, Y. Z., Shiang, R., and Wasmuth, J. J. (1995). Another mutation that results in the substitution of an unpaired cysteine residue in the extracellular domain of FGFR3 in thanatophoric dysplasia type I. *Hum. Mol. Genet.* 4, 2175–2177. doi: 10.1093/hmg/4.11.2175

Tee, J. B., Choi, Y., Dnyanmote, A., Decambre, M., Ito, C., Bush, K. T., et al. (2013). GDNF-independent ureteric budding: role of PI3K-independent activation of AKT and FOSB/JUN/AP-1 signaling. *Biol. Open.* 2, 952–959. doi: 10.1242/bio.20135595

Trenker, R., and Jura, N. (2020). Receptor tyrosine kinase activation: from the ligand perspective. *Curr. Opin. Cell Biol.* 63, 174–185. doi: 10.1016/j.ceb.2020.01.016

Turwankar, A., and Ghaskadbi, S. (2019). VEGF and FGF signaling during head regeneration in *Hydra*. *Gene* 717:144047. doi: 10.1016/j.gene.2019.144047

Ullrich, A., and Schlessinger, J. (1990). Signal transduction by receptors with tyrosine kinase activity. *Cell* 61, 203–212. doi: 10.1016/0092-8674(90)90801-k

van Dijk, E. L., Jaszczyszyn, Y., Naquin, D., and Thermes, C. (2018). The third revolution in sequencing technology. *Trends Genet.* 34, 666–681. doi: 10.1016/j.tig.2018.05.008

Wecker, P., Lecellier, G., Guibert, I., Zhou, Y., Bonnard, I., and Berteaux-Lecellier, V. (2018). Exposure to the environmentally-persistent insecticide chlordecone induces detoxification genes and causes polyp bail-out in the coral P. damicornis. *Chemosphere* 195, 190–200. doi: 10.1016/j.chemosphere.2017.12.048

Weiner, H. L., and Zagzag, D. (2000). Growth factor receptor tyrosine kinases: cell adhesion kinase family suggests a novel signaling mechanism in cancer. *Cancer Invest.* 18, 544–554. doi: 10.3109/07357900009012194

Wilson, S. K., Graham, N., Pratchett, M. S., Jones, G. P., and Polunin, N. (2006). Multiple disturbances and the global degradation of coral reefs: are reef fishes at risk or resilient? *Glob. Change Biol.* 12, 2220–2234. doi: 10.1111/j.1365-2486.2006.01252.x

Yang, J., Anishchenko, I., Park, H., Peng, Z., Ovchinnikov, S., and Baker, D. (2020). Improved protein structure prediction using predicted interresidue orientations. *Proc. Natl. Acad. Sci. U.S.A.* 117, 1496–1503. doi: 10.1073/pnas.1914677117

Yu, K. (2012). Coral reefs in the South China Sea: their response to and records on past environmental changes. *Sci. China Earth Sci.* 55, 1217–1229. doi: 10.1007/s11430-012-4449-5

Zuckerkandl, E., and Pauling, L. (1965). "Evolutionary divergence and convergence in proteins," in *Evolving Genes and Proteins*, eds V. Bryson and H. J. Vogel (New York, NY: Academic Press), 97–166. doi: 10.1016/B978-1-4832-2734-4.50017-6

Conflict of Interest: The authors declare that the research was conducted in the absence of any commercial or financial relationships that could be construed as a potential conflict of interest.

Publisher's Note: All claims expressed in this article are solely those of the authors and do not necessarily represent those of their affiliated organizations, or those of the publisher, the editors and the reviewers. Any product that may be evaluated in this article, or claim that may be made by its manufacturer, is not guaranteed or endorsed by the publisher.

frontiers in Physiology

METHODS
published: 25 March 2022
doi: 10.3389/fphys.2022.822900

The Exact Timing of Microinjection of Parthenogenetic Silkworm Embryos Is Crucial for Their Successful Transgenesis

Valeriya Zabelina[1,2,3], Marketa Vrchotova[1,2], Naoyuki Yonemura[3], Hideki Sezutsu[3], Toshiki Tamura[3,4], Vyacheslav Klymenko[5], Frantisek Sehnal[1,2‡], Michal Zurovec[1,2†], Hana Sehadova[1,2] and Ivo Sauman[1,2]**

[1] Biology Center CAS, Institute of Entomology, České Budějovice, Czechia, [2] Faculty of Science, University of South Bohemia, České Budějovice, Czechia, [3] National Agriculture and Food Research Organization, Tsukuba, Japan, [4] Silk Sciences and Technology Research Institute, Ibaraki, Japan, [5] Faculty of Automation and Information Technology in Management, Ryazan State Radio Engineering University, Ryazan, Russia

OPEN ACCESS

Edited by:
Natraj Krishnan,
Mississippi State University,
United States

Reviewed by:
Jian Xu,
East China Normal University, China
Shiping Liu,
Southwest University, China

***Correspondence:**
Hana Sehadova
sehadova@yahoo.com
Ivo Sauman
sauman@entu.cas.cz

†ORCID:
Michal Zurovec
orcid.org/0000-0002-0913-166X

‡Deceased

Specialty section:
This article was submitted to Invertebrate Physiology, a section of the journal Frontiers in Physiology

Received: 26 November 2021
Accepted: 28 February 2022
Published: 25 March 2022

Citation:
Zabelina V, Vrchotova M, Yonemura N, Sezutsu H, Tamura T, Klymenko V, Sehnal F, Zurovec M, Sehadova H and Sauman I (2022) The Exact Timing of Microinjection of Parthenogenetic Silkworm Embryos Is Crucial for Their Successful Transgenesis. Front. Physiol. 13:822900. doi: 10.3389/fphys.2022.822900

The use of parthenogenetic silkworm (*Bombyx mori*) strains, which eliminate the problem of recombination, is a useful tool for maintaining transgenic clonal lines. The generation of genetically identical individuals is becoming an important tool in genetic engineering, allowing replication of an existing advantageous trait combination without the mixing that occurs during sexual reproduction. Thus, an animal with a particular genetic modification, such as the ability to produce transgenic proteins, can reproduce more rapidly than by natural mating. One obstacle to the widespread use of parthenogenesis in silkworm genetic engineering is the relatively low efficiency of downstream transgenesis techniques. In this work, we seek to optimize the use of transgenesis in conjunction with the production of parthenogenetic individuals. We found that a very important parameter for the introduction of foreign genes into a parthenogenetic strain is the precise timing of embryo microinjection. Our modification of the original method increased the efficiency of transgene injection as well as the survival rate of injected embryos. We also provide a detailed description of the methodological procedure including a graphical overview of the entire protocol.

Keywords: transgenesis, parthenogenesis, *Bombyx mori*, embryonic development, genetic engineering, ovary transplantation, overcoming diapause

INTRODUCTION

Transgene insertion is the critical step in the production of transgenic silkworms, but widespread use of this technique is hampered by the tedious selection and maintenance of desired genotypes. However, these procedures could be simplified by the use of parthenoclones. The main advantage of using parthenogenetic strains is that after successful integration of the transgene into the silkworm genome, a single female initiates a clonal lineage with a genome completely identical to that of the mother, which can be easily maintained as pure female populations without sexual reproduction. Subsequent generations have the same expression of the inserted gene and the same morphological and physiological characteristics. This is important for the production of proteins used in medicine, where it is necessary to ensure the same quality and quantity of the desired product (Tomita, 2011;

Tatemastu et al., 2012), leading to the standardization of biotechnological and pharmacological sericulture products.

Parthenogenetic reproduction is induced in susceptible strains of *Bombyx mori* by specific thermal treatment of the unfertilized eggs of virgin females (Astaurov, 1940). The treatment, which involves heat shock followed by rapid cooling, suppresses the first meiotic division and both pronuclei of oocyte I remain diploid. One of them is aborted and the other becomes the nucleus of the oocyte II and initiates division (Klymenko, 2001). Since no crossing over of chromosomes occurs during silkworm oogenesis (Sturtevant, 1915), the pronuclei are genetically identical to the genome of the mother, including the ZW chromosomes that determine female sex (Tazima, 1978; Doroshenko and Klymenko, 2010). A single female initiates a female clonal lineage with the same genetic and morphological traits that are maintained without sexual reproduction (Tazima, 1978). Certain genotypes have been maintained as parthenoclones without sexual reproduction for decades (Astaurov, 1973; Klymenko et al., 2013; Zabelina et al., 2015b).

Considering that all available parthenogenetic strains of *B. mori* are diapausing, a way had to be found to obtain non-diapausing eggs for microinjection of foreign DNA. Therefore, the first successful attempt was to transplant ovaries into the male larval host (Zabelina and Klymenko, 2008; Zabelina et al., 2015a). Because males do not contain sufficient titers of the diapause hormone, eggs in ovaries implanted into male larvae lost embryonic diapause determination (Zabelina et al., 2015a). Recent results also suggest the possibility of overcoming diapause by crossing a diapausing parthenogenetic strain with a bivoltine strain (Zabelina et al., 2021).

The advantage of parthenocloning in the production of homozygous transgenic lines was first recognized by Grenier et al. (2004), who attempted to develop a parthenogenetic polyvoltine strain but failed to use the strain for transgenesis. The first parthenogenetic and simultaneously transgenic strains were constructed 10 years later but resulting efficiency of hatchability was less than 2% (Zabelina et al., 2015b). The parthenogenetic strain was incubated at 15°C and the DNA for the transgenes was injected 12 h after egg activation (AEA) by heat shock. The timing of the developmental stage for injection of developing embryo in 15°C was roughly estimated with respect to the fact that eggs incubated at 15°C developed approximately three times slower than at 25°C, where the optimal stage for DNA injection is determined to 2–6 h AEA for non-parthenogenetic strains (Tamura et al., 2000, 2007). At this stage of development, the energids divide synchronously, migrate to the periphery, and occupy approximately 25% of the anterior-lateral egg surface, where they begin cellularization. We hypothesized that the low efficiency of transgenesis in the parthenogenetic strain could be caused by incorrect estimation of the progress of the embryonic development at different incubation temperatures (15 vs. 25°C).

In this study, we compared in detail the course of early embryogenesis in parthenogenetic strain PK1 with European silkworm strain K23 at two different temperatures. We found out that the rate of early embryogenesis at 15°C is significantly slower than estimated in the previous study (Zabelina et al., 2015b). We have shown that accurate determination of the most appropriate developmental window for transgenic injection of parthenogenetic silkworm strains dramatically increased embryo survival.

MATERIALS AND METHODS

Silkworm Cultures

Silkworm strain K23 (also known as Soviet-5) was used to study embryonic development after normal fertilization. The strain is univoltine, sex-marked in the egg stage and has a very low capacity for parthenogenesis (0.1%) (Strunnikov, 1971; Zabelina and Klymenko, 2008). The univoltine parthenoclone PK1 [also known as P29 (Astaurov, 1973], has been used to study embryonic development after induction of parthenogenesis by heat shock. The PK1 clone is characterized by high viability, the presence of multiple genetic markers, and nearly 100% parthenogenesis in heat shock treated eggs. Strains K23 and PK1 were kindly provided to us by the Agricultural Research Council (Padua, Italy). The non-diapausing parthenogenetic strain 1–31, the F2 brood between the PK1 and bivoltine Cambodia strains (Zabelina et al., 2021), was used for egg microinjection. All silkworms received artificial diet (Cappellozza et al., 2005) and were maintained under standard conditions of 15 or 25°C and a 12:12 h photoperiod.

Transplantation of Ovaries

Transplantation of developing ovaries was used to interrupt diapause programming (Spiridonova et al., 1987). Day 4 PK1 larvae of the 4th instar were used as ovarian donors. Ovaries

FIGURE 1 | An examples of ovary implantation. Implanted PK1 ovaries (iO) positioned between the endogenous testes of the K23 recipient (T). Scale bar: 500 μm.

were dissected from water-anesthetized female larvae (20 min at room temperature) from the dorsal part of the 5th abdominal segment under sterile Ringer's solution. The dissected ovaries were inserted into anesthetized recipient, day 3 male K23 larvae of the 4th instar, through a small incision on the dorsal side of the larva between the 5th and 6th abdominal segments. The donor ovary was carefully placed between the host testes using forceps and a needle. The site of surgery was sterilized with ethanol. Since males do not contain sufficient titers of the diapause hormone, the eggs in the implanted ovaries were not determined for embryonic diapause (Zabelina et al., 2015a). The transplanted ovaries were left in males throughout oogenesis. An example of ovarian implantation is shown in **Figure 1**.

The Collection and Handling of Eggs

Eggs of the standard univoltine strain K23 were obtained as described by Tamura et al. (1990). Newly eclosed adults were mated at 25°C for 3–4 h and then left overnight at 5°C. Males were removed, and females were placed in darkness at 25°C, where they began laying eggs. Newly laid eggs were collected every 15–30 min, transferred to 15 or 25°C, and examined at 3 or 12 h intervals. Sperm penetration into the eggs during their passage through the oviduct triggered embryogenesis (Tazima, 1978; Miya, 2003) and the progress of embryonic development was conveniently measured in hours after egg laying. Hydrochloric acid (HCl) treatment (Astaurov, 1973) was used to break the diapause of K23 eggs incubated at 25°C.

Embryogenesis of unfertilized eggs of parthenogenetic strain PK1 was activated by heat shock treatment (Astaurov, 1940). Transplanted ovaries with fully developed eggs were dissected from newly eclosed adult K23 recipient males. The incision between the thorax and abdomen was made with fine scissors. The ovaries were removed and placed in a beaker of cold water. The dissected ovaries were scrubbed with circular movements of the fingers on a plastic sieve under running water to remove adjacent tissue. After another wash in cold water, the eggs were removed from the sieve, transferred to a gauze square, and placed in a small bag with a rubber band. The ovaries of the control group were collected from adult PK1 females after egg deposition and also placed in a gauze bag. Both groups of collected eggs were then heat shocked in warm water (46°C) for 18 min. To allow the bags to be immersed in the water, the air should be removed from the bags. The bags were then rapidly cooled by immersing them in 15°C water for 10 min. The bags were then dried with a towel and placed in the incubator at a temperature of 15°C and high humidity. The time of egg deposition for non-parthenogenic strains or heat shock activation of eggs of parthenogenic strains is defined as time zero after egg activation (AEA).

To determine the exact timing for injection of transgene DNA into the parthenogenetic strain PK1, we compared the embryogenesis rate of this parthenogenetic strain at 15°C with the univoltine strain K23 incubated at 25°C. The process of maintaining parthenogenetic individuals is based on eggs derived from the ovaries of the parthenogenetic strain PK1 implanted and grown in males of the strain K23, which prevents diapause due to the low content of diapause hormones in these males.

Embryonic developmental stages were determined based on the number and distribution of nuclei stained with propidium iodide and the degree of serosa formation. Based on the analysis of our samples and data published by Ohtsuki and Murakami (1968), Nagy et al. (1994), and Miya (2003), we distinguished 7 stages of early embryogenesis, designated A to G (**Table 1**). From this, we can conclude that in embryos maintained at 15°C, development slows down rapidly in both implants and PK1 and K23 strains.

The Fixation and Staining of Embryos

To remove the chorion and vitelline membrane, which interfere with embryo fixation and staining, eggs selected for cytology were placed in 30% KOH for 6 min followed by 2% NaClO for 3 min (Nagy et al., 1994; You et al., 2013). After washing in PBS (0.1 M, pH 7.4), the eggs were transferred to a fixative consisting of 2.5 ml PBS, 0.5 ml formaldehyde (38%) and 3 ml n-heptane. The samples were shaken for 50 min at 28°C. The fixative formed two liquid phases, the upper of which was discarded. The remaining liquid was carefully replaced with cold methanol in which the eggs were gently shaken for 10 min. The excess solution was removed and briefly washed three times with chilled methanol.

TABLE 1 | Brief description of the stages of early embryogenesis in *B. mori*.

Stage	Characteristics	Hours AEA		
		N25	O25	O15
A	One nucleus in parthenogenetic eggs or 2 pronuclei in fertilized eggs can be detected in exceptional cases.	0	0	0
B	Up to 40 nuclei assembled in the anterior third of the egg, nuclei are widely separated and some divide within the yolk.	7	6–12	12–24
C	Nuclei occupy about half of the anterio-lateral egg surface where they migrate to the periphery and initiate cellularization.	11	6–12	24–36
D	Nuclei occupy entire egg surface and form cellular blastoderm that contains (1) small cells of presumptive germ anlage in the lateral and ventral egg surfaces; (2) Larger preserosa cells peripheral to the germ anlage; (3) primary yolk nuclei in egg interior.	14	12–24	36–48
E	Large gaps between serosa cells, the cells of future germ anlage become more densely packed and begin to sink.	23	24–36	48–60
F	The rudimental anlage is clearly distinguished from the extraembryonic cells. The serosa is nearly continuous.	26	24–36	>72
G	The short anlage is enveloped by serosa and is separated from the extraembryonic cells.	NA	48–60	>72

Hours indicate the approximate time of incubation after egg activation (AEA) when stages were reached in eggs incubated at 25°C (column N25 based on data published by Nagy et al. (1994) and column O25 based on our data) and in eggs incubated at 15°C (column O15).

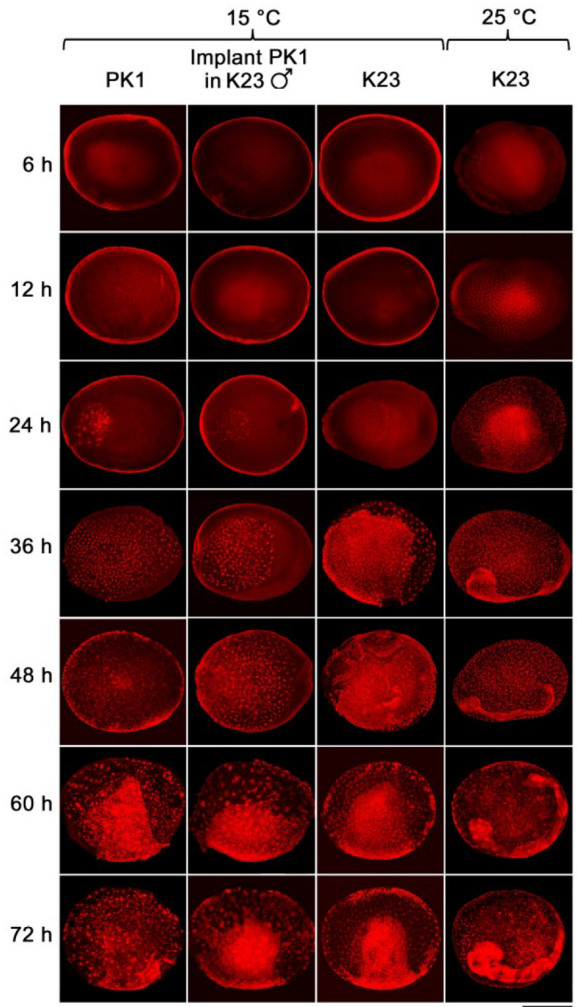

FIGURE 2 | The rate of development of parthenogenetic and univoltine embryos of *B. mori* at different incubation temperatures. Embryogenesis was studied during 72 h AEA. Eggs were incubated at 15°C, except for the last column where embryos were maintained at 25°C. The time after egg activation is indicated on the left side of the panel. PK1, parthenogenetic eggs from PK1 ovaries; implant PK1 in K23 ♂, parthenogenetic PK1 eggs from ovarian implants that developed in K23 males; K23: fertilized eggs from endogenous K23 ovaries. Scale bar: 500 μm.

The eggs were kept in fresh methanol and stored at −20°C. Prior to staining, samples were rehydrated through decreasing methanol series (90%, 70%, 50% and 30% for 15 min each) to PBS.

The cell nuclei were stained with propidium iodide (Sigma, 40 μg/ml), for 15 min in the dark (Nagy et al., 1994). Stained samples were washed three times in PBS for 15 min. Stained embryos were embedded in Vectashield medium (Vector Laboratories) on microscopic slides and stored in the dark at 4°C until examination with a confocal laser scanning microscope (FluoView^{TM} FV1000, Olympus). Multiple Z-stacks images were combined using Imaris software (Bitplane, Oxford Instruments, plc, Tubney Woods, Abingdon, Oxon OX13 5QX, United Kingdom).

Microinjection of Parthenogenetic Eggs

The successful transgenesis of parthenogenetic eggs was reported by Zabelina et al. (2015b) and improved in the following study (Zabelina et al., 2021). The activated eggs of non-diapausing parthenogenetic strain 1–31 were injected with the plasmid vector pPIGA3GFP carrying the GFP gene construct in order to confirm DNA injection (Tamura et al., 2000).

Preparation of plasmid DNA for injection: The plasmid DNA was purified by CsCl gradient ultracentrifugation. The recovered DNA was treated with 70% ethanol, dried by vacuum centrifugation, and dissolved in the injection buffer (5 mM KCl/0.5 mM phosphate buffer at pH 7.0) at a concentration of 200 μg/ml. The prepared DNA solution was stored at −80°C until injection.

Injection of DNA into developing embryos: The injection system consisted of a binocular microscope (Nikon, SMZ 745, Japan) with a stage, an injector (Narishige, IMP300, Japan), a manipulator (Narishige, M152, Japan), and a pipette holder (Narishige, HDD-20, Japan) (Tamura et al., 2007). First, the eggs were fixed on a slide in the same orientation and a small hole was pierced in the ventral side of the egg with a tungsten needle. The tip of a glass capillary was then guided to the location of the hole. By moving the knob on the movable stage of the microscope, the glass capillary could enter the egg. The DNA was then injected using the air pressure of the injector. Activated eggs developing at 15°C were injected with 1–4 nl of 200 μg/ml DNA within 72 h AEA at time points of 12, 18, 24, 30, 48, and 72 h. After injection, the developing embryos were brought to 25°C until hatching. After an additional 4 days of incubation at 25°C, the injected embryos were examined under an Olympus BX51 fluorescence microscope with CCD camera (Olympus DP80, Olympus Corporation, Tokyo, Japan).

Establishing *B. mori* transgenic lines: Parthenogenetic larvae hatched from transgene-injected eggs were reared to imago. Mature eggs were excised from the abdomen, heat shock treated, and examined under a fluorescence microscope for expression of the GFP marker. Transgenic strains were established from the GFP-positive embryos.

RESULTS

Determining Optimal Staging for Transgenesis in the Parthenogenetic Silkworm Strain PK1

We examined the progress of early embryogenesis at 12-h intervals until 72 h after egg activation (AEA, except for the first time point at 6 h AEA) by propidium iodide staining and microscopic analysis (**Figure 2**). Later developmental stages were not examined in this study. Time point zero, i.e., egg activation, is activation of the parthenogenic strains by heat shock treatment or egg deposition in the non-parthenogenic strains. Embryogenesis of the implants was also compared with the development of the parthenogenetic eggs of PK1 left *in situ* in the intact ovaries and with the development of the standard fertilized eggs of K23, both incubated at 15°C (**Figure 2**).

TABLE 2 | Stages of early embryogenesis in *B. mori* embryos incubated at 15°C.

Timing after egg activation (at 15°C)	PK1			Implant PK1 in K23 ♂			K23		
	Stage	%	*n*	Stage	%	*n*	Stage	%	*n*
12 h	A	100	12	A	100	16	A	100	11
24 h	B	100	16	B	100	14	B-C	40–60	12
36 h	C-D	40–60	10	C-D	75–25	15	D-E	80–20	10
48 h	D-E	10–90	11	D-E	65–35	16	E-F	80–20	27
60 h	F	100	14	F	100	2	F	100	12
72 h	F	100	10	F	100	9	F	100	21

Embryonic development was analyzed at 12-h intervals during the first 72 h AEA. Each time point is characterized by developmental stages A-G described in ***Table 1****. PK1, parthenogenetic eggs from PK1 ovaries; implant PK1 in K23 ♂, parthenogenetic PK1 eggs from ovarian implants that developed in K23 males; K23, fertilized eggs from endogenous K23 ovaries; n, number of embryos examined; %, percentage of occurrence of the embryonic developmental stage examined among all eggs in the sample. Stages of embryonic development were determined subjectively by two observers.*

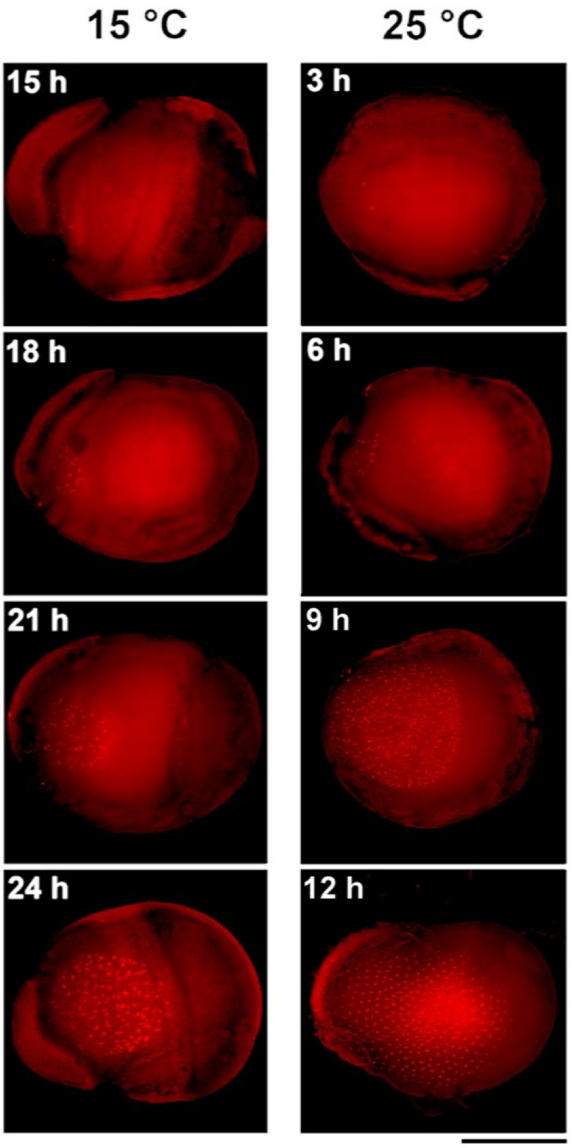

FIGURE 3 | Comparison of early embryogenesis in standard breeding strain K23 incubated at 15°C and 25°C, respectively. The inserted numbers indicate the time after egg activation. Scale bar: 500 μm.

As can be seen from the **Figure 2**, during the first 12 h AEA we did not observe pronuclei at 15°C. Thus, the first nuclei appeared between 12 and 24 h AEA. At the 24 h AEA stage, approximately one-third of the embryo is filled with dividing nuclei. In contrast, K23 embryos kept at 25°C already contain tents of dividing nuclei at 6 h AEA. At the 12 h AEA stage, the embryo is almost completely filled with nuclei. The difference in the rate of embryogenesis between 25 and 15°C increases further at later stages. Embryos developing at 25°C separate distinctly from the serosa between 24 and 36 h, whereas at 15°C the primitive germ band forms at 48 h and the anlage separates distinctly from the serosa at 72 h AEA. Individual strains show individual differences during incubation at 15°C, which become evident at 24 h AEA (**Table 2**). While in K23 about 40% of the tested embryos are at the stage of up to 40 nuclei, which is typical for the other two groups tested, in 60% of the embryos the nuclei occupy about half of the anteriolateral egg surface, migrate to the periphery and start cellularization there. In the implants, on the other hand, development is slightly delayed in the sense that from 36 h AEA onward, a higher percentage of less developed than advanced stages is found in the tested samples. The results of embryonic development at 15°C are summarized in **Table 2**.

To obtain a more detailed picture of the earliest stages of embryogenesis, we examined the development of standard strain K23 every 3 h from 3 to 12 h AEA at 25°C and from 15 to 24 h AEA at 15°C (**Figure 3**). At 25°C, multiple nuclei were already detected at 3 h AEA, consistent with a previous observation that places the first division of the zygote to the time point between 120 and 140 min AEA (Tazima, 1978). At 15°C, the first nuclei were found at 15 h AEA. Based on these data, the most appropriate stage for DNA injection into parthenogenic embryos developing at 15°C is 18–24 h AEA. This stage corresponds to approximately 6 h AEA of embryos developing at 25°C.

Efficiency of Microinjection at Different Stages of Early Embryogenesis

Considering the obtained results, we tested the embryo survival rate after DNA injection at different times AEA in the non-diapausing parthenogenetic *B. mori* 1–31 strain (Zabelina et al., 2021). To determine the most appropriate time point for transgenesis, the plasmid containing the GFP gene expression construct was injected into developing embryos that were

activated by heat shock and maintained at 15°C for up to 72 h AEA. Then the embryos were maintained at 25°C until hatching. Four days later, the injected eggs were examined under a fluorescence microscope to determine the successful microinjection (GFP expression). We also assessed the efficiency of hatchability. The data are summarized in **Table 3** and shown in **Figures 4**, **5**. The highest efficiency of successful microinjection was observed in embryos injected between 12 and 30 h AEA. However, considering the hatchability of larvae after transgene injection, the most appropriate time for transgenesis was set at 18 h AEA (**Table 3**).

Troubleshooting

To improve the survival rate of injected embryos, accurate determination of the optimal stage of embryonic development is critical. Assuming that the early embryonic development rate is similar among the different strains, we recommend the use of 18 h AEA stages. The rate of embryonic development in different strains has been compared in several studies to date. Early embryonic development of diapausing wild-type and non-diapausing *pnd* embryos maintained at 25°C showed no significant difference up to 36 h AEA (Sonobe et al., 1986; Nagy et al., 1994). Also, a comparison of the duration of total embryonic development in four different strains at five different temperatures ranging from 18 to 31°C showed no significant difference in the duration of embryonic development among the four strains (Mochida, 2001). However, in case of problems with survival of injected embryos, the rate of early embryogenesis of a particular strain at a particular temperature must be verified experimentally by morphological observations.

For accurate timing prior to actual transgene injection, we recommend using multiple biological replicates to determine the correct developmental window, especially when using different *B. mori* strains.

To visualize the dividing nuclei, we recommend staining with propidium iodide used in this study, which provides a stronger signal compared to staining with DAPI (**Supplementary Figure 1**). The crucial step for successful nuclear labeling is the precise removal of the chorion and vitelline membrane from the developing embryos.

Graphic Summary of Protocol

(1A) Overcoming diapause by incubation in male.

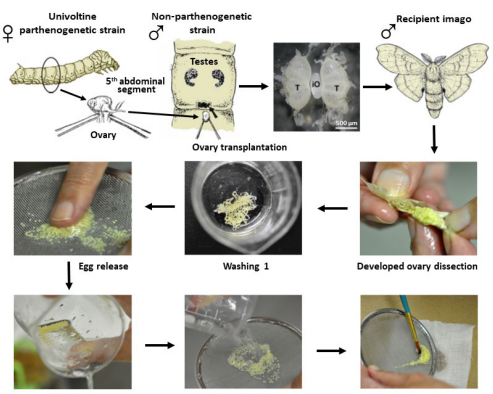

(1B) Overcoming diapause by crossing to bivoltine strain.

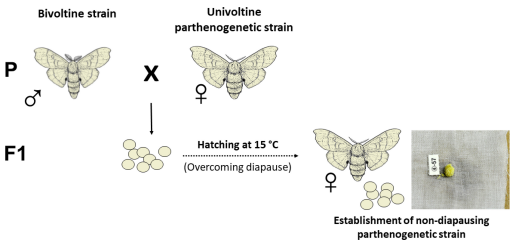

(2) Induction of parthenogenetic development.

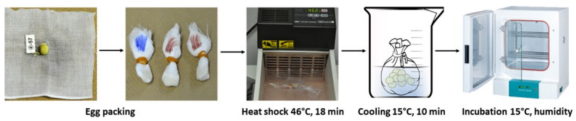

(3) Mechanism of ameiotic parthenogenesis.

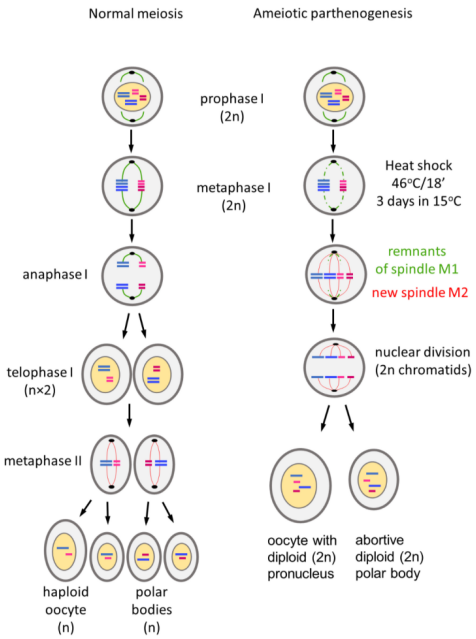

(4) Transgene injection at 18 h after heat shock.

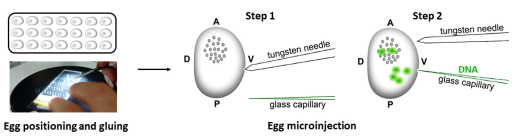

(5) Establishment of transgenic strains.

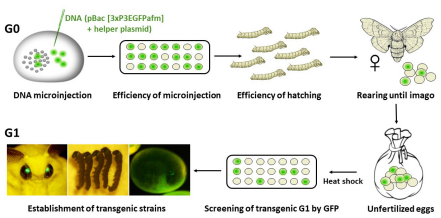

TABLE 3 | Effect of embryonic stage on microinjection efficiency in embryos of parthenogenetic strain *B. mori* 1–31 incubated at 15°C.

Timing of injection after heat-shock activation (at 15°C)	No. of injected eggs	No. of died eggs	Expression of EGFP		Hatched larvae
			Not expressed	Expressed	
12 h	48	12 (25%)	2 (6%)	34 (94%)	0 (0%)
18 h	48	5 (10%)	3 (7%)	40 (93%)	7 (16%)
24 h	48	10 (21%)	2 (5%)	36 (95%)	2 (5%)
30 h	48	12 (25%)	1 (3%)	35 (97%)	1 (3%)
48 h	48	3 (6%)	30 (67%)	15 (33%)	3 (7%)
72 h	47	1 (2%)	33 (72%)	13 (28%)	16 (35%)

GFP-containing DNA plasmid was injected into the heat-shock-activated eggs during the first 72 h AEA at the times indicated in the first column. The number of GFP-positive embryos examined 4 days before hatching reflects the efficiency of microinjection. Mortality of injected embryos and hatchability success of transgenic larvae were also examined. The corresponding percentages are given in parentheses.

DISCUSSION

The introduction of key molecular biology techniques in silkworms opens the door to the genetic manipulations required for basic research and for the use of silkworms as tools for biotechnological production of recombinant proteins. Following the introduction of transgenesis and targeted mutagenesis methods, there is a need to increase the efficiency of transferring important traits and their combinations to progeny by producing genetically identical individuals. In this work, we focus on the optimal matching of the methods used for genetic modification with induced parthenogenesis, which allows the production of silkworm parthenoclones.

A common problem in genetic manipulations is the detection and maintenance of genetic changes in modified individuals, which depends largely on the laborious genotyping of offspring in each generation. Induced parthenogenesis, which allows the production of identical individuals, ensures the transmission of desired traits without the admixture that occurs during sexual reproduction (Grenier et al., 2004; Zabelina et al., 2015b, 2021).

The technique of silkworm transgenesis is based on the injection of DNA constructs into the embryo at a very early stage of nuclear division, before the formation of the cellular blastoderm (Tamura et al., 2000, 2007; Uhlirova et al., 2002; Tomita et al., 2003; Inoue et al., 2005; Royer et al., 2005; Dai et al., 2007; Zhong et al., 2007; Zhao et al., 2010). The transgene, along with adjacent DNA, is randomly inserted into the genome of future somatic or germ cells. Transgenic cells (or individuals) can be detected by markers encoded in the construct.

Today, there is a number of techniques that can be used to edit the genome of various organisms, including insects. One of these is *piggyBac* technology (Tamura et al., 2000), which uses a transposon-derived vector discovered in the lepidopteran *Trichoplusia ni* (Cary et al., 1989) to introduce various genetic constructs (genes) into different insect species. However, the disadvantage of this method is that it does not allow precise targeting of the inserted genetic information. In contrast, endonuclease-based techniques such as zinc fingers, TALENs, and more recently CRISPR/Cas9 methods enable precise targeted genome editing, especially modification of selected genes. Targeted mutagenesis methods use essentially the same basic scheme of embryo microinjection and differ only in the quality and quantity of injected material and the detection of induced genetic changes (Takasu et al., 2010, 2016a,b). Both types of transgenic approaches have different applications in genetic engineering. Another option for transgenesis is homologous recombination, which has the advantage that whole genes or parts of them can be exchanged *in situ*. This method has

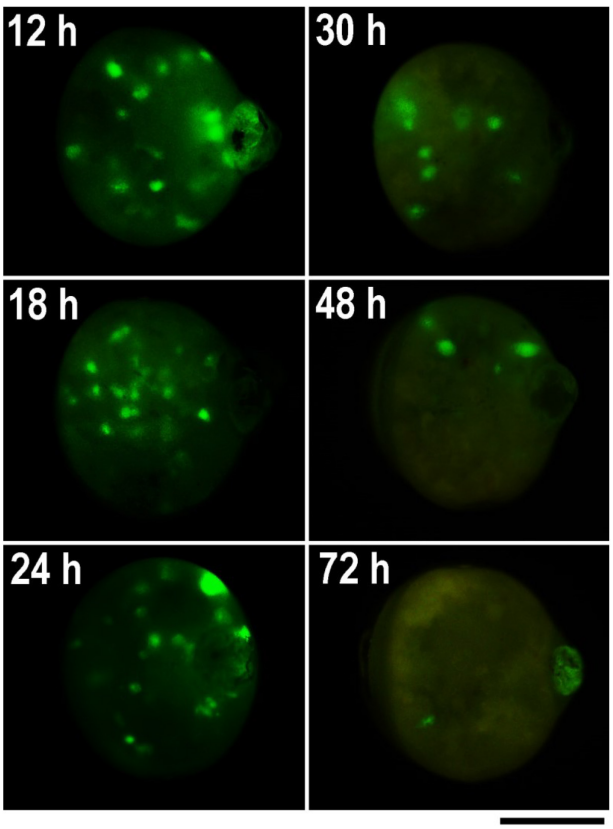

FIGURE 4 | GFP expression in parthenogenetic embryos of *B. mori* 1–31 incubated at 15°C illustrating efficiency of microinjection at different developmental stages. The GFP-containing DNA plasmid was injected into the heat-shock-activated eggs during the first 72 h AEA in times specify by numbers in each figure. GFP expression was examined 4 days before hatching. Time AEA is indicated by the inset numbers. Scale bar: 500 μm.

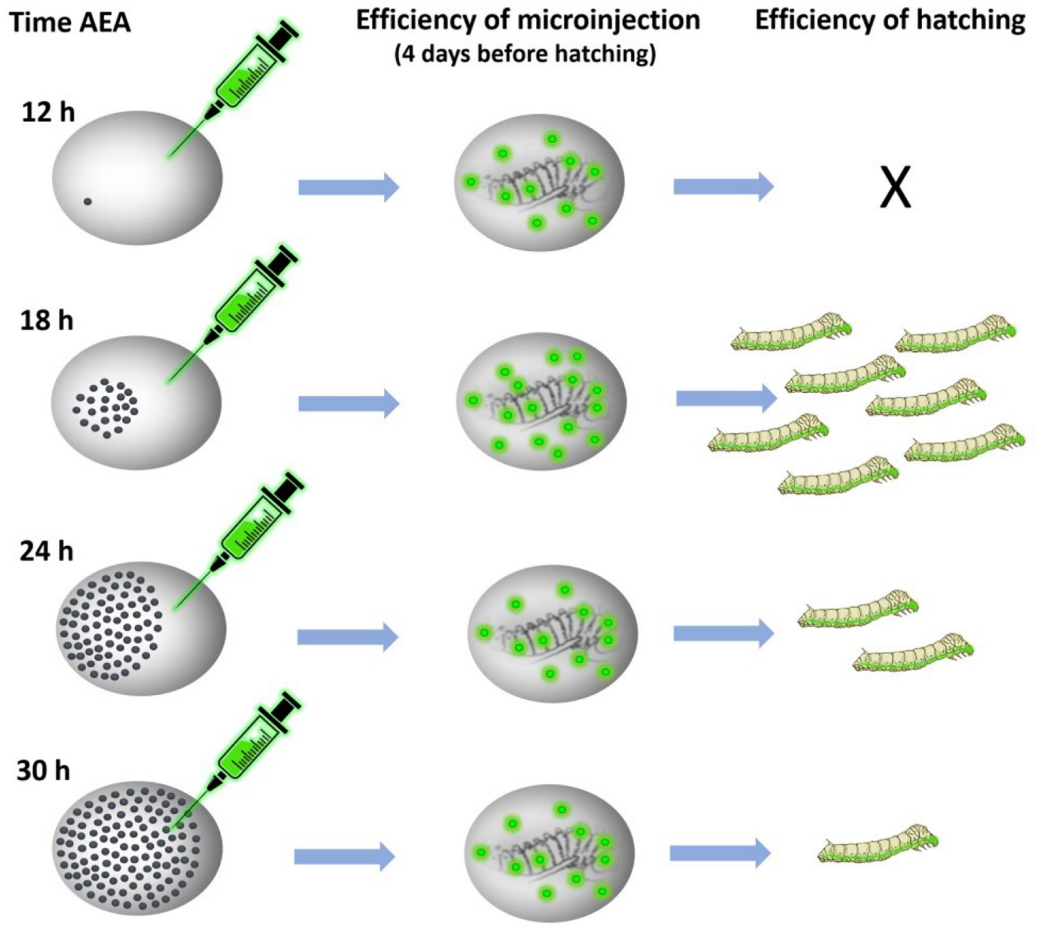

FIGURE 5 | Schematic representation of the procedure of transgene microinjection. Time AEA, time after egg activation.

been successful in *B. mori* using a baculovirus-derived vector, but with extremely low efficiency that precludes routine use (Yamao et al., 1999).

Success of transgenesis depends greatly on accurate staging of target embryos. Injection should be performed before blastoderm formation, i.e., no later than 12 h AEA at 25°C (Tazima, 1978). Tamura et al. (1990) have shown that injection of transgenes under standard conditions at 25°C is efficient during the first 8 h AEA, whereas injections 4 h later (after blastoderm formation) are ineffective. Standard strains developing at 25°C were therefore injected 2–6 h after oviposition (Tamura et al., 1990; Uhlirova et al., 2002), with a hatching rate of about 40% (Tamura et al., 2007). The parthenogenetic strain developing at 15°C was injected 12 h AEA, with a hatching rate of less than 2% (Zabelina et al., 2015b). Subsequent experiments with non-diapausing parthenoclones, where the developmental window for injection was extended from 12 to 18 h AEA, increased the percentage of hatchability by about 10-fold (Zabelina et al., 2021). Since our work shows that the embryonic stage corresponding to 2–6 h at 25°C was reached later during incubation at 15°C than the originally estimated 12 h after heat shock, between 18 and 24 h (**Figures 2**, **3** and **Table 2**), the likely reason for the low efficiency of hatchability in the previous study (Zabelina et al., 2015b) could be the inappropriate timing of DNA injection into the clonal strains.

We tested this assumption using the non-diapausing parthenogenetic line 1–31 (Zabelina et al., 2021) and showed that DNA injection at the correct developmental stage increased the percentage of hatching embryos from 0% at 12 h AEA to 16% at 18 h AEA (**Figure 5**). Thus, injection of DNA at the correct embryonic developmental stage significantly increases the hatchability of eggs and improves the efficiency of transgenic silkworm production as well as targeted mutagenesis. We believe that a detailed description of the whole procedure of parthenogenesis induction in connection with the production of transgenic silkworms will allow a wide application of this method in further research.

DATA AVAILABILITY STATEMENT

The original contributions presented in the study are included in the article/**Supplementary Material**, further inquiries can be directed to the corresponding author/s.

AUTHOR CONTRIBUTIONS

VZ, VK, FS, TT, HaS, and IS: conceptualization and study design. VZ, MV, NY, TT, and HaS: experiment performance. VZ, MV, TT, HaS, and IS: data analysis. FS, HaS, and TT: supervision. FS, MZ, HaS, and IS: writing—original draft. VZ, MV, NY, HaS, TT, VK, FS, MZ, HiS, and IS: manuscript revision and editing. All authors contributed to the article and approved the submitted version.

FUNDING

This research was supported by European Community's Program Interreg Bayern Tschechische Republik Ziel ETZ 2021–2022 no. 331 and European Regional Development Fund (REGGEN ATCZ207).

ACKNOWLEDGMENTS

We would like to thank Frantisek Marec for his help with the ameiotic parthenogenesis diagram. We would also like to thank Roman Neuzil and Stanislav Vrba for technical support.

SUPPLEMENTARY MATERIAL

The Supplementary Material for this article can be found online at: https://www.frontiersin.org/articles/10.3389/fphys.2022.822900/full#supplementary-material

Supplementary Figure 1 | The nuclei in embryos of parthenogenetic PK1 strain incubated at 15°C 24 h after egg activation stained by propidium iodide (red) and by DAPI (blue). Scale bars: 500 μm.

REFERENCES

Astaurov, B. L. (1940). *Artificial Parthenogenesis in the Silkworm, Bombyx mori L.* Saint Petersburg: AN SSSR.

Astaurov, B. L. (1973). Selection for high ability for artificial thermic parthenogenesis and obtaining clones of the silkworm advanced in this direction. *Genetika* 9, 93–106.

Cappellozza, L., Cappellozza, S., Saviane, A., and Sbrenna, G. (2005). Artificial diet rearing system for the silkworm *Bombyx mori* (Lepidoptera : Bombycidae): effect of vitamin C deprivation on larval growth and cocoon production. *Appl. Entomol. Zool.* 40, 405–412. doi: 10.1303/aez.2005.405

Cary, L. C., Goebel, M., Corsaro, B. G., Wang, H. G., Rosen, E., and Fraser, M. J. (1989). Transposon mutagenesis of baculoviruses: analysis of *Trichoplusia* ni transposon IFP2 insertions within the FP-locus of nuclear polyhedrosis viruses. *Virology* 172, 156–169. doi: 10.1016/0042-6822(89)90117-7

Dai, H. J., Jiang, R. J., Wang, J., Xu, G. J., Cao, M. X., Wang, Z. G., et al. (2007). Development of a heat shock inducible and inheritable RNAi system in silkworm. *Biomol. Eng.* 24, 625–630. doi: 10.1016/j.bioeng.2007.10.004

Doroshenko, K. A., and Klymenko, V. V. (2010). Cloning *Bombyx mori* L. female genotypes by implantation of donor's ovaries into parthenoclonal females. *Séricologia* 50, 187–197.

Grenier, A. M., Da Rocha, M., Jalabert, A., Royer, C., Mauchamp, B., and Chavancy, G. (2004). Artificial parthenogenesis and control of voltinism to manage transgenic populations in *Bombyx mori*. *J. Insect. Physiol.* 50, 751–760. doi: 10.1016/j.jinsphys.2004.06.002

Inoue, S., Kanda, T., Imamura, M., Quan, G. X., Kojima, K., Tanaka, H., et al. (2005). A fibroin secretion-deficient silkworm mutants Nd-s(D), provides an efficient system for producing recombinant proteins. *Insect. Biochem. Mol. Biol.* 35, 51–59. doi: 10.1016/j.ibmb.2004.10.002

Klymenko, V. V. (2001). Parthenogenesis and cloning in the silkworm *Bombyx mori* L.: problems and prospects. *J. Insect. Biotechnol. Sericol.* 70, 156–164.

Klymenko, V. V., Lysenko, N. G., and Liang, H. (2013). Parthenocloning in genetics and breeding of the silkworm. *Anim. Breed. Genet.* 47, 40–56.

Miya, K. (2003). *The Early Embryonic Development of Bombyx mori - Ultrastructural Point of View*. Sagamihara: Gendaitosho.

Mochida, Y. (2001). *Formulation of the Relationship Between Incubation Temperature and Growth Rate in Embryonic Development in Post-Diapausing Eggs of Silkworm, Bombyx mori, and Their Low Development Threshold Temperature*. Ibaraki: Institute of Sericulture.

Nagy, L., Riddiford, L., and Kiguchi, K. (1994). Morphogenesis in the early embryo of the lepidopteran *Bombyx mori*. *Dev. Biol.* 165, 137–151. doi: 10.1006/dbio.1994.1241

Ohtsuki, Y., and Murakami, A. (1968). Nuclear division in the early embryonic development of the silkworm, *Bombyx mori* L. *Zool. Mag.* 77, 383–387.

Royer, C., Jalabert, A., Da Rocha, M., Grenier, A. M., Mauchamp, B., Couble, P., et al. (2005). Biosynthesis and cocoon-export of a recombinant globular protein in transgenic silkworms. *Trans. Res.* 14, 463–472. doi: 10.1007/s11248-005-4351-4

Sonobe, H., Maotani, K., and Nakajima, H. (1986). Studies on embryonic diapause in the pnd mutant of the silkworm, *Bombyx mori*: genetic control of embryogenesis. *J. Insect. Physiol.* 32, 213–220.

Spiridonova, T. L., Shchegelskaya, E. A., and Klymenko, V. V. (1987). Gonad transplantation in the larvae of Lepidoptera. *Izvestija Akad Nauk Moldavskoj SSR* 2, 69–71.

Strunnikov, V. A. (1971). Obtaining silkworm hybrids whose ova can be separated into white (female) and dark (male). *Dokl. Akad. Nauk. SSSR* 201, 1223–1226.

Sturtevant, A. H. (1915). No crossing over in the female of the silkworm moth. *Am. Nat.* 49, 42–44. doi: 10.1086/279453

Takasu, Y., Kobayashi, I., Beumer, K., Uchino, K., Sezutsu, H., Sajwan, S., et al. (2010). Targeted mutagenesis in the silkworm *Bombyx mori* using zinc finger nuclease mRNA injection. *Insect. Biochem. Mol. Biol.* 40, 759–765. doi: 10.1016/j.ibmb.2010.07.012

Takasu, Y., Kobayashi, I., Tamura, T., Uchino, K., Sezutsu, H., and Zurovec, M. (2016a). Precise genome editing in the silkworm *Bombyx mori* using TALENs and ds- and ssDNA donors - A practical approach. *Insect. Biochem. Mol. Biol.* 78, 29–38. doi: 10.1016/j.ibmb.2016.08.006

Takasu, Y., Tamura, T., Goldsmith, M., and Zurovec, M. (2016b). Targeted mutagenesis in *Bombyx mori* using TALENs. *Methods Mol. Biol.* 1338, 127–142. doi: 10.1007/978-1-4939-2932-0_11

Tamura, T., Kanda, T., Takiya, S., Okano, K., and Maekawa, H. (1990). Transient expression of chimeric CAT genes injected into early embryos of the domesticated silkworm *Bombyx mori*. *Jpn. J. Genet.* 65, 401–410. doi: 10.1266/jjg.65.401

Tamura, T., Kuwabara, N., Uchino, K., Kobayashi, I., and Kanda, T. (2007). An improved DNA injection method for silkworm eggs drastically increases the efficiency of producing transgenic silkworms. *J. Insect. Biotech. Sericol.* 76, 155–159.

Tamura, T., Thibert, C., Royer, C., Kanda, T., Abraham, E., Kamba, M., et al. (2000). Germline transformation of the silkworm *Bombyx mori* L. using a piggyBac transposon-derived vector. *Nat. Biotechnol.* 18, 81–84. doi: 10.1038/71978

Tatemastu, K., Sezutsu, H., and Tamura, T. (2012). Utilization of transgenic silkworms for recombinant protein production. *J. Biotechnol. Biomater.* 9:4.

Tazima, Y. (1978). *The Silkworm: An Important Laboratory Tool*. Tokyo: Kodansha Ltd.

Tomita, M. (2011). Transgenic silkworms that weave recombinant proteins into silk cocoons. *Biotechnol. Lett.* 33, 645–654. doi: 10.1007/s10529-010-0498-z

Tomita, M., Munetsuna, H., Sato, T., Adachi, T., Hino, R., Hayashi, M., et al. (2003). Transgenic silkworms produce recombinant human type III procollagen in cocoons. *Nat. Biotechnol.* 21, 52–56. doi: 10.1038/nbt771

Uhlirova, M., Asahina, M., Riddiford, L. M., and Jindra, M. (2002). Heat-inducible transgenic expression in the silkmoth *Bombyx mori*. *Dev. Genes Evol.* 212, 145–151. doi: 10.1007/s00427-002-0221-8

Yamao, M., Katayama, N., Nakazawa, H., Yamakawa, M., Hayashi, Y., Hara, S., et al. (1999). Gene targeting in the silkworm by use of a *Baculovirus*. *Genes Dev.* 13, 511–516. doi: 10.1101/gad.13.5.511

You, Z., Sun, C., Chen, L., Yao, Q., and Chen, K. (2013). A novel method of silkworm embryo preparation for immunohistochemistry. *Biotechnol. Lett.* 35, 1209–1214. doi: 10.1007/s10529-013-1202-x

Zabelina, V., Klymenko, V., Tamura, T., Doroshenko, K., Liang, H., Sezutsu, H., et al. (2015a). Genome engineering and parthenocloning in the silkworm, *Bombyx mori*. *J. Biosci.* 40, 645–655. doi: 10.1007/s12038-015-9548-y

Zabelina, V., Uchino, K., Mochida, Y., Yonemura, N., Klymenko, V., Sezutsu, H., et al. (2015b). Construction and long term preservation of clonal transgenic silkworms using a parthenogenetic strain. *J. Insect. Physiol.* 81, 28–35. doi: 10.1016/j.jinsphys.2015.06.011

Zabelina, V., Yonemura, N., Uchino, K., Iizuka, T., Mochida, Y., Takemura, Y., et al. (2021). Production of cloned transgenic silkworms by breeding non-diapausing parthenogenetic strains. *J. Insect. Physiol.* 132:104265. doi: 10.1016/j.jinsphys.2021.104265

Zabelina, V. Y., and Klymenko, V. V. (2008). Ovary transplantation in the silkworm *Bombyx mori* L.: parthenocloning by eggs produced in male recipient. *Séricologia* 48, 123–128.

Zhao, A. C., Zhao, T. F., Zhang, Y. S., Xia, Q. Y., Lu, C., Zhou, Z. Y., et al. (2010). New and highly efficient expression systems for expressing selectively foreign protein in the silk glands of transgenic silkworm. *Trans. Res.* 19, 29–44. doi: 10.1007/s11248-009-9295-7

Zhong, B. X., Li, J. Y., Chen, J. E., Ye, J., and Yu, S. D. (2007). Comparison of transformation efficiency of piggyBac transposon among three different silkworm *Bombyx mori* strains. *Acta Biochim. Biophys. Sin.* 39, 117–122. doi: 10.1111/j.1745-7270.2007.00252.x

Conflict of Interest: The authors declare that the research was conducted in the absence of any commercial or financial relationships that could be construed as a potential conflict of interest.

Publisher's Note: All claims expressed in this article are solely those of the authors and do not necessarily represent those of their affiliated organizations, or those of the publisher, the editors and the reviewers. Any product that may be evaluated in this article, or claim that may be made by its manufacturer, is not guaranteed or endorsed by the publisher.

frontiers | Frontiers in Physiology

ORIGINAL RESEARCH
published: 13 April 2022
doi: 10.3389/fphys.2022.836106

Methods for the Cost-Effective Production of Bacteria-Derived Double-Stranded RNA for *in vitro* Knockdown Studies

Thomas-Wolf Verdonckt and Jozef Vanden Broeck*

Molecular Developmental Physiology and Signal Transduction Research Group, Animal Physiology and Neurobiology Division, Department of Biology, KU Leuven, Leuven, Belgium

OPEN ACCESS

Edited by:
Pamela Imperadore, Zoological Station Anton Dohrn, Italy

Reviewed by:
Veli Vural Uslu, RLP AgroScience, Germany
Ramesh Raju Vetukuri, Swedish University of Agricultural Sciences, Sweden

***Correspondence:**
Thomas-Wolf Verdonckt
thomaswolf.verdonckt@kuleuven.be

Specialty section:
This article was submitted to Invertebrate Physiology, a section of the journal Frontiers in Physiology

Received: *15 December 2021*
Accepted: *08 March 2022*
Published: *13 April 2022*

Citation:
Verdonckt T-W and Vanden Broeck J (2022) Methods for the Cost-Effective Production of Bacteria-Derived Double-Stranded RNA for in vitro Knockdown Studies. Front. Physiol. 13:836106. doi: 10.3389/fphys.2022.836106

RNA interference (RNAi) is a highly conserved pathway for the post-transcriptional regulation of gene expression. It has become a crucial tool in life science research, with promising potential for pest-management applications. To induce an RNAi response, long double-stranded RNA (dsRNA) sequences specific to the target gene must be delivered to the cells. This dsRNA substrate is then processed to small RNA (sRNA) fragments that direct the silencing response. A major obstacle to applying this technique is the need to produce sufficiently large amounts of dsRNA in a very cost-effective manner. To overcome this issue, much attention has been given to the development and optimization of biological production systems. One such system is the *E. coli* HT115 strain transformed with the L4440 vector. While its effectiveness at inducing knockdowns in animals through feeding of the bacteria has been demonstrated, there is only limited knowledge on the applicability of bacteria-derived dsRNA for *in vitro* experiments. In this paper, we describe and compare methods for the economical (43.2 €/mg) and large-scale (mg range) production of high-quality dsRNA from the HT115 bacterial system. We transformed the bacteria with constructs targeting the *Helicoverpa*-specific gene *Dicer2* and, as a non-endogenous control, the *Green Fluorescent Protein* gene (*GFP*). First, we compared the total RNA extraction yields of four cell-lysis treatments: heating, lysozyme digestion, sonication, and a control protocol. Second, we assessed the quality and purity of these extracted dsRNAs. Third, we compared methods for the further purification of dsRNAs from crude RNA extracts. Finally, we demonstrated the efficiency of the produced dsRNAs at inducing knockdowns in a lepidopteran cell line. The insights and results from this paper will empower researchers to conduct otherwise prohibitively expensive knockdown studies, and greatly reduce the production times of routinely or large-scale utilized dsRNA substrates.

Keywords: DsRNA (Double-stranded RNA), HT115 strain, insect, lepidoptera, RNAi–RNA interference, pest control

1 INTRODUCTION

RNA interference (RNAi) is a highly conserved pathway that has become an important tool for loss of function research in both clinical and fundamental research. It enacts post-transcriptional gene silencing through the sequence-specific sequestration or degradation of mRNAs. This process is mediated through an RNA-induced silencing complex (RISC) with the main effector protein being a member of the argonaute family. The RISC is directed to the target mRNA by a complementary small-RNA (sRNA). In arthropods, the cytoplasmic presence of dsRNA activates the small-interfering RNA (siRNA) mediated RNAi (siRNAi) pathway. This siRNAi pathway thus allows the targeted knockdown of genes through the delivery of sequence-specific dsRNA to animal or cellular model systems (Zotti and Smagghe 2015).

The RNAi technology is being developed as a promising biofriendly alternative to current insect pest management strategies (Mezzetti et al., 2020). To this end, the most direct in-field application procedure consists in the spraying of "naked", complexed, or encapsulated dsRNA onto the host plants or pest insects. It is estimated that such treatments would require 2–10 g of dsRNA per hectare (Zotti et al., 2018).

The efficacy of RNAi is highly dependent on the targeted insect species, tissues and genes. The order of Lepidoptera, comprising moths and butterflies, includes many of the most damaging pest species to agriculture. This insect order is characterized by its refractoriness to the application of RNAi technology (Terenius et al., 2011), partly due to the presence of RNAi efficiency-related nucleases (REases) that degrade dsRNA substrates before they can be processed by the RNAi machinery (Singh et al., 2017; Guan et al., 2018). For these species, several micrograms of dsRNA are required to achieve significant knockdowns when delivered to the hemocoel under experimental settings, with in-field applications expected to be even more demanding (Xu et al., 2016).

A crucial requirement for the application of the RNAi technology in the lab or field is therefore the cost-effective production of dsRNA. Three main approaches are commonly used to produce dsRNA in experimental settings. Synthesis from NTPs is a rapidly advancing technology, with industrial costs as low as ~$60 USD per Gram (Zotti et al., 2018). A second approach is *in vitro* synthesis through RNA-dependent RNA polymerases. The MEGAscript™ RNAi Kit (Thermo Scientific) allows to produce dsRNA at a cost of ~$3000 USD for 10 mg. A third option is the production of dsRNA through fermentation. In this process, the dsRNA is synthetized in transgenic cells. This is expected to become the most available and cost-effective method for the large-scale production of dsRNA in the laboratory setting, with target costs near $4 USD per 1 g (Zotti et al., 2018). Still, these prices are yet to become commercially feasible, and custom orders for *in vitro* transcription (IVT) constructs up to 500 bp in size are still billed at ≥$500 USD for 10 mg.

One such system is the bacterial HT115 (DE3) (Takiff et al., 1989) strain of *E. coli*, an RNase III-deficient bacterium. As such, it cannot degrade dsRNA, which allows for its accumulation in the cytoplasm. It can express the bacteriophage T7 polymerase gene from an inducible (Lac) promoter. When transformed with expression plasmids containing T7 promoter sequences, HT115 can produce large quantities of sequence-specific dsRNAs. The L4440 plasmid (Timmons and Fire, 1998) contains two T7 promoters flanking a multiple cloning site and an ampicillin resistance gene.

HT115 bacteria were first transformed with the L4440 plasmid in 2003 (Tenllado et al., 2003) and have since then become a popular tool for functional studies in invertebrate physiology. To this end, the kinetics of dsRNA production in batch cultures have been assayed and production optimized (Papić et al., 2018).

The system is mainly used for direct feeding of induced bacteria to research animals in a process termed bacterium-mediated RNA interference (bmRNAi) (Timmons and Fire, 1998; Goodfellow et al., 2019; Kunte et al., 2020). Recent publications reaffirm its useability in the important lepidopteran pest genera *Spodoptera* and *Helicoverpa* (Vatanparast et al., 2021; Wan et al., 2021; Wang et al., 2021).

For functional research, it is very desirable to produce cost-effective dsRNAs that can be administered via injection or transfection to the research organism. Delivery of live or inactivated bacteria into the hemocoel of orthopteran insects was shown to trigger a knockdown of the target gene (Vogel, 2020). This approach is however unpractical in *Helicoverpa* pests due to the immune responses generated upon the presence of bacteria in the hemolymph (Li et al., 2019). Injections of HT115 bacteria-derived dsRNA extracted using commercial kits was shown to be effective at inducing target gene knockdowns in a lepidopteran species (Wan et al., 2021). As a result, research has focused on developing a cost-effective protocol for the isolation of dsRNA from the bacterial cells. A one-step protocol was published for the extraction of total nucleic acids from the bacteria using cost-effective reagents (Posiri et al., 2013). Still, the one-step phenol-guanidine based protocol (Chomczynski and Sacchi, 1987) is often favored for its RNA-isolation specificity.

Increased physiological effects observed during *in vivo* studies suggest that heating or sonication of bacteria facilitates release of dsRNA into the gut lumen, likely by compromising the integrity of the bacterial cell wall or fragmenting the dsRNA constructs (Kim et al., 2015; Vatanparast and Kim, 2017). Ahn et al. demonstrated that these pre-treatments likewise increase the total RNA yield during phenol-guanidine extractions (Ahn et al., 2019). However, to date, little is known about the reliability of these and other pre-treatments, with no replicate data available, nor is it known how these treatments impact the efficacy of extracted dsRNA at inducing an RNAi response.

The total RNA extracted from the bacterial cells needs to be purified for application in knockdown experiments. Two main techniques are described in literature. The first is digestion of non-specific nucleic acids with DNases and RNases. The second consists of the selective precipitation of dsRNA using lithium chloride salt solutions (Diaz-Ruiz and Kaper, 1978). Little is known about the yield of the described techniques nor the quality of the purified dsRNAs.

In the current paper, we compare different protocols for the cost-effective extraction and purification of dsRNA from HT115 bacterial cells expressing *dsRNA* constructs of the *Green Fluorescent Protein* (*GFP*) or the *Helicoverpa*-specific gene *Dicer2* (*Dcr2*). Therefore, we assay the impact of three pre-treatments on the efficiency of total RNA extraction with phenol-guanidine. Furthermore, we analyze the quality and quantity of the resulting dsRNA extracts. In addition, we evaluate the applicability of two dsRNA purification approaches on their yield and cost-efficiency. Finally, we demonstrate the useability of thus derived dsRNA for *in vitro* knockdown studies in a lepidopteran cell line.

2 MATERIALS AND METHODS

2.1 Gene Sequence Retrieval and Phylogenetic Analysis

The *Helicoverpa armigera Dicer* transcript sequences were identified through the BLAST (Altschul et al., 1990) algorithm by using orthologous genes from closely related species or model organisms as queries and *H. armigera* transcriptome shotgun assemblies (TSAs) as search databases. TSA hits were verified manually on completeness, open reading frames and protein translations via the SnapGene software (Insightful Science) and conserved domains identified through the Conserved Domain Database (Lu et al., 2020). The identified *Helicoverpa armigera* Dicer protein sequences were aligned with known insect proteins through the MUSCLE (Edgar, 2004) algorithm on the MEGA7 (Kumar et al., 2016) platform using default parameters and 200 iterations. The aligned sequences were then exported to IQ-TREE (Nguyen et al., 2015) version 1.6.12 and their phylogenetic relationship was calculated by automatically determining the best substitution model through ModelFinder (Kalyaanamoorthy et al., 2017), performing 10.000 ultrafast bootstraps (Hoang et al., 2018) and carrying out a 1,000 replicates SH-aLRT (Guindon et al., 2010) test. The resulting maximum likelihood tree was uploaded to iTOL (Letunic and Bork, 2021) for rooting and rendering. The identified transcripts and a phylogenetic analysis are presented in the supplementary data (**Supplementary Table S1**; **Supplementary Figure S1**).

2.2 Vector Construction and Bacterial Transformation

The L4440 vector was digested with the HindIII-HF® (New England BioLabs) DNA restriction enzyme following manufacturer's instructions. The *Helicoverpa Dicer2* sequence was amplified from a cDNA library of adult female *Helicoverpa armigera* using the Q5® High-Fidelity DNA Polymerase (New England BioLabs) with Q5 high GC enhancer and primers with 5′ overhangs (sequences available in **Supplementary Table S2**) with a total reaction volume of 25 µL. The PCR was carried out with an initial denaturation at 98°C for 30 s, followed by 35 cycles of 98°C for 10 s, 64.6°C for 30 s and 72°C for 30 s, followed by a final extension at 72°C for 2 min. 20 µL of the PCR product was purified with the GenElute™ PCR Clean-Up Kit (Merck) following manufacturer's instructions. A Gibson assembly was performed with a 1:2 mass to mass ratio of the digested L4440 vector and the purified PCR products using the NEBuilder® HiFi DNA Assembly Master Mix (New England BioLabs). The assembled vectors were transformed into competent HT115 (DE3) *E. coli* cells. Briefly, 10 µL of assembled vector was added to 100 µL competent cells and carefully mixed by stirring. The cells were incubated on ice for 30 min and then transformed via a heat shock treatment of 42°C for 40 s. The cells were then allowed to grow in 250 µL LB medium for 1.5 h. Hereafter, 150 µL of the transformed bacteria were plated on LB agar plates containing ampicillin (50 µg/ml) and tetracycline (12.5 µg/ml). The plates were incubated at 37°C overnight. Individual colonies were picked and grown in 5 ml LB with ampicillin (50 µg/ml) and tetracycline (12.5 µg/ml) with shaking overnight. Plasmids were extracted from 2 ml of the grown cells using the GenElute™ HP Plasmid Miniprep Kit (Merck) following manufacturer's instructions. The extracted plasmids were sequenced via sanger sequencing (LGC, Biosearch Technologies) to verify the sequence of the cloned insert.

2.3 Bacterial Culturing and Induction of dsRNA Expression

HT115 bacteria containing the L4440-*HaDcr2* or L4440-*GFP* constructs (insert sequences in **Supplementary Table S3**, L4440-*GFP* assembly described in Vogel, 2020) were plated onto LB plates with ampicillin (50 µg/ml) and tetracycline (12.5 µg/ml) and incubated overnight at 37°C.

Individual colonies were picked and resuspended in 20 µL MilliQ water. 2 µL of the resuspended cells were used in colony PCR reactions using 6.5 µL REDTaq® DNA polymerase (Merck) and 2 µL each of the gene specific forward and reverse primers (10 µM) for a total reaction volume of 12.5 µL. For each colony, PCR reactions were run to verify the bacterial strain and the presence of the correct L4440 plasmid. The bacterial strain identity was established using primers located 5' upwards and within the T7 polymerase genomic insert (primers HT115 forward and HT115 reverse, respectively). The presence of the L4440 plasmids was assayed using the M13 forward primer and an insert-specific reverse primer (*GFP* reverse or *Dicer2* reverse). All primer sequences are available in **Supplementary Table S2**. The PCR reactions were run with the following conditions: 96°C for 5 min; then 25 cycles of 96°C for 45 s, 53°C 45 s, 72°C for 1 min; then a final elongation step of 72°C for 3 min. The PCR product sizes were visualized as described in **Section 2.6**. The agarose gel results are displayed in **Supplementary Figure S2.**

Cells from verified colonies were grown in 5 ml selective LB medium with ampicillin (50 µg/ml) and tetracycline (12.5 µg/ml) at 37°C with shaking overnight. 4 ml of the cells were then transferred to 400 ml fresh selective LB medium and incubated again at 37°C with shaking for 4 hours. Hereafter, the optical density (OD) of the cell culture was assayed using a Ultrospec® 10 Cell Density Meter (Biochrom). Once the OD was above 0.4, the bacterial cells were induced with sterile filtered Isopropyl β-d-1-thiogalactopyranoside (IPTG) to a final concentration of 1 mM.

Five hours after the induction, the cells were pelleted by centrifugation (4,000 rcf for 10 min at 4°C), they were resuspended in 1 ml Milli-Q® water (MilliporeSigma) (henceforth abbreviated to "MQ") and transferred to a 15 ml falcon tube.

2.4 Bacterial Total RNA Extraction

The collected cells were freeze-thawed 10 times using liquid nitrogen. Next, MQ was added to a final volume of 4 ml (100x concentrated). They were stored at −80°C until further usage.

Four alternative protocols were evaluated to increase the release of RNA from the bacterial cells. The protocols differed in the treatments applied prior to RNA extraction (the pre-treatments). The applied pre-treatments consisted of either (A) the digestion of the bacterial cell wall with lysozyme, (B) the disruption of the bacterial cells via sonication, (C) the lysis of the bacterial cells via heating in QIAzol, or (D) a control protocol where no pre-treatment was applied. The pre-treatments were carried out as follows:

(A) **Lysozyme Digestion**: 100 µL of cells were pelleted by centrifugation (10,000 rcf for 5 min at 4 °C). The supernatant was removed, and the pellet treated with 100 µL of a lysozyme digestion mix consisting of 1.3 µL of 10 mg/ml lysozyme solution (in 50% v/v glycerol), 5.2 µL of 0.5 M EDTA, 13 µL Triton X-100 and 1.3 ml MQ water at 37 °C for 30 min. The digested cells and supernatants were then combined and mixed with 1 ml of QIAzol.

(B) **Sonication**: 100 µL bacterial cell suspension was sonicated on ice for three cycles of 30 s on and 30 s off using the SLPe digital sonifier (Brandson) at 10% amplitude. The sonicated cells were then mixed with 1 ml QIAzol.

(C) **Heating**: 100 µL of bacterial cell suspension was mixed with 1 ml of QIAzol by vortexing for 5 s. The homogeneous mixture was then incubated for 30 min in a 60°C oven.

(D) **Control (no Pre-Treatment)**: 100 µL of bacterial cell suspension was mixed with 1 ml of QIAzol by vortexing for 5 s.

The QIAzol-cell mixtures were then incubated at RT for 5 min. Hereafter, 0.2 ml of chloroform was added and the samples vortexed for 15 s. The samples were left at rest for 10 min and then centrifuged at 12,000 rcf for 15 min at 4°C. After phase separation, the aqueous phase had a volume of approximately 700 µL. To avoid contamination from the interphase, 600 µL of the aqueous phase was taken and transferred to a clean 1.5 ml Eppendorf tube. 500 µL of isopropanol was added and the samples briefly vortexed. Hereafter the samples were left to stand for 7 min, then spun at 12,000 rcf for 10 min at 4°C. The supernatants were removed, and the RNA pellet washed with 1 ml of 70% (v/v) EtOH in RNase-free water. The samples were then once more spun at 7,500 rcf for 5 min at 4 °C. The supernatants were removed, and the RNA pellet was left to dry for 10 min, after which the RNA was resuspended in 180 µL RNase-free water. The absorbance at 260 nm (A_{260}) was assessed through a NanoPhotometer® N60 (Implen), and the total RNA concentration estimated using a conversion factor of 40 µg/ml/A_{260}. The absorbance measurements are provided in the **Supplementary Table S4**.

Furthermore, the scalability of the protocol was assessed by extracting the total RNA from 800 ml of induced bacterial culture. The heating pre-treatment was applied. Briefly, the bacteria were pelleted by centrifugation (4,000 rcf for 10 min at 4°C) and resuspended in MQ. The cells were split in two equal volumes. 40 ml of QIAzol was added to each volume and the mixtures vortexed until homogeneous. The mixtures were then incubated in a 60°C water bath for 30 min; 8 ml chloroform was added to each tube and the mixtures briefly vortexed. The combined volume was distributed over three 50 ml centrifuge tubes with sealing cap (Nalgene). Phase separation was allowed to occur for 7 min, then the samples were spun at 12,000 rcf in a Multifuge X1R (Heraeus) for 15 min at 4°C. The supernatants (~13 ml per tube) were collected in new 50 ml falcon tubes and combined with 9 ml isopropanol. The mixtures were incubated at RT for 7 min then again spun at 12,000 rcf for 15 min at 4 °C. The resulting RNA pellets were washed three times with 5 ml 70% (v/v) EtOH in RNase-free water, pelleting the RNA by centrifuging at 7,500 rcf for 5 min at 4°C between each wash. Finally, the remaining traces of EtOH were removed from the RNA pellets via evaporation and the RNA from all tubes combined and dissolved in 10 ml RNase-free water.

2.5 dsRNA Purification

Total RNA extracts were treated for the purification of the dsRNA fraction. Two approaches were employed, enzymatic digestion of DNA and/or ssRNA, and selective precipitation of dsRNA.

2.5.1 Enzymatic Digestion

To digest the ssRNA fraction, the total RNA was treated with RNase A (Thermo Scientific). As RNase A can also cleave dsRNA under low salt conditions (Libonati and Sorrentino, 2001), two buffers were compared in their ability at shielding the dsRNA from degradation. These were (1) a NaCl-based buffer and (2) the TURBO™ DNase digestion buffer (Thermo Scientific), hereafter referred to as "TURBO buffer".

(1) NaCl Buffer: 1.125 A_{260} units (1 A_{260} unit is defined as the amount of nucleic acid that produces an OD of 1 in 1 ml) of total RNA were diluted to a volume of 90 µL with RNase-free water and mixed with 10 µL of a 10x RNase digestion buffer consisting of 300 mM NaCl, 10 mM Tris-HCl and 5 mM EDTA with neutral pH. The mixture was incubated at 37 °C for 30 min. Hereafter, 1 µL of 10 mg/ml RNase A (Thermo Scientific) was added and the sample incubated at 37°C for an additional hour.

(2) TURBO Buffer: Ahn et al. (2019) demonstrated that the TURBO buffer can be used to purify dsRNA from bacterial total RNA extracts, with the added benefit of allowing a simultaneous DNase digestion. To this end, 1.125 A_{260} units of total RNA were diluted to a volume of 90 µL with RNase-free water and mixed with 10 µL of 10x TURBO™ DNase digestion buffer (Thermo Scientific). The mixture was incubated at 37°C for 30 min. Hereafter, 1 µL of 2 U/µl TURBO™ DNase (Thermo Scientific) and 1 µL of 10 mg/

ml RNase A (Thermo Scientific) were added and the sample was incubated at 37°C for an additional hour.

The RNA was then extracted from the digested samples following the QIAzol extraction protocol, with 500 µL QIAzol. This resulted in a 350 µL water phase. The RNA was precipitated with 350 µL isopropanol and washed with 0.5 ml 70% (v/v) EtOH in RNase-free water. The purified dsRNA was then resuspended in 50 µL RNase-free water.

2.5.2 Selective Precipitation

The dsRNA fraction was purified via selective precipitation in a LiCl solution. This protocol is hereafter referred to as "LiCl precipitation". For this protocol, 1.125 A_{260} units of total RNA were diluted to a final volume of 150 µL using RNase-free water. 1/3rd volume of 8M ice-chilled RNase-free LiCl (Merck) was added to the sample and mixed for a final concentration of 2 M LiCl. The mix was incubated at −20°C for 30 min, then centrifuged at 16,000 rcf for 30 min at 4°C. The supernatant was carried over to a new clean tube and combined with ½ volume of 8 M RNase-free ice-chilled LiCl to a final concentration of 4 M. The samples were incubated at −20°C overnight, then once more centrifuged at 16,000 rcf for 30 min at 4°C. The supernatants were discarded, and the dsRNA pellet washed with 500 µL 70% (v/v) EtOH in RNase-free water. The samples were again centrifuged at 16,000 rcf for 5 min at 4°C. The supernatants were removed, and the pellet allowed to dry. The dsRNA was then resuspended in 50 µL RNase-free water.

The scalability of the LiCl precipitation protocol was assessed on 5 ml of RNA extracted from 400 ml induced bacteria. The given protocol was followed until the dsRNA pellet was obtained. The pellet was washed thrice with 5 ml 70% (v/v) EtOH in RNase-free water and the sample spun at 4,000 rcf for 10 min at 4°C. The supernatant was removed, and the pellet allowed to dry. The dsRNA was then resuspended in 1 ml RNase-free water.

The A_{260} of the purified dsRNA solutions was assessed with a NanoPhotometer® N60 (Implen). The absorbance measurements are provided in **Supplementary Table S6**. The dsRNA concentration was then calculated using a conversion factor of 46 µg/ml/A_{260}, as determined by Strezsak et al. (2021).

2.6 Agarose Gel Electrophoresis

To visualize the size of the PCR products, or the size and integrity of dsRNA strands in RNA extracts or purifications; the nucleic acids were run on a non-denaturing 1% agarose gel in TAE buffer at 120V for half to 2 hours (precise timing given in figure descriptions). The gel was stained with the GelRed® (Biotium) nucleic acid stain and imaged on a ProXima 2000 series platform (Isogen).

2.7 *In vitro* dsRNA Synthesis

L4440 plasmids containing the target constructs were used as templates for PCR reactions using the REDTaq® DNA polymerase. For each reaction, 2.5 ng of plasmid was combined with 6.25 µL REDTaq® and 0.5 µL of forward and reverse primers with T7 overhangs (10 µM) with a final volume of 12.5 µL. The primer sequences are shown in **Supplementary Table S2.**

The PCR was run as follows: 98°C for 5 min, followed by 5 cycles of 98°C for 45 s, 55°C for 45 s and 72°C for 1 min. This was followed by 35 cycles of 98°C for 45 s, 60°C for 45 s and 72°C for 1 min. Finally, the reaction mixture was incubated at 72°C for 2 min and then stored at 4°C. 8 µL of the PCR products were used as substrates for MEGAscript™ T7 transcription reactions (Thermo Scientific). dsRNA was produced and purified following manufacturer's instructions.

2.8 Knockdown in a Cell Line

Helicoverpa zea derived RP-*Hz*GUT-AW1 cells (Goodman et al., 2004) were kept in Ex-Cell® 420 (Merck) medium supplemented with 10% fetal bovine serum (Sigma-Aldrich), 100 U/ml penicillin (Gibco), 100 mg/ml streptomycin (Life Technologies) and 0.25 µg/ml amphotericin B (Sigma-Aldrich). The cells were grown at 27.5°C and subpassaged 1/3 at 90% confluency.

To assess viability and concentration, 10 µL of scraped RP-*Hz*GUT-AW1 cells were mixed 1:1 with 0.4% Trypan Blue (Sigma-Aldrich) and loaded onto a cell counting slide. Cell viability and concentration were measured with the Bio Rad TC20™ Automated Cell Counter.

Cells with a viability above 95% were plated at a density of 2.5 × 10^5 cells/well in 24-well plates. They were left to attach for 3 hours, after which time they were washed with 200 µL of non-supplemented Ex-Cell® 420 (Merck) medium and then treated with the transfection medium.

The transfection medium was prepared by combining 450 ng dsRNA (2.5 µg/ml condition) or 90 ng dsRNA (0.5 µg/ml condition) with 90 µL non-supplemented Ex-Cell® 420 (Merck) and letting the mixture incubate at room temperature for 30 min. In parallel, 90 µL of non-supplemented Ex-Cell® 420 (Merck) was mixed with 3.7 µL Escort IV (Sigma-Aldrich) transfection reagent and likewise left to incubate at RT for 30 min. After the incubation period, the two volumes were combined and the lipoplexes allowed to form for an additional 20 min at RT. The resulting 180 µL transfection mixture was then added directly to the cells. The cells were placed overnight at 27.5°C, after which the transfection medium and non-adherent cells were removed and replaced by 500 µL of supplemented Ex-Cell® 420 (Merck) medium. The cells were grown for one more day after which they were loosened by pipetting and collected in 1.5 ml tubes. The cell viability and concentration were assayed as described above. The collected RP-*Hz*GUT-AW1 cells were pelleted by spinning for 10 min at 1,000 rcf and 4 °C. The supernatant was removed, and the cells resuspended in 10 µL Milli-Q® water. The cells were then stored at −80°C.

2.9 RP-*Hz*GUT-AW1 RNA Extraction and cDNA Synthesis

Total RNA was extracted from the frozen RP-*Hz*GUT-AW1 cells with the RNeasy Lipid Tissue Mini Kit (Qiagen) following manufacturer's instructions. The DNase digestion step was included to remove potential genomic DNA contamination. Quality and quantity of the extracted RNA were assessed with a NanoPhotometer® N60 (Implen) using a conversion factor of 40 µg/ml/A_{260}. cDNA was synthetized from 400 ng RNA in a

TABLE 1 | Percentage of A_{260} units retained after treatment of total RNA (%$A_{260\ dsRNA}$) from *dsGFP* or *dsDcr2* producing bacteria for all combinations of pre-treatments and purification methods tested.

%$A_{260\ dsRNA}$ *GFP*	Purification method			Average per pre-treatment
	LiCl precipitation	NaCl buffer	TURBO buffer	
Pre-treatment				
Lysozyme	14.1	16.9	16.8	15.9
Sonication	20.9	20.6	20.2	20.6
Heating	18.2	18.0	16.4	17.5
Control	21.6	20.9	20.6	21.0
Average per purification method	18.7	19.1	18.5	
%A_{260} dsRNA *Dcr2*				
Pre-treatment				
Lysozyme	11.4	13.5	12.9	12.6
Sonication	17.5	17.9	18.4	17.9
Heating	15.4	13.9	16.2	15.2
Control	18.0	16.8	17.3	17.4
Average per purification method	15.6	15.5	16.2	

10 µL reaction using the PrimeScript First Strand cDNA Synthesis Kit (TaKaRa) following manufacturer's instructions.

2.10 Quantitative Real Time PCR

Target gene expression was assessed through a QuantStudio™ 3 Real-Time PCR System (Thermo Scientific). All PCR reactions were carried out in duplicate with 5 µL Fast SYBR™ Green Master Mix (Thermo Scientific), 0.375 µL 10 µM of the forward and reverse primers, and 4.25 µL cDNA (synthetized from 6.67 ng RNA). All qPCR primers used are presented in **Supplementary Table S2**.

Primer efficiency was determined through relative standard curves with 5x serial dilutions. Specificity and primer-dimer formation were assessed through melting curves. Only primers with efficiencies between 90 and 110% with single melt peaks were used. Gene expression was determined through the delta-delta Ct method (Livak and Schmittgen, 2001). The *Helicoverpa zea* housekeeping genes actin (GenBank: AF286061.1) and arginine kinase (GenBank: HM068068.1) were selected for normalization from a list of candidates through the geNorm algorithm in the NormqPCR package (Perkins et al., 2012).

2.11 Statistical Analysis

Data analysis was carried out using the GraphPad Prism 8 software. To assay for significant differences in the concentration of RNA extracts dependent on the pre-treatment applied and the dsRNA construct used, a two-way ANOVA was performed. A *post hoc* Tukey's multiple comparisons test was carried out to identify which pre-treatments yielded significantly different RNA concentrations. Next, the impact of three independent variables (pre-treatment, extraction method and dsRNA construct) was assessed on: (1) the fraction of dsRNA in the total RNA samples, and on (2) the final dsRNA production yield. To this end, repeated measure two-way ANOVA tests were performed using: (1) the percentage of A_{260} units retained after purification (**Table 1**) or (2) the calculated dsRNA yields (**Table 2**), respectively. No sphericity was assumed, and *p*-values adjusted with the Geisser-Greenhouse method. For both tests, *post hoc* Tukey's multiple comparisons tests were used to identify which pre-treatments significantly differed. The effect of the type of dsRNA used for transfection of RP-*Hz*GUT-AW1 on the viability and cell count was determined with a one-way ANOVA. The significance of the resulting gene knockdowns was calculated through multiple *t*-tests, with alpha = 0.05. Each knock down condition was analyzed individually, without assuming a consistent SD. To assay possible differences in the knockdown efficiencies of the tested dsRNA types, a one-way ANOVA with Brown-Forsythe and Welch tests was applied. All analysis results are provided in the text or in the **Supplementary Tables S5, 7–9**.

3 RESULTS

Bacterial systems allow the production of complex organic molecules in a highly scalable and cost-effective manner. As such they are attractive candidates for the production at medium to large-scale of dsRNA constructs in a laboratory setting. Up to date, bacterially produced dsRNA is rarely applied for *in vitro* studies, partly due to as yet inefficient or unreliable extraction techniques, and partly due to the lack of trust in the purity and effectiveness of bacteria-derived dsRNA. Some major obstacles that need to be overcome are: (1) the

efficient extraction and (2) the purification of the dsRNA from the bacterial cells, including the removal of biological contaminants. The protocols developed for this purpose must be (3) scalable while maintaining the quality of the final product. The produced dsRNA should (4) not be cytotoxic and (5) perform on par with other commercially available alternatives. Based on the results presented in this paper we demonstrate that the applied methods satisfy each of these criteria.

3.1 Pre-Treatments Reliably Improve Total RNA Extraction Efficiency

A major challenge to the production of dsRNA from bacterial systems is the efficient release of the dsRNA from the cells without affecting its integrity. A commonly applied technique is the use of phenol/guanidine-based lysis reagents. While efficient for most eukaryotic cells and tissues, this method often results in low yields due to the presence of a rigid bacterial cell wall. To overcome this issue, we assayed how the total RNA extraction yield of a control protocol was affected when applying three pre-treatments prior to extraction. The control protocol consisted of an incubation in a phenol/guanidine-based lysis reagent for 5 minutes at room temperature. The designator "control" was chosen as this treatment is commonly found in phenol/guanidine-based protocols, and thus functioned as a baseline through which the impact of additional pre-treatments could be established. The pre-treatments were: (A) digestion of the bacterial cell wall with lysozyme, (B) sonication of the bacterial cells, and (C) heating of the cells in lysis reagent. For this purpose, 100x concentrated and freeze-thawed bacterial cells containing the L4440-*HaDcr2* or L4440-*GFP* constructs were aliquoted in 100 µL volumes and subjected to the described pre-treatments. Per condition four replicates were included in this analysis. Total RNA was then extracted from the pre-treated and control cells. The A_{260} of the total RNA was measured (**Supplementary Table S4**), the concentration calculated with a conversion factor of 40 µg/ml/A_{260} and the RNA was run on an agarose gel. To find whether the pre-treatments affected the extraction efficiency, a two-way ANOVA was applied (statistics collected in **Supplementary Table S5**) on the collected *dsGFP* and *dsDcr2* data. The results indicated that the pre-treatments as well as the identity of the dsRNA construct significantly affected the extraction efficiency ($p < 0.0001$). A *post hoc* Tukey's multiple comparisons test shows that all pre-treatments significantly ($p < 0.0001$) differed from each other and the control (**Figure 1**). Sonication resulted in the highest increase relative to the control, with an average of 2.9-fold, followed by heating with a 2.2-fold increase and digestion with a 1.8-fold increase.

400 ng of total RNA from *dsGFP* or *dsDcr2* expressing bacteria extracted through each treatment were run on a 1% agarose gel (**Figure 2A**). As a negative control, total RNA from non-induced cells transformed with the *L4440-GFP* construct and extracted via the heating pre-treatment was likewise run on a 1% agarose gel (**Figure 2B**). The *dsGFP* and *dsDcr2* constructs with an expected size of 775 bp and 712 bp respectively, were at ~700 bp and ~650 bp due to the higher electrophoretic mobility of dsRNA compared to the dsDNAs represented in the ladder. As expected, the *dsGFP* band was missing in the negative control sample. For all treatments and constructs the dsRNA band was present at the expected distance. The intensity of the dsRNA band varied between treatments. The band intensity is dependent on (A) the fraction dsRNA in the total RNA and (B) the degree of degradation of the dsRNA. Total RNA extracted through the control method displayed the strongest dsRNA band, indicating a large fraction of dsRNA; while the RNA extracted from sonicated cells displayed the weakest band with a strong smear underneath the construct, suggesting band degradation.

3.2 Purification Protocols Yield Enriched and Intact dsRNA

The total RNA extracted from the bacteria must be treated to isolate the dsRNA fraction and remove undesired bacterial RNAs. In this study we compared the efficiency and practicality of two distinct purification approaches. The first consisted in the selective precipitation of dsRNA through lithium chloride. This method will be referred to as "LiCl precipitation" throughout the text. The second approach was based on the enzymatic digestion of ssRNA with RNase A. To this end, two nucleic acid digestion buffers were tested: a NaCl-based buffer (henceforth called "NaCl buffer"), and the commercial TURBO™ DNase digestion buffer (henceforth called "TURBO buffer"). As the TURBO buffer was designed for the TURBO™ DNase, a concurrent digestion of the DNA fraction was caried out for this method. For all three purification methods, the *dsGFP* and *dsDcr2* fractions were purified from 1.125 A_{260} units total RNA of one sample obtained through each of the extraction treatments (24 samples total). The absorbance of the purified dsRNA (available in **Supplementary Table S6**) was used to calculate the percentage of A_{260} units retained after purification (**Table 1**). For simplicity, this percentage (which serves as a proxy for the fraction dsRNA in the total RNA extracts) will be referred to as "$\%A_{260\ dsRNA}$" in the text.

A repeated measure two-way ANOVA (not assuming sphericity) analysis indicates that the purification methods had no impact on the $\%A_{260\ dsRNA}$ ($p = 0.9945$, **Figure 3A**), while finding a significant dependence on the extraction pre-treatments ($p = 0.0007$, **Figure 3B**). Furthermore, the analysis indicates that the dsRNA construct also had a highly significant impact ($p < 0.0001$, **Figure 3C**). A *post hoc* Tukey test shows that the sonication pre-treatment and the no pre-treatment control differed significantly from the lysozyme and heating pre-treatments ($p \leq 0.0040$), with no significant difference within the two pairs (**Supplementary Table S7**; **Figure 3B**). The data presented in **Table 1** show that the control and sonication treatments yielded the largest fraction (~20.8 and ~17.7%$A_{260\ dsRNA}$ for *dsGFP* and *dsDcr2*, respectively) of dsRNA in the total RNA extracts. The data also indicate that the selective precipitation of dsRNA with lithium chloride and the

TABLE 2 | dsRNA production yield (µg ds*GFP* or ds*Dcr2* per ml bacterial culture) for all combinations of pre-treatments and purification methods tested.

µg/ml ds*GFP*	Purification method			Average per pre-treatment
	LiCl precipitation	NaCl buffer	TURBO buffer	
Pre-treatment				
Lysozyme	3.19	3.51	3.48	3.39
Sonication	7.98	8.06	8.09	8.04
Heating	5.56	4.82	4.38	4.92
Control	2.69	2.51	2.48	2.56
Average per purification method	4.86	4.73	4.61	
µg/ml ds*Dcr2*				
Pre-treatment				
Lysozyme	3.71	4.63	4.42	4.25
Sonication	9.21	9.08	9.36	9.22
Heating	6.30	5.68	6.60	6.19
Control	3.23	3.10	3.20	3.18
Average per purification method	5.61	5.62	5.89	

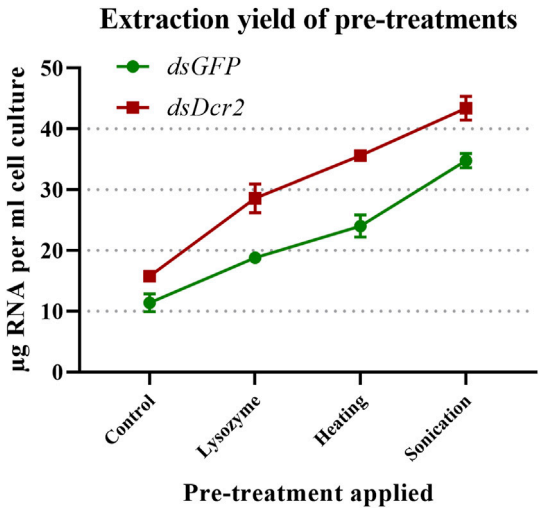

FIGURE 1 | Impact on total RNA extraction efficiency of three pre-treatments. Concentrated bacterial cells expressing two dsRNA constructs (*dsGFP* or *dsDcr2*) were freeze-thawed ten times and then subjected to cell-disruption treatments. The total RNA was then extracted through a phenol/guanidine-based method and the concentration measured through a spectrophotometer. Four replicates were tested for each condition (32 samples in total). Symbols indicate the mean, error bars the standard deviation. All pre-treatments significantly ($p < 0.0001$, two-way ANOVA with Tukey's multiple comparisons test) increased the extraction yields compared to the control method and differed between each other.

enzymatic digestion of nucleic acids yielded comparable purification efficiencies (~18.8 and ~15.8%$A_{260\ dsRNA}$ for *dsGFP* and *dsDcr2*, respectively).

The purified dsRNA fractions were analyzed through agarose gel electrophoresis to verify the removal of bacterial ssRNA or DNA (**Figure 2C**) and assess the integrity and intensity of the purified dsRNA band (**Figure 4**). The data show that the purification via LiCl precipitation or RNase A digestion with the NaCl buffer did not affect the integrity of the dsRNA bands. In contrast, RNase A digestion with the TURBO buffer resulted in a visibly lower band intensity, suggesting degradation.

Starting from the absorbance data of the purified dsRNA and total RNA, we can calculate the amount of purified dsRNA per milliliter of bacterial cell culture for each combination of pre-treatments and purification methods (**Table 2**). The amount of purified dsRNA was calculated using a conversion factor of 46 µg/ml/A_{260} (Strezsak et al., 2021). A repeated measure two-way ANOVA (not assuming sphericity) analysis once more indicated that the purification method had no impact on the final production yield of dsRNA per ml cell culture ($p = 0.9935$). The most determining factor was the pre-treatment applied (94% of variation, $p < 0.0001$), although the dsRNA construct also had a significant impact (5% of variation, $p = 0.0002$). A *post hoc* Tukey's multiple comparisons test confirmed that all pre-treatments significantly differed between each other ($p \leq 0.0086$). The full statistical results are given in **Supplementary Table S6**. The data indicate that the sonication pre-treatment yielded the largest amount of dsRNA per volume unit of bacterial cell culture, with an average 3.0-fold increase compared to the control for both dsRNA constructs. The second largest amount was obtained through the heating pre-treatment with a 1.9-fold increase (**Figure 5**).

3.3 dsRNA Production Protocols Are Scalable

A major advantage of the studied dsRNA extraction and purification protocols is their high scalability. To test whether the dsRNA production yields are independent from the bacterial sample size, *dsGFP* was extracted from 400 ml of induced bacterial culture using the heating pre-treatment and purifying the dsRNA through LiCl precipitation. This procedure yielded a total quantity of 1.67 mg dsRNA, or 4.18 µg dsRNA per ml cell culture. The latter value is comparable to the calculated yield of 5.56 µg/ml with smaller volume purifications (10 ml bacterial culture). The

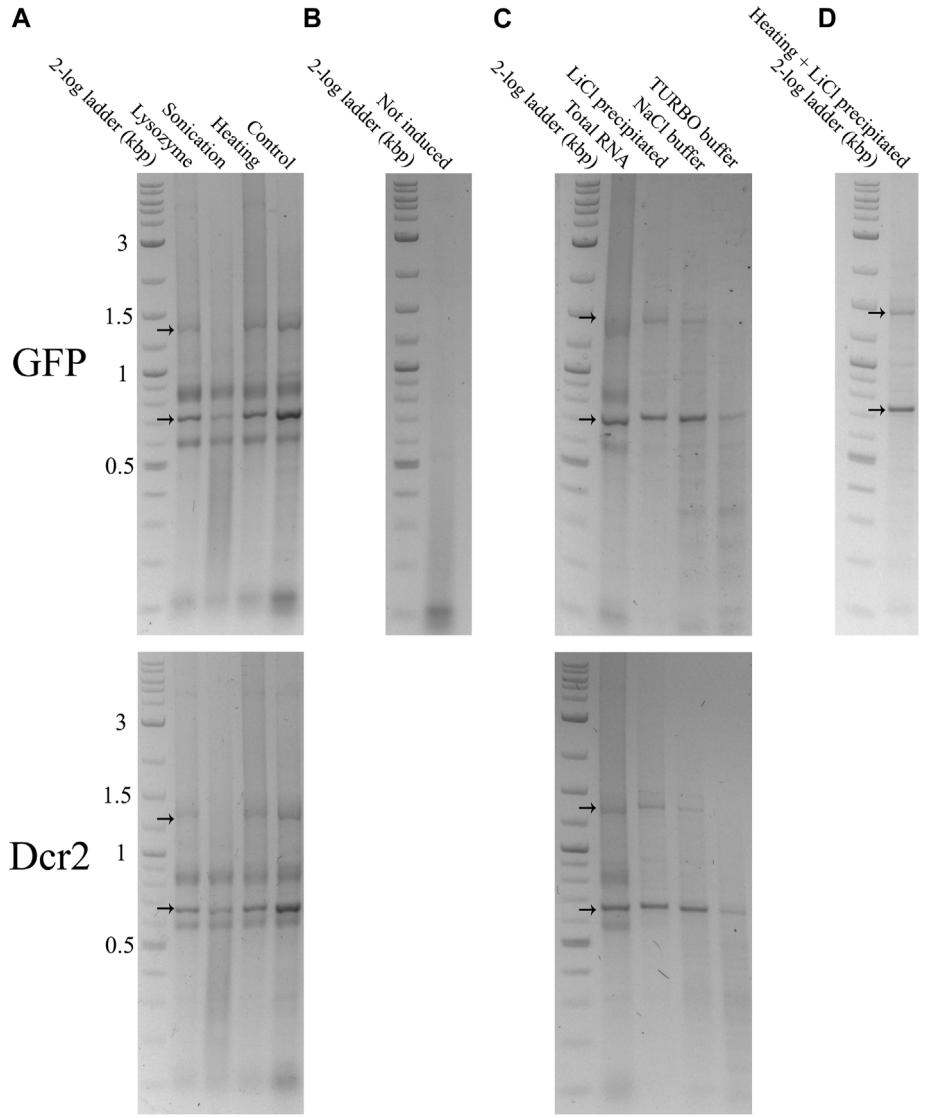

FIGURE 2 | Total and purified RNA extracted from HT115 (DE3) bacteria transformed with a L4440-*GFP* (upper gels) or L4440-*Ha*Dcr2 (lower gels) expression construct was loaded into 1% agarose gels in TAE buffer. The RNA was separated by size through electrophoresis at 120V for 2 h. The nucleic acids were imaged with the GelRed® (Biotium) stain under UV light. Arrows indicate the *dsGFP* and *dsDcr2* bands at the ~700 bp and ~650 bp positions of the DNA ladder and the persistent secondary structure dsRNA band at ~1,400 bp and ~1,300 bp respectively. **(A)**: 400 ng total RNA extracted from induced bacteria treated with a control protocol or three pre-treatments. **(B)**: 400 ng total RNA extracted using the heating pre-treatment from non-induced bacteria. **(C)**: Comparison between 400 ng total RNA extracted from induced bacteria with the heating pre-treatment and dsRNA purified from 400 ng total RNA through three purification methods. The band intensities indicate the efficiency of the applied dsRNA purification protocols. Thus, the "Heating" lane in panel A is equal to the "Total RNA" lane in panel **(C)**. **(D)**: 92 ng dsRNA purified from 400 ml of induced bacterial culture using the heating pre-treatment and LiCl precipitation.

dsRNA band integrity and purity were also maintained (**Figure 2D**).

3.4 Bacteria-Derived dsRNA is Not Cytotoxic to Cultured Cells

A major concern over the useability of bacteria-derived dsRNA in cell line experiments is the impact on cell fitness of possible chemical or biological contaminants. To exclude this possibility, RP-*Hz*GUT-AW1 cells were treated with 2.5 μg/ml *in vitro* or *in vivo* produced *dsGFP* constructs. The cells were then assayed for their viability through an automated cell counter. As the transfection protocol involves a washing step, whereby cells that detached due to possible cytotoxic effects would have been removed, the cell concentration was also assayed, and functions as a measurement of the cell adherence and growth ability. Qualitative and quantitative assays indicated that dsRNAs obtained from sonicated or heated cells and purified through lithium chloride precipitation or digestion by RNase A in the NaCl buffer, had the highest yield. Because of this, the experiment was carried out for all combinations of these methods. One-way ANOVA analyses of viable or adherent cell counting show that there was no significant difference between the

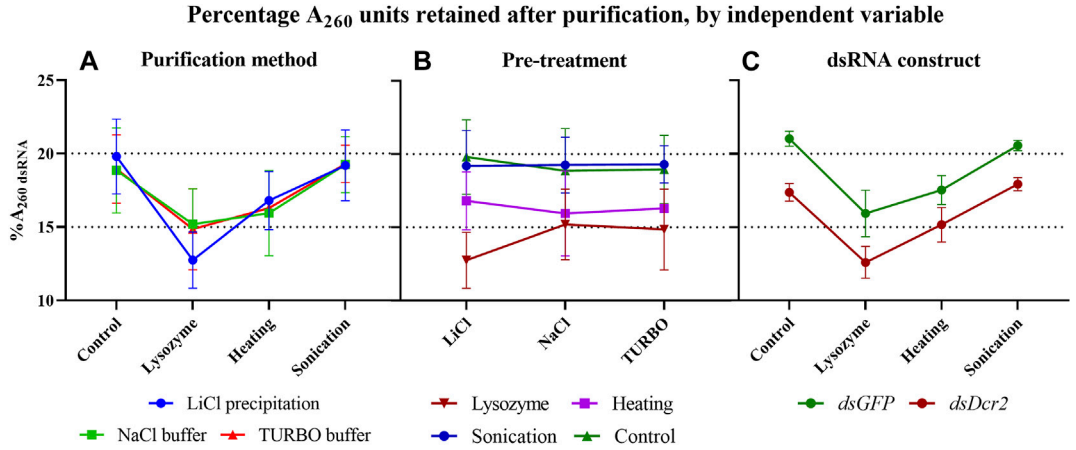

FIGURE 3 | In these graphs, the data of **Table 1** are plotted to highlight the impact of the three independent variables (purification method, pre-treatment, and dsRNA construct) on the percentage of A_{260} units retained following dsRNA purification (%$A_{260\ dsRNA}$). When the data are sorted on the y-axis by one variable (pre-treatment for panel **(A,C)**, or purification method for panel **(B)** and pooled as replicates by a second variable (dsRNA construct for panel A and B, or purification method for panel **(C)**, the effect of the third variable can be visualized. Symbols indicate the mean, error bars the standard deviation. **(A)**: The purification methods have no significant impact ($p = 0.9945$) on the %$A_{260\ dsRNA}$. **(B)**: The pre-treatments have a major effect ($p = 0.0007$) on the %$A_{260\ dsRNA}$. **(C)**: The *GFP* construct results in a higher %$A_{260\ dsRNA}$ than the *Dicer2* construct ($p < 0.0001$). Statistical analysis performed with a repeated measure two-way ANOVA.

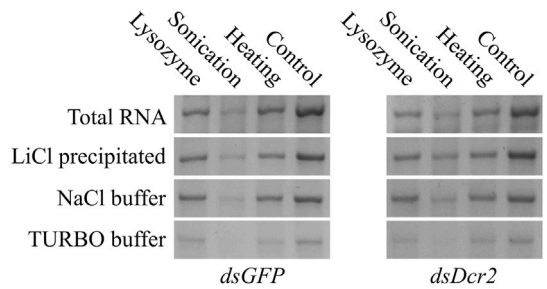

FIGURE 4 | Comparison of *dsGFP* (~700 bp) and *dsDcr2* (~650 bp) bands of total and purified RNA. For each condition, 400 ng total RNA or dsRNA purified from 400 ng total RNA were loaded onto a 1% agarose gel in TAE buffer. The RNA was separated by size through agarose gel electrophoresis at 120V for 2 h. The nucleic acids were imaged with the GelRed® (Biotium) stain under UV light.

conditions tested, neither in terms of cell viability ($p = 0.1359$) nor adherence or growth ($p = 0.2970$, **Figure 6**).

3.5 Bacteria-Derived dsRNA is Applicable for Cellular Knockdown Experiments

A major use of dsRNA is the induction of targeted knockdowns through RNA interference. In insects, this process displays a considerable variety of efficiency, with some orders, such as Lepidoptera, requiring high doses of dsRNA for eliciting a significant silencing effect (Shukla et al., 2016). The proposed method for the production of dsRNA in the order of milligrams is particularly interesting for these less sensitive species. For this reason, the ability of bacteria-derived dsRNA at inducing knockdowns was tested in a lepidopteran gut-derived insect cell line. 2.5×10^5 RP-*Hz*GUT-AW1 cells were treated with either 0.5 or 2.5 µg/ml dsRNA complexed with Escort IV transfection reagent overnight. The transfection medium and non-adhering cells were removed and replaced with complete growth medium. One day after treatment the cells were collected and the *Dicer2* transcript levels assayed through quantitative RT-PCR (qRT-PCR) (**Figure 7**).

For each dsRNA type and concentration, the qRT-PCR ddCt data were normalized against the mean of the control samples and analyzed using multiple *t*-tests. The analysis shows that all dsRNA treatments resulted in significant knockdowns (statistics collected in **Supplementary Table S9**). Next, Brown-Forsythe and Welch ANOVA tests were conducted on the *dsDcr2* ddCt data for each dsRNA concentration. However, no significant difference among the means of the dsRNA types was observed (for 0.5 µg/ml $p = 0.1056$ and $p = 0.2355$; for 2.5 µg/ml $p = 0.7495$ and $p = 0.7270$). These results indicate that the bacteria-derived dsRNA was equally as effective at inducing target gene knockdown as the *in vitro* produced dsRNA, for both concentrations tested.

4 DISCUSSION

The HT115 (DE3) bacterial system in conjunction with the L4440 expression plasmid is a valuable and reliable tool for inducing RNAi in invertebrate species (Timmons et al., 2001). It enables researchers to conduct otherwise prohibitively expensive experiments, requiring manageable development cost and time. Up to date, the system has mainly been applied for *in vivo* feeding studies through bmRNAi (Goodfellow et al., 2019; Taning et al., 2020). In this study, we sought to optimize the isolation of dsRNA from the bacterial production system and demonstrate the usability of thus derived nucleic acids for *in vitro* and *in vivo* knockdown experiments.

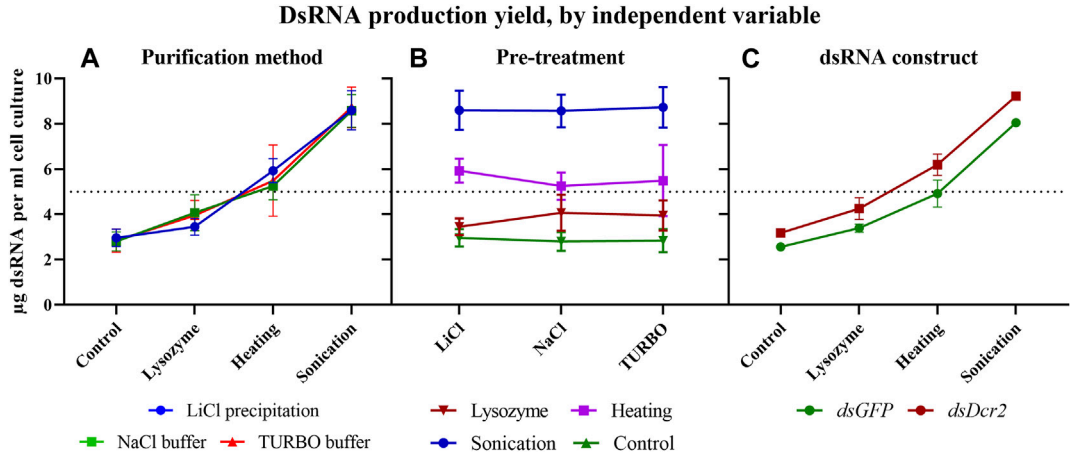

FIGURE 5 | The production yield of dsRNA per ml of bacterial culture is dependent on the pre-treatments applied and the dsRNA construct. The data of **Table 2** were sorted as described in **Figure 4** to visualize the impact of the experimental variables on dsRNA yield. Symbols indicate the mean, error bars the standard deviation. **(A)**: Purification methods did not impact the final production yield of dsRNA per ml cell culture ($p = 0.9935$). **(B)**: The pre-treatments had a major effect on the final production yield of dsRNA per ml cell culture ($p < 0.0001$). **(C)**: The dsRNA construct had an impact on the final production yield of dsRNA per ml cell culture ($p = 0.0002$). Statistical analysis was performed with a repeated measure two-way ANOVA.

4.1 Pre-Treatments Reliably Improve Total RNA Extraction Efficiency

One of the limiting factors in the extraction of dsRNA produced in bacteria is the presence of the bacterial cell wall, which hinders the release of dsRNA from the cytoplasm. Two techniques applied to disrupt the cell wall are heating and sonication of the bacterial cells. The heating pre-treatment causes denaturation of organic polymers and disrupts the cell membrane, increasing the porosity of the bacteria and facilitating dsRNA release. The heating treatment can be applied before or after the addition of phenol/guanidine-based lysis reagents. When applied before, bacterial cells are heated to 95–100°C for 10–100 min (Kim et al., 2015; Vatanparast and Kim, 2017; Ahn et al., 2019). This process was shown to greatly increase extraction yields of total RNA from the cells. If the heating is carried out after the addition of the lysis reagent, the sample is heated to 60–70°C for 10–30 min (Sarathi et al., 2008; Ahn et al., 2019). A single heating step after the addition of the lysis reagent is to be preferred, due to possible degradation of the dsRNA in a high-temperature environment rich in polyvalent ions (Ai et al., 2018) and the possibly increased dsRNase activity of bacterial single-stranded RNases under non-physiological conditions (Grünberg et al., 2021). The sonication treatment causes shearing of the bacterial cells through acoustic cavitation. BmRNAi experiments show that sonication increases phenotypic effects, including the insecticidal activity of HT115 cells expressing dsRNA targeting vital genes (Kim et al., 2015; Vatanparast and Kim, 2017; Ahn et al., 2019). The authors hypothesized that this observed increase was due to the improved cellular release. This hypothesis conflicts with typically low RNAi efficiencies observed when feeding naked dsRNA to the animals (Terenius et al., 2011; Lim et al., 2016; Xu et al., 2016). An alternative explanation could be found in the fragmented nature of sonicated dsRNA. A hampered endosomal escape is thought to be one of the limiting factors in RNAi efficiency in Lepidoptera. While tissues and cells of these species promptly take up dsRNA from the environment, the substrate accumulates in acidic endocytic compartments but is never processed into siRNAs (Shukla et al., 2016; Yoon et al., 2017). Diversifying the size distribution of the delivered dsRNA fragments could improve endosomal escape and thus RNAi efficiency.

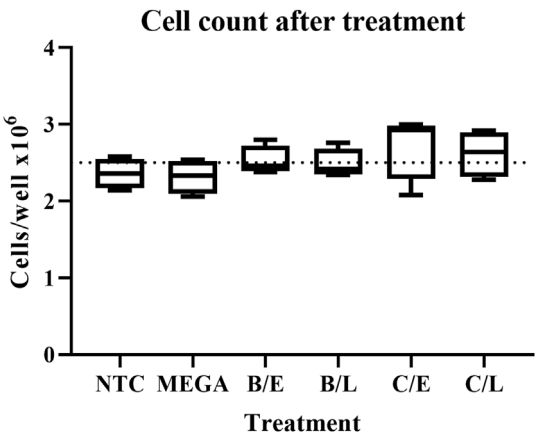

FIGURE 6 | Effect on adherence and growth of RP-*Hz*GUT-AW1 cells of transfection with dsRNA produced *in vitro* or in bacteria. Cells were placed in 24-well plates at > 95% viability and treated with 2.5 µg/ml lipoplexed *dsGFP* or empty lipoplexes overnight. The transfection medium and loose cells were then removed and replaced by complete cell medium. The cells were left to grow for one more day, after which they were collected, and their concentration measured. Four replicates were tested for each condition. Boxplots with min to max whiskers. Dotted line indicates the seeding levels of the cells before treatment. No significant differences were observed ($p > 0.05$) when applying one-way ANOVA analyses. NTC = no-template control consisting of empty lipoplexes; MEGA = dsRNA produced *in vitro* by using the MEGAscript kit; B = sonication pre-treatment; C = heating pre-treatment; E = RNase A digestion in NaCl buffer; L = LiCl precipitation.

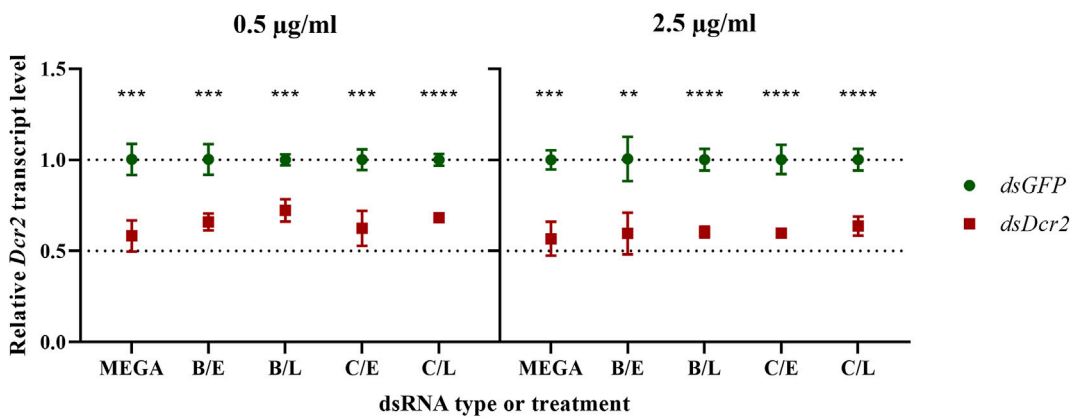

FIGURE 7 | Bacteria-derived dsRNA is effective at inducing a knockdown in the RP-*Hz*GUT-AW1 cell line. Bacteria-derived or MEGAscript produced dsRNA targeting *GFP* or the *Helicoverpa Dicer2* gene was transfected into these gut-derived cells of *Helicoverpa zea*. Transcript levels were assessed 1 day after treatment. Symbols indicate the mean, error bars the standard deviation. Four replicates were tested per condition. All experimental treatments yielded significant knockdowns as assessed through multiple unpaired parametric *t*-test (** $p \leq 0.01$; *** $p \leq 0.001$; **** $p \leq 0.0001$). MEGA = dsRNA produced *in vitro* by using the MEGAscript kit; B = sonication pre-treatment; C = heating pre-treatment; E = NaCl digested dsRNA; L = LiCl precipitated dsRNA.

The data presented in this paper prove for the first time with statistical significance the increase of RNA extraction yield brought forth by three pre-treatments ($p < 0.0001$, **Supplementary Table S5**). We showed that sonication was the most effective at releasing RNA from the cells (**Figure 1**), albeit at the cost of reduced dsRNA band integrity (**Figure 4**; **Figure 2A**), with a 2.9-fold increased yield compared to a control condition. We also demonstrated that heating the cells in lysis reagent increased the yield by 2.2-fold compared to a control condition while maintaining band integrity. Both treatments proved more effective than an enzymatic digestion of the bacterial cell wall using lysozyme. Notably, while increasing the total amount of RNA extracted per volume of bacterial cells, the heating and lysozyme pre-treatments seemed to decrease the relative fraction of dsRNA, as evidenced by the lower band intensity when a fixed amount of total RNA was separated by gel electrophoresis (**Figure 2A**) and by the lower residue ($\%A_{260\ dsRNA}$) when purifying the dsRNA fraction ($p \leq 0.004$, **Supplementary Table S7**; **Table 1**; **Figure 3B**).

Besides the pre-treatments, the dsRNA construct also had a significant impact on the total RNA extraction efficiency ($p < 0.0001$), contributing to 17% of total variation (**Figure 1**; **Supplementary Table S5**). As the ANOVA analysis indicates that this variation is largely independent from the techniques assayed in this study (only 1.6% of variation was assigned to an interaction between the pre-treatments and the dsRNA constructs), the presented experimental data do not allow to conclusively identify the causal factors. We hypothesize that a varying concentration and growth phase of the bacterial cells, as well as the unequal size and sequence of the two dsRNA constructs, might have contributed to the observed results. It may therefore be more appropriate to assign this variation to the cell samples, rather than to the dsRNA constructs. While outside the scope of this paper, follow up studies could make use of biological replicates for each construct to clarify this.

4.2 Purification Protocols Yield Enriched and Intact dsRNA

The bacterial total RNA was treated to enrich the dsRNA fraction via either selective precipitation or enzymatic digestion. The results presented in this study show that the type of purification method contributed to under 0.12% of the variation seen in the percentage of retained A_{260} units ($\%A_{260\ dsRNA}$), with no significant difference found ($p = 0.9945$) (**Figure 3A**; **Supplementary Table S7**). Thus, the choice of which purification method to apply should mainly rely on other aspects, such as the cost of the protocol, the ease of use, available equipment, downstream application, and qualitative properties of the purified dsRNAs. Selective precipitation was carried out following the protocol described by Diaz-Ruiz and Kaper (1978). This protocol has the advantage of removing the ssRNA fraction as well as possible DNA remnants that were carried over during the phenol/guanidine RNA extraction. Of all protocols tested, the LiCl based fractionation requires the least hands-on time, reagents, and equipment. Furthermore, this protocol is easily scalable and applicable to a wide range of dsRNA concentrations, while maintaining equal or better dsRNA integrity than the enzymatic digestion alternatives (**Figure 2C**). Enzymatic removal was carried out using RNase A. The bovine RNase A selectively cleaves ssRNA under high salt conditions, but can degrade dsRNA if the ionic strength becomes too low (Libonati and Sorrentino, 2001). Total RNA was treated with bovine RNase A in a NaCl based digestion buffer with an ionic strength of I = 0.36. This buffer efficiently shielded the dsRNA from degradation, maintaining the intensity of the dsRNA band comparable to that after pre-treatment (**Figure 4**). While this method does not make use of DNases, the purified dsRNA fraction is expected to contain

little or no DNA since the RNA-specific phenol/guanidine extraction was applied twice. In parallel, a combined digestion of ssRNA and dsDNA was attempted as described by Ahn et al. (2019), using bovine RNase A and TURBO™ DNase I. The TURBO™ DNase I was engineered to tolerate higher salt concentrations, maintaining at least 50% of its activity in solutions with up to 200 mM monovalent salt (product manual). The experimental results presented in this paper suggest that the 1x TURBO buffer was not capable of sufficiently shielding the dsRNA from the enzymatic activity of RNase A, with a clear reduction of dsRNA band intensity and increased smearing that were visible for all samples (**Figure 4**; **Figure 2C**). Still, the recovered fraction of nucleic acids after treatment was equal to that of other purification methods. Thus, while the dsRNA was qualitatively more degraded, it was quantitatively maintained. The 1x TURBO DNase buffer contains 75 mM monovalent salt (Decker et al., 2019), and increasing the ionic strength of this buffer with additional monovalent salts such as NaCl might further increase the protection of the dsRNA against degradation and thus improve its yield after the double-digestion step.

4.3 Pre-Treatments and Biological Samples Affect Composition of Released RNA

In **Section 4.1** we determined that the pre-treatment had a major effect on the amount of RNA that could be extracted from the bacterial cells, as it increased RNA yield up to 2.9-fold compared to the control protocol and accounted for 80% of all variation (**Supplementary Table S5**). We could however not yet make statements regarding the amount of extracted dsRNA. The data on the percentage of A_{260} units retained following purification of dsRNA ($\%A_{260\ dsRNA}$, **Table 1**) confirm the previous observation that the pre-treatments differentially promoted the release of total RNA and dsRNA from the cells, as observed by varying band intensities on total RNA gels (**Figure 2A**). Indeed, while for the no pre-treatment control ~19% of A_{260} was dsRNA derived, this value significantly decreased (**Supplementary Table S7**) upon further degradation of the cell wall, to ~16% for the heating treatment and ~14% for the lysozyme digestion treatment (**Figure 3B**). We hypothesize that increasing the porosity of the cell wall may ease the release of large RNAs more than that of smaller molecules such as the dsRNA constructs. An inverse relation between RNA size and release from the cell could also explain why for sonication, where dsRNA fragmentation was observed, the $\%A_{260\ dsRNA}$ was quasi equal to that of the control treatment (~19%). Still, these statements are speculative and further research is required to pinpoint the causal factors. Interestingly, the dsRNA constructs (or as explained in **Section 4.1**, the cell samples) also had a major effect on the $\%A_{260\ dsRNA}$ (32% of total variation, $p < 0.0001$). As seen in **Figures 1**, **3C**, the *dsDcr2* expressing cells released more total RNA with a lower $\%A_{260\ dsRNA}$ than the *dsGFP* expressing cells. This could be explained by a higher porosity of the *dsDcr2* expressing cells, along with an inverse relation between RNA size and cellular release. As concluded in **Section 4.1**, the characteristics of the biological samples and their impact on dsRNA production are outside the scope of this paper but could form an interesting topic for further research.

4.4 dsRNA Production Yield is Mainly Determined by the Pre-Treatment Applied

Using the total RNA absorbance and $\%A_{260\ dsRNA}$ data (**Supplementary Table S4**; **Table 1**, respectively), we can calculate the yield of dsRNA per ml of bacterial culture (**Table 2**; **Figure 5**). An ANOVA analysis reveals that the pre-treatment was the major determinant of dsRNA yield ($p < 0.0001$), accounting for 94% of observed variation and increasing dsRNA yield up to 3.0-fold compared to the no pre-treatment control (**Supplementary Table S8**). From these data, we can conclude that researchers should chose the pre-treatment based on their production priorities. If dsRNA band integrity is desired, the heating method will increase the production yield 1.9-fold without compromising the dsRNA qualitatively. On the other hand, if the main goal is the highest yield, the sonication treatment will increase output 3.0-fold. The dsRNA construct (or cell sample) was also found to contribute to 5% of observed dsRNA yield variation. This value is much lower than the 17% seen for the total RNA yield variation, and 32% seen for the $\%A_{260\ dsRNA}$ variation, suggesting that the purification step reduced the variation derived from the pre-treatments.

4.5 dsRNA Production Protocols Are Cost-Effective and Scalable

The experimental data presented in this paper were obtained by treating aliquots of 10 ml bacterial cell culture. To prove the scalability of selected protocols, purified *dsGFP* was produced from a 400 ml bacterial culture. The cells were pre-treated with the heating step and the dsRNA purified via LiCl precipitation. This resulted in intact dsRNA (**Figure 2D**) with an efficiency of 4.18 µg dsRNA per ml cell culture and a total of 1.67 mg dsRNA. These values are in the range of efficiencies obtained for smaller-scale extractions (5.56 µg/ml). The material cost of production has been calculated at 72.2€ (**Supplementary Table S10**), for a price of 43.2 €/mg. The prices listed are those available to the authors at the time of writing. They may be subject to change over time or vary between countries. As discussed in the introduction, at the time of writing, researchers in small to medium sized labs have very limited options to obtain custom dsRNA. Ordering from external companies is currently priced at ≥$500 USD for 10 mg. While this price is only slightly higher than that of the presented protocols, it does not account for shipping costs, VAT, nor the average 2–3 weeks waiting period. The value that researchers give to a speedy and *in situ* production of their custom dsRNAs is underlined by the still mainstream usage of small-scale production kits, such as the MEGAscript™ RNAi Kit (Thermo Scientific), with high production costs of ~$3000 USD for 10 mg. As such, the protocols presented in this paper offer researchers a cost-effective and readily available alternative to produce dsRNAs.

The largest cost of the methods described in this paper stems from the phenol/guanidine-based lysis reagent (40 €/mg of dsRNA) (**Supplementary Table S10**). Future optimization steps should therefore seek to reduce the required lysis reagent volume or find alternative RNA release methods. Posiri et al. (2013) published a promising "cheap" one-step method that allows the efficient release of total nucleic acids from bacterial cells. Papić et al. (2018) demonstrated the useability of this protocol for large-scale

extractions on fed-batch cultures. The major downside of this novel protocol is the co-extraction of large quantities of DNA from the bacterial cells. This requires further purification steps that risk driving up the hands-on time and production cost. The authors did not attempt to isolate the dsRNA fraction limiting the useability of the product for research purposes.

4.6 Bacteria-Derived dsRNA is Not Cytotoxic to a *Helicoverpa* Derived Cell Line and Applicable for Cellular Knockdown Experiments

dsGFP produced through the protocols presented in this paper was assayed on its cytotoxicity in a lepidopteran derived cell line. *Helicoverpa zea* RP-*Hz*GUT-AW1 cells (Goodman et al., 2004) were transfected with 2.5 μg/ml of either *in vitro* or bacteria-derived dsRNA and their viability and adhesion were assayed. The data indicate that neither cell adhesion or growth ($p = 0.2970$, **Figure 6**), nor viability ($p = 0.1359$) were significantly affected by the bacterial dsRNA relative to a non-template control. The ability of bacteria-derived dsRNA to induce knockdowns was assessed by transfecting the RP-*Hz*GUT-AW1 cells with two concentrations (0.5 μg/ml or 2.5 μg/ml) of either *dsGFP* or *dsDcr2* targeting the *Helicoverpa Dicer2* gene. *In vitro* synthetized dsRNA was employed as a positive control. The data show that bacteria-derived dsRNA performs on-par with *in vitro* alternatives (**Figure 7**), for both concentrations tested. The average decrease (±SD) in relative *Dicer2* transcript levels was 39.9 ± 2.5% at 2.5 μg/ml and 34.5 ± 5.4% at 0.5 μg/ml.

The results presented in this paper demonstrate the feasibility, cost-effectiveness, and efficiency of producing bacteria-derived dsRNA in the mg range under laboratory settings. It aims to boost confidence in the useability of bacteria-derived dsRNA for *in vitro* research by demonstrating that it performs as specifically and efficiently as popular synthetic alternatives. Further research could be conducted to assess the useability of bacteria-derived dsRNA for inducing *in vitro* or *in vivo* knockdowns targeting refractory genes, like the Argonaute proteins. In particular, it is possible that dsRNA extracted through the sonication treatment might display distinct knockdown efficiencies due to a broader spectrum of dsRNA sizes, possibly aiding the uptake into the cytoplasm or escape from endocytic bodies.

DATA AVAILABILITY STATEMENT

The original contributions presented in the study are included in the article/**Supplementary Material**, further inquiries can be directed to the corresponding author.

AUTHOR CONTRIBUTIONS

Conceptualization, methodology, investigation, original draft preparation and writing: T-WV; Review and editing, project management and supervision: JV; Funding acquisition: JV and T-WV.

FUNDING

This work was funded by the Research Foundation of Flanders (FWO), grant number G093119N, and the Special Research Fund of KU Leuven, grant number C14/19/069. T-WV was supported by FWO with a PhD fellowship, grant number 1S83719N.

ACKNOWLEDGMENTS

We want to express our gratitude to Professor Guy Smagghe (Ghent University) for providing us with the RP-*Hz*GUT-AW1 cell line. We also thank Dr. Elise Vogel for providing the L4440-*GFP* construct. Furthermore, we would like to thank Paulien Peeters for technical assistance, and Claire Pietermans for aiding in preliminary research.

SUPPLEMENTARY MATERIAL

The Supplementary Material for this article can be found online at: https://www.frontiersin.org/articles/10.3389/fphys.2022.836106/full#supplementary-material

REFERENCES

Ahn, S.-J., Donahue, K., Koh, Y., Martin, R. R., and Choi, M.-Y. (2019). Microbial-Based Double-Stranded RNA Production to Develop Cost-Effective RNA Interference Application for Insect Pest Management. *Int. J. Insect Sci.* 11, 117954331984032. doi:10.1177/1179543319840323

Ai, X., Wei, Y., Huang, L., Zhao, J., Wang, Y., and Liu, X. (2018). Developmental Control of Helicoverpa Armigera by Ingestion of Bacteria Expressing dsRNA Targeting an Arginine Kinase Gene. *Biocontrol Sci. Techn.* 28, 253–267. doi:10.1080/09583157.2018.1441368

Altschul, S. F., Gish, W., Miller, W., Myers, E. W., and Lipman, D. J. (1990). Basic Local Alignment Search Tool. *J. Mol. Biol.* 215, 403–410. doi:10.1016/S0022-2836(05)80360-2

Chomczynski, P., and Sacchi, N. (1987). Single-step Method of RNA Isolation by Acid Guanidinium Thiocyanate-Phenol-Chloroform Extraction. *Anal. Biochem.* 162, 156–159. doi:10.1016/0003-2697(87)90021-2

Decker, C. J., Steiner, H. R., Hoon-Hanks, L. L., Morrison, J. H., Haist, K. C., Stabell, A. C., et al. (2019). DsRNA-seq: Identification of Viral Infection by Purifying and Sequencing dsRNA. *Viruses* 11, 943–21. doi:10.3390/v11100943

Diaz-Ruiz, J. R., and Kaper, J. M. (1978). Isolation of Viral Double-Stranded Rnas Using A LiCl Fractionation Procedure. *Prep. Biochem.* 8, 1–17. doi:10.1080/00327487808068215

Edgar, R. C. (2004). MUSCLE: Multiple Sequence Alignment with High Accuracy and High Throughput. *Nucleic Acids Res.* 32, 1792–1797. doi:10.1093/nar/gkh340

Goodfellow, S., Zhang, D., Wang, M.-B., and Zhang, R. (2019). Bacterium-mediated RNA Interference: Potential Application in Plant protection. *Plants* 8, 572. doi:10.3390/plants8120572

Goodman, C. L., Wang, A. A., Nabli, H., McIntosh, A. H., Wittmeyer, J. L., and Grasela, J. J. (2004). Development and Partial Characterization of Heliothine Cell Lines from Embryonic and Differentiated Tissues. In Vitro *Cel Dev. Biol. Anim.* 40, 89–94. doi:10.1290/1543-706x(2004)040<0089:dapcoh>2.0.co;2

Grünberg, S., Coxam, B., Chen, T.-H., Dai, N., Saleh, L., Corrêa, I. R., et al. (2021). *E. coli* RNase I Exhibits a strong Ca2+-dependent Inherent

Double-Stranded RNase Activity. *Nucleic Acids Res.* 49, 5265–5277. doi:10.1093/nar/gkab284

Guan, R.-B., Li, H.-C., Fan, Y.-J., Hu, S.-R., Christiaens, O., Smagghe, G., et al. (2018). A Nuclease Specific to Lepidopteran Insects Suppresses RNAi. *J. Biol. Chem.* 293, 6011–6021. doi:10.1074/jbc.RA117.001553

Guindon, S., Dufayard, J.-F., Lefort, V., Anisimova, M., Hordijk, W., and Gascuel, O. (2010). New Algorithms and Methods to Estimate Maximum-Likelihood Phylogenies: Assessing the Performance of PhyML 3.0. *Syst. Biol.* 59, 307–321. doi:10.1093/sysbio/syq010

Hoang, D. T., Chernomor, O., Von Haeseler, A., Minh, B. Q., and Vinh, L. S. (2018). UFBoot2: Improving the Ultrafast Bootstrap Approximation. *Mol. Biol. Evol.* 35, 518–522. doi:10.1093/molbev/msx281

Kalyaanamoorthy, S., Minh, B. Q., Wong, T. K. F., Von Haeseler, A., and Jermiin, L. S. (2017). ModelFinder: Fast Model Selection for Accurate Phylogenetic Estimates. *Nat. Methods* 14, 587–589. doi:10.1038/nmeth.4285

Kim, E., Park, Y., and Kim, Y. (2015). A Transformed Bacterium Expressing Double-Stranded RNA Specific to Integrin β1 Enhances Bt Toxin Efficacy against a Polyphagous Insect Pest, Spodoptera Exigua. *PLoS One* 10, e0132631. doi:10.1371/journal.pone.0132631

Kumar, S., Stecher, G., and Tamura, K. (2016). MEGA7: Molecular Evolutionary Genetics Analysis Version 7.0 for Bigger Datasets. *Mol. Biol. Evol.* 33, 1870–1874. doi:10.1093/molbev/msw054

Kunte, N., McGraw, E., Bell, S., Held, D., and Avila, L. A. (2020). Prospects, Challenges and Current Status of RNAi through Insect Feeding. *Pest Manag. Sci.* 76, 26–41. doi:10.1002/ps.5588

Letunic, I., and Bork, P. (2021). Interactive Tree of Life (iTOL) V5: an Online Tool for Phylogenetic Tree Display and Annotation. *Nucleic Acids Res.* 49, W293–W296. doi:10.1093/nar/gkab301

Li, T., Yan, D., Wang, X., Zhang, L., and Chen, P. (2019). Hemocyte Changes during Immune Melanization in bombyx Mori Infected with *Escherichia coli*. *Insects* 10, 301–15. doi:10.3390/insects10090301

Libonati, M., and Sorrentino, S. (2001). "Degradation of Double-Stranded RNA by Mammalian Pancreatic-type Ribonucleases," in *Methods in Enzymology* (Cambridge, MA: Academic Press), 234–248. doi:10.1016/S0076-6879(01)41155-4

Lim, Z. X., Robinson, K. E., Jain, R. G., Sharath Chandra, G., Asokan, R., Asgari, S., et al. (2016). Diet-delivered RNAi in Helicoverpa Armigera - Progresses and Challenges. *J. Insect Physiol.* 85, 86–93. doi:10.1016/j.jinsphys.2015.11.005

Livak, K. J., and Schmittgen, T. D. (2001). Analysis of Relative Gene Expression Data Using Real-Time Quantitative PCR and the 2−ΔΔCT Method. *Methods* 25, 402–408. doi:10.1006/meth.2001.1262

Lu, S., Wang, J., Chitsaz, F., Derbyshire, M. K., Geer, R. C., Gonzales, N. R., et al. (2020). CDD/SPARCLE: The Conserved Domain Database in 2020. *Nucleic Acids Res.* 48, D265–D268. doi:10.1093/nar/gkz991

Mezzetti, B., Smagghe, G., Arpaia, S., Christiaens, O., Dietz-Pfeilstetter, A., Jones, H., et al. (2020). RNAi: What Is its Position in Agriculture? *J. Pest Sci.* 93, 1125–1130. doi:10.1007/s10340-020-01238-2

Nguyen, L.-T., Schmidt, H. A., Von Haeseler, A., and Minh, B. Q. (2015). IQ-TREE: A Fast and Effective Stochastic Algorithm for Estimating Maximum-Likelihood Phylogenies. *Mol. Biol. Evol.* 32, 268–274. doi:10.1093/molbev/msu300

Papić, L., Rivas, J., Toledo, S., and Romero, J. (2018). Double-stranded RNA Production and the Kinetics of Recombinant *Escherichia coli* HT115 in Fed-Batch Culture. *Biotechnol. Rep.* 20, e00292. doi:10.1016/j.btre.2018.e00292

Perkins, J. R., Dawes, J. M., McMahon, S. B., Bennett, D. L., Orengo, C., and Kohl, M. (2012). ReadqPCR and NormqPCR: R Packages for the reading, Quality Checking and Normalisation of RT-qPCR Quantification Cycle (Cq) Data. *BMC Genomics* 13, 296. doi:10.1186/1471-2164-13-296

Posiri, P., Ongvarrasopone, C., and Panyim, S. (2013). A Simple One-step Method for Producing dsRNA from *E. coli* to Inhibit Shrimp Virus Replication. *J. Virol. Methods* 188, 64–69. doi:10.1016/j.jviromet.2012.11.033

Sarathi, M., Simon, M. C., Venkatesan, C., and Hameed, A. S. S. (2008). Oral Administration of Bacterially Expressed VP28dsRNA to Protect *Penaeus monodon* from white Spot Syndrome Virus. *Mar. Biotechnol.* 10, 242–249. doi:10.1007/s10126-007-9057-6

Shukla, J. N., Kalsi, M., Sethi, A., Narva, K. E., Fishilevich, E., Singh, S., et al. (2016). Reduced Stability and Intracellular Transport of dsRNA Contribute to Poor RNAi Response in Lepidopteran Insects. *RNA Biol.* 13, 656–669. doi:10.1080/15476286.2016.1191728

Singh, I. K., Singh, S., Mogilicherla, K., Shukla, J. N., and Palli, S. R. (2017). Comparative Analysis of Double-Stranded RNA Degradation and Processing in Insects. *Sci. Rep.* 7, 17059. doi:10.1038/s41598-017-17134-2

Strezsak, S. R., Beuning, P. J., and Skizim, N. J. (2021). Complete Enzymatic Digestion of Double-Stranded RNA to Nucleosides Enables Accurate Quantification of dsRNA. *Anal. Methods* 13, 179–185. doi:10.1039/d0ay01498b

Takiff, H. E., Chen, S. M., and Court, D. L. (1989). Genetic Analysis of the Rnc Operon of *Escherichia coli*. *J. Bacteriol.* 171, 2581–2590. doi:10.1128/jb.171.5.2581-2590.1989

Taning, C. N., Arpaia, S., Christiaens, O., Dietz-Pfeilstetter, A., Jones, H., Mezzetti, B., et al. (2020). RNA-based Biocontrol Compounds: Current Status and Perspectives to Reach the Market. *Pest Manag. Sci.* 76, 841–845. doi:10.1002/ps.5686

Tenllado, F., Martínez-García, B., Vargas, M., and Díaz-Ruíz, J. (2003). Crude Extracts of Bacterially Expressed dsRNA Can Be Used to Protect Plants against Virus Infections. *BMC Biotechnol.* 3, 3. doi:10.1186/1472-6750-3-3

Terenius, O., Papanicolaou, A., Garbutt, J. S., Eleftherianos, I., Huvenne, H., Kanginakudru, S., et al. (2011). RNA Interference in Lepidoptera: An Overview of Successful and Unsuccessful Studies and Implications for Experimental Design. *J. Insect Physiol.* 57, 231–245. doi:10.1016/j.jinsphys.2010.11.006

Timmons, L., and Fire, A. (1998). Specific Interference by Ingested dsRNA. *Nature* 395, 854. doi:10.1038/27579

Timmons, L., Court, D. L., and Fire, A. (2001). Ingestion of Bacterially Expressed dsRNAs Can Produce Specific and Potent Genetic Interference in *Caenorhabditis elegans*. *Gene* 263, 103–112. doi:10.1016/S0378-1119(00)00579-5

Vatanparast, M., and Kim, Y. (2017). Optimization of Recombinant Bacteria Expressing dsRNA to Enhance Insecticidal Activity against a Lepidopteran Insect, Spodoptera Exigua. *PLoS One* 12, e0183054–23. doi:10.1371/journal.pone.0183054

Vatanparast, M., Kazzazi, M., Sajjadian, S. M., and Park, Y. (2021). Knockdown of Helicoverpa Armigera Protease Genes Affects its Growth and Mortality via RNA Interference. *Arch. Insect Biochem. Physiol.* 108, 1–21. doi:10.1002/arch.21840

Vogel, E. (2020). *Optimizing RNA Interference for Insect Pest Control*. Doctoral dissertation. KU Leuven. Available at: https://lirias.kuleuven.be/retrieve/578827. Accessed from December 15, 2021.

Wan, X.-S., Shi, M.-R., Xu, J., Liu, J.-H., and Ye, H. (2021). Interference Efficiency and Effects of Bacterium-Mediated RNAi in the Fall Armyworm (Lepidoptera: Noctuidae). *J. Insect Sci.* 21, 8–9. doi:10.1093/jisesa/ieab073

Wang, X.-F., Chen, Z., Wang, X.-B., Xu, J., Chen, P., and Ye, H. (2021). Bacterial-mediated RNAi and Functional Analysis of Natalisin in a Moth. *Sci. Rep.* 11, 4662. doi:10.1038/s41598-021-84104-0

Xu, J., Wang, X.-F., Chen, P., Liu, F.-T., Zheng, S.-C., Ye, H., et al. (2016). RNA Interference in Moths: Mechanisms, Applications, and Progress. *Genes* 7, 88. doi:10.3390/genes7100088

Yoon, J.-S., Gurusamy, D., and Palli, S. R. (2017). Accumulation of dsRNA in Endosomes Contributes to Inefficient RNA Interference in the Fall Armyworm, Spodoptera Frugiperda. *Insect Biochem. Mol. Biol.* 90, 53–60. doi:10.1016/j.ibmb.2017.09.011

Zotti, M. J., and Smagghe, G. (2015). RNAi Technology for Insect Management and Protection of Beneficial Insects from Diseases: Lessons, Challenges and Risk Assessments. *Neotrop. Entomol.* 44, 197–213. doi:10.1007/s13744-015-0291-8

Zotti, M., dos Santos, E. A., Cagliari, D., Christiaens, O., Taning, C. N. T., and Smagghe, G. (2018). RNA Interference Technology in Crop protection against Arthropod Pests, Pathogens and Nematodes. *Pest Manag. Sci.* 74, 1239–1250. doi:10.1002/ps.4813

Conflict of Interest: The authors declare that the research was conducted in the absence of any commercial or financial relationships that could be construed as a potential conflict of interest.

Publisher's Note: All claims expressed in this article are solely those of the authors and do not necessarily represent those of their affiliated organizations, or those of the publisher, the editors and the reviewers. Any product that may be evaluated in this article, or claim that may be made by its manufacturer, is not guaranteed or endorsed by the publisher.

frontiers | Frontiers in Physiology

METHODS
published: 19 April 2022
doi: 10.3389/fphys.2022.878062

FISH for All: A Fast and Efficient Fluorescent *In situ* Hybridization (FISH) Protocol for Marine Embryos and Larvae

Periklis Paganos, Filomena Caccavale, Claudia La Vecchia, Enrico D'Aniello, Salvatore D'Aniello and Maria Ina Arnone**

Department of Biology and Evolution of Marine Organisms, Stazione Zoologica Anton Dohrn, Naples, Italy

In situ hybridization is one the most commonly used techniques for developmental and evolutionary biology and has extensively contributed to the identification of distinct cell types and cell states, as well dissecting several molecular mechanisms involved in physiological processes. Moreover, it has been used as a tool to compare distinct gene expression patterns and, therefore, genetic programs across animal species. Nowadays, the predominance of transcriptomics in science has imposed the need to establish a reliable, fast and easy whole mount *in situ* hybridization protocol. Here we describe a fluorescent *in situ* hybridization protocol that is rapid, accurate and applicable in a great variety of marine species.

Keywords: gene expression, whole-mount FISH, echinoderms, mollusks, tunicates, cephalochordates, development

OPEN ACCESS

Edited by:
Fernando Ariel Genta, Oswaldo Cruz Foundation (Fiocruz), Brazil

Reviewed by:
Minwei Huang, South China Sea Institute of Oceanology (CAS), China
Roberto Feuda, University of Leicester, United Kingdom

****Correspondence:***
Periklis Paganos
periklis.paganos@szn.it
Maria Ina Arnone
miarnone@szn.it

Specialty section:
This article was submitted to Invertebrate Physiology, a section of the journal Frontiers in Physiology

Received: *17 February 2022*
Accepted: *31 March 2022*
Published: *19 April 2022*

Citation:
Paganos P, Caccavale F, La Vecchia C, D'Aniello E, D'Aniello S and Arnone MI (2022) FISH for All: A Fast and Efficient Fluorescent In situ Hybridization (FISH) Protocol for Marine Embryos and Larvae. Front. Physiol. 13:878062. doi: 10.3389/fphys.2022.878062

INTRODUCTION

A key element for understanding the development, physiology and evolutionary origins of an organism is gathering information on the cell types they harbor. Cell type identification relies on the characterization of distinct morphological features, often linked to their functionality and the reconstruction of their molecular fingerprint. This reconstruction can be done at different levels, spanning from assessing the chromatic accessibility that is linked to differential gene expression, to estimating the differential gene expression itself by identifying the spatiotemporal expression pattern of specific gene products (mRNAs and proteins). Traditionally, *in situ* hybridization has been broadly used to detect mRNA molecules within the cells by using labeled antisense RNA probes that hybridize to the specific target. The probe-mRNA hybrid is recognized by an antibody conjugated with specific enzymes that upon administration of their substrate produce either colored compounds or fluorescence.

Nowadays, technologies that allow the capturing of transcriptomes at a single cell resolution and the integration of such mRNA readout data to specific cell types, through spatial transcriptomics, have led to the creation of extensive cell type inventories in various taxa across the evolutionary tree (Sebe-Pedros et al., 2018; Swapna et al., 2018; Cao et al., 2019; Chestnut et al., 2020; Paganos et al., 2021; Qi et al., 2021). The expansion of such inventories reinforced the need to develop reliable *in situ* hybridization protocols as the computationally-predicted cell type need to be validated. Ideally, such protocols should provide high efficiency both in terms of detectability, as well as experimental time, and to be compatible with various organisms.

TABLE 1 | List of gene markers used to test uFISH protocol in mollusks, echinoderms, tunicates and cephalochordates.

Gene symbol	Gene Name	Species
Act	Actin	*M. galloprovincialis*
Cdx	Caudal type homeobox	*S. purpuratus; P. miniata*
Fbsl	Fibrosurfin-like	*S. purpuratus*
Fgf9/16/20	Fibroblast growth factor 9/16/20	*S. franciscanus*
FoxE	Forkhead box E	*B. lanceolatum*
Hnf6	Hepatocyte nuclear factor 6	*C. robusta*
ManRC1a	Macrophage mannose receptor 1	*A. lixula*
Pax6	Paired box 6	*P. lividus*
Pdx1	Pancreas/duodenum Homeobox 1	*S. purpuratus*
Spec1	Calcium-binding SPEC 1A	*S. purpuratus*
SynB	Synaptotagmin B	*L. variegatus*
Vasa	ATP-dependent RNA helicase vasa	*S. purpuratus*

In this study, we developed and tested a whole-mount fluorescent *in situ* hybridization (FISH) method, with broad applicability on many marine embryos and larvae. This protocol allows an overnight hybridization and the whole procedure can be completed within 2 or 3 days, depending on the number of probes used (single or double *in situ* hybridization). Moreover, the main advantage of this protocol is that, with minor methodological adaptions (from fixation to the actual *in situ* hybridization procedure), it is compatible with many marine organisms. Here we show FISH data obtained in mollusks, echinoderms, tunicates and cephalochordates.

MATERIALS AND METHODS

Probe Synthesis

Probe synthesis was performed as previously described by: 1) Perillo et al. (2021) for the sea urchin species *Strongylocentrotus purpuratus*, *Strongylocentrotus franciscanus, Lytechinus variegatus*, *Paracentrotus lividus*, *Arbacia lixula*, and the starfish *Patiria miniata;* 2) Annona et al. (2017) for the amphioxus species *Branchiostoma lanceolatum*; 3) D'Aniello et al., 2011 for the sea squirt *Ciona robusta* (previously named *Ciona intestinalis*); 4) Balseiro et al. (2013) for the Mediterranean mussel *Mytilus galloprovincialis*. In summary, probes were synthetized from linearized, cloned and amplified DNA fragments corresponding to each gene of interest that were used as a template for *in vitro* transcription. In the case of digoxigenin and fluorescein labelled probes, labeling was carried out during the *in vitro* transcription according to the manifacturers' quidelines (Roche), while for DNP labelled probes, non-labelled RNA was synthetized and was labelled post-transcriptionally, according to the manifacturer's instructions (Mirus corporation). The gene makers as well as the species in which each was used are listed in **Table 1**.

Animal Collection

Adult individuals of the sea urchin species *P. livdus* and *A. lixula* were collected from the Gulf of Naples (Italy); adult *C. robusta* individuals were collected from the Gulf of Taranto (Italy); the sea urchin *S. purpuratus* and starfish *P. miniata* were collected from the Gulf of Santa Catalina (CA, United States) and distributed by Patrick Leahy (Kerckhoff Marine Laboratory, California Institute of Technology, Pasadena, CA, United States). All the aforementioned species were housed in circulating aquaria at Stazione Zoologica Anton Dohrn (Naples, Italy). Adult individuals of *M. galloprovincialis* were purchased from Irsvem Srl, a commercial shellfish farm (Naples, Italy) and were used immediately for spawning. *B. lanceolatum* embryos and larvae were reared from animals collected in Argelès-sur-mer (France) and spawned at Observatoire Océanologique de Banyuls-sur-Mer (France). The sea urchin *S. franciscanus* larvae were collected from adult individuals collected from the Gulf of Santa Catalina (CA, United States) and spawned at Kerckhoff Marine Laboratory.

In vitro Fertilization of Gametes and Rearing of Embryos and Larvae

Sea urchin: Gametes were obtained by vigorous shaking of the adult individuals: zygotes were formed after the fertilization of eggs with approximately 1:1,000 dry sperm diluted in filtered sea water (FSW) and embryos were let to grow according to their species salinity and temperature biological needs. In detail, *A. lixula* and *P. lividus* larvae were cultured at 18°C in Mediterranean FSW, *L. variegatus* larvae at 23°C in artificial sea water (ASW) and *S. purpuratus* as well as *S. franciscanus* at 15°C in Mediterranean FSW diluted 9:1 with deionized water and Pacific Ocean FSW respectively. *L. variegatus* larvae were a gift from Dr. Margherita Perillo.

Starfish: Gametes from the batstar *P. miniata* male and female individuals were collected by performing a 4 mm diameter incision on one side of each animal's arm. A piece of each gonad was extracted and placed in calcium and magnesium-free ASW. In case of female gametes, immature eggs were treated with 10 μM 1-Methyladenine in Mediterranean FSW for 1 hour until the germinal vesicle (GV) disappears, indication of their maturity. Mature eggs were then fertilized with approximately 1: 1,000 dry sperm diluted in FSW and zygotes were let to grow at 15°C in Mediterranean FSW diluted 9:1 with deionized water.

Sea squirt: Gametes from *C. robusta* male and female individuals were taken separately for *in vitro* fertilization followed by chemical dechorionation and fertilization (D'Aniello, 2009). Embryos were let to grow until the stage of interest at 18°C in Mediterranean FSW.

Mussel: Sexually mature specimens of *M. galloprovincialis* were mechanically stimulated for the spawning. Approximately, 20–30 mussels were placed in a tank with Mediterranean FSW at 18°C and spread to easily monitor the spawning. When mussels began to spawn, each individual was washed and then transferred into a Becker containing 200 ml of Mediterranean FSW to isolate males and females. Mature eggs were fertilized with an eggs/sperm ratio 1:15 in a volume of 50 ml. The resulting zygotes were let to grow at 18°C in Mediterranean FSW until the developmental stage of interest.

Amphioxus: *B. lanceolatum* gametes were obtained during late spring/early summer period and the spawning was induced by applying thermal shock (Fuentes et al., 2007). Mature gametes

were collected and directly used for the *in vitro* fertilization. Embryos were let to grow at 18°C in Mediterranean FSW.

Fixation

Fixation is an essential step and needs to be performed properly to ensure the mRNA integrity of the samples. All embryos and larvae were fixed in 4% PFA in MOPS Buffer (4% paraformaldehyde, 0.1 M MOPS pH 7, 0.5 M NaCl in DEPC MQ water). Fixation was carried out either for 1 h at room temperature (RT) or overnight at 4°C (both types of fixation gave similar results in all the mentioned species). After fixation was complete, specimens were washed 3–5 times with MOPS buffer (0.1 M MOPS pH 7, 0.5 M NaCl and 0.1% Tween-20 in nuclease-free water) and then gradually dehydrated by passing them through 50%, 60% and finally 70% ice cold ethanol. Samples in 70% ethanol were kept at −20°C until use. The dehydration process can be skipped in case the samples will be used immediately.

Whole-Mount Fluorescent *in situ* Hybridization (FISH)

***Day 1*:** The first day of the FISH procedure includes the rehydration of the specimen and their incubation with the specific antisense RNA probes. **Rehydration:** Embryos/larvae stored in 70% ethanol were placed in 1.5 ml Eppendorf tubes and were gradually rehydrated in MOPS buffer and washed 3–5 times at RT. The duration of each wash was 15 min. In the case of *Branchiostoma lanceolatum*, FISH was also performed on embryos and larvae that were treated with proteinase K (5 μg/ml) to facilitate probe penetration as previously described in Annona et al., 2017. **Pre-hybridization:** After rehydration was complete, MOPS buffer was replaced by hybridization buffer [50% formamide, 0.1 M MOPS pH 7, 0.5 M NaCl and 0.1% Tween-20, 1 mg/ml Bovine serum albumin (BSA) in nuclease-free water] that does not contain any probes and the specimen were kept at 65°C for 3 h. Within this time interval, hybridization buffer was exchanged once to ensure there are no MOPS buffer residues and that the specimens are incubated in the proper hybridization buffer concentration. **Hybridization:** After the pre-hybridization step, specimens were then incubated overnight at 65°C in the hybridization buffer containing the probe. The probe/hybridization buffer solution was preheated for 5–10 min at 70°C followed by 5 min on ice, a step necessary to denature the probe molecules. The antisense RNA probes (labelled with either digoxigenin, fluorescein or dinitrophenol) were used at a final concentration of 0.3–0.5 ng/μl.

Day 2: The second day of the FISH procedure includes all the steps ranging from removing the non-hybridized probe residuals and incubating with the appropriate antibody conjugated with horseradish peroxidase (HRP) to signal detection and imaging. **Post-hybridization:** The probe/hybridization buffer solution was replaced with hybridization buffer that does not contain probes and specimens were incubated for 1 h and 30 min at 65°C. This wash step was performed two times in total. Next, the embryos/larvae were washed 3–5 times with MOPS buffer at RT. The interval of each wash was 15 min. **Blocking and antibody incubation:** Specimens were incubated in the TSA Plus blocking reagent (0.5% blocking reagent in MOPS buffer) for 30 min at RT. The TSA Plus blocking reagent can also be substituted by a homemade blocking solution containing 1 mg/ml BSA and 4% Sheep serum in MOPS buffer. During the blocking step, the antibody solution (1:1,000 of either anti-DIG or anti-DNP or anti-FLUO HRP-conjugated in blocking solution depending on how the probe was labelled) was also let to incubate for 30 min at RT. Next, the blocking solution was replaced with the antibody-containing solution and incubated for 1 h at 37°C. The antibody incubation is followed by MOPS buffer washes (3–5 times) to ensure the removal of the unbound antibody molecules. The duration of each wash was 15 min. **Staining:** The specimens were incubated with 0.005% H_2O_2 in TBS 1x (amplification buffer) for 15 min. From this step and onwards specimens must always be kept in the dark. Next, amplification buffer was replaced by the cyanine-containing solution (Cy3 or Cy5 diluted 1:400 in amplification buffer) and left to incubate for 15 min. Samples were then washed for 15 min, 3–5 times, with MOPS buffer to remove the cyanine residuals. At this point, MOPS buffer containing DAPI (final concentration of 1 μg/ml) was added and the specimens were ready to be observed, **Double FISH**: In case of a double FISH, the staining step performed as described, is followed by a 30 min incubation of the samples with a solution containing 1% H_2O_2 in MOPS buffer that allows the inactivation of the HRP-conjugate to the antibody detecting the first probe. Thereafter, a second round of "blocking and antibody incubation" and of "staining" are provided. For the second staining it is important to use the appropriate antibody according to the labeling of the second probe and a Cyanine different from the one used in the first staining to avoid the false co-localization of the two probes used. For both single and double FISH, the last MOPS buffer wash of the "staining" step was replaced with MOPS buffer containing DAPI in a final concentration of 1 μg/ml and samples were mounted observation with a Zeiss LSM 700 confocal microscope. A protocol format of the FISH procedure can be found in **Supplementary Material S1**.

RESULTS

Reconstruction of gene expression patterns is of high importance for understanding the molecular fingerprint of distinct cell types and for gaining insight into their functions. In this study we developed a fast fluorescent *in situ* hybridization protocol that we then tested on a variety of marine organisms.

This protocol is the result of modifications of a previous one developed by our group and used in echinoderms (two sea urchin and one starfish species) (Perillo et al., 2021). These modifications are regarding the formamide content of the hybridization buffer, which percentage was lowered (from 70% in Perillo et al., 2021 to 50% in the present work) and the subsequent increase of the hybridization temperature (from 50°C in Perillo al., to 65°C here) that led to the acceleration of the whole procedure from approximately 10 days to 2–3 days in total. In addition, one of the most exciting outcomes of the FISH protocol was that we

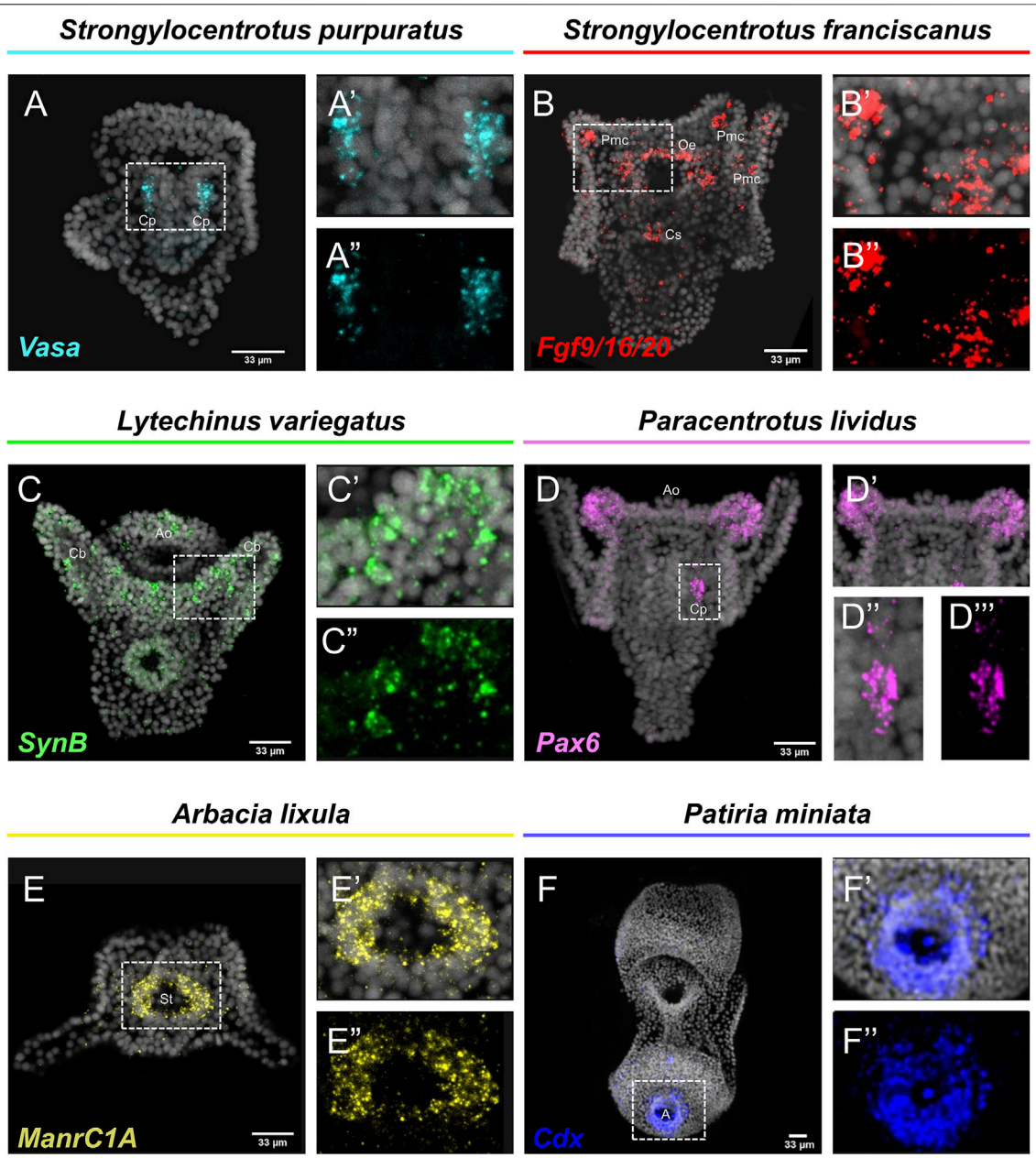

FIGURE 1 | Expression patterns of known gene markers in echinoderm representatives through FISH. FISH of *S. purpuratus* larva with antisense probe for *Vasa* **(A–A'')**, *S. franciscanus* larva with antisense probe for *Fgf9/16/20* **(B–B'')**, *L. variegatus* larva with antisense probe for *SynB* **(C–C'')**, *P. lividus* larva with antisense probe for *Pax6* **(D–D'')**, *A. lixula* with antisense probe for *ManrC1A* **(E–E'')** and *P. miniata* larva with antisense probe for *Cdx* **(F–F'')**. Nuclei are stained with DAPI (in grey). All images are stacks of merged confocal Z sections. A, Anus; Ao, Apical organ; Cb, Ciliary band; Cp, Coelomic pouches; Cs, Cardiac sphincter; Oe, Oral ectoderm; Pmc, Primary mesenchyme cell; St, Stomach.

applied it not only to additional echinoderms species, but also to other species representatives of the mollusks, tunicates and cephalochordates.

In detail, here we present FISH examples for five sea urchin species (*S. purpuratus*, *S. franciscanus*, *L. variegatus*, *P. lividus* and *A. lixula*), the starfish *P. miniata*, the mollusk *M. galloprovincialis*, the tunicate *C. robusta* and the cephalochordate *B. lanceolatum*.

Echinoderms

Embryos and larvae from six echinoderm species were used to test the efficiency of the FISH protocol, for which we used antisense probes designed against gene markers known to label distinct cell types. In detail, FISH for the small micromere descendant cells gene marker *Vasa* (Juliano et al., 2006; Paganos et al., 2021), resulted in the detection of *Vasa* transcripts accumulated in the coelomic pouches of the *S. purpuratus* pluteus larva, structures

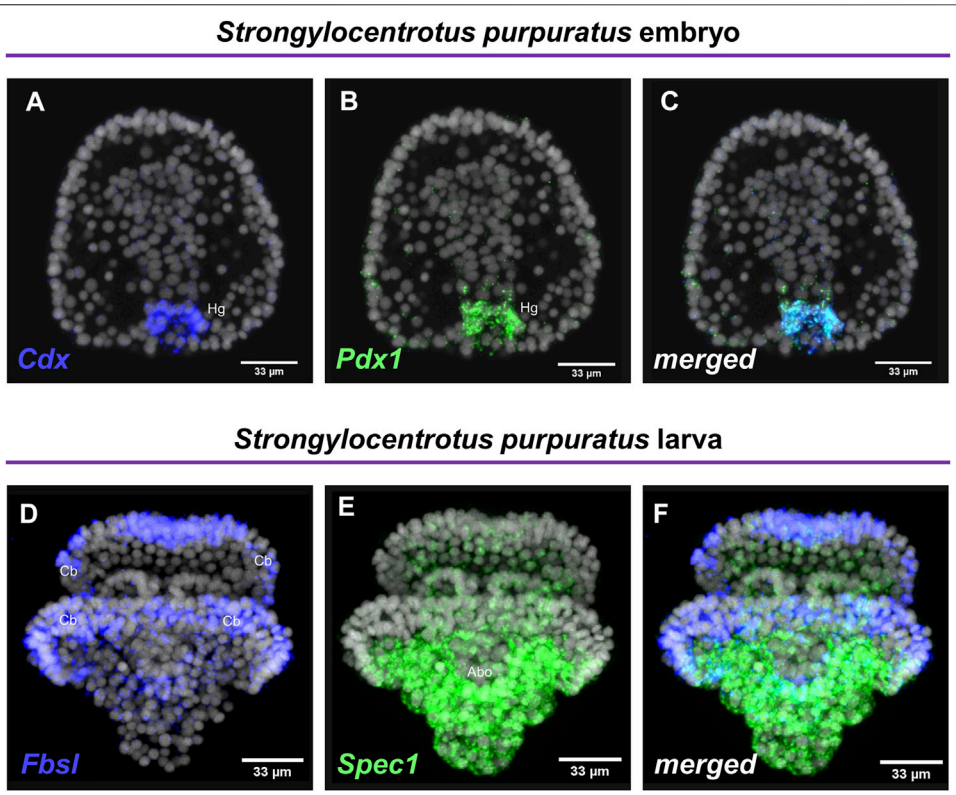

FIGURE 2 | Examples of double FISH. Double FISH of *S. purpuratus* embryos at gastrula stage using antisense RNA probes against *Cdx* **(A)** and *Pdx1* **(B)**. The overlay of the two channels is shown in panel **(C)**. Double FISH of *S. purpuratus* pluteus larvae using antisense RNA probes against *Fbsl* **(D)** and *Spec1* **(E)**. The overlay of the two channels is shown in panel **(F)**. Nuclei are labelled with DAPI (in grey). All images are stacks of merged confocal Z sections. Abo, Aboral ectoderm; Cb, Ciliary band; Hg, Hindgut.

that are formed mainly by small micromere descendant cells (**Figures 1A–A∋**). Transcripts for the Fgf signaling ligand, *Fgf9/16/20,* were detected in the skeletogenic primary mesenchyme cells (Pmc) located in the oral and post-oral arms as well as oral ectoderm and cardiac sphincter cells of the *S. franciscanus* pluteus larva (**Figures 1B–B∋**) domains known to be *Fgf9/16/20* positive in the larvae of other sea urchin species (Röttinger et al., 2008; Paganos et al., 2021). Using a specific antisense probe for the sea urchin pan-neuronal marker *SynB* we were able to detect transcripts present in scattered neurons all across the ciliary band and the apical plate of the *L. variegatus* sea urchin larva (**Figures 1C–C∋**), in agreement with previous studies (Burke et al., 2006; McClay et al., 2018; Tsironis et al., 2021). Moreover, FISH for the *Pax6* gene in the *P. lividus* larva was able to fully reconstruct its expression domains including two bilaterally symmetric ectodermal patches that correspond to the oral arms of the larva and the coelomic pouch domains (**Figures 1D–D∋**), in agreement with published FISH data (Tsironis et al., 2021). Furthermore, FISH for the midgut specific gene marker *ManrC1a* revealed the presence of its transcripts in a specific domain of the digestive tract of the *A. lixula* larva already described for other species (Annunziata et al., 2014) (**Figures 1E–E∋**). Lastly, using the antisense probe against the parahox gene *Cdx* we were able to reconstruct the same expression profile of this gene in the posterior gut of the *P. miniata* starfish larva (**Figures 1F–F∋**), as previously shown by our group using a different FISH protocol (Annunziata et al., 2013). Finally, to assess whether the accelerated hybridization process had any impact on FISH performed with more than one probes, we used this protocol to performed double FISH on *S. purpuratus* embryos and larvae. Strikingly, our data suggest that the hybridization conditions of the FISH do not affect the ability of more than one probe to hybridize or lower the efficiency of the hybridization. Examples of this can be found in **Figure 2** in which we demonstrate that genes known to be co-localized, as shown by different hybridization conditions in the past, are still found to be co-localized through FISH. In detail, *Cdx* and *Pdx1* transcripts co-localize in cells located in the hindgut region of the gastrula embryo (**Figures 2A–C**) similar to what has been previously demonstrated (Cole et al., 2009). Moreover, we were able to clearly discriminate the expression of genes known to never co-localize as in the case of *Fbsl* and *Spec1*, maker genes of the ciliary band and of the aboral ectoderm respectively (Paganos et al., 2021). Using the FISH protocol, *Fbsl* and *Spec1* showed distinct accumulation of transcripts (**Figures 2D–F**) in the same domains we expected from the already published expression pattern data.

Mollusk, Tunicates and Cephalochordates

Once we demonstrated that this fast FISH protocol is able to reconstruct the same expression domains of well-known

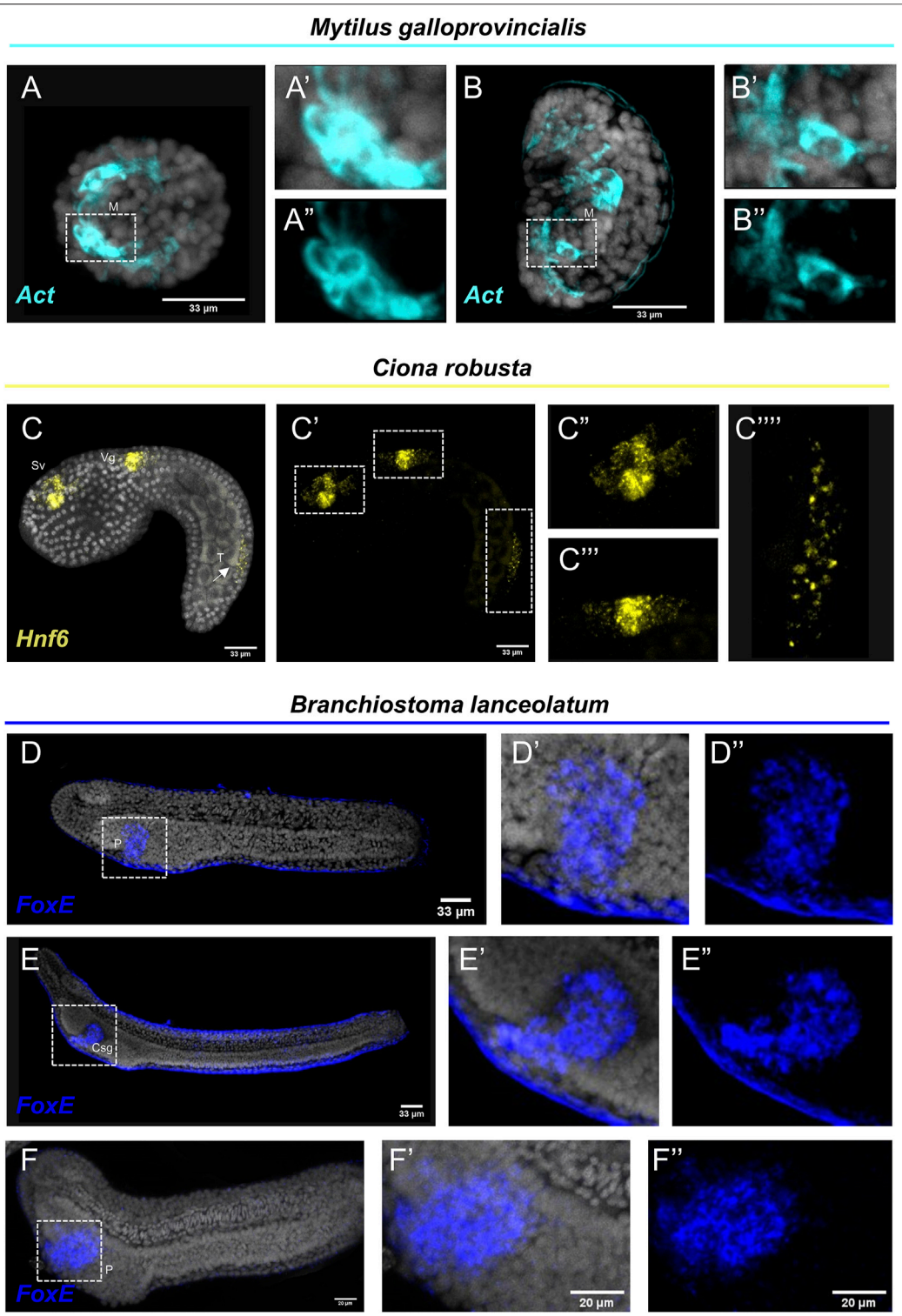

FIGURE 3 | Expression patterns of known gene markers in mollusk, tunicate and cephalochodate representatives through FISH. FISH of *M. galloprovincialis* embryos **(A–A'')** and larvae **(B–B'')** with antisense probe for *Actin*; *C. robusta* embryo with antisense probe for *Hnf6* **(C–C'')**; *B. lanceolatum* embryo **(D–D'')** and larva **(E–E'')** not treated and treated with Proteinase K **(F–F'')** with antisense probe for *FoxE*. Nuclei are labelled with DAPI (in grey). All images are stacks of merged confocal Z sections. Csg, club-shaped gland; M, Muscle; P, Pharyngeal endoderm; Vg, Visceral ganglion; Sv, Sensory vesicle; T, Tail. Arrow indicates positive cells in the posterior neural tube.

echinoderm cell type markers, we set out to investigate whether the FISH protocol is also applicable to other marine organisms.

Interestingly, FISH for the *M. galloprovincialis Actin* gene resulted in the detection of transcripts in bilaterally symmetric populations of muscles in the embryo (**Figures 3A–A∋**) and in a larger population of muscles on the interior of the shell at the veliger larva (**Figures 3B–B∋**). Such expression patterns are in agreement with previous studies using chromogenic *in situ* hybridization protocols (Balseiro et al., 2013).

C. robusta embryo was used as a representative of the tunicate clade. FISH using an antisense probe against *hnf6,* a member of the Cut homeobox gene family, fully reconstructed its previously described expression domains (D'Aniello et al., 2011) along the anterior-posterior axis including precursors of the sensory vesicle, of the visceral ganglion and distinct cell populations of the posterior neural tube (**Figures 3C–C‴**). Interestingly, the *hnf6* signal localized in the tail of the *C. robusta* embryo (**Figure 3C‴′**) is an expression domain that, according to the authors who first described it, is hard to detect as it appears only after prolonging the staining time (Pezzotti et al., 2014). Nevertheless, this is another piece of evidence supporting that our protocol can easily and clearly reconstruct complex expression patterns in *C. robusta* embryos.

Last but not least, we tested the efficiency of the FISH protocol on a representative of the cephalochordate clade, the amphioxus species *Branchiostoma lanceolatum*. *FoxE* is a transcription factor known to be expressed during the amphioxus embryogenesis from neurula until the larva stage. It has been previously demonstrated by chromogenic *in situ* hybridization, that *FoxE* is specifically expressed ventrally on the right side of pharyngeal endoderm at the late neurula stage, while at larva stage its expression is detected in the club-shaped gland (Aldea et al., 2015). FISH for the *FoxE* gene with our protocol shows accumulation of transcripts in the aforementioned domains at both developmental stages (**Figures 3D–E∋**), highlighting that FISH is also applicable on this marine species. However, among all the species tested, *B. lanceolatum* specimens displayed the highest degree of background to signal ratio, which could potentially indicate probe trapping in the *epidermis*. To account for this, we also performed our FISH protocol on specimen that after rehydration were treated with Proteinase K (**Figures 3F–F∋**) that is known to improve probe penetration in this taxon. Indeed, while the specificity of the signal between treated and not treated specimens is unaltered, the background around the *epidermis* was almost completely abolished.

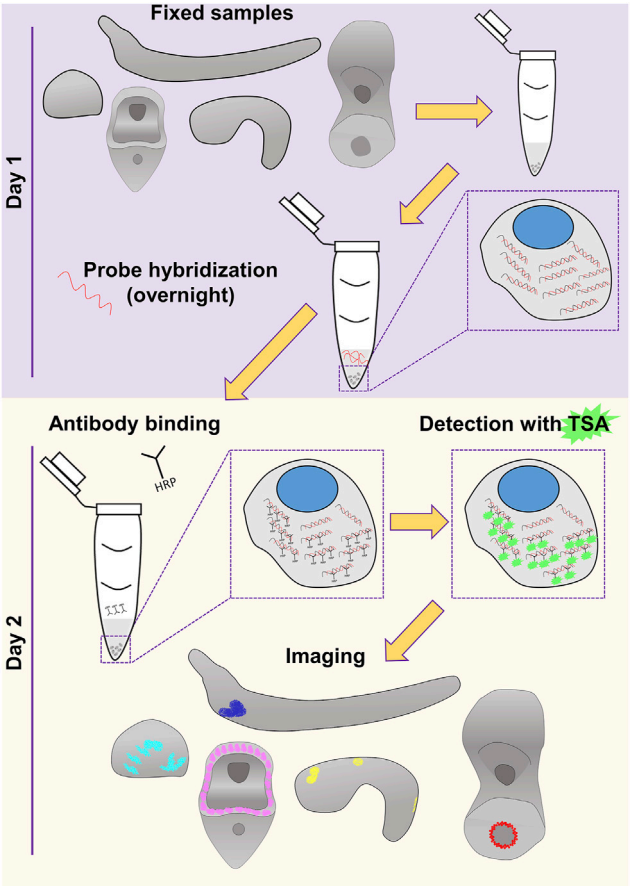

FIGURE 4 | Overview of the FISH procedure described in this study. Schematics of the embryos and larvae used to test the protocol are represented in gray. Color code of the staining corresponds to what used in **Figures 1–3**.

DISCUSSION

Nowadays, extensive cell type inventories are being generated for taxa across the evolutionary tree in an attempt to understand the molecular fingerprint, function and evolutionary origins of cell types and thus animals. Current technologies allow the computational reconstruction of cell types either through the use of single cell transcriptomics or spatial transcriptomics. However, the need to verify such computationally based predictions and the challenges to develop reliable molecular biology tools towards this end still remain. This is the main reason why classical methods to visualize gene expression have not gone obsolete and it is highly unlikely they will in the near future. In this work, we provide evidence of our FISH protocol being such a reliable tool that allows the accurate, easy and fast identification of expression domains. An overview of the protocol is depicted in **Figure 4**.

In the case of echinoderms, FISH dramatically reduces the time required for whole mount FISH procedure from 10 days to only 2–3 days in total, without compromising the quality of the FISH. This feature can be of great importance when considering the higher number of genes that can be analyzed within the additional time offered by FISH. Regarding the mussel *M. galloprovincialis,* there are only a few for whole-mount ISH protocols available, mostly for chromogenic *in situ* hybridization (Murray et al., 2003; Balseiro et al., 2013). Surprisingly, this is the first study to use whole-mount FISH to detect mRNAs present during *M. galloprovincialis* embryonic development. Concerning the tunicate and cephalochordate representatives, *C. robusta* and *B. lanceolatum,* respectively, FISH might be an easier

alternative utilizing less reagents in terms of variety and potentially requiring less experimental time when compared to existing protocols (Yu and Holland, 2009; D'Aniello et al., 2011; Annona et al., 2017). Nonetheless, depending on the intrinsic properties of the sample, minor adaptations could be introduced as in the case of *C. robusta* and *B. lanceolatum* that chemical dechorionation and Proteinase K treatment respectively, are advised to obtain a reduced background to signal ratio.

Overall, it is important that the experimental conditions are kept as similar as possible for most comparisons with a biological significance, taking into consideration of the intrinsic properties of the samples to be analyzed. Towards this end, we believe that using a universal *in situ* protocol for marine organisms, similar to how we universally use other molecular biology techniques (such as PCR, RNA-seq) could potentially ease cross-species comparisons by removing the heterogeneity in how samples are processed. Overall, our FISH protocol has the potential to be an extremely useful resource for Evo-Devo community by allowing FISH to be performed in species previously thought impossible. Whether this protocol could also be applied on non-marine species is still an open question, although we believe that adaptation of the solutions used to the osmotic needs of terrestrial or freshwater organisms should be sufficient to ensure its functionality also to such specimens. Nonetheless, further information and experimentation are needed to achieve this goal and thus testing of this protocol in additional taxa is required.

DATA AVAILABILITY STATEMENT

The original contributions presented in the study are included in the article/**Supplementary Material**, further inquiries can be directed to the corresponding authors.

AUTHOR CONTRIBUTIONS

Conceptualization, PP and MA; methodology, PP and FC; validation, PP and FC resources, PP, FC, CL, ED'A, SD'A, and MA; writing—original draft preparation, PP; writing—review and editing, PP, FC, CL, ED'A, SD'A, and MA; visualization, PP and FC; supervision, MA.

FUNDING

PP was supported by Marie Curie ITN EvoCELL (H2020 Grant Number: 766053 to MA). FC was supported by MUR CIR_0029 Human Capital. SD'A and FC were supported by Assemble Plus project (BA010618 and 360BA0619) for visiting at Observatoire Océanologique de Banyuls-sur-Mer (France). CL was supported by a Ph.D. fellowship co-founded by Stazione Zoologica Anton Dohrn, Napoli, Italy and Università Politecnica delle Marche, Ancona, Italy.

ACKNOWLEDGMENTS

The authors would like to thank Davide Caramiello for taking care of the adult animals at Stazione Zoologica and Dr. Margherita Perillo for providing us with sea urchin larvae that are not available in our institute. The authors are also grateful to Erica Riccio for her irreplaceable contribution.

SUPPLEMENTARY MATERIAL

The Supplementary Material for this article can be found online at: https://www.frontiersin.org/articles/10.3389/fphys.2022.878062/full#supplementary-material

REFERENCES

Aldea, D., Leon, A., Bertrand, S., and Escriva, H. (2015). Expression of Fox Genes in the Cephalochordate *Branchiostoma L. Front. Ecol. Evol.* 3, 80. doi:10.3389/fevo.2015.00080

Annona, G., Caccavale, F., Pascual-Anaya, J., Kuratani, S., De Luca, P., Palumbo, A., et al. (2017). Nitric Oxide Regulates Mouth Development in Amphioxus. *Sci. Rep.* 7, 8432. doi:10.1038/s41598-017-08157-w

Annunziata, R., Martinez, P., and Arnone, M. I. (2013). Intact Cluster and Chordate-Like Expression of ParaHox Genes in a Sea Star. *BMC Biol.* 11, 68. doi:10.1186/1741-7007-11-68

Annunziata, R., Perillo, M., Andrikou, C., Cole, A. G., Martinez, P., and Arnone, M. I. (2014). Pattern and Process during Sea Urchin Gut Morphogenesis: The Regulatory Landscape. *Genesis* 52, 251–268. doi:10.1002/dvg.22738

Balseiro, P., Moreira, R., Chamorro, R., Figueras, A., and Novoa, B. (2013). Immune Responses during the Larval Stages of *Mytilus G*: Metamorphosis Alters Immunocompetence, Body Shape and Behavior. *Fish. Shellfish Immunol.* 35, 438–447. doi:10.1016/j.fsi.2013.04.044

Burke, R. D., Osborne, L., Wang, D., Murabe, N., Yaguchi, S., and Nakajima, Y. (2006). Neuron-Specific Expression of a Synaptotagmin Gene in the Sea Urchin *Strongylocentrotus P. J. Comp. Neurol.* 496, 244–251. doi:10.1002/cne.20939

Cao, C., Lemaire, L. A., Wang, W., Yoon, P. H., Choi, Y. A., Parsons, L. R., et al. (2019). Comprehensive Single-Cell Transcriptome Lineages of a Proto-Vertebrate. *Nature* 571, 349–354. doi:10.1038/s41586-019-1385-y

Chestnut, B., Casie Chetty, S., Koenig, A. L., and Sumanas, S. (2020). Single-Cell Transcriptomic Analysis Identifies the Conversion of Zebrafish Etv2-Deficient Vascular Progenitors into Skeletal Muscle. *Nat. Commun.* 11, 2796. doi:10.1038/s41467-020-16515-y

Cole, A. G., Rizzo, F., Martinez, P., Fernandez-Serra, M., and Arnone, M. I. (2009). Two ParaHox Genes, SpLox and SpCdx, Interact to Partition the Posterior Endoderm in the Formation of a Functional Gut. *Development* 136, 541–549. doi:10.1242/dev.029959

D'Aniello, E., Pezzotti, M. R., Locascio, A., and Branno, M. (2011). Onecut Is a Direct Neural-Specific Transcriptional Activator of Rx in *Ciona I. Develop. Biol.* 355, 358–371. doi:10.1016/j.ydbio.2011.05.584

D'Aniello, E. (2009). Studies on RX Gene Function and its Involvement in *Ciona I* Ocellus Differentiation. PhD thesis PhD thesis The Open University. doi:10.21954/ou.ro.0001004c

Fuentes, M., Benito, E., Bertrand, S., Paris, M., Mignardot, A., Godoy, L., et al. (2007). Insights into Spawning Behavior and Development of the European Amphioxus (*Branchiostoma L*). *J. Exp. Zool.* 308B, 484–493. doi:10.1002/jez.b.21179

Juliano, C. E., Voronina, E., Stack, C., Aldrich, M., Cameron, A. R., and Wessel, G. M. (2006). Germ Line Determinants Are Not Localized Early in Sea Urchin Development, but Do Accumulate in the Small Micromere Lineage. *Develop. Biol.* 300, 406–415. doi:10.1016/j.ydbio.2006.07.035

McClay, D. R., Miranda, E., and Feinberg, S. L. (2018). Neurogenesis in the Sea Urchin Embryo Is Initiated Uniquely in Three Domains. *Development* 145 (21), dev167742. doi:10.1242/dev.167742

Murray, H. M., Gallant, J. W., Perez-Casanova, J. C., Johnson, S. C., and Douglas, S. E. (2003). Ontogeny of Lipase Expression in Winter Flounder. *J. Fish Biol.* 62, 816–833. doi:10.1046/j.1095-8649.2003.00067.x

Paganos, P., Voronov, D., Musser, J. M., Arendt, D., and Arnone, M. I. (2021). Single-Cell RNA Sequencing of the *Strongylocentrotus P* Larva Reveals the Blueprint of Major Cell Types and Nervous System of a Non-Chordate Deuterostome. *Elife* 10, e70416. doi:10.7554/eLife.70416

Perillo, M., Paganos, P., Spurrell, M., Arnone, M. I., and Wessel, G. M. (2021). Methodology for Whole Mount and Fluorescent RNA *In Situ* Hybridization in Echinoderms: Single, Double, and Beyond. *Methods Mol. Biol.* 2219, 195–216. doi:10.1007/978-1-0716-0974-3_12

Pezzotti, M. R., Locascio, A., Racioppi, C., Fucci, L., and Branno, M. (2014). Auto and Cross Regulatory Elements Control Onecut Expression in the Ascidian Nervous System. *Develop. Biol.* 390, 273–287. doi:10.1016/j.ydbio.2014.03.011

Qi, J., Crinier, A., Escalière, B., Ye, Y., Wang, Z., Zhang, T., et al. (2021). Single-Cell Transcriptomic Landscape Reveals Tumor Specific Innate Lymphoid Cells Associated with Colorectal Cancer Progression. *Cel Rep. Med.* 2, 100353. doi:10.1016/j.xcrm.2021.100353

Röttinger, E., Saudemont, A., Duboc, V., Besnardeau, L., Mcclay, D., and Lepage, T. (2008). FGF Signals Guide Migration of Mesenchymal Cells, Control Skeletal Morphogenesis [Corrected] and Regulate Gastrulation during Sea Urchin Development. *Development* 135, 353–365. doi:10.1242/dev.014282

Sebé-Pedrós, A., Saudemont, B., Chomsky, E., Plessier, F., Mailhé, M.-P., Renno, J., et al. (2018). Cnidarian Cell Type Diversity and Regulation Revealed by Whole-Organism Single-Cell RNA-Seq. *Cell* 173, 1520–1534. doi:10.1016/j.cell.2018.05.019

Swapna, L. S., Molinaro, A. M., Lindsay-Mosher, N., Pearson, B. J., and Parkinson, J. (2018). Comparative Transcriptomic Analyses and Single-Cell RNA Sequencing of the Freshwater Planarian Schmidtea Mediterranea Identify Major Cell Types and Pathway Conservation. *Genome Biol.* 19, 124. doi:10.1186/s13059-018-1498-x

Tsironis, I., Paganos, P., Gouvi, G., Tsimpos, P., Stamopoulou, A., Arnone, M. I., et al. (2021). Coup-TF: A Maternal Factor Essential for Differentiation along the Embryonic Axes in the Sea Urchin *Paracentrotus L. Dev. Biol.* 475, 131–144. doi:10.1016/j.ydbio.2020.12.012

Yu, J. K., and Holland, L. Z. (2009). Amphioxus Whole-Mount *In Situ* Hybridization. *Cold Spring Harb Protoc.* 2009(9), pdb.prot5286. doi:10.1101/pdb.prot5286

Conflict of Interest: The authors declare that the research was conducted in the absence of any commercial or financial relationships that could be construed as a potential conflict of interest.

Publisher's Note: All claims expressed in this article are solely those of the authors and do not necessarily represent those of their affiliated organizations, or those of the publisher, the editors and the reviewers. Any product that may be evaluated in this article, or claim that may be made by its manufacturer, is not guaranteed or endorsed by the publisher.

frontiers | Frontiers in Physiology

ORIGINAL RESEARCH
published: 25 April 2022
doi: 10.3389/fphys.2022.882792

Identification and Validation of Reference Genes for Gene Expression Analysis in *Monochamus saltuarius* Under *Bursaphelenchus xylophilus* Treatment

Jiaxing Li, Ningning Fu, Lili Ren* and Youqing Luo*

Beijing Key Laboratory for Forest Pest Control, Beijing Forestry University, Beijing, China

OPEN ACCESS

Edited by:
Fernando Ariel Genta,
Oswaldo Cruz Foundation, Brazil

Reviewed by:
Benshui Shu,
Zhongkai University of Agriculture and Engineering, China
Lifeng Zhou,
Zhejiang A & F University, China

****Correspondence:***
Lili Ren
lily_ren@bjfu.edu.cn
Youqing Luo
youqingluo@126.com

Specialty section:
This article was submitted to Invertebrate Physiology, a section of the journal Frontiers in Physiology

Received: *25 February 2022*
Accepted: *21 March 2022*
Published: *25 April 2022*

Citation:
Li J, Fu N, Ren L and Luo Y (2022) Identification and Validation of Reference Genes for Gene Expression Analysis in Monochamus saltuarius Under Bursaphelenchus xylophilus Treatment. Front. Physiol. 13:882792. doi: 10.3389/fphys.2022.882792

A special mutual relationship exists between the pine wood nematode (PWN) *Bursaphelenchus xylophilus* and its vector beetles of genus *Monochamus*, which enables PWN to spread, at the same time provides longhorned beetles with more weak hosts. PWN are attracted to the pupal chambers and then carried inside the trachea of beetle adults, which is a necessary part to complete the *B. xylophilus* infection cycle. The growth and immune responses of the vector beetle will affect this carrying process, however, they were rarely studied in *Monochamus saltuarius*. Real-time quantitative polymerase chain reaction (RT-qPCR), one of the most common methods for quantitative gene expression analysis, was performed to explore the key genes and pathways involved in the growth, development and immune responses of *M. saltuarius* at different developmental stages associated with infection of PWN and PWN treatment conditions. To enhance the accuracy of RT-qPCR data, the expression of target genes needs to be normalized with reference genes, which are stably expressed under varied experimental conditions. In our study, the stability of 14 candidate reference genes in *M. saltuarius* samples at different developmental stages associated with infection of PWN or PWN treatment conditions was evaluated using delta Ct, geNorm, NormFinder, BestKeeper and RefFinder algorithms. Moreover, *KLF* gene was used to validate the stability of the selected reference genes. Under experimental conditions of this study, *RPL7* and *TER* were suitable reference genes at different developmental stages associated with infection of PWN. *RPL7* and *RPS5* were considered the most stable reference genes in the pupae treated with PWN. *RPS5* and *SNX6* could be used as reference genes in the adults treated with PWN. *RPL7*, *EF1-γ*, and *RPS5* could be used as stable reference genes in all the samples. This work is the first to evaluate reference genes in *M. saltuarius*, laying a foundation for further gene expression experimental procedures and understanding the phoretic relationship between *M. saltuarius* and *B. xylophilus*.

Keywords: *Monochamus saltuarius*, *Bursaphelenchus xylophilus*, RT-qPCR, reference genes, developmental stages

BACKGROUND

Pine wilt disease is one of the most dangerous and devastating diseases caused by *Bursaphelenchus xylophilus* (pine wood nematode; PWN) worldwide. *B. xylophilus* originated in North America, and was introduced to Japan, Korea, China, Portugal, and other countries, causing serious damage in these invasion areas (Dropkin and Foudin, 1979; Mamiya, 1988; Cheng et al., 1983; Han et al., 2008; Khan, 1991; Manuel et al., 1999; Abelleira et al., 2011). PWN is transmitted to dead or dying trees by its insect vector, the *Monochamus* beetles, during oviposition or maturation feeding (Akbulut and Stamps, 2012; Kim et al., 2020; Li et al., 2020).

In China, PWN was first widely spread and damaged in southern area, then spread to northern and other regions. In the southern area, *Monochamus alternatus* as a main vector of the PWN was widely studied. However, *Monochamus saltuarius* emerged as a new and unique vector in Liaoning Province, China (Yu and Wu, 2018), although it was regarded as a common vector in Korea and Japan (Sato, 1987; Kim et al., 2006). It greatly promotes the transmission of *B. xylophilus* to *Larix* spp., *Pinus koraiensis*, *Pinus sylvestris* var. *mongolica*, and *Pinus tabuliformis* (Yu and Wu, 2018; Yu et al., 2019; 2020). Therefore, the research about interaction between *B. xylophilus* and *M. saltuarius* is of significance to prevent and control the prevalence of pine wilt disease in north of China.

Gene expression is an important method to study the potential function of insect genes in different conditions. Real-time quantitative polymerase chain reaction (RT-qPCR), one of the most common methods for quantitative gene expression analysis, has the characteristics of high accuracy, specificity, sensitivity, and rapidity (Bustin, 2002; Bustin et al., 2005; Valasek and Repa, 2005). However, the quality and quantity of RNA extraction, polymerase amplification efficiency, and cDNA synthesis efficiency can all lead to systematic errors during RT-qPCR operation (Klein, 2002; Fleige and Pfaffl, 2006). To eliminate these errors, various strategies have been used to normalize RT-qPCR data, and using internal controls or reference genes has become the most reliable method (Silver et al., 2006; Borowski et al., 2014; Silveira et al., 2021). Nevertheless, there are no absolute stable reference genes because of spatio-temporal specificity of genes and variable experimental conditions. So, it is necessary to screen suitable reference genes according to specific experimental materials and conditions for RT-qPCR analysis.

Studies of reference genes in insects are common. In coleoptera, reference gene screening has been performed in approximately twenty insect species, such as *Dendroctonus valens*, *Harmonia axyridis*, and Cerambycidae species, *Monochamus alternatus, Anoplophora glabripennis* (Toutges et al., 2010; Rajarapu et al., 2012; Shi et al., 2013; Barros Rodrigues et al., 2014; Wang et al., 2014; Song et al., 2015; Tan et al., 2015; Feng et al., 2016; Rodrigues et al., 2017; Yang et al., 2018; Yang et al., 2020; Zhang et al., 2020; Zheng et al., 2020; Guo et al., 2021; Sellamuthu et al., 2021). And common reference genes for Coleoptera studies include *ACT* (actin), *β-TUB* (beta-tubulin), *α-TUB* (alpha-tubulin), *RPs* (ribosomal proteins), *18S rRNA* (18S ribosomal RNA), *28S* rRNA (28S ribosomal RNA), *EF1-α* (elongation factor1-α) and so forth (Toutges et al., 2010; Zhang et al., 2020; Guo et al., 2021). These genes are involved in normal cell metabolic processes. However, reference genes in *M. saltuarius* have not been reported. Therefore, we required to find the appropriate reference genes for gene expression analysis under different PWN treatments.

In this study, we aimed to identify the optimal reference genes in *M. saltuarius* at different developmental stages associated with infection of PWN or PWN treatment conditions. Based on prior experimental reports regarding reference genes in Coleoptera and other insects, 14 candidate reference genes including sorting nexin 6 (*SNX6*), phospholipid-transporting ATPase (*ATPase*), palmitoyltransferase ZDHHC15 isoform X2 (*ZDhhc15*), transcription factor A, mitochondrial-like (*TFAM*), 60S ribosomal protein L18 (*RPL18*), 60S ribosomal protein L7 (*RPL7*), 40S ribosomal protein S5 (*RPS5*), transitional endoplasmic reticulum ATPase TER94 (*TER*), transmembrane and ubiquitin-like domain-containing protein 1 (*Tmub1*), eukaryotic translation initiation factor 4B (*EIF*), elongation factor 1-gamma (*EF1-γ*), cytochrome c oxidase subunit 7C (*COX7*), tubulin alpha-1 chain (*α-TUB*), and triosephosphate isomerase (*TPI*) were selected from the genome and transcriptome data of *M. saltuarius* (unpublished data). Five algorithms were used to evaluate reference genes stability and perform a comprehensive ranking. In addition, the expression profile of the Krüppel-like factor luna (*KLF*) gene was used to verify our result. This study provides valuable information for further exploration on the growth and immune mechanism of *M. saltuarius*, and serves as a reference for exploring its phoretic relationship with *B. xylophilus*.

MATERIALS AND METHODS

Insect

In August and December 2020, the fourth and fifth instar larvae of *M. saltuarius* were collected from Dahuofang Forest Farm, Fushun City, Liaoning Province, China. To ensure the absence of *B. xylophilus* all times, after sterilizing the larvae surface with 75% alcohol, the fifth instar larvae were incubated at artificial media at 25°C with 75% relative humidity. All procedures were performed at the Plant Quarantine Laboratory, Beijing Forestry University, Beijing, China.

Sample Treatment

Samples collected at different developmental stages associated with infection of PWN in *M. saltuarius* included two instar larval stages (L4 and L5), 1-day-age pupae (P1), 5-days-age pupae (P5), 10-days-age pupae (P10), and newly emerged adult (1-day-old) males (AM) and females (AF). Three independent biological replicates were performed at each stage, and each replicate was derived using an individual beetle. All samples were immediately frozen in liquid nitrogen and stored at −80°C for RNA extraction.

To test the effect of *B. xylophilus* on *M. saltuarius*, the artificial co-culture medium of *B. xylophilus* and *M. saltuarius* was prepared using the previous method (Li et al., 2021). Fifth

TABLE 1 | Primer sequences and amplification characteristics of candidate reference genes.

Accession Number	Symbol	Gene Name	Primer sequence (5′to3′)	Size (bp)	E (%)	R^2 Value
Gene_ MSAL09320	*SNX6*	sorting nexin-6	F: CGTTATGAGGAGGAACCC AAATA R: CTCATGGTTCCTTCACCTTCTC	119	97	0.998
Gene_ MSAL04397	*ATPase*	probable phospholipid-transporting ATPase	F: GAACTCGGCAGGATCTCTTATT R: ATAGCTGACCGTACCCAAATG	99	90	0.994
Gene_ MSAL02314	*ZDhhc15*	Palmitoyltransferase ZDHHC15 isoform X2	F: CGAGGTGTTGGTACAGACAAA R: GCGTGAGTGTACAGGGTATTC	144	109	0.998
Gene_ MSAL10600	*TFAM*	transcription factor A, mitochondrial-like	F: CAATGGCAGACTGGGAAGAA R: CTGCCTGGTTTCAACTGTCTA	115	97.1	0.991
Gene_ MSAL00760	*RPL18*	60S ribosomal protein L18	F: AACGGTATTGATGCAAGGTAGA R: GGAACGTACTAGTGGCTTAGTG	103	104.2	0.998
Gene_ MSAL00096	*RPL7*	60S ribosomal protein L7	F: GGCAACGCATTCCCATAAC R: CTTGGACCGACTGTGAAGAT	109	105.4	0.998
Gene_ MSAL00148	*RPS5*	40S ribosomal protein S5	F: CGTAGGGTAAACCAGGCTATC R: GAGGAACCCTTAGCAGCATTA	122	94.7	0.999
Gene_ MSAL03702	*TER*	transitional endoplasmic reticulum ATPase TER94	F: GTCGTTGCTCTTTCACAAGC R: CAAGGCTGGATGGACACTAC	203	100.2	0.998
Gene_ MSAL09667	*Tmub1*	transmembrane and ubiquitin-like domain-containing protein 1	F: CGTAGTCTGCCTTCTGAC AATAA R: ACATCTCCTCCAACCTACCA	97	90.9	0.999
Gene_ MSAL09352	*EIF*	eukaryotic translation initiation factor 4B	F: CGACGATAGGGATGATCG TAAAG R: CCTTTCCCTTGGTTCTGACATA	124	94.3	0.998
Gene_ MSAL06575	*EF1-γ*	elongation factor 1-gamma	F: ACAGCAACGCTATCGCTTAT R: TCACCTTCGGCAAATCCTATC	103	90.7	0.999
Gene_ MSAL03188	*COX7*	cytochrome c oxidase subunit 7C, mitochondrial-like	F: GTGGTGTACCTGGAGCGAAT R: GTCTCAAGATGAGGAAAG GTGC	114	91.8	1.000
Gene_ MSAL09430	*α-TUB*	tubulin alpha-1 chain	F: CCCTTACCCACGTATTCACTTC R: TGGTAATTTCAGCCACGGATAG	98	91.7	1.000
Gene_ MSAL06278	*TPI*	triosephosphate isomerase	F: ATCGGTGAGACCTTAGAGGAA R: CACGTTCGACCAGTCTTTGA	102	94	0.999
Gene_ MSAL01719	*KLF*	Krüppel-like factor luna	F: GCAGAGACTTTGACTCCTCCC R: GGCTCGCACTCTGACTATTGT	144	95.4	0.998

instar larvae with weights ranging from 300 to 500 mg were selected from Dahuofang Forest Farm in December 2020. After sterilizing the larvae surface with 75% alcohol, the fifth instar larvae inoculated in the artificial co-culture medium were cultured with *B. xylophilus* at 25°C and 75% relative humidity. The growth and developmental stage of beetles was observed once every 24 h. After the beetle larvae pupated, 5-days-age pupae (BP5), 10-days-age pupae (BP10), and newly emerged adult (1-day-old) males (BAM) and females (BAF) were collected respectively. Three biological replicates were performed at each stage, and each replicate included one sample. All samples were immediately frozen in liquid nitrogen and stored at −80°C for RNA extraction.

RNA Extraction and cDNA Synthesis

Total RNA from all 33 samples at different developmental stages associated with infection of PWN and PWN treatment conditions were extracted using EASY Spin Plus Tissue/Cell RNA Extraction Kit (Aidlab, China). Quality and quantity of total RNA were evaluated using 1.2% (w/v) agarose gel electrophoresis and NanoDrop 2,000 spectrophotometry. The PrimeScript™ RT Reagent Kit (Takara, China) was used to synthesize the first strand cDNA of each sample according to the manufacturer's protocol. Obtained cDNAs were diluted 5-fold and stored at −20°C for subsequent RT-qPCR experiments.

Selection of Candidate Reference Genes and Primer Design

Fourteen candidate reference genes with relatively high transcript abundance and stable expression [fragments per kilobase of transcript per million mapped reads (FPKM) value >20 and a fold change in expression <2] were selected based on the transcriptome and genome data (unpublished data) of *M. saltuarius*. These genes were *SNX6*, *ATPase*, *ZDhhc15*, *TFAM*, *RPL18*, *RPL7*, *RPS5*, *TER*, *Tmub1*, *EIF*, *EF1-γ*, *COX7*, *α-TUB*, and *TPI* (**Supplementary Table S1**). Their coding DNA sequences were obtained from *M. saltuarius* genome data (GeneBank: OM471799–OM471813), and primers were designed using the web software Primer 3.0 (https://bioinfo.ut.ee/primer3-0.4.0/) and IDT (https://sg.idtdna.com/pages). The primers used for amplification are listed in **Table 1**.

RT-qPCR Analysis

RT-qPCR was performed using Bio-Rad CFX Connect real-time PCR instrument (Bio-Rad, United States) with TB Green® Premix

Ex Taq™ II (Takara, Japan). A 25-μl reaction volume consisted of 12.5 μl of TB Green Premix Ex Taq II (2×), 1 μl of forward and reverse primers (10 μM), respectively, 1 μl of cDNA template, and 9.5 μl of RNA-free water. Amplification conditions were as follows: initial denaturation at 95°C for 30 s, followed by 40 cycles at 95°C for 5 s and 60°C for 30 s. Then, we performed a melt curve analysis using the default parameters with a steady increase in temperature from 65 to 95°C. All RT-qPCR assays were performed in three biological replicates, each biological replicate with three technical replicates. The amplification efficiency (E) and correlation coefficients (R^2) were determined for each gene using the standard curves with a 5-fold dilution series of the template (1, 1/5, 1/25, 1/125, and 1/625), where R^2 was the slope of the standard curve. Amplification efficiency was calculated according to the equation: E% = (10 [−1/slope]−1) × 100%.

Stability Analysis of Candidate Reference Genes

Five algorithms, including delta Ct, geNorm, NormFinder, BestKeeper and RefFinder, were used to analyze the expression stability of the candidate reference genes in different groups. The delta Ct algorithm (based on the delta Ct method) was used to calculate the mean standard deviation (SD) of the paired genes in each sample to assess the gene expression stability. Genes with lower SD value had more stable expression (Silver et al., 2006). The GeNorm was used to calculate the M value based on the pairwise variation between two reference genes. If the M value was less than 1.5, it could be considered a suitable reference gene. The smaller the M value, the higher the stability of gene. The optimal number of reference genes was determined by calculating pairwise variation (V_n/V_{n+1}) by geNorm. A value of V_n/V_{n+1} less than 0.15 indicated that the most suitable reference gene number is n without introducing n + 1 (Vandesompele et al., 2002). In NormFinder, the S value of reference gene according to variance analysis decided the stability of candidate reference genes. The lower the S value, the more stable they were (Andersen et al., 2004). Before using geNorm or NormFinder analysis, the original Ct values were converted to $2^{-\Delta Ct}$ values (ΔCt = original Ct value − lowest Ct value in each group). BestKeeper evaluated the expression stability of all candidate reference genes by calculating the SD and stability value (SV) based on the original Ct values. A gene could not be used as an internal reference gene if the SD value was more than 1 (Pfaffl et al., 2004). Similarly, genes with lower SD and SV values had more stable expression. Finally, the comprehensive ranking of candidate reference genes under different conditions was obtained according to RefFinder (Xie et al., 2012).

Validation of Reference Genes

Krüppel-like transcription factor luna (*KLF*) belongs to a family of 15 different zinc finger proteins of the C2H2 type that are involved invertebrate development, and which controls cell proliferation, growth and differentiation. De Graeve et al. (2003) proposed that *KLF* was a novel transcriptional determinant of *Drosophila* development (De Graeve et al., 2003). Therefore, the *KLF* gene was selected as target gene to validate the stability of the selected reference genes based on the transcriptome data. The primers used are shown in **Table 1**.

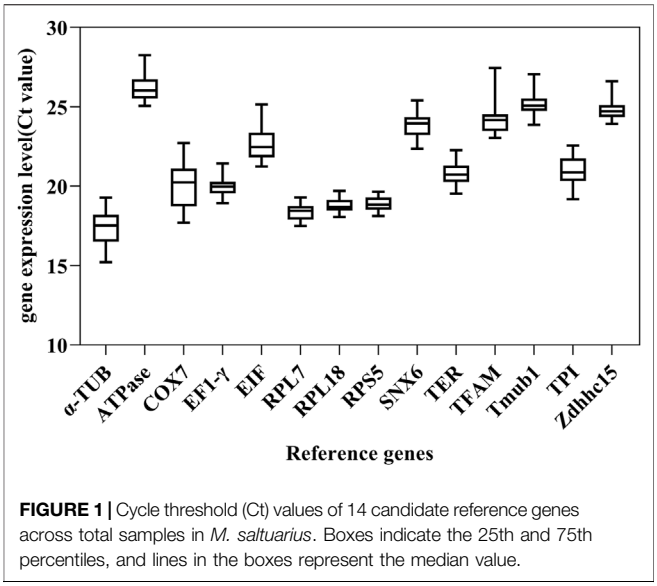

FIGURE 1 | Cycle threshold (Ct) values of 14 candidate reference genes across total samples in *M. saltuarius*. Boxes indicate the 25th and 75th percentiles, and lines in the boxes represent the median value.

We used RT-qPCR (method same as above) to detect the *KLF* expression level in *M. saltuarius* samples at different developmental stages associated with infection of PWN and PWN treatment conditions. The relative quantification of the *KLF* gene was calculated using the $2^{-\Delta\Delta Ct}$ method (Livak and Schmittgen, 2001). One-way analysis of variance (ANOVA) followed by post-hoc Tukey's honestly significant difference (HSD) test on SPSS Statistics Software was used to determine the significance of *KLF* expression levels at different developmental stages associated with infection of PWN and PWN treatment conditions (Wu et al., 2021; Fu et al., 2022).

RESULTS

Primer Performance Analysis of Candidate Reference Genes

A total of 14 candidate reference genes were selected for gene-normalization studies in different samples. RT-qPCR products showed a single peak in the melting curve analysis (**Supplementary Figure S1**) and 1.2% agarose gel electrophoresis showed a specific band for each gene (**Supplementary Figure S2**). The amplification efficiency (E) values of all candidate genes ranged from 90% (*ATPase*) to 109% (*ZDhhc15*), and regression analysis of all primer pairs showed a correlation coefficient (R^2) greater than 0.99 (**Table 1**). These results indicated that all primer pairs designed for the candidate reference genes had good efficiency and specificity in RT-qPCR amplification. Therefore, the primers of these candidate reference genes were used for further analysis.

TABLE 2 | Expression stability ranking of the 14 candidate reference genes based on five algorithms.

Conditions	Genes	Delta Ct		geNorm		NormFinder		BestKeeper		RefFinder	
		Avg. Ct	Rank	M	Rank	SV	Rank	SD + CV	Rank	GM	Rank
Developmental Stages	TER	0.71	1	0.55	6	0.27	1	0.54	6	2.45	1
	RPL7	0.76	4	0.38	1	0.36	6	0.44	3	2.91	2
	RPS5	0.89	9	0.38	2	0.43	9	0.40	1	3.08	3
	Zdhhc15	0.73	2	0.48	4	0.31	3	0.52	5	3.31	4
	EF1-γ	0.74	3	0.52	5	0.29	2	0.48	4	3.31	5
	RPL18	0.77	6	0.41	3	0.34	5	0.43	2	3.66	6
	Tmub1	0.77	5	0.56	7	0.33	4	0.58	7	5.60	7
	SNX6	0.80	7	0.59	8	0.40	7	0.63	8	7.48	8
	ATPase	0.86	8	0.61	9	0.43	10	0.83	10	8.71	9
	TFAM	0.92	10	0.67	10	0.43	8	0.82	9	9.49	10
	α-TUB	1.00	12	0.71	11	0.57	13	0.86	12	11.72	11
	EIF	0.95	11	0.76	12	0.54	12	0.98	13	11.72	12
	TPI	1.01	13	0.80	13	0.49	11	0.86	11	12.49	13
	COX7	1.36	14	0.88	14	0.78	14	1.23	14	14.00	14
Pupae treated with PWN	RPL7	0.57	1	0.13	1	0.11	1	0.18	1	1.00	1
	RPS5	0.60	2	0.13	2	0.16	3	0.21	2	1.68	2
	RPL18	0.66	5	0.28	3	0.15	2	0.24	3	3.87	3
	EF1-γ	0.65	4	0.50	7	0.18	6	0.37	5	4.53	4
	TFAM	0.65	3	0.48	6	0.21	7	0.45	6	4.56	5
	Tmub1	0.75	7	0.36	4	0.17	4	0.35	4	5.29	6
	TER	0.70	6	0.43	5	0.18	5	0.46	7	5.96	7
	TPI	0.79	8	0.60	10	0.27	10	0.54	10	8.94	8
	ATPase	0.79	9	0.53	8	0.28	11	0.49	9	8.97	9
	SNX6	0.80	10	0.56	9	0.26	9	0.61	12	10.44	10
	EIF	0.80	11	0.63	11	0.21	8	0.60	11	10.46	11
	Zdhhc15	1.00	13	0.72	13	0.34	13	0.47	8	11.51	12
	α-TUB	0.96	12	0.67	12	0.30	12	0.82	14	12.47	13
	COX7	1.11	14	0.77	14	0.35	14	0.73	13	13.74	14
Adults treated with PWN	RPS5	0.41	2	0.12	2	0.10	2	0.19	1	1.41	1
	SNX6	0.40	1	0.17	3	0.05	1	0.21	2	1.57	2
	RPL7	0.43	3	0.12	1	0.12	3	0.23	3	2.28	3
	EF1-γ	0.44	4	0.22	4	0.12	4	0.31	5	4.23	4
	Zdhhc15	0.48	5	0.27	5	0.20	8	0.29	4	4.73	5
	TFAM	0.50	6	0.30	6	0.13	5	0.40	9	6.64	6
	Tmub1	0.52	7	0.34	7	0.18	6	0.42	10	7.65	7
	TER	0.56	8	0.37	8	0.23	12	0.47	11	8.66	8
	COX7	0.59	11	0.45	11	0.23	10	0.34	6	9.45	9
	ATPase	0.58	9	0.40	9	0.19	7	0.55	12	9.67	10
	TPI	0.60	12	0.47	12	0.23	11	0.38	7	10.49	11
	EIF	0.59	10	0.42	10	0.22	9	0.63	13	10.68	12
	RPL18	0.64	13	0.49	13	0.25	13	0.39	8	11.51	13
	α-TUB	0.79	14	0.54	14	0.30	14	0.73	14	14.00	14
Total samples	RPL7	0.73	1	0.32	1	0.26	2	0.43	3	1.57	1
	EF1-γ	0.74	2	0.48	4	0.23	1	0.46	4	2.38	2
	RPS5	0.83	6	0.32	1	0.39	7	0.39	1	2.55	3
	RPL18	0.81	5	0.44	3	0.33	5	0.39	2	3.50	4
	TER	0.76	3	0.56	6	0.30	3	0.57	7	4.41	5
	Tmub1	0.77	4	0.53	5	0.31	4	0.56	6	4.68	6
	Zdhhc15	0.85	8	0.61	8	0.38	6	0.50	5	6.62	7
	SNX6	0.83	7	0.59	7	0.39	8	0.64	8	7.48	8
	ATPase	0.85	9	0.63	9	0.41	9	0.77	10	9.24	9
	TFAM	0.91	10	0.67	10	0.43	10	0.72	9	9.74	10
	EIF	0.94	11	0.72	11	0.46	11	0.84	12	11.24	11
	TPI	1.08	12	0.81	13	0.60	12	0.80	11	11.98	12
	α-TUB	1.09	13	0.76	12	0.63	13	0.95	13	12.74	13
	COX7	1.46	14	0.90	14	0.95	14	1.31	14	14.00	14

Note: Avg. Ct, average cycle threshold; M, expression stability value; SV, stability value; SD + CV, standard deviation and coefficient of variation; GM, geometric mean.

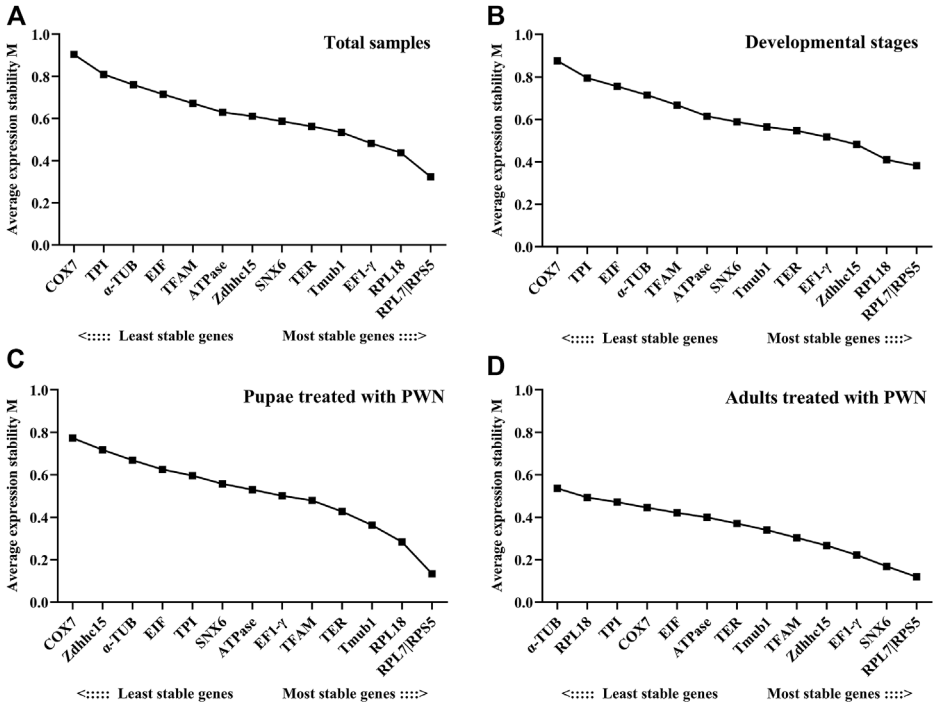

FIGURE 2 | Average expression stability and ranking of candidate reference genes calculated by geNorm. Candidate reference genes with lower M values were more stable. The least stable genes are listed on the left, and the most stable genes are listed on the right. **(A)** Total samples. **(B)** Developmental stages associated with infection of PWN. **(C)** Pupae treated with PWN. **(D)** Adults treated with PWN.

Expression Analysis of Selected Reference Genes

Transcript abundance and cycle threshold (Ct) variation are important parameters for screening reference genes. The Ct value of 14 candidate reference genes across 33 samples showed a wide range of expression levels and significant differences. Ct values of these candidate reference genes ranged from 14.98 to 27.14 for total samples. Among these, *α-TUB, RPL7* and *RPL18* were the most abundant transcripts (average Ct = 17.41, 18.34, 18.74, respectively). The least frequently expressed reference gene were *Zdhhc15*, Tmub1, and *ATPase* (average Ct = 24.80, 25.19, 26.21, respectively). According to the SD values, variance in Ct values increased in the following order: *RPS5* < *RPL18* < *RPL7* < *EF1-γ* < *Zdhhc15* < *TER* < *Tmub1* < *SNX6* < *ATPase* < *TPI* < *TFAM* < *EIF* < *α-TUB* < *COX7* (**Figure 1**).

Expression Stability of Candidate Reference Genes in Different Developmental Stages Associated With Infection of PWN and PWN Treatments

To identify the most suitable reference genes of *M. saltuarius* under the three conditions—different developmental stages associated with infection of PWN, PWN treatment at the pupal stage, and PWN treatment at the adult stage, their expression stability was evaluated using five algorithms as elaborated below.

Delta Ct Analysis

For candidate reference genes in total samples, *RPL7*, *EF1-γ,* and *TER* were more stable than other reference genes (average SD = 0.73, 0.74, 0.76, respectively). For different treatments (**Table 2**), *TER*, *Zdhhc15* and *EF1-γ* had the most stable expression levels (average SD = 0.71, 0.73, 0.74, respectively) at different developmental stages associated with infection of PWN. *RPL7*, *RPS5*, and *TFAM* were the most stable reference genes (average SD = 0.57, 0.60, 0.65, respectively) in PWN-treated pupal groups; while *SNX6*, *RPS5*, and *RPL7* were the most stable reference genes (average SD = 0.40, 0.41, 0.43, respectively) in PWN-treated adult groups. On the whole *α-TUB*, *COX7*, and *TPI* were the least stable under most conditions.

GeNorm Analysis

Among all samples, *RPL7* and *RPS5* were the most stable reference genes, similar with the results found in the sample sets of different developmental stages associated with infection of PWN and all PWN treatment conditions (**Figure 2**). In addition, we found that the most unstable genes greatly varied in different experimental conditions. In developmental stages associated with infection of PWN and total samples, the M values of *COX7* and *TPI* were higher than other genes. In pupae treated with PWN, *COX7* and *Zdhhc15* had the least stability. In adults treated with

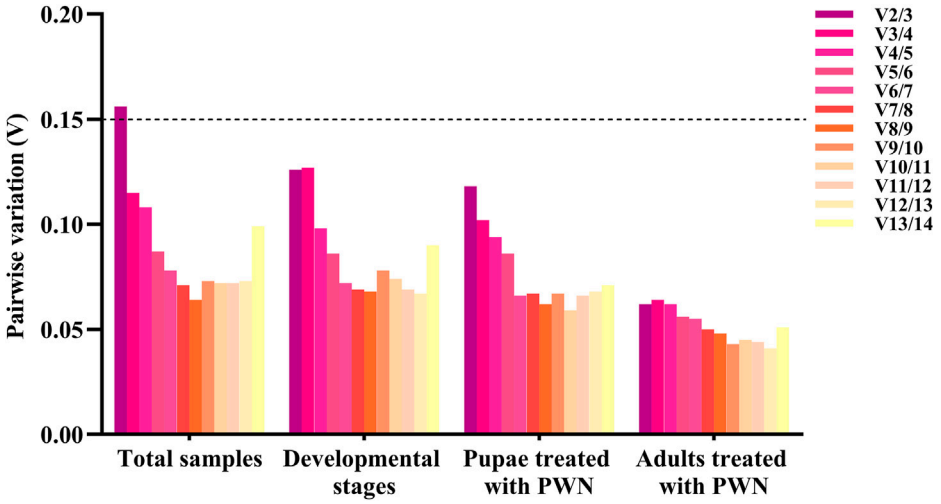

FIGURE 3 | Pairwise variation (V) of 14 reference genes in different conditions calculated by geNorm. The threshold value for assessing the optimal number of reference genes for RT-qPCR normalization is 0.15.

PWN, *α-TUB* and *RPL18* exhibited the most unstable expression levels.

The pairwise changes (V_n/V_{n+1}) were calculated using geNorm with a threshold value of 0.15 to assess the number of reference genes for all treatment conditions. Three groups including different developmental stages associated with infection of PWN, pupae treated with PWN, and adults treated with PWN, V2/3 values were all <0.15 (0.126, 0.118, and 0.062, respectively), indicating that two reference genes were sufficient for RT-qPCR normalization. In 33 total samples, the V2/3 value was 0.156, which was greater than the split-off value, and the V3/4 value was 0.115. Therefore, three reference genes were needed to normalize the expression of the target gene in all samples (**Figure 3**).

NormFinder Analysis

At different developmental stages associated with infection of PWN, the most stable genes were *EF1-γ* and *TER*. In pupae treated with PWN, *RPL7*, and *RPL18* had the strongest stability (**Table 2**). In adults treated with PWN, *SNX6*, and *RPS5* were the most stable reference genes. In total samples, *EF1-γ* and *RPL7* were the best reference genes combination. Unsurprisingly, *α-TUB* and *COX7* were also the least stable genes in most cases.

BestKeeper Analysis

For BestKeeper algorithm, the most stable genes showed the lowest SD ± CV values, and genes with an SD value >1 were considered unstable. In total samples, *RPS5*, *RPL18,* and *RPL7* were the most stable genes. For different developmental stages associated with infection of PWN and pupae treated with PWN, two conditions had similar results that *RPS5*, *RPL18*, and *RPL7* were identified as the most stable genes, but *α-TUB*, *COX7*, *EIF*, and *SNX6* were poor stable genes. Whereas the PWN-treated adult group was slightly different from the above. For adults treated with PWN, *RPS5*, *SNX6*, and *RPL7* showed the highest stability; *ATPase*, *α-TUB*, and *EIF* had the least stable expression level (**Figure 4**). In some groups, *COX7*, whose SD value was greater than 1, was considered an unstable reference gene.

RefFinder Analysis: Comprehensive Stability Analysis of Reference Genes

The RefFinder program was used to obtain a comprehensive reference gene ranking based on the geometric mean of four algorithms. The expression stabilities of candidate reference genes in all samples decreased in the order: *RPL7* > *EF1-γ* > *RPS5* > *RPL18* > *TER* > *Tmub1* > *Zdhhc15* > *SNX6* > *ATPase* > *TFAM* > *EIF* > *TPI* > *α-TUB* > *COX7*. The stability ranking at different developmental stages associated with infection of PWN was as the following: *TER* > *RPL7* > *RPS5* > *Zdhhc15* > *EF1-γ* > *RPL18* > *Tmub1* > *SNX6* > *ATPase* > *TFAM* > *α-TUB* > *EIF* > *TPI* > *COX7*. The stability ranking at pupae treated with PWN was: *RPL7* > *RPS5* > *RPL18* > *EF1-γ* > *TFAM* > *Tmub1* > *TER* > *TPI* > *ATPase* > *SNX6* > *EIF* > *Zdhhc15* > *α-TUB* > *COX7*, and at adults treated with PWN was *RPS5* > *SNX6* > *RPL7* > *EF1-γ* > *Zdhhc15* > *TFAM* > *Tmub1* > *TER* > *COX7* > *ATPase* > *TPI* > *EIF* > *RPL18* > *α-TUB*. The comprehensive analysis showed that *RPL7*, *EF1-γ*, and *RPS5* genes were the most stable reference genes combination for total samples. *RPL7*, *RPS5*, and *RPL18* were the most suitable reference genes in pupae treated with PWN. *RPS5*, *SNX6*, and *RPL7* were the most suitable reference genes in adult treated with PWN (**Table 2**). *TER*, *RPL7*, and *RPS5* were the optimal reference genes at different developmental stages associated with infection of PWN.

Validation of the Selected Reference Genes

To verify the reliability of the selected reference genes, *KLF* was used as the target gene for RT-qPCR analysis. We used the four most stable candidate reference genes (*RPL7, RPS5, SNX6,* and *TER*), the combination of these stable genes (*RPL7* + *RPS5* + *EF1-γ, RPL7* + *RPS5, RPS5*+*SNX6,* and *RPL7*+*TER*), and two most

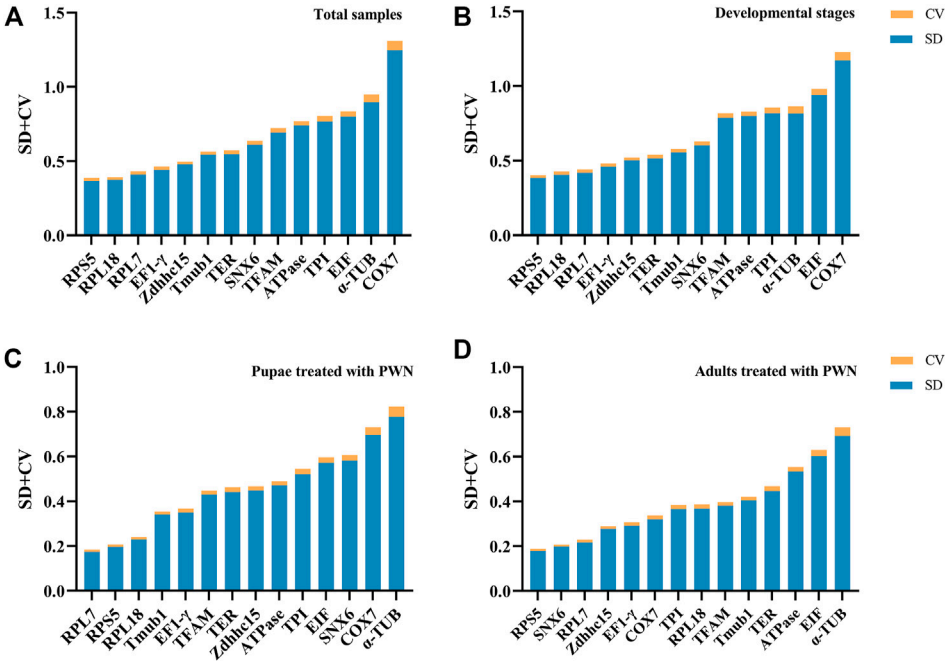

FIGURE 4 | Stability rankings of 14 candidate reference genes by BestKeeper. Blue bars represent standard deviation (SD) of average Ct values, and yellow bars represent coefficients of variation (CV). **(A)** Total samples. **(B)** Developmental stages associated with infection of PWN. **(C)** Pupae treated with PWN. **(D)** Adults treated with PWN.

unstable reference genes (*α-TUB, COX7*) in different treatment conditions to normalize the expression of *KLF* (**Figure 5**).

In the pupae treated with PWN, the relative expression level of *KLF* was significantly up-regulated in BP5 and BP10 groups compared to control groups (P5, P10), which was normalized by the top-ranked gene (*RPL7*, *RPS5* or their combinations). Similar expression-profile changes were obtained by the combination of stable reference genes (*RPL7* + *RPS5* + *EF1-γ*), and there were no significant differences among those normalized by *RPL7*, *RPS5* individually, and *RPL7* + *RPS5*. However, the normalization by the least stable reference gene (*TER*, *α-TUB*, and *COX7*) led to a strong bias in the expression level of *KLF* in different treatments. *α-TUB* and *COX7* significantly decreased the transcription of *KLF* in BP10, and *TER* decreased in BP5. In the adults treated with PWN, although the expression trends were very similar, normalization with the unstable reference gene *TER* and *α-TUB* increased the expression level of *KLF* in BAF and BAM, which resulted in larger standard deviation values. At the different developmental stages associated with infection of PWN, the expression levels of *KLF* normalized by *RPL7* and *TER* individually, or *RPL7* + *TER* were different with *COX7* and *RPS5*. When normalized by *RPS5*, the expression of *KLF* increased in every developmental stage (L5, P1, P5, P10, AF and AM), and significantly decreased in AF and AM stages normalized by *COX7*.

DISCUSSION

M. saltuarius is a unique vector of *B. xylophilus* in northeast China. Its molecular physiology and the function of genes has been actively explored with the unpublished genomes, and recent transcriptomic advances have provided an opportunity for exploring the interspecific interaction mechanism between *M. saltuarius* and *B. xylophilus*, which was in favour of controlling the spread of pine wilt disease to north China. Therefore, it is necessary to probe gene function and quantify gene expression in *M. saltuarius*. Due to high sensitivity, rapidity, specificity, and accuracy, RT-qPCR is an effective method to study this mechanism. To reduce some inter-sample errors, appropriate reference genes are needed to normalize target genes (Zhao et al., 2022). However, there is no research on the reference genes of *M. saltuarius*. We systematically selected the reliable inference genes for standardization of gene expression by using five assessment algorithms (delta Ct, geNorm, NormFinder, BestKeeper, and RefFinder) in *M. saltuarius* at different developmental stages associated with infection of PWN and treated with PWN at the pupal and adult stages.

In our results, some candidate reference genes varied with different algorithms. *TER* ranked first in delta Ct and NormFinder, whereas it ranked sixth in geNorm and BestKeeper at different developmental stages associated with infection of PWN in *M. saltuarius*. The ranking of genes by different software was diverse, probably because different programs have different algorithmics, and the differences in the scaling systems used by the algorithms can also lead to these variations (Zhai et al., 2014; Sagri et al., 2017). Although the ranking order varies depending on the analysis program used, the overall trend was similar. For instance, in the adults treated with PWN, *RPS5, SNX6, RPL7, EF1-γ*, and *Zdhhc15* were all the top five stable genes in the delta Ct, geNorm, BestKeeper, and RefFinder. According to the geNorm,

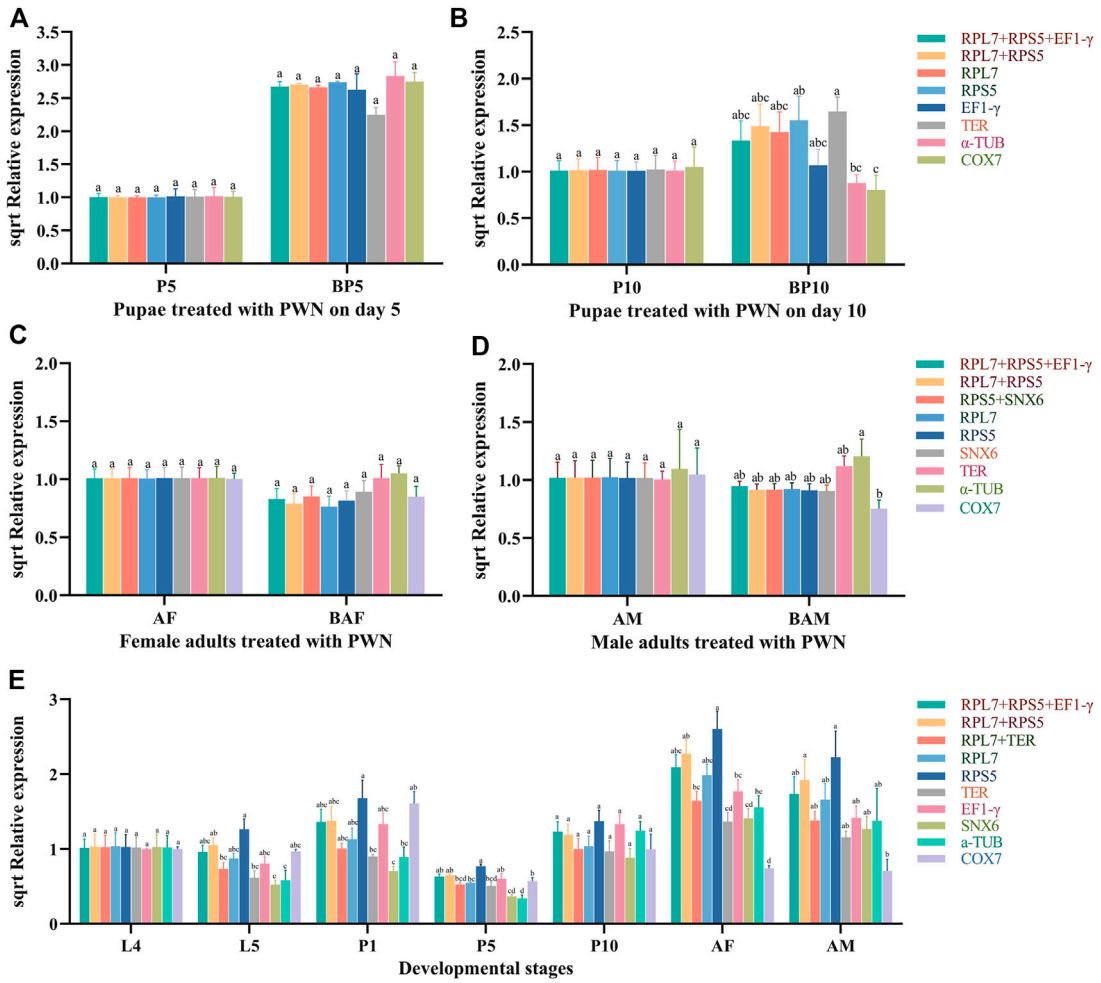

FIGURE 5 | Relative expression levels of *KLF* normalized by candidate reference genes. Different letters indicate the significant differences in *KLF* expression levels (ANOVA, HSD, $p < 0.05$). Sqrt (Relative expression) represents the square root of the relative expression value. **(A)** Pupae treated with PWN on day 5. **(B)** Pupae treated with PWN on day 10. **(C)** Female adults treated with PWN. **(D)** Male adults treated with PWN. **(E)** Developmental stages associated with infection of PWN in *M. saltuarius*.

NormFinder, RefFinder, and BestKeeper, PWN, *RPL7*, *RPS5*, and *RPL18* were all the top three most stable genes in the pupae treated with PWN. Therefore, in practical application, the results provided by these algorithms are required to be considered comprehensively.

Most studies have found that two or more reference genes rather than a single reference gene can increase the accuracy of relative quantification (Vandesompele et al., 2002; Haller et al., 2004; Veazey and Golding, 2011). In our study, the optimal number of reference genes was calculated by geNorm. Most experimental conditions showed values below the proposed 0.15 cut-off value at V2/3. This result indicated that combining the top two reference genes would be adequate for the normalization of gene expression data at developmental stages associated with infection of PWN and PWN treatment conditions.

In this study, the stability of reference genes in *M. saltuarius* could differ under various experimental conditions. *TER* and *RPL7* were stable reference genes at different developmental stages associated with infection of PWN. At the same time, *RPL7* + *RPS5* and *RPS5* + *SNX6* were identified as optimal reference genes in pupal stage treated with PWN, adult stage treated with PWN, respectively. Previous studies have also shown that no reference gene has always been stably expressed under different experimental conditions, in which species, growth stage, tissue, temperature, strain, population, and pesticide varied. Sellamuthu et al. (2021) showed that *β-TUB, Eef2* and *RPS3* were the most stable gene under different developmental stages and sex, while *UBQ* and *V-ATPase* were the most stable genes after Juvenile Hormone III treatment in *Ips sexdentatus* (Sellamuthu et al., 2021). *β-TUB* expression was also stable in *Aquatica leii* at different developmental stages, but *GST* was the most stably gene under different temperatures (Yang et al., 2020). Similarly, *RPS32* was stably expressed in different tissues of *Agasicles hygrophila* while showing lower stability under different nutritional conditions (Guo et al., 2021).

Besides, it was observed that *B. xylophilus* induced more variations in the Ct values in *M. saltuarius*. In *M. alternatus*, PWN caused significant changes at the physiological and molecular level. Zhao et al. (2016) found that ascarosides

secreted by dispersal juveniles (LIII) of *B. xylophilus* could facilitate *M. alternatus* pupation by upregulating ecdysone-dependent gene expression. When dispersal juveniles (LIV) of *B. xylophilus* entered the vector beetle, PWN affected the gene expression of Toll signal pathway (Zhou et al., 2018). In this study, the stable reference genes at PWN treatment conditions were different from normal developmental stages. This result suggested that *B. xylophilus* can also cause variations in transcript levels in *M. saltuarius*.

Among the 14 reference genes studied in this study, ribosomal proteins exhibited more stability compared to other candidate genes in relation to different biotic (developmental stages and PWN treatment) factors. Ribosomal protein genes, which play an important role in ribosome biogenesis, protein translation, and cell development, were one of the most stable reference genes in diverse biotic and abiotic conditions in many insects (Zhou et al., 2015). In *Tribolium castaneum* and *Coccinella septempunctata,* ribosomal proteins exhibited a high level of stability at different developmental stages (Yang et al., 2016; Lü et al., 2018). In different sexes of *M ylabris cichorii,* and *I. sexdentatus*, *RPL22* and *RPS3*, respectively, were the most suitable reference genes for RT-qRCR normalization (Wang et al., 2014; Sellamuthu et al., 2021). Our results demonstrated that the ribosomal proteins were also transcriptionally conserved in *M. saltuarius* under PWN treatment.

The genes of tubulin, a protein that maintains the cytoskeletal structure and morphology in eukaryotic cells, are also frequently used as reference genes (Caridi et al., 2019). For example, *α-TUB* was stably expressed in *Drosophila melanogaster* exposed to different temperatures (Fleur et al., 2011). In *Antheraea pernyi*, *α-TUB* was suitable reference gene for normalizing RT-qPCR data infected by multicapsid nucleopolyhedrovirus (Zhao et al., 2019). However, *α-TUB* was unstable as reference genes under certain conditions, such as in *Spodoptera litura* larvae treated with azadirachtin (Lu et al., 2018). In our research, *α-TUB* showed instability under PWN treatment conditions. *COX* responds to a wide variety of metabolic states and is also considered a novel reference gene for different tissues in *A. hygrophila* and *Spodoptera frugiperda* (Guo et al., 2021; Shu et al., 2021), while was inconsistent with our results. In *M. saltuarius* subjected to several experimental conditions (different developmental stages, adults treated with PWN, and all samples), *COX7* was particularly unstable reference gene. These results suggested that reference genes differ from species to species.

KLF is a key DNA-binding transcriptional factor that regulates various pathways that pertain to insect metamorphosis, metabolism, and other cellular mechanisms, and was selected as the target gene (Weber et al., 2014). The overall transcription pattern of *KLF* normalized with the most stable internal reference genes was similar to the transcriptome data at different developmental stages associated with infection of PWN and PWN treatment. At different developmental stages, the expression level of *KLF* increased at emergence period (AF and AM) when normalized by the top ranked genes and their combinations. On the contrary, normalization with *COX7* showed the lowest transcription of *KLF* in adults (AF and AM). Under certain conditions, normalizing with unsuitable reference genes affected the gene expression and resulted in more significant standard deviations (Lü et al., 2018). The expression level of *KLF* in the pupae treated with PWN (BP5 and BP10) was higher than pupae treated without PWN when normalized by the top ranked genes and their combinations, and the same expression pattern was also observed in *M. alternatus* (Zhao et al., 2016). However, normalization by the least stable reference gene resulted in a strong bias. The transcriptions of *KLF* significantly decreased in the pupae treated with PWN (BP10). Similar results were observed in the condition of adults treated with PWN. Consequently, our findings confirmed the importance of selecting and validated accurate reference genes for RT-qPCR analysis to avoid the misinterpretation of target gene transcription data.

CONCLUSION

This is the first study evaluating reference genes in *M. saltuarius*. We evaluated the stability of 14 candidate reference genes in samples from this beetle at different developmental stages associated with infection of PWN and PWN treatment conditions by delta Ct, geNorm, NormFinder, BestKeeper and RefFinder algorithms. We concluded that *RPL7* and *TER* were suitable reference genes at different developmental stages associated with infection of PWN. *RPL7* and *RPS5* were considered the most stable reference genes in pupae treated with PWN. *RPS5* and *SNX6* could be used as reference genes in adults treated with PWN. *RPL7*, *EF1-γ*, and *RPS5* could be used as stable reference genes in all the samples. Overall, *RPL7* and *RPS5* were the most stable reference genes for *M. saltuarius* under different conditions. Our results could provide stable reference genes for RT-qPCR gene expression analysis of *M. saltuarius*, also lay a foundation for the study of its phoretic relationship with *B. xylophilus*.

DATA AVAILABILITY STATEMENT

The data presented in the study are deposited in the GenBank repository. The names of the repository and accession numbers can be found below: https://www.ncbi.nlm.nih.gov/genbank/; OM471799, OM471800, OM471801, OM471802, OM471803, OM471804, OM471805, OM471806, OM471807, OM471808, OM471809, OM471810, OM471811, OM471812, OM471813.

AUTHOR CONTRIBUTIONS

JL carried out the majority of the bioinformatics studies and participated in performing the experiments. NF was involved in experimental data analysis. JL and NF wrote the manuscript. LR and YL participated in the design of the study and helped to draft the manuscript. All authors have read and agreed to the published version of the manuscript.

FUNDING

This study was funded by the National Key Research and Development Program of China (2021YFD1400900) and the Chinese National Natural Science Foundation (31870642).

ACKNOWLEDGMENTS

We gratefully acknowledge Xiaoyu Xin, Sixun Ge, and Zhenxiao Li (Beijing Forestry University, Beijing), for kind assistance in specimen collection. We also thank the staff of Liaoning Station of Forest and Grassland Pest Management in Shenyang for their support in our collection work.

SUPPLEMENTARY MATERIAL

The Supplementary Material for this article can be found online at: https://www.frontiersin.org/articles/10.3389/fphys.2022.882792/full#supplementary-material

REFERENCES

Abelleira, A., Picoaga, A., Mansilla, J. P., and Aguin, O. (2011). Detection of *Bursaphelenchus Xylophilus*, Causal Agent of Pine Wilt Disease on *Pinus pinaster* in Northwestern Spain. *Plant Dis.* 95, 776. doi:10.1094/PDIS-12-10-0902

Akbulut, S., and Stamps, W. T. (2012). Insect Vectors of the Pinewood Nematode: a Review of the Biology and Ecology of *Monochamus* Species. *For. Pathol* 42, 89–99. doi:10.1111/j.1439-0329.2011.00733.x

Andersen, C. L., Jensen, J. L., and Ørntoft, T. F. (2004). Normalization of Real-Time Quantitative Reverse Transcription-PCR Data: a Model-Based Variance Estimation Approach to Identify Genes Suited for Normalization, Applied to Bladder and colon Cancer Data Sets. *Cancer Res.* 64 (15), 5245–5250. doi:10.1158/0008-5472.CAN-04-0496

Barros Rodrigues, T., Khajuria, C., Wang, H., Matz, N., Cunha Cardoso, D., Valicente, F. H., et al. (2014). Validation of Reference Housekeeping Genes for Gene Expression Studies in Western Corn Rootworm (*Diabrotica Virgifera Virgifera*). *Plos One* 9 (10), e109825. doi:10.1371/journal.pone.0109825

Borowski, J. M., Galli, V., da Silva Messias, R., Perin, E. C., Buss, J. H., dos Anjos e Silva, S. D., et al. (2014). Selection of Candidate Reference Genes for Real-Time PCR Studies in Lettuce under Abiotic Stresses. *Planta* 239, 1187–1200. doi:10.1007/s00425-014-2041-2

Bustin, S. A., Benes, V., Nolan, T., and Pfaffl, M. W. (2005). Quantitative Real-Time RT-PCR - a Perspective. *J. Mol. Endocrinol.* 34, 597–601. doi:10.1677/jme.1.01755

Bustin, S. (2002). Quantification of mRNA Using Real-Time Reverse Transcription PCR (RT-PCR): Trends and Problems. *J. Mol. Endocrinol.* 29, 23–39. doi:10.1677/jme.0.0290023

Caridi, C. P., Plessner, M., Grosse, R., and Chiolo, I. (2019). Nuclear Actin Filaments in DNA Repair Dynamics. *Nat. Cell Biol.* 21 (9), 1068–1077. doi:10.1038/s41556-019-0379-1

Cheng, H. R., Lin, M. S., Li, W. Q., and Fang, Z. D. (1983). Pine Wilt Disease on *Pinus Thunbergii* Parl in Nanjing. *Forest Pest and Disease* 4, 1–5.

De Graeve, F., Smaldone, S., Laub, F., Mlodzik, M., Bhat, M., and Ramirez, F. (2003). Identification of the Drosophila Progenitor of Mammalian Krüppel-like Factors 6 and 7 and a Determinant of Fly Development. *Gene* 314, 55–62. doi:10.1016/S0378-1119(03)00720-0

Dropkin, B. H., and Foudin, A. S. (1979). Report of the Occurrence of *Burasphelenchus lignicolus* Induced Pine Wilt Disease in Missouri. *Plant Dis. Rep.* 63, 904–905.

Feng, B., Guo, Q. S., Mao, B. P., and Du, Y. J. (2016). Identification and Validation of Reference Genes for qRT-PCR Analysis in Chemosensory Tissue of *Monochamus Alternatus*. *Acta Entomologica Sinica* 59, 427–437.

Fleige, S., and Pfaffl, M. W. (2006). RNA Integrity and the Effect on the Real-Time qRT-PCR Performance. *Mol. Aspects Med.* 27, 126–139. doi:10.1016/j.mam.2005.12.003

Fu, N., Li, J., Wang, M., Ren, L., Zong, S., and Luo, Y. (2022). Identification and Validation of Reference Genes for Gene Expression Analysis in Different Development Stages of *Amylostereum Areolatum*. *Front. Microbiol.* 12, 827241. doi:10.3389/fmicb.2021.827241

Guo, Y.-Q., Yang, Y., Chai, Y., Gao, L.-L., and Ma, R. (2021). Identification and Evaluation of Reference Genes for Quantitative PCR Normalization in Alligator Weed Flea Beetle (Coleoptera: Chrysomelidae). *J. Insect Sci.* 21 (5), 9. doi:10.1093/jisesa/ieab067

Haller, F., Kulle, B., Schwager, S., Gunawan, B., Heydebreck, A. v., Sültmann, H., et al. (2004). Equivalence Test in Quantitative Reverse Transcription Polymerase Chain Reaction: Confirmation of Reference Genes Suitable for Normalization. *Anal. Biochem.* 335, 1–9. doi:10.1016/j.ab.2004.08.024

Han, H., Chung, Y.-J., and Shin, S.-C. (2008). First Report of Pine Wilt Disease on *Pinus Koraiensis* in Korea. *Plant Dis.* 92, 1251. doi:10.1094/PDIS-92-8-1251A

Khan, V. H. (1971). The Pine Wilt Disease Caused by *Bursaphelenchus xylophilus* in Nigeria. *Pakistan J. Nematol.* 9 (1), 57–59.

Kim, B.-N., Kim, J. H., Ahn, J.-Y., Kim, S., Cho, B.-K., Kim, Y.-H., et al. (2020). A Short Review of the Pinewood Nematode, *Bursaphelenchus Xylophilus*. *Toxicol. Environ. Health Sci.* 12, 297–304. doi:10.1007/s13530-020-00068-0

Kim, M., Kim, J., Han, J., Kim, Y., Yoon, C., and Kim, G. (2006). Mating Behavior of Pine Sawyer, *Monochamus Saltuarius* Gebler (Coleoptera: Cerambycidae). *J. Asia-pac. Entomol.* 9 (3), 275–280. doi:10.1016/s1226-8615(08)60303-9

Klein, D. (2002). Quantification Using Real-Time PCR Technology: Applications and Limitations. *Trends Mol. Med.* 8, 257–260. doi:10.1016/s1471-4914(02)02355-9

Li, J. X., Ren, L. L., Luo, Y. Q., and Xin, X. Y. (2021). *A Method and Application of a Culture Medium for Co-culture of Monochamus Saltuarius and Pine Wood Nematode. CN113475628A*. Beijing, China: China National Intellectural Property Administration.

Li, M., Li, H., Sheng, R.-C., Sun, H., Sun, S.-H., and Chen, F.-M. (2020). The First Record of *Monochamus Saltuarius* (Coleoptera; Cerambycidae) as Vector of *Bursaphelenchus Xylophilus* and its New Potential Hosts in China. *Insects* 11, 636. doi:10.3390/insects11090636

Livak, K. J., and Schmittgen, T. D. (2001). Analysis of Relative Gene Expression Data Using Real-Time Quantitative PCR and the 2−ΔΔCT Method. *Methods* 25, 402–408. doi:10.1006/meth.2001.1262

Lü, J., Yang, C., Zhang, Y., and Pan, H. (2018). Selection of Reference Genes for the Normalization of RT-qPCR Data in Gene Expression Studies in Insects: A Systematic Review. *Front. Physiol.* 9, 1560. doi:10.3389/fphys.2018.01560

Lu, Y., Yuan, M., Gao, X., Kang, T., Zhan, S., Wan, H., et al. (2018). Identification and Validation of Reference Genes for Gene Expression Analysis Using Quantitative PCR in *Spodoptera Litura* (Lepidoptera: Noctuidae). *Plos One* 8 (7), e68059. doi:10.1371/journal.pone.0068059

Mamiya, Y. (1988). History of pine Wilt Disease in Japan. *J. Nematol.* 20, 219–226.

Manuel, M. M., Helen, B., Maria, A. B., Ana, C. P., Wolfgang, B., and Kai, M. (1999). First Report of *Bursaphelenchus Xylophilus* in Portugal and in Europe. *Nematology* 1 (7), 727–734.

Pfaffl, M. W., Tichopad, A., Prgomet, C., and Neuvians, T. P. (2004). Determination of Stable Housekeeping Genes, Differentially Regulated Target Genes and Sample Integrity: BestKeeper - Excel-based Tool Using Pair-wise Correlations. *Biotechnol. Lett.* 26, 509–515. doi:10.1023/b:bile.0000019559.84305.47

Ponton, F., Chapuis, M.-P., Pernice, M., Sword, G. A., and Simpson, S. J. (2011). Evaluation of Potential Reference Genes for Reverse Transcription-qPCR Studies of Physiological Responses in *Drosophila melanogaster*. *J. Insect Physiol.* 57 (6), 840–850. doi:10.1016/j.jinsphys.2011.03.014

Rajarapu, S. P., Mamidala, P., and Mittapalli, O. (2012). Validation of Reference Genes for Gene Expression Studies in the Emerald Ash Borer (*Agrilus Planipennis*). *Insect Sci.* 19, 41–46. doi:10.1111/j.1744-7917.2011.01447.x

Rodrigues, T. B., Dhandapani, R. K., Duan, J. J., and Palli, S. R. (2017). RNA Interference in the Asian Longhorned Beetle:Identification of Key RNAi Genes and Reference Genes for RT-qPCR. *Sci. Rep.* 7 (1), 1–10. doi:10.1038/s41598-017-08813-1

Sagri, E., Koskinioti, P., Gregoriou, M.-E., Tsoumani, K. T., Bassiakos, Y. C., and Mathiopoulos, K. D. (2017). Housekeeping in Tephritid Insects: the Best Gene Choice for Expression Analyses in the Medfly and the Olive Fly. *Sci. Rep.* 7, 45634. doi:10.1038/srep45634

Sato, H. S. T. A. (1987). Transmission of *Bursaphelenchus Xylophilus* Nickle (Nematoda, Aphelenchoididae) by *Monochamus Saltuarius* (Gebler) (Coleptera, Cerambycidae). *J. Jpn. Soc. Hortic. Sci.* 69, 492–496.

Sellamuthu, G., Amin, S., Bílý, J., Synek, J., Modlinger, R., Sen, M. K., et al. (2021). Reference Gene Selection for Normalizing Gene Expression in *Ips Sexdentatus* (Coleoptera: Curculionidae: Scolytinae) under Different Experimental Conditions. *Front. Physiol.* 12. doi:10.3389/fphys.2021.752768

Shi, X.-Q., Guo, W.-C., Wan, P.-J., Zhou, L.-T., Ren, X.-L., Ahmat, T., et al. (2013). Validation of Reference Genes for Expression Analysis by Quantitative Real-Time PCR in *Leptinotarsa decemlineata* (Say). *BMC Res. Notes* 6, 93. doi:10.1186/1756-0500-6-93

Shu, B.-s., Yu, H.-k., Dai, J.-h., Xie, Z.-g., Qian, W.-q., and Lin, J.-t. (2021). Stability Evaluation of Reference Genes for Real-Time Quantitative PCR Normalization in *Spodoptera Frugiperda* (Lepidoptera: Noctuidae). *J. Integr. Agric.* 20, 2471–2482. doi:10.1016/S2095-3119(20)63298-1

Silveira, G. O., Amaral, M. S., Coelho, H. S., Maciel, L. F., Pereira, A. S. A., Olberg, G. G. O., et al. (2021). Assessment of Reference Genes at Six Different Developmental Stages of *Schistosoma Mansoni* for Quantitative RT-PCR. *Sci. Rep.* 11, 16816. doi:10.1038/s41598-021-96055-7

Silver, N., Best, S., Jiang, J., and Thein, S. L. (2006). Selection of Housekeeping Genes for Gene Expression Studies in Human Reticulocytes Using Real-Time PCR. *BMC Mol. Biol* 7, 33. doi:10.1186/1471-2199-7-33

Song, W., Wang, X. J., Guo, R. J., Zhang, W., Zhang, Z. Q., and Li, M. L. (2015). Selection of Reference Genes for qRT-PCR Analysis of *Dastarcus Helophoroides*. *Acta Agriculturae Boreali-occidentalis Sinica.* 24, 156–161.

Tan, Q.-Q., Zhu, L., Li, Y., Liu, W., Ma, W.-H., Lei, C.-L., et al. (2015). A De Novo Transcriptome and Valid Reference Genes for Quantitative Real-Time PCR in *Colaphellus Bowringi*. *Plos One* 10, e0118693. doi:10.1371/journal.pone.0118693

Toutges, M. J., Hartzer, K., Lord, J., and Oppert, B. (2010). Evaluation of Reference Genes for Quantitative Polymerase Chain Reaction across Life Cycle Stages and Tissue Types of *Tribolium castaneum*. *J. Agric. Food Chem.* 58, 8948–8951. doi:10.1021/jf101603j

Valasek, M. A., and Repa, J. J. (2005). The Power of Real-Time PCR. *Adv. Physiol. Edu.* 29, 151–159. doi:10.1152/advan.00019.2005

Vandesompele, J., De Preter, K., Pattyn, F., Poppe, B., Van Roy, N., De Paepe, A., et al. (2002). Accurate Normalization of Real-Time Quantitative RT-PCR Data by Geometric Averaging of Multiple Internal Control Genes. *Genome Biol.* 3 (7), research0034.1. doi:10.1186/gb-2002-3-7-research0034

Veazey, K. J., and Golding, M. C. (2011). Selection of Stable Reference Genes for Quantitative Rt-PCR Comparisons of Mouse Embryonic and Extra-embryonic Stem Cells. *Plos One* 6, e27592. doi:10.1371/journal.pone.0027592

Wang, Y., Wang, Z.-K., Huang, Y., Liao, Y.-F., Yin, Y.-P., and Tu, J. (2014). Identification of Suitable Reference Genes for Gene Expression Studies by qRT-PCR in the Blister Beetle Mylabris Cichorii. *Mylabris Cichorii. J. Insect Sci.* 14, 94. doi:10.1093/jis/14.1.94

Weber, U., Rodriguez, E., Martignetti, J., and Mlodzik, M. (2014). Luna, a Drosophila KLF6/KLF7, Is Maternally Required for Synchronized Nuclear and Centrosome Cycles in the Preblastoderm Embryo. *Plos One* 9, e96933. doi:10.1371/journal.pone.0096933

Wu, Y., Zhang, C., Yang, H., Lyu, L., Li, W., and Wu, W. (2021). Selection and Validation of Candidate Reference Genes for Gene Expression Analysis by RT-qPCR in Rubus. *Ijms* 22, 10533. doi:10.3390/ijms221910533

Xie, F., Xiao, P., Chen, D., Xu, L., and Zhang, B. (2012). miRDeepFinder: a miRNA Analysis Tool for Deep Sequencing of Plant Small RNAs. *Plant Mol. Biol.* 80, 75–84. doi:10.1007/s11103-012-9885-2

Yang, C., Preisser, E. L., Zhang, H., Liu, Y., Dai, L., Pan, H., et al. (2016). Selection of Reference Genes for RT-qPCR Analysis in *Coccinella septempunctata* to Assess Un-intended Effects of RNAi Transgenic Plants. *Front. Plant Sci.* 7, 1672. doi:10.3389/fpls.2016.01672

Yang, X.-J., Zheng, H.-L., Liu, Y.-Y., Li, H.-W., Jiang, Y.-H., Lin, L.-B., et al. (2020). Selection of Reference Genes for Quantitative Real-Time PCR in *Aquatica Leii* (Coleoptera: Lampyridae) under Five Different Experimental Conditions. *Front. Physiol.* 11. doi:10.3389/fphys.2020.555233

Yang, X., Pan, H., Yuan, L., and Zhou, X. (2018). Reference Gene Selection for RT-qPCR Analysis in *Harmonia axyridis*, a Global Invasive Lady Beetle. *Sci. Rep.* 8. doi:10.1038/s41598-018-20612-w

Yu, H. Y., Wu, H., Huang, R. F., Wang, J., Zhang, R. X., and Song, Y. S. (2020). Isolation and Identification of pine wood Nematode from *Pinus Sylvestris* in Fushun, Liaoning Province. *For. Pest Dis.* 39, 6–10.

Yu, H. Y., and Wu, H. (2018). New Host Plants and Vectors of pine wood Nematodes Were Found in Liaoning Province. *For. Pest Dis.* 37, 61.

Yu, H. Y., Wu, H., Zhang, X. D., Wang, L. M., Zhang, X. F., and Song, Y. S. (2019). Report on Infection of pine wood Nematode in Natural Condition of Larch. *For. Pest Dis.* 38, 7–10.

Zhai, Y., Lin, Q., Zhou, X., Zhang, X., Liu, T., and Yu, Y. (2014). Identification and Validation of Reference Genes for Quantitative Real-Time PCR in *Drosophila Suzukii* (Diptera: Drosophilidae). *Plos One* 9, e106800. doi:10.1371/journal.pone.0106800

Zhang, Y., Chen, J., Chen, G., Ma, C., Chen, H., Gao, X., et al. (2020). Identification and Validation of Reference Genes for Quantitative Gene Expression Analysis in *Ophraella communa*. *Front. Physiol.* 11. doi:10.3389/fphys.2020.00355

Zhao, L., Zhang, X., Wei, Y., Zhou, J., Zhang, W., Qin, P., et al. (2016). Ascarosides Coordinate the Dispersal of a Plant-Parasitic Nematode with the Metamorphosis of its Vector Beetle. *Nat. Commun.* 7, 12341. doi:10.1038/ncomms12341

Zhao, X., Geng, Y., Hu, T., Zhao, Y., Yang, S., and Hao, D. (2022). Evaluation of Optimal Reference Genes for qRT-PCR Analysis in *Hyphantria cunea* (Drury). *Insects* 13, 97. doi:10.3390/insects13010097

Zhao, Z., Wang, L., Yue, D., Ye, B., Li, P., Zhang, B., et al. (2019). Evaluation of Reference Genes for Normalization of RT-qPCR Gene Expression Data forTrichoplusia niCells DuringAntheraea pernyi(Lepidoptera: Saturniidae) Multicapsid Nucleopolyhedrovirus (AnpeNPV) Infection. *J. Insect Sci.* 19. doi:10.1093/jisesa/iey133

Zheng, C., Zhao, D., Xu, Y., Shi, F., Zong, S., and Tao, J. (2020). Reference Gene Selection for Expression Analyses by qRT-PCR in *Dendroctonus Valens*. *Insects* 11, 328. doi:10.3390/insects11060328

Zhou, J., Zhao, L.-L., Yu, H.-Y., Wang, Y.-H., Zhang, W., Hu, S.-N., et al. (2018). Immune Tolerance of Vector Beetle to its Partner Plant Parasitic Nematode Modulated by its Insect Parasitic Nematode. *FASEB j.* 32, 4862–4877. doi:10.1096/fj.201800247R

Zhou, X., Liao, W.-J., Liao, J.-M., Liao, P., and Lu, H. (2015). Ribosomal Proteins: Functions beyond the Ribosome. *J. Mol. Cell Biol.* 7, 92–104. doi:10.1093/jmcb/mjv014

Conflict of Interest: The authors declare that the research was conducted in the absence of any commercial or financial relationships that could be construed as a potential conflict of interest.

frontiers | Frontiers in Physiology

METHODS
published: 26 April 2022
doi: 10.3389/fphys.2022.856369

Fluorescent Microscopy-Based Detection of Chitin in Intact *Drosophila melanogaster*

J. Flaven-Pouchon[1,2] *and B. Moussian*[1,3]*

[1]Interfaculty Institute of Cell Biology, University of Tübingen, Tübingen, Germany, [2]Instituto de Neurociencia, Universidad de Valparaíso, Valparaiso, Chile, [3]INRAE, CNRS, Institut Sophia Agrobiotech, Université Côte d'Azur, Nice, France

Chitin is the major scaffolding component of the insect cuticle. Ultrastructural analyses revealed that chitin adopts a quasi-crystalline structure building sheets of parallel running microfibrils. These sheets called laminae are stacked either helicoidally or with a preferred orientation of the microfibrils. Precise control of chitin synthesis is mandatory to ensure the correct chitin assembly and in turn proper function of cuticular structures. Thus, evaluation of chitin-metabolism deficient phenotypes is a key to our understanding of the function of the proteins and enzymes involved in cuticle architecture and more generally in cuticle biology in insects. Usually, these phenotypes have been assessed using electron microscopy, which is time-consuming and labor intensive. This stresses the need for rapid and straightforward histological methods to visualize chitin at the whole tissue level. Here, we propose a simple method of chitin staining using the common polysaccharide marker Fluorescent brightener 28 (FB28) in whole-mount *Drosophila melanogaster*. To overcome the physical barrier of FB28 penetration into the cuticle, staining is performed at 65°C without affecting intactness. We quantify FB28 fluorescence in three functionally different cuticular structures namely wings, dorsal abdomens and forelegs by fluorescence microscopy. We find that, as expected, cuticle pigmentation may interfere with FB28 staining. Down-regulation of critical genes involved in chitin metabolism, including those coding for chitin synthase or chitinases, show that FB28 fluorescence reflects chitin content in these organs. We think that this simple method could be easily applied to a large variety of intact insects.

Keywords: chitin, FB28, cuticle, drosophila, appendages

OPEN ACCESS

Edited by:
Natraj Krishnan, Mississippi State University, United States

Reviewed by:
Subhash Rajpurohit, Ahmedabad University, India
Mônica Ferreira Moreira, Federal University of Rio de Janeiro, Brazil

***Correspondence:**
B. Moussian
bernard.moussian@uni-tuebingen.de

Specialty section:
This article was submitted to Invertebrate Physiology, a section of the journal Frontiers in Physiology

Received: *17 January 2022*
Accepted: *28 March 2022*
Published: *26 April 2022*

Citation:
Flaven-Pouchon J and Moussian B (2022) Fluorescent Microscopy-Based Detection of Chitin in Intact Drosophila melanogaster. Front. Physiol. 13:856369. doi: 10.3389/fphys.2022.856369

INTRODUCTION

The polysaccharide chitin is a major component of the insect cuticle. Chitin fibers are bundled building higher order chitin microfibrils that in turn are arranged in parallel forming horizontal sheets called laminae. Within the cuticle, laminae are stacked either helicoidally or with a preferred direction of the microfibrils along the apical-basal axis of the cuticle. Synthesis and organization of chitin within the cuticle requires the membrane-inserted glycosyltransferase chitin synthase, chitin binding proteins and chitin modifying enzymes including chitinases, chitin deacetylases and the DOMON domain Knickkopf (Knk) proteins (Moussian, 2010; Muthukrishnan et al., 2012). Impairment of chitin synthase activity by introduction of mutations into the respective gene, by reduction of its transcript levels by RNA interference (RNAi) or by administration of insecticides targeted against the chitin

synthase are lethal. Likewise, the activity of chitin synthesis, organization and modification associated proteins and enzymes is essential for insects. Hence, chitin organization shapes the architecture of the cuticular tissue and is the support for the large diversity of cuticular proteins (CPRs) characterized by the presence of the conserved chitin binding domain R&R. Nevertheless, this chitin binding domain is not sufficient to fix cuticular proteins and the cuticle undergoes a sclerotization step after its synthesis. This step is induced by the so-called tanning hormone Bursicon and its receptor DLGR2 encoded by the *rickets* (*rk*) gene (Baker and Truman, 2002; Luo et al., 2005). Following its release, oxidized catechols transported to the cuticle leading to the formation of adducts between cuticular proteins and chitin resulting in a stable chitin/CPRs network (Schaefer et al., 1987; Andersen, 2010). Evaluation of chitin synthesis, organization and modification deficient phenotypes is central to the understanding of the function of the proteins and enzymes involved in chitin metabolism and more generally the cuticle biology. Usually, these phenotypes are analyzed by transmission electron microscopy. As this method is rather labor intensive and time consuming, a rapid and simple protocol would allow fast and efficient scoring of the phenotypes. Since decades, chitin staining has been carried out in various Fungi and Arthropods using Calcofluor M2R, also known as Fluorescent brightener 28 (FB28) (Harrington and Hageage, 2003). Brighteners were originally used in textile industry and FB28 interest as a stable fungal-cell staining agent was firstly demonstrated by M. Darken (Darken, 1961; Darken, 1962). FB28 was then shown to bind longitudinally to polysaccharide microfibers including chitin (Harrington and Raper, 1968; Herth and Schnepf, 1980). In Insects, chitin staining using FB28 has been limited to thin organs sections such as epidermis, wings or gut (Pesch et al., 2016; Dong et al., 2020; Zhang et al., 2021) or embryos (Moussian et al., 2005). On the other hand, various chitin quantification methods have been applied to insects albeit limited to whole body extracts analysis (Farnesi et al., 2012; Chen et al., 2013; Henriques et al., 2020). Here, we propose a simple, unexpansive and rapid method to stain with FB28 the insect model *Drosophila melanogaster* without prior dissection, thereby allowing chitin detection and quantification at the whole tissue level.

METHODS

Visualizing chitin content at the level of a whole tissue is of interest since cuticular structures can be particularly complex and variable in an insect especially in the imago. The simple method we propose here was developed to address this need. FB28 has been routinely used in a large panel of organisms to visualize chitin extracellular matrices. Novel chitin staining reagents, namely Direct Yellow 98 and Direct Red 23, have been proposed as more stable and specific alternatives than FB28 but their current price limits their use for large-scale applications (Hoch et al., 2005; Sviben et al., 2020). Thus, we used FB28 as a chitin marker for whole-body staining. Unfortunately, FB28 does not penetrate intact *Drosophila melanogaster* at 25°C (**Supplementary Figure S1**). We had previously been successful in staining intact *Drosophila* using Eosin Y by varying the staining temperature (Wang et al., 2016). Hot Eosin Y experiments showed that epicuticular lipids are differentially distributed on the insect exoskeleton and that they play a major role to prevent xenobiotics penetration. Following the same rationales, we developed a Hot FB28 staining protocol to facilitate FB28 penetration and therefore chitin detection at the tissue level. Importantly, our method must address four major concerns: 1) FB28 intensity could reflect FB28 penetrability through the epicuticular lipidic barrier. 2) FB 28 intensity could reflect autofluorescence in the blue spectrum (resilin content). 3) FB28 intensity could be affected by cuticular pigmentation. 4) FB28 intensity could reflect the density of cuticular protein covalently bound to chitin. Assessing these four concerns likely improves the faith that FB28 intensity could precisely reflect chitin content in a given cuticular structure. If so, FB28 intensity should be affected by the down-regulation of chitin-metabolism genes. In this study, we provide several clues to address these concerns.

Hot FB28 Staining of Intact Flies

Groups of 5 48 h-old females were housed in 2 ml plastic vials, kept at −20°C until staining. Flies were washed during 5 min either with chloroform or distilled water. Chloroform was shown to be the most efficient polar solvent to remove cuticular lipids (CHCs) and facilitate dye penetration (Wang et al., 2016). Then, flies were briefly rinsed with 70% ethanol and then distilled water. Once the 2 ml vials were dry, 1 ml of PBST containing FB28 was added and vials were transferred on a warming agitator at 300 rpm during 20 or 60 min using different temperature (50 °C, 60 °C or 65 °C). After staining, flies were bathed 5 times (5 min each), 1 time in PBST and 4 times in distilled water. During these washes, vials were placed in a vertical agitator. Then, wings, dorsal abdomens or forelegs were dissected in PBS and mounted in Polymount medium (Polyscience, Inc.©). GAL4 drivers with differential expression in epidermis for these three structures have been extensively characterized and allow a direct comparison in the same individual. For abdomen staining, the abdomen content of 2 h-old flies was removed before staining. After staining, dorsal abdomen was simply detached from the thorax and mounted.

FB28 Intensity Quantification

Samples were imaged under a Nikon binocular (Nikon AZ100) using Lumencor light engine® illuminator and UV filter (Nikon EX330-380 DM 400, BA 420). The same acquisition parameters were kept for all pictures. The objective used was Nikon AZ plan Fluor 5x1. Pictures were taken using three different expositions for the different tissue (900 ms for wings, 300 ms for dorsal abdomen, 600 ms for forelegs). Pictures were then analyzed with ImageJ. Color channels were split, and the blue channel was used to measure mean grey values of the measured zones.

Measures zone were selected according to *engrailed*, *pannier* or *distalless* expression pattern as illustrated in the respective main figures. Polygons selection tool was used to delimit each zone. For wings, polygons strictly followed the *engrailed* expression pattern excluding the anterior veins and proximal veins network thereby focusing on inter vein areas (polygons selection in **Figure 2A**). For abdomens, measurments were made in the third tergite excluding the melanized posterior part (red rectangle in **Figure 3A**). Moreover, polygon selections in *pnr* + area were not taken in the very center of the segment to avoid melanization traces and to stay as much as possible in the same plan as the *pnr*-polygonal selection. For legs, polygon selections were taken in tarsal segments, tibia and femur (illustrated in **Figure 5A**) avoiding articulations enriched in resilin, a component which auto fluoresces in the blue spectrum (Lerch et al., 2020) To evaluate correlation between FB28 intensity and cuticle pigmentation in pigmentation mutants, pigmentation was measured using mean grey value (MGV) in the entire (indicated as a red rectangle in **Figure 4A**) third tergite as previously described (Flaven-Pouchon et al., 2020). In order to produce a more intuitive score for which darker cuticles had larger values, the final score was obtained by subtracting MGV from 250. Thus, the score was obtained using the following formula:

$$\text{Pigmentation} = -\text{MGV} + 250$$

The value of 250 was chosen arbitrarily because it was the smallest value that produced positive values for all readings.

Statistics

FB28 intensity measurements are shown using scattergrams representing all data of a group and its mean (red cross). Statistically significant differences were determined using one-way ANOVA followed by a Tukey HSD post hoc analysis when samples were normally distributed or by a Kruskal Wallis test followed by Conover-Iman post hoc analysis when strong deviation from normality was detected in each sample (Shapiro test and QQ plot). All statistical analyses were performed using XLSTAT 2016©.

MATERIAL

Fly Husbandry and Crosses

Fly stocks were raised on standard cornmeal/molasses/yeast food and maintained at 22 °C. Unless noted, fly stocks were obtained from the *Drosophila* Bloomington stock center (BL; Bloomington, United States) and the Vienna Drosophila Research Center. Strains used in this study were w^{1118}, *en*-GAL4 (BL 30564), *pnr*-GAL4 (BL 3039), *dll*-GAL4 (BL 3038), UAS-*cht6* RNAi (BL 54823), UAS-*cht10* RNAi (BL 57160), UAS-*knk* RNAi (VDRC 106302), UAS-*kkv* RNAi (VDRC 100327). UAS-*tBur* was kindly provided by A. Kopin. As down-regulation of these genes are mostly lethal during embryological and larval development, all GAL4 drivers used in this study were crossed preliminarily with *tub*-GAL80^{ts} to restrict RNAi expression to metamorphosis. All crosses were performed at 25 °C, progeny was raised at 18 °C until pupariation and then placed at 29 °C. The $yellow^1$ and w^{1118} strains derived from stocks of the Nüsslein-Volhard laboratory; the tan^3 (BL 132) mutant stock was purchased from the Bloomington stock center, the *ebony* mutant strain was made by CRISPR/Cas9 in the background of wild-type Tübingen 2018 flies (Mokeev et al., 2021).

Reagents

Fluorescent brightener 28 (1 mg/ml) in PBST (Tween 1%) solution kept at 4°C in dark place. Purchased from Sigma Aldrich.

Chloroform chemical grade >98%. Purchased from Sigma Aldrich.

Distilled water.

Polymount medium polyscience Inc.©.

Equipments

Eppendorf Thermomixer content (300 RPM) for FB28 staining.

Vertical rotator to rinse the samples.

Dissection material: Dumont forceps Cat5, Vanna's spring scissors (Fine science tool©).

RESULTS

FB28 Applied at High Temperature Leads to Homogenous Wing Staining

We first used the *Drosophila* wing, the simplest chitin containing tissue, as a model to develop this protocol. Importantly, without FB28 staining, *Drosophila* wings did not show any autofluorescence with our acquisition parameter (**Supplementary Figure S1A**). We used different staining temperature during 20 min to maximize FB28 fluorescence (435 nm). As a first concern, FB28 fluorescence intensity can result from both chitin density in the observed organ and FB28 penetration across epicuticular lipidic barrier. To discriminate between these two possibilities, we systematically prewashed some flies (C+) with chloroform to remove cuticular hydrocarbons (CHCs) and compared them with PBS-washed flies (C-) (**Figure 1A**). At 50°C, 60°C, and 65°C, we observed that C+ control flies (w^{1118}) were significantly more fluorescent than their PBS counterparts (**Figure 1B**) showing that at 65°C, the epicuticular barrier still limits FB28 penetration. Interestingly, we did not observe significant differences in C+ flies between 60 and 65°C or in C- flies between 60 and 65°C, which suggested that raising even more the temperature would not increase FB28 intensity. Moreover, higher temperature may eventually injure the tissues lowering the interpretability of the FB28 intensity. Thus, we decided to increase staining time from 20 to 60 min to possibly enhance FB28 penetration. In such conditions, we observed that FB28 stained homogeneously all inter-venous area of the wing and could not observe differences between C+ and C- flies. Of note, staining of the wing veins was highly variable, independently of staining temperature or duration, except for the anterior

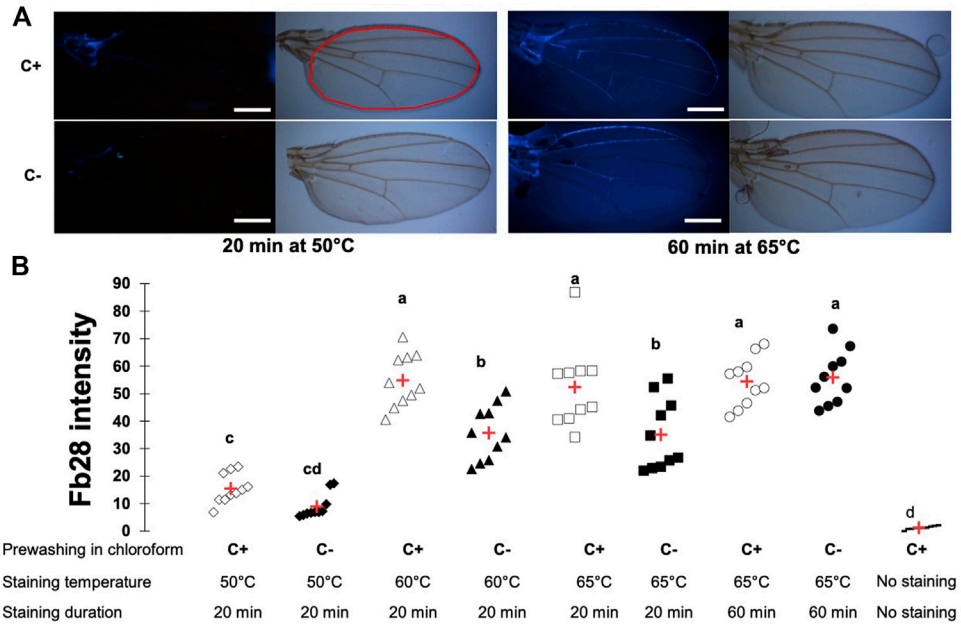

FIGURE 1 | FB28 staining of the whole *Drosophila* wing requires high temperature and duration to be penetration-independent. **(A)** Pictures from wings of 48 h-old control female flies (*w1118*) stained with FB28 at 50° or 65°C during 20 min or 60 min. Upper pictures were taken in bright field. Lower pictures were taken with DAPI filter. To remove epicuticular hydrocarbons, flies were prewashed with chloroform (C+) or washed with PBS as a control (C-). Red line in the white light picture (on the right) indicates the zone used for quantification. Scale bars = 0.3 mm **(B)** FB28 intensity quantification in the whole wing excluding longitudinal veins. Data are represented as scattergrams showing all data points with the mean (red crosses). C+ and C- individuals are represented with empty and black filled markers respectively. Different marker shapes indicate different temperatures. Different letters indicate statistically significant differences (one-way Kruskall-Wallis test followed by a Conover-Iman procedure, p-value < 0.001). n = 10 in each group.

longitudinal vein and the thorax-proximal vein network, which were robustly stained above 50°C. Taken together, these results show that staining whole flies with FB28 during 60 min at 65°C results in a homogenous and CHCs independent FB28 intensity in the wing. Hence, we used these staining parameters in all subsequent experiments.

Down-Regulation of Chitin-Metabolism Related Genes Affects FB28 Intensity in the Wing

To ensure that our protocol could be used to reliably quantify chitin content in a specific organ, we sought to down-regulate genes participating in chitin production or organization and hypothesized their down-regulation should affect FB28 intensity. We therefore selected the genes coding for the chitin synthase 1 (*krotzkopf verkehrt*, *kkv*), the chitin organizing protein *knickkopf* (*knk*), and two chitinases, *cht10* and *cht6*, which belong to the same expression group as *kkv* in the developing wing (Sobala and Adler, 2016). Additionally, we selected the gene coding for the tanning-hormone Bursicon receptor DLGR2 (*rk*) whose down-regulation in the wing leads to cuticle misfolding independently of tanning (Flaven-Pouchon et al., 2020). To down-regulate these genes in the wing, we expressed UAS-RNAi transgenes using the *engrailed*-GAL4 (*en*-GAL4) driver. As some of these genes are lethal during early development, we always restricted RNAi expression to metamorphosis using *tub*-GAL80^{TS} transgene (see Material and Method). Conveniently, *engrailed* expression in the wing is restricted to the posterior half of the wings (Brower, 1986) allowing a direct comparison between anterior and posterior wing halves in the same fly (illustrated in **Figure 2A**). We first down-regulated *cht6* and *cht10* in the wing. *en* > *cht6* RNAi females showed decreased FB28 intensity in the posterior half of the wing (*en*+) compared to *en* > GFP control flies (**Figure 2B**). By contrast, *en* > *cht10* females showed a two-fold increase compared to *en* > GFP females thereby confirming our previous observations (Dong et al., 2020). Interestingly, anterior halves of the wings (*en*-) showed similar FB28 intensities for all genotypes except for *en* > *cht6* RNAi females. Indeed, FB28 intensity of *en*-area in these flies was significantly lower than in control flies suggesting that *cht6* may function in a non-cell autonomous manner. We then down-regulated *kkv* and *knk*; 100% of *en* > *kkv* RNAi flies lacked their posterior wing halves and could therefore not been analyzed. In *en* > *knk* RNAi females, FB28 intensity was highly variable and not significantly different from *en* > GFP females. However, we could see abnormal vein doubling in some flies confirming an organizational role of *knk* in the wing (Li et al., 2017). At last, we down-regulated the Bursicon receptor and observed a 4-fold increase in FB28 intensity compared to *en* > GFP females suggesting that Bursicon signaling strongly affects chitin metabolism. Nonetheless, Bursicon signaling is known to affect wing epidermis mesenchymal transition during wing

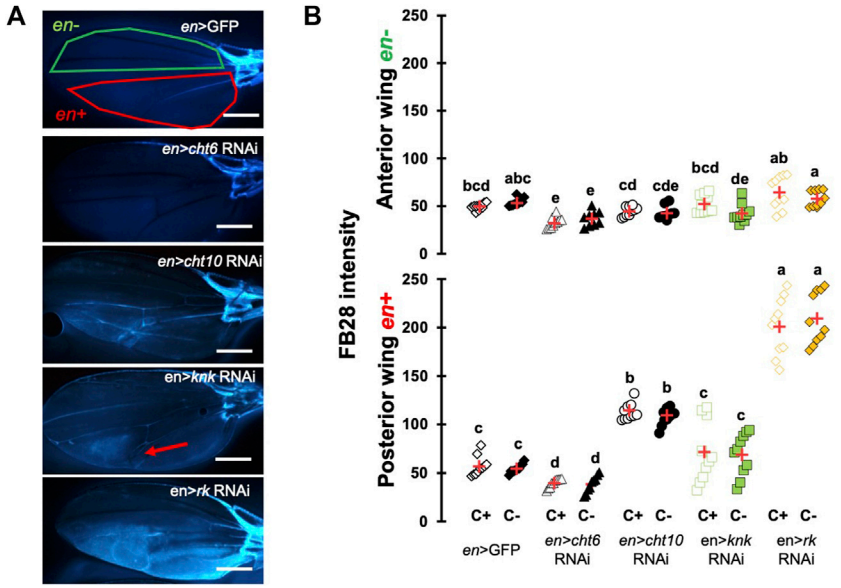

FIGURE 2 | FB28 hot staining combined with transgene differentially expressed in the wing reveal how specific genes affect chitinous content. **(A)** 48 h-old female wings stained with FB28 (65°C during 60 min). Pictures were taken from flies prewashed with chloroform (C+) before staining. *en*-GAL4 was used to specifically drive RNAi expression in the posterior half of the wing. Three chitin-related genes, *chitinase 6* (*cht6*), *chitinase 10* (*cht10*) and *knickkopf* (*knk*) were down-regulated. Additionally, the gene coding for the "tanning-hormone" receptor *DLGR2* (*rk*) was down-regulated. Red line indicates the zone used for quantification of *engrailed* expressing zone (*en*+). Green line indicates the zone used for quantification of *engrailed* non-expressing zone (*en*-). Red arrow in *en* > *knk* RNAi wing indicates a vein doubling in the *en* + area. Scale bar = 0.3 mm. **(B)** FB28 intensity quantification in *en*-zone (upper panel) and *en* + zone (lower panel). Data are represented as scattergrams showing all data points with the mean (red crosses). C+ and C- individuals are represented with empty and black filled markers respectively. Different marker shapes/colors represent the different genotypes. Different letters indicate statistically significant differences (one way Kruskall-Wallis test followed by a Conover-Iman procedure, *p*-value < 0.001). *n* = 10 in each group.

expansion. Thus, high FB28 intensity in these flies could be due to accumulation of FB28 between dorsal and ventral cuticle layers rather than faithfully reflecting the chitin content. Taken together, these results show that down-regulation of genes participating in chitin metabolism affect FB28 intensity in the wing and establish our method as a relevant chitin quantification method for the *Drosophila* wing.

Down-Regulation of Chitin-Metabolism Related Genes Affects FB28 Intensity in the Abdomen

One major advantage of *D. melanogaster* wings to observe chitin staining is the lack of pigmentation of the non-venous cuticle. We examined whether our protocol could allow chitin quantification in melanized tissues and focused on the dorsal abdomen. After FB28 staining of 48 h-old flies, dorsal abdomens were dissected, and fluorescence was observed at 455 nm. Clearly, FB28 intensity is drastically reduced in 48 h-old abdomen suggesting dark pigmentation may affect quantification (**Supplementary Figure S1C**). To bypass this limitation, we used 2 h-old flies in which pigmentation is lighter. Of note, abdomen tanning in *D. melanogaster* is timely controlled by Bursicon hormone release, which starts around 1 h after adult eclosion under normal conditions (Peabody et al., 2009). After various locomotor behavior including abdominal and proboscis contraction, abdomens start tanning. To easily visualize how the selected genes down-regulation affects FB28 intensity in the abdomen, we drove RNAi expression using *pannier*-GAL4 (*pnr*) (Calleja et al., 2000). Conveniently, *pnr*-GAL4 expression pattern is restricted to the central part of dorsal abdomen epidermis and allows a direct comparison between central abdomen and the lateral sides of the abdomen as illustrated in **Figure 3A**. To limit impact of the melanization appearing in the posterior extremity of each segment, we restricted FB28 intensity measurement to the anterior part of the segment. Unfortunately, staining whole flies with FB28 at 65°C resulted in adverse unexpected effects. Indeed, after such treatment, soft tissues below the abdomen cuticle become highly sticky therefore making the cleaning of abdomen cuticle adventurous. To bypass this trouble, we simply pre-dissected the flies partially before staining. With the help of microdissection scissors, we cut the genitalia and removed the abdomen content. With our method, *pnr* > *cht6* RNAi females showed a decreased FB28 intensity in the *pnr* + area relatively to the *pnr*-area (**Figure 3B**). By contrast, FB28 intensity in *pnr*+ was higher in *pnr* > *cht10* RNAi abdomen confirming our observations in wings. Interestingly, *pnr* > *knk* RNAi females exhibited a more variable FB28 phenotype. In these flies, *pnr* + areas often contained alternances of dark and light FB28 intensities suggesting planar disorganization of chitin (**Figure 3B**). Overall, *pnr* > *knk* RNAi abdomens did not show significant differences from *pnr* > GFP controls. Down-regulation of chitin synthase *kkv* using pnr-GAL4 led to high mortality during pupariation but several escapers could be analyzed. As expected, *pnr* > *kkv* RNAi abdomens exhibited a lower FB28 intensity compared to *pnr* > GFP controls.

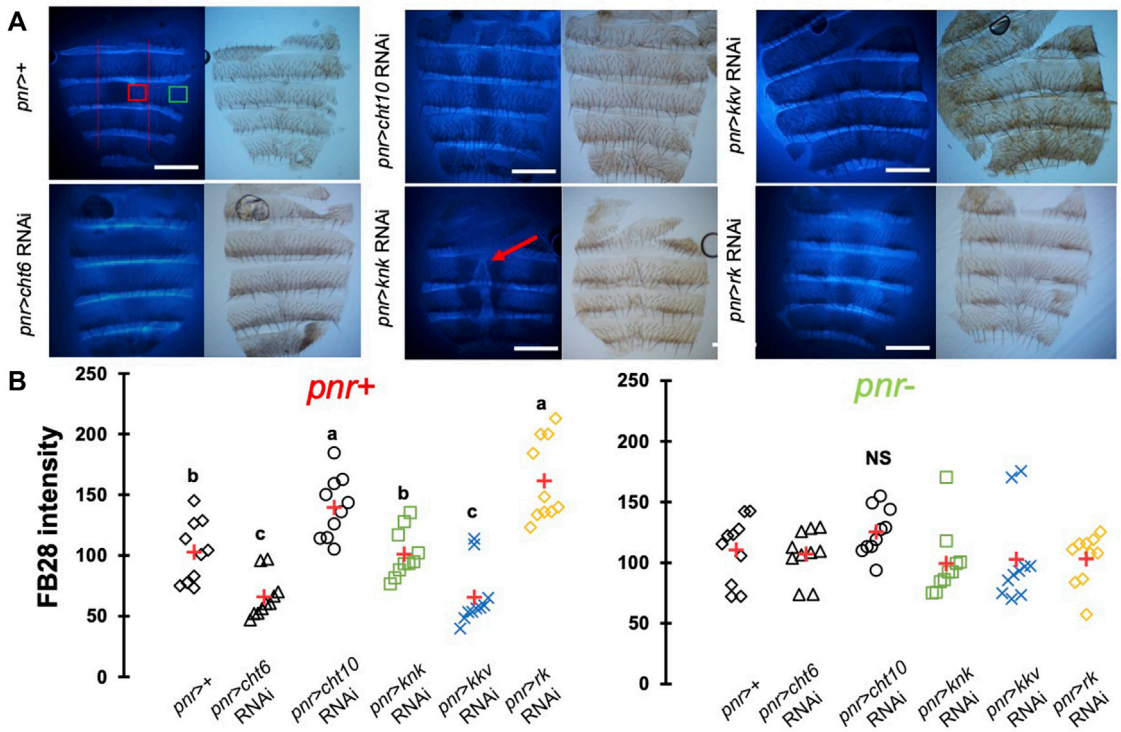

FIGURE 3 | FB28 hot staining combined with transgene differentially expressed in the abdominal epidermis reveal how specific genes affect chitinous content. **(A)** 3 h-old female dorsal abdomens stained with FB28 (65°C during 60 min). *pannier* -GAL4 was used to specifically drive RNAi expression in the central part of the abdomen. Four chitin-related genes, *chitinase 6* (*cht6*), *chitinase 10* (*cht10*), *knickkopf* (*knk*) and *chitin synthase 1* (*kkv*) were down-regulated. Additionally, the gene coding for the "tanning-hormone" receptor *DLGR2* (*rk*) was down-regulated. Red line indicates the zone used for quantification of *pannier* expressing zone (*pnr+*). Green line indicates the zone used for quantification of *pnr* non-expressing zone (*pnr-*). Scale bar = 0.3 mm. **(B)** FB28 intensity quantification. FB28 intensity in *pnr* + zone (right) and *pnr*-zone (left) are shown. Data are represented as scattergrams showing all data points with the mean (red crosses). Different marker shapes/colors represent the different genotypes. Different letters indicate statistically significant differences (one way ANOVA test followed by a Tukey HSD procedure, *p*-value < 0,0001). *n* = 10 in each group.

Additionally, downregulation of *rk* resulted in a marked increase in FB28 intensity compared to *pnr* > GFP controls. Contrary to the wing, this result cannot be explained by an accumulation of FB28 between two different cuticle layers which strongly suggests that bursicon signaling affects chitin metabolism. Finally, we further studied how pigmentation levels could affect FB28 intensity by applying our protocol to flies mutant for *yellow*, *tan* and *ebony*, three genes whose roles in tanning pathways have been extensively investigated (Spana et al., 2020). In brief, the Yellow enzyme is critical to convert dopamine and DOPA into black melanins, whereas Ebony converts Dopamine into NBAD thereby addressing the Dopamine pool to NBAD sclerotization pathway (Wittkopp et al., 2009). *Tan* encodes a NBAD hydrolase which catalyzes the reverse reaction of Ebony (Wright, 1987; True et al., 2005). As expected, *ebony* and *yellow* mutant flies showed abnormal pigmentation compared to their respective controls, whereas *tan* mutant flies did not show any significant pigmentation phenotype (**Figures 4A,B**). However, we did not detect significant correlations between pigmentation and the FB28 signal in *yellow*, *tan* and *ebony* mutant flies neither in their respective background control flies (Canton S and Tübingen 2018 strains, respectively) indicating that pigmentation does not negatively affect FB28 intensity (**Figure 4C**). Thus, another factor is likely to explain FB28 intensity decrease in 48 h-old abdomens compared to immature imago abdomens. Interestingly, in *tan* mutant flies that, again, did not show any pigmentation differences compared to control flies, the FB28 intensity was strongly decreased (**Figure 4D**). This suggests that NBAD sclerotization could significantly impact FB28 binding to chitin. Taken together, these results establish hot FB28 staining as a reliable method to quantify chitin content in the young abdomen.

Down-Regulation of Chitin-Metabolism Related Genes Affects FB28 Intensity in Drosophila Forelegs

To further investigate whether our method could work with other cuticular organs, we applied our method to the *Drosophila* foreleg. Legs are an interesting cuticular tissue for our method because their pigmentation is homogenous lacking strong melanization. Moreover, with hard, soft, elastic and adhesive cuticle parts, legs are among the most complex cuticular structures found in insects. Following the same rational as for wings and abdomen, we drove RNAi expression using *distalless*-GAL4, which mainly expresses in the distal tarsal segments during leg development (Gorfinkiel et al., 1997). *dll*-GAL4 expression gradually decreases in the proximal segments. As

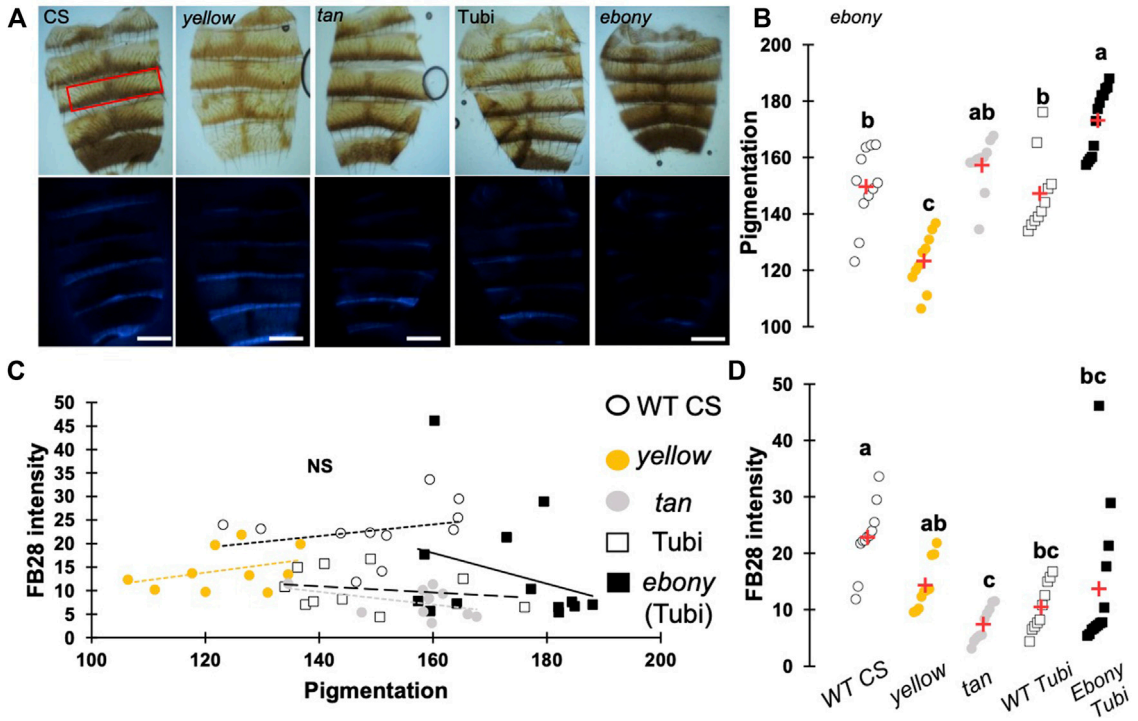

FIGURE 4 | Pigmentation in 48 h-old abdomens poorly affects FB28 intensity compared to sclerotization levels. **(A)** Images of control flies (WT CS), *yellow* mutant flies and *tan* mutant flies. *ebony* mutants were obtained from wild-type Tübingen 2018 (Tubi) flies. Bright Field images (upper panel) and blue filtered images (lower panel) are shown. Scale bars = 0.3 mm **(B)** Quantification of cuticle pigmentation. Pigmentation was measured using the mean grey value in the third tergite as represented by a red rectangle in A. **(C)** Quantification of FB28 intensity expressed as a function of pigmentation. No correlation between pigmentation and FB28 were observed (Pearson correlations: $-0.4 < r < 0.3$, p-values ≥ 0.2). **(D)** Quantification of FB28 intensity alone. *tan* mutant flies showed a significantly lower FB28 intensity compared to wild-type flies. *ebony* mutant flies showed a significant, albeit variable, higher FB28 intensity. Data are represented as scattergrams showing all data points with the mean (red crosses). Different marker shapes/colors represent the different genotypes. Different letters indicate statistically significant differences (one way Kruskall-Wallis test followed by a Conover-Iman procedure, p-value < 0,0001). n > 10 in each group.

illustrated in **Figure 5A**, we first checked unstained legs that do not show any fluorescence. With our acquisition parameters, we did not observe fluorescence without FB28 staining. We then applied our staining method on four genotypes, *dll* > *kkv* RNAi, *dll* > *knk* RNAi, *dll* > *rk* RNAi and a *ddl*>+ control (**Figure 5**). We measured FB28 intensity in the three major division of the legs, namely the most distal tarsal segments, the intermediary tibia and the proximal femur (illustrated in **Figure 5A**). We observed in C+ *ddl*-GAL4 controls that FB28 intensity varies between these three segments (**Figure 5C**); femurs exhibiting the most intense staining, whereas FB28 intensity was lower in tarsal segments and the tibia (Friedman test, $p < 0,0001$, followed by a Nemenyi procedure). Interestingly, we observed a significant difference between C+ and C- *ddl*-GAL4 controls only in tarsal segments which suggests CHC quantity on the tarsal segments is higher than in more proximal parts of the leg. Generally, we observed FB28 intensity in dll > *knk* RNAi forelegs exhibited high variability. Nevertheless, FB28 intensity in C+, *ddl* > *knk* RNAi forelegs was significantly higher in tarsal segments than in C+ *dll*>+ controls. On the other hand, FB28 intensity in *ddl* > *kkv* RNAi forelegs appeared overall weaker than in *dll*>+ controls particularly in the tarsa and the femur. Finally, we observed that FB28 intensity in *ddl* > *rk* RNAi forelegs was generally stronger than in control *dll*>+ forelegs but showed a higher variability in tibia and femur segments. Taken together, these results show hot FB28 staining can be applied to the foreleg for chitin quantification and illustrate the need for a FB28 penetrability control when this method is applied.

In summary, we described in this study a rapid method to stain chitin in *Drosophila* whole body to allow chitin detection in whole tissues and provide both qualitative and quantitative information about chitin-containing structures. The down-regulation of chitin-related genes affected chitin detection in three independent tissues pointing to the robustness of our method. Particular attention must be paid to FB28 penetration versus chitin staining and we proposed a simple control to facilitate interpretation of the results.

DISCUSSION

FB28 Intensity: Factors Limiting Its Interpretation

Using the wing to establish our Hot FB28 staining protocol, we determined 65°C as the optimal temperature to homogeneously stain non-venous parts of the *Drosophila* wing. Lower

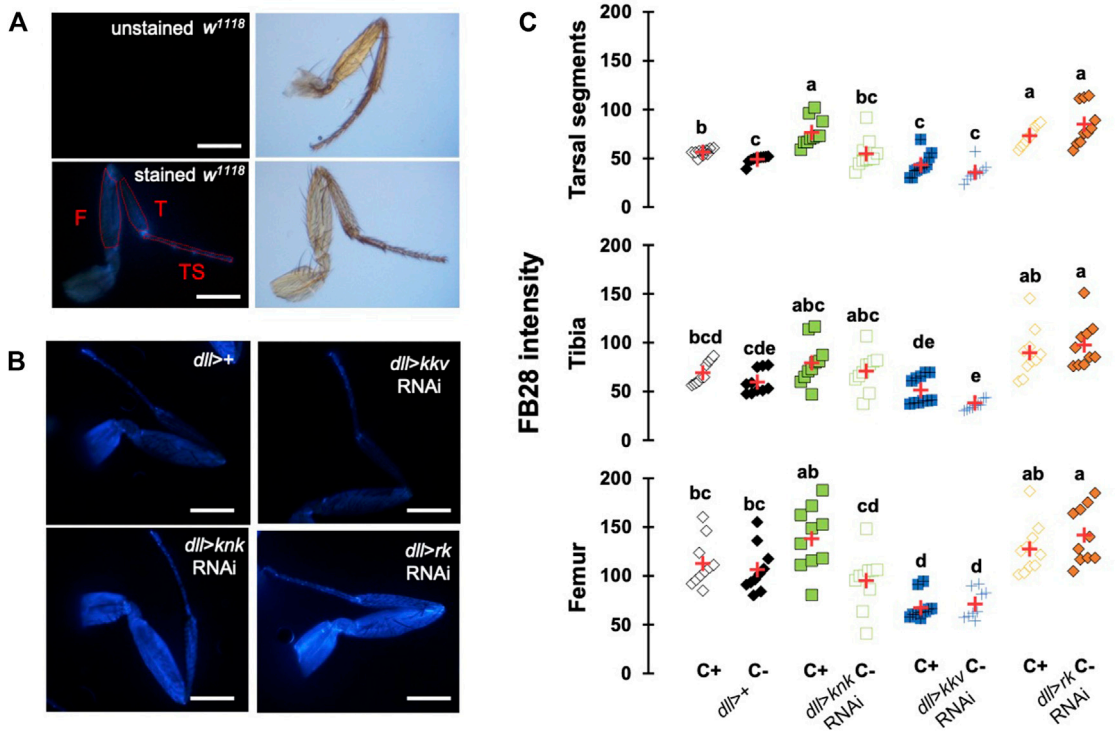

FIGURE 5 | FB28 hot staining combined with transgene differentially expressed in the legs reveal how specific genes affect chitinous content. **(A)** Absence of autofluorescence in unstained *w1118* legs (upper pictures). Fluorescence is only seen after FB28 staining (lower panel). Pictures of the leg by bright field are shown on the right. Scale bars = 0.5 mm. **(B)** Female forelegs stained with FB28 (65°C during 60 min). Pictures were taken from flies prewashed with chloroform (C+) before staining. *Distalless*-GAL4 was used to specifically drive RNAi expression in the *Drosophila* leg. *dll*-GAL4 is gradually expressed from the most distal part of the legs (tarsal segments) to the junction with the thorax. Two chitin-related genes *knickkopf* (*knk*) and *chitin synthase 1* (*kkv*) were down-regulated. Additionally, the "tanning-hormone" receptor *DLGR2* (*rk*) was down-regulated. Scale bars = 0.3 mm **(C)** FB28 intensity quantification. FB28 intensity in tarsal segments (TS), tibia (T) and femur (F) were measured as illustrated by the red lines in **(A)**. Data are represented as scattergrams showing all data points with the mean (red crosses). Different marker shapes/colors represent the different genotypes. Different letters indicate statistically significant differences (one way Kruskall-Wallis test followed by a Conover-Iman procedure, p-value < 0,0001). n = 10 in each group.

temperatures revealed circular staining patterns in the posterior half of the wing, whose shape is similar as in previous observations with hot Eosin Y staining (**Supplementary Figure S1D**, Wang et al., 2016). These observations suggest that temperatures below 65°C are not sufficient to homogeneously abolish the epicuticle lipidic barrier in non-venous part of the wings. Intriguingly, staining of the wing veins was highly variable between wings, even after 1 hour of staining or chloroform washing, except for the anterior marginal vein and the wing hinge, which was always stained even at 50°C. Interestingly, stronger staining of the wing hinge was similarly observed after Eosin Y staining suggesting that the cuticular inward barrier is particularly weak in the wing hinge (Dong et al., 2019). Moreover, high variability of distal veins staining suggests that FB28 diffusion trough the veins is limited. Higher temperatures could help homogenizing veins staining at the cost of a higher risk of tissue disruption. These differences of dye penetration within a single cuticular structure stresses the need of a penetration control. Thus, in intact flies staining, we systematically washed a separate group of flies with chloroform to remove cuticular lipids and to assess that there was no difference with water-washed flies. Overall, we did not see significant differences of FB28 between C+ flies and C- thereby confirming that staining *Drosophila* at 65°C during 60 min are appropriate conditions to rule out the possibility that FB28 penetration affects FB28 intensity. The only exception are the tarsal segments in which chloroform treatment slightly increased FB28 intensity in *en* > GFP controls. This suggests a stronger lipidic barrier is present in these distal segments which is not surprising given that *Drosophila* legs, as gustatory sensors, are daily exposed to xenobiotics (Ling et al., 2014; Gonzalez et al., 2018).

On the other hand, cuticle autofluorescence can be part of the FB28 intensity measurement. In particular, the rubber-like protein matrix resilin has excitation and emission maxima in the range of 320 and 415 nm, respectively, while FB28 shows a maximum excitation and emission at 300 and 480 nm, respectively (Vincent and Wegst, 2004). Resilin has been shown to be particularly present in insect articulations as well as wings hinges (Ardell and Andersen, 2001; Lerch et al., 2020). However, with our acquisition parameters, we did not see any fluorescence without FB28 staining (**Figure 4A**; **Supplementary Figure S1A,B**). This is likely to be explained by the low magnification we used to visualize the tissues and quantify

FB28 intensity (5 × 1). Still, we recommend to always assess autofluorescence especially when visualizing the stained tissue at high magnifications.

One other concern of our method is the impact of melanization on FB28 intensity. Indeed, FB28 intensity in 48 h-old flies is strongly reduced (**Supplementary Figure S1C**). Thus, we focused our analyses on young dorsal abdomens (2 h after eclosion), which are less melanized. Interestingly, we observed pigmentation decrease after the down-regulation of *knk*, *rk* and in a lesser extent with *cht10* (**Figure 3**). However, these decreases do not correlate with FB28 intensity as the strongest pigmentation defects observes in *pnr* > *knk* RNAi did not results in a higher FB28 intensity. This suggests that low levels of pigmentation do not interfere with FB28 intensity. Conversely, FB28 staining of 48 h-old mutants of the tanning pathway did not show any correlation between pigmentation and FB28. These results suggest that FB28 intensity is hardly affected by the darkening of the mature cuticle, yet we have not applied our protocol to insects that are completely black such as *Tenebrio molitor*. Interestingly, we observed that FB28 intensity was lower in the abnormal black-melanin pattern of the wings of *ebony* mutant flies (**Supplementary Figure S3**). This suggests that black melanin may compete with FB28 for chitin binding or alter detection of the FB28 emission. In highly pigmented arthropods, various chemical methods have been proposed to remove melanins from the cuticle (Stuben and Linsenmair, 2009; Younes et al., 2015; Khayrova et al., 2021). However, these treatments are likely to affect the quality and/or the quantity of the chitin fibers particularly through chitin deacetylation and depolymerization (Qin et al., 2002; Younes et al., 2015). Overall, our data suggest that pigmentation is not the major concern that limits the interpretability of FB28 intensity. Importantly, the marked FB28 intensity drop that we observed between 2 h-old and 48 h-old abdomens calls for another explanation than pigmentation.

When staining a cuticular structure with FB28, we assume that there is a competition between the dye molecule which binds to chitin fibers and all endogenous chitin-binding compounds including CPRs, pigments and sclerotizing agents. Thus, the sclerotization state of a given cuticular structure could strongly affect FB28 intensity. Interestingly, we observed strong decrease of FB28 intensity in abdomens and wings of the NABD hydrolase mutant *tan* and in a lesser extent in *yellow* mutants (**Figure 4D**, **Supplementary Figure S3**). This strongly suggests that over-sclerotization of the cuticle as expected in these two mutant flies leads to a decrease in FB28 intensity. On the other hand, results we obtained by down-regulating the tanning-hormone receptor *rickets* suggest that sclerotization defects increase drastically FB28 binding. However, we recently challenged the view that Bursicon/Rk signaling in the epidermis is related to tanning (Flaven-Pouchon et al., 2020). Moreover, *rk* expression is maximal in 3 days-old pupae (Graveley et al., 2011). Thus, we cannot exclude that Bursicon/Rk signaling in the epidermis impacts chitin content through regulation of chitin-related genes during metamorphosis. Further experiments shall address the impact of *rk* down-regulation on chitin metabolism genes transcriptions. Overall, discriminating between chitin polymer availability for FB28 binding and chitin content is a real challenge in FB28 stained intact tissues. One simple solution to this concern consists in analyzing the target tissue soon after ecdysis when sclerotization is not completed which unfortunately restricts the analysis of chitin content to specific stages. Various methods have been proposed to quantify chitin after chemical extraction from biological samples (Lehmann and White, 1975; Tsurkan et al., 2021). Recently, FB28 fluorescence spectrophotometry has been proposed as a fast and efficient method to quantify chitin after mechanical extraction from insect samples (Henriques et al., 2020). We think that this method could be complementarily applied after hot FB28 staining and tissue pooling and would, because of chemical separation and release of the components, decrease the impact of sclerotization state on the chitin content quantification.

In *Drosophila*, chitin synthesis is mainly achieved by the chitin synthase *kkv*, which is highly expressed during metamorphosis (Gagou et al., 2002; Moussian et al., 2005; Sobala and Adler, 2016). As expected, down-regulating the chitin synthase *kkv* during metamorphosis led to high pupal mortality with the three drivers we used (*en*, *dll* and *pnr*). However, we could obtain adult escapers of the *pnr* > *kkv* RNAi and *dll* > *kkv* RNAi genotypes, which showed a decrease in FB28 intensity. These results are particularly important as they establish that hot FB28 staining as a relevant method for chitin content detection in intact insects. Additionally, down-regulation of the chitin organizer gene *knk* overall did not change significantly FB28 intensity in wings or abdomens. Interestingly, FB28 staining was more heterogeneous in *pnr* zones (**Figure 3**) and venous malformation appeared in the *en* zone (**Figure 2**) suggesting chitin organization defects. Previous studies showed that *knk* down-regulation induced chitin fiber disorganization in the procuticle and less lamination in the wing cuticle decreasing indirectly inward barrier efficiency (Moussian et al., 2006; Li et al., 2017). With hot FB28 staining, we did not observe any significant change in FB28 intensity. FB28 intensity in *dll* > *knk* RNAi tarsal segment was slightly higher, which could be explained by inward barrier impairment rather by a higher chitin content. Of note, *knk* down-regulation decreases abdomen pigmentation as it decreases pupal wing melanization confirming that chitin organization is a determinant for pigmentation (Li et al., 2017). Together, these data are not in agreement with the finding that chitin amounts are reduced in the red flour beetle *Tribolium castaneum* and the migratory locust *Locusta migratoria* after *knk* knock-down (Chaudhari et al., 2011; Yu et al., 2021).

Hot FB28 Staining Reveal Opposite Role of Two Chitinases

In insects, chitinases genes are more and more seen as cuticle architects and not only chitin recyclers (Pesch et al., 2016; Noh et al., 2018; Behr and Riedel, 2020). Among *Drosophila* chitinases, we recently showed that *cht10* down-regulation in the wings resulted in increase of chitin amounts possibly through uncoupling with the chitin synthase Kkv activity (Dong et al., 2020). Our results confirm these observations and suggest that the *cht10* function is conserved in various cuticular structures. Conversely, *cht6* down-regulation led to FB28 intensity decrease in all observed organs suggesting opposite roles between *cht10* and *cht6*. Interestingly, *cht6* down-regulation in

the posterior wing half additionally affected the anterior wing half suggesting that *cht6* function in the wing is not tissue-autonomous, whereas *cht10* function is. These results call for a precise dissection of the localization of chitinase action, which could easily be achieved using the CRISPR tools panel available in *Drosophila* and other insect models (Rylee et al., 2018; Port et al., 2020).

In summary, our results illustrate a simple and rapid staining method of an intact insect allowing chitin detection at the tissue level. Once several aspects of cuticle biology are kept in mind, this method could be used in various insects to study the impact of genes down-regulation or insecticide applications on chitin content in whole insects.

DATA AVAILABILITY STATEMENT

The original contributions presented in the study are included in the article/**Supplementary Material**, further inquiries can be directed to the corresponding author.

AUTHOR CONTRIBUTIONS

JF-P and BM conceived and designed the research and prepared the final manuscript. JF-P collected, sorted, dissected flies, stained all tissues and did all analyses. JF-P wrote the first draft. All authors have read and approved the final manuscript.

FUNDING

This research was supported by FONDECYT (National Fund for Scientific and Technological Development, Chile) postdoctoral scholarships #3180496 (to JF-P.), and the Centro Interdisciplinario de Neurociencia de Valparaiso (CINV) Millennium Institute grant P09-022-F supported by the Millennium Scientific Initiative of the Ministerio de Economia, Fomento y Turismo. The contribution of BM was financed by the German Research Foundation (DFG MO1714/9).

SUPPLEMENTARY MATERIAL

The Supplementary Material for this article can be found online at: https://www.frontiersin.org/articles/10.3389/fphys.2022.856369/full#supplementary-material

Supplementary Figure S1 | (A) No fluorescence was observed in wings in the absence of FB28 staining. w^{1118} 48h-old female wing. Picture taken by bright field on the left. **(B)** No fluorescence was observed in abdomen in the absence of FB28 staining. w^{1118} 2h-old female wing. Picture taken by bright field on the left. **(C)** Abdomen of 48h-old *pnr* > *rk* RNAi 48h-old females after hot FB28 staining. FB28 fluorescence is strongly reduced in the melanized center (red arrows). **(D)** w^{1118} 48h-old female wing after hot FB28 staining at 60°C. Fluorescence patterns in posterior wings were observed in most flies and were similar to previous observations with Eosin Y penetration. Scale bars = 0.55 mm

Supplementary Figure S2 | Relative FB28 intensity of the *pnr* zone in the abdomen after RNAi down-regulation of chitin-related genes. *Pnr* zone data from Figure 3 are expressed as a percentage of *pnr*—zone from the same figure. Data are represented as scattergrams showing all data points with the mean (red crosses). Different marker shapes/colors represent the different genotypes. Different letters indicate statistically significant differences (one way Krushall-Wallis test followed by a Conover-Iman procedure, p-value < 0.0001). n = 10 in each group.

Supplementary Figure S3 | FB28 intensity in 48h-old wing from *yellow ebony* and *tan* mutant flies. **(A)** Bright field images (upper pannel) and blue filtered images (lower pannel) are shown. Scale bar = 0.3 mm. **(B)** Quantification of FB28 intensity in the wing. *yellow ebony* and *tan* showed a significantly lower FB28 intensity. Please note in *ebony* wings FB28 intensity follow the black melanin patterns. Data are represented as scattergrams showing all data points with the mean (red crosses). Different marker shapes/colors represent the different genotypes. Different letters indicate statistically significant differences (one way Krushall-Wallis test followed by a Conover-Iman procedure, p-value < 0.0001). n = 10 in each group.

REFERENCES

Andersen, S. O. (2010). Insect Cuticular Sclerotization: A Review. *Insect Biochem. Mol. Biol.* 40, 166–178. doi:10.1016/j.ibmb.2009.10.007

Ardell, D. H., and Andersen, S. O. (2001). Tentative Identification of a Resilin Gene in *Drosophila melanogaster*. *Insect Biochem. Mol. Biol.* 31, 965–970. doi:10.1016/S0965-1748(01)00044-3

Baker, J. D., and Truman, J. W. (2002). Mutations in theDrosophilaglycoprotein Hormone Receptor,rickets, Eliminate Neuropeptide-Induced Tanning and Selectively Block a Stereotyped Behavioral Program. *J. Exp. Biol.* 205, 2555–2565. doi:10.1242/jeb.205.17.2555

Behr, M., and Riedel, D. (2020). Glycosylhydrolase Genes Control Respiratory Tubes Sizes and Airway Stability. *Sci. Rep.* 10 (10), 1–14. doi:10.1038/s41598-020-70185-w

Brower, D. L. (1986). Engrailed Gene Expression in Drosophila Imaginal Discs. *EMBO J.* 5, 2649–2656. doi:10.1002/j.1460-2075.1986.tb04547.x

Calleja, M., Herranz, H., Estella, C., Casal, J., Lawrence, P., Simpson, P., et al. (2000). Generation of Medial and Lateral Dorsal Body Domains by the Pannier Gene of Drosophila. *Development* 127, 3971–3980. doi:10.13039/10000805410.1242/dev.127.18.3971

Chaudhari, S. S., Arakane, Y., Specht, C. A., Moussian, B., Boyle, D. L., Park, Y., et al. (2011). Knickkopf Protein Protects and Organizes Chitin in the Newly Synthesized Insect Exoskeleton. *Proc. Natl. Acad. Sci. U.S.A.* 108, 17028–17033. doi:10.1073/PNAS.1112288108/-/DCSUPPLEMENTAL

Chen, L., Yang, W.-J., Cong, L., Xu, K.-K., and Wang, J.-J. (2013). Molecular Cloning, Characterization and mRNA Expression of a Chitin Synthase 2 Gene from the oriental Fruit Fly, Bactrocera Dorsalis (Diptera: Tephritidae). *Ijms* 14, 17055–17072. doi:10.3390/ijms140817055

Darken, M. A. (1962). Absorption and Transport of Fluorescent Brighteners by Microorganisms. *Appl. Microbiol.* 10, 387–393. doi:10.1128/aem.10.5.387-393.196210.1128/am.10.5.387-393.1962

Darken, M. A. (1961). Applications of Fluorescent Brighteners in Biological Techniques. *Science* 133, 1704–1705. doi:10.1126/science.133.3465.1704

Dong, W., Dobler, R., Dowling, D. K., and Moussian, B. (2019). The Cuticle Inward Barrier inDrosophila Melanogasteris Shaped by Mitochondrial and Nuclear Genotypes and a Sex-specific Effect of Diet. *PeerJ* 7, e7802–21. doi:10.7717/peerj.7802

Dong, W., Gao, Y. H., Zhang, X. B., Moussian, B., and Zhang, J. Z. (2020). Chitinase 10 Controls Chitin Amounts and Organization in the wing Cuticle of Drosophila. *Insect Sci.* 27, 1198–1207. doi:10.1111/1744-7917.12774

Farnesi, L. C., Brito, J. M., Linss, J. G., Pelajo-Machado, M., Valle, D., and Rezende, G. L. (2012). Physiological and Morphological Aspects of *Aedes aegypti* Developing Larvae: Effects of the Chitin Synthesis Inhibitor Novaluron. *PLoS One* 7, e30363. doi:10.1371/journal.pone.0030363

Flaven-Pouchon, J., Alvarez, J. V., Rojas, C., and Ewer, J. (2020). The Tanning Hormone, Bursicon, Does Not Act Directly on the Epidermis to Tan the Drosophila Exoskeleton. *BMC Biol.* 18, 17. doi:10.1186/s12915-020-0742-5

Gagou, M. E., Kapsetaki, M., Turberg, A., and Kafetzopoulos, D. (2002). Stage-specific Expression of the Chitin Synthase DmeChSA and DMeChSB Genes

during the Onset of drosophila Metamorphosis. *Insect Biochem. Mol. Biol.* 32, 141–146. doi:10.1016/S0965-1748(01)00101-1

Gonzalez, D., Fraichard, S., Grassein, P., Delarue, P., Senet, P., Nicolaï, A., et al. (2018). Characterization of a Drosophila Glutathione Transferase Involved in Isothiocyanate Detoxification. *Insect Biochem. Mol. Biol.* 95, 33–43. doi:10.1016/J.IBMB.2018.03.004

Gorfinkiel, N., Morata, G., and Guerrero, I. (1997). The Homeobox Gene Distal-Less Induces Ventral Appendage Development in Drosophila. *Genes Dev.* 11, 2259–2271. doi:10.1101/gad.11.17.2259

Graveley, B. R., Brooks, A. N., Carlson, J. W., Duff, M. O., Landolin, J. M., Yang, L., et al. (2011). The Developmental Transcriptome of *Drosophila melanogaster*. *Nature* 471, 473–479. doi:10.1038/NATURE09715

Harrington, B. J., and Hageage, G. J. (2003). Calcofluor White: A Review of its Uses and Applications in Clinical Mycology and Parasitology. *Lab. Med.* 34, 361–367. doi:10.1309/eph2tdt8335gh0r3

Harrington, B. J., and Raper, K. B. (1968). Use of a Fluorescent Brightener to Demonstrate Cellulose in the Cellular Slime Molds. *Appl. Microbiol.* 16, 106–113. doi:10.1128/am.16.1.106-113.1968

Henriques, B. S., Garcia, E. S., Azambuja, P., and Genta, F. A. (2020). Determination of Chitin Content in Insects: An Alternate Method Based on Calcofluor Staining. *Front. Physiol.* 11, 117. doi:10.3389/fphys.2020.00117

Herth, W., and Schnepf, E. (1980). The Fluorochrome, Calcofluor white, Binds Oriented to Structural Polysaccharide Fibrils. *Protoplasma* 105, 129–133. doi:10.1007/BF01279855

Hoch, H. C., Galvani, C. D., Szarowski, D. H., and Turner, J. N. (2005). Two New Fluorescent Dyes Applicable for Visualization of Fungal Cell walls. *Mycologia* 97, 580–588. doi:10.1080/15572536.2006.11832788

Khayrova, A., Lopatin, S., and Varlamov, V. (2021). Obtaining Chitin, Chitosan and Their Melanin Complexes from Insects. *Int. J. Biol. Macromolecules* 167, 1319–1328. doi:10.1016/j.ijbiomac.2020.11.086

Lehmann, P. F., and White, L. O. (1975). Chitin Assay Used to Demonstrate Renal Localization and Cortisone-Enhanced Growth of Aspergillus fumigatus Mycelium in Mice. *Infect. Immun.* 12, 987–992. doi:10.1128/iai.12.5.987-992.1975

Lerch, S., Zuber, R., Gehring, N., Wang, Y., Eckel, B., Klass, K.-D., et al. (2020). Resilin Matrix Distribution, Variability and Function in Drosophila. *BMC Biol.* 18. doi:10.1186/s12915-020-00902-4

Li, K., Zhang, X., Zuo, Y., Liu, W., Zhang, J., and Moussian, B. (2017). Timed Knickkopf Function Is Essential for wing Cuticle Formation in *Drosophila melanogaster*. *Insect Biochem. Mol. Biol.* 89, 1–10. doi:10.1016/j.ibmb.2017.08.003

Ling, F., Dahanukar, A., Weiss, L. A., Kwon, J. Y., and Carlson, J. R. (2014). The Molecular and Cellular Basis of Taste Coding in the Legs of Drosophila. *J. Neurosci.* 34, 7148–7164. doi:10.1523/JNEUROSCI.0649-14.2014

Luo, C.-W., Dewey, E. M., Sudo, S., Ewer, J., Hsu, S. Y., Honegger, H.-W., et al. (2005). Bursicon, the Insect Cuticle-Hardening Hormone, Is a Heterodimeric Cystine Knot Protein that Activates G Protein-Coupled Receptor LGR2. *Proc. Natl. Acad. Sci. U.S.A.* 102, 2820–2825. doi:10.1073/pnas.0409916102

Mokeev, V., Flaven-Pouchon, J., Wang, Y., Gehring, N., and Moussian, B. (2021). Ratio between Lactobacillus Plantarum and Acetobacter Pomorum on the Surface of *Drosophila melanogaster* Adult Flies Depends on Cuticle Melanisation. *BMC Res. Notes* 14. doi:10.1186/S13104-021-05766-7

Moussian, B. (2010). Recent Advances in Understanding Mechanisms of Insect Cuticle Differentiation. *Insect Biochem. Mol. Biol.* 40, 363–375. doi:10.1016/j.ibmb.2010.03.003

Moussian, B., Schwarz, H., Bartoszewski, S., and Nüsslein-Volhard, C. (2005). Involvement of Chitin in Exoskeleton Morphogenesis inDrosophila Melanogaster. *J. Morphol.* 264, 117–130. doi:10.1002/JMOR.10324

Moussian, B., Ta¨ng, E., Tonning, A., Helms, S., Schwarz, H., Nüsslein-Volhard, C., et al. (2006). Drosophila Knickkopf and Retroactive Are Needed for Epithelial Tube Growth and Cuticle Differentiation through Their Specific Requirement for Chitin Filament Organization. *Development* 133, 163–171. doi:10.1242/dev.02177

Muthukrishnan, S., Merzendorfer, H., Arakane, Y., and Kramer, K. J. (2012). "Chitin Metabolism in Insects," in *Insect Molecular Biology and Biochemistry* (Academic Press), 193–235. doi:10.1016/B978-0-12-384747-8.10007-8

Noh, M. Y., Muthukrishnan, S., Kramer, K. J., and Arakane, Y. (2018). A Chitinase with Two Catalytic Domains Is Required for Organization of the Cuticular Extracellular Matrix of a Beetle. *PLOS Genet.* 14, e1007307. doi:10.1371/JOURNAL.PGEN.1007307

Peabody, N. C., Pohl, J. B., Diao, F., Vreede, A. P., Sandstrom, D. J., Wang, H., et al. (2009). Characterization of the Decision Network for wing Expansion in Drosophila Using Targeted Expression of the TRPM8 Channel. *J. Neurosci.* 29, 3343–3353. doi:10.1523/JNEUROSCI.4241-08.2009

Pesch, Y.-Y., Riedel, D., Patil, K. R., Loch, G., and Behr, M. (2016). Chitinases and Imaginal Disc Growth Factors Organize the Extracellular Matrix Formation at Barrier Tissues in Insects. *Sci. Rep.* 6, 18340. doi:10.1038/srep18340

Port, F., Strein, C., Stricker, M., Rauscher, B., Heigwer, F., Zhou, J., et al. (2020). A Large-Scale Resource for Tissue-specific CRISPR Mutagenesis in Drosophila. *Elife* 9. doi:10.7554/eLife.53865

Qin, C. Q., Du, Y. M., and Xiao, L. (2002). Effect of Hydrogen Peroxide Treatment on the Molecular Weight and Structure of Chitosan. *Polym. Degrad. Stab.* 76, 211–218. doi:10.1016/S0141-3910(02)00016-2

Rylee, J. C., Siniard, D. J., Doucette, K., Zentner, G. E., and Zelhof, A. C. (2018). Expanding the Genetic Toolkit of *Tribolium castaneum*. *PLoS One* 13, e0195977. doi:10.1371/JOURNAL.PONE.0195977

Schaefer, J., Kramer, K. J., Garbow, J. R., Jacob, G. S., Stejskal, E. O., Hopkins, T. L., et al. (1987). Aromatic Cross-Links in Insect Cuticle: Detection by Solid-State 13 C and 15 N NMR. *Science* 235, 1200–1204. doi:10.1126/science.3823880

Sobala, L. F., and Adler, P. N. (2016). The Gene Expression Program for the Formation of Wing Cuticle in Drosophila. *Plos Genet.* 12, e1006100. doi:10.1371/journal.pgen.1006100

Spana, E. P., Abrams, A. B., Ellis, K. T., Klein, J. C., Ruderman, B. T., Shi, A. H., et al. (2020). *SPeck*, First Identified in *Drosophila melanogaster* in 1910, Is Encoded by the Arylalkalamine N-Acetyltransferase (AANAT1) Gene. *G3 Genes|Genomes|Genetics* 10 (9), 3387–3398. doi:10.1534/g3.120.401470

Stuben, M., and Linsenmair, K. E. (2009). Advances in Insect Preparation: Bleaching, Clearing and Relaxing Ants (Hymenoptera: Formicidae). *Myrmecological News* 12, 15–21.

Sviben, S., Spaeker, O., Bennet, M., Albéric, M., Dirks, J.-H., Moussian, B., et al. (2020). Epidermal Cell Surface Structure and Chitin-Protein Co-assembly Determine Fiber Architecture in the Locust Cuticle. *ACS Appl. Mater. Inter.* 12, 25581–25590. doi:10.1021/acsami.0c04572

True, J., Yeh, S.-D., Hovemann, B. T., Kemme, T., Meinertzhagen, I. A., Edwards, T. N., et al. (2005). Drosophila Tan Encodes a Novel Hydrolase Required in Pigmentation and Vision. *PLOS Genet.* preprint, e63. doi:10.1371/JOURNAL.PGEN.001006310.1371/journal.pgen.0010063.eor

Tsurkan, M. V., Voronkina, A., Khrunyk, Y., Wysokowski, M., Petrenko, I., and Ehrlich, H. (2021). Progress in Chitin Analytics. *Carbohydr. Polym.* 252, 117204. doi:10.1016/j.carbpol.2020.117204

Vincent, J. F. V., and Wegst, U. G. K. (2004). Design and Mechanical Properties of Insect Cuticle. *Arthropod Struct. Dev.* 33, 187–199. doi:10.1016/j.asd.2004.05.006

Wang, Y., Yu, Z., Zhang, J., Moussian, B., and Moussian, B. (2016). Regionalization of Surface Lipids in Insects. *Proc. R. Soc. B.* 283, 20152994. doi:10.1098/rspb.2015.2994

Wittkopp, P. J., Stewart, E. E., Arnold, L. L., Neidert, A. H., Haerum, B. K., Thompson, E. M., et al. (2009). Intraspecific Polymorphism to Interspecific Divergence: Genetics of Pigmentation in drosophila. *Science* 326, 540–544. doi:10.1126/SCIENCE.1176980/SUPPL_FILE/WITTKOPP.SOM.PDF

Wright, T. R. F. (1987). The Genetics of Biogenic Amine Metabolism, Sclerotization, and Melanization in Drosophila Melanogaster. *Adv. Genet.* 24, 127–222. doi:10.1016/S0065-2660(08)60008-5

Younes, I., Rinaudo, M., Harding, D., and Sashiwa, H. (2015). Chitin and Chitosan Preparation from Marine Sources. Structure, Properties and Applications. *Mar. Drugs* 13, 1133–1174. doi:10.3390/MD13031133

Yu, R. R., Zhang, R., Liu, W. M., Zhao, X. M., Zhu, K. Y., Moussian, B., et al. (2021). The DOMON Domain Protein LmKnk Contributes to Correct Chitin Content, Pore Canal Formation and Lipid Deposition in the Cuticle of *Locusta migratoria* during Moulting. *Insect Mol. Biol.* 31, 127–138. doi:10.1111/IMB.12745

Zhang, M., Ma, P. J., Zhang, T. T., Gao, Z. M., Zhao, P., Liu, X. J., et al. (2021). Roles of LmCDA1 and LmCDA2 in Cuticle Formation in the Foregut and Hindgut of *Locusta migratoria*. *Insect Sci.* 28, 1314–1325. doi:10.1111/1744-7917.12874

Conflict of Interest: The authors declare that the research was conducted in the absence of any commercial or financial relationships that could be construed as a potential conflict of interest.

Publisher's Note: All claims expressed in this article are solely those of the authors and do not necessarily represent those of their affiliated organizations, or those of the publisher, the editors and the reviewers. Any product that may be evaluated in this article, or claim that may be made by its manufacturer, is not guaranteed or endorsed by the publisher.

frontiers | Frontiers in Physiology

METHODS
published: 04 May 2022
doi: 10.3389/fphys.2022.883858

Thorax-Segment- and Leg-Segment-Specific Motor Control for Adaptive Behavior

*Elzbieta Hammel, Charalampos Mantziaris, Joscha Schmitz, Ansgar Büschges† and Matthias Gruhn *†*

Animal Physiology, Biocenter, Mathematisch-Naturwissenschaftliche Fakultät, Universität zu Köln, Cologne, Germany

We have just started to understand the mechanisms underlying flexibility of motor programs among segmental neural networks that control each individual leg during walking in vertebrates and invertebrates. Here, we investigated the mechanisms underlying curve walking in the stick insect *Carausius morosus* during optomotor-induced turning. We wanted to know, whether the previously reported body-side specific changes in a two-front leg turning animal are also observed in the other thoracic leg segments. The motor activity of the three major leg joints showed three types of responses: 1) a context-dependent increase or decrease in motor neuron (MN) activity of the antagonistic MN pools of the thorax-coxa (ThC)-joint during inside and outside turns; 2) an activation of 1 MN pool with simultaneous cessation of the other, independent of the turning direction in the coxa-trochanteral (CTr)-joint; 3) a modification in the activity of both FTi-joint MN pools which depended on the turning direction in one, but not in the other thorax segment. By pharmacological activation of the meso- or metathoracic central pattern generating networks (CPG), we show that turning-related modifications in motor output involve changes to local CPG activity. The rhythmic activity in the MN pools of the ThC and CTr-joints was modified similarly to what was observed under control conditions in saline. Our results indicate that changes in meso- and metathoracic motor activity during curve walking are leg-joint- and thorax-segment-specific, can depend on the turning direction, and are mediated through changes in local CPG activity.

Keywords: motor control, turning, modulation, insect, locomotion, walking, adaptive behavior

OPEN ACCESS

Edited by:
Graziano Fiorito,
Stazione Zoologica Anton Dohrn, Italy

Reviewed by:
Akira Sakurai,
Georgia State University, United States
Bart R. H. Geurten,
University of Göttingen, Germany

****Correspondence:***
Matthias Gruhn
mgruhn@uni-koeln.de

†These authors share senior authorship

Specialty section:
This article was submitted to Invertebrate Physiology, a section of the journal Frontiers in Physiology

Received: *25 February 2022*
Accepted: *20 April 2022*
Published: *04 May 2022*

Citation:
Hammel E, Mantziaris C, Schmitz J, Büschges A and Gruhn M (2022) Thorax-Segment- and Leg-Segment-Specific Motor Control for Adaptive Behavior. Front. Physiol. 13:883858. doi: 10.3389/fphys.2022.883858

INTRODUCTION

Rhythmic locomotor activity in both vertebrates and invertebrates results from interactions between the activity of central pattern generating networks (CPGs) and sensory feedback that tunes the activity to the demands of the environment (Grillner, 2003; Büschges and Gruhn, 2008; Bidaye et al., 2018; Akay, 2020; Akay and Murray, 2021). Particularly insects have been used for long to investigate the neuronal control of coordinated limb movements. This has led to a good understanding of the basic principles underlying simple stepping patterns and straight walking. We know, for example, that the activity of motor neurons during leg stepping is generated by tonic excitation, shaped by inhibition related to CPG activity. Its magnitude and phase are modulated by position and load feedback from the own and from neighboring legs (e.g., Büschges et al., 2004; Ludwar et al., 2005a; Ludwar et al., 2005b; Büschges et al., 2008; Rosenbaum et al., 2010).

In contrast to studies investigating the fundamentals of a basic step, most studies on variations of stepping movements that are required for behavioral flexibility have been limited to observations of limb kinematics. Particularly for turning, kinematics studies have shown, that it comes along with leg-specific changes in the tarsal placement, leg excursion angles and even stepping direction along the two body sides of the animal (Jindrich and Full, 1999; Dürr and Ebeling, 2005; Frantsevich and Cruse, 2005; Mu and Ritzmann, 2005; Gruhn et al., 2009; Bender et al., 2011; Dallmann et al., 2016; Dürr et al., 2018; Deangelis et al., 2019; Pfeffer et al., 2019). Using setups with a slippery walking surface for the stick insect (Gruhn et al., 2006; Gruhn et al., 2009) has helped demonstrating that these turning-related leg-specific kinematics largely result from the motor output to each individual leg, and do not depend on mechanical coupling between the legs or even on the presence of neighboring legs. This implies that the observed leg-specific kinematics must directly emerge from nervous system output.

Only recently, we have learned about certain changes in neural activity, both at the level of the premotor and motor networks, which may be responsible for the observed turning-related changes in kinematics: extracellular recordings and stimulation of the central complex in the cockroach, as well as by the identification of single neurons in *Drosophila* have shown that the seemingly simple behavioral transition from straight walking to turning is initiated by changes in the descending drive from the central complex of the cerebral ganglion (Ridgel et al., 2007; Guo and Ritzmann, 2013; Martin et al., 2015; Bidaye et al., 2020). Work in the cockroach and the stick insect showed that turning also involves the modification of local reflexes in the front (Mu and Ritzmann, 2008) and middle legs (Hellekes et al., 2012). In addition, changes in the local processing of sensory load and movement feedback further downstream in the thoracic ganglia have been reported (Gruhn et al., 2016; Schmitz et al., 2019). Finally, optomotor-induced turning behavior affects local motoneuron activity in a body side-specific fashion, and CPGs of the thoraco-coxal joint appear to be involved in this (Gruhn et al., 2016). Depending on the role of the leg as an inside or outside leg with respect to the turning direction, these modifications of local reflexes or CPG activity can also occur independently from each other, as was recently shown for the middle leg in the turning stick insect (Gruhn et al., 2016; Schmitz et al., 2019). Apart from the findings in the stick insect mesothoracic thorax-coxa-(ThC)-joint (Gruhn et al., 2016), only a few examples for behavior-dependent modification of CPG activity are known from vertebrates such as turtles, where a single network is known to produce various behaviors such as swimming or scratching (Field and Stein, 1997a; Field and Stein, 1997b; Stein, 2018), or to regulate different speeds as found in zebrafish (Ausborn et al., 2012; Ampatzis et al., 2014).

In the stick insect, each joint of a leg is apparently controlled by an individual pattern generating network (Büschges et al., 1995; Bässler and Büschges, 1998; Bidaye et al., 2018; Mantziaris et al., 2020). The central coupling among CPGs is so weak that a so called "fictive coordinated locomotion" of all muscle groups of a leg is not observed in recordings of leg nerve activity in deafferented preparations (Dean, 1989; Büschges et al., 1995; Ludwar et al., 2005a; Borgmann et al., 2009; Mantziaris et al., 2017). The relative independence of pattern generators and the modulation of their activities are a hallmark for the generation of behavioral flexibility with the same network structures, and a differential regulation of the joint motor networks and CPGs is suggested by the above-mentioned turning kinematics data (Dürr and Ebeling 2005; Gruhn et al., 2009; Dürr et al., 2018).

Based on the turning-related changes in the motor activity of the stick insect middle leg ThC-joint and the observed differences in leg-specific kinematics during curve walking, we raise the question whether the side specificity is typical for each leg on one side of the body, and even for each joint of a leg. We also ask, whether these joint-specific changes in motor activity are mediated by CPG activity. To investigate these questions, we systematically recorded the motor neuron (MN) activity related to the three main leg joints of the stick insect meso- and metathoracic legs during inside and outside turning of the front legs in regular saline. We also studied the effect of the optical turning stimuli on contralateral motor activity in ganglia treated with the CPG-activating muscarinic agonist pilocarpine, in order to study whether the different local joint CPGs are involved in changes of joint-specific motor activity.

MATERIALS AND METHODS

All experiments were performed at room temperature (21°C–24°C) on adult female stick insects of the species *C. morosus* (Brunner von Wattenwyl, 1907) that were raised on blackberry leaves *ad libitum* and kept at a 12 h:12 h light dark cycle. The experiments were carried out on an air cushioned table (MICRO-g, TMC, Peabody, MA, United States) surrounded by a darkened Faraday cage.

Preparation and Experimental Design

For all experiments, all legs except for the two front legs were amputated at mid-coxa (Fischer et al., 2001). The animal was fixed ventral side down with dental cement (two-component glue, Protemp II, ESPE, Seefeld, Germany) onto a foam platform, which was thinner than the width of the insect (3 mm × 5 mm × 100 mm, W × H × L) and was mounted on a brass tube. The head and front legs protruded from the front of the stick allowing their free movement. The rod was positioned above a 13.5 cm × 13.5 cm polished acrylic glass plate at a height of about 8–12 mm to ensure resting angles of the front leg FTi-joint of about 110°. The plate was covered with a lubricant composed of 95% glycerin and 5% water to create a slippery surface (Gruhn et al., 2006) which allows unrestricted leg movements of the stationary animal. Turning in different directions was elicited by a progressive striped pattern displayed on two curved LED screens in front of the animal. Stepping either occurred spontaneously or was elicited by briefly touching the abdomen with a paintbrush. Sequences recorded during stimulation were not analyzed. All stepping sequences were filmed from above at 75 frames per second.

EMG electrodes were placed approximately 1–2 mm apart in the proximal half of the *flexor tibiae* muscle of both front legs, by

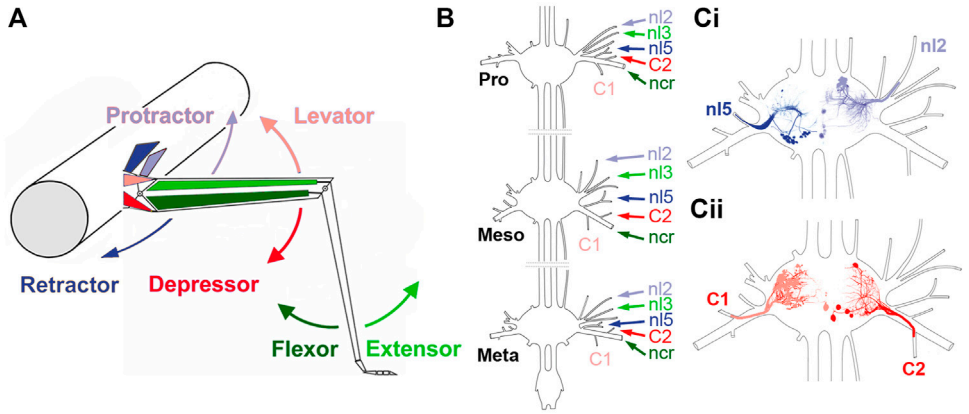

FIGURE 1 | Summary of the stick insect leg segments, with an overview of the thoracic ganglia and relevant nerves. **(A)** Schematic representation of the middle leg and the mesothoracic body-segment, with the location of the muscles responsible for the movement direction that is depicted by the arrows. **(B)** Sketch of the three thoracic ganglia in the stick insect and the location of the relevant leg nerves that are being recorded in this study (Pro: prothorax, Meso: mesothorax; Meta: metathorax). **(Ci,Cii)** Sketches of a mesothoracic ganglion, showing the location of motor neurons of *protractor* (nl2) and *retractor coxae* (nl5) motor neurons **(Ci)**, and *levator* (C1) and *depressor trochanteris* (C2) that project through the respective lateral leg nerves.

punching two small holes into the cuticle using stainless steel minuten pins (0.15 mm), and inserting the cut ends of two twisted copper wires (OD 40 µm). The wires were fixed by applying a small amount of dental cement at the insertion points. The dorsal side of the thorax was opened, the gut was moved aside, and connective tissue was carefully removed to expose the meso- and metathoracic ganglia and the respective leg nerves. The remaining leg stumps were mechanically immobilized with dental cement applied to the coxa. All mesothoracic and metathoracic nerve roots, except for the nerves on which electrodes were placed, were cut prior to the recording to exclude local sensory input (deafferentation), and the body cavity was filled with saline (Weidler and Diecke, 1969).

Pro- and *retractor coxae* MN activity was recorded from nerves nl2 and nl5. *Levator* and *depressor trochanteris* MN activity was recorded from C1 and C2 nerves. The C1 nerve contains the axons of a large number of LevTr MNs (9–11 MNs, 1 CI, and 3 DUM cells; Goldammer et al., 2012). The C2 nerve innervating the *depressor trochanteris muscle* contains only the three large axons of the fast *depressor trochanteris MN* (FDTr, largest amplitude), the slow *depressor trochanteris MN* (SDTr, medium sized amplitude), and the common inhibitor (CI) (Schmitz, 1986). *Extensor tibiae* MN activity was recorded from nerve nl3 (Marquart, 1940; Graham, 1985, **Figure 1**). For recordings of the *flexor tibiae* MN the femur was cut in the proximal third and the stump fixed at an angle of apx. 75° with respect to the body long axis. The *extensor* and *flexor tibiae* muscles control extension and flexion of the leg tibia about the FTi-joint. The ExtTi is innervated by only 3 MNs: the fast *extensor tibiae* (FETi, largest spike amplitude) the slow *extensor tibiae* (SETi, medium spike amplitude), and the CI1 (Godden, 1972; Bässler, 1977; Bässler and Storrer, 1980; Bässler and Wegner, 1983). The flexor, on the other hand, is innervated by small branches of the *ncr*. These branches contain axons of 8–25 MNs, 1–2 DUM cells, and the CI2 and CI3 (Goldammer et al., 2012) which cannot be individually distinguished from each other. The leg was opened dorsally, and the *extensor tibiae* muscle as well as its muscle apodeme were carefully removed to gain access to the *nervus cruris* (*ncr*) and its side branches innervating the flexor.

Split-bath experiments were generally conducted as described in Borgmann et al. (2007), Borgmann et al. (2009) on either the mesothoracic, the metathoracic or both ganglia, being left interconnected in all cases. In brief, the body cavity was fixed with 0.2 mm stainless steel minuten pins, and a 5 mm piece of the cuticle anterior to the attachment points of the retractor muscle, and posterior to the target ganglion was removed, leaving only the anterior and posterior connectives, and the largest tracheae intact. We transiently removed saline from the body cavity, to build a vaseline (white Vaseline, Bad Apotheke, Bad Rothenfelde, Germany) rim separating the meso- and metathoracic body cavities. Care was taken to seal the area around the connectives and tracheae. At the end, the separated areas of the body cavity were refilled with saline and checked for leaks. After control experiments conducted in *Carausius* saline, saline was replaced in the examined ganglion compartment with a 3 mM pilocarpine solution in saline (Büschges et al., 1995).

Electrophysiology

For EMGs of the *flexor tibiae* muscles of front legs, the electrodes were placed as described above. Nerve activity was recorded extracellularly from the nerves specified above using monopolar hook electrodes (modified after Schmitz et al., 1988). The signal was pre-amplified 100-fold (electronics workshop, Zoological Institute, Cologne, Germany), band-pass filtered (100–2,000 Hz), when necessary further amplified 10–1,000-fold, adapted to the signal-to-noise ratio. A reference electrode was placed in the abdomen of the animal. MNs were easily identifiable, as the investigated MNs had axons with the largest diameter in their respective leg nerve and therefore showed the largest amplitudes in the extracellular recordings (identification of MNs based on AP amplitude: Pearson et al.,

1970; nl3: Bässler and Storrer, 1980; further information: nl2, nl5: Graham and Wendler, 1981; all leg nerves: Goldammer et al., 2012, **Figure 1**).

For intracellular recordings, the mesothoracic ganglion was stabilized using cactus spines on a ganglion holder covered with wax. The ganglion sheath was treated with proteolytic enzyme (Pronase E, Merck, Germany) for around 30 s. Intracellular recordings were performed using sharp glass microelectrodes (filled with 3 M KAc/0.1M KCl; R 15–25 MΩ). The electrodes were pulled with the Sutter Microelectrode puller (P-1000, Sutter Instruments, Novato, CA, United States). The intracellular signals were recorded in bridge mode, and amplified with an intracellular amplifier (SEC-10L, npi electronics, Tamm, Germany).

All electrophysiological signals were digitized using the MICRO 1401 II analog-digital converter (CED, Cambridge, United Kingdom) and recorded with the data acquisition and analysis software Spike2 (version 7.01, CED, Cambridge, MA, United Kingdom) on a personal computer running Windows 7 (Microsoft, Corporation, Redmond, WA, United States). To determine the stepping direction of the front legs, video files were synchronized with the respective Spike2 recordings, using a MATLAB (R2011b) script (kindly provided by Dr. Till Bockemühl).

Data Analysis

Spiking activity of phasically active units, and the onset of *flexor tibiae* activity during front leg stepping were marked and saved in separate event channels (minimum interval: 3 ms) for each turning direction. The time series of the units were extracted by defining a threshold crossing through them which excluded common inhibitor (CI) spikes and spikes related to ventilatory activity that was synchronously active in all nerves (Graham and Wendler, 1981). Common inhibitor activity was easily discernible through its presence in multiple nerve recordings. As bursts, we defined bouts of spike activity with simultaneous cessation of activity in the nerve innervating the respective antagonist.

Data were first analyzed with respect to the step cycle of the front leg, which corresponds to the period between adjacent onsets of *flexor tibiae* muscle activity. Phase histograms with a bin size of 30° (i.e., 12 bins) were used to show the distribution of motoneuronal activity in the step cycle in each recording. The bin with the largest number of spike events indicates the phase of the FL step cycle at which motor neurons were maximally active (see Circular Statistics, next paragraph). The same approach was used for comparing activity between motor neuron pools on the inside and outside with respect to the turning direction.

Circular statistics were used to relate the neuronal activity to the step cycle of the ipsilateral front leg. The start of front leg flexor activity was defined by the beginning of the stance phase (ground contact), because of their tight correlation (Gruhn et al., 2006; Rosenbaum et al., 2010). MN activity was often not uniform throughout each step cycle, and polar plots were used to display the angle of maximal neuronal activity (see above). The Hodges-Ajne test was used to detect general deviations from uniformity (MATLAB toolbox). The mean vectors of the maxima, including their lengths, were computed *via* the MATLAB toolbox for circular statistics (Berens, 2009). Data from the intracellular recordings were tested for normal distribution with the Shapiro-Wilk test. Based on the result of the normal distribution test, the data were further analyzed with non-parametric tests at a significance threshold of $p = 0.05$ (Kruskal–Wallis test and the Dunn´s Multiple Comparison Test). For the Cross-correlation analysis the time series of the rectified and smoothed (time constant of 0.07 s) protractor, retractor, levator and depressor MN activity were exported with a sampling rate of 1,000 Hz and the signals were cross-correlated using a custom-written script in Matlab. The time constant used for smoothing ensured a good representation of the signals. An exaggeration of large-amplitude action potentials was not observed. All signals were smoothed 100-fold and their z-score was calculated before cross-correlating the full length of the recording intervals illustrated in each figure. Cross-correlations were calculated using the "xcorr" Matlab function after normalizing each data sequence, so that the autocorrelations at zero time lag are equal with 1, according to the formula:

$$\hat{R}_{xy,coeff}(m) = \frac{1}{\sqrt{\hat{R}_{xx}(0)\hat{R}_{yy}(0)}}\hat{R}_{xy}(m)$$

The correlograms depict the correlation coefficient in the time lag window (−5 s, 5 s) (**Figure 2**). Between stepping sequences, pro- and retractor MNs are tonically active (Büschges and Schmitz, 1991). FL stepping frequency during turning sequences was either compared to pilocarpine-activated burst frequencies of the motor neuron pools residing on the inside and outside relative to the turning direction, or compared to the pilocarpine burst onsets in the meso- or metathoracic nerves under pilocarpine when the animal was quiescent.

The number of animals is represented by "N", and the number of analyzed hemiganglia by "Ń", as in many animal preparations leg nerves of both hemiganglia were recorded simultaneously. Thus, "Ń" corresponds to the actual number of experiments. The letter "n" corresponds to the number of FL steps analyzed in phase histograms.

RESULTS

When intact stick insects walk in a curved path, leg kinematics drastically change (Dürr and Ebeling, 2005; Gruhn et al., 2006; Gruhn et al., 2009). Apart from the drastic changes in protractor and retractor activity, recording EMG activity in the middle leg of the turning animal revealed only minor changes in strength of *flexor tibiae* and *depressor trochanteris* muscle activity, when comparing straight walking to inside or outside steps, respectively (Gruhn et al., 2006; Rosenbaum et al., 2010; Gruhn et al., 2011; Rosenbaum et al., 2015). Therefore, we first asked whether the observed changes in the motor output concern only premotor networks controlling the ThC-joint, or whether similar mechanisms are also active in the premotor networks that control the more distal CTr- and FTi-joints. For this purpose, we used a reduced preparation with all legs removed except the two front legs, that performed curved walking on a slippery surface due to an optomotor stimulation. At the same time, we recorded extracellularly from the deafferented meso- and metathoracic leg nerves nl2 (innervates *protractor coxae, ProCx*),

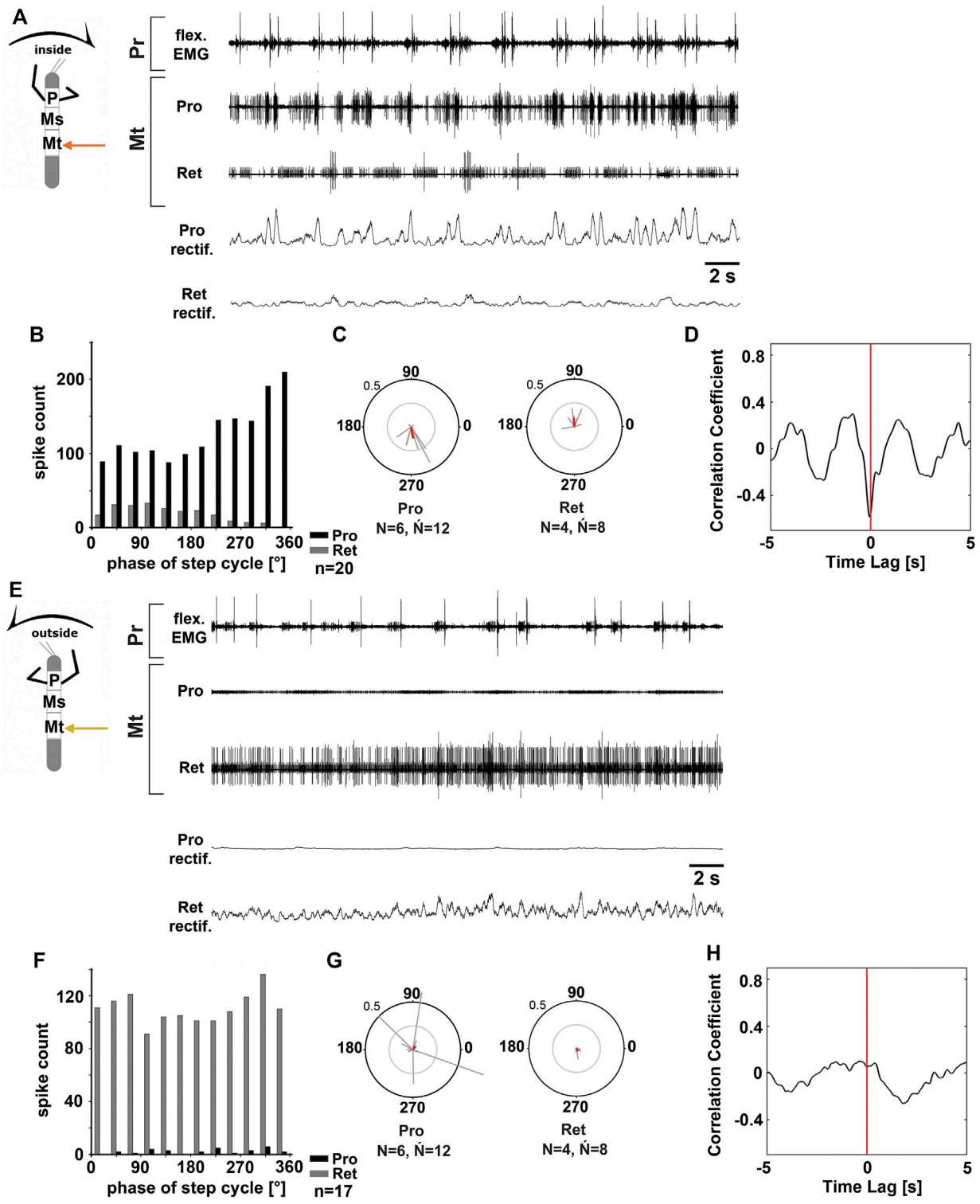

FIGURE 2 | Motor output of the metathoracic *protractor* and *retractor coxae* MN pools in the deafferented ganglion during front leg (FL) inside **(A–D)** and outside **(F,H)** stepping of the same animal. **(A)** FL flexor EMG recording (top), together with extracellular recordings of the ipsilateral protractor (nl2 nerve, second trace) and retractor (nl5 nerve, third trace) nerve during an inside stepping sequence, as well as the rectified protractor and retractor activities (fourth and fifth trace); **(B)** Phase histogram of protractor and retractor nerve activity from the experiment in **(A)** with respect to the FL step cycle; **(C)** Polar plots with the spike event maxima (grey vectors) and their mean (red) for the metathoracic protractor (left) and retractor (right) with respect to the FL step cycle; **(D)** cross-correlation analysis of the protractor and retractor activity. **(E)** FL flexor EMG (top), together with extracellular recordings of the ipsilateral protractor (second trace) and retractor (third trace) nerve during an

(*Continued*)

FIGURE 2 | outside stepping sequence, as well as the rectified protractor and retractor activities (fourth and fifth trace); **(F)** Phase histogram of protractor and retractor nerve activity from the experiment in **(E)** with respect to the FL step cycle; **(G)** Polar plots with the spike event maxima (grey vectors) and their mean (red) leg for the metathoracic protractor (left) and retractor (right) with respect to the FL step cycle; **(H)** cross-correlation analysis of the protractor and retractor activity. *N* = number of animals; *Ń* = number of hemiganglia; *n* = number of analyzed steps. Pr, Mt: Pro- and Metathoracic location of the recording, respectively; Pro, Ret: *protractor coxae* and *retractor coxae* motor neuron activity from nerves nl2 and nl5, respectively. The sketch indicates a stick insect with front legs in a flexed (inside) or stretched (outside) position, and the arrow above indicating the turning direction, the arrow on the side the recorded thoracic segment.

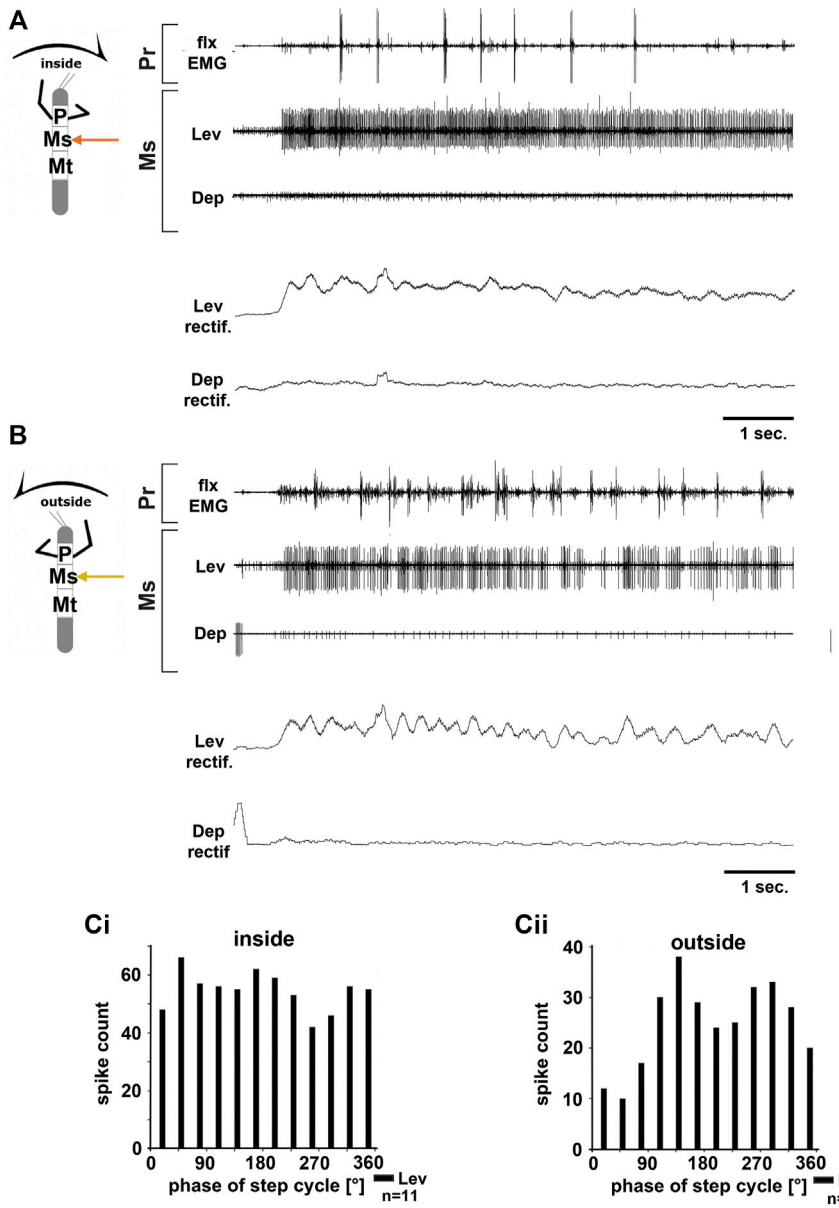

FIGURE 3 | Motor output of the mesothoracic *levator* and *depressor trochanteris* MN pools in the deafferented ganglion during front leg (FL) inside **(A,Ci)** and outside **(B,Cii)** stepping from the same animal. **(A)** FL flexor EMG recording (top), together with extracellular recordings of the ipsilateral levator (C1 nerve, second trace) and depressor (C2 nerve, third trace) nerve during an inside stepping sequence, and the respective rectified activities (fourth and fifth trace); **(B)** FL flexor EMG (top), together with extracellular recordings of the ipsilateral levator (second trace) and depressor (third trace) nerve during an outside stepping sequence, and the respective rectified activities (fourth and fifth trace); **(Ci)** Phase histogram of levator and depressor nerve activity from the experiment in **(A)** with respect to the FL step cycle during inside stepping; **(Cii)** Phase histogram of levator and depressor nerve activity from the experiment in **(B)** with respect to the ipsilateral FL step cycle during outside stepping. *n* = number of analyzed steps. Pr, Ms: Pro- and Mesothoracic location of the recording, respectively; Lev, Dep: *levator trochanteris* and *depressor trochanteris* motor neuron activity from nerves C1 and C2, respectively. The sketch indicates a stick insect with front legs in a flexed (inside) or stretched (outside) position, and the arrow above indicating the turning direction, the arrow on the side the recorded thoracic segment.

nl5 (*retractor coxae, RetCx*), C1 (*levator trochanteris, LevTr*), C2 (*depressor trochanteris, DepTr*), nl3 (*extensor tibiae, ExtTi*) and from branches of nervus cruris (ncr) innervating the *flexor tibiae* (*FlxTi*; for a summary of the leg anatomy and innervating nerves, **Figure 1**), and recorded the activity from above with video to monitor the walking direction. For simplicity reasons, we call the recording site that is on the side of the inside stepping front leg "inside", and that of the outside stepping front leg "outside".

Protractor and Retractor Coxae in the Meso- and Metathorax

Gruhn et al. (2016) previously showed a turning direction-dependent change in the strength of activity of mesothoracic ProCx and RetCx MN pools on the respective inside and outside. In addition, similar to findings by Borgmann et al. (2007) for treadwheel stepping, the mesothoracic inside MN pools showed alternating activity coupled to the FL steps, while no such rhythmicity was present on the outside (Gruhn et al., 2016). Moreover, Borgmann et al. (2007) showed that FL stepping has a weaker influence on the meta- than on the mesothoracic ThC-MN activity. All these findings considered, we therefore tested if there is also a difference in the turning-related motor output between the metathoracic ThC-joints.

Figure 2 shows the typical activity in the metathoracic nl2 (protractor) and nl5 (retractor) nerves during inside (**Figures 2A–D**) and outside steps (**Figures 2E–H**) of the ipsilateral front legs. The results in the metathoracic ThC-MN pools are very similar to those in the mesothorax during the respective behavior of the front legs for both sides.

On the inside, MN activity in metathoracic ProCx MNs was strong, while RetCx MN activity was weak (N = 6, $\acute{N}$ = 12) (**Figure 2A**). ProCx MN activity was coupled to the front leg steps with a mean vector pointing towards 265° (N = 6, $\acute{N}$ = 12; 11 out of 12 experiments, **Figures 2B,C**), while RetCx MN activity showed a preferred coupling to FL stepping in only four out of 12 experiments (average peak at around 90°, **Figure 2C**). On the outside, activity in the metathoracic RetCx MNs increased (**Figure 2E**) and was usually strongly tonic, while activity in the ProCx MNs was strongly decreased compared to the activity in the same nerve when recorded on the inside. In 50% of the experiments, RetCx MN activity showed occasional coupling to the front leg steps, but without a consistent phase relationship (**Figures 2F,G**), and maximal ProCx MN activity never showed a consistent phase relationship to the front leg steps (**Figures 2F,G**). Cross-correlation analysis confirmed the alternation between metathoracic ProCx and RetCx MN activity when recorded on the inside, whereas no such coupling was detected when recorded on the outside (**Figures 2D,H**).

In summary, during front leg turning steps, the metathoracic ProCx and RetCx MNs were activated in a similar manner as the respective mesothoracic MN pools. ProCx MNs were strongly activated and mostly rhythmic on the inside, whereas their activity decreased on the outside. At the same time, RetCx MN activity was strongly increased over ProCx MN activity on the outside, and not systematically coupled to the front leg steps.

Levator and Depressor Trochanteris in the Meso- and Metathorax

The observed changes in the motor output of the left and right side of the body during curve walking, but not between the meso- and metathorax may suggest a similar control mechanism for the ThC joints among thoracic ganglia. However, whether a similar activation pattern also applies to the other leg joint MN pools remained unclear. We therefore investigated the motor output that drives the next more distal leg joint, the coxa-trochanter (CTr)-joint, which allows the leg to be lifted by the *levator trochanteris* muscle during leg swing and be depressed towards the substrate by the *depressor trochanteris* muscle during leg stance. The two muscles are innervated by the meso- and metathoracic leg nerves C1 and C2, respectively.

In all animals, the change in mesothoracic C1 and C2 nerve activity upon font leg stepping was independent of the turning direction. LevTr MN activity on both the inside and the outside increased drastically and persisted throughout the entire walking sequence (N = 4, $\acute{N}$ = 6), whereas any spontaneous SDTr MN activity in C2 seized with the beginning of the walking sequence, and only common inhibitor (CI) activity was observed in these recordings (N = 3, $\acute{N}$ = 6, **Figures 3A,B**). No cross-correlation analysis was performed due to the lack of DepTr MN activity in the mesothoracic C2 nerve during FL turning steps. Occasionally, a modulation in the LevTr MN activity during FL steps is apparent, however, without a preferred phase with respect to the front leg (**Figures 3B,Ci,Cii**).

Unlike in the ThC-joint, no turning-specific difference in MN activity was seen in the CTr-joint. Thus, we wanted to know whether differences in the control of the CTr-joint existed between the meso- and metathorax. Using a similar preparation, we recorded from metathoracic nerves C1 and C2 during front leg curve walking. Again, independent of walking direction, LevTr MN activity was drastically increased, and terminated as soon as front leg stepping ended (N = 6, $\acute{N}$ = 6). **Figures 4A,B** give examples for metathoracic C1 and C2 activity during front leg inside (**Figure 4A**) and outside steps (**Figure 4B**). In contrast to the mesothoracic C2 recording, we observed SDTr MN activity in the metathoracic C2 recording in 50% of the experiments with inside turns (N = 3, $\acute{N}$ = 3) and during 83% of the experiments with outside turns (N = 6, $\acute{N}$ = 5). Still DepTr MN activity was so scarce that no cross-correlation analysis was performed, and. despite occasional modulation of the LevTr MN activity, no phase coupling with respect to the ipsilateral front leg steps (**Figures 4Ci,Cii**) was detected.

In summary, front leg curve stepping sequences, initiate strong meso- and metathoracic LevTr MN activity, independent of the turning direction, and without phase coupling to the ipsilateral front leg step cycle. At the same time, activity of the mesothoracic DepTr MNs ceases or is greatly reduced in the metathorax.

Extensor and Flexor Tibiae in the Meso- and Metathorax

Recording the motor activity of the two proximal leg joints in the inside and outside turning FL preparation revealed fundamental

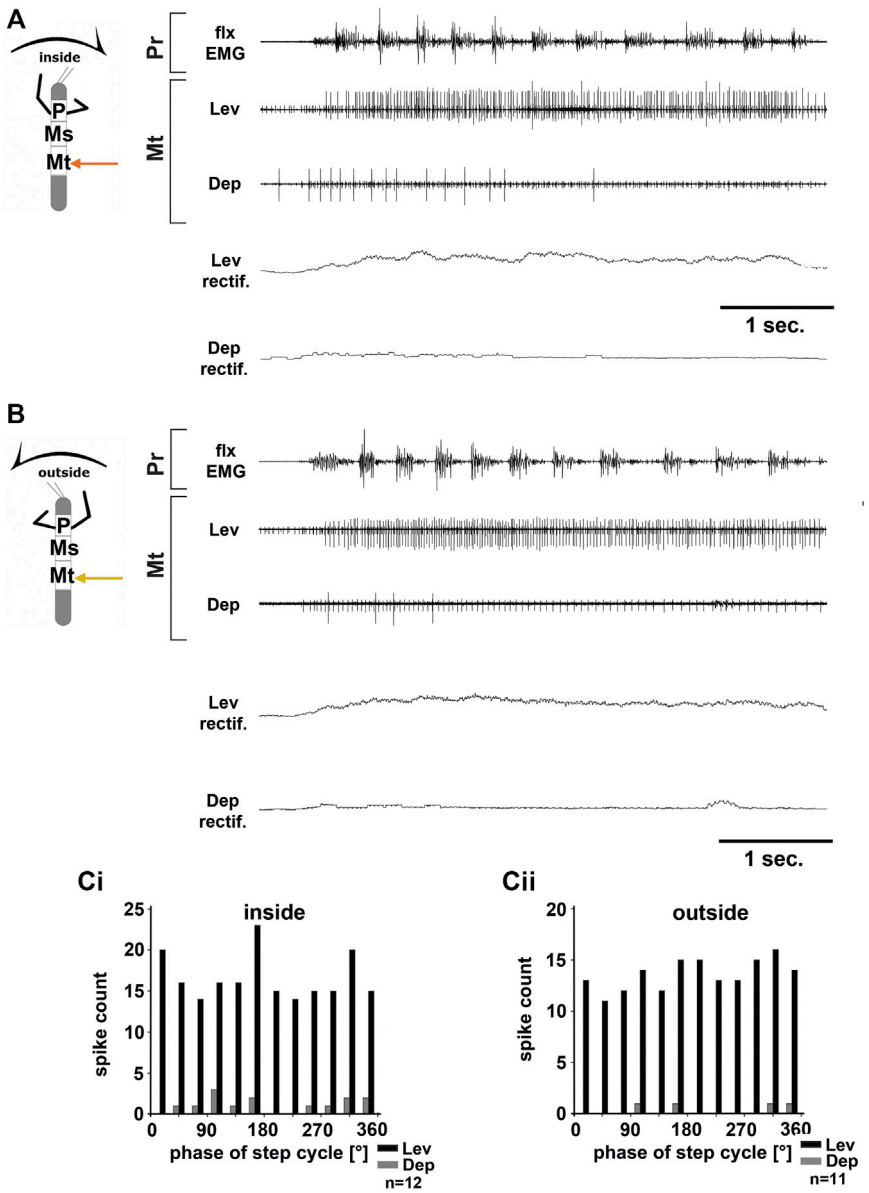

FIGURE 4 | Motor output of the metathoracic *levator* and *depressor trochanteris* MN pools in the deafferented ganglion during front leg (FL) inside **(A,Ci)** and outside **(B,Cii)** stepping from the same animal. **(A)** FL flexor EMG recording (top), together with extracellular recordings of the ipsilateral levator (C1 nerve, second trace) and depressor (C2 nerve, third trace) nerve during an inside stepping sequence, and the respective rectified activities (fourth and fifth trace); **(B)** FL flexor EMG (top), together with extracellular recordings of the ipsilateral levator (second trace) and depressor (third trace) nerve during an outside stepping sequence, and the respective rectified activities (fourth and fifth trace); **(Ci)** Phase histogram of levator and depressor nerve activity from the experiment in **(A)** with respect to the FL step cycle during inside stepping; **(Cii)** Phase histogram of levator and depressor nerve activity from the experiment in **(B)** with respect to the ipsilateral FL step cycle during outside stepping. *n* = number of analyzed steps. Pr, Mt: Pro- and Metathoracic location of the recording, respectively; Lev, Dep: *levator trochanteris* and *depressor trochanteris* motor neuron activity from nerves C1 and C2, respectively. The sketch indicates a stick insect with front legs in a flexed (inside) or stretched (outside) position, and the arrow above indicating the turning direction, the arrow on the side the recorded thoracic segment.

differences in the motor control between the two joints, body sides, and partially even between ganglia. Thus, we next sought to investigate, whether each leg joint is indeed subject to individual control mechanisms, or whether only one of the joints is controlled in a turning specific manner. For this, we recorded the activity of the motor neuron pools that control the FTi-joints of the meso- and metathoracic segments.

We first recorded mesothoracic extensor (nl3) activity during FL turning. Throughout the experiments, no consistent pattern of ExtTi MN activity during either inside or outside front leg steps was discernible. Within the nl3 recordings, SETi and FETi APs were readily distinguishable in all experiments (N = 7, $\acute{N}$ = 10). There was always spontaneous SETi activity, whereas FETi activity appeared only with the begin of a stepping sequence.

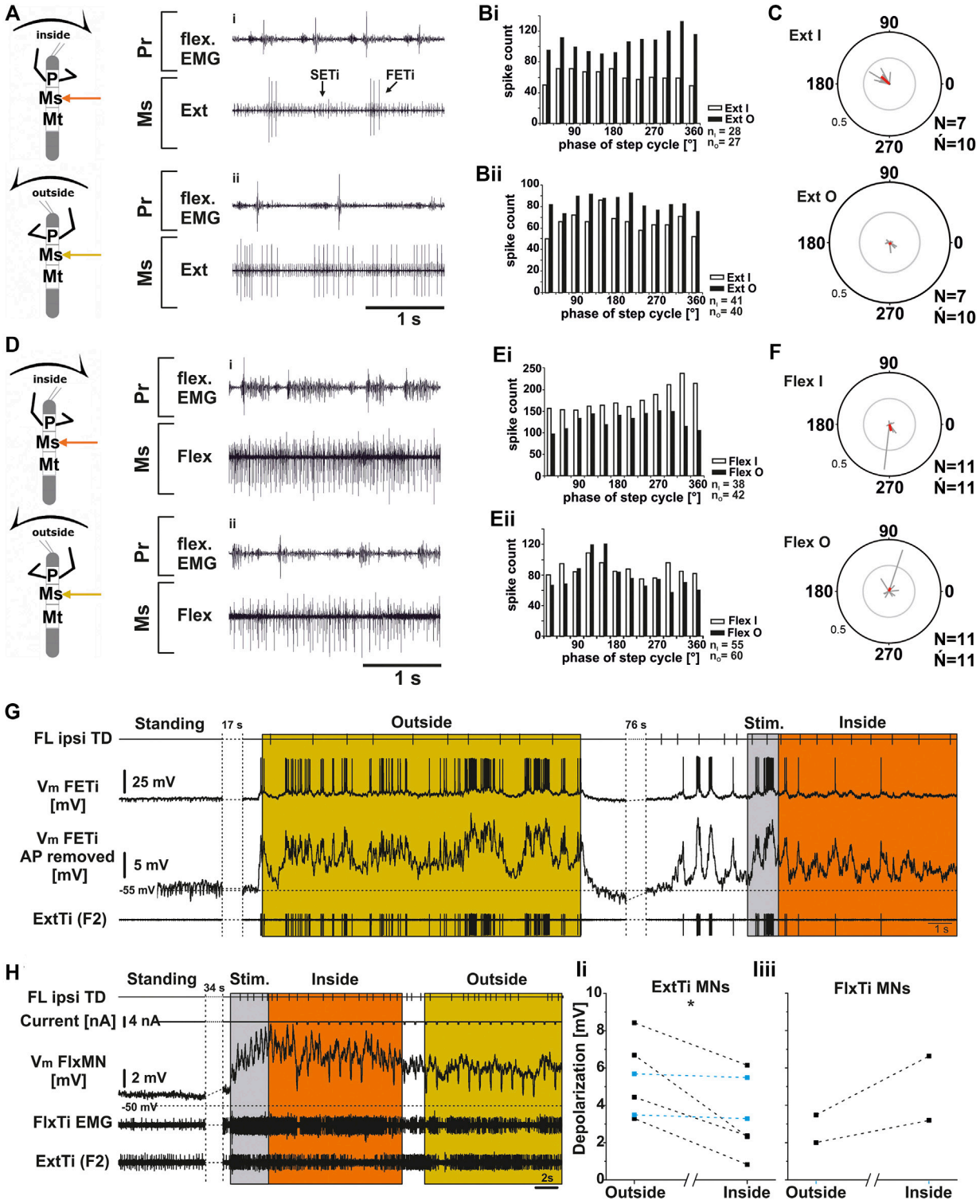

FIGURE 5 | Mesothoracic *extensor* **(A–C)**; **(G,Ii)** and *flexor tibiae* **(D–F; H,Iii)** MN output in the deafferented ganglion during front leg (FL) inside and outside stepping. **(A)** flexor EMG of the front leg (top trace and third trace), together with extracellular recordings of the ipsilateral mesothoracic extensor nerve (nl3) during inside (i) and outside (ii) stepping sequences; **(Bi,Bii)**. Phase histograms of extensor nerve activity from the experiment shown in A **(Bi)**, and an additional experiment to show variability between experiments **(Bii)**, comparing inside and outside activity in the same animal with respect to FL step cycle. **(C)** Polar plots with spike event maxima (grey vectors) and their mean (red) for the extensor with respect to FL step cycle during inside (top) and outside (bottom) stepping; **(D)** flexor EMG recording of the FL (top trace and third trace), together with extracellular recordings of the ipsilateral mesothoracic flexor nerve (ncr) during an exemplary inside (i) and outside (ii) stepping

(*Continued*)

FIGURE 5 | sequence; **(Ei,Eii)**. Phase histograms of flexor nerve activity from walking sequences in **(Di)**, and **(Dii) (Ei)**, and a from second experiment to show the variability, comparing inside and outside activity in the same animal with respect to FL step cycle. **(F)** Polar plots with spike event maxima (grey vectors) and their mean (red) for the flexor with respect FL step cycle during inside (top) and outside (bottom) stepping; **(G–I)**: Tonic depolarization in ExtTi and FlxTi MNs during outside and inside stepping. **(G)** V_m of a fast extensor tibiae MN [FTi, with APs (second trace) and with APs mathematically removed (third trace)] during outside (yellow) and inside (orange) steps of the ipsilateral front leg (FL, top trace). In both situations V_m is depolarized over V_{rest}, but the depolarization during outside leg stepping is increased over that during inside stepping. An extracellular recording of the F2 nerve with the ExtTi MN is shown in the bottom trace, Stim. (grey) marks a phase of brush strokes to the abdomen. **(H)** Flexor tibiae (FlxTi) MN recording (third trace) shows a stronger increase in tonic depolarization during inside (orange) leg stepping over that during outside stepping (yellow, top trace). Second trace shows current injection for input resistance measurements. Fourth trace and bottom trace show FlxTi EMG and extracellular F2 nerve recording. **(I)** Comparison of the amount of tonic depolarization in **(Ii)** ExtTi MNs and **(Iii)** FlxTi MNs between outside and inside stepping; blue lines show experiments with no change; significance value: $p < 0.05$ (*). $\acute{N}$ = number of experiments, (~) approximately equal activity between inside and outside; N = number animals; $\acute{N}$ = number of analyzed hemiganglia; n = number of analyzed steps. Pr, Ms: Pro- and Mesothoracic location of the recording resp.; Flex/FlxTi, Ext/ExtTi: *flexor tibiae* and *extensor tibiae* activity, respectively. FETi: *fast extensor tibiae* motor neuron; V_m: membrane potential. The sketch indicates a stick insect with front legs in a flexed (inside) or stretched (outside) position, and the arrow above indicating the turning direction, the arrow on the side the recorded thoracic segment.

In all experiments outside ExtTi MN activity was greater than that on the inside in most walking sequences (**Figures 5Ai,Bi**). However, in five experiments there were also interspersed walking sequences with similar ExtTi MN activity between both sides (phase plot from another experiment in **Figure 5Bii**). Phase coupling of inside ExtTi MN activity to the front leg steps was observed in seven out of ten experiments (**Figure 5C** "Ext I", mean phase around 140°), whereas outside ExtTi MN activity was phase coupled in only three out of 10 experiments (**Figure 5C**, "Ext O").

Similarly, mesothoracic FlxTi MN activity, as recorded from the *ncr*, showed no consistent activity pattern (N = 11, $\acute{N}$ = 11). FlxTi MN activity was stronger during inside stepping sequences in nine out of 11 experiments. However, two animals showed no difference in activity throughout the experiment, irrespective of the walking direction, and in five of the other nine experiments, walking sequences with similar FlxTi MN activity between inside and outside stepping were equally observed. A representative example of original data is shown in **Figures 5Di,ii, 5Ei** for an experiment with stronger inside than outside activity, and in **Figure 5Eii**, there is an example showing similar FlxTi MN activity irrespective of the turning direction as phase histogram. FlxTi MN activity was never consistently coupled to the front leg step cycles (**Figure 5F**).

From previous work, it is known that motor neuron activity during stepping can be generated by a combination of tonic depolarizing drive as well as phasic excitation from sense organs, and phasic inhibition from the joint CPG (Büschges, 1998; Büschges et al., 2004; Ludwar et al., 2005b; see summary in Büschges and Schmidt, 2015). Currently it is unclear how the observed differences in MN activity during turning are produced. In a first attempt at elucidating the underlying mechanisms, we also recorded intracellularly from extensor and flexor MNs of the mesothoracic FT-joint (**Figures 5G–I**). We evaluated the depolarization of ExtTi and FlxTi MNs during induced turns and compared it to the resting membrane potential (V_m) in the quiescent animal. We compared the V_m from six ExtTi MNs recorded during outside or inside stepping of the front legs in multiple walking sequences from six animals. During curve walking the V_m was always more depolarized compared to the resting animal. However, in four out of six animals and in the pooled data, the change in V_m of the ExtTi MNs from the inactive animal to that during outside stepping was greater than that during inside stepping ($p < 0.05$; **Figures 5G,Ii**). In the other two animals, the depolarization was the same between the two sides. The mesothoracic FlxTi MNs were equally depolarized upon stepping of the front legs as has been described before (Ludwar et al., 2005b; Westmark et al., 2009). However, the change in the V_m of the FlxTi MNs during turning of the front legs differed from the effect on ExtTi MNs, as the depolarization recorded during outside turns was smaller compared to that during inside turns (N = 2). These findings are in line with the changes observed in the extracellular recordings shown above in **Figures 5A,D**.

We also recorded the extracellular activity of ExtTi and FlxTi MNs in the metathoracic segment. Similar to the findings in the mesothoracic segment, we neither detected for the ExtTi, nor the FlxTi MNs a characteristic activity pattern, irrespective of the turning direction (**Supplementary Figure S1**). For the ExtTi MN, we found walking sequences in all experiments, during which the motor neuron activity was similar for both inside and outside MN pools (N = 4, $\acute{N}$ = 6). However, in all animals there were also walking sequences with higher ExtTi MN activity during outside than during inside FL stepping (N = 4, $\acute{N}$ = 5), whereas in two animals, walking sequences with the opposite effect were found (N = 2, $\acute{N}$ = 3). In contrast to the mesothoracic ExtTi MN activity, metathoracic ExtTi MN activity showed no preferred phase coupling to the front leg step cycle (**Supplementary Figures 1A–C**). Similar results were obtained for FlxTi MN activity (**Supplementary Figures 1D–F**). In all eight animals, walking sequences were found, where inside and outside FlxTi MN activity was the same. However, four animals showed walking sequences in which either the activity of the outside or the inside FlxTi MNs was greater during FL turning (N = 4, $\acute{N}$ = 4). Similar to the extensor recordings, no phase coupling of the activity to the front leg step cycle was detected on either side during turning.

In summary, for the mesothoracic ExtTi and FlxTi MNs recorded either on the inside or on the outside, no clear activity patterns were observed. However, outside ExtTi MN activity tends to be stronger compared to inside ExtTi MNs, whereas FlxTi MN activity shows the opposite effect, namely stronger activity on the inside in comparison to the outside. Similar to the protractor coxae MN activity, there is an, albeit weak phase coupling of the mesothoracic ExtTi MN activity to front leg step cycle. The concomitant changes in the V_m could suggest a task-specific change in the excitatory drive to the two antagonistic MN pools of the FTi-joint, which may be at least

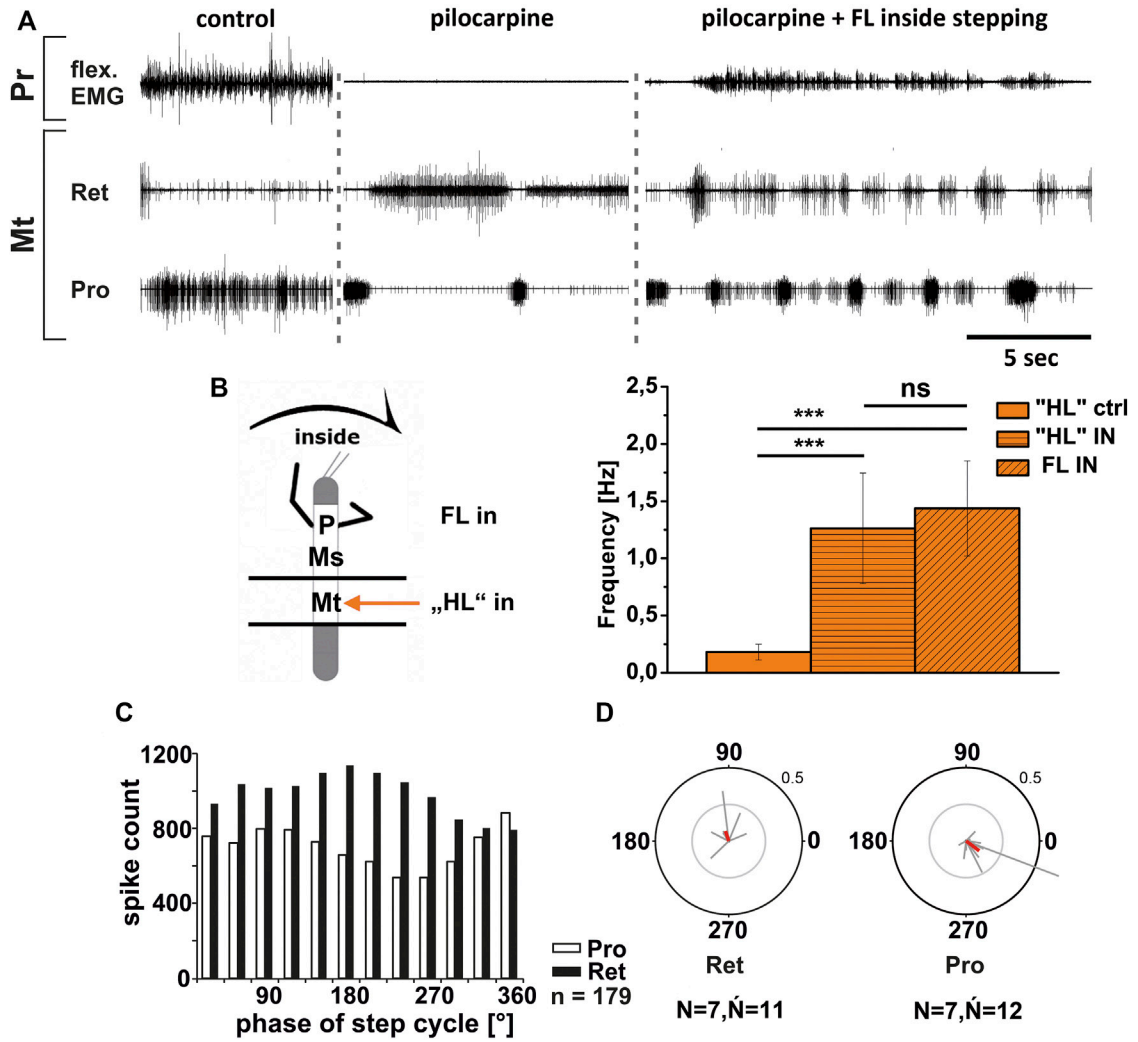

FIGURE 6 | Motor output of *protractor* (Pro) and *retractor* (Ret) *coxae* MN pools in the pilocarpine activated deafferented metathoracic ganglion during front leg (FL) inside stepping; **(A)**. FL Flexor EMG ("flex", top), together with extracellular recordings of the ipsilateral metathoracic retractor (nl5 nerve, second trace) and protractor (nl2 nerve, third trace) nerve during control inside steps, in pilocarpine w/o FL steps, and during inside stepping under pilocarpine application; **(B)**. Schematic of experimental split-bath configuration with comparison of nl2 pilocarpine control Burst frequency ("HL"ctrl) with deafferent HL-segment nl2 burst frequency ("HL"IN) during inside steps of the front legs (FL IN) from 21 walking sequences in 11 experiments (significance level <0.001) **(C)**. Phase histogram of retractor and protractor nerve activity under pilocarpine during inside stepping, with respect to the FL step cycle; **(D)**. Polar plots with the spike event maxima (grey vectors) and their means (red) for the metathoracic retractor (left) and protractor (right) during pilocarpine application with respect to the FL step cycle; *N* = number of animals; *Ń* = number of analyzed hemiganglia; *n* = number of analyzed steps. The sketch indicates a stick insect with front legs in a flexed (inside) or stretched (outside) position, and the arrow above indicating the turning direction, the arrow on the side the recorded thoracic segment. The black bars symbolize the vaseline barrier.

partly responsible for the observed changes in the motor output to this joint during turning. In the metathorax, there was also no specific activity pattern for the metathoracic ExtTi and FlxTi MNs observed irrespective of the FL turning direction. In addition, there was no phasic influence from the front legs.

Involvement of Central Pattern Generators in the Control of Turning-Related Motor Output

Movement of each leg in the stick insect is known to be mediated by separate joint CPGs that control each of the three main leg joints (Büschges et al., 1995). Gruhn et al. (2016) could show that the specific changes in motor output during turning involved changes in CPG activity. Considering the weak coupling among CPGs that control the antagonistic joint MN pools within and between thoracic segments (Büschges et al., 1995; Mantziaris et al., 2017), and since the motor output of the MN pools showed clear joint- and thorax-segment-specific differences during turning, the question arose, whether CPGs are also involved in the observed changes in the other joints. We therefore used the split-bath approach from Borgmann et al. (2007) and Gruhn et al. (2016) in which the muscarinic ACh agonist pilocarpine (3 mM in stick insect saline) was applied selectively to either the meso- or

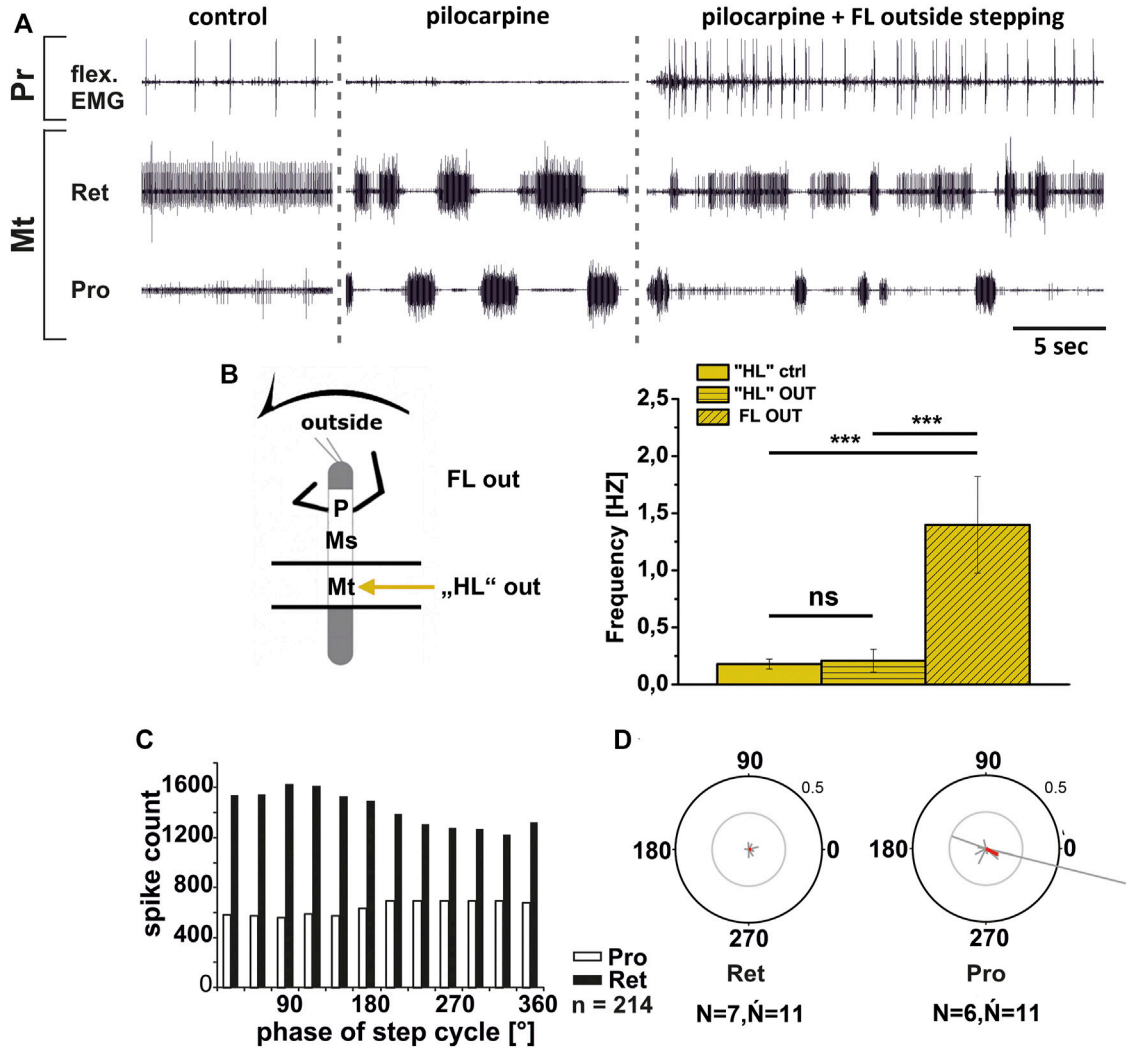

FIGURE 7 | Motor output of *protractor* (Pro) and *retractor* (Ret) *coxae* MN pools in the pilocarpine activated deafferented metathoracic ganglion during front leg (FL) outside stepping; **(A)**. FL Flexor EMG ("flex", top), and extracellular recordings of the ipsilateral metathoracic retractor (second trace) and protractor (third trace) nerve during control outside steps, in pilocarpine w/o FL steps, and during outside stepping under pilocarpine application; **(B)**. Schematic of experimental split-bath configuration with comparison of nl2 pilocarpine control Burst frequency ("HL"ctrl) with deafferent HL-segment nl2 burst frequency ("HL"OUT) during outside steps of the front legs (FL OUT) from 14 walking sequences in 10 experiments (significance level <0.001); **(C)**. Phase histogram of retractor and protractor nerve activity under pilocarpine during outside stepping, with respect to the FL step cycle; **(D)**. Polar plots with the spike event maxima (grey vectors) and their means (red) for the metathoracic retractor (left) and protractor (right) during pilocarpine application with respect to the FL step cycle; *N* = number of animals; *Ń* = number of analyzed hemiganglia; *n* = number of analyzed steps. Pr: Prothoracic/FL segment. The sketch indicates a stick insect with front legs in a flexed (inside) or stretched (outside) position, and the arrow above indicating the turning direction, the arrow on the side the recorded thoracic segment. The black bars symbolize the vaseline barrier.

the metathoracic ganglion, to initiate CPG activity. Subsequently, we elicited FL turning steps to investigate potential effects on the elicited rhythm.

Metathoracic Thorax-Coxa Joint

First, we investigated the effect of FL turning on the pilocarpine-induced rhythmic output of the metathoracic ThC-joint CPG. Gruhn et al. (2016) reported for the respective mesothoracic CPG, that the pilocarpine rhythm on the inside speeds up with the onset of stepping, and that ProCx MN bursts had a similar phase relationship to the front leg steps as in the control without pilocarpine. In contrast, no change in the mean frequency of the pilocarpine rhythm but an increase in the strength of RetCx MN activity were reported.

Similar to these reported findings, metathoracic inside ProCx MN activity increased while RetCx MN activity decreased upon FL turning steps (**Figure 6A**). This was true independent of whether pilocarpine was applied only on the metathoracic ganglion or on the abdominal body cavity as well. Pilocarpine-induced bursting frequency increased from an average of 0.18 Hz (SD 0.07) to 1.26 Hz (SD 0.48), which was not significantly different from the respective FL stepping frequency (1.44 Hz, SD 0.42; **Figure 6B**). Inside ProCx MN activity was significantly coupled to FL steps in eight out of 12 experiments, with a mean

phase of 300°, while inside RetCx MN activity had a preferred phase of 105° (six out of 11 experiments, $N = 7$, $\hat{N}_{Pro} = 12$, $\hat{N}_{Ret} = 11$; **Figures 6C,D**). Outside RetCx MN activity and RetCx MN bursts were stronger and often prolonged during FL turning compared to the pilocarpine rhythm in quiescence, similar to the changes observed in mesothoracic activity (Gruhn et al., 2016) (**Figure 7A**). However, the pilocarpine-induced average bursting frequency of the RetCx MNs in the quiescent animal (0.18 Hz, SD 0.043), and during outside FL steps (0.21 Hz, SD 0.01) did not differ significantly, while both were significantly slower than the stepping frequency of the ipsilateral FL (1.4 Hz, SD 0.42; **Figure 7B**). No systematic phase coupling to the outside FL step cycle for either the ProCx MNs ($N = 6$, $\hat{N} = 11$) or the RetCx MN bursts was found ($N = 7$, $\hat{N} = 11$), where only five out of 11 and three out of 11 experiments, respectively, showed significant coupling (**Figures 7C,D**).

In summary, the pharmacologically activated metathoracic ProCx and RetCx MN activity was clearly modified in both turning directions. Inside ProCx MN activity, and outside RetCx MN activity are stronger compared to the control bursts in the quiescent animal. In addition, on the inside and not on the outside, the pilocarpine rhythm shows significant increase in bursting frequency and phase coupling to the ipsilateral FL in most experiments. This effect is in line with the results in the mesothoracic ganglion, and indicates a change of local CPG activity in parallel with the turning direction of the front legs.

Mesothoracic and Metathoracic Coxa-Trochanter Joint

In contrast to the ThC-joint, no side-specific change in MN activity was detected in recordings of CTr-joint LevTr and DepTr MN pools during either inside or outside turning of the ipsilateral front legs in both the meso- and the metathoracic ganglion. However, given the weak coupling between joint CPGs, we asked, whether also this lack of side-specific activity is mediated through changes in CPG activity. After establishment of a pilocarpine-induced rhythmic alternation between mesothoracic LevTr and DepTr MN activity, front leg curve walking was induced. The results are summarized in **Figures 8**, **9** for inside and outside stepping, respectively. With the beginning of FL stepping and independent of the turning direction, LevTr MN bursts were prolonged and DepTr MN activity ceased entirely throughout the walking sequence in all experiments ($N = 5$, $\hat{N} = 14$). Walking sequences with single APs in the C2 recording were observed in four experiments, and only rarely, occasional DepTr MN bursts during single walking sequences were observed ($N = 2$, $\hat{N} = 3$, **Figures 8Aii**,Cii, **9Aii**,Cii). Accordingly, no systematic coupling of either the inside or the outside LevTr and DepTr MN activity with respect to the ipsilateral FL step cycle was observed (**Figures 8C**, **9C**). Despite the clear increase in LevTr MN, and decrease in DepTr MN activity, the pilocarpine-induced bursting frequency of 0.24 Hz (SD 0.05) during inside stepping sequences was on average unchanged compared to the control bursts with 0.29 Hz (SD 0.09). However, this was significantly different from the respective FL stepping frequency (2.2 Hz, SD 0.74; **Figure 8D**). A similar response was found in the outside turning animals, where the average control burst frequency (0.31 Hz, SD 0.09) was not significantly different from the bursting frequency of 0.18 Hz (SD 0.1) during FL turning even though the rhythm sometimes appeared to be locked in levator phase. Both bursting frequencies were significantly lower than the FL stepping frequency of 1.96 Hz (SD 0.47; **Figure 9D**).

Although DepTr MNs in the mesothorax hardly ever showed activity during control conditions, we observed occasional slow DepTr MN activity in the metathorax in about 50% of the experiments. We wanted to know whether this difference was also reflected in the changes in activity under pilocarpine influence. We therefore recorded the activity of the same 2 MN pools in the metathoracic ganglion after pilocarpine application and during FL curve stepping. The results are summarized in **Figure 10**. As in the mesothorax, in all experiments LevTr MN activity was stronger ($N = 4$, $\hat{N} = 7$), and DepTr MN activity weaker ($N = 3$, $\hat{N} = 6$) during turning sequences of the ipsilateral front legs, independent of the direction (**Figures 10A,B**). In all animals, sequences were observed, where DepTr MN activity was absent throughout front leg stepping. However, in five out of six experiments in which C2 activity was recorded, there were FL stepping sequences, during which intermittent bursts of DepTr MNs occurred ($N = 3$, $\hat{N} = 5$). Again, no systematic coupling of either LevTr MN or DepTr MN activity with respect to the ipsilateral FL step cycle was observed, irrespective of the turning direction (**Figures 10C,D**). Similar to what was observed in the mesothorax, the respective control burst frequencies of 0.23 Hz (inside, SD 0.09), and 0.3 Hz (outside, SD 0.11) did not significantly differ from the frequencies of 0.19 Hz (inside, SD 0.15) and 0.24 Hz (outside, SD 0.12), while the FL stepping frequency was always significantly higher (inside: 2.16 Hz, SD 0.32; outside: 1.87 Hz, SD 0.08; **Figures 10E,F**) compared to the frequency of the MN rhythm.

In summary, coxa-trochanteral MN pools of the pilocarpine-activated meso- and metathorax showed a similar activation pattern as during control conditions without pilocarpine. This change of the regular, alternating pilocarpine rhythm to a clear increase in LevTr MN activation suggests that also at the level of this joint, CPGs are involved in the changes of the motor output in response to FL turning behavior. The occurrence of occasional DepTr MN bursts in the metathoracic C2 recording during stepping sequences suggests that the metathoracic CPG may be more weakly affected by FL turning than the mesothoracic CPG.

DISCUSSION

For turns, insects produce leg-specific changes in kinematics that differ from those observed in a regular straight walking pattern (Strauss and Heisenberg, 1990; Jindrich and Full, 1999; Mu and Ritzmann, 2005; Dürr and Ebeling, 2005; Gruhn et al., 2009; Cruse et al., 2009; Gruhn et al., 2011). Front and middle legs on the inside of the turn typically pull the body into the turning direction, while the outside front, middle and hind legs push the

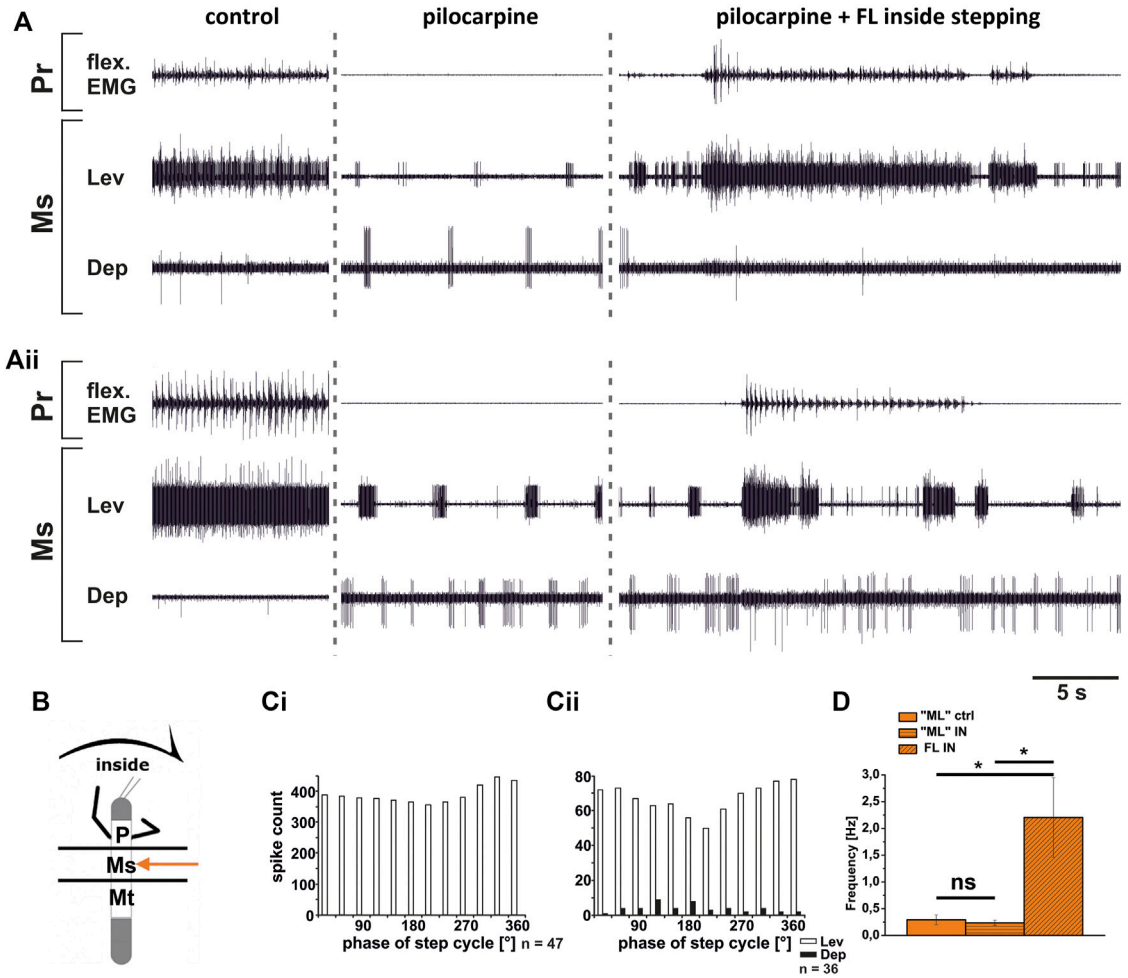

FIGURE 8 | Motor output of *levator* (Lev) and *depressor* (Dep) *trochanteris* MN pools in the pilocarpine activated deafferented mesothoracic ganglion (Ms) during front leg (FL) inside stepping; **(Ai,Aii)** two examples for FL Flexor EMG ("flex", top), together with extracellular recordings of the ipsilateral mesothoracic levator (C1 nerve, second trace) and depressor (C2 nerve, third trace) nerve during control inside steps, in pilocarpine w/o FL steps, and during inside stepping under pilocarpine application; **(B)**. Schematic of experimental split-bath configuration; **(Ci,Cii)** Phase histograms of levator and depressor nerve activity under pilocarpine during inside stepping from the animals in **(Ai,Aii)**, with respect to the FL step cycle; **(D)**. Comparison of pilocarpine C1 control Burst frequency ("ML"ctrl) with deafferent ML-segment C1 burst frequency ("ML"IN) during inside steps of the front legs (FL IN) from 18 walking sequences in three experiments (significance level <0.05); *n* = number of analyzed steps. Pr: prothoracic/FL segment. ns: not significant. The sketch indicates a stick insect with front legs in a flexed (inside) or stretched (outside) position, and the arrow above indicating the turning direction, the arrow on the side the recorded thoracic segment. The black bars symbolize the vaseline barrier.

body around the curved path, and the inside hind legs often act as a pivot. Given the fact that limb movements are generally controlled by a large number of different muscles which often act synergistically (Santuz et al., 2019; Akay and Murray 2021), the conclusions drawn from kinematic analysis are limited. However, it seems clear that they are the result from an interplay of centrally generated output with local and intersegmental sensory feedback (Ritzmann and Zill 2017; Bidaye et al., 2018; Mantziaris et al., 2020; Akay and Murray, 2021). Understanding the contribution of each of these components, not only requires to know the anatomical connectivity, but also to understand the contribution of the single components in a reduced but still behaving preparation. For this purpose, larger insects such as the stick insect offer an ideal choice to elucidate the neuronal mechanisms for walking pattern generation and sensorimotor integration. For stick insect turning, known neuronal mechanisms underlying the observed motor flexibility include local, body-side specific changes in processing of sensory feedback and body-side dependent changes in motor output that involve influences on CPG activity of the most proximal ThC leg joint (Gruhn et al., 2016; Schmitz et al., 2019). However, it was unclear, whether the observed changes in the motor output during curve walking of the front legs concern only premotor networks controlling the ThC-joint, or also those of the more distal CTr- and FTi-joints, including the involvement of CPG activity. Our results are summarized in **Figure 11**.

We found that major differences exist in the turning-related motor output for the MN pools that control the movement of all three main leg joints. The metathoracic ThC-joint shows the

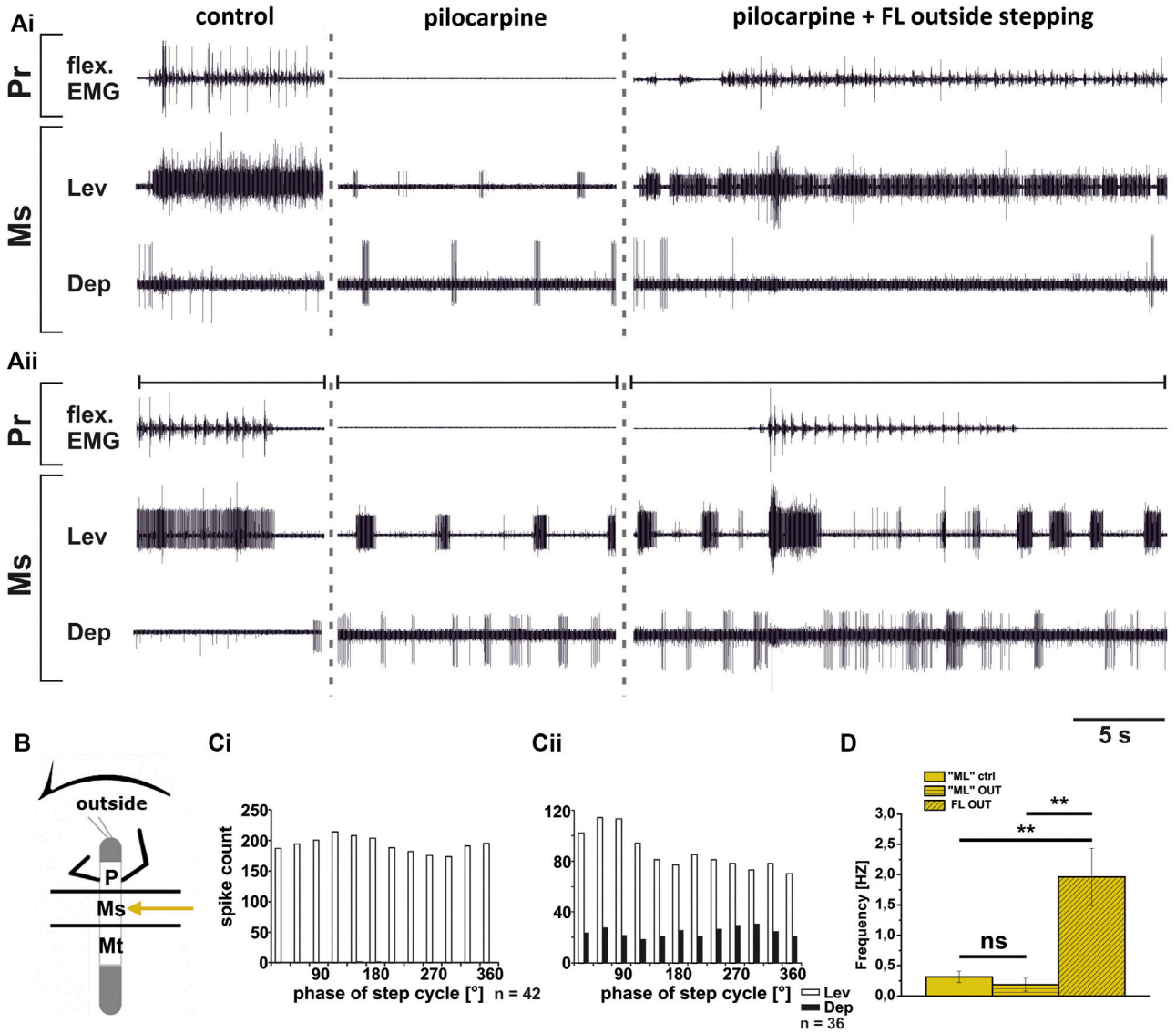

FIGURE 9 | Motor output of *levator* (Lev) and depressor (Dep) *trochanteris* MN pools in the pilocarpine activated deafferented mesothoracic ganglion (Ms) during front leg (FL) outside stepping; **(Ai,Aii)** two examples for FL Flexor EMG ("flex", top), together with extracellular recordings of the ipsilateral mesothoracic levator (C1 nerve, second trace) and depressor (C2 nerve, third trace) nerve during control outside steps, in pilocarpine w/o FL steps, and during outside stepping under pilocarpine application; **(B)**. Schematic of experimental split-bath configuration; **(Ci,Cii)**. Phase histograms of levator and depressor nerve activity under pilocarpine during outside stepping from the animals in **(Ai,Aii)**, with respect to the FL step cycle; **(D)**. Comparison of pilocarpine C1 control Burst frequency ("ML"ctrl) with deafferent ML-segment C1 burst frequency ("ML"OUT) during inside steps of the front legs (FL OUT) from 25 walking sequences in five experiments (significance level <0.01); *n* = number of analyzed steps. Pr: prothoracic/FL segment. ns: not significant. The sketch indicates a stick insect with front legs in a flexed (inside) or stretched (outside) position, and the arrow above indicating the turning direction, the arrow on the side the recorded thoracic segment. The black bars symbolize the vaseline barrier.

same pronounced body side-specific differences during inside and outside steps of the front leg that have been described for the mesothorax (Gruhn et al., 2016): the ProCx MNs in both thoracic segments are strongly activated on the inside and only weakly on the outside, whereas the opposite was observed in the RetCx MNs. At the same time the activity on the inside of the turn is rhythmic and phase-coupled to the FL steps, whereas the activity on the outside is tonic and not phase-coupled. Finally, during inside and outside turning, the changes in MN activity are mediated through influences on CPG activity as shown in our experiments with pharmacological activation of the CPG networks.

In contrast, CTr-joint MNs show no turning-related differences in activity. Independent of the turning direction, the LevTr MN activity is strongly increased, whereas DepTr MN activity ceases. This effect is equally mediated through changes in CPG activity, as the pharmacologically activated pilocarpine rhythm shows an increase of the LevTr MN activity during inside and outside turns, similar to the result without pilocarpine, and sometimes the rhythm even appeared

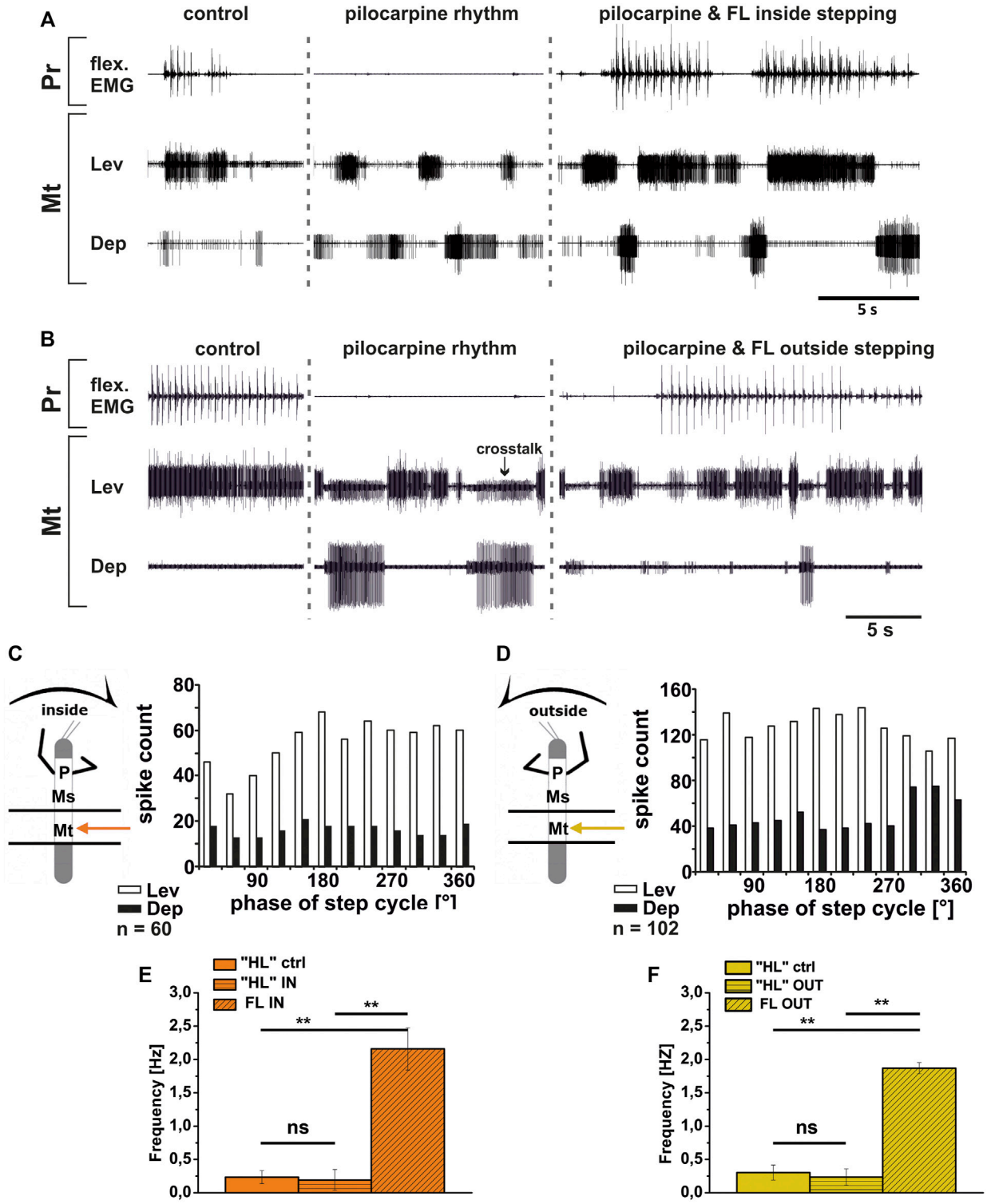

FIGURE 10 | Motor output of *levator* (Lev) and *depressor* (Dep) *coxae* MN pools in the pilocarpine activated deafferented metathoracic ganglion (Mt) during front leg (FL) inside **(A,C)** and outside **(B,D)** stepping; **(A,B)**. FL Flexor EMG ("flex", top), together with extracellular recordings of the ipsilateral metathoracic levator (C1 nerve, second trace) and depressor (C2 nerve, third trace) nerve during control inside **(A)** or outside **(B)** steps, in pilocarpine w/o FL steps, and during inside and outside stepping under pilocarpine application, respectively; **(C,D)**. Phase histograms of levator and depressor nerve activity under pilocarpine during inside **(C)** and outside **(D)** stepping, with respect to the FL step cycle; **(E,F)**. Comparison of pilocarpine C1 control Burst frequency ("HL"ctrl) with deafferent HL-segment C1 burst frequency ("HL"IN/OUT) during inside/outside steps of the front legs (FL IN/OUT) from 14 inside, and 7 outside walking sequences in 4, respectively Three experiments (significance level <0.01); *n* = number of analyzed steps. ns: not significant; Pr: prothoracic segment. The sketch indicates a stick insect with front legs in a flexed (inside) or stretched (outside) position, and the arrow above indicating the turning direction, the arrow on the side the recorded thoracic segment. The black bars symbolize the vaseline barrier.

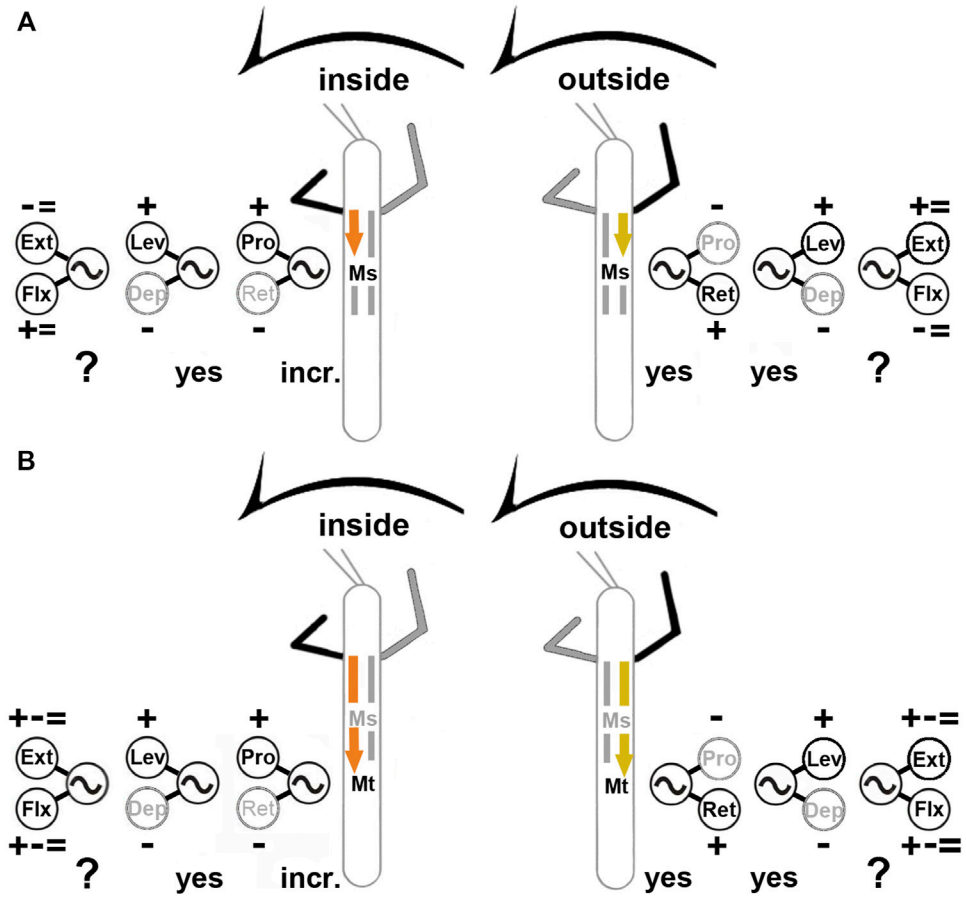

FIGURE 11 | Summary of observed influences on the meso- **(A)** and metathoracic **(B)** MN pools during inside (left) and outside (right) turning of the front legs. "+": increase in MN activity, "–": decrease in MN activity, " = ": no change in MN activity found; "incr.": increase in CPG frequency; "yes"**:** CPG affected; "?": effect on CPG not tested. Ext: extensor tibiae; Flx: flexor tibiae; Lev: levator trochanteris; Dep: depressor trochanteris; Pro: protractor coxae; Ret: retractor coxae. Ms, Mt: meso- and metathoracic segment, respectively. The sketch indicates a stick insect with front legs in a flexed (inside) or stretched (outside) position, and the arrow above indicating the turning direction, the arrow on the side the recorded thoracic segment. Note that "+ – = " above the extensor and below the flexor MN pools denotes that there were examples of increased, decreased and unchanged MN activity.

locked in levator phase. The strength of this effect on the activity of the CTr-joint MNs appears to weaken from meso- to metathorax.

MNs of the FTi-joint show both, side-specific differences and thorax segment-specific differences in activation, however to a much lesser extent. In contrast to the two more proximal joints, FTi-joint MN activity is highly variable and does not show systematic task-specific changes. Whereas on the outside of the mesothorax, ExtTi MN activity increases compared to FlxTi MN activity, the opposite occurs on the inside. In 50% of the experiments, however, walking sequences with equal activity between contralateral sides were found for both MN pools. In the metathorax, the activity of the ExtTi and FlxTi MN pools increased or decreased in both turning situations, and contralateral sides showed often similar activity in response to FL turning (**Figure 11**). Overall, we thus present two major findings: 1) the turning-related motor output differs strongly among the three major leg joints and also between the ipsilateral meso- and metathoracic hemisegments; 2) the turning-related effect to the thoracic CPGs decreases from the meso- to the metathorax.

Motor Control Mechanisms During Turning

Our results highlight the independent control of the different leg joints and thoracic segments in the stick insect (Büschges et al., 1995; Akay et al., 2001; Fischer et al., 2001; Bucher et al., 2003; Borgmann et al., 2012; Büschges and Borgmann, 2013), and show that this relative independence persists during turning, if not even being strengthened. Particularly pronounced changes during turning of the stick insect occur in the leg kinematics at the level of the ThC-joint in *protractor* (ProCx) and *retractor coxae* (RetCx) muscle activation during different walking conditions (Dürr and Ebeling, 2005; Cruse et al., 2009; Rosenbaum et al., 2010; Gruhn et al., 2011). The inside hind leg has been shown to produce on average smaller front to back excursions than the ipsilateral middle leg, and it may act like a pivot, around which the animal turns, when the curve is tight. The outside hind leg moves with a strong front to back excursion, similar to the

mesothoracic outside leg (Dürr and Ebeling, 2005; Cruse et al., 2009; Gruhn et al., 2009), which is in line with a variety of other walking insect and crustacean species (e.g., Frantsevitch and Mokrushov, 1980; Strauss and Heisenberg, 1990; Cruse and Saavedra, 1996; Frantsevich and Cruse, 2005; Mu and Ritzmann, 2005).

Under experimental conditions, when a front leg is stepping straight on a treadmill, ipsilateral metathoracic ThC-motor neurons have been reported to become mostly tonically active, and ProCx MNs receive phasic modulatory input in the meso- and to a lesser extent in the metathorax from the stepping front leg (Borgmann et al., 2007). Outside activity is never phase-coupled to the front leg, neither in the meso- nor in the metathoracic ThC-joint. Finally, during inside steps of the front leg, both, meso- and metathoracic ThC-neurons receive phasic signals from the front leg and/or the premotor networks governing FL MNs (Gruhn et al., 2016). Together with our findings, this implies that there is a gradient of descending influence that creates the characteristic motor output from outside to straight, and finally to inside steps. The tonic activity in the metathorax during front leg outside and straight stepping points to the potential importance of local sensory feedback during these two situations, and suggests that the influence from the stepping front leg onto the metathoracic ProCx and RetCx MNs might be weaker than in the mesothorax (Borgmann et al., 2007). When, however, the middle leg is present (but not stepping), rhythmic activation of ProCx and RetCx MN activity through FL stepping can be observed (Borgmann et al., 2009). This will be discussed further below. All in all, however, the similarity in the activity between the two posterior thoracic segments suggests a very similar central control mechanism for this joint.

In the CTr-joint, we observed a lack of the occurrence of turning-direction specific motor patterns. This may be related to the fact that each leg, independent of the direction the animal turns into and even irrespective of any condition the stick insect may encounter, needs to be off the ground during swing and on the ground during stance. The tonic activity of the LevTr MNs and the lack of activity in the DepTr MNs, resembles the situation in the deafferented outside turning ThC-joint MNs, with strong tonic RetCx MN activity and weak to absent ProCx MN activity. Interestingly, in the CTr-joint the swing MNs are tonically active, whereas in the ThC-joint stance MNs are, A strong tonic activation of middle leg levator, and a suppression of its antagonist the depressor has also been reported for the straight stepping single FL preparation (Borgmann et al., 2012). This motor output changed as soon as the middle leg campaniform sensilla (CS) were stimulated. The load stimulus terminated LevTr and initiated DepTr MN activity. This suggests that local load feedback may be crucial for the switch between the antagonists in the CTr-joint irrespective of leg function. Based on the strong effect of load stimuli, and the lack of patterning influence from the front leg, Borgmann et al. (2012) suggested a hierarchy in the strength of inter-leg influence onto the local pattern generating networks which decreases from proximal to distal joints. Our results provide further evidence for this hypothesis, and go beyond, by suggesting that such a gradient may also exist from rostral to caudal between the meso- and metathoracic segments, as we could show that the observed suppression of depressor activity was reduced in the metathoracic CTr-joint. Borgmann et al. (2012) and our results differ from a study by Ludwar et al. (2005a), who reported that front leg stepping activated DepTr MN activity in the deafferented mesothorax which was also phase-coupled to the front leg in six out of nine experiments. Currently, we have no explanation for this discrepancy. The only difference between the approach in Ludwar et al. (2005a) and that in Borgmann et al. (2012) was that in the latter study, the mesothoracic ganglion was not deafferented, while the only difference between Ludwar et al. (2005a) and our study was that walking in our approach happened with reduced sensory input from the front leg due to the use of a slippery surface. Thus, it could be that load information from the front leg plays a different role as soon as local sensory feedback is missing.

The lack of a clear, turning-related motor output of the FTi-joint MNs to the flexor and extensor tibiae muscles further supports the idea of a weaker central drive to the more distal joints and even more so in the more caudal metathoracic segment. Similar to our results, Hellekes et al. (2012) reported a strong, turning-related mesothoracic ExtTi MN output during outside, and strong mesothoracic FlxTi MN output during inside turns of the front legs, when other legs were also still attached. This is likely due to central drive, which is also confirmed by the results of our intracellular recordings where 66% of the ExtTi MNs were more strongly depolarized during outside vs. inside turns. No comparable data exist for the metathoracic MN pools, but it is plausible that intracellular data from the metathoracic FTi-joint MN pools would show more variability in this segment.

Involvement of Central Pattern Generating Networks in the Expression of Turning-Related Motor Output

The finding that changes in motor output of the deafferented meso- and metathoracic ganglia during FL turning were leg-segment, and partly thorax-segment-specific raised the possibility that not all changes in the meso- and metathorax were mediated through modification of local CPG activity as is the case for the mesothoracic ThC-joint (Gruhn et al., 2016). In arthropods, the muscarinic agonist pilocarpine has long been used to induce fictive locomotion (crayfish: Chrachri and Clarac, 1990; locust: Ryckebusch and Laurent, 1993; hawkmoth: Johnston and Levine, 2002; cockroach: Fuchs et al., 2011) or to elicit rhythmic motoneuronal patterns in individual MN pools (stick insect: Büschges et al., 1995), and demonstrated that each of the three major stick insect leg joints in each leg is controlled by an individual CPG (Büschges et al., 1995). Therefore, we hypothesized that if pilocarpine-elicited CPG activity were altered during front leg curve stepping, it could be concluded that CPGs are involved in the turning related changes in motor output.

The changes in the pilocarpine-induced rhythm of the metathoracic ThC-joint CPG during turning, were body-side specific, similar to the changes during control conditions, and

similar to the changes reported for the mesothoracic ProCx- and RetCx MN pools by Gruhn et al. (2016). During inside steps the rhythm was phase-coupled to the front leg step cycle, albeit to a lesser extent than in the mesothorax. On the outside, RetCx MN bursts were lengthened, and not systematically coupled to the FL steps. DepTr MN bursts were always strongly suppressed, and LevTr MN bursts lengthened during stepping sequences independent of the walking direction. In the metathorax, occasional alternation of levator and depressor bursts occurred during walking sequences. The high variability in the MN pools of the FTi-joint during front leg turning under control conditions, even within a single animal, and thus the lack of a good reference, prevented us to study potential changes in the activity of the FTi-joint CPG.

Borgmann et al. (2009) reported that pilocarpine-elicited activity of the ThC-joint MNs was similar in the meso- and metathorax, with strong entrainment of the patterned CPG activity by the stepping of a single front leg on a tread wheel with a phase preference between 300° and 330°. This effect of FL straight stepping onto the metathoracic ipsilateral thoracic ThC-joint CPGs resembles the effect we observed during inside stepping. Thus, during inside stepping the decreasing gradient in activation strength postulated for the meso- and metathoracic ThC-joint by Borgmann et al. (2007) appears to be less prominent than during straight stepping. This may be due to a more prominent role of sensory input based on the FL kinematics during inside turns. However, as mentioned above, Borgmann et al. (2009) also showed that the presence of the middle leg allows the activation of alternating metathoracic ProCx and RetCx MN activity in the absence of pharmacological CPG activation, demonstrating the importance of additional local sensory input for the activation of the CPGs *in vivo*.

For the next distal CTr-joint, a gradient in activation strength during FL turning steps is apparent even during pilocarpine-induced CPG activation. The CTr-joint pilocarpine rhythm is shaped towards the same activity as in regular saline, namely stronger burst in the LevTr MNs. The fact that the typical pilocarpine alternation is still occurring in the metathoracic CTr-joint CPG during FL curve stepping demonstrates that any descending input preventing the alternating activity in the mesothorax is weaker in the metathorax, and supports our hypothesis according to which the descending influence that coincides with the FL curve stepping is weaker in the meta- compared to the mesothorax. The only data that exist so far on intersegmental influences in the pilocarpine activated CTr-joint MNs in the stick insect are from Mantziaris et al. (2017), Daun et al. (2019), and Mantziaris et al. (2020), who studied the central coupling between the three thoracic CTr CPGs without descending input from the head ganglia, and after complete deafferentation of all ganglia. Mantziaris et al. did observe weak coupling between ipsilateral CPGs of the same joint and proposed that central pathways between them exist that exert a coordinating influence. Furthermore, Daun et al. (2019) found that the central coupling between the prothoracic and the meso- or metathoracic ganglia was generally weaker than coupling between the two more posterior ganglia. This suggests that turning-related changes that are seen in the meso- and metathoracic CTr-joint MN activity are likely not to come from the activity of the FL CPGs, otherwise we would expect a patterned influence coupled to the FL steps. The neural control that alters CPG activity in the CTr-joint is thus more likely to derive from neural networks or inputs arising anterior to the thoracic ganglia. This, however, stresses how crucial local sensory feedback is for the generation of a functional motor pattern. Interestingly, a study by Knebel et al. (2017) in the locust reported a strong coupling between the pro- and mesothoracic ganglia after pharmacological activation, suggesting a less flexible control of leg movements in this species.

Interplay of Central and Sensory Inputs for the Motor Output During Turning

The motor output in the deafferented meso- and metathoracic ganglia does not resemble a functional motor output observed during walking of an intact animal. Translated into actual movement, the inside middle and hind leg motor output would produce a front-to-back movement of the lifted leg, together with occasional flexion movements around the FTi-joint. The outside legs would be permanently retracted, lifted, and most likely also stretched. It appears that this output only represents a necessary default activation, on which each joint depends to perform the kinematic changes observed during turning *in vivo*. The pronounced differences in the motor output to the ThC-joint possibly relate to the very strong alterations in the forward and backward movement of the inside and outside legs leading to changes in anterior and posterior extreme positions (AEP, PEP) (Dürr and Ebeling, 2005; Gruhn et al., 2009). The lack of a body side-specific activity of the CTr-joint MN pools points to the importance of this joint to determine stance and swing, independent of any direction, while the observed activation patterns in the FTi-joint fits to the role of the flexor as a stance and the extensor as a swing phase muscle, independent of the body side. They also fit to the role of both muscles to serve body height control through co-activation, but also reflect the relatively large kinematic variability in this joint during turning (Dürr and Ebeling, 2005; Gruhn et al., 2009).

This stresses the importance of an integration of CPG activity with sensory input in order to shape the functional motor output *in vivo*. According to our results, the activity of the different joint MN pools suggests that the impact of central descending influences on the motor output weakens while the dependence of motor output on local sensory feedback increases from rostral to caudal and from proximal to distal. This importance of local sensory feedback on timing and magnitude of the motor output is known from the stick insect and has been studied in great detail (Hess and Büschges, 1997; Hess and Büschges, 1999; Akay et al., 2001; Bucher et al., 2003; Akay et al., 2004; Büschges and Gruhn, 2008; Gebehart et al., 2021; Gebehart and Büschges 2021). Interaction of central and peripheral influences for the generation of functional motor outputs are known from crustaceans and stick insects (Sillar et al., 1987; Bucher et al., 2003; Borgmann et al., 2009; Borgmann et al., 2012; Gebehart and Büschges 2021; Gebehart et al., 2021), and may even affect the

timing and strength of MN activity in the adjacent thoracic segment (Sillar et al., 1987). At present, however, due to the experimental restrictions of our study, we cannot be conclusive about the interactions between central and peripheral inputs and their weighing at the level of each joint during turning.

In the meso- and the metathorax, the ThC-joint MNs of the inside leg, even when completely deafferented, show a rhythmic, alternating output that is in phase with the front leg step cycle. For this joint and this turning direction, the dependence on local feedback appears to be necessary to uncouple the two neighboring legs from one another. The outside ThC-joint MNs are often not switching from RetCx to ProCx MN activity, but the activity appears to be locked in RetCx phase of activity. Here, a strong dependence on load feedback has been postulated for the mesothorax, based on the alteration of the processing of load feedback in this segment during turning (Gruhn et al., 2016) and is likely to be present in the metathorax as well.

The absence of alternating activity between LevTr and DepTR MN pools of the CTr-joint resembles the outside activity of the ThC-joint MN pools, and implies a similar dependence of CPG activity on local sensory input during turning-related movements. This dependence on local sensory input in the CTr-joint has been known to arise from load signals from the campaniform sensilla (CS) (Akay et al., 2007; Rosenbaum et al., 2010; Borgmann et al., 2012; Zill et al., 2015; Gebehart et al., 2021), as well as feedback from the femoral chordotonal organ (fCO), which monitors position- and movement of the tibia (Hess and Büschges, 1999; Bucher et al., 2003; Gebehart et al., 2021). It is possible that the processing of this input, which has been shown to have access to the CTr-joint CPG, is modified during turning, similar to the load feedback in the mesothoracic ThC-joint MNs (Gruhn et al., 2016). The lack of a difference in the CTr-joint MN activity of the two body sides may be due to the difference in the functional role of the joint, as the leg has always to be on the ground during stance independent of its role as an outside or inside leg.

The apparent failure of the deafferented preparation to produce a consistent turning-related output in FTi-joint MNs, which is especially evident in the metathorax, suggests a weakening of turning-related intersegmental and central influences towards the metathorax for this joint as well. From the extracellular recordings, it appears that activity modification during turning is much weaker and less consistent in the metathoracic FTi-joint MNs, probably because the central drive has a weaker effect. The importance of sensory feedback in the FTi-joint control system has also long been known (Graham and Bässler, 1981; Hofmann et al., 1985; Bässler, 1993; Akay et al., 2001; Schmitz et al., 2015; Zill et al., 2015; Zill et al., 2017). Schmitz et al. (2015) observed in a different experimental setup, that 19% of middle leg steps into a hole without ground contact failed to elicit flexor tibiae EMG activity. They attributed the observed effect to the failure of local load feedback to drive FlxTi MN, which are known to be activated above firing threshold by tarsal touchdown (Gruhn et al., 2006; Berendes et al., 2013; Schmitz et al., 2015). We also know that signaling of movement feedback from the fCO in the mesothoracic ganglion is locally processed during turning to promote active flexion in the inside, but not in the outside leg (Hellekes et al., 2012). Furthermore, Gebehart and Büschges (2021) have recently shown that temporal differences in the reporting of load and movement feedback are a crucial factor for the integration of this sensory information in the pre-motor interneurons. Therefore, absence of sensory feedback in the deafferented preparation we used may have contributed to the observed variability in motor output to this joint. The presumed increase in dependence on local sensory input towards the metathorax has been mentioned above and seems to be valid for all three joints. Given the proximity of the metathoracic legs to the center of mass of the stick insect body (Cruse, 1976; Dallmann et al., 2016), it is conceivable that the necessity of load feedback for the patterning may be even more pronounced for the metathoracic than the mesothoracic motor circuits. So far, however, we have no information about the influence of load feedback in the metathoracic walking legs and future studies should focus on such sensory influences on the metathoracic motor activity.

In summary, we have presented evidence showing that the motor output to the three main leg joints of the meso- and the metathoracic legs of the stick insect, i.e., the ThC, the CTr-, and the FTi-joints, during turning is not only joint-specific, but also differs depending on the thoracic segment. We show that changes in the activity during turning are most likely mediated by influences on local CPG activities, and that the respective influences on segmental CPGs weaken caudally towards the metathorax. We conclude from our results that the turning-related motor output strongly depends on local or inter-leg sensory feedback, in order to be shaped into the functional inside or outside stepping pattern observed in the intact behaving stick insect. Future experiments will have to address the sources of this descending influence that is causal for the observed activity changes during turning, the mechanisms behind the decreasing influence of the central drive, and the change in local sensory processing observed in the mesothoracic ThC- and FTi-joints.

DATA AVAILABILITY STATEMENT

The raw data supporting the conclusion of this article will be made available by the authors, without undue reservation.

AUTHOR CONTRIBUTIONS

EH performed experiments, analyzed data, prepared figures, contributed funding and wrote the first draft of the MS; CM analyzed data, contributed to the figures and co-wrote the MS; JS performed experiments, analyzed data, and prepared figures; AB supervised the experiments and data analysis, figure generation, provided funding and co-authered the MS; MG supervised and performed experiments, analyzed data, prepared figures and co-authored the MS.

FUNDING

The work was Supported by DFG grant Bu857 to AB and Konrad-Adenauer-Stiftung to EH.

ACKNOWLEDGMENTS

The authors would like to thank Till Bockemühl for valuable help with the data analysis, and Moritz Haustein for valuable comments and input on the study and the manuscript. We would also like to thank Michael Dübbert and Jan Sydow for their excellent technical support.

SUPPLEMENTARY MATERIAL

The Supplementary Material for this article can be found online at: https://www.frontiersin.org/articles/10.3389/fphys.2022.883858/full#supplementary-material

Supplementary Figure S1 | Two examples each of the metathoracic *extensor* **(A–C)** and *flexor tibiae* **(D–F)** MN output in the deafferented ganglion during front leg (FL) inside and outside stepping. **(A)** flexor EMG of the front leg (top trace and third trace), together with extracellular recordings of the ipsilateral metathoracic extensor nerve (nl3) during inside (i,iii) and outside (ii,iv) stepping sequences; **(Bi,ii)** Phase histograms of extensor nerve activity from the walking sequences in **(Ai,ii)** and **(Aiii,iv)**, comparing inside (I) and outside (O) activity in the same animal with respect to FL step cycle. **(C)** Polar plots with spike event maxima (grey vectors) and their mean (red) for the extensor with respect to FL step cycle during inside (top, I) and outside (bottom, O) stepping; **(D)** flexor EMG recording of the FL (top trace and third trace), together with extracellular recordings of the ipsilateral metathoracic flexor nerve (ncr) during inside (i,iii) and outside (ii,iv) stepping sequences; **(Ei,ii)**. Phase histograms of flexor nerve activity from experiments in **(Di,ii)** and **(Diii,iv)**, comparing inside (I) and outside (O) activity in the same animal with respect to FL step cycle. **(F)** Polar plots with spike event maxima (grey vectors) and their mean (red) for the flexor with respect FL step cycle during inside (top, I) and outside (bottom, O) stepping; N = number animals; Ń = number of analyzed hemiganglia; *n* = number of analyzed steps. Pr, Mt: Pro- and Metathoracic location of the recording, respectively; Flex/FlxTi, Ext/ExtTi: *flexor tibiae* and *extensor tibiae* activity, respectively. The sketch indicates a stick insect with front legs in a flexed (inside) or stretched (outside) position, and the arrow above indicating the turning direction, the arrow on the side the recorded thoracic segment.

REFERENCES

Akay, T., and Murray, A. J. (2021). Relative Contribution of Proprioceptive and Vestibular Sensory Systems to Locomotion: Opportunities for Discovery in the Age of Molecular Science. *Int. J. Mol. Sci.* 22 (3), 1467–1485. doi:10.3390/ijms22031467

Akay, T., Bässler, U., Gerharz, P., and Büschges, A. (2001). The Role of Sensory Signals from the Insect Coxa-Trochanteral Joint in Controlling Motor Activity of the Femur-Tibia Joint. *J. Neurophysiology* 85, 594–604. doi:10.1152/jn.2001.85.2.594

Akay, T., Haehn, S., Schmitz, J., and Büschges, A. (2004). Signals from Load Sensors Underlie Interjoint Coordination during Stepping Movements of the Stick Insect Leg. *J. Neurophysiol.* 92, 42–51. doi:10.1152/jn.01271.2003

Akay, T., Ludwar, B. C., Göritz, M. L., Schmitz, J., and Büschges, A. (2007). Segment Specificity of Load Signal Processing Depends on Walking Direction in the Stick Insect Leg Muscle Control System. *J. Neurosci.* 27, 3285–3294. doi:10.1523/jneurosci.5202-06.2007

Akay, T. (2020). Sensory Feedback Control of Locomotor Pattern Generation in Cats and Mice. *Neuroscience* 450, 161–167. doi:10.1016/j.neuroscience.2020.05.008

Ampatzis, K., Song, J., Ausborn, J., and El Manira, A. (2014). Separate Microcircuit Modules of Distinct V2a Interneurons and Motoneurons Control the Speed of Locomotion. *Neuron* 83 (4), 934–943. doi:10.1016/j.neuron.2014.07.018

Ausborn, J., Mahmood, R., and El Manira, A. (2012). Decoding the Rules of Recruitment of Excitatory Interneurons in the Adult Zebrafish Locomotor Network. *Proc. Natl. Acad. Sci. U. S. A.* 109 (52), E3631–E3639. doi:10.1073/pnas.1216256110

Bässler, U., and Büschges, A. (1998). Pattern Generation for Stick Insect Walking Movements-Multisensory Control of a Locomotor Program. *Brain Res. Rev.* 27, 65–88. doi:10.1016/s0165-0173(98)00006-x

Bässler, U., and Storrer, J. (1980). The Neural Basis of the Femur-Tibia-Control-System in the Stick Insect Carausius Morosus. *Biol. Cybern.* 38, 107–114. doi:10.1007/bf00356037

Bässler, U., and Wegner, U. T. A. (1983). Motor Output of the Denervated Thoracic Ventral Nerve Cord in the Stick Insect *Carausius Morosus*. *J. Exp. Biol.* 105, 127–145. doi:10.1242/jeb.105.1.127

Bässler, U. (1977). Sensory Control of Leg Movement in the Stick Insect *Carausius Morosus*. *Biol. Cybern.* 25, 61–72. doi:10.1007/bf00337264

Bässler, U. (1993). The Femur-Tibia Control System of Stick Insects - A Model System for the Study of the Neural Basis of Joint Control. *Brain Res. Rev.* 18, 207–226. doi:10.1016/0165-0173(93)90002-h

Bender, J. A., Simpson, E. M., Tietz, B. R., Daltorio, K. A., Quinn, R. D., and Ritzmann, R. E. (2011). Kinematic and Behavioral Evidence for a Distinction between Trotting and Ambling Gaits in the cockroachBlaberus Discoidalis. *J. Exp. Biol.* 214 (12), 2057–2064. doi:10.1242/jeb.056481

Berendes, V., Dübbert, M., Bockemühl, T., Schmitz, J., Büschges, A., and Gruhn, M. (2013). A Laser-Supported Lowerable Surface Setup to Study the Role of Ground Contact during Stepping. *J. Neurosci. Methods* 215, 224–233. doi:10.1016/j.jneumeth.2013.03.024

Berens, P. (2009). CircStat: A MATLAB Toolbox for Circular Statistics. *J. Stat. Softw.* 31, 1–21. doi:10.18637/jss.v031.i10

Bidaye, S. S., Bockemühl, T., and Büschges, A. (2018). Six-legged Walking in Insects: How CPGs, Peripheral Feedback, and Descending Signals Generate Coordinated and Adaptive Motor Rhythms. *J. Neurophysiol.* 119, 459–475. doi:10.1152/jn.00658.2017

Bidaye, S. S., Laturney, M., Chang, A. K., Liu, Y., Bockemühl, T., Büschges, A., et al. (2020). Two Brain Pathways Initiate Distinct Forward Walking Programs in Drosophila. *Neuron* 108 (3), 469–485. doi:10.1016/j.neuron.2020.07.032

Borgmann, A., Scharstein, H., and Büschges, A. (2007). Intersegmental Coordination: Influence of a Single Walking Leg on the Neighboring Segments in the Stick Insect Walking System. *J. Neurophysiol.* 98, 1685–1696. doi:10.1152/jn.00291.2007

Borgmann, A., Hooper, S. L., and Büschges, A. (2009). Sensory Feedback Induced by Front-Leg Stepping Entrains the Activity of Central Pattern Generators in Caudal Segments of the Stick Insect Walking System. *J. Neurosci.* 29, 2972–2983. doi:10.1523/jneurosci.3155-08.2009

Borgmann, A., Toth, T. I., Gruhn, M., Daun-Gruhn, S., and Büschges, A. (2012). Dominance of Local Sensory Signals over Inter-segmental Effects in a Motor System: Experiments. *Biol. Cybern.* 105, 399–411. doi:10.1007/s00422-012-0473-y

Brunner von Wattenwyl, K. (1907). Die Insektenfamilie der Phasmiden. Leipzig: Wilhelm Engelmann, Vol. 2.

Bucher, D., Akay, T., Dicaprio, R. A., and Büschges, A. (2003). Interjoint Coordination in the Stick Insect Leg-Control System: the Role of Positional Signaling. *J. Neurophysiol.* 89, 1245–1255. doi:10.1152/jn.00637.2002

Büschges, A., and Borgmann, A. (2013). Network Modularity: Back to the Future in Motor Control. *Curr. Biol.* 23, R936–R938. doi:10.1016/j.cub.2013.09.021

Büschges, A., and Schmidt, J. (2015). Neuronal Control of Walking: Studies on Insects. *e-Neuroforum* 6, 105–112. doi:10.1007/s13295-015-0017-8

Büschges, A., and Schmitz, J. (1991). Nonspiking Pathways Antagonize the Resistance Reflex in the Thoraco-Coxal Joint of Stick Insects. *J. Neurobiol.* 22 (3), 224–237. doi:10.1002/neu.480220303

Büschges, A., Schmitz, J., and Bässler, U. (1995). Rhythmic Patterns in the Thoracic Nerve Cord of the Stick Insect Induced by Pilocarpine. *J. Exp. Biol.* 198, 435–456. doi:10.1242/jeb.198.2.435

Büschges, A., Akay, T., Gabriel, J. P., and Schmidt, J. (2008). Organizing Network Action for Locomotion: Insights from Studying Insect Walking. *Brain Res. Rev.* 57, 162–171. doi:10.1016/j.brainresrev.2007.06.028

Büschges, A. (1998). Inhibitory Synaptic Drive Patterns Motoneuronal Activity in Rhythmic Preparations of Isolated Thoracic Ganglia in the Stick Insect. *Brain Res.* 783, 262–271. doi:10.1016/s0006-8993(97)01370-x

Büschges, A., and Gruhn, M. (2008). Mechanosensory Feedback in Walking: From Joint Control to Locomotor Patterns. *Adv. Insect Physiol.* 34, 193–230. doi:10.1016/S0065-2806(07)34004-6

Büschges, A., Ludwar, B. C., Bucher, D., Schmidt, J., and Dicaprio, R. A. (2004). Synaptic Drive Contributing to Rhythmic Activation of Motoneurons in the Deafferented Stick Insect Walking System. *Eur. J. Neurosci.* 19, 1856–1862. doi:10.1111/j.1460-9568.2004.03312.x

Chrachri, A., and Clarac, F. (1990). Fictive Locomotion in the Fourth Thoracic Ganglion of the Crayfish, *Procambarus clarkii*. *J. Neurosci.* 10, 707–719. doi:10.1523/jneurosci.10-03-00707.1990

Cruse, H., and Saavedra, M. (1996). Curve Walking in Crayfish. *J. Exp. Biol.* 199 (7), 1477–1482. doi:10.1242/jeb.199.7.1477

Cruse, H., Ehmanns, I., Stübner, S., and Schmitz, J. (2009). Tight Turns in Stick Insects. *J. Comp. Physiol. A* 195, 299–309. doi:10.1007/s00359-008-0406-3

Cruse, H. (1976). The Function of the Legs in the Free Walking Stick insect,Carausius Morosus. *J. Comp. Physiol.* 112, 235–262. doi:10.1007/bf00606541

Dallmann, C. J., Dürr, V., and Schmitz, J. (2016). Joint Torques in a Freely Walking Insect Reveal Distinct Functions of Leg Joints in Propulsion and Posture Control. *Proc. Biol. Sci.* 283, 20151708. doi:10.1098/rspb.2015.1708

Daun, S., Mantziaris, C., Tóth, T., Büschges, A., and Rosjat, N. (2019). Unravelling Intra- and Intersegmental Neuronal Connectivity between Central Pattern Generating Networks in a Multi-Legged Locomotor System. *PLOS ONE* 14 (8), e0220767. doi:10.1371/journal.pone.0220767

Dean, J. (1989). Leg Coordination in the Stick Insect Carausius Morosus: Effects of Cutting Thoracic Connectives. *J. Exp. Biol.* 145, 103–131. doi:10.1242/jeb.145.1.103

Deangelis, B. D., Zavatone-Veth, J. A., and Clark, D. A. (2019). The Manifold Structure of Limb Coordination in Walking Drosophila. *eLife* 8, 46409ff. doi:10.7554/eLife.46409

Dürr, V., and Ebeling, W. (2005). The Behavioural Transition from Straight to Curve Walking: Kinetics of Leg Movement Parameters and the Initiation of Turning. *J. Exp. Biol.* 208, 2237–2252. doi:10.1242/jeb.01637

Dürr, V., Theunissen, L. M., Dallmann, C. J., Hoinville, T., and Schmitz, J. (2018). Motor Flexibility in Insects: Adaptive Coordination of Limbs in Locomotion and Near-Range Exploration. *Behav. Ecol. Sociobiol.* 72, 15. doi:10.1007/s00265-017-2412-3

Field, E. C., and Stein, P. S. G. (1997a). Spinal Cord Coordination of Hindlimb Movements in the Turtle: Interlimb Temporal Relationships during Bilateral Scratching and Swimming. *J. Neurophysiology* 78, 1404–1413. doi:10.1152/jn.1997.78.3.1404

Field, E. C., and Stein, P. S. G. (1997b). Spinal Cord Coordination of Hindlimb Movements in the Turtle: Intralimb Temporal Relationships during Scratching and Swimming. *J. Neurophysiology* 78, 1394–1403. doi:10.1152/jn.1997.78.3.1394

Fischer, H., Schmidt, J., Haas, R., and Büschges, A. (2001). Pattern Generation for Walking and Searching Movements of a Stick Insect Leg. I. Coordination of Motor Activity. *J. Neurophysiol.* 85, 341–353. doi:10.1152/jn.2001.85.1.341

Frantsevich, L. I., and Cruse, H. (2005). Leg Coordination during Turning on an Extremely Narrow Substrate in a Bug, *Mesocerus Marginatus* (Heteroptera, Coreidae). *J. Insect Physiol.* 51, 1092–1104. doi:10.1016/j.jinsphys.2005.05.008

Frantsevitch, L. I., and Mokrushov, P. A. (1980). Turning and Righting in *Geotrupes* (Coleoptera, Scarabaeidae). *J. Comp. Physiol. A* 136 (4), 279–289.

Fuchs, E., Holmes, P., Kiemel, T., and Ayali, A. (2011). Intersegmental Coordination of Cockroach Locomotion: Adaptive Control of Centrally Coupled Pattern Generator Circuits. *Front. Neural Circuits* 4, 125. doi:10.3389/fncir.2010.00125

Gebehart, C., and Büschges, A. (2021). Temporal Differences between Load and Movement Signal Integration in the Sensorimotor Network of an Insect Leg. *J. Neurophysiol.* 126 (6), 1875–1890. doi:10.1152/jn.00399.2021

Gebehart, C., Schmidt, J., and Büschges, A. (2021). Distributed Processing of Load and Movement Feedback in the Premotor Network Controlling an Insect Leg Joint. *J. Neurophysiol.* 125 (5), 1800–1813. doi:10.1152/jn.00090.2021

Godden, D. H. (1972). The Motor Innervation of the Leg Musculature and Motor Output during Thanatosis in the Stick insectCarausius Morosus Br. *J. Comp. Physiol.* 80, 201–225. doi:10.1007/bf00696491

Goldammer, J., Büschges, A., and Schmidt, J. (2012). Motoneurons, DUM Cells, and Sensory Neurons in an Insect Thoracic Ganglion: a Tracing Study in the Stick Insect Carausius Morosus. *J. Comp. Neurol.* 520, 230–257. doi:10.1002/cne.22676

Graham, D., and Bässler, U. (1981). Effects of Afference Sign Reversal on Motor Activity in Walking Stick Insects (*Carausius Morosus*). *J. Exp. Biol.* 91, 179–193. doi:10.1242/jeb.91.1.179

Graham, D., and Wendler, G. (1981). The Reflex Behaviour and Innervation of the Tergo-Coxal Retractor Muscles of the Stick insectCarausius Morosus. *J. Comp. Physiol.* 143, 81–91. doi:10.1007/bf00606071

Graham, D. (1985). "Pattern and Control of Walking in Insects," in *Advances in Insect Physiology* (London: Academic Press), 31–140. doi:10.1016/s0065-2806(08)60039-9

Grillner, S. (2003). The Motor Infrastructure: from Ion Channels to Neuronal Networks. *Nat. Rev. Neurosci.* 4 (7), 573–586. doi:10.1038/nrn1137

Gruhn, M., Hoffmann, O., Dübbert, M., Scharstein, H., and Büschges, A. (2006). Tethered Stick Insect Walking: a Modified Slippery Surface Setup with Optomotor Stimulation and Electrical Monitoring of Tarsal Contact. *J. Neurosci. Methods* 158, 195–206. doi:10.1016/j.jneumeth.2006.05.029

Gruhn, M., Zehl, L., and Büschges, A. (2009). Straight Walking and Turning on a Slippery Surface. *J. Exp. Biol.* 212, 194–209. doi:10.1242/jeb.018317

Gruhn, M., Rosenbaum, P., Bollhagen, H. P., and Büschges, A. (2011). Studying the Neural Basis of Adaptive Locomotor Behavior in Insects. *J. Vis. Exp.* 50, e2629. doi:10.3791/2629

Gruhn, M., Rosenbaum, P., Bockemühl, T., and Büschges, A. (2016). Body Side-specific Control of Motor Activity during Turning in a Walking Animal. *eLife* 5, e13799. doi:10.7554/eLife.13799

Guo, P., and Ritzmann, R. E. (2013). Neural Activity in the Central Complex of the Cockroach Brain Is Linked to Turning Behaviors. *J. Exp. Biol.* 216, 992–1002. doi:10.1242/jeb.080473

Hellekes, K., Blincow, E., Hoffmann, J., and Büschges, A. (2012). Control of Reflex Reversal in Stick Insect Walking: Effects of Intersegmental Signals, Changes in Direction, and Optomotor-Induced Turning. *J. Neurophysiol.* 107, 239–249. doi:10.1152/jn.00718.2011

Hess, D., and Büschges, A. (1997). Sensorimotor Pathways Involved in Interjoint Reflex Action of an Insect Leg. *J. Neurobiol.* 33, 891–913. doi:10.1002/(sici)1097-4695(199712)33:7<891::aid-neu3>3.0.co;2-3

Hess, D., and Büschges, A. (1999). Role of Proprioceptive Signals from an Insect Femur-Tibia Joint in Patterning Motoneuronal Activity of an Adjacent Leg Joint. *J. Neurophysiol.* 81, 1856–1865. doi:10.1152/jn.1999.81.4.1856

Hofmann, T., Koch, U. T., and Bässler, U. (1985). Physiology of the Femoral Chordotonal Organ of the Stick Insect *Cuniculina Impigra*. *J. Exp. Biol.* 114, 207. doi:10.1242/jeb.114.1.207

Jindrich, D. L., and Full, R. J. (1999). Many-legged Maneuverability: Dynamics of Turning in Hexapods. *J. Exp. Biol.* 202 (Pt 12), 1603–1623. doi:10.1242/jeb.202.12.1603

Johnston, R., and Levine, R. (2002). Thoracic Leg Motoneurons in the Isolated CNS of Adult Manduca Produce Patterned Activity in Response to Pilocarpine, Which Is Distinct from that Produced in Larvae. *Invertebr. Neurosci.* 4, 175–192. doi:10.1007/s10158-002-0019-4

Knebel, D., Ayali, A., Pflüger, H.-J., and Rillich, J. (2017). Rigidity and Flexibility: The Central Basis of Inter-leg Coordination in the Locust. *Front. Neural Circuits* 10, 112. doi:10.3389/fncir.2016.00112

Ludwar, B. C., Göritz, M. L., and Schmidt, J. (2005a). Intersegmental Coordination of Walking Movements in Stick Insects. *J. Neurophysiol.* 93, 1255–1265. doi:10.1152/jn.00727.2004

Ludwar, B. C., Westmark, S., Büschges, A., and Schmidt, J. (2005b). Modulation of Membrane Potential in Mesothoracic Moto- and Interneurons during Stick Insect Front-Leg Walking. *J. Neurophysiol.* 94, 2772–2784. doi:10.1152/jn.00493.2005

Mantziaris, C., Bockemühl, T., Holmes, P., Borgmann, A., Daun, S., and Büschges, A. (2017). Intra- and Intersegmental Influences Among Central Pattern Generating Networks in the Walking System of the Stick Insect. *J. Neurophysiol.* 118, 2296–2310. doi:10.1152/jn.00321.2017

Mantziaris, C., Bockemühl, T., and Büschges, A. (2020). Central Pattern Generating Networks in Insect Locomotion. *Dev. Neurobiol.* 80 (1-2), 16–30. doi:10.1002/dneu.22738

Marquart, F. (1940). Beiträge zur Anatomie der Muskulatur und der peripheren Nerven von *Carausius* (*Dixipus) morosus*. *Zool. Jahrbücher Abt. Anat. Ontol. Tiere* 66, 63–128.

Martin, J. P., Guo, P., Mu, L., Harley, C. M., and Ritzmann, R. E. (2015). Central-complex Control of Movement in the Freely Walking Cockroach. *Curr. Biol.* 25, 2795–2803. doi:10.1016/j.cub.2015.09.044

Mu, L., and Ritzmann, R. E. (2005). Kinematics and Motor Activity during Tethered Walking and Turning in the Cockroach, *Blaberus Discoidalis*. *J. Comp. Physiol. A* 191, 1037–1054. doi:10.1007/s00359-005-0029-x

Mu, L., and Ritzmann, R. E. (2008). Interaction between Descending Input and Thoracic Reflexes for Joint Coordination in Cockroach: I. Descending Influence on Thoracic Sensory Reflexes. *J. Comp. Physiol. A* 194, 283–298. doi:10.1007/s00359-007-0307-x

Pearson, K. G., Stein, R. B., and Malhotra, S. K. (1970). Properties of Action Potentials from Insect Motor Nerve Fibres. *J. Exp. Biol.* 53, 299–316. doi:10.1242/jeb.53.2.299

Pfeffer, S. E., Wahl, V. L., Wittlinger, M., and Wolf, H. (2019). High-speed Locomotion in the Saharan Silver Ant, Cataglyphis Bombycina. *J. Exp. Biol.* 222 (29), jeb198705. doi:10.1242/jeb.198705

Ridgel, A. L., Alexander, B. E., and Ritzmann, R. E. (2007). Descending Control of Turning Behavior in the Cockroach, Blaberus Discoidalis. *J. Comp. Physiol. A* 193, 385–402. doi:10.1007/s00359-006-0193-7

Ritzmann, R. E., and Zill, S. N. (2017). "Control of Locomotion in Hexapods," in *The Oxford Handbook of Invertebrate Neurobiology*. Editor J. E. Byrne (Oxford University Press. Oxford Handbooks Online). doi:10.1093/oxfordhb/9780190456757.013.20

Rosenbaum, P., Wosnitza, A., Büschges, A., and Gruhn, M. (2010). Activity Patterns and Timing of Muscle Activity in the Forward Walking and Backward Walking Stick InsectCarausius Morosus. *J. Neurophysiol.* 104, 1681–1695. doi:10.1152/jn.00362.2010

Rosenbaum, P., Schmitz, J., Schmidt, J., and Büschges, A. (2015). Task-dependent Modification of Leg Motor Neuron Synaptic Input Underlying Changes in Walking Direction and Walking Speed. *J. Neurophysiol.* 114, 1090–1101. doi:10.1152/jn.00006.2015

Ryckebusch, S., and Laurent, G. (1993). Rhythmic Patterns Evoked in Locust Leg Motor Neurons by the Muscarinic Agonist Pilocarpine. *J. Neurophysiol.* 69 (5), 1583–1595. doi:10.1152/jn.1993.69.5.1583

Santuz, A., Akay, T., Mayer, W. P., Wells, T. L., Schroll, A., and Arampatzis, A. (2019). Modular Organization of Murine Locomotor Pattern in the Presence and Absence of Sensory Feedback from Muscle Spindles. *J. Physiol.* 597 (12), 3147–3165. doi:10.1113/jp277515

Schmitz, J., Büschges, A., and Delcomyn, F. (1988). An improved electrode design for en passant recording from small nerves. *Comp. Biochem. Physiol. Part A Physiol.* 91, 769–772. doi:10.1016/0300-9629(88)90963-2

Schmitz, J., Gruhn, M., and Büschges, A. (2015). The Role of Leg Touchdown for the Control of Locomotor Activity in the Walking Stick Insect. *J. Neurophysiol.* 113, 2309–2320. doi:10.1152/jn.00956.2014

Schmitz, J., Gruhn, M., and Büschges, A. (2019). Body Side-specific Changes in Sensorimotor Processing of Movement Feedback in a Walking Insect. *J. Neurophysiol.* 122 (5), 2173–2186. doi:10.1152/jn.00436.2019

Schmitz, J. (1986). The Depressor Trochanteris Motoneurones and Their Role in the Coxo-Trochanteral Feedback Loop in the Stick Insect *Carausius Morosus*. *Biol. Cybern.* 55, 25–34. doi:10.1007/bf00363975

Sillar, K. T., Clarac, F., and Bush, B. M. (1987). Intersegmental Coordination of Central Neural Oscillators for Rhythmic Movements of the Walking Legs in Crayfish, *Pacifastacus Leniusculus*. *J. Exp. Biol.* 131, 245–264. doi:10.1242/jeb.131.1.245

Stein, P. S. G. (2018). Central Pattern Generators in the Turtle Spinal Cord: Selection Among the Forms of Motor Behaviors. *J. Neurophysiol.* 119 (2), 422–440. doi:10.1152/jn.00602.2017

Strauss, R., and Heisenberg, M. (1990). Coordination of Legs During Straight Walking and Turning in Drosophila Melanogaster. *Journal of Comparative Physiology. A, Sensory, Neural, and Behavioral Physiology* 167. doi:10.1007/BF00192575

Weidler, D. J., and Diecke, F. P. J. (1969). The Role of Cations in Conduction in the Central Nervous System of the Herbivorous Insect Carausius Morosus. *Z. Vergl. Physiol.* 64, 372–399. doi:10.1007/bf00340433

Westmark, S., Oliveira, E. E., and Schmidt, J. (2009). Pharmacological Analysis of Tonic Activity in Motoneurons during Stick Insect Walking. *J. Neurophysiol.* 102, 1049–1061. doi:10.1152/jn.91360.2008

Zill, S. N., Chaudhry, S., Büschges, A., and Schmitz, J. (2015). Force Feedback Reinforces Muscle Synergies in Insect Legs. *Arthropod Struct. Dev.* 44, 541–553. doi:10.1016/j.asd.2015.07.001

Zill, S. N., Neff, D., Chaudhry, S., Exter, A., Schmitz, J., and Büschges, A. (2017). Effects of Force Detecting Sense Organs on Muscle Synergies Are Correlated with Their Response Properties. *Arthropod Struct. Dev.* 46, 564–578. doi:10.1016/j.asd.2017.05.004

Conflict of Interest: The authors declare that the research was conducted in the absence of any commercial or financial relationships that could be construed as a potential conflict of interest.

Publisher's Note: All claims expressed in this article are solely those of the authors and do not necessarily represent those of their affiliated organizations, or those of the publisher, the editors and the reviewers. Any product that may be evaluated in this article, or claim that may be made by its manufacturer, is not guaranteed or endorsed by the publisher.

frontiers | Frontiers in Physiology

METHODS
published: 30 May 2022
doi: 10.3389/fphys.2022.882413

Optimization of Whole Mount RNA Multiplexed *in situ* Hybridization Chain Reaction With Immunohistochemistry, Clearing and Imaging to Visualize Octopus Embryonic Neurogenesis

Ali M. Elagoz[1,2], *Ruth Styfhals*[1,2,3], *Sofia Maccuro*[1,2], *Luca Masin*[2,4], *Lieve Moons*[2,4] *and Eve Seuntjens*[1,2]*

[1]Laboratory of Developmental Neurobiology, Department of Biology, KU Leuven, Leuven, Belgium, [2]Leuven Brain Institute, KU Leuven, Leuven, Belgium, [3]Department of Biology and Evolution of Marine Organisms, Stazione Zoologica Anton Dohrn, Naples, Italy, [4]Laboratory of Neural Circuit Development and Regeneration, Department of Biology, KU Leuven, Leuven, Belgium

OPEN ACCESS

Edited by:
Natraj Krishnan,
Mississippi State University,
United States

Reviewed by:
Robyn J. Crook,
San Francisco State University,
United States
Camino Gestal,
Spanish National Research Council
(CSIC), Spain

***Correspondence:**
Eve Seuntjens
eve.seuntjens@kuleuven.be

Specialty section:
This article was submitted to
Invertebrate Physiology,
a section of the journal
Frontiers in Physiology

Received: 23 February 2022
Accepted: 02 May 2022
Published: 30 May 2022

Citation:
Elagoz AM, Styfhals R, Maccuro S,
Masin L, Moons L and Seuntjens E
(2022) Optimization of Whole Mount
RNA Multiplexed in situ Hybridization
Chain Reaction With
Immunohistochemistry, Clearing and
Imaging to Visualize Octopus
Embryonic Neurogenesis.
Front. Physiol. 13:882413.
doi: 10.3389/fphys.2022.882413

Gene expression analysis has been instrumental to understand the function of key factors during embryonic development of many species. Marker analysis is also used as a tool to investigate organ functioning and disease progression. As these processes happen in three dimensions, the development of technologies that enable detection of gene expression in the whole organ or embryo is essential. Here, we describe an optimized protocol of whole mount multiplexed RNA *in situ* hybridization chain reaction version 3.0 (HCR v3.0) in combination with immunohistochemistry (IHC), followed by fructose-glycerol clearing and light sheet fluorescence microscopy (LSFM) imaging on *Octopus vulgaris* embryos. We developed a code to automate probe design which can be applied for designing HCR v3.0 type probe pairs for fluorescent *in situ* mRNA visualization. As proof of concept, neuronal (*Ov-elav*) and glial (*Ov-apolpp*) markers were used for multiplexed HCR v3.0. Neural progenitor (*Ov-ascl1*) and precursor (*Ov-neuroD*) markers were combined with immunostaining for phosphorylated-histone H3, a marker for mitosis. After comparing several tissue clearing methods, fructose-glycerol clearing was found optimal in preserving the fluorescent signal of HCR v3.0. The expression that was observed in whole mount octopus embryos matched with the previous expression data gathered from paraffin-embedded transverse sections. Three-dimensional reconstruction revealed additional spatial organization that had not been discovered using two-dimensional methods.

Keywords: fluorescent *in situ* hybridization, immunohistochemistry, tissue clearing, cephalopod, brain development, invertebrate, light sheet imaging

1 INTRODUCTION

The recently increased availability of genomic information has spurred molecular research on several cephalopod species, including *Octopus vulgaris* (Albertin et al., 2015; Kim et al., 2018; Zarrella et al., 2019; Li et al., 2020). *O. vulgaris* or the common octopus, is a cosmopolitan species, and has been the subject of many seminal studies of neural anatomy and behavior (Young, 1971, 1983; Fiorito et al., 1990; Amodio and Fiorito, 2013). How the octopus has

expanded its brain and how the nervous system is able to generate these complex cognitive behaviors are matters of growing research interest.

As evolutionary novel features arise during the development of organisms, studying embryonic development of the nervous system in cephalopods can give important insights into these research questions. *O. vulgaris* spawns several hundreds of thousands of small-sized eggs that develop, depending on the water temperature, in roughly 40 days to independently feeding and swimming paralarvae (Naef, 1928; Deryckere et al., 2020). The central brain develops from placodes to cords and lobes, which represent the adult brain lobes, although only containing about 200,000 cells at hatching. Despite the huge difference in size, this larval brain is able to control a number of innate behaviors. Our recent work showed that the larval brain derives from a neurogenic zone located around the eye placode that expresses evolutionary conserved neurogenic transcription factors (Deryckere et al., 2021).

The study of spatial gene expression has been instrumental in defining the molecular patterning and gene function during embryogenesis. In non-model species such as cephalopods, antibody tools are not readily available and often too expensive to develop. Methods that allow detection of mRNA expression *in situ* are more widely applicable. The recent development of *in situ* hybridization chain reaction version 3.0 (HCR v3.0) offers a robust, sensitive, versatile and low-cost method for simultaneous detection of multiple mRNAs in cells or tissues of any organism (Choi et al., 2014; Choi et al., 2016, 2018; Schwarzkopf et al., 2021). The method seems to outcompete traditional colorimetric *in situ* hybridization because of its robustness and the option for multiplexing, and other branched DNA probe methods such as RNAscope because of the much lower cost, despite the latter being highly sensitive and easier in use (Jones and Howat, 2020).

In order to follow up on organ morphogenesis, technologies have been developed that allow three-dimensional (3D) imaging of whole embryos or organs, often combined with marker gene labeling techniques. Besides classical confocal microscopy, that allows for high resolution imaging at the cellular level, light sheet fluorescence microscopy (LSFM) revolutionized imaging speed of optically transparent organisms including several aquatic embryonic and larval specimens (Santi, 2011). In addition, several methods have been developed to optically clear fixed tissue samples using organic solvent-based methods (e.g. iDISCO+, uDISCO, and BABB) or water-based methods (e.g. CUBIC, fructose-glycerol, and TDE) (Richardson and Lichtman, 2015). While these methods often preserve the fluorescent signals generated by genetic labeling in transgenic animal lines, or after immunohistochemistry, currently there is no publication presenting the compatibility of these clearing methods with HCR v3.0 treated cephalopod samples.

Organ development, such as the nervous system, can be complex to understand only using two-dimensional (2D) imaging. 3D imaging can provide an additional perspective. Here, we add to the existing methodology an automation of probe design, and optimized clearing protocol that retains the signal generated by HCR v3.0 in whole mount *O. vulgaris* embryos, even in combination with immunohistochemistry. These methods will advance gene expression analysis in non-model species such as cephalopods. Moreover, we present data on developmental stage XV as an experimental stage, which is mid-organogenesis, and the embryos have developed eye pigmentation which is successfully cleared by the proposed protocol in order to visualize the brain by LSFM. We also include immunohistochemistry to prove that sequential detection of mRNA and protein is feasible using our combined method. Combining visualization of mRNA and protein can be useful for a number of reasons. First of all, it provides flexibility to the researcher in the case where not for all genes under investigation antibodies are available. Secondly, expression information gathered at the mRNA level and protein levels might be different. For instance, the respective protein can be secreted, which means that mRNA could be detected in a different location than the protein. Our data confirmed previous findings using HCR v3.0 on transverse sections (Deryckere et al., 2021; Styfhals et al., 2022) and showed the power of this technique to map marker gene expression in 3D during organogenesis.

2 MATERIALS AND METHODS

2.1 Animals

Live *Octopus vulgaris* embryos were received from the Instituto Español de Oceanografía (IEO, Tenerife, Spain). Embryos were incubated until reaching the developmental stage XV in the closed standalone system located at the Laboratory of Developmental Neurobiology (KU Leuven, Belgium). The size of an octopus egg, from the stalk till micropyle, is 2 mm × 0,7 mm and a stage XV octopus embryo, from the top of the mantle till the end of arms, is approximately 1,25 mm × 0,88 mm. The stage XV embryos were fixed in 4% paraformaldehyde (PFA) in phosphate buffered saline (PBS) overnight, followed by a wash of Diethyl pyrocarbonate-treated phosphate buffered saline (PBS-DEPC). Embryos were manually dechorionated using tweezers (Dumont #5 Forceps—Biology/Inox, FST) in PBS-Tween (PBST). Embryos were dehydrated into 100% Methanol (MeOH) following a series of graded MeOH/PBST washes, each for 10 min: 25% MeOH/75% PBST, 50% MeOH/50% PBST, 75% MeOH/25% PBST, 100% MeOH, 100% MeOH. Dehydrated embryos were kept at −20°C overnight or until further use.

2.2 *In situ* Hybridization Chain Reaction Version 3.0 with(out) Immunohistochemistry

2.2.1 Probe Design

Easy_HCR was used during generation of HCR v3.0 type probe pairs for fluorescent *in situ* mRNA visualization. *Ov-apolpp, Ov-ascl1*, *Ov-elav,* and *Ov-neuroD* were already designed as previously described in Deryckere et al., 2021 and Styfhals et al., 2022. The 33, 33, 27, and 26 split-initiator probe pairs were designed for *Ov-apolpp, Ov-ascl1*, *Ov-elav,* and *Ov-neuroD*, respectively (**Supplementary Table ST1**).

DNA Oligo Pools were ordered from Integrated DNA Technologies, Inc (probe sets are presented in **Supplementary Table ST1**) and dissolved in Nuclease-Free Distilled Water (Invitrogen). HCR amplifiers with B1-Alexa Fluor-546, B2-Alexa Fluor-647 and B3-Alexa Fluor-488 were obtained from Molecular Instruments, Inc.

2.2.2 Hybridization Chain Reaction v3.0

The protocol is based upon the Molecular Instruments' (MI) HCR v3.0 protocol for whole mount mouse embryos (*Mus Musculus*) (Choi et al., 2018) with some small adaptations. Briefly, multiple octopus embryos were processed simultaneously due to their small size in 0.5 ml Eppendorf tubes. The volume of the solutions used in each step was 100 µl. During the preparation of fixed whole mount octopus embryos, the desired amount of octopus embryos were transferred to 0.5 ml Eppendorf tubes, thawed on ice and gradually moved to room temperature (in total half an hour). The rehydration of octopus embryos was carried out at room temperature. The octopus embryos were permeabilized by treating them for 15 min at room temperature using proteinase K (Roche, 10 µg/ml in PBS-DEPC). During the detection stage, the probe solutions were prepared by adding 0.4 pmol of each probe to 100 µl of probe hybridization buffer. Probes were omitted in negative controls. During the amplification stage, pre-amplification was carried out for at least 30 min. 3 pmol for Hairpin H1 and 3 pmol for Hairpin H2 were separately prepared (2 µl of 3 µM stock each hairpin was snap cooled: 95°C for 90 s, 5 min on ice followed by 30 min at room temperature) and added to a total of 100 µl of amplification buffer. After overnight amplification, excess hairpins were removed by 3 × 100 µl 5xSSCT washes at room temperature in the dark. The embryos were incubated in 1:2000 DAPI in 5xSSCT for 2 h followed by a 5xSSCT wash for 5 min. Then, embryos were transferred to the fructose-glycerol clearing solution described in Dekkers et al., 2019 for at least 2 days. Fructose-glycerol clearing solution was prepared by dissolving 29,72 g of fructose in 33 ml of glycerol and 7 ml of distilled water on a magnetic stirrer. A Refractometer was used to measure the refractive index of the fructose-glycerol clearing solution to validate its value being 1.45. The refractive index needs to match to the sample chamber used for imaging. A step-by-step protocol for whole mount HCR v3.0 with IHC is provided in protocol. io (dx.doi.org/10.17504/protocols.io.bxz6pp9e).

2.2.3 Immunohistochemistry

When HCR was combined with IHC, the incubation in DAPI in the HCR protocol was included in the IHC section of the protocol. The embryos were directly processed for IHC after the last excess hairpin removal wash. The whole protocol of IHC was carried out at 4°C. Embryos were incubated with the primary antibody (1:1,000 rabbit anti-phospho-histone H3 (Ser10)) (Millipore 06–570) for the following 2 days after the HCR protocol. Afterwards, the embryos were washed with 5xSSCT three times for 2 h followed by adding the secondary antibody donkey anti-rabbit Alexa 488 (Life Technologies) at a final concentration of 1:300 diluted in antibody diluent (Roche) and incubated overnight. The excess secondary antibody was washed with 5xSSCT twice for 2 h and the embryos were incubated in 1:2000 DAPI in 5xSSCT for 2 h followed by 5xSSCT wash for 5 min. Fructose-glycerol clearing was performed as described above.

2.3 Light Sheet Fluorescence Microscopy Imaging and Analysis

Imaging was done using Zeiss Z1 Light sheet fluorescence microscopy (LSFM) (Carl Zeiss AG, Germany). The cleared and stained embryos were glued from their mantle on a metal plunger and immersed in low-viscosity immersion oil mix, as described in Deryckere et al., 2021. A refractometer was used to measure the refractive index of the immersion oil to match the refractive index of fructose-glycerol clearing solution. The z-stack coronal planes of the embryo was acquired in a series of tiles with a 20x/1.0—refractive index 1.45 detection objective and 10x/0.2 illumination objectives. 2 µm/slice was chosen. The number of tiles was determined by considering the top-left and bottom-right coordinates and 20% tile overlap. The acquired tiles were stitched together using ARIVIS (Vision4D, Zeiss Edition 3.1.4). Then, image analysis such as manual reconstruction of the brain and stellate ganglia, 3D rendering, and background reduction were also carried out using this software. Furthermore, fluorescent background was removed and signal-to-background ratio on light sheet images was optimized on ARIVIS software (**Supplementary Figure SF2**).

3 RESULTS AND DISCUSSION

In this study, we report for the first time on optimization of whole mount RNA multiplexed *in situ* hybridization chain reaction (HCR) combined with immunohistochemistry, clearing and imaging to visualize *Octopus vulgaris* embryonic neurogenesis. An overview of the methodology pipeline is depicted in **Figure 1**.

3.1 Manual Segmentation Versus Hybridization Chain Reaction to Visualize the Developing Nervous System

In order to benchmark our method, we first delineated the central nervous system of developmental stage XV octopus embryo using histological nuclear staining only (**Figure 2**). The embryo was stained by using the nuclear marker DAPI (**Figures 2A–C**). Afterwards, the central brain (supra-esophageal and sub-esophageal masses, and laterally located optic lobes) as well as stellate ganglia were manually segmented and reconstructed based on Marquis, 1989 (**Figures 2D–I**, **Supplementary Video SV1**). Next, the developing nervous system of a developmental stage XV octopus embryo was visualized by HCR using the pan-neuronal marker *Ov-elav* (**Figure 2J–L**). To reduce the time of probe pair design, *in silico* validation and ordering, we developed an automated tool called Easy_HCR (available on

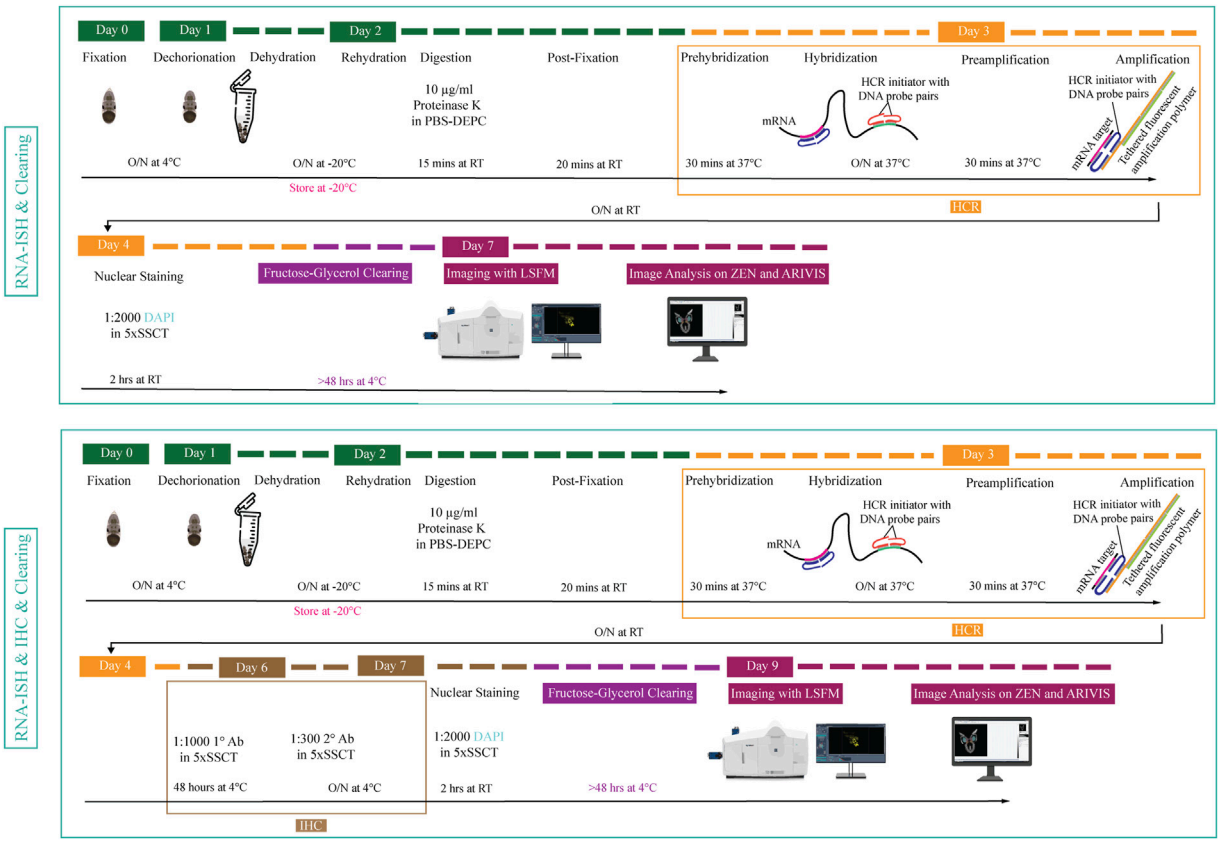

FIGURE 1 | Overview of experimental pipeline for *Octopus vulgaris* embryos. RNA *in situ* hybridization chain reaction version 3.0 (RNA-ISH) and immunohistochemistry (IHC) are followed by fructose-glycerol clearing and imaging with Light Sheet Fluorescence Microscopy (LSFM). The final images (3D images and Z-stack planes) as well as videos are acquired, processed and analyzed with ZEN (black edition) and ARIVIS VISION4D v.3.1.4 software. For developmental stage XV embryo (its size is approximately 1,25 mm x 0,88 mm), RNA-ISH & Clearing & Imaging & Image Analysis takes approximately 7 days whereas, RNA-ISH & IHC & Clearing & Imaging & Image Analysis takes around 9 days. (This figure is designed using a resource from freepik.com).

https://github.com/SeuntjensLab/Easy_HCR). Easy_HCR is a set of jupyter notebooks made to automate the creation of probe pairs for hybridization chain reaction (HCR). It is based on insitu_probe_generator (Kuehn et al., 2021). These notebooks feature automated blasting and probe pair filtering to minimize off-target effects, checking regions of local similarity on custom databases using BLAST+ (Basic Local Alignment Search Tool) and probe list formatting for easy ordering from Integrated DNA Technologies, Inc. (IDT) (Camacho et al., 2009). Custom database creation is necessary when Easy_HCR is used for other organisms. We recommend to design at least 20 split-initiator probe pairs per gene. Easy_HCR is available on GitHub via https://github.com/SeuntjensLab/Easy_HCR.

While both manual segmentation and *Ov-elav* HCR created a 3D view on the nervous system, manual segmentation was far more time-consuming and heavily dependent on the expert's interpretation. *Ov-elav* HCR clearly delineated the neuronal cells and revealed the precise location of the gastric ganglion as well as the two buccal ganglia. Furthermore, manual segmentation is only feasible if the brain has developed to a certain point which allows experts to be able to unequivocally distinguish it from the surrounding tissues. Therefore, HCR combined with Light sheet imaging is a more accurate and less time-consuming method to visualize organ morphogenesis.

3.2 Multiplexing *in situ* Hybridization Chain Reaction

As a next step, we multiplexed HCR mRNA detection by combining the pan-neuronal marker (*Ov-elav*) with a glial marker (*Ov-apolpp*). As controls, we measured autofluorescence on each channel as well as performed HCR using only-hairpins without any probe conditions (**Supplementary Figure SF1**). *Ov-elav* expression was visualized in the central brain masses, optic lobes, stellate, mouth and gastric ganglia as well as the neurons in the arms, while *Ov-apolpp* was mainly expressed within the neuropil located in the central brain, optic lobes and arms (**Figure 3**). The expression of *Ov-elav* and *Ov-apolpp* observed in whole mount octopus embryos matches the expression data seen on

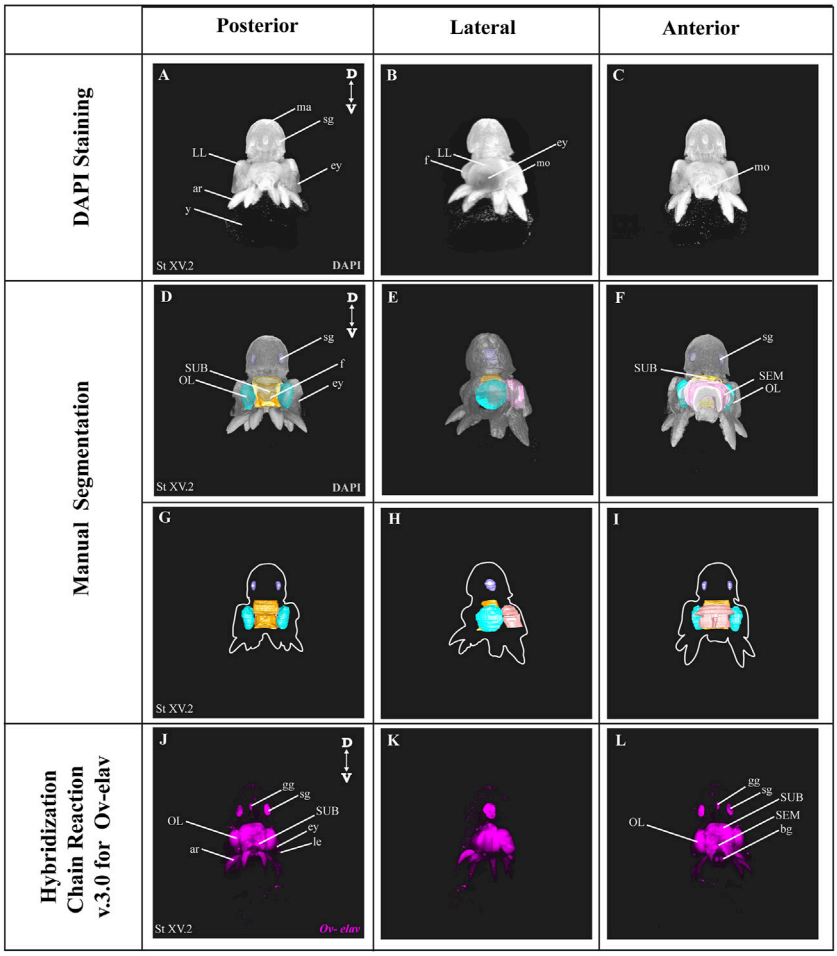

FIGURE 2 | Manual Segmentation vs. *in situ* hybridization chain reaction. **(A–C)** Maximum intensity projection of DAPI-stained developmental stage XV octopus embryo in 3D view. **(D–F)** 3D volumetric octopus embryo with manually reconstructed central brain as well as stellate ganglia. *Color legend: light blue, optic lobes; pink, supraesophageal mass; orange, subesophageal mass; and dark blue, stellate ganglia*. **(G–I)** Manually reconstructed central brain as well as stellate ganglia. **(J–L)** *in situ* hybridization chain reaction (HCR) for *Ov-elav* on a developmental stage XV embryo. A stage XV octopus embryo is approximately 1,25 mm × 0,88 mm, from the top of the mantle till the end of the arms. *Abbreviations: ar, arm; bg, buccal ganglia; D, dorsal; ey, eye; fu, funnel; gg, gastric ganglion; le, lens; LL, lateral lip; ma, mantle; n, neuropil; OL, optic lobe; SEM, supraesophageal mass; sg, stellate ganglion; SUB, subesophageal mass; V, ventral; y, yolk.*

transverse sections (Deryckere et al., 2021; Styfhals et al., 2022). The z-stack overview and 3D view of the multiplexed HCR of *Ov-elav* and *Ov-apolpp* is provided in the Supplementary Information (**Supplementary Videos SV2–4**).

3.3 Combining Whole Mount Multiplexed *in situ* Hybridization Chain Reaction With Immunohistochemistry

After optimization of multiplexed HCR v3.0 on whole mount octopus embryos, we tested its compatibility with immunohistochemistry. Multiplexed hybridization of neuronal progenitor (*Ov-ascl1*) and neuronal precursor (*Ov-neuroD*) markers was followed by an immunostaining for the mitotic marker phosphorylated-histone H3 (PH3) (**Figure 4**). *Ov-ascl1* was mainly expressed in the neurogenic lateral lips and retina, while *Ov-neuroD* was mainly expressed in the transition zones connecting the neurogenic area with the central brain (**Figures 4F–H**). The expression of *Ov-neuroD* in the transition zone is outlined in **Figure 4H**. Previously, we had manually segmented the posterior transition zone based on the visualization of *Ov-neuroD* expression on transversal paraffin sections, and found it to be a bow-shaped structure (Deryckere et al., 2021). By combining *Ov-neuroD* HCR with 3D imaging, we confirmed the bow-shaped expression pattern but also revealed that it is actually shaped as a double bow, both sides being connected to each other posteriorly (**Supplementary Video SV7**). Also *Ov-ascl1* expression observed in whole mount octopus embryos fitted with the expression pattern observed on transverse sections (Deryckere et al., 2021). PH3+ cells were mainly present on the skin, retina, lateral lips and arms (**Figure 4E**). The z-stack overview as well as 3D view of the multiplexed HCR of *Ov-ascl1*

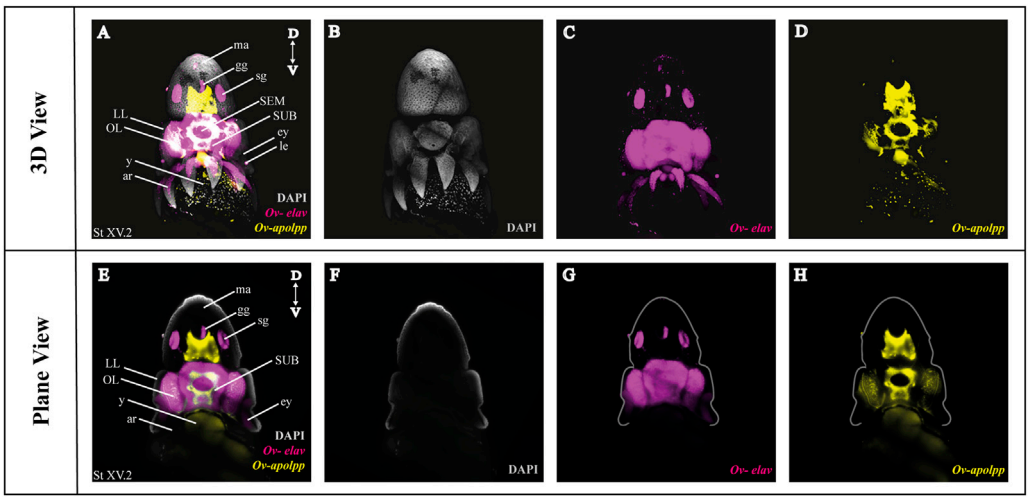

FIGURE 3 | Whole Mount HCR v3.0 followed by fructose-glycerol clearing on an *Octopus vulgaris* embryo (developmental stage XV) imaged with LSFM. Top panel illustrates the merged 3D view from the posterior side of the embryo, and bottom panel shows a single plane of a coronal section. **(A)** Overview image showing the expression of *Ov-elav and Ov-apolpp* on a Stage XV embryo in 3D. Note that only high-level expression is retained on the merged view. DAPI (in grey) is used for nuclear labelling. **(B–D)** 3 individual channels from **(A)**. **(E)** Overview image showing the expression of *Ov-elav and Ov-apolpp* on a coronal section of Stage XV embryo. **(F–H)** 3 individual channels from **(E)**. *Abbreviations: ar, arm; D, dorsal; ey, eye; fu, funnel; gg, gastric ganglion; LL, lateral lip; ma, mantle; n, neuropil; OL, optic lobe; SEM, supraesophageal mass; sg, stellate ganglion;SUB, subesophageal mass; V, ventral; y, yolk.*

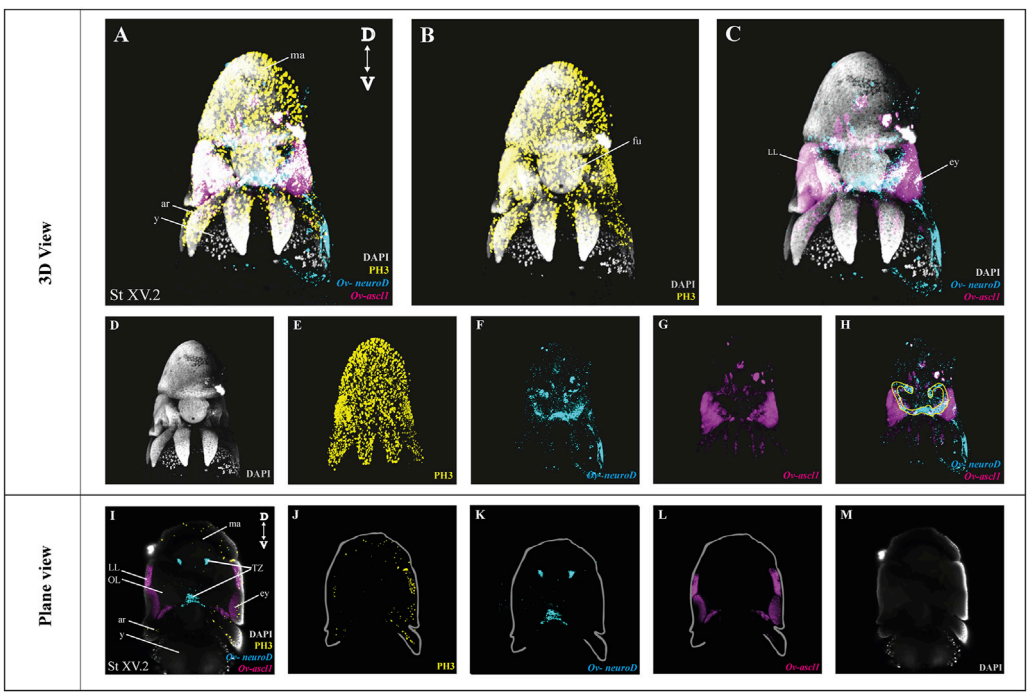

FIGURE 4 | Whole Mount multiplexed HCR v3.0-IHC followed by fructose-glycerol clearing on an *Octopus vulgaris* embryo (developmental stage XV) imaged with LSFM to visualize neurogenesis. **(A)** Overview image showing the expression of *Ov-ascl1 and Ov-neuroD* and presence of mitotic cells (PH3+) on a Stage XV embryo in 3D view. DAPI (in grey) is used for nuclear labelling. **(B)** Image illustrating mitotic PH3+ cells with DAPI which is an indication of successful IHC after HCR. **(C)** Multiplexed HCR Image of *Ov-ascl1 and Ov-neuroD* with DAPI. **(D–G)** Separate channels from **(A)**. **(H)** Overlay of *Ov-ascl1 and Ov-neuroD* show mutually exclusive expression. Yellow line indicates the transition zone area. **(I)** Overview image showing the expression of *Ov-ascl1 and Ov-neuroD* and presence of mitotic cells (PH3+) on a coronal section of Stage XV embryo. **(J–M)** 4 individual channels from **(I)**. *Abbreviations: ar, arm; D, dorsal; ey, eye; fu, funnel; LL, lateral lip; ma, mantle; OL, optic lobe; SUB, subesophageal mass; V: ventral; y, yolk.*

TABLE 1 | Comparison of different water-based clearing methods and their compatibility with HCR on whole mount octopus embryos and paralarvae.

Clearing method	Clearing performance	Signal Intensity of HCR after clearing	Observations
CUBIC	++	–	Incomplete removal of eye pigmentation which hinders the brain imaging. Tissue swelling observed
60% TDE	+	Not tested	The pigmented tissue, especially eyes and chromatophores, is not cleared. Tissue shrinkage observed
DEEP-Clear	+++	–	Minimal disturbance from eye pigmentation during acquisition after clearing
Fructose-glycerol	++	+++	Pigmented tissue is cleared adequately, which allows brain imaging. Tissue shrinkage observed

and *Ov-neuroD* with IHC of PH3 is provided in the Supplementary Information (**Supplementary Videos SV5–7**).

3.4 Comparing Different Water-Based Clearing Methods and Their Compatibility With HCR

Four different (CUBIC, TDE, DEEP-clear and fructose-glycerol) water-based clearing methods were compared for their clearing performance as well as to evaluate whether the signal intensity of HCR was retained after clearing on octopus embryos (see also **Table 1**) (Costantini et al., 2015; Nguyen, 2017; Dekkers et al., 2019; Pende et al., 2020). CUBIC (Clear, Unobstructed Brain/Body Imaging Cocktails and Computational analysis) clearing had mild clearing properties since the eye pigmentation was not completely removed which hindered brain imaging during acquisition. Furthermore, swelling of the tissue was observed. Also, no signal was observed when CUBIC was carried out after HCR on octopus embryos. TDE (60% 2,2′-thiodiethanol in PBS-DEPC) immersion was the worst-performing clearing method since no clearing of the pigmented tissue was observed even after several days of incubation. Therefore, its compatibility with HCR was not tested. The DEEP-Clear (DEpigmEntation-Plus-Clearing method) was the best to clear the octopus samples since the majority of the eye pigmentation was cleared which allowed minimal disturbance of the brain, yet it also completely wiped out the HCR signal. Fructose-glycerol clearing was the only option to sufficiently clear and at the same time preserve the HCR signal after clearing, even though some tissue shrinkage was observed (**Table 1**).

HCR with different clearing methods has been published over the last few years (Shah et al., 2016; Nguyen, 2017; Kramer et al., 2018; Kumar et al., 2021; Lin et al., 2018; Sanchez et al., 2019; Bruce et al., 2021; Vianello et al., 2021). Although CUBIC clearing was not compatible with HCR in octopus embryos, positive results have been published on rat brains (Nguyen, 2017). It was shown that both CUBIC and CLARITY clearing could be used for clearing the rat brains to visualize *Arc* mRNA (Nguyen, 2017). PACT (passive CLARITY technique) tissue hydrogel embedding and clearing has been used after single molecule HCR in cell culture and whole mount zebrafish embryos (Shah et al., 2016). HCR in combination with fructose-glycerol clearing has been used for intact tails (somites and presomitic mesoderm) of mouse embryos and afterwards, further adapted by the Lütolf group for gastruloids (3D aggregates of mouse embryonic stem cells) (Sanchez et al., 2019; Vianello et al., 2021). Recently, glycerol (50–70%) clearing was used for a wide range of whole mount samples (Bruce et al., 2021). Apart from the water-based clearing methods tested, solvent-based methods, such as iDISCO+ and uDISCO, have been used successfully in combination with HCR (Kramer et al., 2018; Lin et al., 2018). The compatibility and efficiency of HCR with CLARITY and iDISCO+ in fresh-frozen rodent brain tissues and postmortem human brain blocks was previously tested (Kumar et al., 2021). An alternative for clearing methods is fluorescence tomography or confocal imaging (Guo et al., 2019; Duckhorn et al., 2021). For instance, combination of whole mount HCR with fluorescence tomography has been used for finding the exact location of *Cre* mRNA in a Thy1-Cre mouse brain (Guo et al., 2019).

4 CONCLUSION

Our aim was to report an optimized protocol for whole mount HCR v3.0 and its compatibility with IHC as well as a water-based tissue clearing method on octopus embryos for understanding neural anatomy and neurogenesis in 3D. We believe that the proposed experimental pipeline can be adapted to other model and non-model organisms. Also, HCR has a wide range of applications in various fields, such as in biomedical purposes. For instance, it can be used for studying development and creating developmental atlases for specific systems or for understanding diseases such as pathogen detection and behavior in chronic infections (Choi, Beck and Pierce, 2014; Bi, Yue and Zhang, 2017; Wu et al., 2021). Whole mount HCR provides a more precise 3D view compared to manual segmentation based solely on nuclear labeling. Our automated tool Easy_HCR can be used for automated probe pair design. Comparison of 4 different water-based clearing protocols should help the experimenter to pick the most robust method when performing whole mount HCR in combination with 3D imaging.

DATA AVAILABILITY STATEMENT

Easy_HCR is available on GitHub via https://github.com/SeuntjensLab/Easy_HCR. The original contributions presented in the study are included in the article/**Supplementary Material**, further inquiries can be directed to the corresponding author.

AUTHOR CONTRIBUTIONS

AE, RS, SM, and LMa performed the experiments. AE, RS, and SM analyzed and interpreted the data. ES supervised the study. AE and ES wrote the original draft of the manuscript. All authors contributed to review and editing.

FUNDING

AE and LMa were supported by Fonds Wetenschappelijk Onderzoek (FWO), Belgium; FR/11D4120N and SB/1S42720N, respectively. RS was supported by a fellowship in Stazione Zoologica Anton Dohrn, Italy. ES was supported by KU Leuven, Belgium (ID-N/20/007 and C14/21/065).

ACKNOWLEDGMENTS

The authors would like to thank Eduardo Almansa (Instituto Español de Oceanografía, Santa Cruz de Tenerife, Spain) for his support and supplying us with octopus eggs. We would like to thank Astrid Deryckere for helping us to initialize the study, and all members of the Seuntjens and Arckens labs for critical discussions.

SUPPLEMENTARY MATERIAL

The Supplementary Material for this article can be found online at: https://www.frontiersin.org/articles/10.3389/fphys.2022.882413/full#supplementary-material

REFERENCES

Albertin, C. B., Simakov, O., Mitros, T., Wang, Z. Y., Pungor, J. R., Edsinger-Gonzales, E., et al. (2015). The octopus Genome and the Evolution of Cephalopod Neural and Morphological Novelties. *Nature* 524 (7564), 220–224. doi:10.1038/nature14668

Amodio, P., and Fiorito, G. (2013). *Observational and Other Types of Learning in Octopus, Handbook of Behavioral Neuroscience*. R. Menzel, P. Benjamin (Eds.). Academic Press, 293–302. doi:10.1016/B978-0-12-415823-8.00023-X

Bi, S., Yue, S., and Zhang, S. (2017). Hybridization Chain Reaction: A Versatile Molecular Tool for Biosensing, Bioimaging, and Biomedicine. *Chem. Soc. Rev.* 46, 4281–4298. doi:10.1039/c7cs00055c

Bruce, H. S., Jerz, G., Kelly, S. R., McCarthy, J., Pomerantz, A., Senevirathne, G., et al. (2021). *Hybridization Chain Reaction (HCR)* in Situ *Protocol*. doi:10.17504/protocols.io.bunznvf6

Camacho, C., Coulouris, G., Avagyan, V., Ma, N., Papadopoulos, J., Bealer, K., et al. (2009). BLAST+: Architecture and Applications. *BMC Bioinforma.* 10, 421. doi:10.1186/1471-2105-10-421

Choi, H. M. T., Beck, V. A., and Pierce, N. A. (2014). Next-generation *In Situ* Hybridization Chain Reaction: Higher Gain, Lower Cost, Greater Durability. *ACS Nano* 8 (5), 4284–4294. doi:10.1021/nn405717p

Choi, H. M. T., Calvert, C. R., Husain, N., Huss, D., Barsi, J. C., Deverman, B. E., et al. (2016). Mapping a Multiplexed Zoo of mRNA Expression. *Dev. Camb.* 143 (19), 3632–3637. doi:10.1242/dev.140137

Choi, H. M. T., Schwarzkopf, M., Fornace, M. E., Acharya, A., Artavanis, G., Stegmaier, J., et al. (2018). Third-generation *In Situ* Hybridization Chain Reaction: Multiplexed, Quantitative, Sensitive, Versatile, Robust. *Dev. Camb.* 145 (12), 1–10. doi:10.1242/dev.165753

Costantini, I., Ghobril, J.-P., Di Giovanna, A. P., Mascaro, A. L. A., Silvestri, L., Müllenbroich, M. C., et al. (2015). A Versatile Clearing Agent for Multi-Modal Brain Imaging. *Sci. Rep.* 5, 1–9. doi:10.1038/srep09808

Dekkers, J. F., Alieva, M., Wellens, L. M., Ariese, H. C. R., Jamieson, P. R., Vonk, A. M., et al. (2019). High-resolution 3D Imaging of Fixed and Cleared Organoids. *Nat. Protoc.* 14 (6), 1756–1771. doi:10.1038/s41596-019-0160-8

Deryckere, A., Styfhals, R., Elagoz, A. M., Maes, G. E., and Seuntjens, E. (2021). Identification of Neural Progenitor Cells and Their Progeny Reveals Long Distance Migration in the Developing octopus Brain. *eLife* 10, 69161. doi:10.7554/eLife.69161

Deryckere, A., Styfhals, R., Vidal, E. A. G., Almansa, E., and Seuntjens, E. (2020). A Practical Staging Atlas to Study Embryonic Development of *Octopus vulgaris* under Controlled Laboratory Conditions. *BMC Dev. Biol.* 20 (1), 1–18. doi:10.1186/s12861-020-00212-6

Duckhorn, J. C., Junker, I., Ding, Y., and Shirangi, T. R. (2021). *Combined* in Situ *Hybridization Chain Reaction and Immunostaining to Visualize Gene Expression in Whole-Mount Drosophila Central Nervous Systems*. bioRxiv 2021.08.02.454831. doi:10.1101/2021.08.02.454831

Fiorito, G., Von Planta, C., and Scotto, P. (1990). Problem Solving Ability of *Octopus vulgaris* Lamarck (Mollusca, Cephalopoda). *Behav. Neural Biol.* 53 (2), 217–230. doi:10.1016/0163-1047(90)90441-8

Guo, W., Liu, X., Hu, Q., Huang, F., Li, N., Zhang, Q., et al. (2019). Whole-mount *In Situ* Hybridization of Mouse Brain to Precisely Locate mRNAs via Fluorescence Tomography. *J. Biophot.* 12 (4), e201800249–8. doi:10.1002/jbio.201800249

Jones, J., and Howat, W. J. (2020). Guidelines for the Optimization and Validation of *In Situ* Hybridization. *Methods Mol. Biol.* 2418, 3–17. doi:10.1007/978-1-0716-0623-0_1

Kim, B.-M., Kang, S., Ahn, D.-H., Jung, S.-H., Rhee, H., Yoo, J. S., et al. (2018). The Genome of Common Long-Arm octopus Octopus Minor. *GigaScience* 7 (11), 1–7. doi:10.1093/gigascience/giy119

Kramer, E. E., Steadman, P. E., Epp, J. R., Frankland, P. W., and Josselyn, S. A. (2018). Assessing Individual Neuronal Activity across the Intact Brain: Using Hybridization Chain Reaction (HCR) to DetectArcmRNA Localized to the Nucleus in Volumes of Cleared Brain Tissue. *Curr. Protoc. Neurosci.* 84 (1), e49. doi:10.1002/cpns.49

Kuehn, E., Clausen, D. S., Null, R. W., Metzger, B. M., Willis, A. D., and Özpolat, B. D. (2021). Segment Number Threshold Determines Juvenile Onset of Germline Cluster Expansion in Platynereis Dumerilii. *J. Exp. Zoology Part B Mol. Dev. Evol.bioRxiv,* 1–16. doi:10.1002/jez.b.2310016

Li, F., Bian, L., Ge, J., Han, F., Liu, Z., Li, X., et al. (2020). Chromosome-level Genome Assembly of the East Asian Common octopus (Octopus Sinensis) Using PacBio Sequencing and Hi-C Technology. *Mol. Ecol. Resour.* 20 (6), 1572–1582. doi:10.1111/1755-0998.13216

Lin, R., Feng, Q., Li, P., Zhou, P., Wang, R., Liu, Z., et al. (2018). A Hybridization-Chain-Reaction-Based Method for Amplifying Immunosignals. *Nat. Methods* 15 (4), 275–278. doi:10.1038/nmeth.4611

Marquis, V. F. (1989). Die Embryonalentwicklung des Nervensystem von *Octopus vulgaris* Lam. (Cephalopoda, Octopoda), eine histologische Analyse. *Verhandl. Naturf. Ges. Basel.* 99 (1), 23

Naef, A. (1928). "Die Cephalopoden. Embryologie. *Fauna Flora Golf Neapel*, 35, 1–357. English translation by Boletzky, S.V., 2001. The Cephalopoda-Embryology. Smithsonian Institution Press, Washington, District of Columbia, USA.

Nguyen, M. (2017). *Optimization of Whole Brain Clearing Techniques for the Molecular Investigation of Arc*. Arizona: University of Arizona.

Pende, M., Vadiwala, K., Schmidbaur, H., Stockinger, A. W., Murawala, P., Saghafi, S., et al. (2020). A Versatile Depigmentation, Clearing, and Labeling Method for Exploring Nervous System Diversity. *Sci. Adv.* 6 (22), 365. doi:10.1126/sciadv.aba0365

Richardson, D. S., and Lichtman, J. W. (2015). Clarifying Tissue Clearing. *Cell.* 162, 246–257. doi:10.1016/j.cell.2015.06.067

Sanchez, P. G., and Miyazawa, H.Instruments, Molecular. (2019). *Hybridization Chain Reaction (HCR) Protocol for Tails of Mouse Embryos*. doi:10.17504/protocols.io.7pyhmpw

Santi, P. A. (2011). Light Sheet Fluorescence Microscopy. *J. Histochem Cytochem.* 59, 129–138. doi:10.1369/0022155410394857

Schwarzkopf, M., Liu, M. C., Schulte, S. J., Ives, R., Husain, N., Choi, H. M. T., et al. (2021). Hybridization Chain Reaction Enables a Unified Approach to Multiplexed, Quantitative, High-Resolution Immunohistochemistry and *In Situ* Hybridization. *Development*, 148, 148. doi:10.1242/DEV.199847

Shah, S., Lubeck, E., Schwarzkopf, M., He, T.-f., Greenbaum, A., Sohn, C. h., et al. (2016). Single-molecule RNA Detection at Depth via Hybridization Chain Reaction and Tissue Hydrogel Embedding and Clearing. *Dev. Camb.* 143 (15), 8560. doi:10.1242/dev.138560

Styfhals, R., Zolotarov, G., Hulselmans, G., Spanier, K. I., Poovathingal, S., Elagoz, A. M., et al. (2022). *Cell Type Diversity in a Developing octopus Brain*. bioRxiv, 1–34. doi:10.1101/2022.01.24.477459

Vianello, S., Park, J., and Lutolf, M. (2021). *Hybridization Chain Reaction (HCR) Protocol for Gastruloids (ESC Aggregates)*. doi:10.17504/protocols.io.bcwfixbn

Wu, J., Lv, J., Zheng, X., and Wu, Z.-S. (2021). Hybridization Chain Reaction and its Applications in Biosensing. *Talanta* 234, 122637. doi:10.1016/j.talanta.2021.122637

Young, J. Z. (1971). *The Anatomy of the Nervous System of* Octopus vulgaris. Oxford, UK: Clarendon Press.

Young, J. Z. (1983). The Distributed Tactile Memory System of Octopus. *Proc. R. Soc. Lond. Ser. B. Biol. Sci.* 218 (1211), 135

Zarrella, I., Herten, K., Meas, G. E., Tai, S., Yang, M., and Seuntjens, E. (2019). The Survey and Reference Assisted Assembly of the *Octopus vulgaris* Genome. *Scientific Data* 6(1), 1–8.

Conflict of Interest: The authors declare that the research was conducted in the absence of any commercial or financial relationships that could be construed as a potential conflict of interest.

Publisher's Note: All claims expressed in this article are solely those of the authors and do not necessarily represent those of their affiliated organizations, or those of the publisher, the editors and the reviewers. Any product that may be evaluated in this article, or claim that may be made by its manufacturer, is not guaranteed or endorsed by the publisher.

frontiers | Frontiers in Physiology

TYPE Review
PUBLISHED 09 September 2022
DOI 10.3389/fphys.2022.928013

OPEN ACCESS

EDITED BY
Fernando Ariel Genta,
Oswaldo Cruz Foundation (Fiocruz), Brazil

REVIEWED BY
Pedro M. Costa,
New University of Lisbon, Portugal
Susana Camarillo-Coop,
Universidad Juárez Autónoma de Tabasco, Mexico

*CORRESPONDENCE
Paul L. R. Andrews,
pandrews@sgul.ac.uk

SPECIALTY SECTION
This article was submitted to Invertebrate Physiology, a section of the journal Frontiers in Physiology

RECEIVED 25 April 2022
ACCEPTED 01 August 2022
PUBLISHED 09 September 2022

CITATION
Andrews PLR, Ponte G and Rosas C (2022), Methodological considerations in studying digestive system physiology in octopus: limitations, lacunae and lessons learnt.
Front. Physiol. 13:928013.
doi: 10.3389/fphys.2022.928013

Methodological considerations in studying digestive system physiology in octopus: limitations, lacunae and lessons learnt

Paul L. R. Andrews[1]*, Giovanna Ponte[1] and Carlos Rosas[2]

[1]Department of Biology and Evolution of Marine Organisms, Stazione Zoologica Anton Dohrn, Naples, Italy, [2]Unidad Multidisciplinaria de Docencia e Investigación, Facultad de Ciencias, Universidad Nacional Autónoma de México, Sisal, Yucatán, Mexico

Current understanding of cephalopod digestive tract physiology is based on relatively "old" literature and a "mosaic of data" from multiple species. To provide a background to the discussion of methodologies for investigating physiology we first review the anatomy of the cephalopod digestive tract with a focus on *Octopus vulgaris*, highlighting structure-function relationships and species differences with potential functional consequences (e.g., absence of a crop in cuttlefish and squid; presence of a caecal sac in squid). We caution about extrapolation of data on the digestive system physiology from one cephalopod species to another because of the anatomical differences. The contribution of anatomical and histological techniques (e.g., digestive enzyme histochemistry and neurotransmitter immunohistochemistry) to understanding physiological processes is discussed. For each major digestive tract function we briefly review current knowledge, and then discuss techniques and their limitations for the following parameters: *1*) Measuring motility *in vitro* (e.g., spatiotemporal mapping, tension and pressure), *in vivo* (labelled food, high resolution ultrasound) and aspects of pharmacology; *2*) Measuring food ingestion and the time course of digestion with an emphasis on understanding enzyme function in each gut region with respect to time; *3*) Assessing transepithelial transport of nutrients; *4*) Measuring the energetic cost of food processing, impact of environmental temperature and metabolic rate (flow-through/intermittent respirometry); *4*) Investigating neural (brain, gastric ganglion, enteric) and endocrine control processes with an emphasis on application of molecular techniques to identify receptors and their ligands. A number of major knowledge lacunae are identified where available techniques need to be applied to cephalopods, these include: *1*) What is the physiological function of the caecal leaflets and intestinal typhlosoles in octopus? *2*) What role does the transepithelial transport in the caecum and intestine play in ion, water and nutrient transport? *3*) What information is signalled from the digestive tract to the brain regarding the food ingested and the progress of digestion? It is hoped that by combining discussion of the physiology of the cephalopod digestive system with an overview of techniques and identification of key knowledge gaps that this will encourage a more systematic approach to research in this area.

KEYWORDS

octopus, digestive tract, digestive gland, motility, digestion, secretion, welfare, Directive 2010/63/EU

Introduction

The digestive system (DS) in cephalopods includes an epithelium-lined muscular tract (DT), and glands (salivary glands and digestive gland [DG]± appendages). The DS physically and chemically degrades food, absorbs nutrients and processes them for metabolism. The DG has a major role in detoxification of ingested potential toxins (e.g., domoic acid, metals) but the "barrier function" of the epithelium also contributes to defence of the organism. The DS is also responsible for excretion of waste products (faeces, including mucus and sloughed epithelial cells) and voiding of undigested and indigestible matter (i.e. faeces, vomit).

Studying the physiology of the cephalopod DS can be justified from a pure science perspective, particularly contributing to comparative and evolutionary studies. For example, comparison with fish as the main predators of cephalopods in the same ecological niches has been considered mainly from a brain evolution perspective (e.g., Ponte et al., 2021), but this should be broadened to include the DS which processes food to "fuel" brain tissue. In "Cephalopods and fish: The limits of convergence," Packard (1972) commented on similarities in relation to the caecum but other comparisons between fish and cephalopod digestive tracts are unexplored. There are also applied research justifications to consider: *1*) Optimising diets at all life stages in aquaculture; *2*) Understanding the consequences of dietary change in the wild; *3*) Understanding adaptations to environmental change; *4*) Assessing the impact of ingestion of plastics and other contaminants on the digestive tract, health and welfare; *5*) Animal welfare in the laboratory, public display and aquaculture (*see* Sykes et al., 2017, for detailed discussion).

This review considers techniques used to study the physiological processes underlying key functions of the digestive system in cephalopods with a particular focus on octopuses as these have been the subject of most recent studies.

To provide a background we briefly describe the range of food eaten by cephalopods and then the anatomy of the cephalopod DT highlighting major species differences.

The range of substances ingested: challenges for the digestive system

Villanueva et al. (2017) commented that food sources ranged from "detritus to birds." All cephalopods are carnivorous with cephalopods, fish, gastropods and crustacea amongst the most common foods depending upon the species and habitat. Chemically, the diet is dominated by proteins and lipids. However, field studies have widened the range of food types to include for example, gelatinous fauna by the giant deep-sea octopus (*Haliphron atlanticus*, Hoving and Haddock, 2017) and various types of detritus (e.g., faecal pellets, gelatinous zooplankton) by vampire squid (*Vampyroteuthis infernalis*, Hoving and Robison, 2012).

The digestive system also deals with non-prey items. Examples include, microplastics in the water, adherent to, or ingested by the prey. Evidence for microplastic ingestion has been published for wild and cultured cuttlefish (*Sepia officinalis*, Oliveira et al., 2020), common octopus (*Octopus vulgaris*, Pedà et al., 2022), jumbo squid (*Dosidicus gigas*: Braid et al., 2012; Rosas-Luis, 2016), vampire and mid-water squid (*V. infernalis* and *Abralia veranyi*, Ferreira et al., 2022). Although no adverse effects are reported, the potential for harm, particularly from obstruction of the ducts linking the caecum and digestive gland is considerable (for discussion *see* Oliveira et al., 2020). Plant matter (e.g., seaweed, bull kelp, eelgrass) has been found in the cephalopod digestive tract (Boucaud-Camou and Boucher-Rodoni, 1983; Braid et al., 2012). In theory, non-prey items could be digested by enzymes, ejected unchanged by defaecation or vomiting/regurgitation or remain in the tract where, if accumulated, they could cause an obstruction.

Food ingestion will be accompanied by seawater, potentially containing dissolved or suspended chemical contaminants. The first report of metals in the cephalopod DG was in 1975 (Martin and Flegal, 1975; Bustamante et al., 1998) with high levels of cadmium, copper, iron, silver and zinc in *Loligo opalescens*, *Ommastrephes bartrami*, and *Sthenoteuthis oualaniensis*. The metal concentrations were considered sufficient to be toxic. Bustamante et al. (2006) reviewed the DG and muscle mercury content in 20 cephalopod species concluding that the DG did not store mercury, but demethylated it allowing accumulation in organic form in muscle. Rodrigo and Costa (2017) identified the DG as the main metal accumulation organ and concluded that metallothionines were not the only detoxification mechanism with spherulae (high MWt. protein and metal association) chelating metals (*see* also, Bustamante et al., 2006). B-esterases have recently been implicated in metabolism of plastic additives in the DG of *O. vulgaris* and *S. officinalis* (Omedes et al., 2022).

The biochemical pathways involved in processing metals and other potentially toxic chemicals (e.g., domoic acid) in the DG, their subsequent distribution to other tissues (e.g., brain, muscle) and the functional consequences (e.g., impaired metabolism, modified neuronal function) require further study, especially considering the important role of cephalopods in the marine ecosystems.

TABLE 1 Selected key publications that include detailed descriptions of the anatomy and histology of the digestive system and its innervation in a range of cephalopod species.

Species	Comment	References
Gross anatomy of the digestive system in adults		
Loligo vulgaris, Loligo forbesii, Alloteuthis media, Alloteuthis subulata	Detailed description of *Loligo vulagris* and comments on other species. Summary of pre-1930s literature	Bidder (1950)
Loligo vulgaris	Monograph on the common squid including description of the digestive system and feeding	Williams (1909)
Eledone cirrhosa	Monograph with very detailed diagrams of the digestive system	Isgrove (1909)
Octopus vulgaris, Abralia trigonura, Loligo vulgaris, Vampyroteuthis infernalis	Diagrams of gross anatomy and a tabulated comparison of digestive organs between Nautloidoea and several species of Coleoidea	Mangold and Young (1998)
Todarodes pacificus, Loligo bleekeri, Loligo edulis, Watasenia scintillans, Sepia lycidas, Euprymna morsei	Diagrams of gross anatomy of six Decapodiform cephalopods and data on some organ weights	Omura and Endo (2016)
Octopus americanus	Diagram and brief description of digestive tract	Avendaño et al. (2020)
Nautilus pompilius	Original description of external and internal anatomy of Nautilus	Owen (1832)
		Westermann and Schipp (1998b), also comments on *Nautilus macromphalus*
Sepia officinalis	Monograph with very detailed diagrams of the digestive system	Tompsett (1939)
Enteroctopus megalocyathus	Basic description and photograph of digestive tract	Garri and Lauria de Cidre (2013)
Cirrothauma	Diagram and description of digestive tract in a finned octopod	Aldred et al. (1983)
Sepia officinalis, Octopus vulgaris, Loligo vulgaris	General description of anatomy and importantly a photograph of the tract in each species	Guerra (2019)
Gross anatomy of the digestive system in paralarvae		
Octopus vulgaris	3D reconstruction during the first month of life and also data on embryos	Fernández-Gago et al. (2017)
Octopus vulgaris	Detailed colour images of the digestive tract in live feeding paralarvae taking advantage of their transparency at this life stage	Nande et al. (2017)
Histology of the digestive tract		
Enteroctopus megalocyathus	Sections of several regions but particularly the caecum	Garri and Lauria de Cidre (2013)
Octopus vulgaris	Haematoxylin & Eosin stained section of several regions	Emam et al. (2016)
Nautilus pompilius on *Nautilus macromphalus*	Sections from all main regions and also scanning electron microscopy of caecum	Westermann and Schipp (1998b)
Octopus vulgaris	Detailed survey of all regions of the digestive tract	Fernández-Gago et al. (2019)
Octopus vulgaris	Detailed survey of all regions of the digestive tract	Anadón (2019)
Loligo vulgaris, Loligo forbesii, Alloteuthis media, Alloteuthis subulata	Histology of epithelium in oesophagus stomach and caecum and diagrammatic reconstructions of caecal wall	Bidder (1950)
Eledone cirrosa Illex illecebrosus	Study of histological changes occurring during the course of digestion	Boucher-Rodoni (1976)
Histopathology of the digestive tract		
Octopus vulgaris	Histopathology changes in the caecum and intestine caused by *Aggregata octopiana*	Gestal et al. (2002)
Multiple species	Comprehensive review of pathogens and diseases including those affecting the digestive tract	Gestal et al. (2019)
Histology of digestive gland (DG)		
Octopus vulgaris		Rodrigo and Costa (2017)
		Fernández-Gago et al. (2019)
Enteroctopus mergalocythus		Garri and Lauria de Cidre (2013)
Sepia officinalis		Costa et al. (2014)
Nautilus pompilius L. and Nautilus macromphalus		Ruth et al. (1999)
Euprymna tasmanica (dumpling squid)	Investigation of potential lipid storage in DG.	Moltschaniwskyj and Johnston (2006)
Enzyme and mucus histochemistry		
Octopus vulgaris	Detailed survey of mucus and granule secreting cells in all regions of the tract	Fernández-Gago et al. (2019)

(Continued on following page)

TABLE 1 (*Continued*) Selected key publications that include detailed descriptions of the anatomy and histology of the digestive system and its innervation in a range of cephalopod species.

Species	Comment	References
Innervation of the digestive system		
Eledone cirrhosa	Detailed diagrams of the gastric ganglion and associated nerves	Isgrove (1909)
Octopus vulgaris	Detailed description of the extrinsic (visceral and sympathetic) innervation	Young (1967; 1971)
	Molecular study of the neurochemistry of the gastric ganglion	Baldascino et al. (2017)
Sepia officinalis	Focus on the nerve plexuses within the wall of the digestive tract	Alexandrowicz (1928)

Sea water drinking occurs in marine teleosts and elasmobranchs and is an important component of fluid and ionic homeostasis (for review *see*: Grosell, 2010; Takei, 2021). Haemolymph osmolarity measured in *O. vulgaris, O. insularis* and *O. ocellatus* ranged from ~940 to ~1170 mOsm/kg (Amado et al., 2015; Sakamoto et al., 2015) so is slightly hypo-osmotic or iso-osmotic with sea water. The values are comparable to marine osmoconforming fish but considerably higher than the osmoregulating teleosts (Takei, 2021). Wells and Wells (1989; 1993) investigated water uptake in *O. vulgaris* and concluded that the digestive gland appendage ("pancreas") is one site of fluid and ion transport. Of relevance to this is the finding in squid (*L. vulgaris*) and cuttlefish (*S. officinalis*) hatchlings (Hu et al., 2010) that the appendage shows Na^+/K^+ ATPase immunoreactivity; this is significant as this ion exchange pump is responsible for generating the local osmotic gradient in the lateral intercellular spaces responses for transepithelial water transport but there are no physiological studies of fluid/ionic transport in cephalopod gut. Wells and Wells (1989, p. 219) describe rectal ingestion of sea water in *O. vulgaris* and Mangold and Young (1998) include "intake of seawater" in their list of intestinal functions in cephalopods. Furthermore, Bidder (1950) reports that water is drawn into the intestine of "larval" *L. vulgaris* and that this may occur in adults monitored by the processes of specialised rectal cells and involving the anal leaflets. These latter observations require investigation using modern physiological techniques.

A brief introduction to the anatomy of the cephalopod digestive system: implications for physiology

The structure and function of organs is related. As a background, we briefly describe the anatomy of the digestive tract in *O. vulgaris*, highlighting poorly understood aspects in relation to function and then discuss the main anatomical differences from other cephalopods to emphasise the necessity to study a variety of species.

Table 1 summarises publications describing the gross anatomy of the digestive system in a range of cephalopod species and also provides references to specific topics of relevance to understanding physiology.

The anatomy of the digestive tract in *O. vulgaris*: relationships to physiology

The buccal mass comprising the beak, radula and associated muscles is the point at which food enters the body with the size of the bolus determined by the gape of the beak and the bite force. The food is mixed with secretions from the anterior and posterior salivary glands which contain digestive enzymes but also in the case of the posterior glands toxins used to subdue or kill prey (*see* below for details and Ponte and Modica, 2017).

From the buccal mass, pieces of food are propelled along the cuticle lined oesophagus which passes between the sub- and supra-oesophageal lobes of the brain linked by the connectives. The distensibility of the oesophagus and the encircling brain tissue will limit the bolus size together with the compressibility of the food by the oesophageal muscle which in its proximal part has functional characteristics of striated muscle (Andrews and Tansey, 1983a).

Following passage along the oesophagus, the bolus enters the crop with very limited evidence for a sphincter between the two structures (for details *see* Sykes et al., 2020). Diagrams of the digestive tract in *O. vulgaris* (*see* Figure 1) sometimes show a bridge of tissue linking each posterior salivary gland to the anterior crop and this can also be seen in published pictures (for *O. vulgaris see* fig. 1 in Baldascino et al., 2017; for *O. americanus see* fig. 3 in Avendaño et al., 2020). Although this structure appears like a duct transporting salivary secretions into the crop, this has not been demonstrated (G. Ponte and P.L.R. Andrews, unpublished observations). Studies of this structure should be undertaken in paralarvae to investigate patency as the structure in adults may be vestigial. Another possibility is that the connexion serves to hold the salivary glands in position as the crop fills.

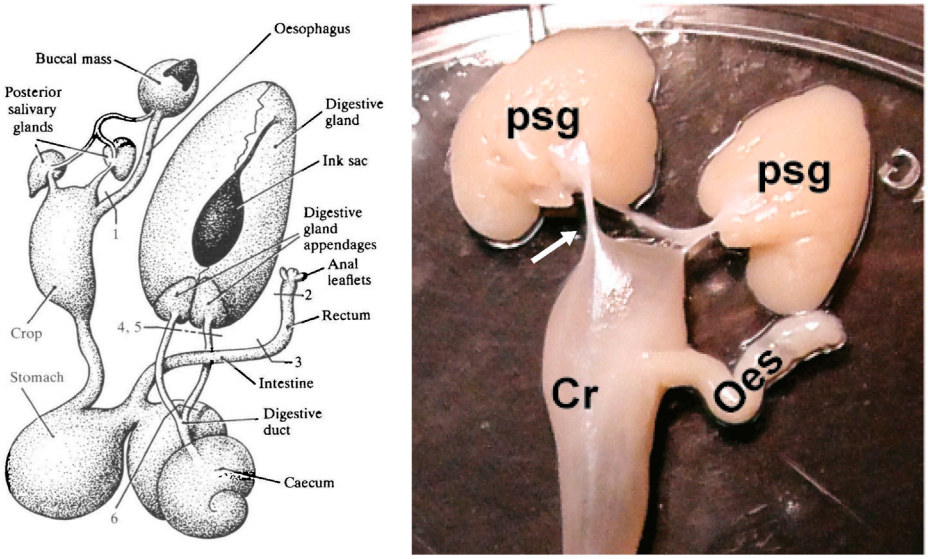

FIGURE 1
The diagram on the left shows the digestive tract of *Octopus vulgaris*. Note that the posterior salivary glands are connected to the buccal mass by a duct which delivers saliva containing digestive enzymes and toxins for injection into prey and each gland is also connected to the crop by a duct-like structure (*see* text for discussion). The labelling of the original is retained with the numbers indicating sites at which the tract was lesioned/ligated for studies of water uptake. Reproduced from Wells and Wells, 1989, p.217 with permission from The Company of Biologists, Cambridge, United Kingdom. The photograph on the right is taken from Baldascino et al., 2017 (Figure 1) and shows the posterior salivary glands (psg) in *Octopus vulgaris* and the connections (arrowed only on the left) to the anterior crop (Cr). The oesophagus (oes) detached from the buccal mass is also visible.

When distended with food, the crop can be seen to have a more distensible anterior half (*see* Figure 2) which accommodates ~75% of the content and a narrower posterior part connecting to the gastric vestibule (Andrews and Tansey, 1983a) with no strong evidence for a sphincter. The gastric vestibule is one of two thin layers of muscle holding the two thick muscle blocks closely apposed and responsible for the movement of one thick block against the other. The stomach has a relatively thick cuticle lining. The anatomical similarity of the stomach in octopus (and to a lesser extent cuttlefish) to that of the koilen-lined "gizzard" present in some species of bird was first noted by Aristotle (1910). The gastric vestibule connects with both the spiral caecum and the intestine with evidence for sphincters between these structures lacking. The major enzymes responsible for digestion (*see* below) originate in the digestive gland, are passed into the caecum (DG ducts) from where they can enter the gastric vestibule to contact the food. The capacity of the stomach in octopus is small in relation to the crop so only relatively small boluses of food can enter for trituration while enzymes continue to act and then the partially digested food progresses to the either caecum or intestine. Alternatively, the crop and stomach may act as a single functional unit with food interchanged between the "hopper" (crop) and "mill" (stomach) until it is physically and chemically degraded and is passed to the caecum or intestine. Currently, there is no definitive evidence to decide between the two, not incompatible, options. The common cavity between the crop, stomach, caecum and intestine means that contents can readily interchange depending upon the intraluminal pressure gradient generated by the muscles in each region.

In *O. vulgaris*, the oesophagus, crop and particularly the stomach are all lined with a cuticle. The cuticle protects the underlying epithelium against abrasion by ingested prey (e.g., crab carapace and limbs, fish bones) and in the stomach provides a surface for trituration. The presence of a continuous, variable thickness, layer of cuticle makes it highly unlikely that the oesophagus, crop or stomach has an absorptive function. However, it should be noted that limited evidence has been provided for uptake of radio-labelled glycine/leucine by the crop in *Nautilus pompilius* (Westermann and Schipp, 1998a) and *O. vulgaris* (Wells, 1978) but uptake into the epithelium does not provide evidence for transepithelial transport.

The caecum is a thin-walled muscular tube, coiled into about two and a half turns forming a cone and lined with lamellae which will increase the surface area. It is stated that the caecum filters food from the stomach "discarding gross particles that pass directly to the intestine" (Anadón, 2019, p. 4). Whilst this is a likely function, together with the addition of mucus to begin formation of faecal ropes, there are no direct studies in octopus demonstrating this but studies of the caecum in squid (Bidder, 1950) are supportive. Additionally, cilia have been to proposed to be responsible for the movement of "fine particles in suspension"

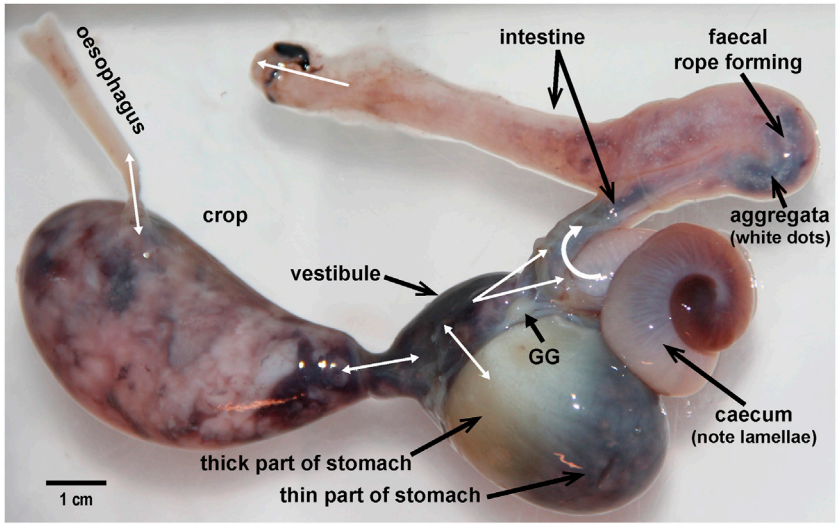

FIGURE 2
The digestive tract removed from an *Octopus vulgaris* weighing 900 g. The main anatomical regions are labelled including the gastric ganglion (GG). Double headed white arrows indicate the potential for bi-directional exchange of material due the existence of a common cavity. For the anal opening although only unidirectional flow (defaecation) is indicated there is some evidence for the entry of sea water *via* this route (*see* text for discussion). Note the "teardrop" shape of the crop distended with food (primarily an octopus arm), the relatively thin and thick parts of the stomach, the caecal lamellae visible through the thin wall, the presence of aggregata in the intestine, and the location of the GG with nerve radiating to adjacent structures.

from the caecum into the digestive gland (Fernández-Gago et al., 2019, p. 331) but no studies have investigated the relative roles of the cilia, caecal muscle constricting the cone or DG duct peristalsis in this process. The large surface area of the caecum is also consistent with an absorptive function, but Fernández-Gago et al. (2019, p. 331) concluded that in *O. vulgaris* that there was "no clear evidence for absorption in the caecum" although Boucaud-Camou et al. (1976) considered it was involved in absorption as is also the case in *N. pompilius* (Westermann and Schipp, 1998b). In the squid the caecum/caecal sac is proposed to have a major role in absorption (Boucher-Rodoni and Mangold, 1977; Boucaud-Camou and Boucher-Rodoni, 1983). Published studies used uptake of radiolabelled molecules by the epithelium or the presence of lipid containing vesicles in the epithelium but have not demonstrated transepithelial transport into the haemolymph from the caecum and this is therefore a major knowledge gap.

The control of the directionality of movement of contents between the common cavities of the crop, stomach and vestibule, caecum (and hence the DG duct) and proximal intestine has not been investigated. Evidence for the presence of sphincters is inconclusive or absent in octopus although there may be a flap-valve between the caecum and the digestive gland duct at the tip of the columella (Budelmann et al., 1997; *see* figure 64A, p. 197) and a thickening of circular muscle at the exit of the ink duct and anus is consistent with it acting as a sphincter (Young, 1967).

The tubular intestine shows little external variation in octopus throughout its course from the stomach vestibule/caecal junction to the anal opening, but turns anteriorly in the middle of its course. Internally, the mucosa has longitudinal folds, two of which on opposite sides are larger forming a "typhlosole" in the proximal intestine. It is assumed that the function of the typhlosole is to increase surface area and whilst this is a logical assumption the question of the reason why a surface area increase is required has not been answered; usually this is to facilitate absorption but it could also be related to secretory capacity (e.g., mucus). It is reported that the epithelium of the typhlosoles is ciliated but that of adjacent intestinal epithelial tissue has a luminal border with microvilli (Anadón, 2019; Fernández-Gago et al., 2019) suggesting a differentiation of function. Ciliary motion would be capable of moving mucus with trapped particles so investigation of the direction of ciliary beating in fresh specimens would be of particular interest. The function of the typhlosoles is not established, but constriction of the circular muscle would lead to the division of the lumen into two channels by apposition of the typhlosoles. A further issue regarding intestinal function in octopus is the extent to which it is involved in transepithelial transport of nutrients, ions and water which has not been investigated directly. In *Loligo* limited evidence was presented by Bidder (1950) for some absorption in the intestine while caecal absorption is in progress noting that the intestine may have a more major role when the gonads enlarge, limiting filling of the caecal sac. The capacity to absorb

nutrients from contents bypassing the caecum/digestive gland but which have been exposed to digestive enzymes would be an advantage, as would involvement in water and ion homeostasis.

The anal opening in *O. vulgaris* has paired muscular anal flaps or wings. Their absence in species lacking an ink sac suggests involvement in inking rather than a digestive tract function but further investigation is required. The flaps are innervated by the atrio-rectal nerve branch of the visceral nerve and Young (1967, figure 18, p. 9) noted the presence of a plexus of fine fibres in the flap commenting "perhaps afferent."

The faeces are formed as mucus coated ropes but their composition has not been studied in any detail and the mechanisms, presumed to be neural, controlling of defaecation are unknown (*see* Ponte et al., 2017 for discussion).

Toxin secretion by the salivary glands: a cornucopia

The toxicity of the exocrine secretions from the posterior salivary glands of *O. vulgaris* was first noted by Lo Bianco working at the Stazione Zoologica Naples, in the early C19th but the toxic fraction was not identified until 1959 (Ghiretti, 1959). Two main constituents were identified with differing biological effects on crabs; amines inducing hyperexcitability and cephalotoxin, lethality. Cephalotoxin is a glycoprotein now known to occur in α and β forms (Cariello and Zanetti, 1977). The current view is that the saliva is a chemical cocktail including tachykinins (i.e. Eledoisin from *Eledone*, Erspamer and Anastasi, 1962), OctTK 1, phospholipase A2, other proteins, and enzymes (e.g., peptidase, hyaluronidase, chitinase) that also play key roles in toxicity of coleoid venom, supplemented by other small organic molecules, peptides, and non-enzymatic proteins (for review *see*: Ruder et al., 2013; Gonçalves and Costa, 2021).

Analysis of the phylogenetic history and molecular evolution of coleoid venom shows comparable diversity and complexity with those found in snakes (Ruder et al., 2013) with evidence of active evolution of some constituents (e.g., cysteine-rich pacifastin and kallikrein). Characterization of the molecular structure and composition of cephalotoxins is still incomplete (maybe except for *Sepia esculenta* cephalotoxin, Ueda et al., 2008). Apart from the glycosylation of the protein, characterization allowed the identification of conserved domains: EGF-like, Sushi, TSP type-1 and LDL-receptor class A (review in Gonçalves and Costa, 2021). Of particular interest is the epidermal growth factor (EGF) domain known to paralyse crustaceans *via* Na_v block; cephalotoxins, should be described as EGF neurotoxins. The increasing availability of cephalopod genomes has provided insights about tissue-specific genes expressed in the posterior salivary gland of three cephalopod species (non-tetrodotoxin-bearing octopods vs. tetrodotoxin in *Hapalochlaena maculosa*; Whitelaw et al., 2020).

Although cephalopod salivary gland research is focused on the nature of the toxins and their biological effects little is known about the physiological mechanisms involved in their secretion, how the ratio of the various constituents is determined, and the neural control of secretion together with the transport of saliva along the ducts. The discrete nature of the salivary glands makes them suitable for *in vitro* studies of intact glands and subsequently isolated cells comparable to those applied to mammalian salivary glands.

Major anatomical differences in the digestive system between species: physiological implications

Knowledge of the physiological consequences of structural similarities and differences in the digestive tract between species ("functional morphology," Mangold and Young, 1998) is essential to understanding how the animal adapts to its ecological niche. Mangold and Young (1998) and Voss (1988) utilised digestive tract morphology for systematics and revealing phylogenetic relationships. A recent review of the structure and function of the digestive system in molluscs makes more general comparisons (Lobo-da-Cunha, 2019).

Crop

The crop is present in Nautiloidea, Vampyromorpha and in most Octopoda but may be reduced or absent in some cirrates (e.g., *Cirrothauma*, Aldred et al., 1983) with Voss (1988) proposing that this is related to a diet of small, soft-bodied prey. Naef (1928) includes a crop in their diagram of a "primitive hypothetical cephalopod." The crop is absent in Sepiodea and Teuthoidea; molecular techniques should be able to identify the gene(s) responsible. As the primary function of the crop is storage, its absence in Sepiodea and Teuthoidea arguably limits their ability to optimise feeding opportunities unless the stomach is adapted to compensate by being more sacculated and distensible than the stomach in Octopoda.

Caecum

A caecum of variable complexity is present in Nautiloidea and Coleoidea but a caecal sac is only present in Teuthoidea and even then, not all Oegopsida (Mangold and Young, 1998) although the functional implications are unknown. The complexity of lamellae in the caecum is less in cuttlefish compared to octopus and squid (Anadón, 2019).

Sphincters

In contrast to the poor evidence for structures (sphincters or valves) in the octopus DT there are more detailed descriptions in *L. vulgaris*. Williams (1909) describes a "very remarkable five-way valve" (p. 36) between the caecum and neighbouring cavities of the gut and also

sphincters at the openings from the oesophagus and the stomach. Attached to the caecal wall, Bidder (1950) describes a solid valve structure reinforced by cartilage with an innervated "sphincter-like" muscle surrounding its edge and capable of regulating the passage of fluid into, or out of, the caecum at various phases of digestion. Additionally, the sac-like posterior caecum can be separated from the more complex anterior portion (appendix, ciliated organ accessible by the digestive gland and intestine) by a "diaphragm-like" sphincter (Bidder, 1950).

Intestine

Regarding the intestine, the principle difference visible externally is the presence of coils or loops (Mangold and Young, 1998) occurring approximately half-way between the junction with the caecum and anal opening. These are present in Sepioidea, Nautiloidea and Octopoda although variably in the Cirrata (e.g., absent in *Cirrothauma*; Aldred et al., 1983) and absent in Teuthoidea and Vampyromorpha. In species with loops and coils the overall intestinal length will be relatively longer in relation to body size but we do not know if the proportions of intestine, rectum and anal regions differs. Loops and coils in the intestine increase the overall luminal surface area for absorption so may indicate differing absorptive capacity. Coiling also increases the relative length of the intestine in relation to body size and potentially the time that digesta spends in the digestive tract, but formal studies supporting this hypothesis are lacking. There have been no comparisons of the coiled area with adjacent regions to investigate structural specialisations and there is insufficient data to identify potential relationships between food type, morphological differences in other structures (e.g., ± crop, ±caecal sac) and intestinal complexity. Internal differences in the intestine have not been reported systematically but transverse septa are present in the proximal intestine of *Nautilus* (Budelmann et al., 1997) but not octopus and the typhlosole is more complex in *Nautilus*.

The above brief descriptions are from a relatively limited number of species but demonstrate that that it would be unwise to extrapolate data on physiology of the digestive tract from one species to another.

Techniques for the study of digestive tract anatomy relevant to physiology

Descriptive morbid anatomy

Post mortem dissection of fresh specimens is the classical method for describing the gross anatomy. In fresh specimens, it is possible to view and measure the distribution of contents and classify their nature, i.e. liquid, solid and colour (Figure 2); note a description of changes in squid stomach contents with time in Wallace et al. (1981) and Boucher-Rodoni (1976) for caecal contents in *Eledone cirrhosa*. Care should be taken in interpretation as the method of killing may modify digestive tract motility (e.g., brain destruction will stimulate neurones; magnesium chloride relaxes smooth muscle; Bacq, 1934) and contractions may occur *post mortem* redistributing contents, particularly liquids. Guidance on dissection techniques is given in Øresand and Oxby's (2021) illustrated guide to the dissection of the bobtail squid, *Sepietta oweniana* and by Guerra (2019) for several species.

Useful data can also be obtained from dissection of fixed specimens but distortion can occur and fixation of entire (larger) animals is a challenge. Freezing intact animals immediately *post mortem* preserves the tissue and maintains anatomical relationships.

Quantitative anatomy

Gross dissection provides largely descriptive, qualitative information on the morphology of the digestive system enabling comparison between species (*see* above). However, quantification of the wet weight of identified tissues provides data enabling further differentiation of species, assessment of the impact of different diets (e.g., natural vs. prepared/synthetic/elaborated) and investigation of potential correlations with environmental changes.

Most DS organ weight data is available for the DG; for example: six decapodiform cephalopods (Omura and Endo, 2016), *O. vulgaris* (García-Garrido et al., 2010; Bastos et al., 2020), *Octopus maya* and *Octopus mimus* (Linares et al., 2015; Pascual et al., 2019) with more limited data for the stomach and caecum (e.g., Omura and Endo, 2016). Detailed analysis of digestive gland weights has shown changes in the weight of the digestive gland in O. *maya* with season and location (Pascual et al., 2019).

Ideally, data on dry weight should also be obtained to differentiate between increase tissue mass compared to increased water content which may be pathophysiological (e.g., oedema).

Imaging techniques

Dissection is a destructive process so should only be used when there are no other methods available. For example, high-field magnetic resonance imaging and micro-computed tomography have been used for external and internal taxonomic description of a preserved specimen of a novel species of dumbo octopus (*Grimpoteuthis imperator*, Ziegler and Sagorny, 2021). The resolution of the digestive system was sufficient to identify all key features (e.g., presence of crop and "pancreatic" portion of the DG, paired hepatic ducts) and also to note that there was only a single posterior

salivary gland and the anal flaps were absent (as was the ink sac). Importantly, collection of this type of imaging data enables construction of 3D models of the viscera so that the relationships of structures can be readily examined. High resolution ultrasound can also be used to image tissue in preserved animals but it has particular utility for anatomical and physiological studies in living animals so is discussed below.

Histology, histochemistry and immunohistochemistry

The following are *selected examples* to illustrate the potential contribution of histological techniques to understanding physiology.

Muscle layers

The muscle layers and the presence of connective tissue has mainly been investigated using haematoxylin and eosin (H&E) and Masson's trichrome (e.g., Anadón, 2019) with a few studies using transmission electron microscopy (reviewed by Budelmann et al., 1997). Histology enables identification of the muscle type (e.g., smooth or striated), the orientation (e.g., circular, longitudinal, oblique) and thickness of the layers in the various regions. This knowledge has functional implications as smooth and striated muscles have different physiological properties. When the muscle is relatively thin it is suggestive of areas of storage and when thicker, indicative of more powerful contractions or sphincter areas. As noted above, evidence for the presence of sphincters in the digestive tract is limited and is an area where histological studies can inform understanding of control processes. The complex valves involving both muscle and mucosal modifications reported in squid (Williams, 1909; Bidder, 1950) require histological investigation particularly to investigate the claim (Bidder, 1950, p. 18) that they are "reinforced by cartilage."

The basic organization of the muscle in the cephalopod digestive tract is an inner layer of longitudinal muscle and an outer layer of circular muscle with some regions having an additional outer longitudinal layer (e.g., *O. vulgaris* oesophagus, Fernández-Gago et al., 2019) or a circular layer mixed with oblique muscles (e.g., thick stomach muscle in *E. megalocyathus*, Garri and Lauria de Cidre, 2013). Significantly, this contrasts with the vertebrate digestive tract where broadly the organisation is an inner circular muscle layer and an outer longitudinal one (Furness, 2006); the functional consequences particularly for the mechanisms underlying peristalsis require investigation.

Epithelial secretions

Using H&E, Fernandez-Gago et al. (2019, p. 324, table 1) surveyed the epithelial cells secreting mucus or a granular secretion throughout the digestive tract of *O. vulgaris* and similar data is available for *E. megalocyathus* (Garri and Lauria de Cidre, 2013). Mucus secretions were classified using alcian blue (acidic/sulphated/carboxylated glycoconjugates) and periodic acid Schiff (neutral glycoconjugates) alone or in combination. Of particular physiological relevance is the differential distribution of the various types of mucus secreting cells in the lamellae and first and second coils of the caecum (Fernández-Gago et al., 2019) in *O. vulgaris*.

Further insights into secretions are gained from studies of ultrastructure (e.g., electron dense granules, rough endoplasmic reticulum) and enzyme immunohistochemistry (Westermann and Schipp, 1998a). In *N. pompilius* digestive tract the most prominent enzymes were acid and alkaline phosphatase and β-glucuronidase, the latter implicated in mucus catabolism but chymotrypsin and trypsin-like enzymes implicated in nutrient digestion were also present (Westermann and Schipp, 1998a).

Morphological changes related to function

In the DG marked quantifiable histological changes occur during the course of digestion. DGs showing large numbers of "boules" are considered to be active as these contain digestive enzymes ready for exocytosis (Bidder, 1957). The number of "boules" decreases with time after feeding and are absent in one to 3 days without food in *O. vulgaris* (Bidder, 1957). Brown and grey bodies associated with the excretion of waste products are seen during the excretory phase (Bidder, 1957; Rodrigo and Costa, 2017).

Neurones and neurotransmitters

The innervation of the digestive tract in cephalopods has been relatively neglected since the detailed anatomical and histological studies by, for example, Alexandrowicz (1928), Bogoraze and Cazal (1946) and Young (1967; 1971) with recent studies only commenting in passing on the presence of neurones (e.g., Anadón, 2019; Fernández-Gago et al., 2019). Here we use studies of the gastric ganglion to exemplify the contribution of histological techniques. The gastric ganglion is a prominent oval structure (~3 mm long in a 500 g – body weight - *O. vulgaris*) located on the external surface of the digestive tract at the junction of the stomach, caecum and intestine (Figure 2). It is composed of a cortical layer of cells with an inner neuropil from which nerve fibres emerge to supply all adjacent regions of the DT including the digestive gland ducts. The neuronal organisation of the ganglion has been investigated using cresyl violet (Andrews and Tansey, 1983a), Picro-Ponceau (Baldascino et al., 2017), Golgi-Cox (Spasiano, 2020) various modifications of Cajal's silver stain methods (Young, 1971) and antibodies for neurofilament 200, neuronal marker acetylated alpha-tubulin and neuronal nuclear antigen (NeuN, Baldascino et al., 2017). The overall organisation of the cells and the connectivity of axons and dendrites closely resembles the organisation of the central nervous system, supporting the view that it is a major peripheral control centre for the digestive tract. Conventional, fluorescence and immuno-histochemistry (including for the presence of

synthetic or destructive enzymes) have identified the presence (usually by "like-immunoreactivity") of potential neurotransmitters including acetylcholine, corticotrophin-releasing factor, dopamine, FMRF-amide, gamma amino butyric acid, 5-hydroxytryptamine, nor-adrenaline, octopamine (*see* Baldascino et al., 2017 for methodological details and references); the functions of these substances now need investigating using the physiological techniques discussed below. Although we have focused on the tract itself there is evidence that the vasculature supplying the tract is innervated (Andrews and Tansey, 1983b) which is of importance in matching blood flow changes to the post prandial metabolic demands.

Methods used for the investigation of major physiological functions of the cephalopod digestive system

The majority of the *in vivo* techniques will be regulated by national legislation (e.g., Directive 2010/63/EU) and/or institutional review. Collection of animals from the wild may also require specific authorisation. Removal of digestive tract tissue for study *in vitro* requires a humane method of killing (*see* Andrews et al., 2013; Fiorito et al., 2015) and although the EU legislation does not currently specify methods for cephalopods, unlike the situation for vertebrates, in Annexe IV the principles to be followed are specified. For all studies involving animals, researchers should carefully consider application of the 3Rs (Fiorito et al., 2014), experimental design, for example by using the Experimental Design Assistant, and consult animal experimentation reporting guidelines such as ARRIVE (Kilkenny et al., 2010; Percie du Sert et al., 2020). Some research on the cephalopod digestive system is of direct relevance to aquaculture so note should be taken of the growing concerns regarding welfare (Jacquet et al., 2019; Birch et al., 2021).

Measuring motility of the digestive tract

Motility describes the way the contraction and relaxation of the muscles of the digestive tract move the secretions (including salivary and DG ducts), the food whilst it is digested and absorbed, and any indigestible components, waste products, adherent mucus and shed epithelial cells.

Whole digestive tract and regional transit time

Whole DT transit time is usually taken as the time from when food enters the gut to when the undigested constituents of that meal leave the DT as faeces but it can also be applied to the time taken for an artificial marker to pass through the DT. Although conceptually it is a simple measurement, the value obtained depends upon the physical and chemical nature of the food, the physiology of the DT which may be influenced by external stressors, ambient temperature in poikilothermic species and any conscious control over motility such as deferral of defaecation. Although whole digestive tract transit time provides some information about the physiology of digestion it gives little insight into each region's contribution to the overall time and hence its function (e.g., how long do different foods spend in the stomach?). Measurements of overall and regional times are required when investigating control of the digestive tract as well as quantifying the impact of different diets and environmental changes (e.g., temperature). Two main methods have been used.

Movement of food labelled with markers

The movement of shrimps (*Crangon crangon*) labelled with barium sulphate was monitored in juvenile *N. pompilius* by taking timed X-ray photographs (Westermann et al., 2002). Although this technique allows non-invasive monitoring of food movement once the shrimps lose their integrity the barium will disperse into the liquid contents of the tract so may move at a different rate from the solid components. Indigestible food entered the rectum 4 h after feeding but spent a further 8 h in the rectum before defaecation; the overall duration of digestion is assessed at 12 h (at 18–19°C). This technique has not been used in other cephalopods but is applicable (particularly to cuttlefish) provided humane methods of restraint during imaging can be developed. X-rays can also be used to monitor the passage of solid radio-opaque markers of different size incorporated into the food.

Food distribution in the digestive tract

This usually involves feeding matched (e.g., weight, sex) groups of animals a known amount of food after a period of food deprivation, e.g., 24 h for *O. vulgaris* or *S. officinalis* (*see* Sykes et al., 2017 for assessment of welfare impact), killing groups at fixed times after feeding and measuring the amount and composition (e.g., pH, enzyme activity, lipid and protein content) of contents in the lumen of each region of the tract; some studies also include biochemical analysis of the digestive gland and haemolymph sampling. The change in the amount and composition of digesta in each region of the gut (and potentially the faeces) can be used to assess the overall time taken to digest food and the contribution of each region. This approach has been used in *Octopus maya*, *O. mimus* and *O. vulgaris* type II from Brazil (Martínez et al., 2012; Linares et al., 2015; Gallardo et al., 2017; Bastos et al., 2020).

Using standardised food intake this method can also be used to estimate the rate at which food leaves the stomach as shown in cuttlefish (Quintela and Andrade, 2002a; b). With a shrimp meal gastric emptying in *S. officinalis* was shown to be faster at higher ambient temperatures; the time for 50% of the meal to be emptied from the stomach was estimated to be 3.5 h at 15.5°C, but 1.6 h at 23°C (Quintela and Andrade, 2002a) but this method does not

allow the relative contributions of the effects of higher temperature on enzyme activity and motility to be identified. Techniques need to be developed to measure the emptying of the solid and liquid components separately as liquid components are likely to empty more quickly; in cephalopods this may be important as in octopus soluble nutrients enter the digestive gland and haemolymph ~ 40 min post ingestion (Rosa et al., 2004; Linares et al., 2015). This food distribution method is readlily applicable to meaure emptying from the stomach in cuttlefish and squid where there is no crop, but in octopus where the crop and stomach act in concert other techniques will need to be developed to measure exchange between the two regions as well as net emptying into the caecum/intestine. Finally, a key reason why measurement of gastric emptying is needed is to understand how the process is regulated to ensure that only suitable processed food enters the caecum and the relationship between gastric emptying and satiety/hunger signals.

The main disadvantages of this technique are that it requires the death of the animal, uses a large number of animals depending on the temporal resolution studied, groups need careful matching so data can be combined to produce a single plot of the timing of various processes, contents may move after death because of the interconnectivity of the gut regions and *post mortem* continuation of motility. However, currently it is the only technique allowing sampling of gut contents (except faeces) enabling detailed biochemical analysis to follow the course of food digestion and also the analysis of exocrine secretions contributing to digestion. If an animal is killed, we urge that optimal use is made of the all the tissues by making them available to other local researchers or making a bank of fixed or frozen tissue; the latter is particularly important for rarer species.

In vitro studies of physiology and pharmacology

In vitro here refers to studies in which either the entire digestive tract, a region (e.g., the crop, the rectum) or a strip of tissue cut from a region is removed from an animal killed humanely is placed in a tissue bath. Functionality is maintained by immersion in a physiological solution (modified Ringer's solution), gassed (to maintain oxygen and the pH of any buffers) and kept within normal body temperature range while measurements are made of muscle contractile activity (e.g., tension or intra-luminal pressure). Here we focus on techniques appliable to either segments of digestive tract or the entire digestive tract but do not discuss *In vitro* techniques applied to studying the working of the buccal mass (Boyle et al., 1979).

With appropriate experimental design and controls the techniques described below can be used to investigate the effects of a range of interventions and conditions applied before the *in vitro* study but which are likely to have prolonged effects. Examples include: *1*) Life stage dependent changes; *2*) Effect of protracted exposure to expected changes in environmental conditions associated with climate change (e.g., sea water acidification); *3*) Comparison of diets with differing composition, energy density and digestibility; *4*) Investigation of functional effects of endogenous agents and/or their receptors which may be identified from genomic studies (e.g., cephalopod G-protein receptors, Ritschard et al., 2019), neuropeptidome analysis (e.g., Zatylny-Gaudin et al., 2016), molecular and immunohistochemical analysis of the gastric ganglion (e.g., Baldascino et al., 2017).

Tension measurement

In vitro recordings of tension from various regions of the digestive tract have been undertaken in *O. vulgaris* (e.g., Andrews and Tansey, 1983a; Takuwa-Kuroda et al., 2003), *S. officinalis* (e.g., Bacq, 1934; Zatylny-Gaudin et al., 2010) and *Doryteuthis pealeii* (e.g., Wood, 1969). However, the paucity of studies shows that this is an under-utilized technique in cephalopods. It is also possible to measure pressure in closed isolated segments of digestive tract (Andrews and Ponte, personal observations).

Two insights into the physiology of digestive tract motility emerge from published studies:

Spontaneous contractile activity. All regions of the digestive tract show varying degrees of spontaneous (i.e., in the absence of overt stimuli) contractile activity with contractions of differing amplitudes and frequencies (Figure 3). Myogenic activity (i.e. not requiring neurones) is particularly important to investigate as in vertebrates, including fish (e.g., *Myoxocephalus scorpius* Brijs et al., 2017b) and humans (Hwang et al., 2009), this is due to activity of the Interstitial Cells of Cajal (ICC) which act as pacemaker cells periodically depolarizing to initiate contraction of adjacent smooth muscle cells (Sanders, 2019). Wood (1969) reported that contractile response of the squid stomach to stretch continued in the presence of tetrodotoxin as did the associated electrical activity providing very preliminary evidence for "myogenic activity." Functional studies, combined with molecular and immunohistochemical studies (e.g., calcium activated chloride channel ANO-1 positive cells) to investigate the presence of ICCs are required to identify whether the fundamental mechanism (ICC-smooth muscle cell) underlying digestive tract contractile activity in vertebrates occurs in cephalopods.

Modulation by a diversity of putative neurotransmitters and hormones. Figure 4 shows a stimulatory effect (increased tone, contraction amplitude and frequency) of nor-adrenaline/adrenaline on the crop, thin part of the stomach and intestine while acetylcholine and nicotine inhibited activity which recovered above baseline levels on washing (Andrews and Tansey, 1983a). This provides preliminary evidence for reciprocal control of motility analogous to divisions of the autonomic nervous system in vertebrates (Olsson, 2009). An inhibitory effect of acetylcholine followed by post-washing

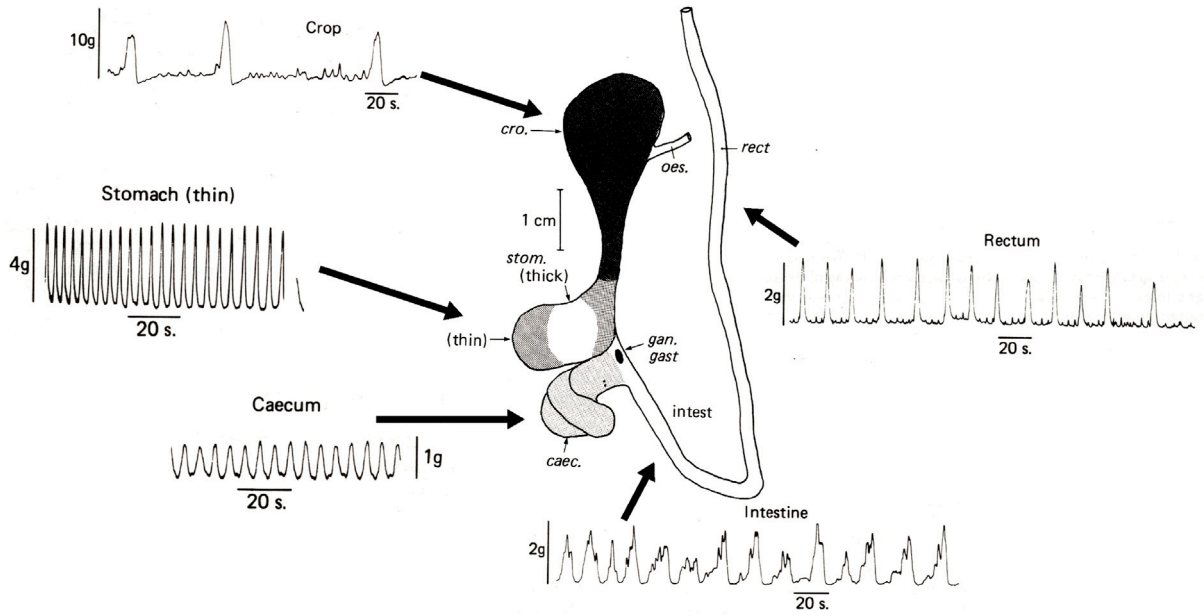

FIGURE 3
Spontaneous contractile activity recorded *in vitro* from longitudinal muscle strips of the main regions of the digestive tract removed immediately *post mortem* from *Octopus vulgaris*. Note that all regions show some spontaneous contractile activity but that the magnitude and frequency differs. Abbreviations: caec = caecum; cro = crop; gan. gast = gastric ganglion; intest = intestine; rect = rectum. Modified from Figures 1 and 4 in Andrews and Tansey, 1983a, pages 111 and 115. Reproduced with the application of an author permissions waiver request from Cambridge University Press.

excitation has also been reported in squid stomach as has the excitatory effect of adrenaline (Bacq, 1934; Wood, 1969). Although responses to the cholinergic and adrenergic receptor agonists are clear, defining receptor types/subtypes involved requires the use of selective or specific receptor antagonists (*see* IUPHRA/BPS Guide to Pharmacology; www.guidetophamacology.org). Whilst many receptors are relatively well characterized in mammalian tissues very little information is available regarding the pharmacology of receptors in cephalopods defined either by agonists or antagonists.

Imaging of contractions: spatiotemporal mapping. The external profile of the digestive tract changes with the progression of contractions and also as the degree of distension of a particular segment is changed by bolus progression. High resolution video recording of the digestive tract followed by automated computer analysis of the apparent diameter enables the generation of "spatiotemporal maps" showing the contractile activity, its magnitude, direction (oro-anal or ano-oral) and speed of travel (*see* Lentle and Hulls, 2018 for review of the method). Spatiotemporal mapping frequently used in mammals to investigate the effects of drugs (e.g., in mouse stomach, Worth et al., 2015) has also been utilised to study motility in the digestive tract of the fish *Oncorhynchus mykiss* (Brijs et al., 2017a) and *Myoxocephalus scorpius* (Brijs et al., 2014; Brijs et al., 2017b). However, it has not been applied to cephalopods, although using cursor measurement of individual video frames at timed intervals Sykes et al. (2020; Figure 3B) demonstrated its applicability to analysis of crop contractions using an *in vitro* preparation in *O. vulgaris*.

Other techniques also applicable *in vitro* to investigate the effect of treatments *in vivo* (e.g., acute food deprivation, adaptation to different diets, pharmacological or surgical interventions to investigate control) on motility measured *in vitro* include the passage of artificial boluses (e.g., Le et al., 2021), electrophysiological studies of muscle using extracellular (e.g., suction electrodes as in squid stomach, Wood, 1969) and intracellular (adapting techniques used in octopus arm muscle, Rokni and Hochner, 2002) recordings.

In vivo imaging

Imaging the digestive tract *in situ* in the living animal (*in vivo*) allows measurement of the movement of food, changes in the physical nature of the contents through the tract and characterisation of the contractile activity. However, methods used currently require some form of restraint or possibly sedation which may themselves affect motility, although in some species it may be possible to train the animal to remain quiescent during monitoring. Whilst X-rays have been used to

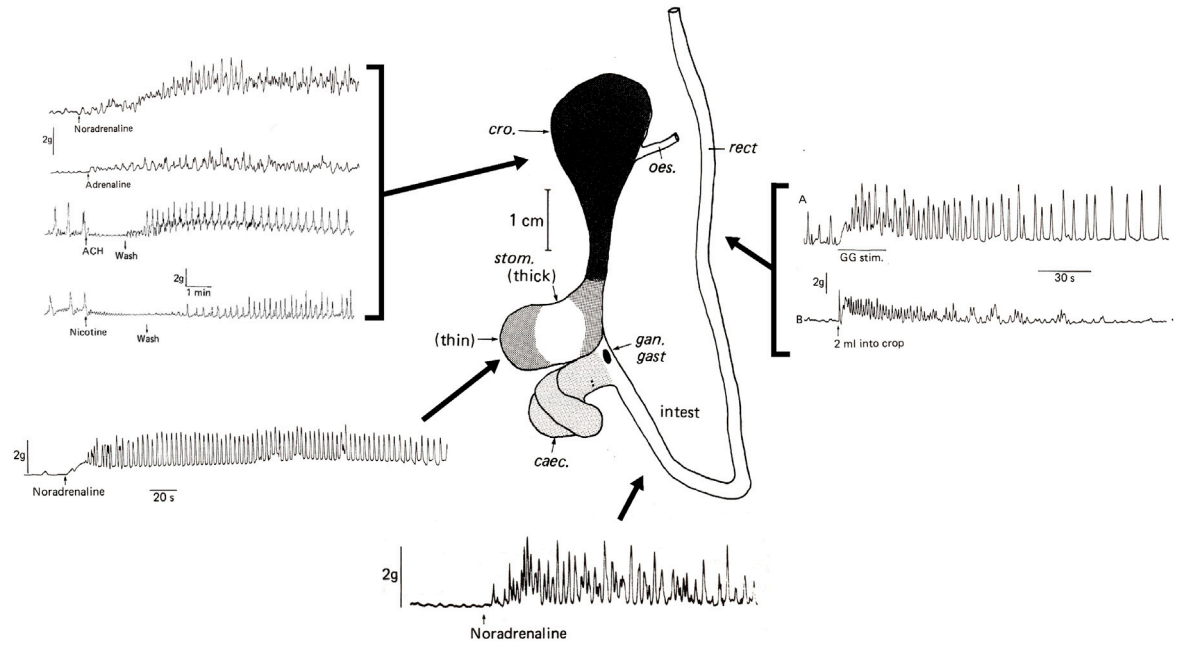

FIGURE 4
The effects of adreno- and cholino-receptor ligands on the *in vitro* contractile activity of main regions of the *Octopus vulgaris* digestive tract. The crop, stomach and intestine all show an increase in contraction amplitude and tone to noradrenaline (1 μg/ml–10 μg/ml) with the response to adrenaline (2 μg/ml) in the crop also shown. Both acetylcholine (ACH; 20 μg/ml) and nicotine (20 μg/ml) cause transient inhibition of ongoing contractile activity in the crop followed by rebound excitation following washing. The upper right -hand panel shows the excitatory effect of gastric ganglion (GG) stimulation (20 V, 0.5 ms, 20 Hz) on the crop and the stimulation of crop motility by fluid distension (2 ml); these two recordings are from *in situ* preparations. Abbreviations: caec, caecum; cro, crop; gan. gast, gastric ganglion; intest, intestine; rect, rectum. Details of methods are in Andrews and Tansey, 1983a. This Figure is modified from Figures 1, 8, 9 and 10 in Andrews and Tansey, 1983a, pages 111, 119, 121 and 122. Reproduced with the application of an author permissions waiver request from Cambridge University Press.

monitor the progress of food mixed with radio-opaque barium sulphate in *N. pompilius* (Westermann et al., 2002) and *S. officinalis* (Ponte et al., 2017, *see* also Figure 1H therein) the low temporal resolution does not provide information about individual contractions. Additionally, movement of the contrast medium may not accurately reflect the bolus movement.

The technique most applicable to cephalopods is the use of high-resolution ultrasound (e.g., VEVO - Visualsonics). In a pilot study of unrestrained *O. vulgaris*, Ponte et al. (2017) were able to show propulsive contractions of the crop in both longitudinal and transverse planes, and constriction of the caecum together with the motion of the complex spirally organised lamellae (*see* figure 1 in Ponte et al., 2017). The method also provides information about the physical characteristics of the lumen contents. This technique should be adaptable to cuttlefish, although the locomotor activity of squid may prevent use without undue restraint. Combination of *in vivo* ultrasound with the *in vitro* techniques outlined above will identify if motility is modified by diets of different composition, and the impact of environmental changes.

The transparency of *O. vulgaris* paralarvae post-hatching, enables direct observation of the digestive tract during feeding allowing observation of the distribution of food in the digestive tract. Analysis of high-resolution video recordings enabled quantification of crop volume, contraction frequency in crop, stomach and intestine, and insights into the overall timing of digestion (Nande et al., 2017). Juvenile and mature individuals of several species of cephalopod are sufficiently transparent for direct observation of the passage of material through parts of the digestive tract and also to see changes in the colour of the digestive gland. Bidder (1950) utilised the transparency of juvenile squid to make observations on the movement ingested pieces of fish (marked with iron saccharate, carmine and Nile blue) in the digestive tract commenting that "the only parts of the digestive system not visible in the living animal are the buccal glands and poison glands and the "pancreas" (Bidder, 1950, p. 8). Direct observation is not an option for cuttlefish species because of the cuttlebone but there are several examples of transparent/semi-transparent squid (e.g., Cranchiide family) and octopus (e.g., Vitreledonellidae family).

Measuring food ingestion rate

Ingestion rate can be measured in experimental settings using live or frozen organisms, pieces of natural or processed (elaborated/synthetic) food and is calculated as the difference between the delivered food and that remaining for at least 2 h after being offered to the animals. The latter time can be established according to the feeding time regularly used in the laboratory depending on the species feeding habits. The percentage of leached nutrients must be measured and depends on the type of the diet. When processed food is used, leaching is measured using the shaking method (Obaldo et al., 2002). For this, 10 samples of 2 g of each diet are placed in 250-ml flasks placed in a horizontal shaker for 2 h (or the time that is estimated in each experimental condition to feed the animals) at the same temperature and water quality used experimentally. After that time, the water is filtered (pre-weighed, Whatman 1441-090 is recommended) to separate the remaining food from the leached water. Original food ($N = 10$) and leached samples of each diet are dried in a convection oven at 60°C for 48 h until constant weight, and then cooled in a desiccator. Dried feed samples are weighed and analysed for dry matter retention. Ingestion rate is calculated according to the following equation:

$$\text{Ingestion rate (I)} = [\text{offered food} - \text{recovered food}] \times [1 - (\text{nutrient leaching})]$$

where offered and recovered food are expressed as dry weight (g) (60°C, 48 h), and unconsumed food as % of the nutrients lost during the shaking procedure (Obaldo et al., 2002). Ingestion rate (I) is expressed as g. ingested food (wet weight) considering the water content obtained after dry sampling at 60°C for 48 h. In the case of fresh or frozen food the same method is used. A review of the stomach contents and ingestion rate in cephalopods by Ibáñez et al. (Ibáñez et al., 2021) gives recommendations for obtaining data of ecological importance.

Measuring the time course of digestion

Digestion time differs between species, with temperature, dissolved oxygen and type of food, among other variables. For that reason, when evaluating the digestive processes, preliminary observations are required to determine the overall duration of digestion and hence sampling frequency. In *O. vulgaris sensu stricto*, *O. vulgaris* type II from Brazil, *O. maya*, and *O. mimus* fed fresh crab at 5% of the body weight it took ~ 400 min to complete the digestion process (Martínez et al., 2012; Linares et al., 2015; Gallardo et al., 2017; Bastos et al., 2020). Depending on the number of animals available, it is possible to take timed samples during the process, but how many animals should be sampled to maintain a balance between 3Rs considerations and data quality? The answer depends on the type of analysis required, but usually a minimum of three animals will be necessary to obtain data that can be statistically analysed (Table 2). Also, it is essential to remember that digestive juice enzyme activity can be highly variable, especially with a mixed diet. For that reason, in this type of study it is highly recommended to use a single type of food to evaluate digestion timing (crustacea are arguably the best diet because their importance in trophic ecology of cephalopods).

TABLE 2 Number of animals sampled in three octopus species when the timing of the digestive process was studied.

O. maya[a]		*O. mimus*[a]		*O. vulgaris* type II[b]	
min	***N***	**min**	***N***	**min**	***N***
0	6	0	5	0	3
20	7	30	3	60	4
40	7	90	3	120	5
80	7	150	3	200	4
120	7	210	3	300	4
180	8	270	3	400	4
240	10	330	3		
360	6	390	3		
480	3				

Note that animals were fed with one piece of crab (*Callinectes* spp for *O. maya* and *O. vulgaris* type II and *Cancer* spp for *O. mimus*) except for animals at time zero. All the animals should be fasted at least by 12 h before the experiment. After fasting, allow the octopus to ingest the crab for enough time to guarantee that animals end the ingestion process; inn *O. maya, O. mimus* and *O. vulgaris* type II this takes around 20–30 min.
[a]Linares et al. (2015).
[b]Bastos et al. (2020).

Table 3 shows the variety of digestive enzymes in octopus species. Although there are probably more than a dozen types of enzyme with different roles, there is evidence suggesting that the acidic enzymes have higher activity during digestion (e.g., Ibarra-García et al., 2018). Based on Boucaud-Camou and Boucher-Rodoni (1983), Martínez et al. (2012) studied the pH of the "gastric juice" (i.e., the fluid found in the stomach but not secreted by the stomach) of *O. maya* during digestion of crab. They found that pH varied between 5.2 and 6, demonstrating, as was previously observed in *O. sinensis* (?) by Morisita (1972 a, b and c, cited by Boucaud-Camou and Boucher-Rodoni, 1983) that the main enzymes in the digestive tract of those octopus species were acidic proteinases. Until now, besides *O. sinensis*(?) and *O. vulgaris* sp. (Table 3) the presence of acidic proteinases has been demonstrated in the gastric juice of *O. mimus, O. maya* (Linares et al., 2015) and *O. vulgaris* type II (Bastos et al., 2020), and in the digestive gland of *O. bimaculoides* (Ibarra-García et al., 2018), *Robsonella fontaniana* (Pereda et al., 2009) and *Enteroctopus megalociathus* (Farías et al., 2010) indicating that the acidic proteinases may be the main type of digestive enzyme in octopus species. It is interesting to note that in some studies

TABLE 3 Enzyme activities detected with different methods in digestive gland (DG), anterior (ASG), and posterior (PSG) salivary gland, gastric juice (GJ) or entire paralarvae (All) of several octopus species.

Enzymes	Activity	Tissue/organ	Species	Stage	Reference
Acid phosphatases	xx	DG	*E. megalocyathus*	J	Farías et al. (2010)
Acid phosphatases	xxx	All	*R. fontaniana*	Pl	Pereda et al. (2009)
Acid proteinases	xxxx	GJ,DG	*O. vulgaris* Type II	PA	Bastos et al. (2020)
Acid proteinases	x	GJ,DG	*O. vulgaris* Type II	PA	Bastos et al. (2021)
Acidic proteases	xxx	DG	*O. vulgaris* s.e	?	Arvy (1960)
Acidic proteases	xxx	GJ	*O. vulgaris* s.e	?	Boucaud-Camou and Boucher-Rodoni (1983)
Alkaline phosphatase	xx	All	*R. fontaniana*	Pl	Pereda et al. (2009)
Alkaline proteases	xxx	PSG	*O. vulgaris* s.e	?	Arvy (1960)
Alkaline proteinases	x	GJ, DG	*O. vulgaris* Type II	PA	Bastos et al. (2020)
Alkaline proteinases	xx	DG	*E. megalocyathus*	J	Martínez-Montaño et al. (2018)
Amylase	xx	DG	*O. bimaculoides*	J	Ibarra-García et al. (2018)
Amylase	xxx	GJ	*O. bimaculoides*	J	Ibarra-García et al. (2018)
Amylase	nd	SG	*O. bimaculoides*	J	Ibarra-García et al. (2018)
Amylase	xx	PSG, DG, Ca	*O. vulgaris* s.e	A	Mancuso et al. (2014)
Carboxypeptidase A	x	PSG	*O. sinensis (?)*	?	Morishita 1974 a,b,c cited by Boucaud-Camou and Boucher-Rodoni (1983)
Carboxypeptidase A	x	DG, GJ	*O. sinensis* (?)	?	Morishita 1974 a,b,c cited by Boucaud-Camou and Boucher-Rodoni (1983)
Carboxypeptidase B	x	DG, PSG	*O. vulgaris* s.e	?	Mancuso et al. (2014)
Cathepsin B	xxxx	DG	*O. maya*	PA	Rosas et al., Unpublished data
Cathepsin D	xxxx	DG, GJ	*O. maya*	J	Martínez et al. (2011)
Cathepsin H	xxxx	DG	*O. maya*	PA	Rosas et al., Unpublished data
Cathepsin L	xxxx	DG	*O. maya*	PA	Rosas et al., Unpublished data
Cathepsin-like	xxxx	DG, GJ, PSG	*O. sinensis* (?)	?	Morishita 1974 a,b,c cited by Boucaud-Camou and Boucher-Rodoni (1983)
Cellulase	xxx	DG	*O. vulgaris* s.e	?	Boucaud-Camou and Boucher-Rodoni (1983)
Chitinase	xx	DG, St	*O. sinensis (?)*	?	Okutani and Kimata (1964)
Chitinase	xx	PSG	*Eledone cirrhosa*	A	Grisley and Boyle (1990)
Chymotrypsin	xx	PSG	*O. sinensis* (?)	?	Morishita 1974 a,b,c cited by Boucaud-Camou and Boucher-Rodoni (1983)
Chymotrypsin	x	All	*O. vulgaris* s.e	Pl	Villanueva et al. (2002)
Chymotrypsin	xxx	PSG,DG,Ca	*O. vulgaris* s.e	A	Mancuso et al. (2014)
Chymotrypsin	xx	GJ	*O. sinensis* (?)	?	Morishita 1974 a,b,c cited by Boucaud-Camou and Boucher-Rodoni (1983)
Chymotrypsin	xx	DG	*Eledone spp*	PA	Boucher-Rodoni (1982)
Chymotrypsin	xxx	PSG	*Eledone cirrhosa*	A	Grisley and Boyle (1987)
Chymotrypsin	xx	DG, GJ	*O. maya*	J	Martínez et al. (2011)
Chymotrypsin	xxx	GJ,DG	*O. vulgaris* Type II	PA	Bastos et al. (2021)
Chymotrypsin	xx	DG	*E. megalocyathus*	J	Farías et al. (2010)
Chymotrypsin	x	DG	*E. megalocyathus*	J	Martínez-Montaño et al. (2018)
Chymotrypsin	xx	DG	*O. bimaculoides*	J	Ibarra-García et al. (2018)
Chymotrypsin	x	GJ	*O. bimaculoides*	J	Ibarra-García et al. (2018)
Chymotrypsin	x	SG	*O. bimaculoides*	J	Ibarra-García et al. (2018)
Dipeptidase	xx	ASG	*O. sinensis (?)*	?	Morishita 1974 a,b,c cited by Boucaud-Camou and Boucher-Rodoni (1983)
D-aspartate oxidase	xx	DG	*O. vulgaris*	?	Tedeschi et al. (1994)
Esterases	xxx	PSG	*O. vulgaris* s.e	?	Arvy (1960)
Glucosaminidase	x	All	*R. fontaniana*	Pl	Pereda et al. (2009)
Leucine amino peptidase	x	DG	*O. maya*	PA	Aguila et al. (2007)
Leucine amino peptidase	x	DG	*E. megalocyathus*	J	Martínez-Montaño et al. (2018)
Lipase	xx	DG	*O. vulgaris* s.e	?	Fernández-Gago et al. (2019)
Lipase	xx	DG	*O. vulgaris* s.e	?	Mancuso et al. (2014)
Lipase	xxx	DG	*E. megalocyathus*	J	Martínez-Montaño et al. (2018)

(Continued on following page)

TABLE 3 (*Continued*) Enzyme activities detected with different methods in digestive gland (DG), anterior (ASG), and posterior (PSG) salivary gland, gastric juice (GJ) or entire paralarvae (All) of several octopus species.

Enzymes	Activity	Tissue/organ	Species	Stage	Reference
Lipase	xx	DG	*O. bimaculoides*	J	Ibarra-García et al. (2018)
Lipase	x	GJ	*O. bimaculoides*	J	Ibarra-García et al. (2018)
Lipase	xxx	SG	*O. bimaculoides*	J	Ibarra-García et al. (2018)
Trypsin	x	PSG	*O. sinensis* (?)	?	Morishita 1974 a,b,c cited by Boucaud-Camou and Boucher-Rodoni (1983)
Trypsin	x	DG	*O. maya*	PA	Aguila et al. (2007)
Trypsin	x	DG, GJ	*O. maya*	J	Martínez et al. (2011)
Trypsin	x	All	*O. vulgaris* s.e	Pl	Villanueva et al. (2002)
Trypsin	x	All	*O. vulgaris* s.e	Pl	Morote et al. (2011)
Trypsin	xxx	PSG, DG,Ca	*O. vulgaris* s.e	A	Mancuso et al. (2014)
Trypsin	xxx	GJ,DG	*O. vulgaris* Type II	PA	Bastos et al. (2021)
Trypsin	x	DG	*E. megalocyathus*	J	Farías et al. (2010)
Trypsin	x	DG	*E. megalocyathus*	J	Martínez-Montaño et al. (2018)
Trypsin	xx	DG	*O. bimaculoides*	J	Ibarra-García et al. (2018)
Trypsin	x	GJ	*O. bimaculoides*	J	Ibarra-García et al. (2018)
Trypsin	x	SG	*O. bimaculoides*	J	Ibarra-García et al. (2018)
α-amylase	xxx	GJ,DG	*O. vulgaris* Type II	PA	Bastos et al. (2021)
α-amylase	x	DG	*E. megalocyathus*	J	Martínez-Montaño et al. (2018)
β-Galactosidase	xx	All	*R. fontaniana*	Pl	Pereda et al. (2009)

Relative magnitude of the enzyme activity reported by authors (x). When the stage of life cycle was not identified a symbol (?) was added. Pl, paralarvae; J, juveniles; PA, pre-adults.

high activities of amylase are reported suggesting that some species *(O. bimaculoides; O. vulgaris sensu stricto)* may have the ability to digest complex carbohydrates (Table 3). Although interesting, these studies require duplication (Table 3) and the sources of complex carbohydrate identified.

It is important to evaluate the pH, temperature, substrate concentration and divalent ions that could specifically regulate digestive enzymes activity in each region of the tract (Martínez et al., 2011; Ibarra-García et al., 2018). Sampling requires the animal to be anaesthetized and killed (e.g., Roumbedakis et al., 2020). As soon as possible the digestive tract should be separated immediately into the crop, stomach, caecum and digestive gland using surgical clamps to avoid mixing the luminal contents. Once separated, the volume and weight of the chyme (the mixture of secretions [e.g., mucus and enzymes], partially digested food and ingested fluid) contained in each region should be measured, immediately frozen in liquid nitrogen, and stored until analysis (depending on the time until analysis, samples can be stored at −20, −40 or −80°C). A wealth of information on the digestive physiology of octopus can be obtained from this type of study particularly when combined with other techniques (e.g., *in vitro* studies of motility or preservation of tissue for IHC; *see* above); measurements are summarised in Figure 5.

In *O. maya, O. mimus* and *O. vulgaris* juveniles and adults, soluble nutrients (e.g., soluble protein, small peptides and amino acids) in the food move quickly to the DG and pass to the circulation becoming available for tissue metabolism, only 40–60 min after ingestion (Rosa et al., 2004; Linares et al., 2015).

The digestive physiology of octopus species and probably of other cephalopods can be divided into two phases: *1*) soluble nutrients pre-digested in the prey (or elaborated food) quickly pass-through the crop, stomach and caecum to the DG and then the haemolymph to be transported to tissues; *2*) more complex nutrients (e.g., myofibrillar proteins, complex lipids) are processed by the simultaneous action of the enzymes (from salivary glands and DG) when food is in the crop with mechanical degradation by concerted action of the crop and stomach, filtration in the caecum and finally entering the DG *via* the ducts as a suspension.

A recent histochemical study of the digestive tract of *O. vulgaris* detected no digestive enzyme presence in the digestive tract epithelium (Fernández-Gago et al., 2019) consistent with the view that chyme formation during the digestive process is predominantly by digestive enzymes secreted from DG with a minor contribution from salivary enzymes. This means that the changes occurring as food passes along the digestive tract are mainly because of the pulses of enzyme production in DG during the digestion phases previously described in cephalopods (Semmens, 2002; Martínez et al., 2011; Linares et al., 2015). The time to digest a meal depends on the species and ambient temperature. For example, in tropical and sub-tropical pre-adults of *O. maya* (26°C; 0.500 kg), *O. mimus* (14°C; 1.2 kg) (Linares et al., 2015) and *O. vulgaris* type II from Brazil (20.8°C) (Bastos et al., 2020) the complete digestive process takes 6–7 h, while

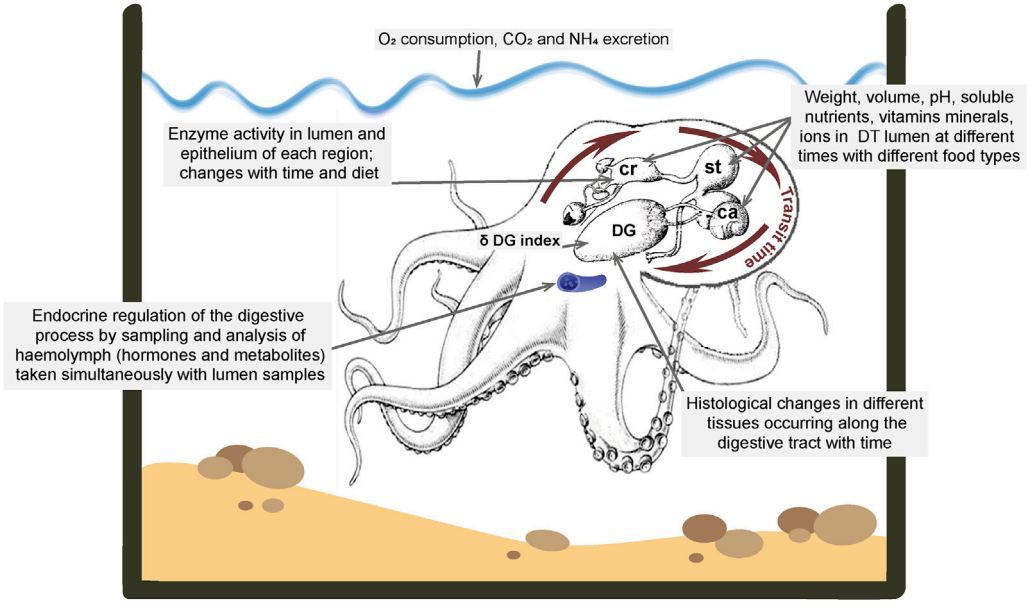

FIGURE 5
Summary of measurements which can be made in octopus to quantify the movement of food through the digestive tract, the digestive processes and the metabolic consequences of digestion. *See* text for details and references. Abbreviations: ca, caecum; cr, crop; DG, digestive gland; DT, digestive tract; st, stomach. Diagram of octopus and digestive tract modified from Gallardo et al., 2017.

in *Octopus cyanea* the entire digestive process was takes around 12 h at 30°C from the beginning of the meal (Boucher-Rodoni, 1973). Although digestion appears is a fast process in octopus species it is necessary to evaluate how temperature is modulating all the physiological, endocrinological and enzymatic mechanisms involved in the process to predict possible consequences in warming scenarios; a meta-analysis would be a useful first step.

Measuring trans-epithelial absorption of material

Once the chyme is in the DG, biochemical process involving absorption and further digestion are activated (Boucaud-Camou and Boucher-Rodoni, 1983; Budelmann et al., 1997). In the DG of *O. maya* fasted for 24 h in laboratory conditions, "resting cells" characterised by few or no heterolysosomes or residual bodies are observed (Martínez et al., 2011). Additionally, an apocrine secretion and cell debris can be observed in the tubular lumen, probably resulting from catabolism in response to food deprivation for 24 h. During the first 1 and 2 h of the postprandial period (PP), digestive cells show nuclei forming a belt at the basal region of each columnar cell as the typical characteristic. Some heterolysosomes appeared inside the digestive cells. Acidophilic chyme in the tubule lumen indicates soluble nutrients in the DG. Once the digestive system in the DG is activated, heterophagosomes in the acinar cells transport amino acids to the haemolymph and then muscle and other tissues. In *O. maya*, *O. mimus* and *O. vulgaris* type II studies suggest that soluble protein is accumulated in muscle tissues initiating the glycosynthetic process (Gallardo et al., 2017; Bastos et al., 2020). After 4 h PP, the digestive cells store heterolysosomes (nutrients). Additionally, heterophagosomes were observed only near the apical zone of the cell, revealing the beginning of complex nutrient transport because of the mechanical digestion of more complex nutrients. Digestive cells showed a brush border (i.e., microvilli) on the apical membrane contacting the lumen. Acidophilic chyme was observed in the centre of the lumen. Peaks of glucose, cholesterol, acylglycerols and soluble protein can be observed with high digestive activity in DG cells. All these processes indicate that nutrients were transformed and transported to the tissues for energy and anabolic processes. At 6 h PP, the digestive cells have a conspicuous brush border and an empty lumen. Digestive cells appear filled with heterolysosomes, without heterophagosomes. At 8 h PP, a reduction in heterolysosomes was be observed, together with residual bodies, cell debris and apocrine secretion in the lumen. The proliferation of nuclei indicated the presence of replacement cells located in the basal lamina of the tubules signalling the end of the process (Boucaud-Camou and Boucher-Rodoni, 1983; Martínez et al., 2011; Gallardo et al., 2017; Fernández-Gago et al., 2019; Bastos et al., 2020).

Measuring the energetic costs of food processing: specific dynamic action and apparent heat increment

Before describing the measurement of metabolic rate we first highlight one of the important parameters derived from its measurement. Many years ago it was recognized that the apparent heat increment (AHI) also termed specific dynamic action, (SDA) could be used as an indicator of the cost of mechanical and biochemical processes associated with the ingestion and assimilation of food (Nixon, 1969). Although muscular tissue is responsible for the mechanical activity, and the epithelium of the tract synthesises and secretes chitin and mucus requiring energy, the digestive gland is the main site of metabolic functions (Boucaud-Camou and Boucher-Rodoni, 1983). Hence, the AHI may result from addition of the energy used in the above processes; depending on the diet and temperature this constitutes a considerable percentage of the daily energy budget in aquatic organisms (Katsanevakis et al., 2005; Aguila et al., 2007; Noyola et al., 2013). In *O. vulgaris* values between 25 and 55% of food conversion efficiency were calculated. When different temperatures were compared it was observed that the peak value of AHI (SDA) of *O. vulgaris* was 64% at 20°C and 42% at 28°C (Katsanevakis et al., 2005) and in *O. cyanea* AHI was 60% of the ingested food (Nixon, 1969; Boucaud-Camou and Boucher-Rodoni, 1983). In *O. maya* it was also demonstrated that the AHI values are dependent on the type of diet with values that oscillate between 9 and 14% of the ingested energy when animals were fed fresh crabs or mixed diets made from fresh crab meat and other ingredients (Aguila et al., 2007; Rosas et al., 2007; Rosas et al., 2008). When temperature was investigated, the AHI values of *O. maya* were relatively higher in animals maintained in optimal temperature ranges (30–48% of routine metabolic rate; 22–26°C) than observed in animals maintained at 30°C (21%) suggesting that in higher temperatures the energy invested in mechanical and biochemical transformation of food is decreased due to additional costs associated with maintaining a higher metabolic rate at higher temperatures (Noyola et al., 2013). That means that depending on the species and its thermal tolerance temperatures beyond the optimal thermal range could affect the general physiological condition of the animals reducing the energy available to be invested in processing food. In larvae of coral reef, tropical fish it was observed that a temperature of 31.5°C does not affect the AHI (SDA) magnitude and duration suggesting that this species (*Amphiprion percula*) is well adapted to temperatures expected even in warming scenarios (McLeod and Clark, 2016).

Measuring metabolic rate

There has been considerable debate about measurement of respiratory metabolism in aquatic animals in the light of new hypotheses related to global warming and physiological adaptation of ectotherms (Sokolova et al., 2012a; Sokolova et al., 2012b; Norin and Clark, 2016; Pörtner et al., 2017). Although the debate has focused on fish (Chabot et al., 2016a), there is a broad consensus on measurement of metabolism in aquatic organisms (Steffensen, 1989; Chabot et al., 2016b; Svendsen et al., 2016). Two types of respirometer have been used:

i) *Flow-through respirometry*. This measures oxygen consumption by quantifying the difference between inlet and outlet oxygen concentration and adjusting the flow of water through the respirometer to maintain a pre-set oxygen content difference. Oxygen consumption is then calculated as the product of water flow through the respirometer per unit time and the difference in oxygen concentration of the water entering and exiting the respirometer. In this respirometer the constant inflow of clean water reduces or eliminates the hypoxia, hypercapnia and nitrogenous waste issues associated with closed-system respirometry, but it introduces mixing and equilibration (washout) problems (Steffensen, 1989), although this can be corrected (Niimi, 1978).
ii) *Intermittent-flow respirometry*. This combines short measurement periods in a recirculating, but closed, respirometer. After some time (determined by the oxygen level in the respirometric chamber: not lower than dissolved oxygen saturation of 80%) the chamber is flushed with clean water to ensure that the water in the respirometer has been thoroughly exchanged to eliminate potential hypoxia, hypercapnia and nitrogenous waste build-up in the chamber (Steffensen, 1989). While this oxygen consumption method is the most popular amongst fish physiologists, it does require more equipment and a slightly more complex experimental setup than the flow-through respirometer (Svendsen et al., 2016). Although both methods have pros and cons, the most important aspect is the accuracy and validity of the measurements.

The development of oxygen sensors to measure dissolved oxygen facilitated experimental work in this area. Although polarographic oxygen probes are still used, optical sensors are considered the best to use in physiological evaluations of metabolic rate of aquatic animals including cephalopods. Much of the data obtained in the last 50 years on octopus species used the home tank as a respirometric chamber and in the many cases as closed respirometers (Wells et al., 1983; O'Dor and Wells, 1987; Wells et al., 1996; Cerezo Valverde and Garcia Garcia, 2005; Katsanevakis et al., 2005). Although those data give useful information about the respiratory physiology of several octopus species, using optical sensors and improving the systems (i.e., Intermittent-flow or flow-through respirometry) will give more precise data as shown in *O. vulgaris* and *O. maya* (Cerezo Valverde and Garcia Garcia, 2004; Aguila et al., 2007; Noyola et al., 2013; Martínez et al., 2014; Meza-Buendía et al., 2021).

Data on oxygen consumption can be used to evaluate the energetic costs of different types of food (natural and elaborated)

if the AHI is measured but also, if ingested food (I), faeces production (F), nitrogen excretion (N) and growth (P) are measured (all expressed in energy units; J day^{-1} g^{-1} or kg^{-1}), these values can be integrated into an energetic flow equation (Wells et al., 1996):

$$\mathbf{I} = F + N + P + R$$

where assimilated energy (As) can be calculated as:

$$As = R + P$$

In this equation $R = R_{AHI} + R_{rut}$, with R_{rut} the metabolic rate of animals before feeding in respirometric chamber. Studies made in *O. maya* show stable R_{rut} values can be obtained in animals conditioned to respirometric chambers for 12–18 h, depending on temperature and the animal size (Roumbedakis et al., 2020; Meza-Buendía et al., 2021). When this type of data is obtained in animals fed different types of food it is possible to know how the nutritional characteristics of the food modulate the quantity of energy that is channelled to growth in comparison to mechanical and biochemical transformation of the ingested food. When pre-adult *O. maya* were fed *Callinectes sapidus* crab, R was 30% of As, but animals fed with elaborated food made from fish meal the R/As, % was between 80 and 90% indicating that a significantly proportion of the ingested energy was used to transform that diet in physiologically useful energy reducing the energy available for growth (Aguila et al., 2007). When an elaborated paste made from crab and squid was used to feed early juveniles of this species, a R/As value of 27%, was obtained. Analysis of R/A% and growth shows that lower values (~30%) are associated with higher growth rates but diets with high R/A% (80–95%) are associated with lower growth as almost all the ingested energy is channelled to maintenance but not growth (Van Heukelem, 1976; Martínez et al., 2014).

Omics and molecular biology

The utility of molecular studies is well illustrated by studies investigating effects of the gastrointestinal parasite *Aggregata octopiana*. Changes in gene expression in tissue from discrete regions of the DS provides insights into physiology. For example, in the octopus gastric ganglion expression of selected genes correlated with increased relative expression of six genes in conditions of high infection (i.e., Sn, Nfkb2, Cckar, SCPRP, Serpinb10, Tlr3) while reduced expression was reported for others (e.g., Litaf, Mirp, Sod1, Prdx6, Gpx1, Rph3al) (Baldascino et al., 2017). The study demonstrated effects of the parasite on a neural structure at a site distant from the locus of infection in the intestinal wall. Transcriptomic analysis of haemocytes identified >500 differentially expressed transcripts in *Aggregata* infected octopus infected with *Aggregata* including genes involved in pathways such as Nuclear Factor-kB, Toll-like receptor, and Complement (e.g., Castellanos-Martínez et al., 2014) or transcriptional variations of diet, temperature, and growth-related genes in paralarvae (e.g., García-Fernández et al., 2019; Garcia De La Serrana et al., 2020).

Proteomics further characterised salivary glands and their secretions. For example, the Southern blue-ringed octopus (*Hapalochlaena maculosa*) is a remarkable exception with loss of proteinaceous toxins due to the presence of tetrodotoxin (Whitelaw et al., 2020). The gland has >600 genes exclusive to *H. maculosa* when compared to *O. bimaculoides* and *Callistoctopus minor*) providing an overall scenario of fewer and more specialized genes expressed by other octopod species, when compared to *Hapalochlaena.*

Although omics and molecular studies provide novel insights it is important that findings are translated where possible into understanding the physiology of the digestive system.

Investigating neural and endocrine control mechanisms

Relatively little is known about how the individual functions described above are controlled, coordinated with each other (e.g., the relationship between the crop, stomach and caecum and the secretory and absorptive phases of DG activity) and with the regulation of food intake. Here we briefly review selected studies to illustrate some of the applicable techniques.

Neural control

a) *The enteric nervous system (ENS).* The ENS comprises the neurones within the wall of the digestive tract which may act as relays between the gastric ganglion and the muscle/epithelium to modulate secretion and motility but which also form independent reflex circuits comprising intrinsic afferent (the subepithelial plexus is reported to consist mainly of sensory cells in cuttlefish, Alexandrowicz, 1928) and efferent neurones (Furness and Stebbing, 2018). Although there is good histological evidence for the presence of intramural neurones throughout the digestive tract in cephalopods (e.g., Alexandrowicz, 1928; Young, 1967) only a limited number of species have been studied, with limited techniques (e.g., no tract tracing studies to define the exact relationship to the GG or immunohistochemistry) and there are no specific functional studies. Involvement of ENS in coordinated peristalsis and mucus secretion is highly probable by analogy with other species (Costa and Furness, 1976; Furness, 2006) as is modulation by extrinsic nerves (e.g., from the gastric ganglion) but these speculations await experimental confirmation using for example *in vitro* pharmacological studies (*see* above), and neurophysiological recordings from enteric neurones as have been performed extensively in mammals (Furness, 2006).

b) *The gastric ganglion (GG).* The structure and neurochemical complexity of the GG is consistent with its proposed role as a peripheral integrative centre but limited studies have only been undertaken in *O. vulgaris.* Electrical stimulation of the GG in *O. vulgaris* increased contractile activity in the crop, stomach, caecum (spiral tightening) and proximal intestine (Andrews and Tansey, 1983a) and there is a single report (Falloise, 1906) of accelerated flow from the digestive gland which could be due to capsule contraction, expulsion of stored secretion or *de novo* synthesised secretions. However, there have been no neurophysiological studies demonstrating the integrative abilities of the GG, the properties of its neurones or how it interfaces with the ENS, although its compact nature and structure (cortical layer of cells) make it ideally suited for these types of study. Neurophysiological studies of the stomatogastric ganglion in other molluscs (e.g., Jing et al., 2007; Daur et al., 2016) provide examples of the techniques and types of study which need to be undertaken.

Although surgical removal of the GG would be a technically simple procedure, it is unlikely to yield results which would be readily interpretable because of its extensive influence. *In vitro* studies of the entire digestive tract in *O. vulgaris* showed that GG removal/local anaesthetic application disrupted coordination of contractions between the crop and stomach and also contracted the crop suggesting removal of a tonic inhibitory effect of the GG on the crop (Andrews and Tansey, 1983a).

Molecular and immunohistochemical studies of the *O. vulgaris* GG (Baldascino et al., 2017) have identified a number of putative peptide neurotransmitters (e.g., cephalotocin, corticotrophin releasing factor, FMRF-amide, octopressin, small cardioactive peptide-related peptide, tachykinin related peptide) and receptors (e.g., cholecystokinin $_{A,B}$, octopressin, orexin receptor$_2$). However, functional studies are limited to showing contraction of the radula muscle (small cardioactive peptide-related peptide tachykinin related peptide, Kanda and Minakata, 2006) and contraction of the crop and stomach (tachykinin related peptide, Kanda et al., 2007) or rectum (octopressin, Takuwa-Kuroda et al., 2003). Detailed studies of the effect of putative peptide neurotransmitters on digestive tract motility and secretions are needed both by investigating their direct effects (*in vitro studies*) and also indirect effects by acting on the GG where they could induce motor program switching (e.g., Kirby and Nusbaum, 2007).

The role of the GG in regulating individual regions of the digestive tract could also be investigated by selective surgical transection (under general anaesthesia, with recovery and including a sham lesion group) of nerves radiating from the ganglion to adjacent structures. Following recovery, urge to eat, food intake, growth, transit time, faecal composition, haemolymph composition and post-prandial metabolism (O_2 consumption) could be measured to identify the impact of the lesion. Such a study would need careful justification, with clearly defined outcomes. Interpretation of the results may be complicated as the sectioned nerves may contain both afferent and efferent fibres and digestion of food is a sequential process with interdependent components.

c) *The central nervous system (CNS), interchange of information with the digestive system, and control of food intake.*

Communication (neural and/or endocrine) between the digestive system and the CNS is essential for the regulation of food intake which requires behaviour change to locate, capture and ingest food at a time when digestion of the previous meal permits. Limited evidence from changes in attack behaviour in *O. vulgaris* at different times after feeding has been used to conclude that the crop sends information on its degree of distension to the CNS (directly or *via* the GG; *see*: Young, 1960; Nixon, 1965). Additionally, as not all nerve fibres degenerate when the sympathetic nerves are cut between the inferior buccal ganglion and oesophagus it is concluded that the nerve contains some afferent fibres (Young, 1965). Neurophysiological studies are required to record from the sympathetic nerves to investigate whether they convey information about crop distension to the CNS in octopus or in the case of cuttlefish and squid from the stomach. If mechanosensitive afferents are present, we hypothesise by analogy with mechanoreceptors in hollow visceral organs of vertebrates, that they will be in-series with the muscle and hence capable of signalling both overall level of distension and contractions (*see* for example Andrews et al., 1980).

A detailed neurophysiological survey of the information carried in the nerves connecting the GG to the DT, the visceral nerves, and the sympathetic nerves connecting with the inferior buccal ganglion and superior buccal lobe is required to understand the relative role(s) played by the CNS, GG and ENS.

The effects of surgical transection of the nerves connecting the CNS and digestive system was investigated by Best and Wells (1983) in *O. vulgaris* but the observations have not been pursued. In food deprived animals the sight of a crab in a sealed glass jar stimulated secretion in the DG, an effect prevented by section of the sympathetic nerves either above or below the crop implying a response driven by the CNS. This is the equivalent of the "cephalic phase" of digestive tract secretions first reported by Pavlov in dogs (Pavlov, 1897). However, the majority of animals (16/18) with sympathetic nerves cut were unable to clean crabs after successfully attacking complicating interpretation. Section of the abdominal and atrio-rectal branches of the visceral nerve was without apparent effect on the ability to clean a crab, the DG response, post-prandial rise in O_2 consumption or growth. Although representing unique observations the

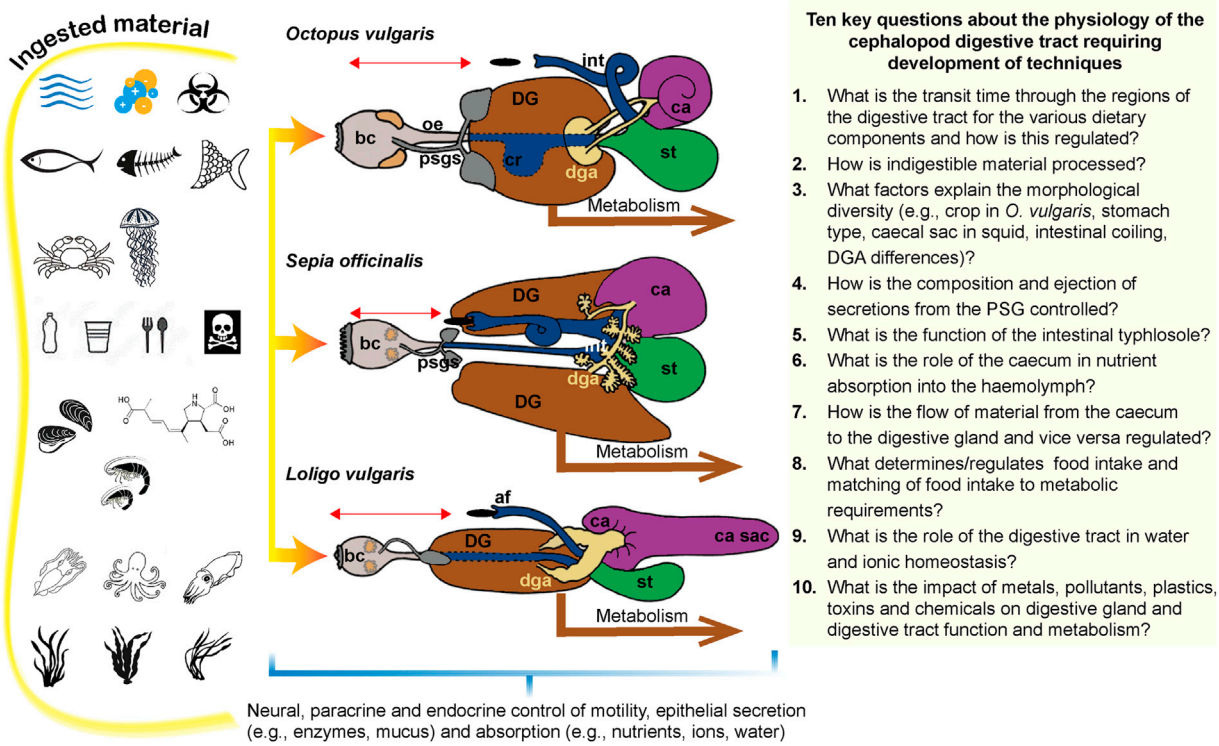

FIGURE 6
Diagram summarising a number of the key issues discussed in the review. The left -hand panel shows some of the diverse range of materials (food and non-food items) which can enter the digestive tract of cephalopods and which it will need to digest/detoxify/metabolise or eject (vomiting or defaecation). From left to right in each row the symbols indicate: water (may also contain dispersed oils), ions, biohazardous material, fish (or pieces), fish bones, fish scales, crustacea, jellyfish, plastic (entire items or fragments depending on animal size), toxins (may be adsorbed to plastics), mussels and other shellfish, domoic acid (may be present in mussels), shrimps, cephalopods (including conspecifics), seaweed and seagrasses (probably incidentally ingested with other food). The middle panel shows gross anatomical features of the digestive tract of an exemplar octopus, cuttlefish and squid to highlight the major gross anatomical differences. The horizontal red line represents the transit time-the time taken from when food enters the digestive tract *via* the beak to when the remains of that meal leave in the faeces (black oval). Abbreviations: af, anal flaps; bc, buccal complex; ca, caecum; cr, crop; DG, digestive gland; dga, digestive gland appendage; int, intestine; oe, oesophagus; psgs, posterior salivary glands; st, stomach. The right -hand panel list 10 key questions which need to be answered about the physiology of the cephalopod digestive tract and which will require the application of some new techniques and development of other to investigate in cephalopods. *See* text for detailed discussion references. The diagram in the middle panel is modified from Lobo-da-Cunha, 2019.

results should be treated with caution until replicated using more refined surgical techniques.

Endocrine control

The control of the DS by substances acting *via* the haemolymph has not been investigated in any detail especially in comparison to the reproductive system in cephalopods (e.g., Zatylny-Gaudin et al., 2016). Hormones synthesised outside the digestive system could regulate any of the DT functions directly or *via* the GG but also the potential for hormones released from the digestive tract to act on the GG or on the CNS for example to regulate food intake should not be overlooked. With the possible exception of the posterior salivary glands (Ponte and Modica, 2017) histological studies have not identified cells with characteristics typical of endocrine or paracrine cells in the digestive system but there have not been any systematic studies. Measurements of haemolymph during food deprivation and post-prandially would be the most obvious approach to identifying hormones linked to digestion with candidates identified from analysis of the genome. Based particularly on molecular studies, the following families are of particular interest: *1*) *secretin* (Cardoso et al., 2010; Mirabeau and Joly, 2013; Tam et al., 2014). A secretin-like substance was isolated from the caecum in *O. vulgaris* and shown to stimulate secretion in the digestive gland (Ledrut and Ungar, 1937). This study should be followed up as a major function of secretin is stimulation of fluid secretion in the vertebrate exocrine pancreas (Bayliss and Starling, 1902); *2*) *vasopressin/oxytocin* (Odekunle et al., 2019). Evidence for the

octopressin receptor in the GG has been obtained (Baldascino et al., 2017) and Odekunle et al. (2019) noted evidence implicating the vasopressin/oxytocin -type signalling from a number of studies of protostomes; *3*) gastrin/cholecystokinin (Zatylny-Gaudin and Favrel, 2014) as there is evidence for cholecystokinin $_{A,B}$ receptors in the GG (Baldascino et al., 2017); *5*) *orexin* (Ritschard et al., 2019). There is limited evidence for the orexin receptor$_2$ in the GG but the ligand in cephalopods is not known although members of the orexin family have been implicated in regulation of food intake in vertebrates (Wong et al., 2011).

Molecular and haemolymph profile studies need to be complemented by studies showing a functional effect of any hormones on the digestive tract. In addition, the effect of reproductive hormones on the digestive tract needs to be investigated as they may be involved in the suppression of food intake which accompanies egg laying and care in several octopus species (e.g., *O. maya*).

Concluding comments

We have reviewed diverse techniques applied to understanding the physiology of the digestive tract which enable it to perform its primary function of processing food into a form which can be utilized. Three themes emerge: *1*) Many of the pivotal studies were published more than 50 years ago and should be replicated using more modern techniques to both confirm and extend the initial findings; *2*) There are a number of major knowledge gaps (Figure 6) (e.g., transepithelial transport in the caecum/intestine) which can be resolved using established physiological techniques (e.g., Ussing chamber, molecular identification of transporters) and assumptions about function are made based primarily upon anatomy (e.g., typhlosole function); *3*) Our understanding of the physiology of the digestive tract in cephalopods is a "mosaic of knowledge" with data on individual DT functions coming from a range of species in different Orders rather than a detailed understanding of the entire digestive tract in representative species (e.g., *O. vulgaris* and *S. officinalis*). As Bidder (1950, p. 41) noted 70 years ago "Until more information is available it is clearly dangerous to combine, as has too often been done, one observation from *Octopus* with another from *Sepia* under the generalisation "In the Cephalopods.""

It is hoped that this review by combining discussion of the physiology of the cephalopod DS with an overview of techniques and identification of key knowledge gaps will stimulate a more systematic approach to research in this area.

Author contributions

All authors made an equivalent contribution to the mansucript.

Funding

CR thanks the PAPIIT program at the National Autonomous University of Mexico for the economic support given to study the digestive physiology of *Octopus maya* (IN 203022). GP and PLRA have been supported by the Stazione Zoologica Anton Dohrn intramural fund.

Acknowledgments

PA wishes to acknowledge that this review was written during the tenure of an honorary Research Fellowship at Stazione Zoologica Anton Dohrn Naples, Italy and would like to thank G. Fiorito (Head of the Department of Biology and Evolution of Marine Organisms, SZN) and the SZN President R. Danovaro. PA and GP wish to thank Dieter Fuchs and Visualsonics, and the Association for Cephalopod Research for their support and advice regarding the use of high-resolution ultrasound to image the octopus digestive system.

Conflict of interest

The authors declare that the research was conducted in the absence of any commercial or financial relationships that could be construed as a potential conflict of interest.

Publisher's note

References

Aguila, J., Cuzon, G., Pascual, C., Domingues, P. M., Gaxiola, G., Sánchez, A., et al. (2007). The effects of fish hydrolysate (CPSP) level on *Octopus maya* (Voss and Solis) diet: Digestive enzyme activity, blood metabolites, and energy balance. *Aquaculture* 273, 641–655. doi:10.1016/j.aquaculture.2007.07.010

Aldred, R. G., Nixon, M., and Young, J. Z. (1983). *Cirrothauma murrayi* Chun, a finned octopod. *Philosophical Trans. R. Soc. Lond. B, Biol. Sci.* 301, 1–54.

Alexandrowicz, J. S. (1928). Notes sur l'innervation du tube digestif cephalopodes. *Archives de zoologie Exp. Gen.* 67, 69–90.

Amado, E. M., Souza-Bastos, L. R., Vidal, E. a. G., Leite, T. S., and Freire, C. A. (2015). Different abilities to regulate tissue hydration upon osmotic challenge in vitro, in the cephalopods *Octopus vulgaris* and *O. insularis*. *Mar. Freshw. Behav. Physiology* 48, 205–211. doi:10.1080/10236244.2015.1024078

Anadón, R. (2019). "Functional histology: The tissues of common coleoid cephalopods," in *Handbook of pathogens and diseases in cephalopods* (Springer), 39–85.

Andrews, P. L., Grundy, D., and Scratcherd, T. (1980). Vagal afferent discharge from mechanoreceptors in different regions of the ferret stomach. *J. Physiol.* 298, 513–524. doi:10.1113/jphysiol.1980.sp013098

Andrews, P. L. R., Darmaillacq, A. S., Dennison, N., Gleadall, I. G., Hawkins, P., Messenger, J. B., et al. (2013). The identification and management of pain, suffering and distress in cephalopods, including anaesthesia, analgesia and humane killing. *J. Exp. Mar. Biol. Ecol.* 447, 46–64. doi:10.1016/j.jembe.2013.02.010

Andrews, P. L. R., and Tansey, E. M. (1983a). The digestive tract of *Octopus vulgaris*: The anatomy, physiology and pharmacology of the upper tract. *J. Mar. Biol. Assoc. U. K.* 63, 109–134. doi:10.1017/s0025315400049845

Andrews, P. L. R., and Tansey, E. M. (1983b). Aminergic innervation of the blood vessels of *Octopus vulgaris*. *Cell Tissue Res.* 230, 229–232. doi:10.1007/BF00216043

Aristotle (1910). *Historia animalium, English translation by D'arcy wenthworth thompson*. Oxford: Clarendon Press.

Arvy, L. (1960). Histoenzymological data on the digestive tract of *Octopus vulgaris* lamarck (cephalopoda). *Ann. N. Y. Acad. Sci.* 90, 929–949. doi:10.1111/j.1749-6632.1960.tb26440.x

Avendaño, O., Roura, Á., Cedillo-Robles, C. E., González, Á. F., Rodríguez-Canul, R., Velázquez-Abunader, I., et al. (2020). *Octopus americanus*: A cryptic species of the *O. vulgaris* species complex redescribed from the caribbean. *Aquat. Ecol.* 54, 909–925. doi:10.1007/s10452-020-09778-6

Bacq, Z. M. (1934). Recherches Sur La Physiologie Du Systéme Nerveux Autonome. V. – Réactions Du Ventricule Médian, Des Chromatophores Et De Divers Organes Isolés d'Un Mollusque Céphalopode (*Loligo Pealii*) A L'Adrénaline, L'Acétylcholine, L'Ergotamine, L'Atropine Et Aux Ions K, Ca et Mg. *Arch. Int. Physiol.* 38, 138–159. doi:10.3109/13813453309145138

Baldascino, E., Di Cristina, G., Tedesco, P., Hobbs, C., Shaw, T. J., Ponte, G., et al. (2017). The gastric ganglion of *Octopus vulgaris*: Preliminary characterization of gene- and putative neurochemical-complexity, and the effect of *Aggregata octopiana* digestive tract infection on gene expression. *Front. Physiol.* 8, 1001. doi:10.3389/fphys.2017.01001

Bastos, P., Fracalossi, D. M., Chimal, M. E., Sánchez, A., and Rosas, C. (2020). Digestive enzymes and timing of digestion in *Octopus vulgaris* type II. *Aquac. Rep.* 16, 100262. doi:10.1016/j.aqrep.2019.100262

Bastos, P., Gallardo, P., Rosas, C., Vieira, F. D. N., Silva, C. P., Oliveira, G. B., et al. (2021). Pelleted diet with thermal treatment of ingredients for *Octopus americanus*: Growth performance and enzymatic activity. *Aquac. Res.* 52, 1106–1117. doi:10.1111/are.14968

Bayliss, W. M., and Starling, E. H. (1902). The mechanism of pancreatic secretion. *J. Physiol.* 28, 325–353. doi:10.1113/jphysiol.1902.sp000920

Best, E., and Wells, M. (1983). The control of digestion in Octopus I: The anticipatory response and the effects of severing the nerves to the gut. *Vie Milieu/Life Environ.* 33, 135–142.

Bidder, A. M. (1957). Evidence for an absorptive function in the liver of *Octopus vulgaris*. *Pubblicazioni della Stazione Zool. Napoli* 29, 139–150.

Bidder, A. M. (1950). The digestive mechanism of the European squids *Loligo vulgaris, Loligo forbesii, Alloteuthis media* and *Alloteutihis subulata*. *J. Cell Sci.* 9, 1–43. doi:10.1242/jcs.s3-91.13.1

Birch, J., Burn, C., Schnell, A., Browning, H., and Crump, A. (2021). *Review of the evidence of sentience in cephalopod molluscs and decapod Crustaceans*. London: London School of Economics and Political Science.

Bogoraze, D., and Cazal, P. (1946). Remarques sur le système stomatogastrique du Poulpe (*Octopus vulgaris* lamarck): Le complexe retro-buccal. *Archives de zoologie expérimentale générale* 84, 115–131.

Boucaud-Camou, E., Boucher-Rodoni, R., and Mangold, K. (1976). Digestive absorption in *Octopus vulgaris* (cephalopoda: Octopoda). *J. Zoology* 179, 261–271. doi:10.1111/j.1469-7998.1976.tb02295.x

Boucaud-Camou, E. V. E., and Boucher-Rodoni, R. (1983). "Feeding and digestion in cephalopods," in *The Mollusca*. Editors A. S. M. Saleuddin and K. M. Wilbur (San Diego: Academic Press), 149–187.

Boucher-Rodoni, R. (1976). Étude histologique du tube digestif de deux Cephalopodes *Eledone cirrosa* (Octopoda) et *Illex illecebrosus* (Teuthoidea), au cours de la digestion. *Cah. Biol. Mar.* 17, 245–260.

Boucher-Rodoni, R. (1982). La glande digestive des céphalopodes, organe de synthèse et de sécrétion d'enzymes digestives. *Cah. Biol. Mar.* 23, 299–318.

Boucher-Rodoni, R., and Mangold, K. (1977). Experimental study of digestion in *Octopus vulgaris* (cephalopoda: Octopoda). *J. Zoology* 183, 505–515. doi:10.1111/j.1469-7998.1977.tb04202.x

Boucher-Rodoni, R. (1973). Vitesse de Digestion d'*Octopus cyanea* (cephalopoda: Octopoda). *Mar. Biol.* 18, 237–242. doi:10.1007/bf00367990

Boyle, P. R., Mangold1, K., and Froesch*, D. (1979). The mandibular movements of *Octopus vulgaris*. *J. Zoology* 188, 53–67. doi:10.1111/j.1469-7998.1979.tb03392.x

Braid, H. E., Deeds, J., Degrasse, S. L., Wilson, J. J., Osborne, J., and Hanner, R. H. (2012). Preying on commercial fisheries and accumulating paralytic shellfish toxins: A dietary analysis of invasive *Dosidicus gigas* (cephalopoda ommastrephidae) stranded in pacific Canada. *Mar. Biol.* 159, 25–31. doi:10.1007/s00227-011-1786-4

Brijs, J., Hennig, G. W., Axelsson, M., and Olsson, C. (2014). Effects of feeding on in vivo motility patterns in the proximal intestine of shorthorn sculpin (*Myoxocephalus scorpius*). *J. Exp. Biol.* 217, 3015–3027. doi:10.1242/jeb.101741

Brijs, J., Hennig, G. W., Gräns, A., Dekens, E., Axelsson, M., and Olsson, C. (2017a). Exposure to seawater increases intestinal motility in euryhaline rainbow trout (*Oncorhynchus mykiss*). *J. Exp. Biol.* 220, 2397–2408. doi:10.1242/jeb.156000

Brijs, J., Hennig, G. W., Kellermann, A.-M., Axelsson, M., and Olsson, C. (2017b). The presence and role of interstitial cells of Cajal in the proximal intestine of shorthorn sculpin (*Myoxocephalus scorpius*). *J. Exp. Biol.* 220, 347–357. doi:10.1242/jeb.141523

Budelmann, B. U., Schipp, R., and Boletzky, S. V. (1997). "Cephalopoda," in *Microscopic anatomy of invertebrates*. Editors F. W. Harrison and A. J. Kohn (New York: Wiley-Liss, Inc.), 119–414.

Bustamante, P., Caurant, F., Fowler, S. W., and Miramand, P. (1998). Cephalopods as a vector for the transfer of cadmium to top marine predators in the north-east Atlantic Ocean. *Sci. Total Environ.* 220, 71–80. doi:10.1016/s0048-9697(98)00250-2

Bustamante, P., Lahaye, V., Durnez, C., Churlaud, C., and Caurant, F. (2006). Total and organic Hg concentrations in cephalopods from the North Eastern Atlantic waters: Influence of geographical origin and feeding ecology. *Sci. Total Environ.* 368, 585–596. doi:10.1016/j.scitotenv.2006.01.038

Cardoso, J. C. R., Vieira, F. A., Gomes, A. S., and Power, D. M. (2010). The serendipitous origin of chordate secretin peptide family members. *BMC Evol. Biol.* 10, 135. doi:10.1186/1471-2148-10-135

Cariello, L., and Zanetti, L. (1977). Alpha- and beta-cephalotoxin: Two paralysing proteins from posterior salivary glands of *Octopus vulgaris*. *Comp. Biochem. Physiol. C. Comp. Pharmacol.* 57, 169–173. doi:10.1016/0306-4492(77)90066-1

Castellanos-Martínez, S., Arteta, D., Catarino, S., and Gestal, C. (2014). De novo transcriptome sequencing of the *Octopus vulgaris* hemocytes using illumina RNA-seq Technology: Response to the infection by the gastrointestinal parasite aggregata octopiana. *PLOS ONE* 9, e107873. doi:10.1371/journal.pone.0107873

Cerezo Valverde, J., and Garcia Garcia, B. N. (2004). Influence of body weight and temperature on post-prandial oxygen consumption of common octopus (*Octopus vulgaris*). *Aquaculture* 233, 599–613. doi:10.1016/j.aquaculture.2003.11.025

Cerezo Valverde, J., and Garcia Garcia, B. (2005). Suitable dissolved oxygen levels for common octopus (*Octopus vulgaris* cuvier, 1797) at different weights and temperatures: Analysis of respiratory behaviour. *Aquaculture* 244, 303–314. doi:10.1016/j.aquaculture.2004.09.036

Chabot, D., Mckenzie, D. J., and Craig, J. F. (2016a). Metabolic rate in fishes: Definitions, methods and significance for conservation physiology. *J. Fish. Biol.* 88, 1–9. doi:10.1111/jfb.12873

Chabot, D., Steffensen, J. F., and Farrell, A. P. (2016b). The determination of standard metabolic rate in fishes. *J. Fish. Biol.* 88, 81–121. doi:10.1111/jfb.12845

Costa, M., and Furness, J. B. (1976). The peristaltic reflex: An analysis of the nerve pathways and their pharmacology. *Naunyn. Schmiedeb. Arch. Pharmacol.* 294, 47–60. doi:10.1007/BF00692784

Costa, P. M., Rodrigo, A. P., and Costa, M. H. (2014). Microstructural and histochemical advances on the digestive gland of the common cuttlefish, *Sepia officinalis* L. *Zoomorphology* 133, 59–69. doi:10.1007/s00435-013-0201-8

Daur, N., Nadim, F., and Bucher, D. (2016). The complexity of small circuits: The stomatogastric nervous system. *Curr. Opin. Neurobiol.* 41, 1–7. doi:10.1016/j.conb.2016.07.005

Emam, W., Ibrahim, A. a. M., and Ghareb, T. (2016). Macro and microscopic structure of the digestive system of *Octopus vulgaris* from Alexandria water on the Mediterranean Sea. *Int. J. Dev.* 5, 27–45. doi:10.21608/idj.2016.146734

Erspamer, V., and Anastasi, A. (1962). Structure and pharmacological actions of eledoisin, the active endecapeptide of the posterior salivary glands of eledone. *Experientia* 18, 58–59. doi:10.1007/BF02138250

Falloise, A. (1906). Contribution à la physiologie comparée de la digestion. La digestion chez les Céphalopodes. *Arch. Intern. Physiol.* 3, 282–296.

Farías, A., Pereda, S. V., Uriarte, I., Dörner, J., Cuzon, G., and Rosas, C. (2010). Evaluating the effects of formulated moist diets on juveniles of patagonian Octopus *Enteroctopus megalocyathus* (gould 1852). *J. Shellfish Res.* 29, 793796–793798. doi:10.2983/035.029.0412

Fernández-Gago, R., Heß, M., Gensler, H., and Rocha, F. (2017). 3D reconstruction of the digestive system in *Octopus vulgaris* cuvier, 1797 embryos and paralarvae during the first month of life. *Front. Physiol.* 8, 462. doi:10.3389/fphys.2017.00462

Fernández-Gago, R., Molist, P., and Rocha, F. (2019). Anatomical and histochemical features of the digestive system of *Octopus vulgaris* Cuvier, 1797 with a special focus on secretory cells. *Acta Zool.* 100, 320–335. doi:10.1111/azo.12257

Ferreira, G. V. B., Justino, A. K. S., Eduardo, L. N., Lenoble, V., Fauvelle, V., Schmidt, N., et al. (2022). Plastic in the inferno: Microplastic contamination in deep-sea cephalopods (*Vampyroteuthis infernalis* and *Abralia veranyi*) from the southwestern Atlantic. *Mar. Pollut. Bull.* 174, 113309. doi:10.1016/j.marpolbul.2021.113309

Fiorito, G., Affuso, A., Anderson, D. B., Basil, J., Bonnaud, L., Botta, G., et al. (2014). Cephalopods in neuroscience: Regulations, research and the 3Rs. *Invert. Neurosci.* 14, 13–36. doi:10.1007/s10158-013-0165-x

Fiorito, G., Affuso, A., Basil, J., Cole, A., De Girolamo, P., D'angelo, L., et al. (2015). Guidelines for the care and welfare of cephalopods in research - a consensus based on an initiative by CephRes, FELASA and the Boyd Group. *Lab. Anim.* 49, 1–90. doi:10.1177/0023677215580006

Furness, J. B., and Stebbing, M. J. (2018). The first brain: Species comparisons and evolutionary implications for the enteric and central nervous systems. *Neurogastroenterol. Motil.* 30, e13234. doi:10.1111/nmo.13234

Furness, J. B. (2006). *The enteric nervous system*. Malden, Mass, USA: Blackwell Publishing.

Gallardo, P., Olivares, A., Martínez-Yáñez, R., Caamal-Monsreal, C., Domingues, P. M., Mascaró, M., et al. (2017). Digestive physiology of *Octopus maya* and *O. mimus*: Temporality of digestion and assimilation processes. *Front. Physiol.* 8, 355. doi:10.3389/fphys.2017.00355

Garcia De La Serrana, D., Pérez, M., Nande, M., Hernández-Urcera, J., Pérez, E., Coll-Lladó, C., et al. (2020). Regulation of growth-related genes by nutrition in paralarvae of the common octopus (*Octopus vulgaris*). *Gene* 747, 144670. doi:10.1016/j.gene.2020.144670

García-Fernández, P., Prado-Alvarez, M., Nande, M., Garcia De La Serrana, D., Perales-Raya, C., Almansa, E., et al. (2019). Global impact of diet and temperature over aquaculture of *Octopus vulgaris* paralarvae from a transcriptomic approach. *Sci. Rep.* 9, 10312. doi:10.1038/s41598-019-46492-2

García-Garrido, S., Hachero-Cruzado, I., Garrido, D., Rosas, C., and Domingues, P. (2010). Lipid composition of the mantle and digestive gland of *Octopus vulgaris* juveniles (Cuvier, 1797) exposed to prolonged starvation. *Aquac. Int.* 18, 1223–1241. doi:10.1007/s10499-010-9335-6

Garri, G. R., and Lauria de Cidre, L. (2013). Microanatomy of the digestive system of *Enteroctopus megalocyathus* (cephalopoda, Octopoda) of the southwest atlantic. *Bol. Invest. Mar. Cost.* 42, 255–274. doi:10.25268/bimc.invemar.2013.42.2.49

Gestal, C., Páez De La Cadena, M., and Pascual, S. (2002). Malabsorption syndrome observed in the common octopus *Octopus vulgaris* infected with *Aggregata octopiana* (Protista: Apicomplexa). *Dis. Aquat. Organ.* 51, 61–65. doi:10.3354/dao051061

Gestal, C., Pascual, S., Guerra, Á., Fiorito, G., and Vieites, J. M. (2019). *Handbook of pathogens and diseases in cephalopods*. Springer International Publishing.

Ghiretti, F. (1959). Cephalotoxin: The crab-paralysing agent of the posterior salivary glands of cephalopods. *Nature* 183, 1192–1193. doi:10.1038/1831192b0

Gonçalves, C., and Costa, P. M. (2021). Cephalotoxins: A hotspot for marine bioprospecting? *Front. Mar. Sci.* 8. doi:10.3389/fmars.2021.647344

Grisley, M., and Boyle, P. (1987). Bioassay and proteolytic activity of digestive enzymes from octopus saliva. *Comp. Biochem. Physiology Part B Comp. Biochem.* 88, 1117–1123. doi:10.1016/0305-0491(87)90014-9

Grisley, M. S., and Boyle, P. R. (1990). Chitinase, a new enzyme in octopus saliva. *Comp. Biochem. Physiology Part B Comp. Biochem.* 95, 311–316. doi:10.1016/0305-0491(90)90081-4

Grosell, M. (2010). "4 - the role of the gastrointestinal tract in salt and water balance," in *Fish physiology*. Editors M. Grosell, A. P. Farrell, and C. J. Brauner (Academic Press), 135–164.

Guerra, Á. (2019). "Functional anatomy: Macroscopic anatomy and post-mortem examination," in *Handbook of pathogens and diseases in cephalopods* (Springer), 11–38.

Hoving, H. J. T., and Haddock, S. H. D. (2017). The giant deep-sea octopus *Haliphron atlanticus* forages on gelatinous fauna. *Sci. Rep.* 7, 44952. doi:10.1038/srep44952

Hoving, H. J. T., and Robison, B. H. (2012). Vampire squid: Detritivores in the oxygen minimum zone. *Proc. Biol. Sci.* 279, 4559–4567. doi:10.1098/rspb.2012.1357

Hu, M. Y., Sucré, E., Charmantier-Daures, M., Charmantier, G., Lucassen, M., Himmerkus, N., et al. (2010). Localization of ion-regulatory epithelia in embryos and hatchlings of two cephalopods. *Cell Tissue Res.* 339, 571–583. doi:10.1007/s00441-009-0921-8

Hwang, S. J., Blair, P. J. A., Britton, F. C., O'driscoll, K. E., Hennig, G., Bayguinov, Y. R., et al. (2009). Expression of anoctamin 1/TMEM16A by interstitial cells of Cajal is fundamental for slow wave activity in gastrointestinal muscles. *J. Physiol.* 587, 4887–4904. doi:10.1113/jphysiol.2009.176198

Ibáñez, C. M., Riera, R., Leite, T., Díaz-Santana-Iturrios, M., Rosa, R., and Pardo-Gandarillas, M. C. (2021). Stomach content analysis in cephalopods: Past research, current challenges, and future directions. *Rev. Fish. Biol. Fish.* 31, 505–522. doi:10.1007/s11160-021-09653-z

Ibarra-García, L. E., Tovar-Ramírez, D., Rosas, C., Campa-Córdova, Á. I., and Mazón-Suástegui, J. M. (2018). Digestive enzymes of the californian two-spot octopus, *Octopus bimaculoides* (pickford and McConnaughey, 1949). *Comp. Biochem. Physiol. B Biochem. Mol. Biol.* 215, 10–18. doi:10.1016/j.cbpb.2017.10.001

Isgrove, A. (1909). *Eledone*. London, UK: Williams & Norgate.

Jacquet, J., Franks, B., Godfrey-Smith, P., and Sánchez-Suárez, W. (2019). The case against Octopus farming. *Issues Sci. Technol.* 35, 37–44.

Jing, J., Vilim, F. S., Horn, C. C., Alexeeva, V., Hatcher, N. G., Sasaki, K., et al. (2007). From hunger to satiety: Reconfiguration of a feeding network by *Aplysia* neuropeptide Y. *J. Neurosci.* 27, 3490–3502. doi:10.1523/JNEUROSCI.0334-07.2007

Kanda, A., and Minakata, H. (2006). Isolation and characterization of a novel small cardioactive peptide-related peptide from the brain of *Octopus vulgaris*. *Peptides* 27, 1755–1761. doi:10.1016/j.peptides.2005.12.006

Kanda, A., Takuwa-Kuroda, K., Aoyama, M., and Satake, H. (2007). A novel tachykinin-related peptide receptor of *Octopus vulgaris*– evolutionary aspects of invertebrate tachykinin and tachykinin-related peptide. *FEBS J.* 274, 2229–2239. doi:10.1111/j.1742-4658.2007.05760.x

Katsanevakis, S., Protopapas, N., Miliou, H., and Verriopoulos, G. (2005). Effect of temperature on specific dynamic action in the common octopus, *Octopus vulgaris* (Cephalopoda). *Mar. Biol.* 146, 733–738. doi:10.1007/s00227-004-1476-6

Kilkenny, C., Browne, W. J., Cuthill, I. C., Emerson, M., and Altman, D. G. (2010). Improving bioscience research reporting: The ARRIVE guidelines for reporting animal research. *PLoS Biol.* 8, e1000412. doi:10.1371/journal.pbio.1000412

Kirby, M. S., and Nusbaum, M. P. (2007). Peptide hormone modulation of a neuronally modulated motor circuit. *J. Neurophysiol.* 98, 3206–3220. doi:10.1152/jn.00795.2006

Le, H. T. M. D., Lie, K. K., Etayo, A., Rønnestad, I., and Sæle, Ø. (2021). Physical and nutrient stimuli differentially modulate gut motility patterns, gut transit rate, and transcriptome in an agastric fish, the ballan wrasse. *PLOS ONE* 16, e0247076. doi:10.1371/journal.pone.0247076

Ledrut, J., and Ungar, G. (1937). Action de la Sécrétine chez L'*Octopus vulgaris*. *Arch. Int. Physiol.* 44, 205–211. doi:10.3109/13813453709145203

Lentle, R. G., and Hulls, C. M. (2018). Quantifying patterns of smooth muscle motility in the gut and other organs with new techniques of video spatiotemporal mapping. *Front. Physiol.* 9, 338. doi:10.3389/fphys.2018.00338

Linares, M., Caamal-Monsreal, C., Olivares, A., Sánchez, A., Rodríguez, S., Zúñiga, O., et al. (2015). Timing of digestion, absorption and assimilation in octopus species from tropical (*Octopus maya*) and subtropical-temperate (*O. mimus*) ecosystems. *Aquat. Biol.* 24, 127–140. doi:10.3354/ab00642

Lobo-da-Cunha, A. (2019). Structure and function of the digestive system in molluscs. *Cell Tissue Res.* 377, 475–503. doi:10.1007/s00441-019-03085-9

Mancuso, M., Giordano, D., Genovese, L., Denaro, M. G., and Caruso, G. (2014). Study of digestive enzymes in wild specimens of *Sepia officinalis* (Linnaeus, 1758) and *Octopus vulgaris* (Cuvier, 1797). *Cah. Biol. Mar.* 55, 445–452.

Mangold, K. M., and Young, R. E. (1998). "The systematic value of the digestive organs," in *Systematics and biogeography of cephalopods*. Editors N. A. Voss, M. Vecchione, R. B. Toll, and M. J. Sweeney (Washington, DC: Smithsonian Institution), 21–30.

Martin, J. H., and Flegal, A. R. (1975). High copper concentrations in squid livers in association with elevated levels of silver, cadmium, and zinc. *Mar. Biol.* 30, 51–55. doi:10.1007/bf00393752

Martínez, R., Gallardo, P., Pascual, C., Navarro, J., Sánchez, A., Caamal-Monsreal, C., et al. (2014). Growth, survival and physiological condition of *Octopus maya* when fed a successful formulated diet. *Aquaculture* 426-427, 310–317. doi:10.1016/j.aquaculture.2014.02.005

Martínez, R., Sántos, R., Álvarez, A., Cuzón, G., Arena, L., Mascaró, M., et al. (2011). Partial characterization of hepatopancreatic and extracellular digestive proteinases of wild and cultivated *Octopus maya*. *Aquacult. Int.* 19, 445–457. doi:10.1007/s10499-010-9360-5

Martínez, R., Santos, R., Mascaró, M., Canseco, L., Caamal-Monsreal, C., and Rosas, C. (2012). Digestive dynamics during chyme formation of *Octopus maya* (Mollusca, Cephalopoda). *Aquac. Res.* 43, 1119–1126. doi:10.1111/j.1365-2109.2011.02915.x

Martínez-Montaño, E., Uriarte, I., Rosas, C., Amthauer, R., Romero, A., and Farías, A. (2018). Replacing live feed with formulated diets in juvenile Patagonian red octopus (*Enteroctopus megalocyathus*). *Aquac. Nutr.* 24, 633–643. doi:10.1111/anu.12589

McLeod, I. M., and Clark, T. D. (2016). Limited capacity for faster digestion in larval coral reef fish at an elevated temperature. *PLOS ONE* 11, e0155360. doi:10.1371/journal.pone.0155360

Meza-Buendía, A. K., Trejo-Escamilla, I., Piu, M., Caamal-Monsreal, C., Rodríguez-Fuentes, G., Diaz, F., et al. (2021). Why high temperatures limit reproduction in cephalopods? The case of *Octopus maya*. *Aquac. Res.* 52, 5111–5123. doi:10.1111/are.15387

Mirabeau, O., and Joly, J.-S. (2013). Molecular evolution of peptidergic signaling systems in bilaterians. *Proc. Natl. Acad. Sci. U. S. A.* 110, E2028–E2037. doi:10.1073/pnas.1219956110

Moltschaniwskyj, N., and Johnston, D. (2006). Evidence that lipid can be digested by the dumpling squid *Euprymna tasmanica*, but is not stored in the digestive gland. *Mar. Biol.* 149, 565–572. doi:10.1007/s00227-006-0246-z

Morote, E., Rodríguez, M., Mancera, J. M., Moyano, F. J., and Muñoz, J. (2011). Las enzimas digestivas como indicadores del estado nutricional en paralarvas de pulpo *Octopus vulgaris* Cuvier, 1797. *Bol. Inst. Español Oceanogr.* 21, 177–186.

Naef, A. (1928). *Die Cephalopoden (Embryologie). Fauna und Flora des Golfes von Neapel. Monographie 35*. Roma, Italy; Berlin, Germany: Bardi; R. Friedländer & Sohn.

Nande, M., Presa, P., Roura, Á., Andrews, P. L. R., and Pérez, M. (2017). Prey capture, ingestion, and digestion dynamics of *Octopus vulgaris* paralarvae fed live zooplankton. *Front. Physiol.* 8, 573. doi:10.3389/fphys.2017.00573

Niimi, A. J. (1978). Lag adjustment between estimated and actual physiological responses conducted in flow-through systems. *J. Fish. Res. Bd. Can.* 35, 1265–1269. doi:10.1139/f78-197

Nixon, M. (1965). Some observations on the food intake and learning in *Octopus vulgaris*. *Pubbl. Staz. Zool. Napoli* 34, 329–339.

Nixon, M. (1969). The time and frequency of responses by *Octopus vulgaris* to an automatic food dispenser. *J. Zoology* 158, 475–483. doi:10.1111/j.1469-7998.1969.tb02163.x

Norin, T., and Clark, T. D. (2016). Measurement and relevance of maximum metabolic rate in fishes. *J. Fish. Biol.* 88, 122–151. doi:10.1111/jfb.12796

Noyola, J., Mascaró, M., Caamal-Monsreal, C., Noreña-Barroso, E., Díaz, F., Re, D., et al. (2013). Effect of temperature on energetic balance and fatty acid composition of early juveniles of *Octopus maya*. *J. Exp. Mar. Biol. Ecol.* 445, 156–165. doi:10.1016/j.jembe.2013.04.008

O'Dor, R. K., and Wells, M. J. (1987). "Energy and nutrient flow," in *Cephalopod life cycles*. Editors R. K. O'dor and M. J. Wells (London: Academic Press), 109–131.

Obaldo, L. G., Divakaran, S., and Tacon, A. G. (2002). Method for determining the physical stability of shrimp feeds in water. *Aquac. Res.* 33, 369–377. doi:10.1046/j.1365-2109.2002.00681.x

Odekunle, E. A., Semmens, D. C., Martynyuk, N., Tinoco, A. B., Garewal, A. K., Patel, R. R., et al. (2019). Ancient role of vasopressin/oxytocin-type neuropeptides as regulators of feeding revealed in an echinoderm. *BMC Biol.* 17, 60. doi:10.1186/s12915-019-0680-2

Okutani, K., and Kimata, M. (1964). Studies on chitinolytic enzyme present in aquatic animals: III distribution of chitinase in digestive organs of a few kinds of aquatic animals. *Bull Jpn. Soc. Sci. Fish.* 30, 574–576. doi:10.2331/suisan.30.574

Oliveira, A. R., Sardinha-Silva, A., Andrews, P. L. R., Green, D., Cooke, G. M., Hall, S., et al. (2020). Microplastics presence in cultured and wild-caught cuttlefish, *Sepia officinalis*. *Mar. Pollut. Bull.* 160, 111553. doi:10.1016/j.marpolbul.2020.111553

Olsson, C. (2009). Autonomic innervation of the fish gut. *Acta Histochem.* 111, 185–195. doi:10.1016/j.acthis.2008.11.014

Omedes, S., Andrade, M., Escolar, O., Villanueva, R., Freitas, R., and Solé, M. (2022). B-esterases characterisation in the digestive tract of the common octopus and the European cuttlefish and their in vitro responses to contaminants of environmental concern. *Environ. Res.* 210, 112961. doi:10.1016/j.envres.2022.112961

Omura, A., and Endo, H. (2016). The functional-morphological adaptive strategy of digestive organs of decapodiform cephalopods. *J. Vet. Med. Sci.* 78, 43–47. doi:10.1292/jvms.15-0185

Øresland, R., and Oxby, G. (2021). *A photo-illustrated dissection guide for bobtail squids*. Sweden: Divers and scientists West Coast Sweden.

Owen, R. (1832). *Memoir on the pearly Nautilus (Nautilus pompilius, linn.)*. London: Richard Taylor.

Packard, A. (1972). Cephalopods and fish: The limits of convergence. *Biol. Rev.* 47, 241–307. doi:10.1111/j.1469-185x.1972.tb00975.x

Pascual, C., Mascaro, M., Rodríguez-Canul, R., Gallardo, P., Sánchez, A. A., Rosas, C., et al. (2019). Sea surface temperature modulates physiological and immunological condition of *Octopus maya*. *Front. Physiol.* 10, 739. doi:10.3389/fphys.2019.00739

Pavlov, I. P. (1897). *The work of the digestive glands*. London, UK: C. Griffin & Company Limited. Translated by W.H. Thompson, 1902.

Pedà, C., Longo, F., Berti, C., Laface, F., De Domenico, F., Consoli, P., et al. (2022). The waste collector: Information from a pilot study on the interaction between the common octopus (*Octopus vulgaris*, cuvier, 1797) and marine litter in bottom traps fishing and first evidence of plastic ingestion. *Mar. Pollut. Bull.* 174, 113185. doi:10.1016/j.marpolbul.2021.113185

Percie du Sert, N., Ahluwalia, A., Alam, S., Avey, M. T., Baker, M., Browne, W. J., et al. (2020). Reporting animal research: Explanation and elaboration for the ARRIVE guidelines 2.0. *PLoS Biol.* 18, e3000411. doi:10.1371/journal.pbio.3000411

Pereda, S. V., Uriarte, I., and Cabrera, J. C. (2009). Effect of diet and paralarval development on digestive enzyme activity in the cephalopod *Robsonella fontaniana*. *Mar. Biol.* 156, 2121–2128. doi:10.1007/s00227-009-1242-x

Ponte, G., and Modica, M. V. (2017). Salivary glands in predatory mollusks: Evolutionary considerations. *Front. Physiol.* 8, 580. doi:10.3389/fphys.2017.00580

Ponte, G., Sykes, A. V., Cooke, G. M., Almansa, E., and Andrews, P. L. R. (2017). The digestive tract of cephalopods: Toward non-invasive in vivo monitoring of its physiology. *Front. Physiol.* 8, 403. doi:10.3389/fphys.2017.00403

Ponte, G., Taite, M., Borrelli, L., Tarallo, A., Allcock, A. L., and Fiorito, G. (2021). Cerebrotypes in cephalopods: Brain diversity and its correlation with species habits, life history, and physiological adaptations. *Front. Neuroanat.* 14, 565109. doi:10.3389/fnana.2020.565109

Pörtner, H.-O., Bock, C., and Mark, F. C. (2017). Oxygen- and capacity-limited thermal tolerance: Bridging ecology and physiology. *J. Exp. Biol.* 220, 2685–2696. doi:10.1242/jeb.134585

Quintela, J., and Andrade, J. P. (2002a). Diel feeding rhythms, daily ration and gastric evacuation rates of *Sepia officinalis* in the Ria Formosa Lagoon (South Portugal). *Bull. Mar. Sci.* 71, 665–680.

Quintela, J., and Andrade, J. P. (2002b). Effects of temperature on gastric evacuation rates in *Sepia officinalis* (Linnaeus, 1758) in laboratory conditions. *Bull. Mar. Sci.* 71, 681–689.

Ritschard, E. A., Fitak, R. R., Simakov, O., and Johnsen, S. (2019). Genomic signatures of G-protein-coupled receptor expansions reveal functional transitions in the evolution of cephalopod signal transduction. *Proc. Biol. Sci.* 286, 20182929. doi:10.1098/rspb.2018.2929

Rodrigo, A. P., and Costa, P. M. (2017). The role of the cephalopod digestive gland in the storage and detoxification of marine pollutants. *Front. Physiol.* 8, 232. doi:10.3389/fphys.2017.00232

Rokni, D., and Hochner, B. (2002). Ionic currents underlying fast action potentials in the obliquely striated muscle cells of the Octopus arm. *J. Neurophysiol.* 88, 3386–3397. doi:10.1152/jn.00383.2002

Rosa, R., Costa, P. R., and Nunes, M. L. (2004). Effect of sexual maturation on the tissue biochemical composition of *Octopus vulgaris* and *O. defilippi* (Mollusca: Cephalopoda). *Mar. Biol.* 145, 563–574. doi:10.1007/s00227-004-1340-8

Rosas, C., Cuzon, G., Pascual, C., Gaxiola, G., Chay, D., López, N., et al. (2007). Energy balance of *Octopus maya* fed crab or an artificial diet. *Mar. Biol.* 152, 371–381. doi:10.1007/s00227-007-0692-2

Rosas, C., Tut, J., Baeza, J., Sánchez, A., Sosa, V., Pascual, C., et al. (2008). Effect of type of binder on growth, digestibility, and energetic balance of *Octopus maya*. *Aquaculture* 275, 291–297. doi:10.1016/j.aquaculture.2008.01.015

Rosas-Luis, R. (2016). Description of plastic remains found in the stomach contents of the jumbo squid *Dosidicus gigas* landed in Ecuador during 2014. *Mar. Pollut. Bull.* 113, 302–305. doi:10.1016/j.marpolbul.2016.09.060

Roumbedakis, K., Alexandre, M. N., Puch, J. A., Martins, M. L., Pascual, C., and Rosas, C. (2020). Short and long-term effects of anesthesia in *Octopus maya* (cephalopoda, octopodidae) juveniles. *Front. Physiol.* 11, 697. doi:10.3389/fphys.2020.00697

Ruder, T., Sunagar, K., Undheim, E. a. B., Ali, S. A., Wai, T.-C., Low, D. H. W., et al. (2013). Molecular phylogeny and evolution of the proteins encoded by coleoid (cuttlefish, Octopus, and squid) posterior venom glands. *J. Mol. Evol.* 76, 192–204. doi:10.1007/s00239-013-9552-5

Ruth, P., Schipp, R., and Arnold, J. M. (1999). Organization and function of the midgut glands of *Nautilus pompilius* L. and *Nautilus macromphalus* SOW. (Cephalopoda, Tetrabranchiata). *Zoology* 102, 196–211.

Sakamoto, T., Ogawa, S., Nishiyama, Y., Akada, C., Takahashi, H., Watanabe, T., et al. (2015). Osmotic/ionic status of body fluids in the euryhaline cephalopod suggest possible parallel evolution of osmoregulation. *Sci. Rep.* 5, 14469. doi:10.1038/srep14469

Sanders, K. M. (2019). "Spontaneous electrical activity and rhythmicity in gastrointestinal smooth muscles," in *Smooth muscle spontaneous activity: Physiological and pathological modulation*. Editors H. Hashitani and R. J. Lang (Singapore: Springer), 3–46.

Semmens, J. M. (2002). Changes in the digestive gland of the loliginid squid *Sepioteuthis lessoniana* (Lesson 1830) associated with feeding. *J. Exp. Mar. Biol. Ecol.* 274, 19–39. doi:10.1016/s0022-0981(02)00165-x

Sokolova, I. M., Frederich, M., Bagwe, R., Lannig, G., and Sukhotin, A. A. (2012a). Energy homeostasis as an integrative tool for assessing limits of environmental stress tolerance in aquatic invertebrates. *Mar. Environ. Res.* 79, 1–15. doi:10.1016/j.marenvres.2012.04.003

Sokolova, I. M., Sukhotin, A. A., and Lannig, G. (2012b). "Stress effects on metabolism and energy budgets in mollusks," in *Oxidative stress in aquatic ecosystems*. Editors D. Abele, J. P. Vazquez-Medina, and T. Zenteno-Savin (Boston: Wiley-Blackwell), 263–280.

Spasiano, E. (2020). *Characterization of the "little brain" of* Octopus vulgaris *(Mollusca, Cephalopoda)*. Naples: Università degli Studi di Napoli "Federico II". MSc Master Degree.

Steffensen, J. F. (1989). Some errors in respirometry of aquatic breathers: How to avoid and correct for them. *Fish. Physiol. Biochem.* 6, 49–59. doi:10.1007/BF02995809

Svendsen, M. B. S., Bushnell, P. G., and Steffensen, J. F. (2016). Design and setup of intermittent-flow respirometry system for aquatic organisms. *J. Fish. Biol.* 88, 26–50. doi:10.1111/jfb.12797

Sykes, A. V., Almansa, E., Cooke, G. M., Ponte, G., and Andrews, P. L. R. (2017). The digestive tract of cephalopods: A neglected topic of relevance to animal welfare in the laboratory and aquaculture. *Front. Physiol.* 8, 492. doi:10.3389/fphys.2017.00492

Sykes, A. V., Almansa, E., Ponte, G., Cooke, G. M., and Andrews, P. L. R. (2020). Can cephalopods vomit? Hypothesis based on a review of circumstantial evidence and preliminary experimental observations. *Front. Physiol.* 11, 765. doi:10.3389/fphys.2020.00765

Takei, Y. (2021). The digestive tract as an essential organ for water acquisition in marine teleosts: Lessons from euryhaline eels. *Zool. Lett.* 7, 10. doi:10.1186/s40851-021-00175-x

Takuwa-Kuroda, K., Iwakoshi-Ukena, E., Kanda, A., and Minakata, H. (2003). Octopus, which owns the most advanced brain in invertebrates, has two members of vasopressin/oxytocin superfamily as in vertebrates. *Regul. Pept.* 115, 139–149. doi:10.1016/s0167-0115(03)00151-4

Tam, J. K. V., Lee, L. T. O., Jin, J., and Chow, B. K. C. (2014). Molecular evolution of GPCRS: Secretin/secretin receptors. *J. Mol. Endocrinol.* 52, T1–T14. doi:10.1530/JME-13-0259

Tedeschi, G., Negri, A., Ceciliani, F., Ronchi, S., Vetere, A., D'aniello, G., et al. (1994). Properties of the flavoenzyme d-aspartate oxidase from *Octopus vulgaris*. *Biochim. Biophys. Acta* 1207, 217–222. doi:10.1016/0167-4838(94)00071-9

Tompsett, D. H. (1939). *Sepia*. Liverpool: The University Press of Liverpool.

Ueda, A., Nagai, H., Ishida, M., Nagashima, Y., and Shiomi, K. (2008). Purification and molecular cloning of SE-cephalotoxin, a novel proteinaceous toxin from the posterior salivary gland of cuttlefish *Sepia esculenta*. *Toxicon.* 52, 574–581. doi:10.1016/j.toxicon.2008.07.007

Van Heukelem, W. F. (1976). *Growth, bioenergetics and life-span of Octopus cyanea and Octopus maya*. Manoa: University of Hawai'i at Manoa.

Villanueva, R., Koueta, N., Riba, J., and Boucaud-Camou, E. (2002). Growth and proteolytic activity of *Octopus vulgaris* paralarvae with different food rations during first feeding, using *Artemia nauplii* and compound diets. *Aquaculture* 205, 269–286. doi:10.1016/s0044-8486(01)00678-0

Villanueva, R., Perricone, V., and Fiorito, G. (2017). Cephalopods as predators: A short journey among behavioral flexibilities, adaptions, and feeding habits. *Front. Physiol.* 8, 1–12. doi:10.3389/fphys.2017.00598

Voss, G. L. (1988). "Evolution and phylogenetic relationships of deep-sea octopods (Cirrata and Incirrata)," in *The Mollusca. Paleontology and neontology of cephalopods*. Editors M. R. Clarke and E. R. Trueman (San Diego: Academic Press), 253–276.

Wallace, I., O'dor, R., and Amaratunga, T. (1981). Sequential observations on the digestive process in the squid *Illex illecebrosus*. *NAFO Sci. Counc. Stud.* 1, 65–69.

Wells, M. J., Clarke, A., and Clarke, M. R. (1996). Energetics: The costs of living and reproducing for an individual cephalopod. *Philosophical Trans. R. Soc. Lond. Ser. B Biol. Sci.* 351, 1083–1104.

Wells, M. J., O'dor, R. K., Mangold, K., and Wells, J. (1983). Diurnal changes in activity and metabolic rate in *Octopus vulgaris*. *Mar. Behav. Physiology* 9, 275–287. doi:10.1080/10236248309378598

Wells, M. J. (1978). *Octopus: Physiology and behaviour of an advanced invertebrate*. Springer Science & Business Media.

Wells, M. J., and Wells, J. (1993). Fluid uptake and the maintenance of blood volume in octopus. *J. Exp. Biol.* 175, 211–218. doi:10.1242/jeb.175.1.211

Wells, M. J., and Wells, J. (1989). Water uptake in a cephalopod and the function of the so-called 'pancreas. *J. Exp. Biol.* 145, 215–226. doi:10.1242/jeb.145.1.215

Westermann, B., Ruth, P., Litzlbauer, H. D., Beck, I., Beuerlein, K., Schmidtberg, H., et al. (2002). The digestive tract of *Nautilus pompilius* (cephalopoda, tetrabranchiata): An X-ray analytical and computational tomography study on the living animal. *J. Exp. Biol.* 205, 1617–1624. doi:10.1242/jeb.205.11.1617

Westermann, B., and Schipp, R. (1998a). Cytological and enzyme-histochemical investigations on the digestive organs of *Nautilus pompilius* (Cephalopoda, Tetrabranchiata). *Cell Tissue Res.* 293, 327–336. doi:10.1007/s004410051124

Westermann, B., and Schipp, R. (1998b). Morphology and histology of the digestive tract of *Nautilus pompilius* and *Nautilus macromphalus* (Cephalopoda, Tetrabranchiata). *Zoomorphology* 117, 237–245. doi:10.1007/s004350050048

Whitelaw, B. L., Cooke, I. R., Finn, J., Da fonseca, R. R., Ritschard, E. A., Gilbert, M. T. P., et al. (2020). Adaptive venom evolution and toxicity in octopods is driven by extensive novel gene formation, expansion, and loss. *GigaScience* 9, giaa120. doi:10.1093/gigascience/giaa120

Williams, L. W. (1909). *The anatomy of the common squid Loligo pealii, Lesueur*. Leiden, Holland: E.J. Brill.

Wong, K. K. Y., Ng, S. Y. L., Lee, L. T. O., Ng, H. K. H., and Chow, B. K. C. (2011). Orexins and their receptors from fish to mammals: A comparative approach. *General Comp. Endocrinol.* 171, 124–130. doi:10.1016/j.ygcen.2011.01.001

Wood, J. D. (1969). Electrophysiological and pharmacological properties of the stomach of the squid *Loligo pealii* (Lesueur). *Comp. Biochem. Physiol.* 30, 813–824. doi:10.1016/0010-406x(69)90036-x

Worth, A. A., Forrest, A. S., Peri, L. E., Ward, S. M., Hennig, G. W., and Sanders, K. M. (2015). Regulation of gastric electrical and mechanical activity by cholinesterases in mice. *J. Neurogastroenterol. Motil.* 21, 200–216. doi:10.5056/jnm14120

Young, J. Z. (1971). *The anatomy of the nervous system of* Octopus vulgaris. London, UK: Oxford University Press.

Young, J. Z. (1965). The buccal nervous system of *Octopus*. *Philosophical Trans. R. Soc. Lond. Ser. B, Biol. Sci.* 249, 27–44.

Young, J. Z. (1967). The visceral nerves of *Octopus*. *Philosophical Trans. R. Soc. Lond. Ser. B, Biol. Sci.* 253, 1–22.

Young, J. Z. (1960). Unit processes in the formation of representations in the memory of *Octopus*. *Proc. R. Soc. Lond. Ser. B. Biol. Sci.* 153, 1–17.

Zatylny-Gaudin, C., Bernay, B., Zanuttini, B., Leprince, J., Vaudry, H., and Henry, J. (2010). Characterization of a novel LFRFamide neuropeptide in the cephalopod *Sepia officinalis*. *Peptides* 31, 207–214. doi:10.1016/j.peptides.2009.11.021

Zatylny-Gaudin, C., Cornet, V., Leduc, A., Zanuttini, B., Corre, E., Le Corguillé, G., et al. (2016). Neuropeptidome of the cephalopod *Sepia officinalis*: Identification, tissue mapping, and expression pattern of neuropeptides and neurohormones during egg laying. *J. Proteome Res.* 15, 48–67. doi:10.1021/acs.jproteome.5b00463

Zatylny-Gaudin, C., and Favrel, P. (2014). Diversity of the RFamide peptide family in mollusks. *Front. Endocrinol.* 5, 178. doi:10.3389/fendo.2014.00178

Ziegler, A., and Sagorny, C. (2021). Holistic description of new deep sea megafauna (Cephalopoda: Cirrata) using a minimally invasive approach. *BMC Biol.* 19, 81. doi:10.1186/s12915-021-01000-9

frontiers | Frontiers in Physiology

TYPE Original Research
PUBLISHED 14 September 2022
DOI 10.3389/fphys.2022.968047

OPEN ACCESS

EDITED BY
Graziano Fiorito,
Stazione Zoologica Anton Dohrn, Italy

REVIEWED BY
Paul Andrews,
St George's, University of London, United Kingdom
Sophie Cohen-Bodénès,
École Normale Supérieure, France

*CORRESPONDENCE
Marta Sprecher,
marta.sprecher@unifr.ch

SPECIALTY SECTION
This article was submitted to Invertebrate Physiology, a section of the journal Frontiers in Physiology

RECEIVED 13 June 2022
ACCEPTED 18 August 2022
PUBLISHED 14 September 2022

CITATION
Sprecher M, Sprecher SG and Spadavecchia C (2022), A pilot investigation of the efficacy and safety of magnesium chloride and ethanol as anesthetics in Loligo vulgaris embryos. *Front. Physiol.* 13:968047. doi: 10.3389/fphys.2022.968047

A pilot investigation of the efficacy and safety of magnesium chloride and ethanol as anesthetics in *Loligo vulgaris* embryos

Marta Sprecher[1]*, Simon G. Sprecher[1] and Claudia Spadavecchia[2]

[1]Department of Biology, University of Fribourg, Fribourg, Switzerland, [2]Department of Clinical Veterinary Medicine, Anaesthesiology and Pain Therapy Section, Vetsuisse Faculty, University of Bern, Bern, Switzerland

The inclusion of cephalopods in the legislation related to the use of animals for experimental purposes has been based on the precautionary principle that these animals have the capacity to experience pain, suffering, distress, and lasting harm. Recent studies have expanded this view and supported it. Handling cephalopod mollusks in research is challenging and whenever more invasive procedures are required, sedation and/or anesthesia becomes necessary. Therefore, finding adequate, safe, and effective anesthetics appears mandatory. Several substances have been considered in sedating cephalopods, in some instances applying those utilized for fish. However, species-specific variability requires more detailed studies. Despite long-lasting experience being linked to classic studies on squid giant axons, evidence of action on putative anesthetic substances is scarce for *Loligo vulgaris* and particularly for their embryos. The aim of the current study was to evaluate effects elicited by immersion of squid embryos in anesthetic solutions and examine whether these forms display a similar reaction to anesthetics as adults do. Different concentrations of ethanol (EtOH; 2, 2.5, and 3%) and magnesium chloride ($MgCl_2$; 1, 1.5, and 1.8%) were tested by adopting a set of indicators aimed at exploring the physiological responses of squid embryos. Forty-two embryos of the common squid *Loligo vulgaris* (stages 27–28) were assigned to three conditions (EtOH, $MgCl_2$, and controls) and video recorded for 15 min (5 min before, 5 min during, and 5 min after immersion in the anesthetic solutions). In each group, the heart rate, respiratory rate, buoyancy, chromatophore activity, and tentacles/arms responses were assessed to evaluate the embryos' vitality and responsiveness to stimulation. Both substances provoked a decrease in heart and respiratory rates and inhibited buoyancy, chromatophores, and tentacles/arms responses; no adverse effects were observed. EtOH had a faster onset of action and faster recovery than $MgCl_2$, being potentially more adequate as an anesthetic for shorter procedures. Even though $MgCl_2$ caused a longer muscle relaxation, the reversibility was not confirmed for the 1.8% concentration; however, lower concentrations triggered similar results as the ones obtained with the highest

EtOH concentrations. We have shown that the late developmental stages of *Loligo vulgaris* embryos could represent a good model to evaluate anesthetics for cephalopods since they can display similar reactions to anesthetics as adults animals do.

KEYWORDS

anesthesia, cephalopods embryos, *Loligo vulgaris*, ethanol, administration and dosage, magnesium chloride ($MgCl_2$)

Introduction

In the last decade, cephalopod mollusks have been included in European Union regulation for the use of live animals by transposition into the national legislation of the Directive 2010/63/EU "on the protection of animals used for scientific purposes." In Switzerland, the Animal Protection Ordinance (Schweizerische-Tierschutzverordnung, 2018) includes cephalopods in Chapter 1 (General Provisions—Aims) and Chapter 6 (Experiments on animals) to be protected by law since 2018. In particular, "Chapter 1" defines the categories of animals that will be protected by the ordinance; "Chapter 6" deals with animal experimentation and defines three types of cephalopods according to their sizes (small, medium, and large), no species-specific recommendation has been provided. The inclusion was based on the precautionary principle (Birch, 2017, 2021) that these animals possess the capacity to experience pain, suffering, distress, and lasting harm, further supported by some more recent findings (EFSA Panel, 2005; Crook et al., 2011; Crook and Walters, 2011; Andrews et al., 2013; Crook et al., 2013; Crook, 2021). Over the last years, an increasing number of studies have been focused on various aspects of the biology, physiology, and ecology of cephalopods. This induced an expansion of the number of species studied and also an increase in the number of studies. Therefore, an increase in attention toward the welfare of these animals is mostly required by the scientific community as well as fisheries. It is remarkable to mention that in the EU Member States, the number of cephalopods used in research in 2018 accounted for over four thousand animals according to (EU, 2019).

To perform animal handling such as for hemolymph withdrawal (Jozet-Alves et al., 2008; Locatello et al., 2013), surgeries such as limb amputation for biomechanical studies, pain or nerve regeneration studies (Imperadore et al., 2019b; Howard et al., 2019; Nesher et al., 2019), or tissue sampling (Mackie, 2008; Ponte and Fiorito, 2015; Zatylny-Gaudin et al., 2016; Baldascino et al., 2017; Imperadore et al., 2019a), the animal should be anesthetized. In mammals, the application of sedation protocols must ensure the "AALLR," meaning analgesia, amnesia, loss of consciousness, loss of control reflexes, and muscle relaxation (Katzung et al., 2021). In cephalopods and, more particularly, in the common squid *Loligo vulgaris*, other criteria are needed to define satisfactory anesthesia, since their physiological characteristics are unique and cannot be easily compared to those of mammals under similar circumstances (Sen and Tanrikul, 2009). Previous work of various laboratories have urged the use of standardized protocols with specific criteria to evaluate satisfactory anesthesia in cephalopods: ventilation rate, chromatophore coloration change, loss of sucker adhesiveness, loss of voluntary or provoked movement, and unresponsiveness to noxious stimuli (Pagano et al., 2011; Gleadall, 2013; Butler-Struben et al., 2018). On the other hand, the major criteria to be observed during sedation on the basis of those used in other aquatic animals (McFarland and Klontz, 1969) include breathing depression, pupil constriction due to flash of light, reaction to pinching eye skin, flabbiness of arms, and the lack of reaction to stimulus. But are the same parameters used for adult animals also comparable to those used for embryos? Do cephalopod embryos display similar reactions as their adults do during anesthesia?

To date, ethanol (EtOH) and magnesium chloride ($MgCl_2$) have been the most used substances to anesthetize cephalopods (Messenger et al., 1985; Butler-Struben et al., 2018; Abbo et al., 2021). Indeed, according to a recent review, out of 48 studies in which procedures for "anesthetizing" cephalopods were mentioned, 17 reported $MgCl_2$, 23 EtOH in seawater, 3 a combination of both, and only 5 a different agent (Fiorito et al., 2015). The wide acceptance of EtOH and $MgCl_2$ is linked to the fact that these substances are easy to use, not reported to be toxic for the user, and do not require special permits for purchase (depending on the country). Furthermore, they are cheap and considered more "eco-friendly" than other substances that have been suggested to be utilized with cephalopods (e.g., isoflurane; Polese et al., 2014) where special equipment is needed, and particularly, attention to disposal is required (Kumar et al., 2013; Varughese and Ahmed, 2021).

Detailed information about the physiological effects of EtOH and $MgCl_2$ in cephalopods remains scarce, especially for *Loligo vulgaris* and, more particularly, for embryos at their latest stages. Most of the recent studies on *Loligo* spp. embryos are either of ecological interest or related to development (Burbach et al., 2014; Rosa et al., 2014; Crawford et al., 2020). Therefore, it is important to not only establish anesthesia protocols but also assess whether the same indicators used for adults may be applied to embryos and determine if embryos respond in the same way to the anesthetics as adults do.

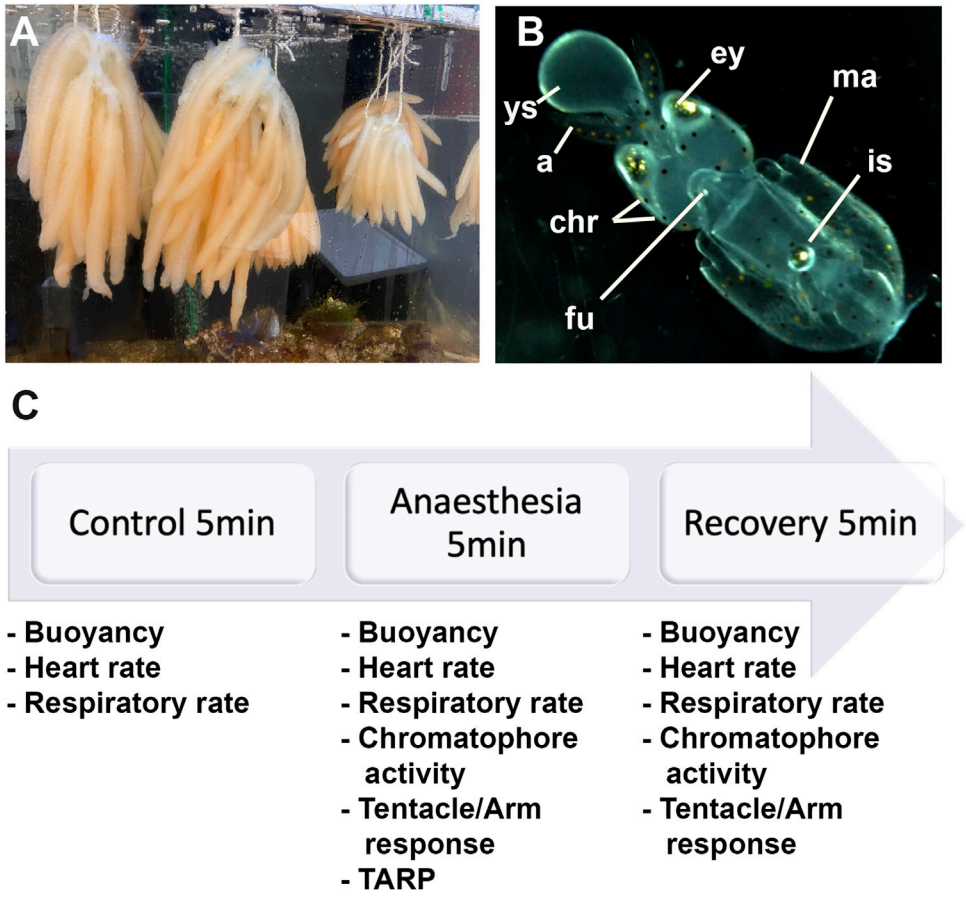

FIGURE 1
(A) Eggs of *Loligo vulgaris* suspended in bundles; each bundle contains between 15 and 30 arms. Each arm contains between 100 and 150 embryos. **(B)** Embryo stages 27–28; ys: external yolk sac, a: arms, ey: eyes, chr: chromatophores, fu: funnel, ma: mantel, is: ink sac. **(C)** Experiment timeline.

Late-stage embryos provide an interesting life stage to explore, considering that their nervous system is well developed and their capacity to learn also appears weeks before hatching as shown for *Sepia* embryos (Darmaillacq et al., 2006; Lee et al., 2020). Another important fact is that embryos can be available in reasonable numbers.

Here, we utilized *L. vulgaris* embryos to evaluate responses to immersion in EtOH and $MgCl_2$ solutions and assess the adequacy of these substances as anesthetics. In our aims, we 1) provide baseline heart rate and respiratory rate data for embryos; 2) describe changes in the heart and respiratory rates, buoyancy, chromatophore activity, and tentacle/arms responses induced by immersion in EtOH (2, 2.5, and 3% in seawater) and $MgCl_2$ (1, 1.5, 1.8% in seawater); 3) compare the responses to anesthetic solutions of squid embryos with the adult data from other studies; and 4) assess the reversibility of anesthesia on the embryos. To the best of our knowledge, our study provides a first baseline and reference for physiological parameters of respiration and heart rate of late-stage *L. vulgaris* embryos.

Materials and methods

Sample collection, housing, and husbandry

Eggs from the species *Loligo vulgaris* were collected during a sampling project of the European Marine Biological Resource Center (EMBRC) France at the Bay of Morlaix on the 22 January 2021. The eggs which are normally attached to a substrate were found in a rocky sandy habitat. The eggs were transported by a commercial courier in 30-L plastic bags with one-thirds seawater and two-thirds oxygen following the procedure by Fuentes et al. (2005). The duration of the transport was 24 h at a temperature of

14°C, and the density was three branches per bag (i.e., less than 3,000 embryos/bag).

Upon arrival in the laboratory, the eggs were incubated in a closed artificial seawater system [Red Sea REEFER 170 Deluxe Aquarium (Black)]. The tank contained 130 L of artificial seawater at a temperature of 14 ± 0.5°C (salinity range: 34–36 ppt; pH range: 7.99–8.13). A 12-h light/dark cycle was set with a crepuscular and a dawn light regime, and Maxspect éclairage LED (RSX 100W) was utilized. The eggs were suspended in bundles (see Figure 1A) in a plastic structure made with PVC. Each bundle comprised between 15 and 30 arms. Each arm hosted between 100 and 150 embryos. Taking into account that the oxygen consumption of one egg mass of octopus is twice the consumption of an adult of an average weight size (Parra et al., 2000) and to provide the best care to warrant adequate care, squid eggs' oxygenation was further facilitated by adding two additional bubblers with air diffusers (Tetra APS 100 and Tetratec AS45).

Experimental setup and embryos

Each procedure was conducted by the same person and under the same conditions. The observations of the embryos were carried out using a stereoscope (Leica Microsystems; Leica Plan APO 1.0×, 10450028; CLS100 LED).

We utilized *L. vulgaris* embryos at developmental stages 27–28 that were identified following the procedure by Arnold et al. (1974) (Figure 1B). At this stage, the yolk matches the length of the arms or the head; the latter representing one-third of the mantle length. Hatching could occur if stimulated artificially. At this stage, the ink sac is pigmented.

The eggs were placed in a Petri dish containing artificial seawater. Salinity and temperature were kept constant at 34 ppt and 14°C, respectively. The eggs were dissected carefully with a forceps (F. S. T, no. 11254-20), and the hatchlings were placed in a three-compartment culture glassware containing artificial seawater (salinity: 34 ppt; temperature: 14°C; formulation of the artificial seawater was 4 kg of artificial sea salt per 100 L of deionized water). The individuals were chosen randomly from three different egg branches; no sex differentiation was performed. The egg cases were dissected to remove the embryos, and once the embryos were out of their cases, no further development was observed.

Samples were randomly attributed to three groups. The first group (N = 18 embryos; EtOH group) served to test three different EtOH concentrations; the second group (N = 18, $MgCl_2$ group) was used to test three different concentrations of $MgCl_2$; and the third group represented the control. Each embryo was tested only for one concentration. Anesthetic solutions were made in artificial seawater, and we did not determine any potential difference in the osmotic pressure of the solutions utilized in the different treatments.

Anesthesia protocol

We identified three phases (5 min each): the control phase (t0), the anesthesia phase (t1), and the recovery phase (t2; Figure 1C). According to the Guidelines for the Care and Welfare of Cephalopods in Research, different times were proposed for anesthesia purposes for different species, but no references exist for *Loligo* and specifically for embryos (Fiorito et al., 2015). The averages suggested were between 8 and 19 min while using a single substance and according to the body size. In addition, the findings of Marking and Meyer (1985) regarding aquatic animals propose 3 min for sedation and 5 min for recovery. Therefore, we decided to use 5 min for each procedure. During the first 5 minutes (control phase; t0), the health status of the embryos was assessed. Then, artificial seawater was removed by a pipette and immediately replaced with the anesthetic solutions (anesthesia phase; t1). Afterward, the anesthetic was changed back to fresh artificial seawater (recovery phase, t2). During the three phases, the heart and respiratory rates were recorded, while the remaining parameters were evaluated only during t1 and t2. We recorded

- heart rate "hr";
- respiratory rate "rr";
- time until loss of buoyancy "TL B" and time to recover buoyancy "TR B″";
- time until loss of chromatophores activity "TL CR" and time to recover chromatophores activity "TR CR";
- time until loss of tentacles/arms response "TL T/A R" and time to recover tentacles/arms response "TR T/A R″"; and
- typical adverse response pattern "TARP" (as defined by Gleadall, 2013).

Anesthetic concentrations suggested for adult cephalopods ranged between 1% and 3% for EtOH and between 1.5% and 3.75% for $MgCl_2$ depending on the species (reviewed in Fiorito et al., 2015). As no specific reference has been identified for *L. vulgaris*, we decided to investigate the effects of 2%, 2.5%, and 3% EtOH, as well as of 1%, 1.5%, and 1.8% $MgCl_2$ (dissolved in 34 ppm artificial seawater). We did not assess the weight of the embryos. The whole procedure was video recorded, and the sequences were used to extract parameters.

Parameter assessment

Heart rate

Like any other cephalopod, *Loligo vulgaris* possess three hearts, the systemic heart and two branchial hearts. Since the beating of three hearts is synchronized, the heart rate of only one heart was counted (typically the right branchial heart). During t0, the heart rate was recorded (as beats/minute) during minutes 1, 3, and 5, then a mean of the three values was calculated. During

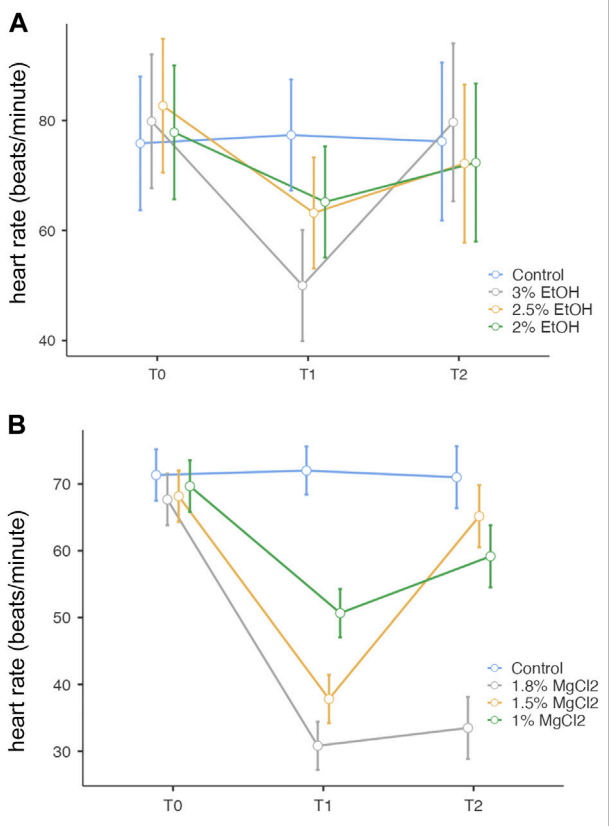

FIGURE 2
(A). Heart rate (beats/minute) before, during, and after anesthesia for the three concentrations of EtOH (3%, 2.5%, and 2%), as well as the control group. The y-axis represents the heart rate in beats per minute, the x-axis displays the three phases of the experiment each lasting 5 min: T0, control phase; T1, sedation phase; and T2, recovery phase. **(B)** Heart rate (beats/minute) before, during, and after anesthesia for the three concentrations of $MgCl_2$ (1.8%, 1.5%, and 1%), as well as the control group. The y-axis represents the heart rate in beats per minute, the x-axis displays the three phases of the experiment, each lasting 5 min: T0, control phase; T1, sedation phase; and T2, recovery phase.

t1, the heart rate was recorded at minutes 6, 8, and 10, and a mean was then calculated. Finally, during t2, the heart rate was assessed at minutes 11, 13, and 15, and the mean was calculated.

Respiratory rate

Cephalopod respiration is a complex movement of the mantle, increases or decreases its size, the first one corresponding to an inspiration (Figures 3A,B) and the increase of pressure in the mantle (Figure 3B) triggering water expulsion through the funnel (expiration) (Bone et al., 1994). During t0, the contractions of the mantle combined with the funnel movements were counted during minutes 1, 3, and 5, then the mean of the three values was calculated. Similarly, during t1, respirations were counted during minutes 6, 8, and 10, and the mean value was calculated. During t2, respirations were counted at minutes 11, 13, and 15, and the mean was calculated.

Time until loss and to recovery of buoyancy "TL B", "TR B"

Buoyancy is the capacity of the embryo to swim in a physiological manner and, if put in an unphysiological position, to return to a physiological one. Buoyancy should be present as proof of good health (Sherrill et al., 2000; Moltschaniwskyj et al., 2007) and thus a core criterion for embryos inclusion in the study. During t0, buoyancy was verified and defined as present or absent. During t1, the time until loss of buoyancy was measured in seconds once the embryo went from a present to an absent state. During t2, embryos were stimulated every 10 s by a gentle touch to the mantle, head, tentacles, and arms, and the time to recovery of buoyancy was recorded.

Time until loss and to recovery of chromatophore activity "TL CR", "TR CR"

Chromatophores are pigmented sacs connected to radial muscles, and each contraction and relaxation of these muscles trigger the pigmented sac to increase or decrease its size, respectively (Mathger and Hanlon, 2007). During t0, the chromatophores were observed, and three states were defined: a relaxed state, half-contracted state, and a contracted state (Figure 5A–C). During t1, the time until loss of chromatophore activity was defined as the time from immersion in the anesthetic bath to loss of chromatophore activity or until a relaxed state was observed and maintained. During t2, the time to recovery of the chromatophore activity was defined as the time from immersion in an anesthetic-free solution to the return of chromatophore pattern changes/change from a relaxed to contracted state.

Time until loss and to recovery of tentacles/arms response "TL T/A R", "TR T/A R"

In cephalopods, such as octopus, a measure of the state of anesthesia is sucker adhesiveness (Sen and Tanrikul, 2009; Pagano et al., 2011). However, for smaller cephalopods, sucker adhesiveness is difficult to evaluate. Moreover, this is particularly difficult to assess in late-stage *L. vulgaris* embryos. Therefore, as an alternative proxy for the responsiveness of the embryo, we assessed tentacles/arms response following a gentle pinch. During t0, the tentacles/arms response was classified as absent or present. During t1, the time until loss of tentacles/arms response or the absence of it was measured. In t2, the time to recovery of tentacles/arms response or its presence was recorded.

Typical adverse response patterns

The typical adverse response pattern (TARP) corresponds to an excitatory phase of immersion in the anesthetic solution that

in some circumstances may be particularly marked, including inking, escape reactions, increased or erratic ventilation, rapid switch in coloration or of the chromatophore tone, rapid jetting movements, convulsions, and defecation (Gleadall, 2013). Any observed adverse reactions were recorded during induction and recovery.

Data analysis

Video recordings of *L. vulgaris* embryos at stages 27–28 (Figure 1B) under different treatments were obtained during experiments, and parameters were noted from video playback. Each video consisted of a 5-min control phase (t0), a 5-min anesthesia phase (t1), and a 5-min recovery phase (t3), as mentioned above.

Statistical analyses were performed using standard statistical functions in jamovi (https://www.jamovi.org/). For all experiments where two conditions are directly compared, we used a t-test (buoyancy, chromatophores activity, and tentacles response), while for the experiments with multiple conditions, we used ANOVA with a Tukey *post hoc* test (heart and respiratory rates). A paired samples t-test was used to determine if there was a significant difference between the means of the embryos anesthetized with EtOH and those anesthetized with $MgCl_2$, for the following parameters: buoyancy, chromatophores activity, and tentacles response. The heart and respiratory rates were assessed using repeated measures ANOVA within factors; three conditions and three repeated measures with a Tukey *post hoc* test. All data are presented as means ± standard error of the mean (SE).

Ethical statement

Ethical review and approval were not required for this study because only embryos were used, which do not fall under the Swiss Animal Protection Ordinance. However, we followed the principles stated in the Guidelines for the Care and Welfare of Cephalopods in Research (Fiorito et al., 2015). After the experiment, the embryos were humanely killed by an increased dose of EtOH every 5 min, starting with 1.5%, then 2.5% until a final concentration of 3.75% was reached, and death was confirmed by mechanical brain/head destruction.

Results

During the experiments, we did not observe mortality at short term, induced from treatment in *L. vulgaris* embryos.

Heart rate

During the control/baseline phase (t0), the heart rate was comparable in all experimental groups: mean ± SE, 79.04 ± 2.92 beats/minute (EtOH group) and 72.07 ± 5.06 beats/minute ($MgCl_2$ group; Figure 2 A and B). It is noteworthy to report that we recorded the lowest observed rate at t0 of 67.67 beats/minute (±3.86) in animals assigned to the 1.8% $MgCl_2$ group, and the highest values noted reached 82.67 beats/minute (±5.83; 2% EtOH group; see Table 1).

During the anesthesia phase (t1), the lowest heart rate was reached under 1.8% $MgCl_2$ at 30.83 beats/minute (±3.61), followed by the rate noted under 1.5% $MgCl_2$ (37.83 beats/minute) and 1% $MgCl_2$ (50.67 beats/minute). The lowest heart rate for the EtOH group was triggered by the 3% EtOH concentration with 50.00 beats/minute (±4.84) followed by the 2.5% EtOH group with 63.17 beats/minute, and finally the 2% EtOH group recorded the highest heart rate for both groups with 65.17 beats/minute (Figure 2 A, B, and Tables 1).

During the recovery phase (t2), animals returned to values comparable to the baseline with the highest heart rates observed for the EtOH group with 79.67 beats/minute (±6.88), 72.33 beats/minute, and 72.17 beats/minute for the 3%, 2%, and 2.5% concentrations, respectively. For the $MgCl_2$ group, the highest values of the heart rate were observed in the 1.5% concentration condition (65.17 ± 4.65 beats/minute), followed by the 1% concentration condition with 59.17 beats/minute and the 1.8% concentration condition with 33.50 beats/minute (see Table 1).

Overall, no significant differences emerged among the groups ($p = 1$, 3% EtOH and 2% EtOH; $p = 0.999$ for the 2.5% EtOH group). By comparing the heart rates between t0 and t1, significant differences resulted (3% EtOH and 2.5% EtOH, $p < 0.001$ and $p = 0.003$, respectively), confirming the heart rate depression during anesthesia. However, no variations existed between t0 and t1 for the 2% EtOH group, confirming that the embryos were too lightly anesthetized, as were those in the control group with $p = 0.113$ and $p = 1$, respectively. During the recovery phase, significant variations were found only for the 3% EtOH group ($p < 0.001$) (see Supplementary Table S1).

Overall, no significant differences were observed during t0 (baseline) between different treatments ($p > 0.05$). However, significant differences existed when comparing before anesthesia (t0) and during anesthesia (t1; $p < 0.001$ for 1.8% and 1.5%, $p = 0.002$ for 1% $MgCl_2$) except for the control group ($p = 1$), thus confirming the heart rate depression induced by anesthesia. When comparing the heart rate between the anesthesia (t1) and recovery (t2) phases, no significant differences were observed for animals exposed to 1.8% $MgCl_2$ since the animals never recovered and the 1% appeared to be only light sedated. $p < 0.001$ for the 1.5% $MgCl_2$ proved to be the more satisfying concentration (Supplementary Table S1).

TABLE 1 Heart rate (beats/minute) of *L. vulgaris* embryos exposed to different EtOH and $MgCl_2$ concentrations and the controls (no anesthetic solution). Measures are summarized (mean, SE, and 95% confidence interval) at the three different phases: baseline, t0; anesthesia, t1; and recovery, t2.

EtOH					
Concentrations	**Time**	**Mean**	**SE**	**95% confidence interval**	
				Lower	**Upper**
Control	T0	75.8	5.83	63.7	88.0
	T1	77.3	4.84	67.2	87.4
	T2	76.2	6.88	61.8	90.5
3% EtOH	T0	79.8	5.83	67.7	92.0
	T1	50.0	4.84	39.9	60.1
	T2	79.7	6.88	65.3	94.0
2.5% EtOH	T0	82.7	5.83	70.5	94.8
	T1	63.2	4.84	53.1	73.3
	T2	72.2	6.88	57.8	86.5
2% EtOH	T0	77.8	5.83	65.7	90.0
	T1	65.2	4.84	55.1	75.3
	T2	72.3	6.88	58.0	86.7
$MgCl_2$					
Control	T0	71.3	3.86	63.3	79.4
	T1	72.0	3.61	64.5	79.5
	T2	71.0	4.65	61.3	80.7
1.8% $MgCl_2$	T0	67.7	3.86	59.6	75.7
	T1	30.8	3.61	23.3	38.4
	T2	33.5	4.65	23.8	43.2
1.5% $MgCl_2$	T0	68.2	3.86	60.1	76.2
	T1	37.8	3.61	30.3	45.4
	T2	65.2	4.65	55.5	74.9
1% $MgCl_2$	T0	69.7	3.86	61.6	77.7
	T1	50.7	3.61	43.1	58.2
	T2	59.2	4.65	49.5	68.9

Respiratory rate

Table 2 summarizes the respiratory rate observed in *L. vulgaris* embryos in different phases and conditions of the experiment. During the t0 phase, the average respiratory rate ranged between 56.29 ± 5.50 and 63.40 ± 6.70 mantle contractions per minute (EtOH and $MgCl_2$ groups, respectively (Figure 3C), with a peak of 68.83 ± 3.86 mantle contractions per minute (mcm), and the lowest values recorded were 51.33 mantle contractions per minute. During anesthesia phase (t1), the respiratory rate was reduced to 12.83 ± 3.64 mcm (3% EtOH) and 14.20 ± 4.49 mcm (1.8% $MgCl_2$; Figure 3 C; Table 2). The second lowest respiratory rates were recorded with 1.5% $MgCl_2$ concentration (18.33) followed by 2.5% EtOH and 2% EtOH groups (30.83 and 31.70 mantle contractions per minute, respectively). The less depressed respiratory rate in squid embryos was observed with the 1% $MgCl_2$ concentration, reaching 36.70 mantle contractions per minute (50.33 mantle contractions per minute for the control group; Table 2). During recovery (t2), the respiratory rate returned to high values of 52.0 ± 4.37 mcm (1% $MgCl_2$), 51.67 mcm (1.5% $MgCl_2$), and 51.68 (3% EtOH group) mantle contractions per minute; 49.17 mcm (2.5% EtOH) and 47.70 mcm for *L. vulgaris* embryos exposed to 2% EtOH concentrations. We registered 49.67 mantle contractions per minute in the control group (Table 2).

No differences were observed during t0 (baseline; see Supplementary Table S2). However substantial differences were noted when t0 (before anesthesia) and t1 (after anesthesia) phases were compared ($p < 0.001$, 1.8%, and 1.5% $MgCl_2$ concentration groups). No differences emerged when embryos exposed to 1% $MgCl_2$ were considered ($p = 0.079$; Supplementary Table S2). In addition, when baseline (t0) and the recovery (t2) phases were considered, we did not find

TABLE 2 Respiratory rate (mantle contractions/minute) of *L. vulgaris* embryos exposed to different EtOH and $MgCl_2$ concentrations and the controls (no anesthetic solution). Measures are summarized (mean, SE, and 95% confidence interval) at the three different phases: baseline, t0; anesthesia, t1; and recovery, t2.

EtOH					
Concentrations	**Time**	**Mean**	**SE**	**95% Confidence interval**	
				Lower	**Upper**
Control	T0	52.8	4.97	42.46	63.2
	T1	50.3	3.64	42.74	57.9
	T2	49.7	5.47	38.25	61.1
3% EtOH	T0	62.0	4.97	51.63	72.4
	T1	12.8	3.64	5.24	20.4
	T2	51.7	5.47	40.25	63.1
2.5% EtOH	T0	59.0	4.97	48.63	69.4
	T1	30.8	3.64	23.24	38.4
	T2	49.2	5.47	37.75	60.6
2% EtOH	T0	51.3	4.97	40.96	61.7
	T1	31.7	3.64	24.07	39.3
	T2	47.7	5.47	36.25	59.1
$MgCl_2$					
Control	T0	52.8	4.39	43.68	62.0
	T1	50.3	4.49	40.96	59.7
	T2	49.7	4.37	40.56	58.8
1.8% $MgCl_2$	T0	68.8	4.39	59.68	78.0
	T1	14.2	4.49	4.80	23.5
	T2	15.2	4.37	6.06	24.3
1.5% $MgCl_2$	T0	58.0	4.39	48.84	67.2
	T1	18.3	4.49	8.96	27.7
	T2	51.7	4.37	42.56	60.8
1% $MgCl_2$	T0	58.7	4.39	49.51	67.8
	T1	36.7	4.49	27.30	46.0
	T2	52.0	4.37	42.89	61.1

significant differences except for the 1.8% $MgCl_2$ group. Comparison between the anesthesia phase (t1) and the recovery (t2) revealed significant differences for the 1.5% ($p < 0.001$) and 1% ($p = 0.078$) $MgCl_2$ groups, showing recovery which appears to be more efficient when the 1.8% concentration was considered (Supplementary Table S2).

Time until loss of buoyancy and time to recovery of buoyancy

Time until loss of buoyancy "TL B″ was shorter on average when using EtOH (54 ± 8.29 s) compared to values recorded with $MgCl_2$ (194 ± 52.61 s; Figure 4 A and B). The faster time until loss of buoyancy was reached when embryos were exposed to 3% EtOH concentration (19.83 ± 3.66 s; Table 3), followed by the 2.5% EtOH concentration and the 2% EtOH concentration (68.33 ± 7.17, and 73.83 ± 10.44 s, respectively). For the $MgCl_2$ group, the TL B took longer (TL B: 107.50 ± 41.60 s, 1.8% $MgCl_2$; 174.50 ± 30.09 s, 1.5% $MgCl_2$; 299.50 ± 3.69 s, 1% $MgCl_2$; Table 3). During the recovery phase after anesthesia (t2), the average time to recovery buoyancy "TR B″ was 198.83 ± 33.25 s for the EtOH group but required 1700.06 ± 1185.52 s for the $MgCl_2$ group, thus suggesting a marked interindividual variability in this case (Table 3). The highest TR B value was observed for embryos exposed to 1.8% $MgCl_2$ (4721.67 ± 855.4 s), followed by animals of the 1.5% $MgCl_2$ concentration (314 ± 21.60 s), then by the 3% EtOH group (223.33 ± 20.00 s) and the 1.5% and 2% EtOH groups (194.67 ± 42.70 and 178.50 ± 44.40 s, respectively). The faster TR B was obtained with 1% $MgCl_2$ concentration at 64.50 ± 12.60 s (Table 3).

No significant differences were obtained for the time until loss of buoyancy among all three EtOH concentrations and the 1.8% $MgCl_2$ concentration (Supplementary Table S3). However,

10.3389/fphys.2022.968047

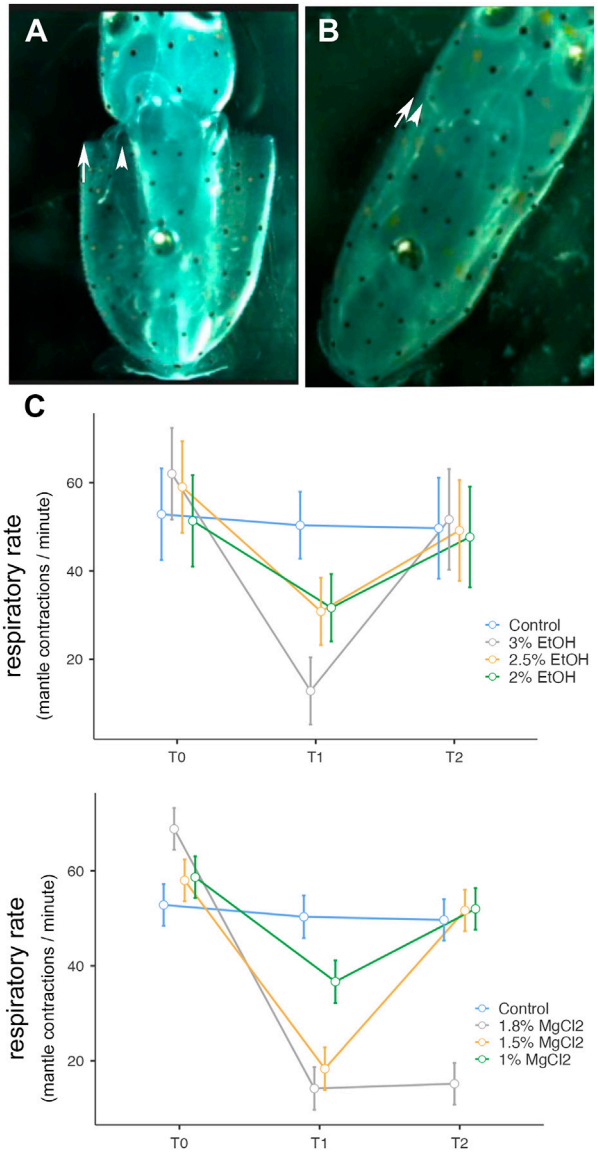

FIGURE 3
(A) Expansion of the mantle. **(B)** Contraction of the mantle. Both **(A)** and **(B)** correspond to one respiration. **(C)** Respiratory rate (mantle contractions/minute) before, during, and after anesthesia for the three concentrations of EtOH (3%, 2.5%, and 2%) and $MgCl_2$ (1.8%, 1.5%, and 1%), as well as the control group. The y-axis represents the respiratory rate, the x-axis displays the three phases of the experiment, each lasting 5 min; T0, control phase; T1, sedation phase; and T2, recovery phase.

significant differences were found in comparing EtOH concentrations and the 1.5% and 1% $MgCl_2$ groups (Supplementary Table S3). Substantial differences existed among groups; the 3% EtOH concentration was significant when compared to the baseline, while the 1.8% and 1.5% $MgCl_2$ concentrations had no significant differences (Supplementary Table S3).

Concerning the time to recover buoyancy, no significant differences existed between the EtOH concentrations and the 1.5% $MgCl_2$ group (Supplementary Table S3). Among the EtOH concentrations, no significant difference emerged for time to recover buoyancy, in contrast to the case of the $MgCl_2$ group (all significant; Supplementary Table S3).

Time until loss of chromatophore activity and time to recovery of chromatophores activity

Time until loss of chromatophore activity "TL CR" was faster on average with EtOH (147.89 ± 14.45 s) than with $MgCl_2$ (168.44 ± 15.26 s; Figure 5D). The faster onset was with the 3% EtOH concentration at 80.50 ± 36.40 s, followed by the 1.8% $MgCl_2$ group (108.50 ± 45.70 s; Table 4). The loss of chromatophore activity was reached in 130.17 ± 41.10 s when squid embryos were exposed to 1.5% $MgCl_2$ concentration and in 163.17 ± 26.30 s when the animals were exposed to 2.5% EtOH concentration (Table 4). On the other hand, TL CR required more than 200 s when the squid embryos were tested with 2% EtOH (200 ± 36.70 s) and 1% $MgCl_2$ (266.67 ± 33.33 s; Table 4).

Recovery of chromatophore tone was quite fast with both $MgCl_2$ and EtOH (61.89 ± 19.91; 70.44 ± 52.69 s, respectively). The fastest recovery was recorded when the lowest $MgCl_2$ concentration (1%) was used (11.17 ± 2.47 s) and the 2.5% EtOH group (45.83 ± 16.13 s; Table 4). More time was required when animals were exposed to the 2% EtOH concentration (68.50 ± 12.03 s; Table 4). On the other hand, 3% EtOH concentration and 1.8% $MgCl_2$ concentration resulted in a longer time to recovery of chromatophore tone (97 ± 51.17; 88.33 ± 17.13 s, respectively; Table 4). It is interesting to note that embryos that exhibited half-contracted or relaxed chromatophore states at the baseline performed a similar pattern during the whole immersion in EtOH until the change to fresh artificial seawater.

There were no significant differences in the time to recovery of chromatophore activity among the three concentrations of EtOH and the three concentrations of $MgCl_2$. However, significant differences were observed between the 1.8% and 1% $MgCl_2$ and between 1.5% and 1% $MgCl_2$ (Supplementary Table S4) groups.

Time until loss and recovery of tentacle response

Time until loss of the tentacles/arms response "TL T/A R" was quicker on average for the $MgCl_2$ concentrations with 96.94 ± 25.26 s and 117.83 ± 37.54 s for the EtOH concentrations (Figure 6 A and B). The faster TL T/AR was achieved by the 1.8% $MgCl_2$ concentration with

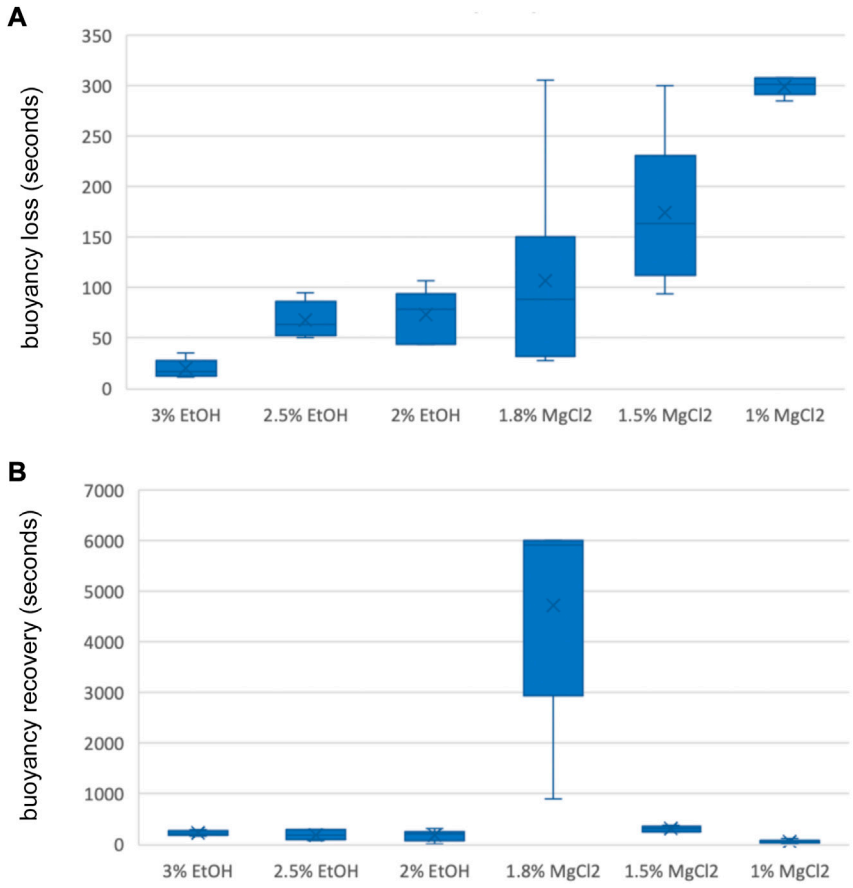

FIGURE 4
(A) Box and whiskers plot with the time until loss of buoyancy response in seconds. The y-axis represents the seconds until loss of buoyancy and the x-axis displays the three EtOH and $MgCl_2$ concentrations. The upper and lower limits show the highest and lowest times, respectively, until the loss of buoyancy, and the mid-point shows the mean. **(B)** Box and whiskers plot with the time to recovery of buoyancy response in seconds. The y-axis represents the seconds to the recovery of buoyancy and the x-axis displays the three EtOH and $MgCl_2$ concentrations. The upper and lower limits show the highest and lowest times, respectively, until recovery of buoyancy, and the mid-point shows the mean.

44.83 ± 11.70 s, followed by 46.33 ± 7.43 s for the 3% EtOH concentration. The second fastest TL T/A R resulted in conditions where animals were exposed to 1.5% $MgCl_2$ concentration (99 ± 16.54 s); this was followed by TL T/A R in animals exposed to 2% $MgCl_2$ concentration (147.67 ± 29.66 s) and 2.5% EtOH (159.51 ± 36.81; Table 5). The slower TL T/A R was observed for squid embryos exposed to 1% $MgCl_2$ concentrations (266.70 ± 33.33 s; Table 5). Time to the recovery of tentacles/arms response "TR T/A R″ was on average quicker for the EtOH (67.94 ± 37.85 s) than was for the $MgCl_2$ (73.28 ± 28.37 s) group. We observed the quickest recovery in the 1% $MgCl_2$ group, followed by the groups exposed to 2.5% EtOH and 2% EtOH (20.17 ± 8.35; 36.67 ± 11.30; 40.33 ± 11.55 s, respectively; Table 5). The longest TR T/A R was obtained for the 3% EtOH concentration (126.83 ± 38.19 s) and 1.8% $MgCl_2$ (117.33 ± 21.75 s; Supplementary Table S5) groups.

Typical adverse response pattern

No TARP reactions (as defined by Gleadall, 2013) were observed throughout the course of the study.

Follow-up of the embryos after the anesthesia protocol

The embryos were monitored for 48 h after anesthesia to assess their vitality and any other adverse effects. Our data show that embryos exposed to $MgCl_2$ can be divided into two groups: the first group are the embryos exposed to 1.8% concentration and the second group are those anesthetized with the 1.5% and 1% $MgCl_2$ concentrations. None of the embryos exposed to 1.8% $MgCl_2$ survived after 6 h. Besides buoyancy, all the other parameters considerably returned to values similar to the

TABLE 3 Time until loss of buoyancy in seconds (TL B) and time to recovery of buoyancy in seconds (TR B) of *L. vulgaris* embryos exposed to different EtOH and $MgCl_2$ concentrations and the controls (no anesthetic solution). Measures are summarized (mean, median, SD, and SE).

	N	Mean	Median	SD	SE
TL B 3% EtOH	6	19.8	16.5	8.98	3.66
TL B 2.5% EtOH	6	68.3	63.5	17.57	7.17
TL B 2% EtOH	6	73.8	79.0	25.56	10.44
TL B 1.8% $MgCl_2$	6	107.5	89.0	101.90	41.60
TL B 15% $MgCl_2$	6	174.5	163.5	73.69	30.09
TL B 1% $MgCl_2$	6	299.5	301.5	9.05	3.69
	N	**Mean**	**Median**	**SD**	**SE**
TR B 3% EtOH	6	223.3	216.5	49.1	20.0
TR B 2.5% EtOH	6	194.7	194.0	104.5	42.7
TR B 2% EtOH	6	178.5	198.0	108.7	44.4
TR B 1.8% $MgCl_2$	6	4721.7	5910.0	2095.2	855.4
TR B 1.5% $MgCl_2$	6	314.0	320.0	53.0	21.6
TR B 1% $MgCl_2$	6	64.5	70.0	30.9	12.6

baseline; the heart and respiratory rates took between 40 min and 1 h to normalize. The chromatophore tone and tentacles/arms response also recovered relatively quickly within 5 min. However, the quickest recovery for the buoyancy was obtained after 2 h 46 min for one embryo and did not occur for the remaining embryos. On the other hand, 8 out of 12 embryos survived 24 h with a decreased heart rate and respiratory rate and only four survived 48 h. In any case, death appeared to be linked to respiratory depression followed by poor oxygenation.

The short life span can be explained by the type of anesthetic but also the fact that embryos had lost their external yolk, leaving them with only their internal yolk to feed them. For the EtOH group, for each concentration, only one embryo was kept for this follow-up. The three embryos those survived 24 h with a proper heart and respiratory rate, buoyancy, chromatophore, and tentacles/arms response were still present. After 48 h, the embryos were still present with a heart rate, but with a lower rate than the baseline, and the respiration was depressed with partial buoyancy.

Discussion

Anesthetic substances

The large diversity of cephalopods, with over 800 species, makes it difficult to standardize the use and dosage of anesthetic solutions. For research purposes, only a few species are currently being studied. However, these species have diverged, adapting to rather different lifestyles and differing in body sizes. While it is challenging to anesthetize different species, it is important to establish some common approaches and standardize the evaluation of anesthetic quality in these animals. In our study, the parameters proposed by Pagano et al. (2011) and Andrews et al. (2013) were investigated as much as the size and physiology of the *Loligo* embryos allowed.

The concentrations of EtOH and $MgCl_2$ used in the present study were based on ranges previously utilized for adult animals (reviewed in Fiorito et al., 2015). Depending on the species and body weight, concentrations ranging from 1 to 3% were suggested for EtOH and from 1.5% to 3.75% for $MgCl_2$. Therefore, in our study the concentrations for the EtOH solution tested were 2%, 2.5%, and 3% and were 1%, 1.5% and 1.8% for $MgCl_2$ in seawater. It seems likely that the body size and age of the animal may affect the efficiency of a given anesthetic. In our study, the comparison of these substances revealed that for the heart rate and respiratory rate, EtOH had a faster onset and recovery than did $MgCl_2$, confirming previous observations reported for adult squids. Indeed, a recent study found that EtOH is less depressive and easier to recover than $MgCl_2$ for octopus and cuttlefish (Abbo et al., 2021). Nevertheless, the return of the chromatophore and tentacle/arm responses was faster for the $MgCl_2$ groups than the EtOH groups.

The mechanisms of $MgCl_2$ and EtOH anesthetic functions in cephalopods is still largely unknown. A recent study in *Sepia pharaonis* showed that $MgCl_2$ enhances the amount of the inhibitory neurotransmitters glycine and tyrosine while reducing the level of dopamine (Yang et al., 2020). In contrast to EtOH, $MgCl_2$ has a prolonged activity, being therefore potentially more suitable for longer procedures. In addition, $MgCl_2$ has been reported to have not only immobilizing properties but also analgesic ones, by acting as a neurotransmitter release blocker and having local anesthetic properties (Butler-Struben et al., 2018). However, the mode of action and physiological mechanism of $MgCl_2$ as an anesthetic have not been fully elucidated and remain to be explored. It has been studied extensively in mice (Wong et al., 1997; Sharko and Hodge, 2008). According to Wong et al. (1997), the use of EtOH resembles the use of volatile anesthetics such as desflurane, both depressing the muscle stretch reflex or monosynaptic reflex while having a quick onset and offset of action as well as an age-related rise of anesthetic potency. The younger the animal, the higher the required dosage; the latter is along the lines of the higher dosage used in our experiment. In addition, EtOH has a hypnotic and sedative effect modulated through metabotropic glutamate receptors requiring $GABA_A$ and NMDA receptors. Even though EtOH analgesic effects are not known in cephalopods, it is notorious to provoke a possible status of loss of consciousness in humans, followed in some cases of amnesia and analgesic effects (Tamerin et al., 1971; Thompson et al., 2017), but state dependency (Goodwin et al., 1969; Bettinger and McIntire, 2004; Rezayof et al., 2008) has been widely reported and may be the cause of such effects.

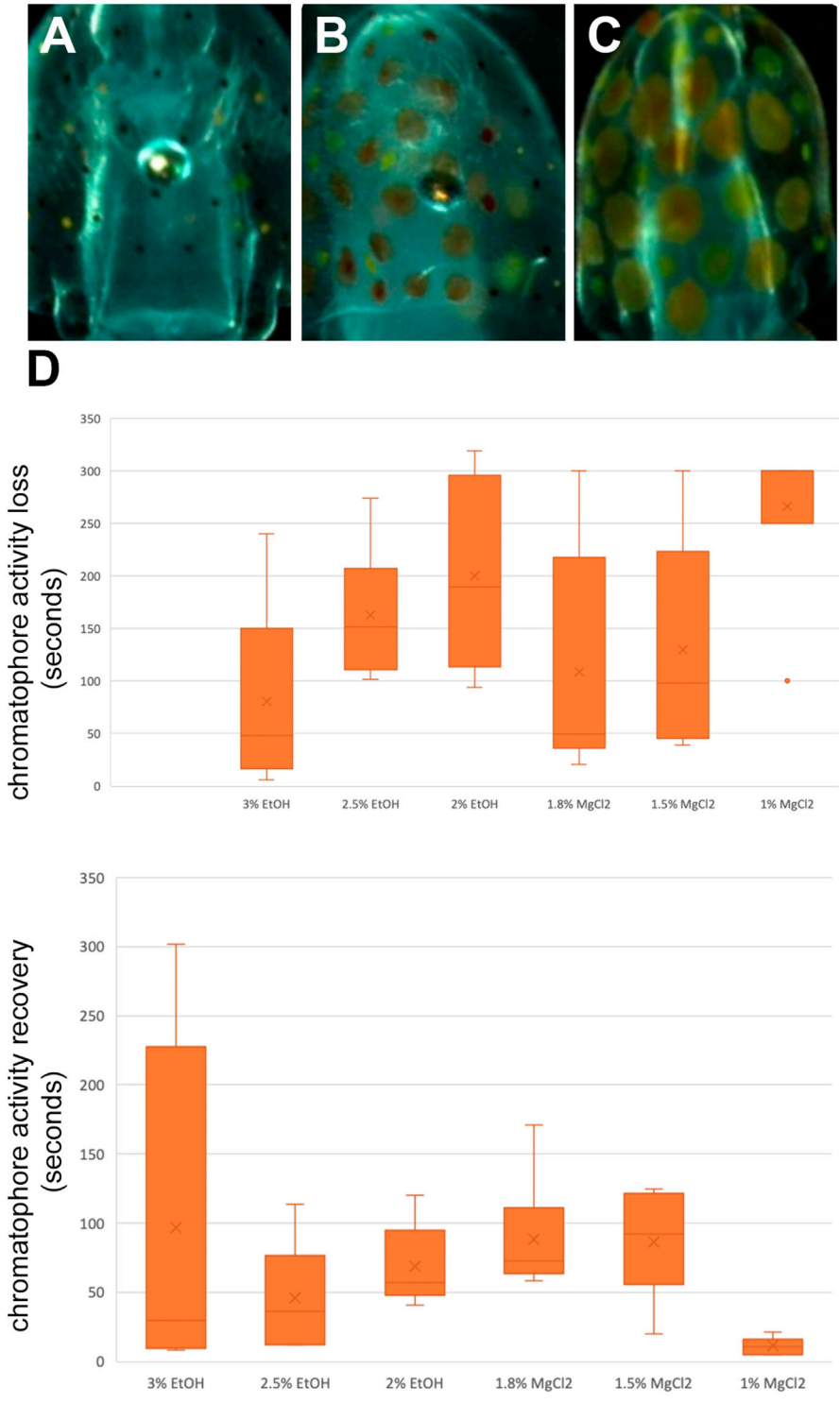

FIGURE 5
(A) Contracted chromatophores corresponding to muscle relaxation. **(B)** A half-contracted chromatophores. **(C)** Completely relaxed chromatophores corresponding to full muscle contraction. **(D)** Box and whiskers plot with the time until the loss or to recovery of chromatophores activity in seconds. The y-axis represents the seconds until the loss or to recovery of chromatophores and the x-axis displays the three EtOH and $MgCl_2$ concentrations. The upper and lower limits show the highest and lowest times, respectively, until loss or to recovery of chromatophore activity, and the mid-point shows the mean.

TABLE 4 Time until loss of chromatophore tone in seconds (TL CR) and time to recovery of chromatophore activity in seconds (TR CR) of *L. vulgaris* embryos exposed to different EtOH and $MgCl_2$ concentrations and the controls (no anesthetic solution). Measures are summarized (mean, median, SD, and SE).

	N	Mean	Median	SD	SE
TL CR 3% EtOH	6	80.5	48.5	89.1	36.4
TL CR 2.5% EtOH	6	163.2	152.0	64.4	26.3
TL CR 2% EtOH	6	200.0	189.5	89.8	36.7
TL CR 1.8% $MgCl_2$	6	108.5	49.5	111.8	45.7
TL CR 1.5% $MgCl_2$	6	130.2	98.0	100.6	41.1
TL CR 1% $MgCl_2$	6	266.7	300.0	81.6	33.3
	N	**Mean**	**Median**	**SD**	**SE**
TR CR 3% EtOH	6	97.0	29.5	125.34	51.17
TR CR 2.5% EtOH	6	45.8	36.5	39.51	16.13
TR CR 2% EtOH	6	68.5	57.0	29.46	12.03
TR CR 1.8% $MgCl_2$	6	88.3	72.5	41.97	17.13
TR CR 15% $MgCl_2$	6	86.2	92.0	38.88	15.87
TR CR 1% $MgCl_2$	6	11.2	11.0	6.05	2.47

In the future, it will be possible to compare different concentrations, combinations of substances, or other anesthetics (e.g., isoflurane; Polese et al., 2014). In the present study, embryos were anesthetized by immersion, which is a minimally invasive approach, largely utilized in fish, cephalopods, and other aquatic organisms. Other administration methodologies exist, such as subcutaneous or intravenous injections, and might be explored for future studies, with appropriate care in terms of monitoring stress and severity degrees.

The heart rate and respiratory rate are basic vital parameters that can be easily recorded during anesthesia for cephalopods and, particularly for, *Loligo vulgaris* embryos, and no reference values are available for these vital parameters in the literature. Therefore, obtaining baseline data before and after anesthesia was one of our main goals.

Heart and respiratory rate

During the baseline phase, the heart rate and respiratory rate were recorded, and they were consistent among all embryos. During anesthesia, the heart and respiratory rates were depressed for both anesthetics, however, important differences among embryos were observed, corroborating the idea that individual susceptibility to anesthetic concentration is present (Butler-Struben et al., 2018). The best EtOH concentration remained 3%, in comparison to the 2.5% and 2% EtOH concentrations (but mortality at the end of the experiment should be carefully considered). For the latter two, the embryos were lightly anesthetized, and the decrease in the heart and respiratory rates showed no significant differences between the three phases (Figure 2 and 3, t1–t2). EtOH 3% concentration displayed the quickest return to the initial baseline: within 1 min. The respiration rate at the 3% EtOH concentration resulted as the lowest of all concentrations and returned similarly to baseline within 3 min, similar to the most optimal $MgCl_2$ concentration. Comparing the heart and respiratory rate parameters, the optimal $MgCl_2$ solution was the 1.5% concentration; the heart rate obtained after anesthesia was equivalent to the 1.8% $MgCl_2$ concentration but lower than the 3% EtOH concentration. The return to baseline was obtained within 6 min instead of nearly 40 min to 1 h for the 1.8% $MgCl_2$ concentration. The respiratory rate attained with the 1.5% concentration was the third lowest rate after the 1.8% $MgCl_2$ concentration and the 3% EtOH concentration. Concerning the recovery, it was reached within the observed 5 min.

Tentacles/arms response

In mammals, the return to a responsive and conscious state following general anesthesia is typically evaluated by looking at eye reflexes, jaw tone, and occurrence of spontaneous movements. In cephalopods, tentacle adhesiveness as well as eye reflexes have been proposed as signs of recovery (Sen and Tanrikul, 2009; Pagano et al., 2011). Due to the smaller size of the embryos used in this study, these parameters would have been difficult to assess. Therefore, the tentacles/arms response to pinch was used instead. This response was lost quickly on average with $MgCl_2$, especially at the 1.8% concentration, than with EtOH, but recovery was never reached for this concentration. Nevertheless, lower dosages of 1% $MgCl_2$ attained the quickest recovery time. Corroborating the mechanism of action of $MgCl_2$ (Yang et al., 2020), indeed $MgCl_2$ not only releases inhibitory neurotransmitters but at the same time also reduces the release of excitatory neurotransmitters, and therefore lower concentrations could have less depressive effects.

Chromatophore tone

Cephalopods possess unique features such as chromatophore activity, allowing adaptation to environmental conditions. Indeed, while submerging the embryos in both anesthetic agents, the chromatophore reacted until a complete contraction (paling). Both $MgCl_2$ and EtOH showed a similar effect and no differences existed among the concentrations for the time until the loss and recovery of function. The faster TL CR was obtained with 3% EtOH, with the longer TR CR being registered for the 1.8% $MgCl_2$ concentration, possibly

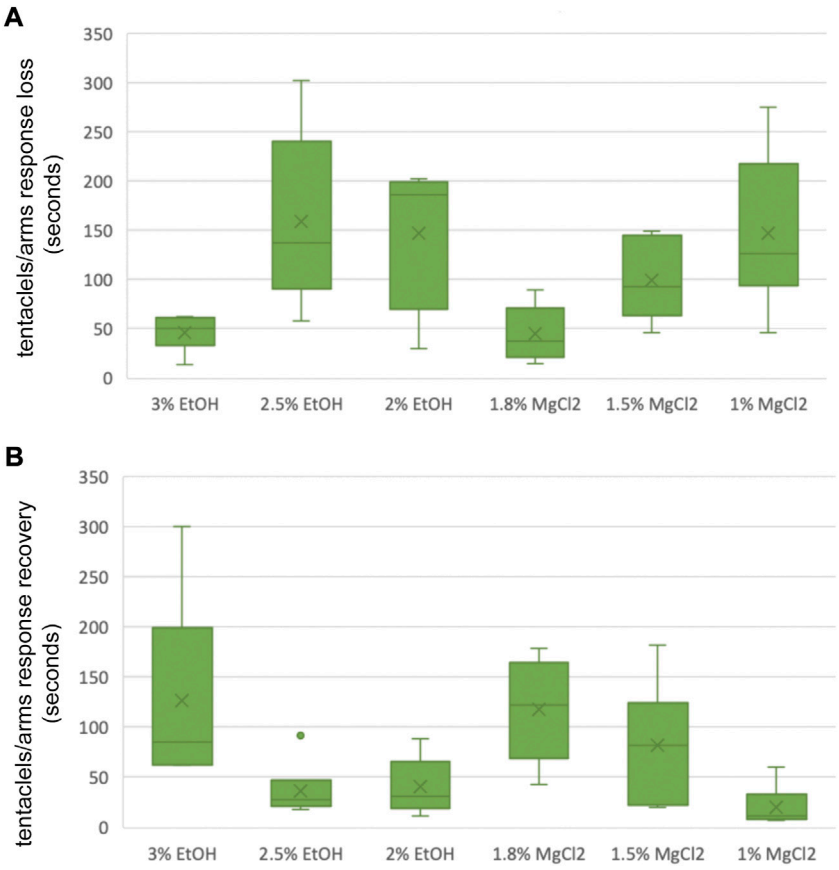

FIGURE 6
(A) Box and whiskers plot with the time until loss of tentacles/arms response in seconds. The y-axis represents the seconds until loss of tentacles/arms response and the x-axis displays the three EtOH and $MgCl_2$ concentrations. The upper and lower limits show the highest and the lowest times, respectively, until the loss of tentacles/arms response, and the mid-point shows the mean. **(B)** Box and whiskers plot with the time to recovery of tentacles/arms response in seconds. The y-axis represents the seconds to recovery of tentacles/arms response and the x-axis displays the three EtOH and $MgCl_2$ concentrations. The upper and lower limits show the highest and the lowest times, respectively, until the recovery of tentacles/arms response, and the mid-point shows the mean.

indicating that at higher concentrations, $MgCl_2$ is a better muscle relaxant than EtOH.

Buoyancy

Buoyancy is another physiological mechanism that healthy squids should display. According to previously published guidelines for aquatic species, anesthesia is considered "effective" if it acts within 3 min of immersion in an anesthetic bath, while recovery should occur within 5 min after returning to an anesthetic-free solution (Marking and Meyer, 1985). Both anesthetics were quite efficient in inducing loss of buoyancy, no significant differences existed for the three EtOH solutions and 1.8% $MgCl_2$. Regarding the recovery of function, it was quicker with EtOH than with $MgCl_2$. Since the 1.8% $MgCl_2$ concentration took longer than 300 s to recover, it indicates a non-recovery of function, and therefore according to the definition of Marking and Meyer (1985), does not fulfill the efficiency criteria. In addition, no significant differences existed between the 3% EtOH, 2.5% EtOH, and 1.5% $MgCl_2$ concentrations for the time to recovery of buoyancy.

TARP

Any adverse response pattern should be documented for embryos. According to Gleadall (2013), there are different adverse responses for embryos, such as inking, defecating, or rapid changes of chromatophore patterns. Immersion in EtOH and $MgCl_2$ solutions was well tolerated by embryos of the common squid *Loligo vulgaris*, and no adverse effects at the tested concentrations were observed, corroborating

TABLE 5 Time until loss of tentacles/arms response in seconds (TL T/A R) and time to recovery of tentacles/arms response in seconds (TR T/A R) of *L. vulgaris* embryos exposed to different EtOH and $MgCl_2$ concentrations and the controls (no anesthetic solution). Measures are summarized (mean, median, SD, and SE).

	N	Mean	Median	SD	SE
TL T/A R 3% EtOH	6	46.3	50.0	18.2	7.43
TL T/A R 2.5% EtOH	6	159.5	137.5	90.2	36.81
TL T/A R 2% EtOH	6	147.7	186.0	72.7	29.66
TL T/A R 1.8% $MgCl_2$	6	44.8	38.0	28.7	11.70
TL T/A R 1.5% $MgCl_2$	6	99.0	93.0	40.5	16.54
TL T/A R 1% $MgCl_2$	6	266.7	300.0	81.6	33.3
	N	**Mean**	**Median**	**SD**	**SE**
TR T/A R 3% EtOH	6	126.8	85.5	93.5	38.19
TR T/A R 2.5% EtOH	6	36.7	27.5	27.7	11.30
TR T/A R 2% EtOH	6	40.3	31.5	28.3	11.55
TR T/A R 1.8% $MgCl_2$	6	117.3	122.0	53.3	21.75
TR T/A R 15% $MgCl_2$	6	82.3	82.0	61.1	24.94
TR T/A R 1% $MgCl_2$	6	20.2	11.0	20.5	8.35

previous reports (Lange and Hartline, 1974; Garcia-Franco, 1992; Ikeda et al., 2009; Mooney et al., 2010; Estefanell et al., 2011).

Conclusion

Following various authors, cephalopods react to anesthesia by changes in the respiratory rate, which appear depressed with the magnitude, depending on the concentration. Similar results were obtained in our study in squid embryos since their respiratory rates went down with differences in depth, depending on the concentrations used. Furthermore, the loss of body color or chromatophore relaxation are the other indicators of the depth of anesthesia. According to the substances used, adults look paler or achromatic. Indeed, for the embryos, this was also the case; their chromatophores relaxed, not allowing the pigmentation to show. Sucking intensity is the only parameter that could not be measured in embryos in this study due to their relative size. Instead, pinching of arms and tentacles was used.

We found that both substances had similar effects on the heart and respiratory rates after immersion, as well as on chromatophores activity, tentacles/arms response, and buoyancy. The main differences between EtOH and $MgCl_2$ appeared during the recovery. Buoyancy was on average more quickly restored following immersion in EtOH than it did in $MgCl_2$. For the 1.8% $MgCl_2$ concentration, buoyancy was not regained, indicating that the safety for $MgCl_2$ at this concentration cannot be guaranteed. On the other hand, no significant differences were observed for anesthetic recovery of the chromatophore and tentacle/arms responses.

It should be noted that considering the marked interindividual variability (also observed here), we cannot exclude that a fixed time frame of exposure to the anesthetic solution and recovery may be insufficient for all animals to attain a similar state for each concentration tested. Further studies may help in disclosing such a possibility.

Even though no adverse response pattern was observed during the experiment for both EtOH and $MgCl_2$ at the investigated concentrations, EtOH seemed to be a more efficient substance for *Loligo vulgaris* embryos than did $MgCl_2$ in circumstances here tested. Not only did embryos regain their heart and respiratory rates quickly but had also recovered physiological responsiveness more rapidly after the EtOH treatment.

Moreover, both substances might at increasing concentrations also be relevant for euthanasia.

The physiological parameters used here represent a critical attempt to standardize the monitoring of embryos, and together with other techniques such as electrophysiology recordings from the pallial nerves (Abbo et al., 2021) or H-NMR spectroscopy (Yang et al., 2020), could elucidate the mechanism of action of $MgCl_2$ and EtOH, in particular, the reversible inhibitory activity of these substances. In future studies, further measures could be included, such as for instance, skin irritation (linked with exposure to EtOH) or corticosteroids production in response to exposure to anesthetics (Chancellor et al., 2021). Such studies are critical to gain deeper knowledge on the effects and safety of anesthetic agents in cephalopods, possibly highlighting differences among species and peculiarities in mechanisms of action.

Data availability statement

The original contributions presented in the study are included in the article/Supplementary Material; further inquiries can be directed to the corresponding author.

Ethics statement

Ethical review and approval were not required for the animal study because only embryos were used for this study, which do not fall under the animal welfare directive.

Author contributions

MS, SS, and CS designed the study. MS performed the experiments and analyzed the data. MS, SS, and CS wrote the manuscript.

Funding

This work was funded by the Swiss National Science Foundation (31003A_149499 to SS.)

Acknowledgments

The authors would like to thank the Station Biologique de Roscoff, CNRS Sorbonne Université, especially R. Garnier and G. Schires. They thank R. Rohr of the Biostatistics platform of the Department of Biology for his help with the statistical analysis. They also thank C. Fritsch, J. Kaldun, and their colleagues at the University of Fribourg for the fruitful discussion and comments.

Conflict of interest

The authors declare that the research was conducted in the absence of any commercial or financial relationships that could be construed as a potential conflict of interest.

Publisher's note

Supplementary material

The Supplementary Material for this article can be found online at: https://www.frontiersin.org/articles/10.3389/fphys.2022.968047/full#supplementary-material

References

Abbo, L. A., Himebaugh, N. E., DeMelo, L. M., Hanlon, R. T., and Crook, R. J. (2021). Anesthetic efficacy of magnesium chloride and ethyl alcohol in temperate Octopus and cuttlefish species. *J. Am. Assoc. Lab. Anim. Sci.* 60 (5), 556–567. doi:10.30802/AALAS-JAALAS-20-000076

Andrews, P. L. R., Darmaillacq, A. S., Dennison, N., Gleadall, I. G., Hawkins, P., Messenger, J. B., et al. (2013). The identification and management of pain, suffering and distress in cephalopods, including anaesthesia, analgesia and humane killing. *J. Exp. Mar. Biol. Ecol.* 447, 46–64. doi:10.1016/j.jembe.2013.02.010

Arnold, J. M., Summers, W. C., Gilbert, D. L., Manalis, R. S., Daw, N. W., and Lasek, R. J. (1974). A guide to laboratory use of the squid Loligo pealei. *Woods Hole*. Mass: Marine Biological Laboratory.

Baldascino, E., Di Cristina, G., Tedesco, P., Hobbs, C., Shaw, T. J., Ponte, G., et al. (2017). The gastric ganglion of *Octopus vulgaris*: Preliminary characterization of gene- and putative neurochemical-complexity, and the effect of *Aggregata octopiana* digestive tract infection on gene expression. *Front. Physiol.* 8 (1001). doi:10.3389/fphys.2017.01001

Bettinger, J. C., and McIntire, S. L. (2004). State-dependency in *C. elegans*. *Genes. Brain Behav.* 3 (5), 266–272. doi:10.1111/j.1601-183X.2004.00080.x

Birch, J. (2017). Animal sentience and the precautionary principle. *Anim. Sentience* 2 (16), 1. doi:10.51291/2377-7478.1200

Birch, J., Burn, C., Schnell, A., Browning, H., and Crump, A. (2021). *Review of the evidence of sentience in cephalopod molluscs and decapod Crustaceans*. London: London School of Economics and Political Science.

Bone, Q., Brown, E., and Travers, G. (1994). On the respiratory flow in the cuttlefish sepia officinalis. *J. Exp. Biol.* 194, 153–165. doi:10.1242/jeb.194.1.153

Burbach, J. P., Grant, P., Hellemons, A. J., Degiorgis, J. A., Li, K. W., and Pant, H. C. (2014). Differential expression of the FMRF gene in adult and hatchling stellate ganglia of the squid Loligo pealei. *Biol. Open* 3 (1), 50–58. doi:10.1242/bio.20136890

Butler-Struben, H. M., Brophy, S. M., Johnson, N. A., and Crook, R. J. (2018). *In vivo* recording of neural and behavioral correlates of anesthesia induction, reversal, and euthanasia in cephalopod molluscs. *Front. Physiol.* 9, 109. doi:10.3389/fphys.2018.00109

Chancellor, S., Abbo, L., Grasse, B., Sakmar, T., Brown, J. S., Scheel, D., et al. (2021). Determining the effectiveness of using dermal swabs to evaluate the stress physiology of laboratory cephalopods: A preliminary investigation. *Gen. Comp. Endocrinol.* 314, 113903. doi:10.1016/j.ygcen.2021.113903

Crawford, K., Diaz Quiroz, J. F., Koenig, K. M., Ahuja, N., Albertin, C. B., and Rosenthal, J. J. C. (2020). Highly efficient knockout of a squid pigmentation gene. *Curr. Biol.* 30 (17), 3484–3490. e3484. doi:10.1016/j.cub.2020.06.099

Crook, R. J. (2021). Behavioral and neurophysiological evidence suggests affective pain experience in octopus. *iScience* 24 (3), 102229. doi:10.1016/j.isci.2021.102229

Crook, R. J., Hanlon, R. T., and Walters, E. T. (2013). Squid have nociceptors that display widespread long-term sensitization and spontaneous activity after bodily injury. *J. Neurosci.* 33 (24), 10021–10026. doi:10.1523/JNEUROSCI.0646-13.2013

Crook, R. J., Lewis, T., Hanlon, R. T., and Walters, E. T. (2011). Peripheral injury induces long-term sensitization of defensive responses to visual and tactile stimuli in the squid Loligo pealeii, Lesueur 1821. *J. Exp. Biol.* 214 (19), 3173–3185. doi:10.1242/jeb.058131

Crook, R. J., and Walters, E. T. (2011). Nociceptive behavior and physiology of molluscs: Animal welfare implications. *ILAR J.* 52 (2), 185–195. doi:10.1093/ilar.52.2.185

Darmaillacq, A.-S., Chichery, R., Shashar, N., and Dickel, L. (2006). Early familiarization overrides innate prey preference in newly hatched *Sepia officinalis* cuttlefish. *Anim. Behav.* 71 (3), 511–514. doi:10.1016/j.anbehav.2005.04.019

Efsa Panel, o. A. H. a. W. (2005). Opinion of the Scientific Panel on Animal Health and Welfare (AHAW) on a request from the Commission related to the "Aspects of the biology and welfare of animals used for experimental and other scientific purposes. *EFSA J.* 292, 1–136. doi:10.2903/j.efsa.2005.292

Estefanell, J., Socorro, J., Afonso, J. M., Roo, J., Fernández-Palacios, H., and Izquierdo, M. S. (2011). Evaluation of two anaesthetic agents and the passive integrated transponder tagging system in *Octopus vulgaris* (Cuvier 1797). *Aquac. Res.* 42 (3), 399–406. doi:10.1111/j.1365-2109.2010.02634.x

EU (2019). Report on the statistics on the use of animals for scientific purposes in the Member States of the European Union in 2015-2017. Available at: https://op.europa.en/en/publication-detail/-/publication/04a890d4-47ff-11ea-b81b-01aa75ed71a1

Fiorito, G., Affuso, A., Basil, J., Cole, A., de Girolamo, P., D'Angelo, L., et al. (2015). Guidelines for the care and welfare of cephalopods in research -A consensus based on an initiative by CephRes, FELASA and the boyd group. *Lab. Anim.* 49 (2), 1–90. doi:10.1177/0023677215580006

Fuentes, L., Iglesias, J., Sánchez, F. J., Otero, J. J., Moxica, C., and Lago, M. J. (2005). Técnicas de transporte de paralarvas y adultos de pulpo (*Octopus vulgaris*). *Bol. Inst. Esp. Oceanogr.* 21 (1-4), 155–162.

Garcia-Franco, M. (1992). Anaesthetics for the squid sepioteuthis sepioidea (mollusca: Cephalopoda). *Comp. Biochem. Physiology Part C Comp. Pharmacol.* 103 (1), 121–123. doi:10.1016/0742-8413(92)90239-4

Gleadall, I. G. (2013). The effects of prospective anaesthetic substances on cephalopods: Summary of original data and a brief review of studies over the last two decades. *J. Exp. Mar. Biol. Ecol.* 447 (11), 23–30. doi:10.1016/j.jembe.2013.02.008

Goodwin, D. W., Powell, B., Bremer, D., Hoine, H., and Stern, J. (1969). Alcohol and recall: State-dependent effects in man. *Science* 163 (3873), 1358–1360. doi:10.1126/science.163.3873.1358

Howard, R. B., Lopes, L. N., Lardie, C. R., Perez, P. P., and Crook, R. J. (2019). Early-life injury produces lifelong neural hyperexcitability, cognitive deficit and altered defensive behaviour in the squid *Euprymna scolopes*. *Philos. Trans. R. Soc. Lond. B Biol. Sci.* 374 (1785), 20190281. doi:10.1098/rstb.2019.0281

Ikeda, Y., Sugimoto, C., Yonamine, H., and Oshima, Y. (2009). Method of ethanol anaesthesia and individual marking for oval squid (Sepioteuthis lessoniana FÃ©russac, 1831 in Lesson 1830â "1831). *Aquac. Res.* 41 (1), 157–160. doi:10.1111/j.1365-2109.2009.02305.x

Imperadore, P., Lepore, M. G., Ponte, G., Pflüger, H.-J., and Fiorito, G. (2019a). Neural pathways in the pallial nerve and arm nerve cord revealed by neurobiotin backfilling in the cephalopod mollusk *Octopus vulgaris*. *Invert. Neurosci.* 19 (2), 5. doi:10.1007/s10158-019-0225-y

Imperadore, P., Parazzoli, D., Oldani, A., Duebbert, M., Buschges, A., and Fiorito, G. (2019b). From injury to full repair: Nerve regeneration and functional recovery in the common octopus, *Octopus vulgaris*. *J. Exp. Biol.* 222 (19), jeb209965. doi:10.1242/jeb.209965

Jozet-Alves, C., Moderan, J., and Dickel, L. (2008). Sex differences in spatial cognition in an invertebrate: The cuttlefish. *Proc. Biol. Sci.* 275 (1646), 2049–2054. doi:10.1098/rspb.2008.0501

Katzung, B., Kruidering-Hall, M., Tuan, R. L., Vanderah, T. W., and Trevor, A. (2021). *Katzung & trevor's pharmacology: Examination and board review*. New York: McGraw-Hill Education.

Kumar, P. S., Kumar, S. S., Mekala, P., Arivuchelvan, A., and Jagadeeswaran, A. (2013). ICT in local self governance: A study of rural India. *Int. J. Comput. Appl.* 83(5), 31–36. doi:10.5120/14453-2714

Lange, G. D., and Hartline, P. H. (1974). Retinal responses in squid and octopus. *J. Comp. Physiol.* 93 (1), 19–36. doi:10.1007/BF00608757

Lee, Y. C., Darmaillacq, A. S., Dickel, L., and Chiao, C. C. (2020). Effects of embryonic exposure to predators on the postnatal defensive behaviors of cuttlefish. *J. Exp. Mar. Biol. Ecol.* 524, 151288. doi:10.1016/j.jembe.2019.151288

Locatello, L., Fiorito, G., Finos, L., and Rasotto, M. B. (2013). Behavioural and immunological responses to an immune challenge in *Octopus vulgaris*. *Physiol. Behav.* 122, 93–99. doi:10.1016/j.physbeh.2013.08.029

Mackie, G. O. (2008). Immunostaining of peripheral nerves and other tissues in whole mount preparations from hatchling cephalopods. *Tissue Cell.* 40 (1), 21–29. doi:10.1016/j.tice.2007.08.005

Marking, L. L., and Meyer, F. P. (1985). *Fisheries* 10 (6), 2–5. doi:10.1577/1548-8446(1985)010<0002:abanif>2.0.co;2

Mathger, L. M., and Hanlon, R. T. (2007). Malleable skin coloration in cephalopods: Selective reflectance, transmission and absorbance of light by chromatophores and iridophores. *Cell. Tissue Res.* 329 (1), 179–186. doi:10.1007/s00441-007-0384-8

McFarland, W. N., and Klontz, G. W. (1969). Anesthesia in fishes. *Fed. Proc.* 28 (4), 1535–1540.

Messenger, J. B., Nixon, M., and Ryan, K. P. (1985). Magnesium chloride as an anaesthetic for cephalopods comparative biochemistry and physiology Part C: Comparative pharmacology 82(1), 203–205. doi:10.1016/0742-8413(85)90230-0

Moltschaniwskyj, N. A., Hall, K., Lipinski, M. R., Marian, J. E. A. R., Nishiguchi, M., Sakai, M., et al. (2007). Ethical and welfare considerations when using cephalopods as experimental animals. *Rev. Fish. Biol. Fish.* 17, 455–476. doi:10.1007/s11160-007-9056-8

Mooney, A. T., Lee, W.-J., and Hanlon, R. T. (2010). Long-duration anesthetization of squid (*Doryteuthis pealeii*). *Mar. Freshw. Behav. Physiology* 43 (4), 297–303. doi:10.1080/10236244.2010.504334

Nesher, N., Maiole, F., Shomrat, T., Hochner, B., and Zullo, L. (2019). From synaptic input to muscle contraction: Arm muscle cells of *Octopus vulgaris* show unique neuromuscular junction and excitation-contraction coupling properties. *Proc. Biol. Sci.* 286 (1278). doi:10.1098/rspb.2019.1278

Pagano, E., Ponte, G., Andrews, P., and Fiorito, G. (2011). A comparative analysis of different anesthetics in *Octopus*: Towards true anesthesia? *J. Shellfish Res.* 30 (3), 1016.

Parra, G., Villanueva, R., and Yúfera, M. (2000). Respiration rates in late eggs and early hatchlings of the common octopus, *Octopus vulgaris*. *J. Mar. Biol. Assoc. U. K.* 80 (3), 557–558. doi:10.1017/S0025315400002319

Polese, G., Winlow, W., and Di Cosmo, A. (2014). Dose-dependent effects of the clinical anesthetic isoflurane on *Octopus vulgaris*: A contribution to cephalopod welfare. *J. Aquat. Anim. Health* 26 (4), 285–294. doi:10.1080/08997659.2014.945047

Ponte, G., and Fiorito, G. (2015). in *Immunohistochemical analysis of neuronal networks in the nervous system of* Octopus vulgaris. Editors A. Merighi and L. Lossi, 61–77.

Rezayof, A., Alijanpour, S., Zarrindast, M.-R., and Rassouli, Y. (2008). Ethanol state-dependent memory: Involvement of dorsal hippocampal muscarinic and nicotinic receptors. *Neurobiol. Learn. Mem.* 89 (4), 441–447. doi:10.1016/j.nlm.2007.10.011

Rosa, R., Trubenbach, K., Pimentel, M. S., Boavida-Portugal, J., Faleiro, F., Baptista, M., et al. (2014). Differential impacts of ocean acidification and warming on winter and summer progeny of a coastal squid (Loligo vulgaris). *J. Exp. Biol.* 217 (4), 518–525. doi:10.1242/jeb.096081

Schweizerische-Tierschutzverordung (2018). Animal protection ordinance: Chapter 1: General Provisions Art 1 Scope et Art 2 Terms. Chapter 6: Animal Experiments, Genetically Modified Animals and Mutants having a Clinical Pathological Phenotype Section 1: Scope, Permitted Deviations Article 112 Scope. Avialable at: https://www.fedlex.admin.ch/eli/cc/2008/416/fr#art_1https://www.fedlex.admin.ch/eli/cc/2008/416/fr#art_2https://www.fedlex.admin.ch/eli/cc/2008/416/de#art_112.

Sen, H., and Tanrikul, T. T. (2009). Efficacy of 2-phenoxyethanol as an anaesthetic for the musky octopus, *Eledone moschata* (lamarck 1799, cephalopoda: Octopodidae). *Turk. J. Vet. Anim. Sci.* 33 (6), 463–467.

Sharko, A. C., and Hodge, C. W. (2008). Differential modulation of ethanol-induced sedation and hypnosis by metabotropic glutamate receptor antagonists in C57BL/6J mice. *Alcohol. Clin. Exp. Res.* 32 (1), 67–76. doi:10.1111/j.1530-0277.2007.00554.x

Sherrill, J., Spelman, L. H., Reidel, C. L., and Montali, R. J. (2000). Common cuttlefish (sepia officinalis) mortality at the national zoological park: Implications for clinical management. *J. Zoo. Wildl. Med.* 31 (4), 523–531. doi:10.1638/1042-7260(2000)031[0523:CCSOMA]2.0.CO;2

Tamerin, J. S., Weiner, S., Poppen, R., Steinglass, P., and Mendelson, J. H. (1971). Alcohol and memory: Amnesia and short-term memory function during experimentally induced intoxication. *Am. J. Psychiatry* 127 (12), 1659–1664. doi:10.1176/ajp.127.12.1659

Thompson, T., Oram, C., Correll, C. U., Tsermentseli, S., and Stubbs, B. (2017). Analgesic effects of alcohol: A systematic review and meta-analysis of controlled experimental studies in healthy participants. *J. Pain* 18 (5), 499–510. doi:10.1016/j.jpain.2016.11.009

Varughese, S., and Ahmed, R. (2021). Environmental and occupational considerations of anesthesia: A narrative review and update. *Anesth. Analg.* 133 (4), 826–835. doi:10.1213/ANE.0000000000005504

Wong, S. M., Fong, E., Tauck, D. L., and Kendig, J. J. (1997). Ethanol as a general anesthetic: Actions in spinal cord. *Eur. J. Pharmacol.* 329 (2-3), 121–127. doi:10.1016/s0014-2999(97)89174-1

Yang, H., Zhao, Y., Song, W., Ye, Y., Wang, C., Mu, C., et al. (2020). Evaluation of the efficacy of potential anesthetic agents on cuttlefish (Sepia pharaonis) juveniles. Aquaculture Reports 1005242.

Zatylny-Gaudin, C., Cornet, V., Leduc, A., Zanuttini, B., Corre, E., Le Corguille, G., et al. (2016). Neuropeptidome of the cephalopod sepia officinalis: Identification, tissue mapping, and expression pattern of neuropeptides and neurohormones during egg laying. *J. Proteome Res.* 15 (1), 48–67. doi:10.1021/acs.jproteome.5b00463

Frontiers in Physiology

Understanding how an organism's components work together to maintain a healthy state

The second most-cited physiology journal, promoting a multidisciplinary approach to the physiology of living systems - from the subcellular and molecular domains to the intact organism and its interaction with the environment.

Discover the latest Research Topics

See more →

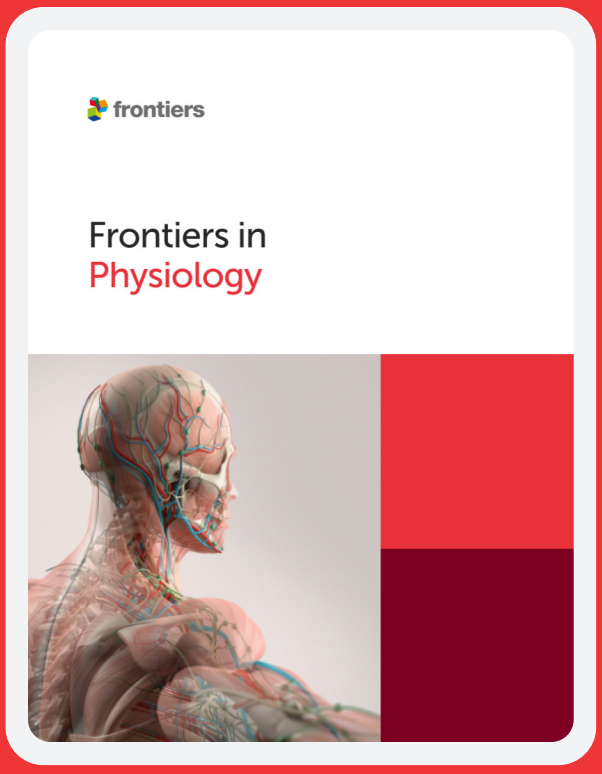

Frontiers

Avenue du Tribunal-Fédéral 34
1005 Lausanne, Switzerland
frontiersin.org

Contact us

+41 (0)21 510 17 00
frontiersin.org/about/contact